# Double-fused long-wavelength vertical-cavity lasers

by

Dubravko Ivan Babić

Ph.D. Dissertation
ECE Technical Report #95-20

August 1995

UNIVERSITY OF CALIFORNIA

Santa Barbara

Double-fused long-wavelength vertical-cavity lasers

A Dissertation submitted in partial satisfaction

of the requirements for the degree of

Doctor of Philosophy

in

Electrical and Computer Engineering

by

Dubravko Ivan Babić

Committee in charge:

Professor John E. Bowers, Chairperson

Professor Evelyn L. Hu, co-Chairperson

Professor Larry A. Coldren

Professor Arthur C. Gossard

August 1995

The dissertation of Dubravko Ivan Babić
is approved

---

Professor Larry A. Coldren

---

Professor Arthur C. Gossard

---

Professor Evelyn L. Hu, co-Chairperson

---

Professor John E. Bowers, Chairperson

August 1995

## ACKNOWLEDGMENTS

My sincerest thanks and appreciation go to my advisers Professors John Bowers and Evelyn Hu for guidance, patience and friendship, and to my committee: Professors Larry Coldren and Arthur Gossard for helpful discussions and advice.

I indebted to Dr. James Dudley, Dr. Klaus Streubel and Dr.-to-be Richard Mirin, for if it wasn't for them, I probably would not be writing these lines now. James pioneered the wafer fusion project at UCSB which has completely changed the course of my research and enabled me to graduate. Klaus grew the active layers for all my lasers, and without a really good active layer in a long-wavelength vertical-cavity laser, you're nowhere. I spent many hours discussing the designs and the physics with Richard, probably not as much time as he spent growing mirrors for me. The UCSB-HP collaboration has been a constant help through the past few years, and I acknowledge the very useful discussions with Drs. Long Yang, Dan Mars, and Kent Carey. I have greatly benefited from collaborating with Dr. Joachim Piprek of University of Delaware, who has modeled the double-fused lasers and whose careful analysis has helped me in the final stages of writing this dissertation.

It would be very hard to mention here everybody with whom I have worked and partied during these six years of graduate school: Archie Holmes, Matt Peters, Dan Mars, and Mark Mondry have provided me with many epilayers for lasers and experiments. I learned processing from John Wasserbauer, Jeff Scott, Jeff Schramm, Gerald Robinson, Torsten Wipiejewski, Eva Strzelecka, Philip Floyd, Nguyen Nguyen, Jeff Yen, Kursad Kiziloglu, and many others. I gratefully acknowledge the help of Jack Whaley, Martin Vandenbroek, and Brian Caralejo. I thank Near Margalit for testing the lasers and verifying that my laser process works, Kehl Sink and Thomas Liljeberg for helping with the electrical test setup, Alan Mar and Judy Karin for help with the optical pumping. I acknowledge Thomas Reynolds for redesigning the GaAs 1000 sputtering machine with me, for help with setting up both optical pumping and electrical testing, getting the computers to work, fixing things in no time, and letting me use his truck to drive to Federal Express at 5:05 PM.

Scott Corzine's help in checking and correcting my theoretical speculations is greatly appreciated. Theoretical discussions with Rajeev Ram were always enlightening. I miss the late-night philosophical discussions with Anish Goyal, the jazz and the blues played by Gilbert Chinn and Mark Comstock. I thank Eva for the sour cherries, Alan for the advice, Dan for being himself, and Paula for being there.

Finally, I could not have done it without the espressos at Roma and Java Jones, the Chocolate Gallery, the Cocteau Twins and Brasilian Music.

This dissertation is dedicated to

Nada, Hrvoje, Tomislav, and Karen

# VITA

| | |
|---|---|
| May 1959 | Born in Zagreb, Croatia |
| July 1982 | Dipl. Ing. in Electrical Engineering<br>Electrotechnical Faculty, University of Zagreb, Croatia. |
| Apr. 1983 – Dec. 1984 | Research Assistant, Electrical & Computer Engineering<br>University of California, Santa Barbara |
| Dec. 1984 | Master of Science, Electrical & Computer Engineering<br>University of California, Santa Barbara |
| Apr. 1985–Feb. 1989 | Design Engineer<br>Avantek, Inc., Santa Clara, California. |
| Sep. 1989 – Aug. 1995 | Graduate Research Assistant,<br>Department of Electrical and Computer Engineering<br>University of California, Santa Barbara |
| Aug. 1995 | Doctor of Philosophy,<br>Electrical and Computer Engineering<br>University of California, Santa Barbara |

## PUBLICATIONS IN TECHNICAL JOURNALS

1. D. I. Babić and H. Kroemer, "The role of non-uniform dielectric permittivity in the determination of heterojunction band offsets by cv-profiling through isotype heterojunctions", *Solid State Electronics*, Vol. 28, No. 10, pp. 1015-1017 (1985).
2. M.A. Rao, E. J. Caine, H. Kroemer, S. I. Long, D. I. Babić, "Determination of valence and conduction band discontinuities at the (Ga,In)P/GaAs heterojunction by cv-profiling", *Journal of Applied Physics*, Vol. 61, No. 2, pp. 643-649 (1987).
3. D. I. Babić, J. J. Dudley, M. Shirazi, E.L. Hu, J. E. Bowers, "Sputter deposition of precision Si/Si3N4 Bragg reflectors using multitasking interactive processing control", *Journal of Vacuum Science and Technology A*, Vol. 9, No. 3, pp. 1113-117 (1991).
4. H. Wada, D. I. Babić, D. L. Crawford, T. E. Reynolds, J. J. Dudley, J. E. Bowers, E. L. Hu, J. L. Merz, B. I. Miller, U. Koren, M. G. Young, "Low Threshold, High Temperature Pulsed Operation of InGaAsP/InP Vertical Cavity Surface Emitting Lasers", *IEEE Photonics Technology Letters*, Vol. 3, No. 11, pp. 977-979 (1991).
5. D. I. Babić, T. E. Reynolds, E. L. Hu, J. E. Bowers, "In-situ characterization of thin film optical coatings using a normal incidence laser reflectometer", *Journal of Vacuum Science and Technology A*, Vol. 10, No. 4, pp. 939-944 (1992).
6. D. I. Babić, and S. W. Corzine, "Analytic Expressions for the Reflection Delay, Penetration Depth and Absorptance of Quarter-Wave Dielectric Mirrors", *IEEE Journal of Quantum Electronics*, Vol. 28, No. 2, pp. 514-524 (1992).
7. M. J. Mondry, D. I. Babić, L. A. Coldren, J. E. Bowers, "Refractive Index of AlGaInAs on InP for Optoelectronic Applications", *IEEE Photonics Technology Letters*, Vol. 4, No. 6, pp. 627-630 (1992).
8. H. Wada, D. I. Babić, M. Ishikawa, J. E. Bowers, "Effects of nonuniform current injection in GaInAsP/InP vertical-cavity lasers", *Applied Physics Letters*, Vol. 60, No. 24, pp. 2974-2976 (1992).

9. D. B. Young, D. I. Babić, S. P. DenBaars, L. A. Coldren, "Epitaxial AlGaAs/AlAs Distributed Bragg Reflectors for Green (550 nm) Lightwaves", *Electronics Letters,* Vol. 28, No. 20, pp. 1873-1874 (1992).
10. J. J. Dudley, M. Ishikawa, D. I. Babić, B. I. Miller, R. Mirin, W. B. Jiang, J. E. Bowers, and E. L. Hu, "144°C operation of 1.3 μm InGaAsP vertical cavity lasers on GaAs substrates", *Applied Physics Letters*, Vol. 61, No. 26, 3095-3097 (1992).
11. M. Shimizu, D. I. Babić, J. J. Dudley, W. B. Jiang, J. E. Bowers, "Thermal Resistance of 1.3-μm InGaAsP Vertical Cavity Lasers", *Microwave and Optical Technology Letters,* Vol. 6, No. 8, pp. 455-457 (1993)
12. D. I. Babić, Y. Chung, N. Dagli, J. E. Bowers, "Modal Reflectivity of Quarter-Wave Mirrors in Vertical Cavity Lasers", *IEEE Journal of Quantum Electronics*, Vol. 29, No. 6, pp. 1950-1962 (1993).
13. J. E. Schramm, D. I. Babić, E. L. Hu, J. L. Merz, "A Reactive Ion Etcher Self-Bias Voltage Regulator", *Journal of Vacuum Science and Technology A*, Vol. 11, No. 5, pp. 2858-2859 (1993).
14. K.-K. Law, and D. I. Babić, "Effect of Layer Thickness Variations on Propagation Delay and Penetration Depth of a Quarter-Wave Distributed Bragg Reflector", *IEEE Photonics Technology Letters*, Vol. 5, No. 11, pp. 1294-1296 (1993).
15. J. J. Dudley, D. I. Babić, R. P. Mirin, L. Yang, B. I. Miller, R. J. Ram, T. E. Reynolds, E. L. Hu, and J. E. Bowers, "Low Threshold, Wafer-Fused Long Wavelength Vertical Cavity Lasers", *Applied Physics Letters*, Vol. 64, No. 12, pp. 1463-1465 (1994).
16. D. I. Babić, R. J. Ram, J. E. Bowers, M. Tan, L. Yang, "Scaling laws for gain-guided vertical-cavity lasers with distributed Bragg reflectors", *Applied Physics Letters*, Vol. 64, No. 14, pp. 1762-1764 (1994).
17. D. I. Babić, J. J. Dudley, K. Streubel, R. P. Mirin, E. L. Hu, J. E. Bowers, "Optically pumped all-epitaxial wafer-fused 1.52 μm vertical-cavity lasers", *Electronics Letters*, Vol. 30, No. 9, pp. 704-706 (1994).
18. I-H. Tan, J. J. Dudley, D. I. Babić, D. A. Cohen, D. B. Young, E. L. Hu, J. E. Bowers, B. I. Miller, U. Koren, M. G. Young, "High quantum efficiency and narrow absorption bandwidth of the wafer-fused resonant

$In_{0.53}Ga_{0.47}As$ photodetectors", *IEEE Photonics Technology Letters,* Vol. 6, No. 7, pp. 811-813 (1994).

19. R. J. Ram, D. I. Babić, R. A. York, J. E. Bowers, "Spontaneous Emission in Microcavities with Distributed Mirrors", *IEEE J. Quantum Electron* , Vol. 31, No. 2, pp. 399-410 (1995).
20. D. I. Babić, J. J. Dudley, K. Streubel, R. P. Mirin, E. L. Hu, J. E. Bowers, "Double-fused 1.52 μm vertical-cavity lasers", *Appl. Phys. Lett.* Vol. 66, No. 9, pp. 1030-1032 (1995).
21. D. I. Babić, K. Streubel, R. P. Mirin, N. M. Margalit, E. L. Hu, J. E. Bowers, "Transverse mode and polarisation characteristics of double-fused 1.52 μm vertical-cavity lasers", *Electronics Letters* , Vol. 31, No. 8, pp. 653-654 (1995).
22. D. I. Babić, K. Streubel, R. P. Mirin, N. M. Margalit, M. G. Peters, E. L. Hu, J. E. Bowers, "Fabrication and characteristics of double-fused vertical-cavity lasers", submitted for publication in *Optical and Quantum Electronics*, June (1995).
23. D. I. Babić, K. Streubel, R. P. Mirin, N. M. Margalit, J. E. Bowers, E. L. Hu, D. E. Mars, L. Yang, K. Carey, "Room-temperature continuous-wave operation of 1.54 μm vertical-cavity lasers", to be published in *IEEE Phot. Technol. Lett.*, November (1995).
24. A. Hawkins, T. E. Reynolds, D. England, D. I. Babić, M. J. Mondry, J. E. Bowers, "Silicon hetero-interface photodetector", submitted to *Appl. Phys. Lett.*

## CONFERENCE PRESENTATIONS

1. H. Wada, D. I. Babić, D. L. Crawford, T. E. Reynolds, J. J. Dudley, J. E. Bowers, E. L. Hu, J. L. Merz, B. I. Miller, U. Koren, M. G. Young, "Low Threshold, High Temperature Pulsed Operation of InGaAsP/InP Vertical Cavity Surface Emitting Lasers", IEEE 49th Annual Device Research Conference, June 17-19, 1991, Boulder, Colorado, Post Deadline Papers Digest, also IEEE Lasers and Electro-Optics Society 1991 Annual Meeting Digest, paper-SDL4.6, San Jose, California, 1991
2. D. I. Babić, T. E. Reynolds, E. L. Hu, J. E. Bowers, "Reactive Sputtering of Si/$SiN_x$ Quarter-wave Dielectric Mirrors using in-situ Laser Reflectometry", Presented at the SPIE Technical Symposium on Microelectronic Processing Integration 1991, San Jose, California, September 1991.
3. D. I. Babić, M. J. Mondry, L. A. Coldren, J. E. Bowers, "Refractive Index of AlGaInAs on InP for Optoelectronic Applications", IEEE Lasers and Electro-Optics Society 1991 Annual Meeting Digest, paper-OE9.6, San Jose, California, 1991.
4. M. Shimizu, J. J. Dudley, D. I. Babić, J. E. Bowers, E. L. Hu, "Thermal design for CW of 1.3μm GaInAsP surface-emitting lasers", Opt. Soc. Am. 1992 Ann. Mtg., Albuquerque, New Mexico, paper FKK4.
5. J. J. Dudley, M. Ishikawa, B. I. Miller, D. I. Babić, R. P. Mirin, W. B. Jiang, M. Shimizu, J. E. Bowers, E. L. Hu, "InGaAsP (1.3 μm) vertical-cavity lasers using GaAs/AlAs mirrors", Opt. Soc. Am. 1992 Ann. Mtg., Albuquerque, New Mexico, paper FKK7.
6. D. I. Babić, J. J. Dudley, M. Shimizu, "High Temperature Long Wavelength Vertical Cavity Lasers", IEEE Lasers and Electro-Optics Society 1992 Ann. Mtg., Boston, November 16-19, paper DLTA 13.1 (**invited**).
7. E. L. Hu, D. I. Babić, J. A. Skidmore, T. Strand, J. Schramm, "In-Situ Monitoring of Etching and Deposition Processes for Optoelectronic Device Fabrication", IEEE Lasers and Electro-Optics Society 1992 Ann. Mtg., Boston, November 16-19, paper AOD 1.2 (**invited**).
8. J. E. Bowers, D. I. Babić, G. Wang, D. Tauber, W. Jiang, R. L. Nagarajan, "Vertical Cavity Laser High Speed Dynamics and Modeling", Integrated

Photonic Research Conference 1993, Palm Springs March 22-24, 1993, paper IWB1 (**invited**).

9. D. I. Babić, Y. Chung, N. Dagli, J. E. Bowers, "Modal Reflectivity of Quarter-Wave Mirrors in Vertical Cavity Lasers", CLEO'93, Baltimore, Paper CTuM7 (1993).
10. R. J. Ram, R. A. York, D. I. Babić, J. E. Bowers, "Classical analysis of microcavity lasers", 1993 Opt. Soc. Am. Ann. Mtg., Toronto, Ontario, Canada, paper. WDD2 (1993).
11. D. I. Babić, R. J. Ram, J. E. Bowers, M. Tan, L. Yang, "Transverse modes in cavities with distributed Bragg reflectors", 1993 Opt. Soc. Am. Ann. Mtg., Toronto, Ontario, Canada, paper. MLL2 (1993).
12. J. J. Dudley, H. Wada, D. I. Babić, T. E. Reynolds, J. E. Bowers, "Long Wavelength Vertical Cavity Lasers", DOD Fiber Optics Conference, McLean, VA, March 1992, (**invited**).
13. J. J. Dudley, D. I. Babić, H. Wada, M. Shimizu, R. P. Mirin, T. E. Reynolds, J. E. Bowers, and E. L. Hu,, "InGaAsP Vertical Cavity Lasers", SPIE OE/LASE 1993, paper 1850-10, Los Angeles, CA January 1993 (**invited**).
14. M. Shimizu, J. J. Dudley, D. I. Babić, W. B. Jiang, and J. E. Bowers, "Conditions for Continuous Wave Operation of 1.3 μm InGaAsP Vertical Cavity Lasers", Optical Fiber Communication Conf./Int. Conf. on Integrated Optics and Optical Fiber Communication (OFC/IOOC), San Jose, CA, February 1993.
15. J. J. Dudley, D. I. Babić, R. P. Mirin, L. Yang, B. I. Miller, R. J. Ram, T. E. Reynolds, E. L. Hu, and J. E. Bowers, "Low Threshold, Electrically Injected InGaAsP (1.3 μm) Vertical Cavity Lasers on GaAs substrates", postdeadline paper IIIB-8, IEEE 51st Device Research Conference, Santa Barbara, CA, June 1993.
16. J.J. Dudley, D. I. Babić, R. P. Mirin, L. Yang, B. I. Miller, R. J. Ram, T. E. Reynolds, E. L. Hu, and J. E. Bowers, "Wafer fused, Low Threshold, Long Wavelength Vertical Cavity Lasers on GaAs substrates", AFCEA Fiber Optics and Photonic Conference, McLean, VA, paper 6-3, March 22-24 (1994).

17. I-H. Tan, C. Reaves, J. J. Dudley, A. L. Holmes Jr., D. I. Babić, E. L. Hu, J. E. Bowers, S. DenBaars, "Low-Temperature Pd Direct Bonding and Electrical Transport Across InP-Pd-GaAs Interfaces", 6th International Conference on InP and Related Materials, Santa Barbara, paper ThG4, March 28-31 (1994).

18. L. Yang, K. Carey, M. Ludowise, W. Perez, D. E. Mars, J. Fouquet, K. Nauka, S. J. Rosner, R. J. Ram, J. J. Dudley, D. I. Babić, J. E. Bowers, "Wafer bonding of InP and GaAs: Interface characterization and device applications", 6th International Conference on InP and Related Materials, Santa Barbara, paper MP36, March 28-31 (1994).

19. D. I. Babić, J. J. Dudley, K. Streubel, R. P. Mirin, E. L. Hu, J. E. Bowers, "Optically pumped all-epitaxial wafer-fused 1.52-μm vertical cavity lasers", 6th International Conference on InP and Related Materials, Santa Barbara, paper WA4, March 28-31 (1994).

20. J. J. Dudley, D. I. Babić, R. P. Mirin, L. Yang, B. I. Miller, E. L. Hu, J. E. Bowers, "Temperature and Transverse Mode Characteristics of InGaAsP (1.3 μm) Vertical Cavity Lasers on GaAs substrates", 6th International Conference on InP and Related Materials, Santa Barbara, paper WA3, March 28-31 (1994).

21. J. E. Schramm, D. I. Babić, E. L. Hu, J. E. Bowers, J. L. Merz, "Anisotropy Control in the Reactive Ion Etching of InP Using Oxygen in Methane/Hydrogen/Argon", 6th International Conference on InP and Related Materials, Santa Barbara, paper WE4, March 28-31 (1994).

22. R. J. Ram, D. I. Babić, R. A. York, J. E. Bowers, "Limitations to Controlling Spontaneous Emission in Microcavities with Distributed Mirrors", 1994 International Semiconductor Laser Conference, Maui, Hawaii paper B24, September 19-29 (1994).

23. J. J. Dudley, D. I. Babić, R. P. Mirin, R. J. Ram, L. Yang, J. E. Bowers, E. L. Hu, "Long wavelength surface emitting lasers on GaAs substrates", Engineering Foundation Third Conference on High Speed Devices for Communications and Interconnects, San Luis Obispo, CA August 14-18 (1994).

24. R. J. Ram, D. I. Babić, R. A. York, J. E. Bowers, "Spontaneous Emission in Microcavities with Distributed Mirrors", 1994 IEEE Lasers and Electro-Optics Annual Mtg., Boston, Massachusetts (**invited**).

25. D. I. Babić, J. J. Dudley, K. Streubel, R. P. Mirin, N. M. Margalit, E. L. Hu, J. E. Bowers, "Double-fused 1.52-μm vertical cavity lasers", 1994 IEEE Laser and Electro-Optics Annual Mtg., Boston, MA, Oct 31 - Nov 4, 1994, paper PD1.3.

26. D.I. Babić, J. J. Dudley, R. P. Mirin, J. E. Bowers, E. L. Hu, "Long-wavelength vertical-cavity lasers", 1994 International Electron Devices Meeting, San Francisco, CA, Dec 11-14 1994, paper 31.1, Technical Digest p. 757 (**invited**).

27. J. E. Bowers, D. I. Babić, J. J. Dudley, R. P. Mirin, R. J. Ram, E. L. Hu, "Long-wavelength vertical-cavity lasers", Fifth Optoelectronics Conference, paper 14D3-1, Makuhari, Chiba, Japan, July 12-15 (1994) (**invited**).

28. D. I. Babić, J. J. Dudley, K. Streubel, R. P. Mirin, J. E. Bowers, E. L. Hu, "Double-fused 1.52 μm vertical-cavity lasers", 1994 IEEE Lasers and Electro-Optics Society Ann. Mtg., Boston, MA, Nov. 14-16, paper PD1.4 (1994).

29. D. I. Babić, J. J. Dudley, K. Streubel, R. P. Mirin, N. M. Margalit, J. E. Bowers, E. L. Hu, "Transverse-mode and polarization characteristics of double-fused 1.52 μm vertical-cavity lasers", 1995 Indium Phosphide and Related Materials Conference, Sapporo, Hokkaido, Japan, paper SB1.2, May 9-13 (1995).

30. D. I. Babić, I-H. Tan, R. P. Mirin, J. E. Bowers, E. L. Hu, "Wafer fusion for optoelectronic applications", 1995 Conference on Lasers and Electro-Optics, Baltimore, MD (1995) (**invited**).

31. D. I. Babić, K. Streubel, R. P. Mirin, N. M. Margalit, J. E. Bowers, E. L. Hu, D. E. Mars, L. Yang, K. Carey, "Room-temperature continuous-wave operation of 1.54 μm vertical-cavity lasers", 10th International Conference on Integrated Optics and Optical Fibre Communications (IOOC'95), paper PD1.5, Hong Kong, June 26-30 (1995).

32. J. Piprek, D. I. Babić, J. E. Bowers, "Modeling and characterization of double-fused 1.54 μm vertical-cavity lasers for CW operation at and above room-temperature", submitted to OELASE'96, San Jose, January 1996.

*"What makes the desert beautiful", said the little prince,*

*is that somewhere it hides a well..."*

Antoine de Saint Exupéry

# Abstract

In recent years, the vertical-cavity laser has emerged as a new coherent light source alongside the conventional in-plane laser owing to its compactness, circular beam profile and ease of integration with other electronic circuitry. The development of long-wavelength 1.3 μm and 1.55 μm vertical-cavity surface-emitting lasers has been fueled by the need for low cost, high speed sources for optical communications and interconnects. However, the practical realization of these lasers has been a difficult process over the last decade due to numerous technological difficulties. It has been recently demonstrated that some of the problems can be efficiently avoided by using the process of *wafer fusion* which enables bonding semiconductors of different lattice constants and optical properties to form a laser cavity. This dissertation discusses the fabrication of vertical-cavity lasers using *two* wafer fusion steps for long-wavelength (optical communication) applications. The ultimate result described in this work is the fabrication of the *first* 1.54 μm vertical-cavity laser operating continuously at room-temperature.

## TABLE OF CONTENTS

Chapter 1

# Introduction to vertical-cavity lasers

The optical fiber and the semiconductor laser have revolutionized the field of information transmission. The development of fiber optic communication systems has been fueled by the growing need for a high bit-rate and high volume communication medium that is more efficient than the coaxial cable. Optical fibers can guide information encoded in light signals uninterrupted over hundreds of kilometers, while the semiconductor laser provides an inexpensive source for such optical transmission. Presently, optical fibers are being installed around the world: across the land and under the oceans. Both commercial telephone and business communications are being conducted over these links. And every such link uses a large number of semiconductor lasers to amplify the signals. Communication applications extend to numerous short distance applications, such as, local area networks, and chip-to-chip communication. Compact disc players and optical storage devices, as well as, laser printing were brought to mass production owing to the inexpensive semiconductor laser. Semiconductor lasers are pushing their way into many other fields where they are replacing large solid state or gas lasers with small devices barely visible to the naked eye.

In recent years, the vertical-cavity laser (VCL) has emerged as a new coherent light source alongside the conventional in-plane laser owing to its compactness, inherent single-longitudinal mode operation, circular beam profile and straightforward integration with other electronic circuitry. Vertical-cavity lasers hold promise of superior performance in many optoelectronic applications and lower manufacturing cost than in-plane lasers. State of the art GaAs-based vertical-cavity lasers operate continuously at room-temperature with sub-100 μA threshold currents. The outstanding performance of these laser greatly relies on their monolithic fabrication process and the quality of Al(Ga)As/GaAs quarter-wave mirrors, which are presently the highest quality epitaxial mirrors that can be routinely fabricated.

The development of long-wavelength 1.3 μm and 1.55 μm vertical-cavity surface-emitting lasers has been driven by the need for low cost, high speed sources for optical communications and interconnects. However, the practical realization of these lasers has been a difficult process over the last decade due to numerous technological difficulties. The most significant problem was the fabrication of mirrors with sufficiently high reflectivity and adequate electrical and thermal properties. It has been recently demonstrated that, using the process of *wafer fusion*, InGaAsP active layers operating at 1.3 μm and 1.55 μm can be bonded to Al(Ga)As/GaAs mirrors, thereby enabling the fabrication of long-wavelength vertical-cavity lasers with mirrors grown on GaAs. This dissertation discusses the fabrication of vertical-cavity lasers using *two* wafer fusion steps to fabricate the *first* 1.54 μm vertical-cavity laser operating continuously at room-temperature.

## 1.1. *Development of vertical-cavity lasers*

In vertical-cavity lasers both the laser oscillation and the laser output occur in the direction perpendicular to the wafer surface. The basic structure of a vertical-cavity lasers includes high reflectivity mirrors, and suitable charge, current and mode confining schemes. The requirements for efficient operation are high cavity finesse and near unity overlap between charge and electromagnetic field. There are many ways to implement this type of structure. The most important parameter determining the shape of the laser cavity is the electrical conductivity of the mirrors. Bringing electrical current through or around the mirrors leads to vastly different contact arrangements, and current and mode confinement schemes. The different implementations of vertical-cavity laser divided by mirror conductivity are shown in Figure 1.1. Epitaxial mirrors are conductive and provide uniform current injection, whereas insulating mirrors require ring-contacts and often lead to current crowding at the edges of active layers. Current and mode confinement, indicated with the shaded areas in Figure 1.1, is required on all of these cavities and can be achieved by wet or dry etching, oxidation or insulating implantation. The active layers utilizing both bulk and quantum wells have been investigated, whereas charge confinement is being accomplished by using epilayers of larger bandgap or by multi-quantum-well barrier structures.

The vertical-cavity laser was invented by Professor Kenichi Iga at Tokyo Institute of Technology in 1977 and was fabricated for the first time in 1979 (Soda, 1979). This device operated pulsed at 77 K with pulsed threshold current of 900 mA and 1.3 μm lasing wavelength. The first room-temperature continuous wave operation of a GaAs

surface-emitting laser was demonstrated by (Koyama, 1988) using an etched-well structure and amorphous dielectric mirrors (shown in Fig. 1.1a).

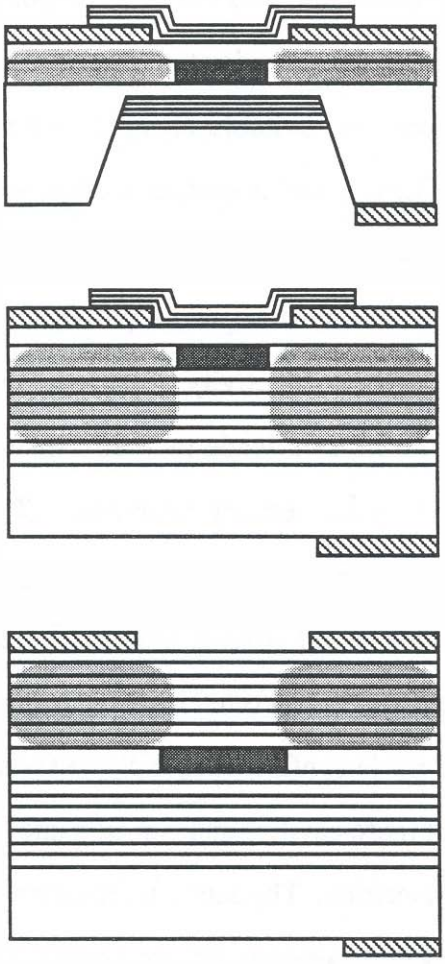


**Fig. 1.1**: Three implementations of vertical-cavity lasers.

The investigation of epitaxially grown mirrors was pursued in an attempt to create a laser cavity in a single epitaxial growth. Since the range of refractive indexes that could be realized with semiconductor alloys was much smaller than that of amorphous dielectrics, the number of quarter-wave layers was much larger. This in turn placed stringent requirements on the precision of the epitaxial growth technology. The material combination that was the first choice for the fabrication of long-wavelength epitaxial mirrors was InGaAsP and InP (Chailertvanitkul, 1985). The Al(Ga)As/GaAs system, first demonstrated by (Sakaguchi, 1988), was to become the material combination of choice for short-wavelength (< 1 μm) GaAs-based vertical-cavity lasers. Mirrors fabricated with AlAs and GaAs are electrically and thermally conductive and have very high reflectivity owing to the large refractive index ratio between GaAs and AlAs.

The first efficient vertical-cavity lasers with threshold currents in the miliamp and sub-miliamp range were fabricated with using AlAs/GaAs mirrors and quantum-well active layers. A quantum-well active region offers higher gain and differential gain at lower transparency than bulk, due to a sharper increase in the density of states and lower non-radiative recombination. The most notable progress in quantum-well GaAs-based vertical-cavity lasers was demonstrated by (Jewell, 1989[a]) and (Geels, 1990). The fabrication of these lasers involved wavelength-size cavity sandwiched between AlAs/GaAs quarter-wave mirrors, as shown in Figure 1.1c, and laterally defined by reaction ion etching. The active layers were realized by compressively-strained InGaAs wells. Since the transition energy of the bound states in the wells (≈980 nm) is below the bandgap of GaAs, the AlAs/GaAs quarter-wave mirrors are transparent at this wavelength and can produce extremely high reflectivities (>99.9%). A more

complete review of these developments is given by (Jewell, 1991) and (Corzine, 1993). Present day GaAs vertical-cavity lasers almost exclusively use quantum-wells and AlGaAs/GaAs based quarter-wave mirrors.

The progress in long-wavelength (1.3 and 1.55 μm) surface-emitting lasers was slower than that of GaAs-based VCLs. Only in recent years has the phosphide growth technology been able to provide the control and active layer quality to fabricate vertical-cavity lasers at optical communication wavelengths. High nonradiative recombination and current leakage, and higher temperature sensitivity of the threshold current already observed in long-wavelength in-plane lasers has just made the realization more difficult (Yano, 1981, O'Gorman, 1992). The most significant issue hindering this development is that there are no epitaxial mirrors lattice matched to InP that match the quality of AlAs/GaAs mirrors in reflectivity, thermal properties and ease of fabrication. This has resulted in a strong effort in developing high quality amorphous mirrors and the investigation of numerous alternate structures for making VCLs.

Until recently, the etched-well laser structure, shown in Figure 1.1a, has been the only structure used for fabrication of 1.3 μm vertical-cavity lasers (Yang, 1990, Wada, 1991, Oshikiri, 1991, Baba, 1993). The state of the art etched-well 1.3-μm VCLs was developed at Tokyo Institute of Technology (Baba, 1993). The top quarter-wave mirror of this laser uses the MgO/Si material combination because of the high thermal conductivity MgO (Tanobe, 1992). The device was mounted upside down on a diamond heatsink using Ga as solder and operated continuous-wave up to 14°C, which is currently the highest continuous wave operating temperature for 1.3

μm VCLs. Similar results (continuous-wave at 13°C) have recently been obtained by (Uchiyama, 1995) using $Al_2O_3$/Si mirrors. All of the reported devices operating at 1.3 μm used bulk active layers. The etched well structure has been also investigated for 1.55 μm wavelength (Deppe, 1990, Uchida, 1993, Lin, 1994, Uomi, 1994). With the maturing phosphide growth techniques, high quality InGaAsP mirrors are becoming available for use at 1.55 μm and devices that use one dielectric and one InGaAsP/InP mirror, such the one shown in Figure 1.1b were fabricated (Tai, 1991, Tadokoro, 1992, Fisher, 1993, 1995, Streubel, 1994). The current and mode confinement in these devices is realized by mesa etching or semi-insulating InP regrowth. Strained and strain-compensated quantum-well active layers have also been investigated using room-temperature optical pumping (Tai, 1991, Lin, 1994). Recently, a low temperature bonding technique using spin-on glass has been used to fabricate low threshold electrically pumped 1.5 μm vertical-cavity lasers with strain-compensated quantum-well active layers (Chua, 1995).

The main problem with long-wavelength vertical-cavity lasers is excessive cavity losses coming from: a) insufficient mirror reflectivity that originates from using lossy materials in the mirrors (below gap absorption in amorphous semiconductors and free-carrier absorption in extrinsic semiconductors), b) scattering at sharp cavity features and rough surfaces (rough epitaxial growth or etched surfaces), c) diffraction losses originating from cavity sections without waveguiding, and d) intracavity absorption originating from free-carrier and intervalence absorption. In addition, continuous-wave operation at room temperature has been difficult to achieve due to high device thermal resistance and high nonradiative recombination inherent to long-wavelength active layers. Amorphous mirrors exhibit relatively poor thermal conductances except

for several materials such as MgO, and silicon carbide. However, the high index material typically used is amorphous silicon which is quite lossy at optical communication wavelengths. Diffraction losses are present in these cavities because vertical-cavity lasers are small wavelength-size open resonators and unless they are carefully designed to provide waveguiding, a considerable fraction of the energy is lost to radiation.

Most of these problems are not as pronounced in GaAs-based vertical-cavity lasers because most of the GaAs VCL use AlAs/GaAs mirrors which have substantially better thermal conductance, are electrically conductive and have a larger refractive index difference than any other epitaxial mirror presently available. It is safe to say that the GaAs-based VCLs owe most of their success to the optical, electrical and thermal properties of AlAs/GaAs mirror in the near infrared. This fact has prompted the idea to use AlAs/GaAs mirrors in conjunction with InGaAsP active layer to fabricate long-wavelength vertical-cavity lasers.

Long-wavelength InGaAsP active layers are grown lattice matched to InP and AlAs/GaAs mirrors are grown on GaAs substrates. Since the lattice constant between GaAs and InP is very different ( $\Delta a/a$ = 3.8%), these materials can not be grown on the same substrate with acceptable quality. However, by using the method of wafer fusion (Liau, 1990), it is possible to bond GaAs and InP and fabricate vertical-cavity lasers operating at 1.3 μm and 1.55 μm. This idea and its first practical implementation, pioneered by James Dudley from UC Santa Barbara (Dudley, 1992, 1993), represents probably the most significant recent advance in long-wavelength vertical-cavity lasers. The first wafer-fused vertical-cavity laser had the structure

shown in Figure 1.1b with an *n*-type AlAs/GaAs bottom mirror and a $Si/SiO_2$ top mirror. This laser exhibited record room-temperature pulsed performance at 1.3 μm.

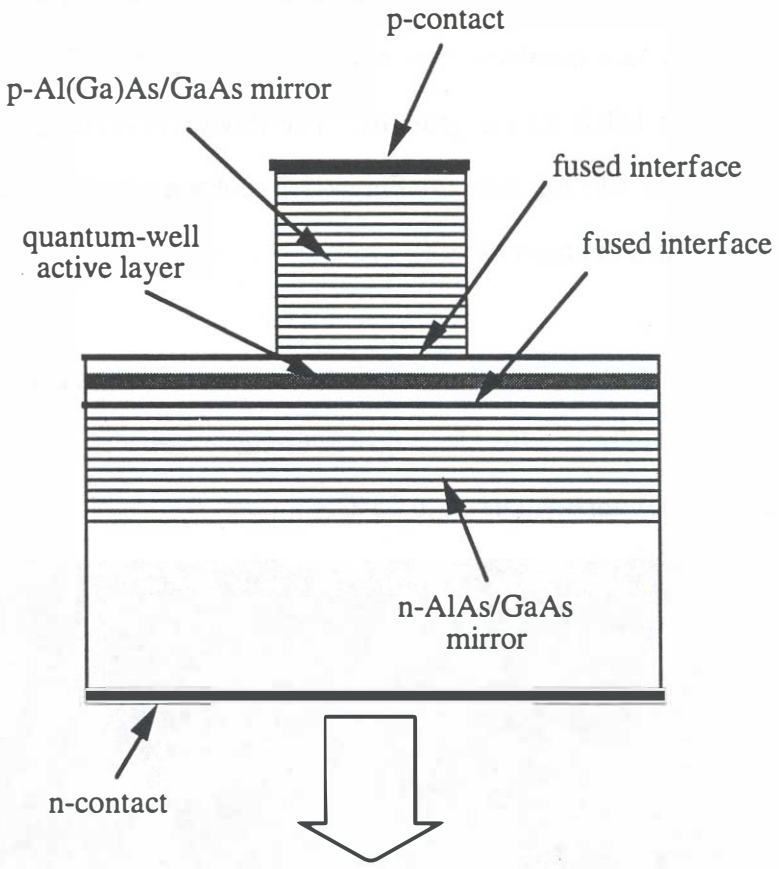


**Fig. 1.2**: The structure of the double-fused vertical-cavity laser.

However, the confirmation of wafer fusion as a viable technique of fabricating vertical-cavity lasers is the realization of room-temperature continuous-wave operating long-wavelength vertical-cavity lasers. To achieve this, the dielectric mirror of the first fused laser had to be replaced with a higher reflectivity epitaxial mirror, while the bulk active layer had to be replaced by one with strain-compensated quantum wells.

The first room-temperature continuous-wave operation of 1.54 μm vertical-cavity lasers was finally achieved with an all-epitaxial wafer-fused laser that uses InGaAsP quantum-well active layer bonded to *two* AlAs/GaAs mirrors on each side. The structure of this *double-fused vertical-cavity laser* is shown schematically in Figure 1.2. The structure involves three epitaxial growths: MOCVD growth of the active layer and two MBE mirror growths. The device is defined with circular contact patterns and reactive ion etching. Figure 1.3 shows a scanning electron micrograph of a finished 12 μm diameter device.

This dissertation describes the design, fabrication and the characteristics of the first generation of double-fused long-wavelength vertical-cavity lasers operating continuously at temperatures up to 33°C.

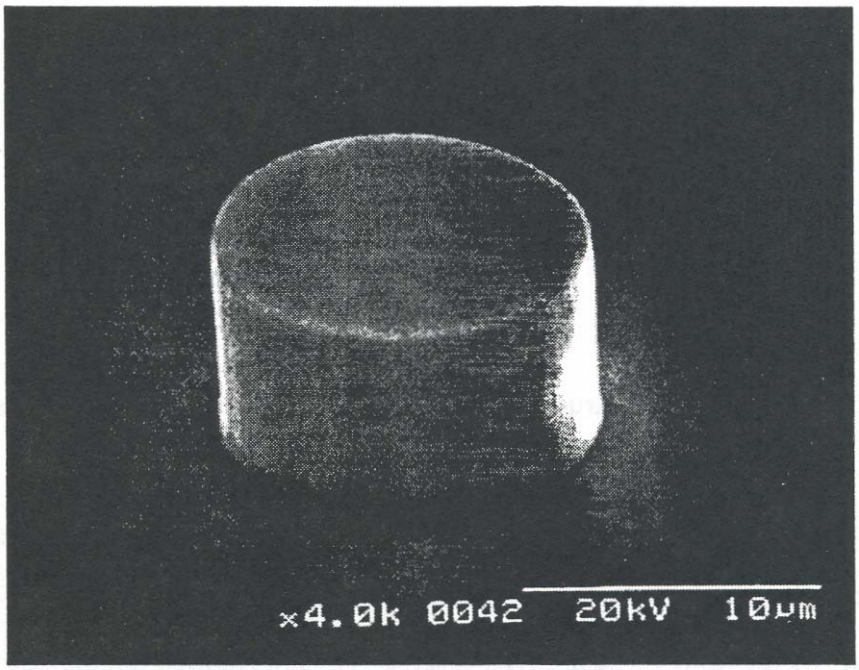


**Fig. 1.3**: Finished 12 μm diameter double-fused 1.54 μm vertical-cavity laser that operates continuously at room temperature.

## 1.2. *Dissertation outline*

The development of long-wavelength vertical-cavity lasers has been a long and complicated process. It involved a number of theoretical analyses, and many processing experiments and device measurements. The experimental parts and the developments that are directly related to the double-fused vertical-cavity lasers are described in the main part of this dissertation, while the theoretical analyses are given in the appendices.

In Chapter 2, we start by describing the main requirements placed on the laser mirrors and cavities for obtaining low threshold and continuous-wave operating lasers. In Chapter 3 we describe the development of the wafer fusion process for bonding GaAs and InP. Chapter 4 discusses the specific design of the double-fused lasers, with special attention paid to the active layer and $p$-mirror design. The fabrication process is described in Chapter 5 and the device results in Chapter 6. In Chapter 7 we analyze the performance of fabricated double-fused lasers and discuss the problems that still need to be solved. The future directions for this research are discussed in Chapter 8, along with a description of a number of devices and device improvements that are expected to further the progress of long-wavelength vertical-cavity lasers. Appendix A describes the transverse field matrix approach of calculating multilayer reflection/transmission coefficients. Appendices B and C describe the theoretical development of quarter-wave mirrors and open resonators with distributed mirrors. Appendix D describes the measurement of the metal-semiconductor reflection coefficient used in Chapter 4 for mirror design. Appendix E contains my personal log of the development of long-wavelength vertical-cavity lasers at UC Santa Barbara.

Chapter 2

# Laser mirrors and cavities

The key issue in fabricating long-wavelength vertical-cavity resonators is the realization of high reflectivity mirrors. Active layers with bandgap energies in the 1.3 μm to 1.6 μm wavelength range are presently grown using InGaAsP and AlInGaAs lattice matched to InP, as shown in Figure 2.1. The immediate choice for long-wavelength quarter-wave epitaxial mirrors is the InGaAsP/InP system lattice matched to InP. The quaternary alloy is used as the high index and InP as the low index material (AlInGaAs will be discussed later). The range of refractive index that can be realized by varying the composition of this alloy is relatively small and requires epitaxial growths of thicknesses greater than 10 μm for a single mirror to achieve sufficient reflectivity for vertical-cavity laser operation. Growing very thick epitaxial layers with high precision is quite demanding on the growth technique and raises issues connected with source depletion and reaction chamber coating. The thermal conductivity of the quaternary InGaAsP alloy is an order of magnitude lower than that of InP and therefore laser cavities that use these materials require a careful thermal design involving heat paths around the mirrors for device cooling. This leaves a small margin of error in the design and the fabrication of these lasers, although it is very likely that with a high degree of control over the epitaxial growth, vertical-cavity

lasers with these mirrors will be possible in the future. For these reasons, many other epitaxial and amorphous mirror material combinations have been investigated in recent years for long-wavelength vertical-cavity laser applications.

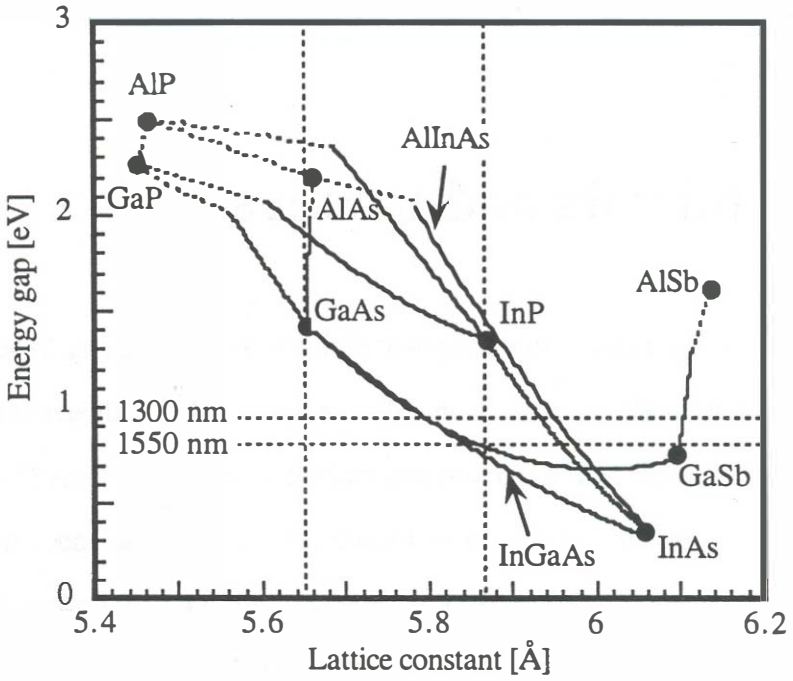


**Fig. 2.1**: Energy-gap vs. lattice constant for III-V alloys relevant for long-wavelength vertical-cavity laser applications. Vertical lines indicate GaAs and InP substrate lattice constants, while the horizontal lines indicate the energies of the 1300 nm and 1550 nm transitions.

A number of problems is simplified by using AlAs/GaAs quarter-wave mirrors in conjunction with the InGaAsP active layers bonded by wafer fusion. The thermal conductivity of these mirrors is better than any other long-wavelength mirror material system, and the relatively large refractive index ratio provides sufficiently high reflectivity to fabricate lasers at long-wavelengths.

## 2.1. *Practical long-wavelength mirrors*

The peak reflectivity of a quarter-wave mirror is determined by the number of quarter-wave layers and the presence of loss. If lossless dielectrics existed, one could in principle realize any value of reflectivity using any two materials with a different refractive index. However, this is limited by two factors: (a) No dielectric is lossless: All materials exhibit some degree of absorption or scattering within bulk of the material or at the interfaces. The maximum reflectivity value that can achieved depends on the refractive indexes and the absorption coefficients of the layers. (b) If the refractive index ratio is small, one must use a large number of layers to achieve high reflectivity. This may not be practical because of stresses associated with thick films, or difficult fabrication due limited control of layer thicknesses during the deposition. We discuss these issues in more detail in the following sections.

### 2.1.1. *Peak reflectivity in the presence of absorption loss*

To illustrate the mutual dependence of loss in the layers and the refractive index difference we consider the maximum achievable reflectivity of a quarter-wave mirror in the presence of absorption loss. The *maximum reflectivity* is a hypothetical value of the mirror reflectivity that would be achieved with an infinite number of layers. The exact calculation for a finite number of layers can be performed using transverse field matrices described in Appendix A. Here we take the advantage of analytic relations (B-78) which are valid for weak absorption. We relate the fractional refractive index difference $\Delta n/\bar{n}$ between the high and low index material in the mirror to the loss in the two layers $\alpha_L$ and $\alpha_H$. Here $\Delta n = n_H - n_L$ and

$\bar{n} = (n_L + n_H)/2$ are the difference and the average refractive index of the two materials in the mirrors. In order to make a plot that can be used for a variety of mirrors we define a dimensionless mirror absorption coefficient as $\lambda\bar{\alpha}/\bar{n}$ where $\lambda$ is the free-space wavelength. The average absorption coefficient is given by $\bar{\alpha} = (\alpha_L + \alpha_H)/2$ if the first layer in the mirror is of high index, or by $\bar{\alpha} = \alpha_L n_H/2n_L + \alpha_H n_L/2n_H$ if the first layer is of low index.

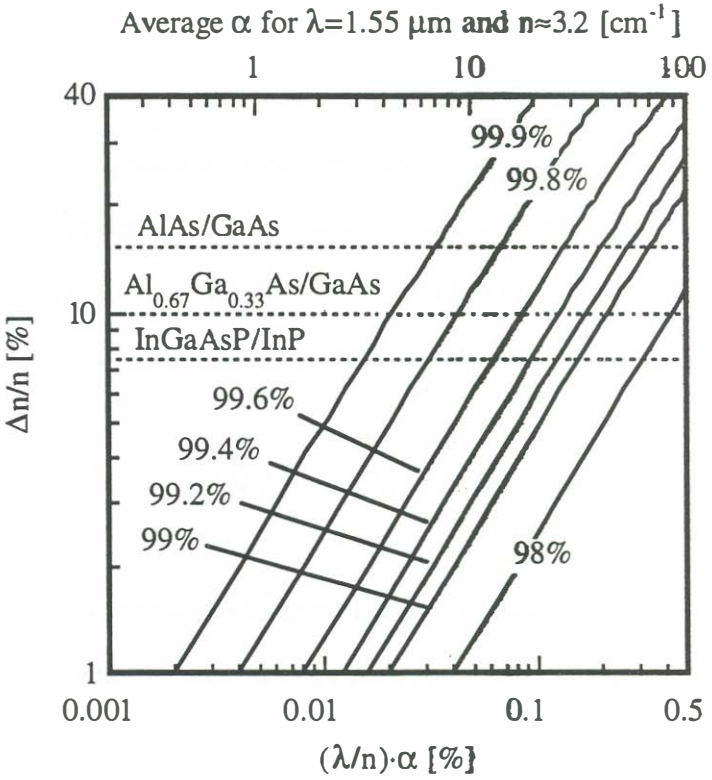


**Fig. 2.2**: The relationship between the fraction refractive index difference $\Delta n/\bar{n}$ and the normalized mirror absorption loss $\lambda\bar{\alpha}/\bar{n}$, where $\lambda$ is the free-space wavelength.

To illustrate the reflectivity dependence on the loss and the refractive index difference, in Figure 2.2 we show a family of constant reflectivity curves in a $\Delta n/\bar{n}$ – $\lambda\bar{\alpha}/\bar{n}$

coordinate system. The curves are determined analytically from (B-78) with no approximations. It is evident that the peak reflection coefficient of a quarter-wave mirror is more susceptible to the presence of absorption if the refractive index difference is small. For these reasons, two materials with a large refractive index difference are preferred for use in vertical-cavity laser applications.

As a practical example, Figure 2.2 also illustrates the maximum achievable reflectivity for three epitaxial quarter-wave mirrors that are presently being used in long-wavelength applications. All three mirrors are tuned to 1550 nm and use the appropriate value of the refractive indexes. The mirror loss is used as a variable here, since it can be varied depending on the mirror doping level. The absolute value of absorption loss is given assuming an approximate value of the average refractive index ($\bar{n} = 3.2$) and is shown on the second abscissa. The AlAs/GaAs mirror, used in wafer-fused VCLs, has a fractional refractive index difference of $\Delta n/\bar{n} \approx 15\%$, while InGaAsP/InP system gives $\Delta n/\bar{n} \approx 8.5\%$. For this reason, with the given amount of loss, the maximum possible reflectivity that can be achieved using the AlAs/GaAs is higher than the InGaAsP/InP material combination. Note that since we are dealing with different material systems, the values of loss are not necessarily equal when the impurity concentrations are equal.

The second means of comparison between mirror optical properties is the number of layers that are required to provide a specified value of reflectivity. We selected three representative mirrors to illustrate this fact. Figure 2.3 shows the reflectivity of AlAs/GaAs, InGaAsP/InP and $Si/SiO_2$ mirrors as function of number of layers. The number of layers required to saturate the reflectivity of the InGaAsP/InP mirror is

almost twice as high as for the AlAs/GaAs mirror. (The average absorption coefficient is kept equal in the two cases). The $Si/SiO_2$ mirror with $\Delta n/\bar{n} \approx 80\%$ requires only a few periods to saturate the reflectivity. However, amorphous silicon is quite lossy at 1550 nm ($\alpha \approx 400 cm^{-1}$, $\lambda\bar{\alpha}/\bar{n} \approx 1.25\%$) and that limits the peak reflectivity.

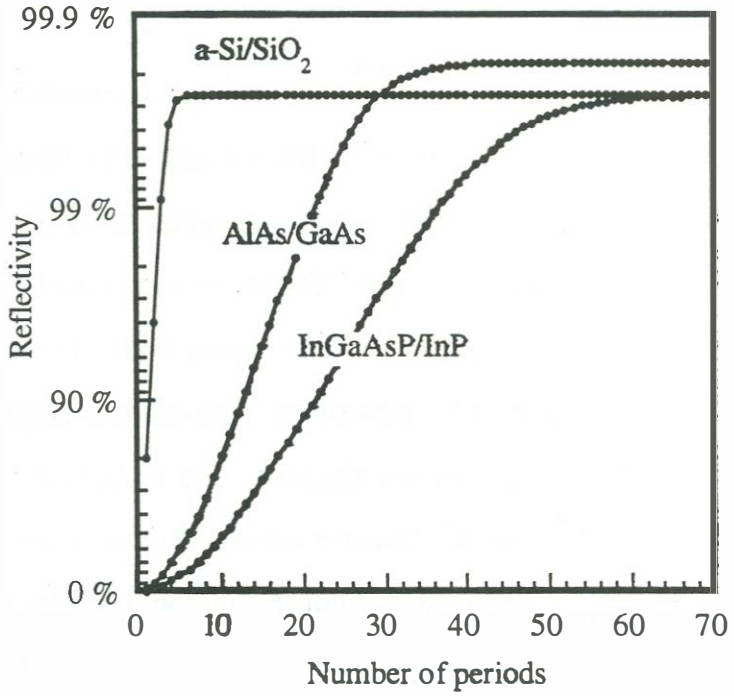


**Fig. 2.3**: Reflectivity as a function of number of layers for three quarter-wave mirrors used for 1.55 μm vertical-cavity lasers.

Besides the optical properties, the vertical-cavity laser design requires a careful consideration of the thermal and electrical properties of the mirror materials and laser structure. Presently, there are a number of materials and techniques used for fabrication of quarter-wave mirrors that are used for long-wavelength applications. We consider the epitaxial and the amorphous mirrors separately.

### 2.1.2. *Epitaxial mirrors*

Epitaxial mirrors realized with compound III-V semiconductor alloys lattice matched to a given substrate exhibit relatively narrow range of refractive index values and thermal conductivities. Binary alloys may have more than an order of magnitude better thermal conductivity than some tertiary and/or quaternary alloys. The main reason for this is the alloy-disorder scattering (Adachi, 1983).

For the realization of long-wavelength vertical-cavity lasers there are several material choices for the fabrication of quarter-wave mirrors. The deciding factor on what material combinations can be used is the wavelength of the fundamental absorption and the range of the refractive index that can be realized in the transparent regime. Semiconductor alloys that are potentially interesting for long-wavelength vertical-cavity lasers can be grown lattice matched to GaAs, InP, GaSb, or Si. Two important properties of the semiconductor refractive index are: 1) all semiconductors exhibit a refractive index decrease below the fundamental absorption edge, and 2) the refractive index at a given wavelength in the transparent regime generally reduces with the energy gap of the semiconductor (Moss, 1959). These properties are illustrated in Figures 2.4 for selected materials which are interesting for long-wavelength mirror applications. Figure 2.4 shows the refractive index at 1550 nm as a function of the energy bandgap of the material, and enables a direct comparison between the achievable refractive index values for compatible materials. Evidently, in order to fabricate a semiconductor quarter-wave mirror one uses a wide bandgap material for the lower of the two indexes and a narrow gap material for the higher. In selecting the narrow gap material or alloy composition care must be taken that the lasing

wavelength is longer than the wavelength of the absorption edge of the mirror material.

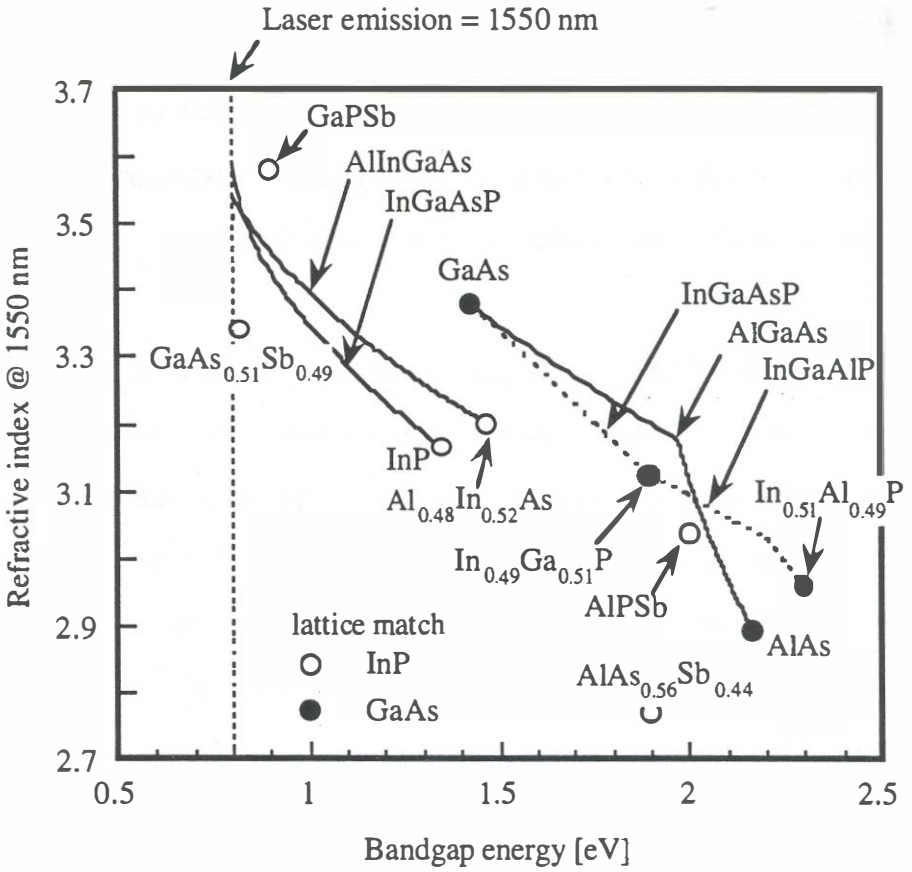


**Fig. 2.4**: Refractive index as a function of energy gap for material lattice matched to GaAs and InP.

The most common choice for vertical quarter-wave mirrors for long-wavelength applications is the InGaAsP/InP or AlInGaAs/AlInAs combination lattice matched to InP. Since the bandgap is a continuous function of the composition (Figure 2.4), an optimum composition exists for the narrow gap choice: The refractive index (at fixed wavelength below the gap) increases as the bandgap decreases, while the absorption

coefficient increases with the proximity of the absorption edge. The smallest bandgap of the InGaAsP alloy used for mirrors at 1.55 μm is in the neighborhood of 0.87 eV (Streubel[a], 1994). The refractive index ratio between this composition and InP is $\Delta n/\bar{n} \approx 8.5\%$ and the mirrors require over 80 layers to achieve reflectivities over 99.5%. For 1.3 μm application the smallest bandgap of the quaternary alloy would have to be around 1150 nm which results in an even smaller refractive index difference ( $\Delta n/\bar{n} \approx 6\%$). For this reason, the InGaAsP/InP mirrors are not used at 1.3 μm.

A large number of researchers have investigated the InGaAsP/InP system for fabrication of mirrors and vertical-cavity lasers (Tai, 1987, Imajo, 1990, Choa, 1991, Streubel[a], 1994). The AlInGaAs/AlInAs system has a very similar, but slightly smaller refractive index difference, as shown in Figure 2.4 (Mondry, 1992). To date a number of researchers have reported such mirrors (Kowalsky, 1991, Guy, 1993), but there have not been reports of vertical-cavity lasers fabricated using this material combination. Optical pumping of a vertical-cavity laser using a 45-period AlInGaAs/AlInAs mirror and a bulk active layer was attempted by this author, but no lasing was observed (Babić[c], 1993). There are other material combinations lattice matched to InP that can be used for fabricating quarter-wave mirrors. They involve mixed group V elements, such as, As/Sb and P/Sb alloys, grown by MBE. Using these materials one can potentially obtain refractive index ratios that are superior to the quaternary/binary long wavelength mirrors, as shown in Figure 2.4. The first attempt to grow such a mirror using InGaAsP/AlAsSb was reported by (Tai, 1989). In recent years, the AlAsSb/GaAsSb lattice matched to InP has been more thoroughly investigated by (Blum, 1994). The AlPSb/GaPSb grown by gas-source molecular

beam epitaxy is also expected to provide very large refractive index ratio (Shimomura, 1994, Anan, 1994).

Changing to a different lattice constant offers a new set of materials. Using GaAs substrates it possible to fabricate AlSb/GaAlSb mirrors (not lattice matched) that would be transparent to 1.55 μm (Tuttle, 1993, Lambert, 1994). The use of Si/AlP system on Si (Babić, 1992c) could be grown by MOCVD and would offer not only a large refractive index difference, but also a possibility of VCL integration on silicon if wafer fusion was also used. An interesting idea for the fabrication of 1.3 μm VCL discussed many times in the optoelectronics community is to slightly increase the GaAs substrate lattice constant using graded InGaAs buffer layers and then grow a strained InGaAs quantum-well active layer. At least one (top) mirror would then have to be grown at a different lattice constant such as is reported by (Otsubo, 1995). No lasers have been reported using this technique, probably because of high density of dislocations propagating from the GaAs substrate. The lattice matching requirement is completely avoided by the use of wafer fusion, where InGaAsP active layers lattice matched to InP are fused to AlAs/GaAs mirrors grown on GaAs.

The more exotic approaches to fabricating quarter-wave mirrors with large refractive index ratio, but using epitaxially grown layers, are air-bridge mirrors and laterally oxidized AlAs/GaAs mirrors. The idea behind both of these types of mirrors is to replace one of the grown epitaxial layers (typically low index AlGaAs or AlAs) with some low index material. The low index material is selectively etched in replaced with a resin in (Ho, 1990) or left empty (air) to form a very high refractive index ratio mirror (Hsin, 1990, Beyler, 1991). The other possibility, being explored in recent

years, is oxidizing AlAs or AlGaAs with very low Ga content to convert the entire AlAs/GaAs quarter-wave mirror to GaAs/$AlO_x$ mirror. The refractive index of $AlO_x$ is almost twice lower than that of AlAs and hence very high reflection coefficients can be realized in this way (MacDougal, 1995). The down side of this process is the reduced thermal conductivity and lack of electrical conductivity.through the mirror.

### 2.1.3. *Amorphous mirrors*

Mirrors deposited by using low temperature (<300°C) techniques, such as, electron-beam evaporation or sputtering are generally amorphous or polycrystalline. These mirrors are electrically insulating, but they exhibit a relatively large range of thermal conductivities: from thermally insulating (0.014 W/Kcm for $SiO_2$) to moderately thermally conductive (2.5 W/Kcm for SiC).

Low temperature deposition techniques offer a wide range of materials and refractive indexes for use both in infrared and visible range. For long-wavelength vertical-cavity-lasers, the most common material combination is $SiO_2$ ($n = 1.46$) as the low index and amorphous silicon as high index ($n \approx 3.6$) material. Silicon dioxide can be deposited by electron-beam evaporation, plasma enhanced chemical vapor deposition, and reactive sputtering (Oshikiri, 1991, Babić, 1991, Scherer, 1992). Owing to the large refractive index ratio these mirrors only require a few periods to achieve high reflectivity. However, their reflectivity is limited by the absorption in amorphous silicon. It is known that in amorphous materials the absorption tail extends deep into the forbidden gap (Stern, 1971). The absorption coefficient of amorphous silicon has been measured to be $\alpha_{a\text{-Si}} \approx 1000\ \text{cm}^{-1}$ at 1300 nm (Babić, 1992) and

$\alpha_{a-Si} \approx 400\ cm^{-1}$ at 1550 nm. The thermal conductivity of silicon oxide and amorphous silicon is quite poor and they can not be used as bottom, heat transferring mirror in VCLs. Thermal conduction of these mirrors can be improved by using MgO (Baba, 1993) and silicon carbide.

## 2.2. *Laser cavity design issues*

The electrical, thermal and optical issues in the designing long-wavelength vertical-cavity lasers rely on the corresponding properties of the mirrors. Cavities with insulating mirrors require ring contacts and hence are susceptible to nonuniform current injection and current crowding. Nonuniform injection has been investigated on 1.3 μm vertical-cavity lasers (Wada, 1992). The detrimental effect of non-uniform injection is the reduced overlap between the mode and the gain profile, and current crowding, which produces a threshold current density increase with the increasing diameter of the device. The lateral carrier profile in vertical-cavity lasers changes even in uniformly injected active layers due to spatial hole burning (Scott, 1993). However, in this case the effects are weaker and can be reduced using suitable current leveling schemes (Scott, 1993). Most importantly, current crowding produces higher power dissipation which in devices with high thermal resistance severely limits the prospects of continuous-wave operation. Consequently, for long-wavelength vertical-cavity lasers, it is advantageous to avoid ring contacts and try to develop uniformly injected structures with conductive mirrors. Furthermore, building cavities with lateral guiding and short cavity lengths is advantageous from the point of reducing diffraction and absorption losses.

The listed issues are substantially improved by the use of AlAs/GaAs with InGaAsP active layers. With two wafer fusion steps we surround the InGaAsP active layer with two mirrors that are electrically and thermally conductive. Once such an epilayer structure is formed by fusion, practically every structure investigated for GaAs-based VCLs can be applied to long-wavelength VCLs. The index-guided post device

fabricated in the course of this work is the simplest structure to build and was therefore used to demonstrate the concept.

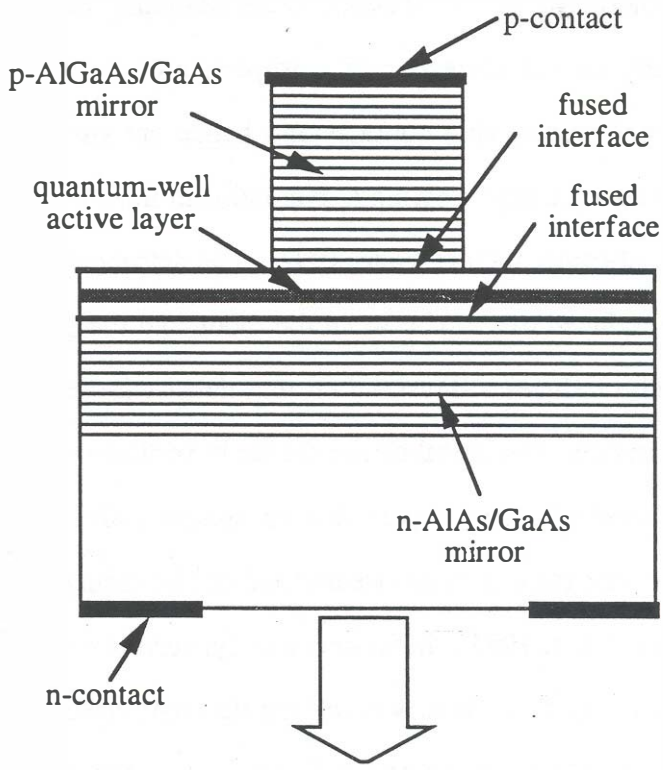


**Fig. 2.5**: A simple index-guided post vertical-cavity laser.

The structure of the fabricated double-fused vertical-cavity laser is schematically illustrated in Figure 2.5. The top mirror is etched by reactive ion etching for current and mode confinement, while the active layer and the bottom mirror are left unpatterned. In most index-guided post VCLs and in this work, the top and bottom mirrors will be $p$ and $n$-type, respectively. This is done because heavily doped $n$-GaAs substrates have much smaller loss than $p$-GaAs (Sec. 4.4). Therefore, the top

of the pillar has the $p$-type contact, while the $n$-type contact is made to the substrate. The post height is several micrometers (5 – 7 μm) depending on the number of mirror periods and the wavelength. The most important geometry dependent loss mechanisms in this structure are sidewall scattering and diffraction loss. The roughness at the waveguide sidewalls produces scattering losses and the free-space propagation though the unguided fraction of the bottom mirror produces coupling losses. These losses are discussed in more detail in Appendix C.

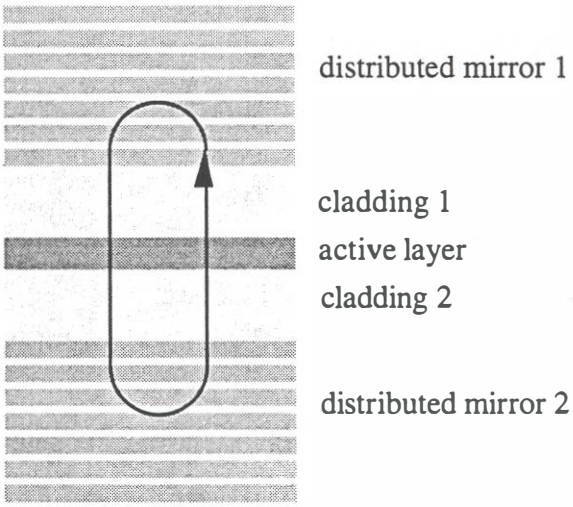


**Fig. 2.6**: Axial structure of a vertical-cavity laser with two epitaxial mirrors.

The axial refractive index profile of this structure is shown in Figure 2.6: A wavelength size cavity ($1-3\lambda$) is sandwiched between two quarter-wave mirrors with reflectivities exceeding 99.5 %. The cladding layers serve as a means of adjusting the cavity length between the mirrors, and centering the active layer at the place where the electromagnetic field in the cavity has a maximum. Owing to the short

cavity length, this structure typically has only one longitudinal mode. The exact determination of this mode can be performed using transverse field matrix approximate described in Appendix A or approximately using the penetration depth approach described in Sec. C.1.3. The losses in this cavity originate from the absorption in the extrinsic epitaxial layers: The cladding and the mirrors. The doping in all of the layers has to be optimized between electrical conduction and absorption loss. The free-carrier absorption in *p*-type GaAs, InP and InGaAsP is higher at long wavelengths than it is at ≈ 1 μm wavelength used in GaAs-based VCLs. For this reasons the design of epitaxial mirrors and cavities for long-wavelength VCLs becomes a more critical issue (Chapter 4). The thermal resistance of this device is quite straightforward to calculate by considering that the active layer and the mirror post are the dominant heat sources in the structure (Sec. 6.6).

## 2.3. *Conclusion*

Some of the difficulties of realizing room-temperature operating vertical-cavity lasers can be effectively solved by using AlAs/GaAs mirrors because of their optical, electrical and thermal properties which when combined outperform all other long-wavelength mirrors. Still, the laser cavity requires a careful design because free-carrier absorption, scattering and diffraction losses are present, and an optimization between these and the electrical and thermal properties is necessary. With this knowledge and the wafer fusion process available to bond InGaAsP active layers to AlAs/GaAs mirrors, the fabrication of a double-fused vertical-cavity laser appears feasible and hold great promise of success in achieving room-temperature continuous-wave operation.

Chapter 3

# Wafer fusion

The method of wafer fusion of InP to GaAs used in the fabrication long-wavelength vertical-cavity lasers was developed through a collaboration between UC Santa Barbara and Hewlett-Packard Laboratories, Palo Alto. The initial developments included studies of physical, electrical and optical properties of fused junctions and are summarized in (Ram, 1995, Dudley, 1993). This chapter approaches the fusion from a more practical point of view, with the desire to repeatably produce fused samples of similar quality and standard size with the goal of fabricating working long-wavelength vertical-cavity lasers.

Epitaxial growth offers a variety of materials for fabrication of optoelectronic devices, but it has the disadvantage of being a relatively high temperature process and requires that the grown materials be lattice matched. In the quest for new devices and simplified fabrication of existing devices, researchers have investigated several alternative methods for creating epitaxial multilayer structures that involve incompatible materials, such as materials with other lattice constants and of non-crystalline structure. One of these is epitaxial growth on lattice mismatched substrates, particularly for the purpose of integration of optoelectronic devices on

silicon (Sugo, 1992, Deppe, 1990, Dobbelaere, 1988). Wafer fusion or bonding is an alternative method for achieving this goal by transferring already grown epilayers and bonding them to a new substrate. When applied to III-V semiconductors, the two methods are very different in the type of crystal quality they can realize. Dislocations present in wafer fused junctions are predominantly edge dislocations and do not introduce any threading dislocations, whereas hetero-epitaxy usually involves mixed dislocations (Ram, 1995).

Semiconductor bonding and/or bonding of semiconductor devices using intermediate layers is several decades old (Haisma, 1994) and has a variety of characteristics that open possibilities for creating novel devices and integration schemes. Some of the characteristics of various types of bonded junctions are listed here: The distance between two directly bonded surfaces is atomically small. There is no externally added compound that is intentionally introduced to enhance the bonding, but sometimes insulators or metals may are used as intermediate layers. Surfaces can be patterned by etching of one or both surfaces and buried three dimensional structures can be fabricated in this manner, where the voids can be filled with other materials. This interface-engineering technology is well suited to specific device applications, such as, permeable-base transistors (Slatter, 1992), bipolar integrated circuits (Shimbo, 1985), pressure sensors (Cristel, 1990), and micro-mechanical applications (Gösele, 1992). Conductive and insulating layers can be buried to provide a variety of current confining or transport schemes. This is particularly interesting for Silicon-On-Insulator applications using the so-called Silicon Direct Bonding technique (Lasky, 1985, Ohashi, 1986). Abrupt dopant variation can be realized across the bonded junction as well (Yamaguchi, 1995).

Bonding can be used to join various compositional states, since crystalline, polycrystalline, and amorphous materials can be bonded. Consequently, samples with different crystallographic orientations can be bonded. Finally, to fabricate vertical-cavity lasers we have taken the advantage of the fact that materials with different lattice constants can be bonded into a composite crystalline solid.

Most of the bonding research interest in the past decade was concentrated on Silicon Direct Bonding (SDB) which was originally introduced as a means of improving Silicon-On-Insulator devices (Lasky, 1985, 1986) using an intermediate silicon oxide layer. Note that the name, *direct bonding* does not mean that silicon is directly bonded to silicon, but rather refers to a generic type of bonding where no intentionally introduced adhesive is used. Around the same time a similar technique for *direct* silicon-to-silicon bonding was reported (Shimbo, 1986). However, even in this case the presence of oxygen at the surface played an important role in the bonding (Bengtsson, 1992). Silicon bonding has found its way to many applications (Harendt, 1991, Ohura, 1987). Reviews of the bonding technology and the physics of the silicon-to-silicon bonding process are given in (Bengtsson, 1992, Haisma, 1994).

Different bonding methods may include intermediate layers used to enhance bonding and/or elevated temperature processing. The key characteristics that differentiate the applications of different bonding techniques are the electrical, thermal, and optical properties of the junctions. The first question in bonding is the process temperature. Many applications require bonding because it may be performed at low temperatures. Low temperature bonding techniques include silicon-nitride direct bonding (Bower,

1993), epitaxial liftoff / Van der Waals bonding technique (Yablonovitch, 1990), and spin-on glass (Chua, 1995). All of these techniques rely on an intermediate layer between the semiconductors. For this reason there is poor or no electrical conductance through the bonded junctions. In many electronic applications, there is no requirement for optical transparency. For such applications, an intermediate metal is very useful, because of higher electrical and thermal conductivity, and also the possibility of bonding at reduced temperatures. A good example of this type of bonding that occurs already at room temperature is Van der Waals bonding using a palladium intermediate layer (Yablonovitch, 1991). If the bonded junction is to be used for surface-normal optoelectronic devices, one simultaneously requires optical transparency, and electrical and thermal conductivity. One of the bonding techniques that offers these properties is wafer fusion of compound semiconductors. First observed by (Liau, 1984), it has now been used by many authors to fabricate optoelectronic devices on GaAs and Si substrates (Liau[a], 1990, Lo, 1991, Mori, 1994). The method is also called *direct bonding* or *bonding by atomic rearrangement.*

The bonding techniques can also be divided into two groups by application: a) Devices are transported and bonded to a new substrate primarily for the purpose of *integration*, and b) bonding dissimilar materials enables the realization of *novel devices* which would not be possible by lattice matched epitaxial or hetero-epitaxial growth. The latter group includes the improvement of device performance by bonding to new substrates for optical transparency or heat sinking. This division is particularly apparent in compound semiconductor bonding: Examples of bonding for integration are wafer fusion of InP to GaAs (Liau[a], 1990, Lo, 1991) and InP to Si (Lo, 1991, Mori, 1994, Wada, 1994) used to fabricate long-wavelength lasers on GaAs and Si

substrates. Examples of fabrication of novel devices using wafer fusion are wafer-fused long-wavelength vertical-cavity lasers (Dudley, 1994, Babić, 1995), resonant-cavity photodetectors (Tan, 1994), silicon hetero-interface photodetectors (Hawkins, 1995), and transparent-substrate light-emitting diodes (Kish, 1994). The critical requirement in these surface-normal optoelectronic devices is the electrical conductivity and optical transparency of the junction. For this reason, no other method that relies on an intermediate insulating or metallic layer for bonding can be used. In wafer fusion, semiconductors, such as, silicon, GaAs, InP are bonded into a new crystalline solid, which as a result can be processed as any other semiconductor. If the two crystals that will be bonded are aligned before bonding, the composite solid will cleave preferentially along the same group of planes as the two constituents, {011} for GaAs and InP. The advantage of wafer fusion is that the bonds between the solids are of the same type as in the original solid and hence the bond between the two parts is as strong as the two crystals forming the new solid.

The topic of this dissertation is the application of wafer fusion to the fabrication of long-wavelength vertical-cavity lasers. Inasmuch as the initial development of wafer fusion was done in a collaboration with Hewlett-Packard company, the exact procedure of pre-fusion surface activation, cleaning and application of the pressure to the samples can not be disclosed. However, the information given in this text brings out the most important facts developed at UCSB and are part of the public domain. Furthermore, a large part of the initial characterization of the bonding has been performed by R. J. Ram and J. J. Dudley and has been published elsewhere (Dudley, 1993, Ram , 1995).

## 3.1. *Wafer fusion technique*

### 3.1.1. *Physics of bonding*

When two macroscopic bodies approach each other at distances smaller than a few hundred nanometers the collective van der Waals forces result in an attraction between the two bodies. If the two bodies are very flat and clean, and their surfaces approach each other at distances smaller than a few nanometers, these circumstances lead to interfacial bonding. This is a complex phenomenon owing to additional interaction between the surface of the bodies by adsorbed layers, static electrical charges, and chemical bonding. Hence, Van der Waals bonding does not completely describe the bonding phenomenon. Once initiated, the bonding will spread through an entire area in the form of a "contact wave", as commonly observed in silicon bonding of large wafers. The silicon-to-silicon bonding relies on the presence of a hydrogen bond between the hydroxyl groups and Van der Waals forces to perform the room-temperature bonding between hydrophilic surfaces, while after annealing at higher temperatures the bonds are replaced by Si-O-Si bonds (Bengtsson, 1992).

Compound semiconductor bonding, InP to GaAs bonding in particular, appears fundamentally different even though at the room-temperature stage the initial attraction and bonding bear some similarity to silicon direct bonding. The bonding of GaAs and InP does not involve oxygen or any other compound other than the fused materials (Liau, 1990a, Ram, 1995). The process of bonding occurs by heating the substrates to temperatures at which the surface of the semiconductors are known to decompose, giving off the Group V element and leaving the surface Group III element rich. In the

well-known process of *proximity annealing* (Williams, 1984) implant annealing of GaAs wafers is performed rapidly by covering the wafer with another GaAs wafer. The intention is to provide local over-pressure of arsenic to prevent surface decomposition. A similar effect is realized when two exceptionally flat surfaces are pressed against each other during the process of wafer fusion. Here the distance between two bonded wafers is much smaller than could ever be realized by simply placing one wafer on top of another, especially if one of the wafers in the proximity anneal has a pattern on it. The surfaces that are fused are as flat as the commercially available epi-ready wafers of InP and GaAs. The epitaxial growth on top of the wafers has a tendency to smooth out the roughness, but also adds growth related defects. The mean square roughness of epilayers is in the meighbourhood of 1 nm.

The process of fusion of GaAs and InP is not fully understood, but is believed to occur by desorption of phosphorus and surface diffusion of indium. This model is described in greater detail by (Dudley, 1993, Ram, 1995, Liau[a], 1990) and relies on the idea of proximity anneal using GaAs as cap for decomposing InP. As molecular phosphorus $P_2$ desorbs from the surface and fills the gaps in the fused junction, indium diffuses laterally and fills voids, later to react with phosphorus again during the cooldown to possibly form an InGaAsP alloy (Liau[a], 1990).

Another effect that enhances the fusion uniformity is the local melting of InP or GaAs under high pressures exerted on microscopic non-uniformities. When two surfaces meet they touch in the places that stand out most. The force used for fusion in this work is between 175 and 200 N on a 8mm×8mm sample (pressure ≈ 0.3GPa). During the first touching of the samples the effective area may be many orders of

magnitude smaller than the wafer surface. The forces acting on small nonuniformities with extra heights can therefore be in the range of hundreds of thousands of Newtons. This force easily bows the wafer, or even breaks it if the obstacle is too large, but it may also enhance the uniformity of fusion through local melting via the so called *ice skater effect*. In ice skating, the pressure of the skate knife melts the ice below it by moving to a different place in the water phase diagram (Pauling, 1970). The ice melts under pressure, rather than heat. This is a self-limiting force because as the fused area increases the force on individual non-uniformities decreases.

### 3.1.2. *Fusion process sequence*

Practically all of the fusion performed in this work was done at 630°C for 20 minutes. Temperatures as low as 600°C were explored, but good quality fusion was observed only above 615°C. However, the parameter space has not been fully investigated, and it is entirely possible that fusion could be obtained at even lower temperatures with proper cleaning and pressure. A number of runs were performed with the fusion temperature of 650°C, but between 630°C and 650°C it was hard observe any difference.

The fusion process is performed in a quartz tube with a retractable three-zone furnace (resistive heaters). The temperature of the samples, which were loaded in a graphite fixture, was monitored using a thermocouple that was located exactly below the fixture. The time dependence of the sample temperature is shown in Figure 3.1. The heating stage is quite short while a cooldown of 4°C/min was used. The sudden decrease of temperature at the end occurred at 250°C when the furnace was retracted.

Very often the furnace was simply shut off around 500°C and then the cooldown started at an approximate rate of 10°C/min.

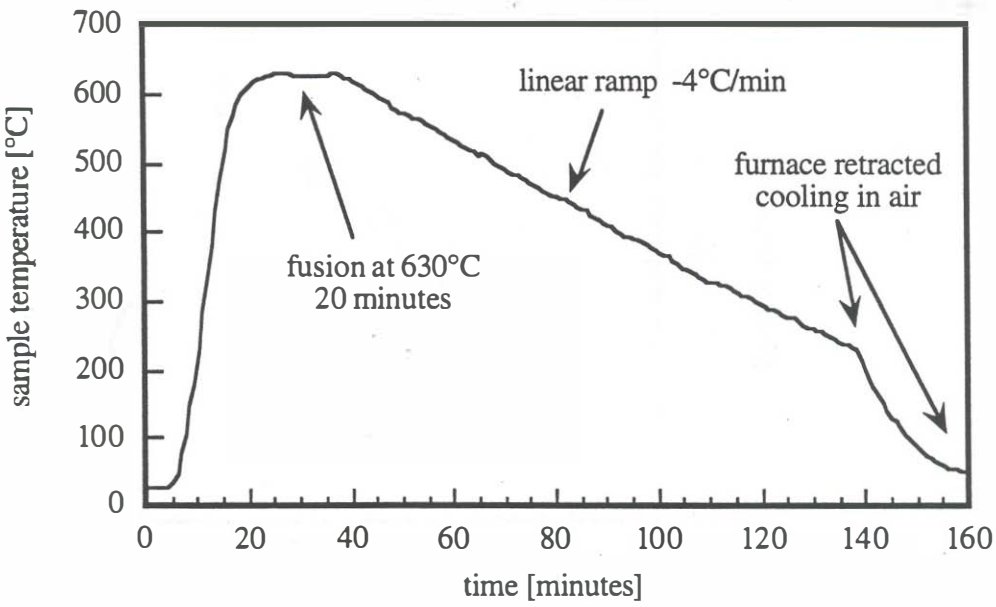


**Fig. 3.1**: Sample temperature profile during a typical fusion run.

3.1.3. *Fixture, force, and sample size*

The pressure during fusion was applied to the samples using a specially designed graphite fixture. In order to ensure that the pressure is approximately equal every time, a calibrated torque wrench was used to tighten the fixture. However, when the fixture force was measured using a calibrated miniature load cell (Entran, ELF-13/5-250), it was observed that the force was not consistent. It varied from run to run depending on the order and the manner in which the fixture was tightened. The relationship between the torque and the measured force used on our fixture is shown in Figure 3.2. Even though the variation was large, it is possible to give an estimate of the force

used for most of the fusion runs used in the fabrication of VCLs in this work. The torque used was almost always 0.55 lb-in.

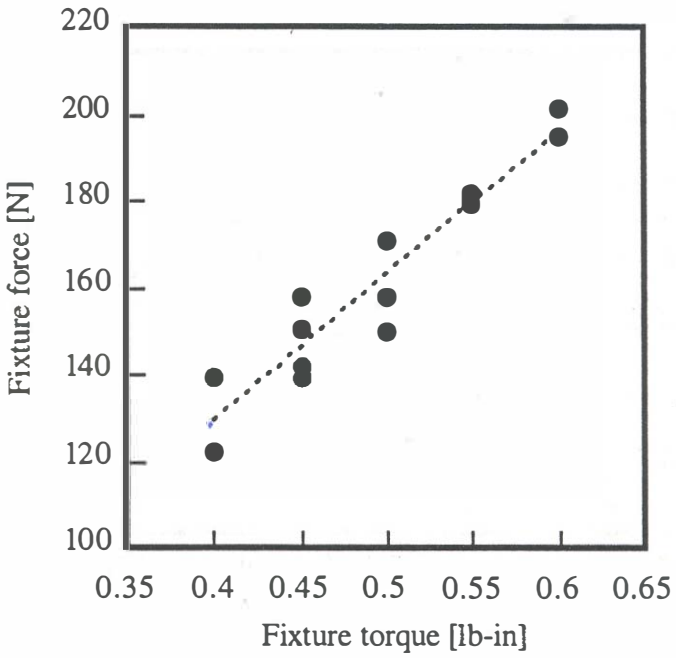


**Fig. 3.2**: Measured relationship between force and the torque used to tighten the graphite fixture used in this work.

The sample size was a compromise between uniformity of pressure and conservation of material. As discussed later in Section 3.3.1, for small samples (3 mm x 5 mm and 4 mm x 4 mm) the fusion was incomplete due to nonuniform pressure in the fixture. Fusion uniformity dramatically improved when larger areas were used, such as, 8 mm x 8 mm and the largest ever used which was 8 mm by 10 mm. Practically all of the fusion experiments in this work were done with samples of 8 mm x 8 mm, or similar size. Furthermore, both samples were always made of equal size (as close as possible). This has made the alignment easier and the uniformity of fusion at the edges much better. Figure 3.3 shows side views of two fused pairs of InP to GaAs

in which the sample sizes were not adjusted to be equal. Furthermore, in the top case the GaAs substrate has been thinned down before fusion. Thinning down was explored for several runs, but no fusion improvement was detected. In fact, the cleaning of the samples after lapping was more difficult since the samples had to be mounted using wax.

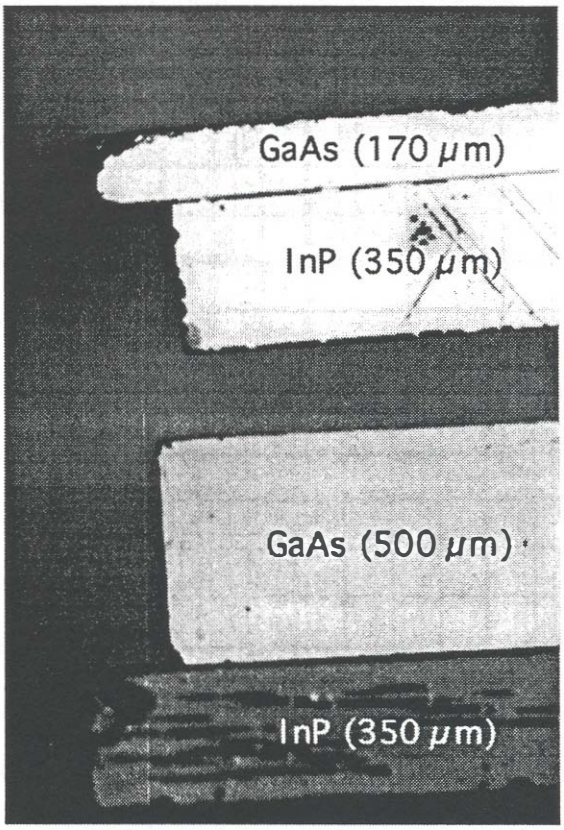


**Fig. 3.3**: Side view of two fused pairs of GaAs and InP substrates. The GaAs substrate in the top case has been thinned down before fusion.

### 3.1.4. *Cleaning*

In general, the process of cleaning consisted of a sequence of oxidation and oxide removal steps. The free surface of GaAs and InP always have some oxygen present in form of oxides, and carbon adsorbed to the surface in the form of hydrocarbons. The cleaning procedure for the fabrication of VCLs using fusion was altered many times to find the optimum, and in many ways the procedure used was adopted simply because it gave more-or-less consistent results rather than through a full understanding of the surface chemistry. Most of the time, the cleaning procedure started with boiling tri-chloro-ethane and acetone, followed by room-temperature isopropanol rinse and nitrogen dry. No water was ever used after the solvent cleaning. If the samples were previously patterned with photoresist (in most cases they were) then at this point the remaining hydrocarbons were removed in a 10 minute low power oxygen plasma. A parallel plate plasma etcher (asher) was used for this purpose at 100 W and 300 mT. The cleanliness of this etcher was always questionable since $CF_4/O_2$ plasma was used in the same system and occasionally there was backstreaming of pump oil. After this step the oxides were removed using 25% HF on both samples or in 3%$NH_4OH$. Hydrofluoric acid is known to be a good non-oxidizing acid for cleaning InP (Knauer, 1989). The GaAs sample sometimes underwent oxide cleaning using hydrochloric acid. The problem with $NH_4OH$ is that it slowly attacks GaAs. Concentrated $NH_4OH$ (≈30%) etches GaAs at a rate of at least 18nm/hour (Margalit, 1995). This is a problem since the cavity length of the fused VCL is directly effected. Other researchers who perform GaAs to InP fusion use a weak mixture of $H_2SO_4$:$H_2O_2$ to remove all of the oxides and organics (Okuno[a], 1995). However, the problem with this etchant is that it also etches GaAs. Only HF does not attack any of the surfaces.

However, the problem with HF is that it leaves a hydrophobic InP surface and perhaps some fluorine (Kissinger, 1991). Fusion to hydrophobic surfaces is a bit harder and several variations, such as diluting HF in solvents, were explored to make the surface hydrophilic. The danger is, of course, in the use of a solvent which may oxidize the surface (Barbé, 1988). This occurs if the solvent contains traces of water.

After the oxide was cleaned, the samples were exposed to 60 minutes of ultraviolet-ozone oxidation. This process step has two functions: to burn off the remaining carbon from the surface, and to create a thin ≈5 nm oxide on the surface (Lu, 1993). The thickness of this oxide is not known exactly, nor was there any attempt to measure it. The reason for this step is to always create an oxide of fixed thickness and composition before the final pre-fusion oxide removal.

Next, the samples are carried over to the fusion setup and there, just before insertion into the fixture and then into the furnace, the last oxide removal was performed. This can be done in concentrated HF or in a mixture of HF and a solvent. The mating of two surfaces to be fused can be performed either dry or wet. In dry mating the oxides are removed and dried before the two surfaces are placed in contact. Since oxygen reacts easily with oxide-free surfaces and hydrocarbons easily adsorb to such surfaces, it is necessary to perform this task in an inert atmosphere, such as a nitrogen glove box. The advantage of this method over wet mating is that there are no liquids trapped between the surfaces during fusion. However, this still does not eliminate the problem of liquids and gases adsorbed at the surface which desorb only at elevated temperatures during fusion. The wet fusion chemical of choice is concentrated HF.

This is a weak, non oxidizing acid and is used by most authors (Okuno, 1995, Lo, 1991, Wada, 1994).

### 3.1.5. *Channels*

Both in wet and dry fusion, hydrocarbons, fluorides or water adsorbed on the surface must eventually desorb from the surface at elevated the temperatures. This problem has been observed and studied many times in connection of silicon-direct-bonding (Ohashi, 1986, Tong, 1990, Yamaguchi, 1995). The desorption of hydrocarbons at 200-800°C results in bubbles and large voids in the fused junctions. One way of eliminating this problem, used in SDB, was to anneal the samples at high temperatures to drive the water or the hydrocarbons in to silicon (Mitani, 1991).

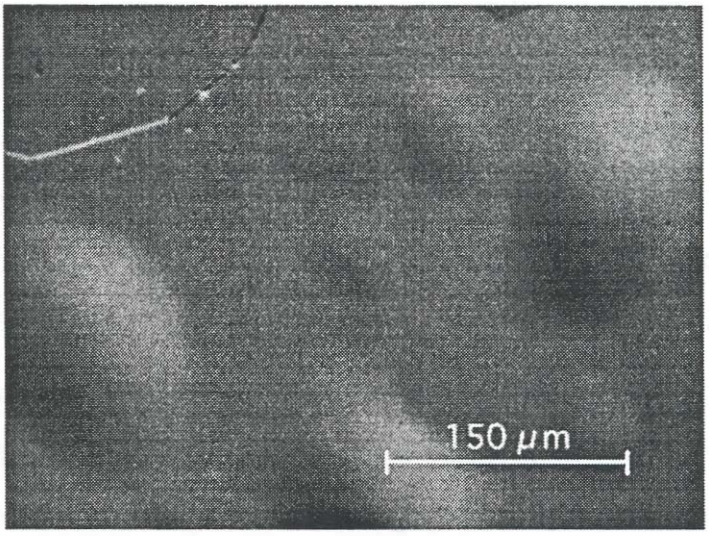


**Fig. 3.4**: Large bubbles in InP epilayers after InP substrate removal.

In this work, it was also observed that large fused areas would very often have a number of bubbles and cracks on it. A photograph of large bubbles is shown in Figure 3.4. In addition to the large bubbles, the fused junction exhibited high density of microscopic voids with typical sizes ranging from 100 nm to several micrometers. These voids were not easily observed without stain-etching, a method for micro-void decoration described in later text (Section 3.2.1.) The problem of cracks, large bubbles and micro-voids was solved by using an array of channels etched in one or both of the substrates (Babić, 1994). This method almost completely eliminates the bubbles and μ-voids over the entire area of the samples ($64 mm^2$).

The method consists of etching one- or two-dimensional arrays of channels that extend to the end of the sample. The function of the channels is to provide an outlet for gases that are released when the temperature of the samples is increased during fusion. In most of the work, only one-dimensional arrays were used, because there were no indications that the fusion was better with a two-dimensional array. This has the advantage of leaving a larger area unpatterned. The channels were patterned using a stripe laser mask with different stripe widths. Three different channel widths were used: 2, 5, and 10 μm, while the pitch was always 150 μm. Most of the time the channels were etched in the InP sample, but sometimes GaAs was etched. The channels in InP were etched using 3:1 $H_3PO_4$:HCl for 20 s. This is a very viscous etchant and for very narrow channels a longer time may be used (30s). The etch depth also depended on whether there was an etch stop layer below the InP surface. When bulk InP wafers were patterned, the etch depth was approximately 500 nm. For vertical-cavity lasers the active-layer cladding thicknesses were 120 nm and 300 nm as described in Chapter 4. Since hydrochloric acid etches InP, but stops on any Ga

containing alloys, the depth of the channels etched in the VCL active layers were always equal to the cladding thickness.

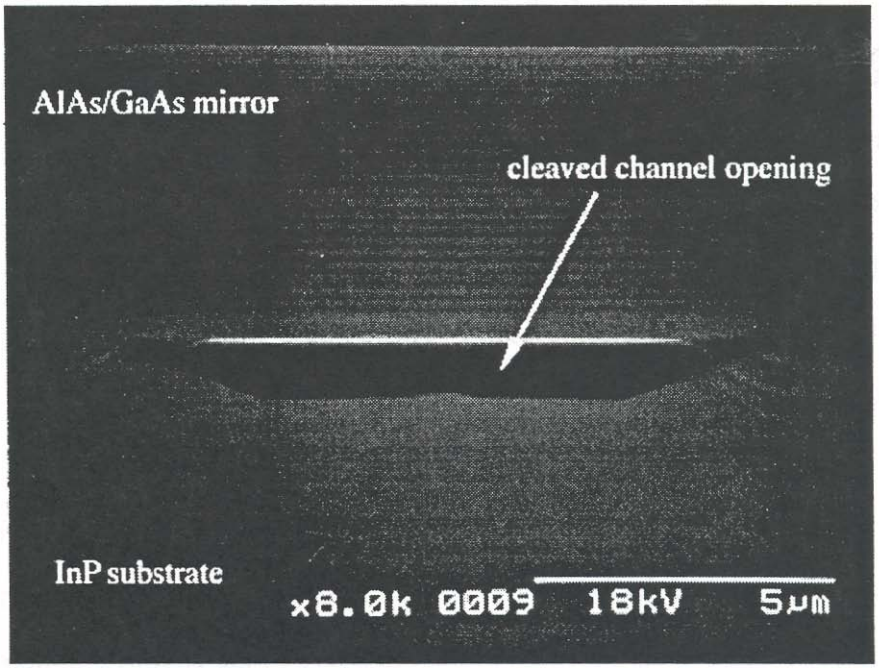


**Fig. 3.5**: Cleaved cross-section of a fused interface between an InP substrate and AlAs/GaAs mirror. The channel has been etched into the InP substrate.

Patterned fusion has been previously used to release the stress in the fused layers. However, stress relaxation does not appear to be the main cause for the improvement in fusion observed when using channels. There are two indications that this true: Fusion is improved even when the channel width equals or is smaller than the epilayer thickness. This can be seen in Figure 3.5 where a channel has been etched in the InP substrate that was subsequently fused to an AlAs/GaAs mirror. The mirror on top of the channel does not show any significant bowing. The presence of bowing would indicate that there is significant stress relaxation in the fused layers. Some stress

relaxation may have occured along the channel edges, which in fact may be observed by a slight nonuniformity in the cleaved edge around the channels. Secondly, if the fusion improvement was a result of stress release by using channels and then one would expect that a two dimensional array of channels would outperform the one-dimensional array, simply because the stress energy would be reduced in both directions. However, no difference was observed between the use of one and two dimensional arrays of channels.

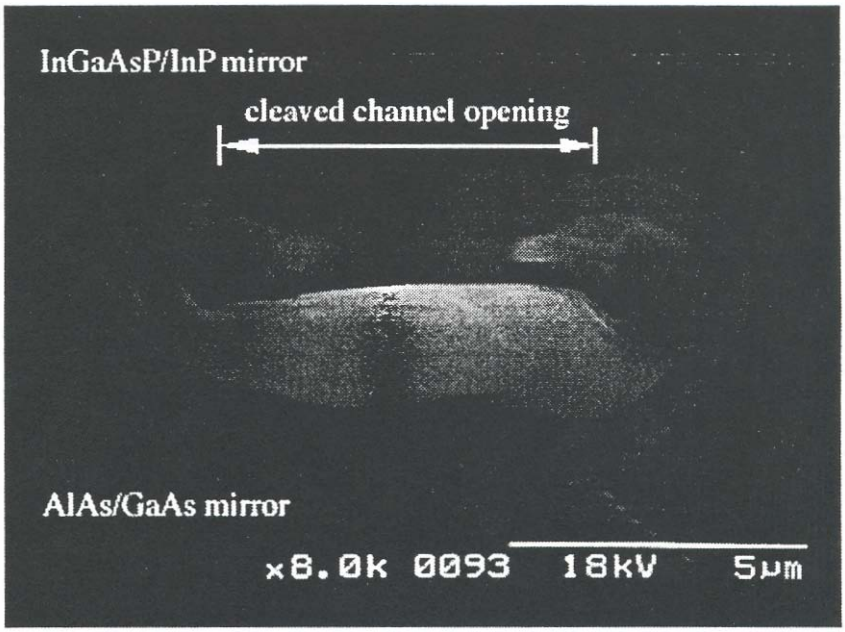


**Fig. 3.6**: Cleaved channel opening from which a dense liquid is pushed out under pressure. The composition of the liquid is not known.

It appears that excess hydrocarbons, water, and possibly contaminants desorbed from the surface of the fused materials and diffused out along the channel. If one cleaves the sample perpendicularly to the channels, sometimes one can observe trapped dense

liquid, as can be seen in the corners of the channel in Fig. 3.5. If the channel has a very small cross-sectional area, the liquid may be under pressure so that upon cleaving it is pushed out. In this case the liquid accumulates at the cleaved channel exit as shown in Figure 3.6. The composition of this liquid is not known, even though it seems very likely that it has a hydrocarbon structure.

The fact that excess hydrocarbons and water must leave the fused junction implies that there is a minimum channel cross section that gives good results. The critical channel cross-sectional area should also depend on the sample size. Since only one size of fused sample was used most of the time, this issue was not investigated. However, during the course of this work it has been found that good quality fusion on an 8 mm x 8 mm sample can be obtained if channels are at least 5 μm wide and 120 nm deep with 150 μm pitch. Recently, this method has been used in Silicon Direct Bonding of large (4") wafers (Yamaguchi, 1995). The channels reported there are an order of magnitude deeper, wider and farther apart.

### 3.1.6. *Orientation*

If one observes wafer fusion on an atomic scale as an attempt to match one crystal with another of similar lattice constant then the orientation of the two samples will be important. There have been very few reports on investigations of fusion of crystals of various orientations (Okuno, 1995a, 1995b). In this work, only (001) InP and GaAs were fused. Even with this restriction there are two ways to orient the samples before fusion: *In-phase* and *anti-phase*, nomenclature taken from (Okuno, 1995). In an ideal

case, illustrated in Figure 3.7, the two surfaces to be fused end with atomic layers from different groups. In that case, realizing the right bond direction is the only obstacle to getting a perfect continuation of the crystal. If the bond directions at the two surfaces are parallel then we have in-phase fusion and the crystal is continued perfectly, while for 90° out of phase we have anti-phase bonding.

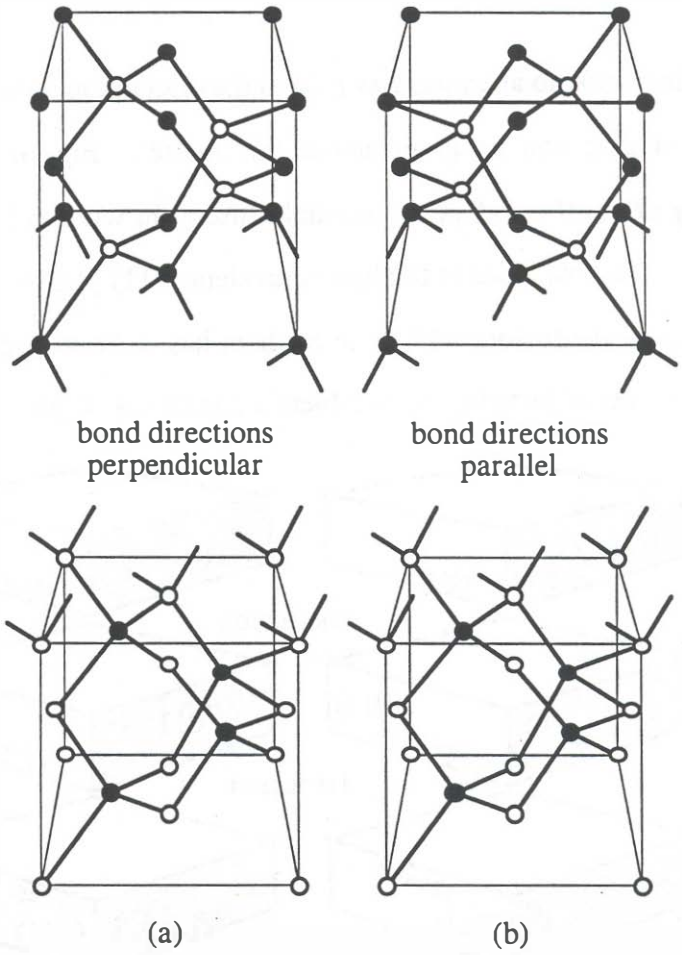


**Fig. 3.7**: (a) Anti-phase, and (b) in-phase bonding between two Zinc Blende crystals.

Preliminary experiments with electrical junctions fabricated using both of these orientations gave contradictory results (Okuno, 1995a, 1995b) and hence it is not clear if it makes any difference what orientation is used in fusion. However, in (Okuno, 1995b) (001) InP was also fused to a (011) GaAs crystal and there the difference in the V-I characteristics was clear: The voltage drop in this case was larger than both in-phase and anti-phase fusion of (001) wafers.

In most of this work no attention was paid to the orientation of the wafers, and hence no consistent data can be given about this matter. Figure 3.8 shows how to intentionally orient the wafers for a double-fused run with anti-phase and in-phase orientations. The basic idea is to align equivalent (011) planes of the samples to be fused for anti-phase fusion, while one of them has to be turned by 90° if in-plane fusion. This is needed because the zinc-blende crystal has $S_4$ point-group symmetry.

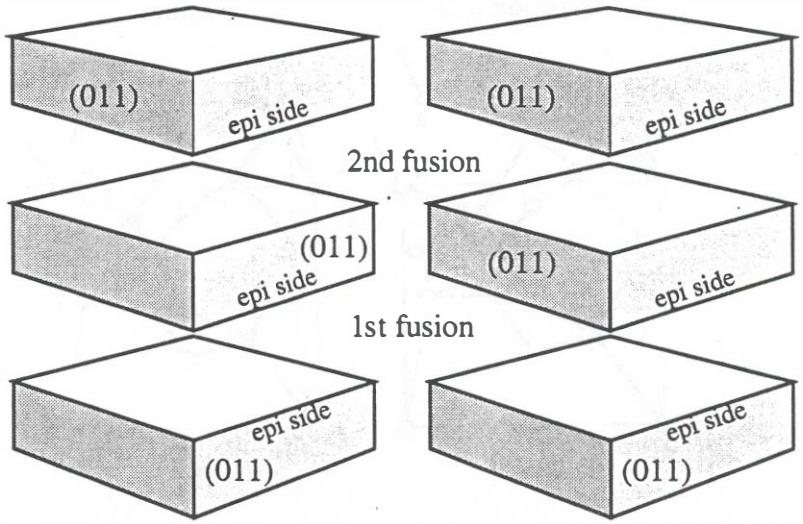


**Fig. 3.8**: Orientation of wafers in double-fusion for making both junctions fused either in-phase or anti-phase.

## 3.2. *Fused interface characterization*

There were two standard tests for fusion quality used in this work: Visual inspection of the fused epilayers after substrate removal, and stain-etching of the cleaved edge. Visual inspection was performed using an optical microscope with a Nomarski interferometer insert. The samples were inspected for bubbles, cracks and continuous fusion extending to the edges of the sample. Stain etching was used to inspect the fused junctions for the presence of microscopic voids. It is important to note that a fused epilayer that appears clean and smooth (see Figure 3.20, for an example), does not imply a fused surface free of microscopic voids.

### 3.2.1. *Stain etching*

This method is most useful for determination of the presence of micro-voids in the junctions. On a cleaved edge, many voids were too small and too thin to locate using the scanning electron microscope, but if selective etching was used to decorate the voids they became very easy to detect. The selective stain-etching of fused junctions was developed as a part of this work, but it has recently come our attention that similar non-selective techniques have been used in characterization of directly bonded silicon junctions (Mitani, 1991).

The principle of the selective strain etching is illustrated in Figure 3.9 and 3.10. The cleaved facet of a fused sample cleaves along the {011} group of planes and is generally flat across the fused junction, as shown in Fig. 3.9a. Even if this is not the

case stain etching will still be very useful in decorating the junctions. To perform the stain-etch, the sample is immersed into a 1:1:50 $H_2SO_4$:$H_2O_2$:$H_2O$ solution for 90 seconds. Sometimes phosphoric acid is used instead of sulfuric. If the fusing is complete then the GaAs side etches uniformly inwards as shown in Figure 3.10(a), while if there are voids present in the fused junctions the etchant enters the void by capillary action and starts etching downwards, as shown in Fig. 3.10(b).

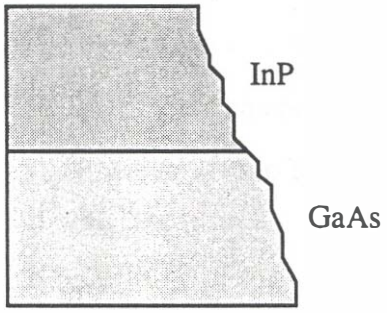


**Fig. 3.9**: Cleaved edge of a well-aligned fused junction before stain-etching.

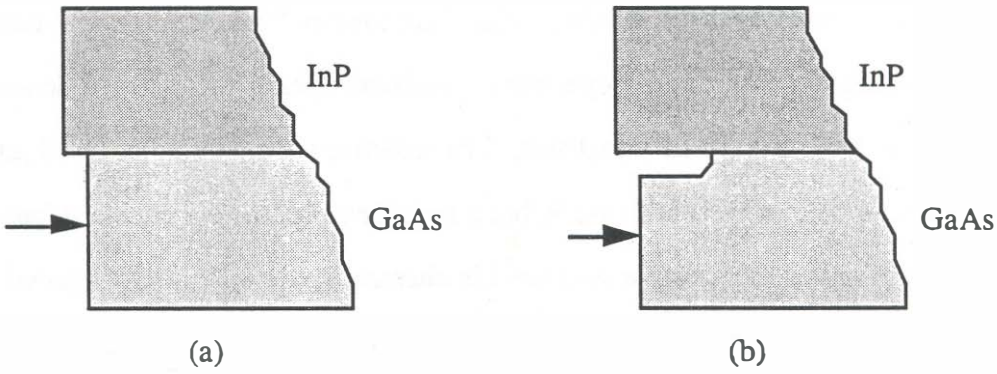


**Fig. 3.10**: Etch profiles of fused junctions after stain etching. (a) etch profile of a completely fused junction, (b) etch profile with micro-voids.

Even though the initial penetration of the etchant into the void is slow, as soon as the etched hole widens the process speeds up to the etch-rate limit present outside of the void. The additional feature of this method is that most of the decorated voids result in etched voids of roughly same size and can seldom be mistaken for some other crystal defect. Figures 3.11 shows an example of decorated micro-voids in a fused junction between an InGaAsP/InP mirror (with bulk active layer) and a GaAs substrate.

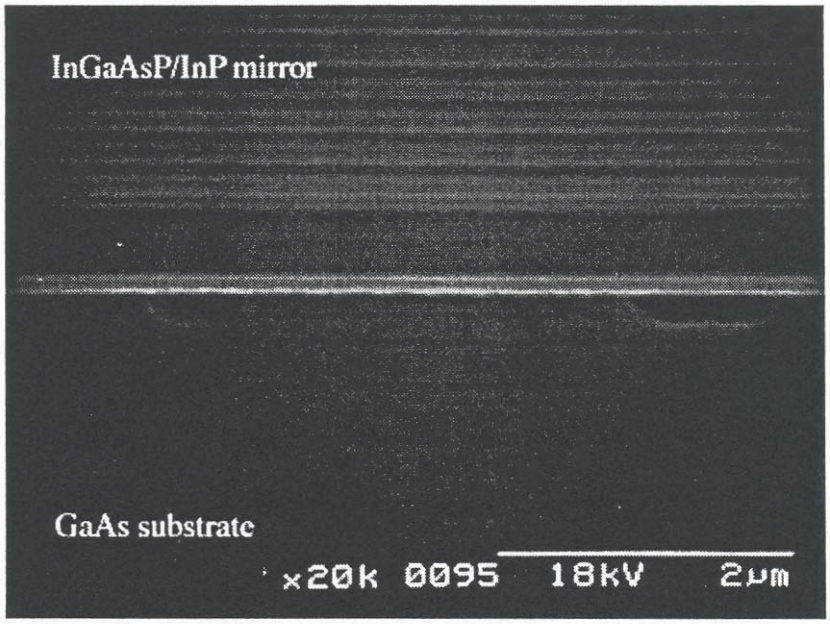


**Fig. 3.11**: Decorated μ-voids in a fused junction.

The use of channels (Section 3.1.5) has almost completely eliminated the problem of micro-voids. A sample that has been fused with channels will exhibit a perfect fused junction after stain etching, according to Fig. 3.10a. An scanning electron micrograph of a junction section with a channel and an adjacent fused junction is shown in Figure 3.12.

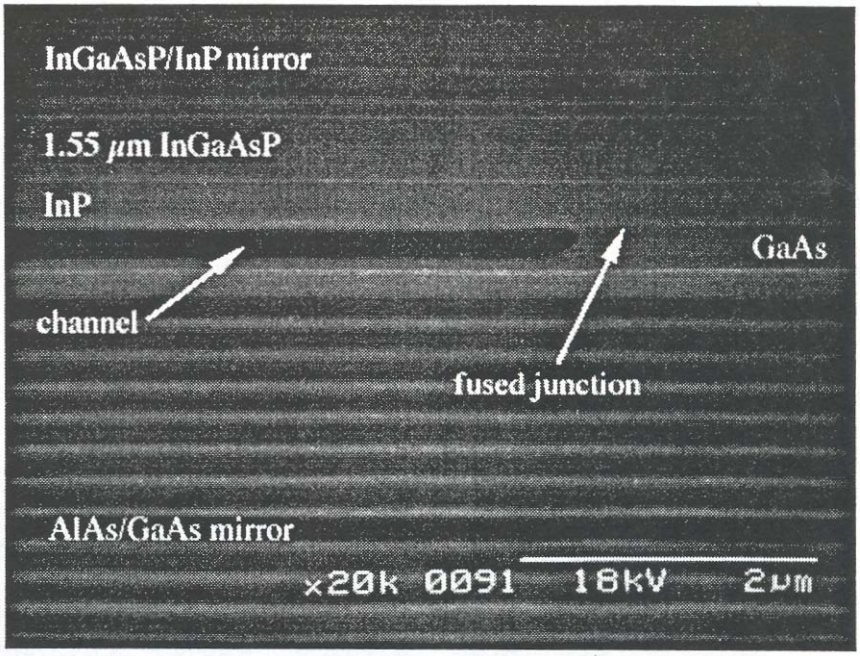


**Fig. 3.12**: Stain-etched fused junction with a channel and a well-fused section next to the channel.

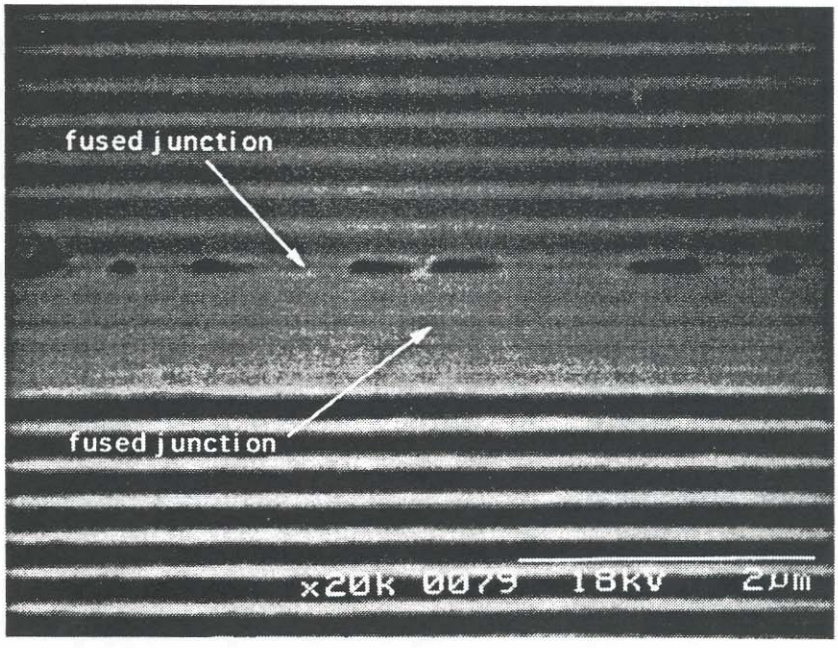


**Fig. 3.13**: Stain-etched double-fused vertical-cavity laser structure of a laser that did not operate due to poor fusion.

A similar comparison can be made in a double-fused structure shown in Figure 3.13 where the first fused junction (between the $n$-type mirror and the active layer) is complete, while the second junction (between the $p$-type mirror and the active layer) has a large debsity of voids. The device shown in Fig. 3.13 is did not lase at room temperature (F152). It has been also been observed that there is some difference in etch rates of $p$ and $n$ GaAs so the time necessary to stain $n$-type is bit longer (more than 120 sec).

In this work, the stain etching method has been intrumental in the development of the repeatble fusion process. The next steps in junction characterization are electrical conduton and optical obsorption.

### 3.2.2. *Auger electron spectroscopy*

Auger-electron spectroscopy (AES) characterization was performed on one failed fusion run. The two fused samples were bulk InP and multilayer GaAs growth, but the mating surfaces were InP and GaAs. The cause of failed fusion is not entirely clear, but the presence of carbon and oxygen at the surface of the samples after fusion indicates that hydrocarbon contamination and/or inadequate oxide removal is the probable cause. Figure 3.14 shows the photograph of the two substrates after they have been removed from the fusion furnace. The darker regions are pitted. The channels were etched only in the InP side.

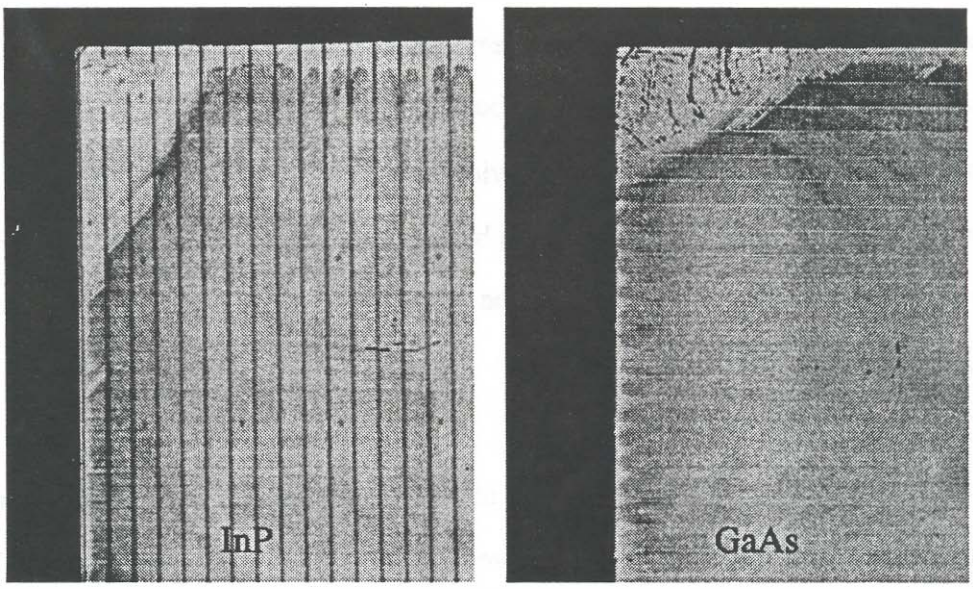


**Fig. 3.14**: Pitted surfaces of GaAs and InP after failed fusion. Channel pitch is 150 μm.

Auger electron spectroscopy was performed on both of these substrates. The samples were taken from the fusion setup directly into the Auger chamber. The AES spectra fro the two samples are shown in Figures 3.15 and 3.16. The visible peaks on the InP sample (Fig. 3.15) reveal the presence of indium, phosphorus, carbon, and oxygen. The latter two indicate that the fusion was probably prevented by carbon contamination and/or insufficient oxide removal before fusion. There exists a possibility that some of the carbon seen in the scan adhered to the surface while the samples were transferred from the fusion setup to the Auger system. However, similar transfers performed on other samples resulted in much smaller carbon peak intensities, and therefore it is believed that the carbon seen in these scans was present at the junction during the attempted fusion.

The AES scan from the GaAs sample is shown in Figure 3.16. Here the peaks show the presence of gallium, arsenic, carbon, and oxygen. Clearly, carbon and oxygen contaminated both surfaces. Interestingly, the phosphorus and indium peaks are also present on the GaAs sample. We believe that this is a confirmation of the postulated fusion reaction (Sec. 3.1.1.) in which, phosphorus desorbs from the surface of InP and adsorbs to both surfaces again during cooling. Meanwhile, mass transport enables indium to coat both surfaces.

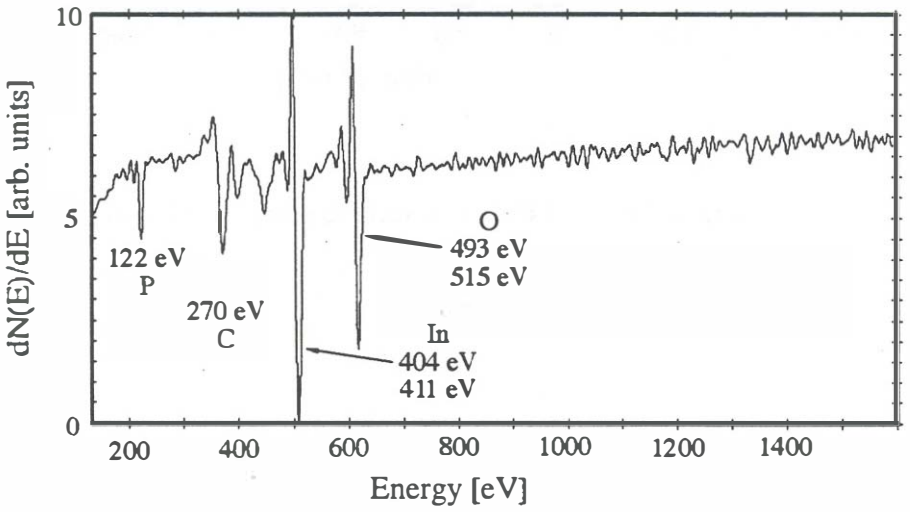


**Fig. 3.15**: AES of InP surface after failed fusion.

The failed fusion of this type, in which the entire sample remains not fused, is quite rare. For this to occur, the entire surface of the sample must be contaminated. Local contamination does not produce such results. In fact, it was observed that a large part of a 8 mm x 8 mm sample can be fused even if visible photoresist contamination exist at the sample edges. Nevertheless, through repeated fusion runs it is has been found

that surface preparation is the most important factor determining the quality of the fusion.

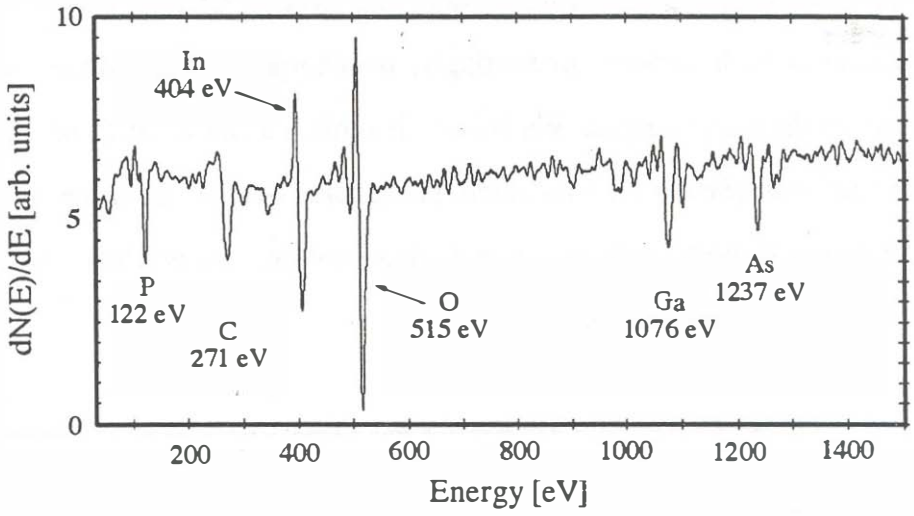


**Fig. 3.16**: AES of GaAs surface after failed fusion.

## 3.3. *Fusion uniformity*

### 3.3.1. *Large scale nonuniformity*

Both InP and GaAs are relatively soft semiconductors and will deform under pressure at elevated temperatures. The fused samples will conform to the surfaces of the fixture, and for this reason it is very important to make sure that the surfaces pressing the fused samples are very flat. In the experiments performed in this work, the GaAs sample often had a polished back side, while the InP was rough. The surfaces of the fixture that press on the samples are typically rough and leave marks on the back the fused samples. If the back surface of the sample is rough, it will be difficult to see any marks. However, if the wafer surface was previously polished (by the manufacturer), then the rough graphite surfaces leave marks on the back of the fused wafers. This is illustrated in Figure 3.17, where back surfaces of InP and GaAs are shown after the fusion (photographed using Nomarski interferometer).

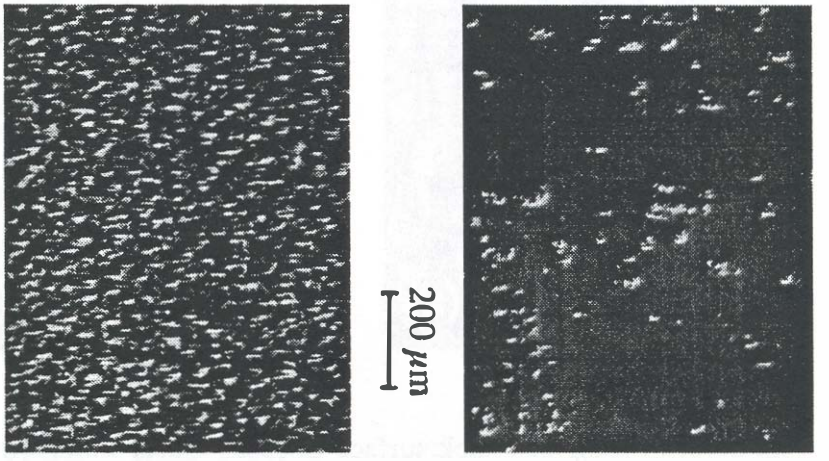


**Fig. 3.17**: Back surface of InP and GaAs after fusion.

One way of telling if this type of sample combination has fused uniformly over a large area is to look at the back of the polished GaAs wafer after fusion. The surface which was originally smooth has become rough and pitted in the places where the sample has fused. In the places where the pressure was not sufficient and fusion did not occur, the back surface of GaAs remained smooth. The comparison of the back GaAs surface for these two cases is shown in Figure 3.18. The two surfaces in this figure were photographed on the same sample which fused only on one side due to off-center pressure. The roughness shown in Fig 3.18(b) is of the same type as the one shown in Fig 3.17(b). The incomplete fusion of this sample was confirmed when the GaAs substrate was removed down to the etch-stop layer. As shown in Figure 3.19, the upper-right half of the sample the epilayers remained floating and disconnected from the InP substrate, while on the lower-left half the epilayers fused.

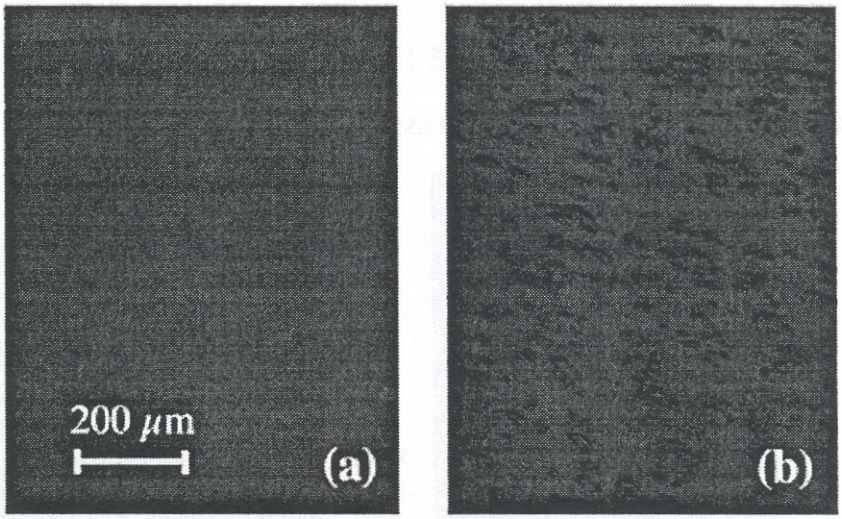


**Fig. 3.18**: (a) Polished back surface of fused GaAs wafer, (b) Back surface of GaAs wafer damaged by fixture pressure in the regions where the epilayers fused.

The uniformity of the pressure on the sample is very dependent on the sample size and the centering of the force. If a sample is too small it is very difficult to center the force and very often the edges or even whole sections of the sample will not fuse, as illustrated on a 3 mm x 5 mm sample in Figure 3.19. For this reason, the sample size is enlarged to the point where repeatable fusion of good uniformity could be performed. For our fixture, sample size of 8 mm x 8 mm was sufficient to give satisfactory results. Both of the samples to be fused are always cleaved to the same size, because it has been found in the course of this work and previously by (Dudley, 1994) that this improves the uniformity.

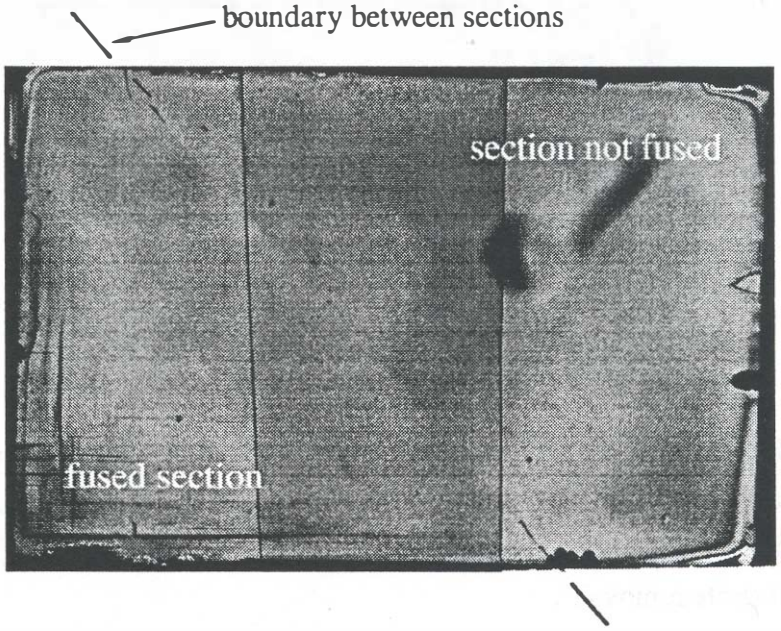


**Fig. 3.19**: Fused InGaAsP/InP epilayers after InP substrate removal. Due nonuniform pressure one half of the sample did not fuse. The sample size is 3 mm x 5 mm.

Perhaps the most stringent test of large scale uniformity is the fusion of the sample edges. This is the region where the fixture force is most likely to deviate from the desired value and produce poor or no fusion. Using a 8 mm x 8 mm sample in our process we were able to achieve uniform fusion to within 200 μm of the sample edges. An example of such fused surface is shown in Figures 3.20. The surface shown is the surface of InGaAsP fused to GaAs with the InP substrate removed, and most of the edge damage comes from undercutting during the substrate removal.

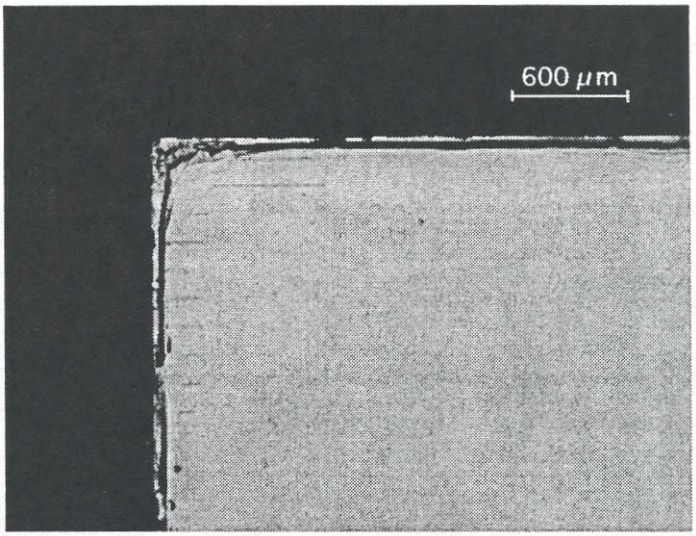


**Fig. 3.20**: A corner of a sample with InGaAsP epilayer fused to GaAs (InP substrate removed). The epilayers are fused almost to the edge. Most of the edge damage is attributed to undercutting during substrate removal.

### 3.3.2. *Surface flatness*

Fusion over nonuniformities in the epilayers reveal some of the mechanical aspects of wafer fusion. Figures 3.21 and 3.22 show examples of fusion over a semiconductor

dust particle that ended up trapped between the mating surfaces, while Figure 3.23 shows fusion over an oval defect. In both figures the bottom surface is an AlAs/GaAs quarter-wave mirror, while the top is an InGaAsP/InP quarter-wave mirror with a bulk active layer and a thick InP bonding layer.

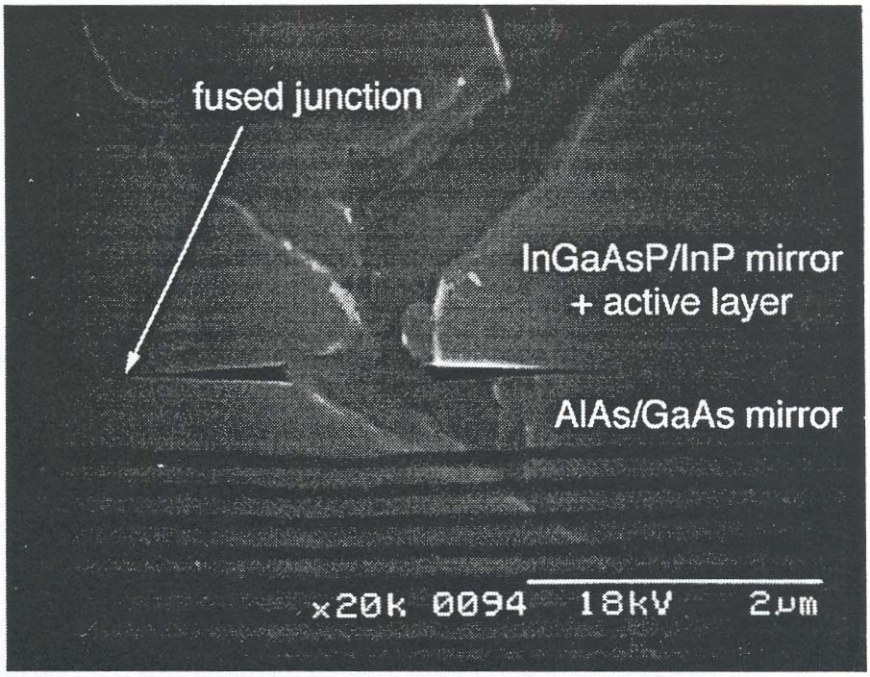


**Fig. 3.21**: Cleaved cross-section of a fused junction with a trapped semiconductor dust particle.

The trapped semiconductor dust particle has produced bowing in the fused epilayers and a void in the fused junction. It is visible from the "as-cleaved" (Figure 3.21), as well as the stain-etched (Figure 3.22) scanning electron micrograph that the ordinary cleaving plane has been disturbed by dislocations formed by the presence of this particle. It is also important to note that the sample has bowed locally, and that the bowing is present in both the InGaAsP/InP and AlAs/GaAs epilayers.

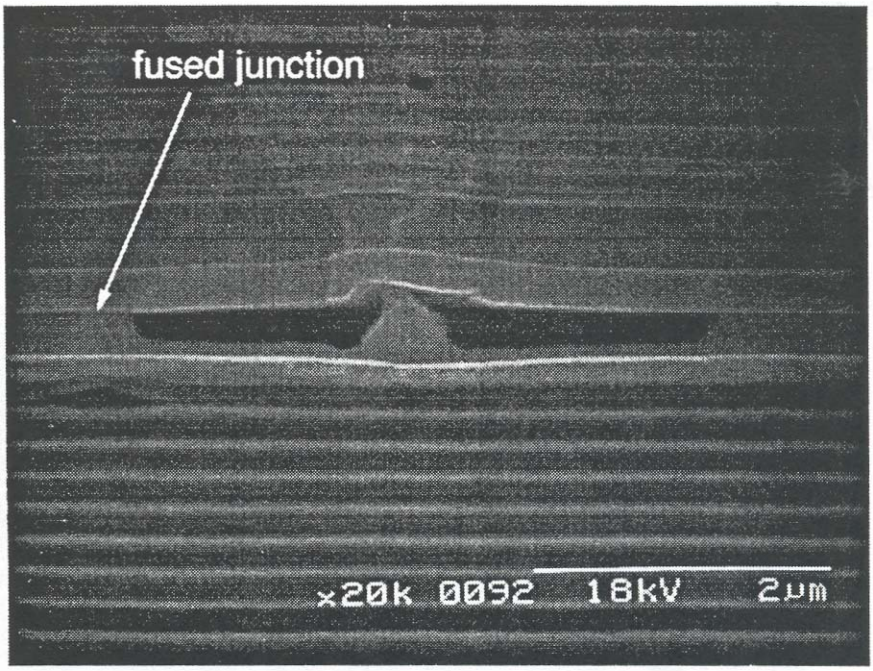


**Fig. 3.22**: Cleaved cross-section of a fused junction with a trapped semiconductor dust particle.

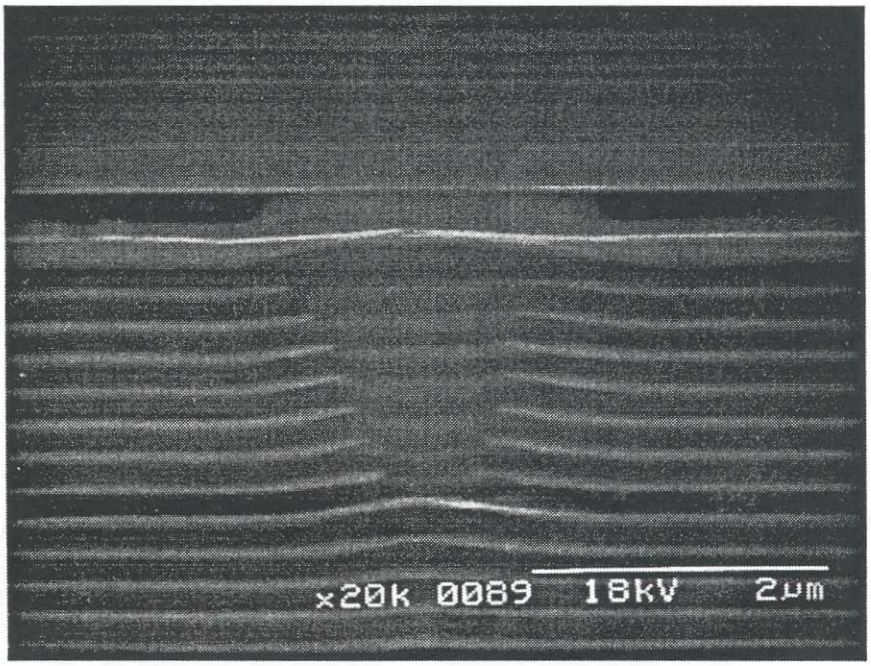


**Fig. 3.23**: Fusion over an oval defect appearing in the AlAs/GaAs mirror. The cleaved edge has been stain-etched.

The disturbance in the fused epilayer was not as pronounced in the fusion over an oval defect shown in Figure 3.23. Stain-etching was used to delineate the voids around both cases, indicating what portion of the area around the defect has not fused: Approximately 5 μm in Figure 3.21, and ≈10 μm in Figure 3.23. The high fusion pressure seems to be important for realization of continuous void-free fusion in the presence of defects. Inasmuch as both fused surfaces will be grown by some epitaxial growth technique for device fabrication the existence of the surface defects is unavoidable.

The InGaAsP/InP mirrors and active layers shown as fusion examples in this chapter were grown by K. Streubel for the single-fused all-epitaxial VCL structure discussed in Section 8.3.

## 3.4. *Conclusions*

In the course of this work, wafer fusion was approached more from the applied and technological perspective rather than from an academic standpoint. This chapter illustrated several practical problems and methods of solution that have brought fusion to sufficient quality to fabricate working vertical-cavity lasers. However, numerous questions remain and need to be investigated in the future. Some of the issues that need to be investigated in the future are listed below.

As set of standard tests should be introduced for characterizing the quality of fused junctions. In this work the standard tests were visual inspection of the fused epilayers and stain-etching of the cleaved fused junction. For applications in optoelectronics the most critical tests involve voltage-current characteristics, carrier recombination and light absorption. Once a set of standard test is established, the process has to be characterized from the standpoint of cleaning procedure, and fusion temperature and time. The time and temperatures of fusion has not been varied in this work, hence questions remain whether the conditions used were optimal. Furthermore, the cleaning procedure and oxide removal has been found to have a deciding influence on the quality of fusion and voltage characteristics. The surface preparation directly determines the type of bonds and contaminants that will be present at the junction. A number of voltage-current measurements through fused junctions have been performed, but no consistent model and junction character has been established.

The most important electrical characterization that should be performed are current-voltage and capacitance-voltage measurements. Both of these methods should be

performed as a function temperature (if possible) to help identify the presence of any potential barriers, surface charges, and most importantly if there is a consistent value of a heterojunction band offset between GaAs and InP. Carrier recombination should be investigated by forward bias voltage-current characteristics and deep-level transient spectroscopy of fused junctions. Optical absorption and scattering is probably very weak at fused junctions, but even very small absorption influences the operation of a vertical-cavity laser. The fused junction absorption can be measured using in-plane waveguides of different length that include fused junctions. The influence of sample orientation on the electrical properties of the junctions is yet to be understood. Finally, one must develop large area fusion to be able to make wafer fusion a manufacturable process.

Chapter 4

# Laser design

The double-fused laser structure offers the possibly of fabricating a great variety of vertical-cavity laser structures that have already been explored for GaAs-based vertical-cavity lasers. By performing two wafer fusion steps and placing two Al(Ga)As/GaAs quarter-wave mirrors on both sides of the InGaAsP active layer, we have in fact created a new epilayer structure which now can be processed in any number of ways used in GaAs VCLs: isolating implantation, reactive ion etching or Zn-diffusion (disordering). To demonstrate the concept and fabricate working VCLs, only the simplest index-guided post structure was fabricated.

The design of double-fused vertical-cavity lasers is described in two parts: We first discuss the issues related to the design of the active layers, and then the quarter-wave mirrors. Special attention has been paid to the design of the $p$-type mirrors since it was found that absorption in extrinsic $p$-GaAs is quite high at long wavelengths.

Prior to this work, the there had been very limited data and few consistent results on 1.55 μm vertical-cavity lasers. The devices reported varied in structure and choice of material, but the task was clear: One had to minimize the cavity losses, and the

electrical and the thermal resistances. In addition, one also had to investigate such structures that would produce working lasers without exhausting every possible design parameter. The philosophy underlying this work was to fabricate a *robust* room-temperature continuous-wave operating 1.55 μm VCL. The *robustness* refers to the simplicity of the design and the fabrication, but primarily to the large freedom in the design parameter space left for future improvements. The room-temperature operating 1.55 μm double-fused vertical-cavity lasers reported in this work use a single mask process and are tested without any special heat-sinking schemes. Plenty of room for improvement has been left in the optical, electrical and especially thermal performance of these lasers. Some of the techniques and structures that promise to improve these devices will be described in Chapter 8.

## 4.1. *The double-fused vertical-cavity laser generations*

The double-fused vertical-cavity laser structure, shown in Fig. 1.2, consists of two MBE-grown quarter-wave mirrors and an MOCVD-grown InGaAsP active layer sandwiched between them. In the course of this work, a number of runs with similar structures have been fabricated. Several different mirror combinations and two different quantum-well active layers were used. Table 4.1 summarizes the double-fused vertical-cavity lasers runs. This chapter first discusses the cavity design (active layer structure and the adjustments to cavity length for correct mode position), quarter-wave mirror design (primarily the optimization of the resistance and the reflectivity of *p*-type mirrors), and discusses the conditions for room-temperature continuous-wave operation of these structures.

| GEN | Run# | Proc. | n-mirror | active | p-mirror | operation | $\lambda$[nm] |
|---|---|---|---|---|---|---|---|
| 1 | F123 | P227 | S201 | KS2290‡ | S207† | RT-pulsed | 1515 |
| | F125 | | | | | RT-pulsed | 1522 |
| | F126 | | S230 | | | RT-pulsed | 1508 |
| | F132 | P236 | S201 | | | RT-pulsed | 1517 |
| | F133 | | | | | RT-pulsed | |
| 2 | F139 | P250 | | | S250†† | RT-pulsed | — |
| | F150 | P260 | | | | NO | — |
| | F151 | | | | | NO | — |
| | F160 | P278 | S276 | | | NO | — |
| | F166 | P283 | S276 | | | RT-pulsed | 1549 |
| | F167 | | S201 | | | RT-pulsed | 1532 |
| 3 | F170 | P290 | S276 | KS2778‡‡ | | RT-CW | 1542 |
| | F171 | P290 | S276 | KS2781‡‡ | | RT-CW | 1558 |

**Table 4.1**: A summary of double-fused vertical-cavity lasers fabricated in the course of this development.

†S207: *p*-AlAs/GaAs linear grading, pulse doping

††S250: *p*-AlGaAs/GaAs parabolic grading, flat-band engineered

‡KS2290: Active layer with separate confinement regions.

‡‡KS2778/81: Active layer without separate confinement regions.

## 4.2. *Active layer*

During the development of vertical-cavity lasers at UC Santa Barbara, various active layer structures were investigated. The first room-temperature pulsed operation at 1.3 μm was obtained using a 600 nm thick InGaAsP active layer (Wada, 1991), while the first wafer fused 1.3 μm vertical-cavity laser used a 300 nm thick bulk InGaAsP active layer (Dudley, 1994). The first wafer fused 1.55 μm VCL structures that operated by optical pumping were also fabricated using bulk InGaAsP active layer (Babić, 1994). There have also been numerous attempts to fabricate electrically pumped VCL structure with unstrained and strained quantum-well active layers, grown both at the Royal Institute of Technology (KTH) in Stockholm and at University of California at Santa Barbara. The first success with electrically pumped devices was obtained using low doped *p*-mirrors and strain-compensated InGaAsP quantum-well active layers grown at KTH. All of the active layers described in this work were grown at KTH.

The general structure of an InP grown active layer for use in a double-fused laser consists of an active region (quantum well or bulk) embedded in an InP cladding. The InP cladding layers are fused to the top-most GaAs layer of the Al(Ga)As/GaAs mirrors. It is possible to realize fusion between (In,Ga)(As,P) alloys and GaAs, but in this work, the fusion was always performed between InP and GaAs. The lasers described in this work use two different strain-compensated active layer structures. They are shown in Figures 4.1 and 4.2. In both cases the active layer had 7 compressively strained quantum wells and 6 strain-compensating barriers. The structures are different in two ways: In structure *A*, the quantum-wells are

surrounded by 183 nm thick 1.3-μm InGaAsP separate confinement layers, while in structure *B* the InP claddings extend all the way to the wells. Furthermore, the structure *A* was grown with the *p*-side down (the *p*-doped layers were grown before the *n*-doped layers). This is particularly difficult in MOCVD due to Zn segregation (zinc floats to the surface) and requires a difficult calibration procedure. Structure *B* was grown with the *n*-doped layers first.

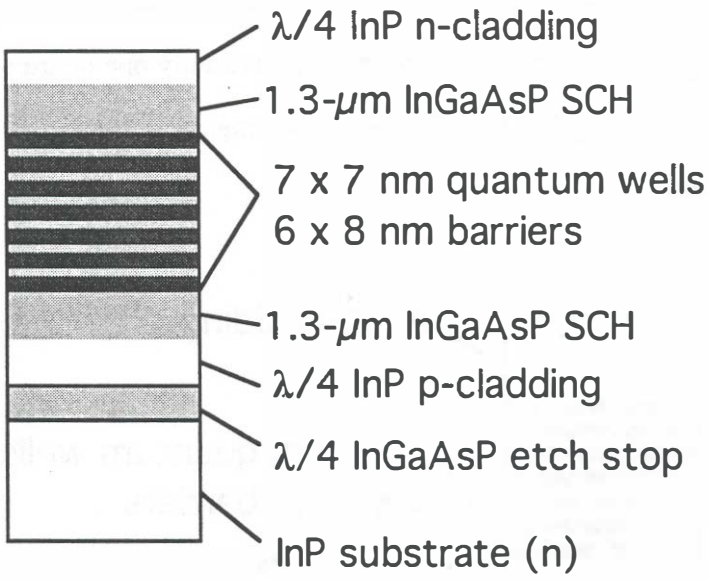


**Fig. 4.1**: Structure A; active layer design with the 1.3 μm InGaAsP separate confinement regions.

The reason structure *A* was grown *p*-side down was that this active layer was originally intended for a single-fused proton implanted VCL. The structure of this laser would be very similar to the single-fused structure shown in Figure E.4, but with current confinement realized with proton implantation in the top *p*-type cladding. It is well known fact that hydrogen forms a complex with Zn (or Be) in GaAs and InP

and that forming insulating layers in $p$-type is easier than in $n$-type InP. Since the semi-insulating layers created by hydrogen implantation are also known to redistribute and anneal out at elevated temperatures, the implantation had to be performed after wafer fusion. High reflectivity of the fused mirror would be ensured by using an $n$-type rather than $p$-type AlAs/GaAs bottom mirror.

In addition to the plans for fabricating an implanted VCL, the active layer also incorporated a structural adjustment for a double fused device. This involved making the etch-stop / contact layer (1.42-μm InGaAsP) exactly one quarter-wavelength thick at 1550 nm. This fact has later become instrumental for double-fused laser cavity resonance tuning.

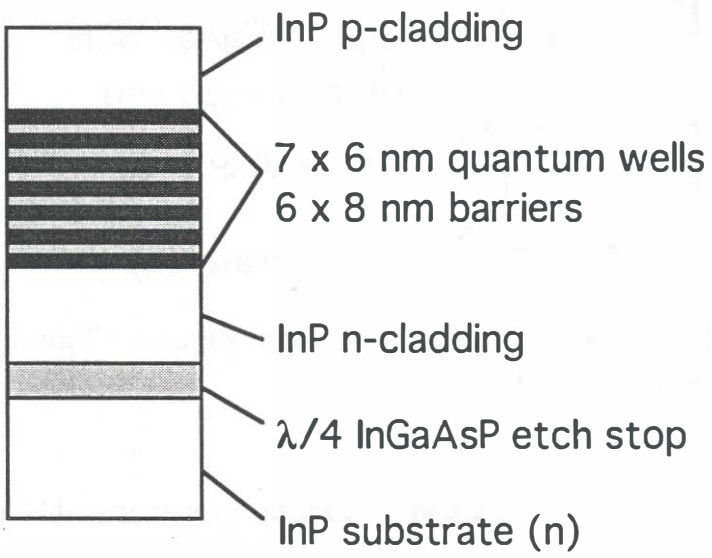


**Fig. 4.2**: Structure *B*; improved active layer design without the separate confinement regions.

| KS2290 | | | | |
|---|---|---|---|---|
| material | comment | doping | Thickness | |
| InP cladding | $\lambda/4$ | $N_D = 5 \cdot 10^{18}$ cm$^{-3}$ | 122.2 nm | |
| Q(1.3μm) | | $N_D = 5 \cdot 10^{18}$ cm$^{-3}$ | 183.6 nm | |
| InGaAsP | +1% cs | undoped | 7 nm | |
| InGaAsP | -0.9% ts | undoped | 8 nm | 6 x |
| InGaAsP | +1% cs | undoped | 7 nm | |
| Q(1.3μm) | | $N_A = 2 \cdot 10^{17}$ cm$^{-3}$ | 183.6 nm | |
| InP cladding | $\lambda/4$ | $N_A = 3 \cdot 10^{18}$ cm$^{-3}$ | 122.2 nm | |
| Q(1.42μm) | $\lambda/4$ | $N_A = 3 \cdot 10^{18}$ cm$^{-3}$ | 114.6 nm | |
| InP buffer | | $N_A = 3 \cdot 10^{18}$ cm$^{-3}$ | 200 nm | |
| InP substrate | | n-type | | |

**Table 4.2**: The layer structure of KS2290 active layer (*A*).

Four different active layers were characterized for use in double-fused vertical-cavity lasers: One with separate confinement regions – structure *A* (wafer KS2290), and three without the separate confinement layers - structure *B* (KS2777, KS2778, KS2781). Most of the results and the upcoming discussions are based only on the results from two wafers: KS2290 and KS2778. The nominal thicknesses and doping levels of these two epilayers are shown in Table 4.2 and 4.3. The wells were grown under constant As/P ratio, and it is believed that it was this fact that kept the wells from disordering during the extended high temperature processing (wafer fusion). There have been indications that strain-compensated quantum wells cannot be used in conjunction with wafer fusion, i.e. direct bonding at temperatures above 600°C

(Chua, 1994), but the strain-compensated wells in question were not grown under the constant As/P ratio.

| KS2778 | | | | |
|---|---|---|---|---|
| material | comment | doping | Thickness | |
| InP cladding | | $N_A = 1 \cdot 10^{18}\,cm^{-3}$ | 217 nm | |
| InP cladding | | undoped | | |
| InGaAsP (qw) | +1% cs | undoped | 6 nm | |
| InGaAsP (bar) | -0.9% ts | undoped | 8 nm | 6 x |
| InGaAsP (qw) | +1% cs | undoped | 6 nm | |
| InP cladding | | $N_D = 5 \cdot 10^{18}\,cm^{-3}$ | 313.8 nm | |
| Q(1.42μm) | $\lambda/4$ | $N_D = 5 \cdot 10^{18}\,cm^{-3}$ | 114.6 nm | |
| InP buffer | | $N_D = 5 \cdot 10^{18}\,cm^{-3}$ | 200 nm | |
| InP substrate | | n-type | | |

**Table 4.3**: The layer structure of KS2778 active layer (*B*).

The room-temperature photoluminescence spectra on all of these samples was obtained using a 790 nm pump laser. The data is shown in Figure 4.3. The photoluminescence intensity of structure *B* epilayers was stronger than that of structure *A*. In both designs, the quantum wells are located at least 200 nm from the fused junctions (Ram, 1995) and the fused junctions are located in regions where majority carrier flow dominates. Therefore, we do not expect to be adversely affected by possible minority carrier recombination at the fused junctions.

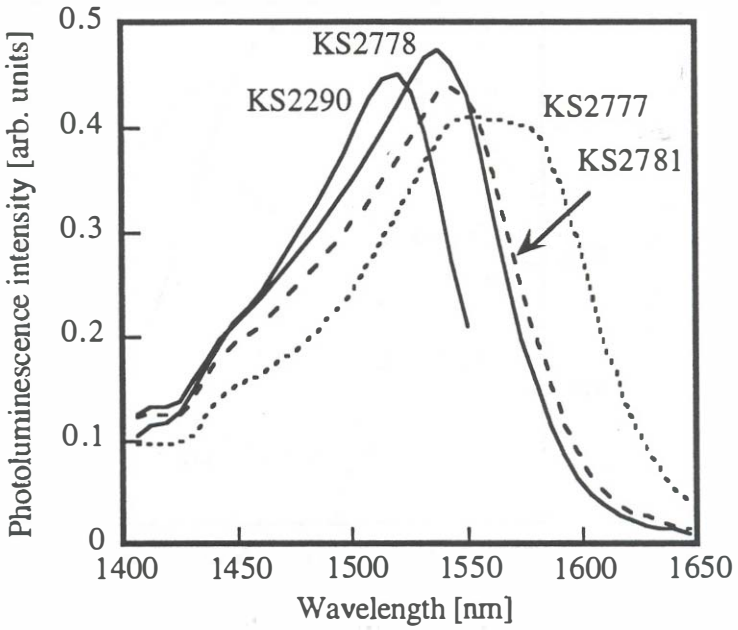


**Fig. 4.3**: The room-temperature photoluminescence spectra of four active layers used in this work.

The main reason for going from structure *A* to *B* was to improve the high-temperature performance of the lasers. In structure *A* the barriers and the separate confinement were approximately of the same composition, letting carriers flow into the separate confinement regions and recombining there. The results discussed in Chapter 7 indicate that this decreased the internal quantum efficiency at elevated temperatures. The elimination of the lower bandgap separate confinement regions and their replacement with large bandgap InP has reduced this leakage. Furthermore, the structure *B* was grown with the *n*-side down, thereby reducing Zn diffusion during the growth and subsequent fusion steps.

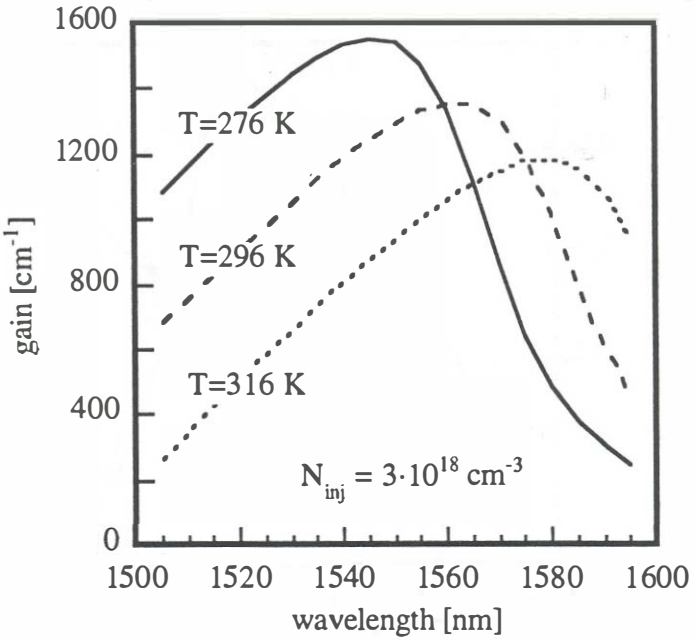


**Fig. 4.4**: Calculated gain as a function of the wavelength for three temperatures, at a constant injection level (Piprek, 1995).

The calculation of gain in strain-compensated wells for these structures was performed by Dr. Joachim Piprek from University of Delaware (Piprek, 1995). The peak gain position has been made to fit the photoluminescence spectra by adjusting the well thickness. More discussion on this topic will be presented in Chapter 7. Figure 4.4 and 4.5 show a summary of gain calculations with 4.75 nm $In_{0.76}Ga_{0.24}As_{0.82}P_{0.18}$ (KS2778). The approximate fits to the calculated gain curves are given by the following relations. The transparency current density is

$$J_{tr}(T) = 76.6 \exp\left(\frac{T-300}{63.8}\right) \ [\mathrm{A/cm^2}] \qquad (4\text{-}1)$$

where the temperature is in degrees Kelvin. The maximum gain at a given current density per well is then given by

$$g(J,T) = 846 \ln\left(\frac{J}{J_{tr}(T)}\right) \quad [\mathrm{cm}^{-1}] \tag{4-2}$$

The wavelength variation of the gain is given by a third-order polynomial fit

$$g(J,T,\lambda) = g(J,T) + 2.66 \cdot \Delta\lambda - 0.247 \cdot \Delta\lambda^2 - 0.00171 \cdot \Delta\lambda^3 \ [\mathrm{cm}^{-1}] \tag{4-3}$$

with $\Delta\lambda = \lambda - 1564$ [nm]. In Chapter 7 these relations are compared to the measured gain-current relationship.

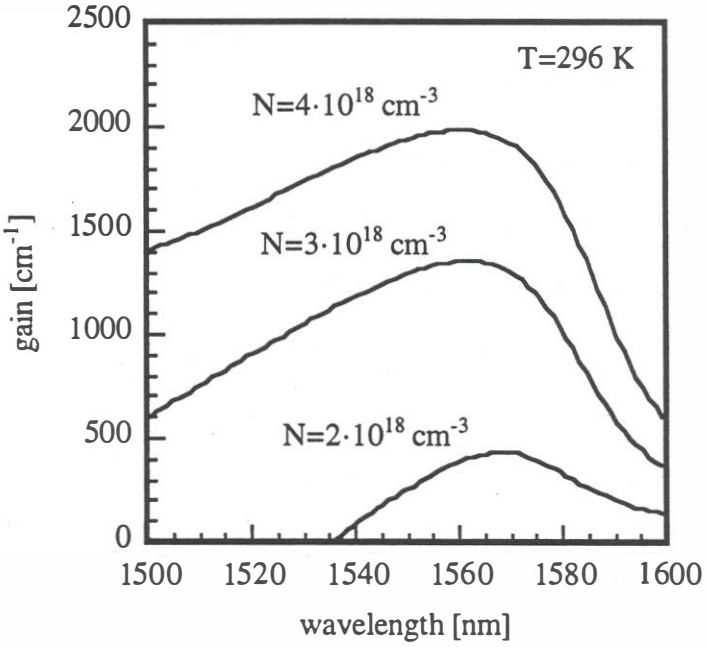


**Fig. 4.5**: Calculated gain as a function of the wavelength for three temperatures at a constant injection level (Piprek, 1995).

The gain spectrum decreases and shifts towards longer wavelengths with increasing temperature, and consequently the threshold current of any semiconductor laser changes with temperature. In vertical-cavity lasers the threshold current dependence on temperature may exhibit a minimum at a some temperature. The parameter that is

most interesting for continuous-wave operating lasers is the rate at which the threshold current changes around and immediately above room temperature. This rate is suitably expressed by the *local characteristic temperature* $T_0$ defined as

$$T_0(T) = dT/d\ln(I_{th}). \qquad (4\text{-}4)$$

evaluated at 300 K. Therefore, the $T_0$ values quoted for vertical-cavity lasers in this work are always $T_0 = dT/d\ln I_{th}|_{T=300\,\mathrm{K}}$.

## 4.3. *Cavity optical length*

### 4.3.1. *Mode adjustment issues*

Given a finished active layer structure, the most important task is to adjust the cavity mode to the right wavelength through two wafer fusion processes. The cavity mode has to be located in the region of highest reflectivity to provide lowest threshold gain and it also has to be placed strategically relative to the gain peak position. It has to appear at the long wavelength side of the gain peak since the gain spectra shift towards longer wavelengths as the device heats up. Heating of the active layer is unavoidable in electrically pumped devices and one must account for this effect when real devices are fabricated. Inasmuch as the gain peak shifts at a rate of about 0.4 nm/°C, a moderate temperature difference of 30°C degrees between the active layer and the heatsink will produce a shift of 12 nm.

There are two factors that influence the mode position: The phase properties of the mirrors and the cavity length. The phase properties of the mirrors can be altered by either changing the center wavelength of the mirror or by changing the ratio of the refractive indexes. Neither of these two methods is as efficient as changing the overall cavity optical length by adding or subtracting some cavity thickness. Therefore, most attention was paid to the adjustment of the optical cavity length.

As it will be shown in this section, the optical thicknesses of all of the active layers used in this work were always slightly shorter than required for a mode position at 1550 nm. In order to shift the cavity mode to the desired wavelength, one had to add

some optical thickness to the mirrors. The first designs (generation 1) did not have any such cavity correction. To adjust the mode in this generation of devices, we took advantage of the variation in the optical thicknesses around the MOCVD and the MBE grown wafers. However, this did not always work out completely, as it can be seen from Table 4.1, where all of these lasers operated at wavelengths that are shorter than 1550 by 25-40 nm. In the later generations of lasers the mode adjustment was performed by specially designing the mirrors. Since the AlAs/GaAs mirrors were grown in-house, modifying the mirror design to adjust the cavity length was the easiest way to adjust the mode position. To exactly determine by how much optical length the cavity should be adjusted one has to measure the cavity optical length. This procedure is described in the next section.

4.3.2. *Measurement of the free-standing-cavity resonance*

Since the double-fused laser cavity is to be built from three separate parts, one has the opportunity to characterize the optical properties of all three parts independently. The mirrors are being characterized by measuring the reflectivity spectra, while the cavity is characterized by measuring its optical length.

In the final double-fused structure, the AlAs/GaAs mirrors will be fused to the two InP cladding layers. To be able to predict the double-fused cavity resonance one must know the phase properties of the two mirrors and the optical length of the cavity in the desired range of wavelengths. The phase properties of the mirrors are determined by fitting calculated to measured reflectivity spectra (fitting the center wavelength, refractive index, and the number of layers). The optical length of the cavity is

determined by measuring the *free-standing cavity* resonance. By free-standing cavity we mean a cavity without the distributed mirrors (and their complicated phase relationship). In our case, a free-standing cavity would be realized by replacing the AlAs/GaAs mirrors with ideal hard mirrors that have equal peak reflectivity and phase $\pi$. (When the Al(Ga)As/GaAs mirrors are tuned exactly to the resonance, their phase, looking from the inside the cavity, is exactly equal to $\pi$). This also ensures that the standing wave pattern has a null at the fused junction. A simplified view of this standing-wave pattern is shown with the case (a) of Fig. 4.6. The approximate length of the free-standing cavity is $3\lambda/2$.

To perform the free-standing cavity resonance measurements, we mount the epilayers on a glass slide using a transparent wax, and remove the substrate and the etch-stop layers from the active layers (*A* and *B*) using wet chemical etching (Sec. 5.1.2). The cavity is now formed by the one InP-to-air and one InP-to-wax reflection which dominate the other reflections in the cavity. The resonant standing-wave pattern of this cavity, illustrated with the case (b) of Fig. 4.6, is a complement of the pattern that is present at the double-fused laser resonance. This occurs because the phases of the mirrors are opposite: The air-InP reflection have phase zero, while the AlAs/GaAs mirror have phase $\pi$. The active layer is now located at the node of the standing wave pattern. To apply the measurement method correctly we need to investigate the relationship between the resonances of the two cases.

Consider now an ideal symmetric cavity with two mirrors that both have the reflection phase either zero of $\pi$ seen from the inside the cavity, as shown in Fig. 4.6. By symmetric cavity we mean a cavity in which the two mirrors are identical. No

generality is lost by using a symmetric cavity for simplicity. Assume also that the cavity is uniform, namely, that the gain region, indicated by shaded areas in Fig. 4.6, has the same optical properties as the rest of the cavity. At resonance, the round trip phase is an integer multiple of $2\pi$. Consequently, the standing wave pattern inside the cavity is always symmetric regardless of the direction of the incident beam. The standing wave pattern changes into its complement when the mirror reflectivity changes from $\pi$, case (a), to zero, case (b). We shall refer to case (a) as the original cavity and to the case (b) as the complementary cavity.

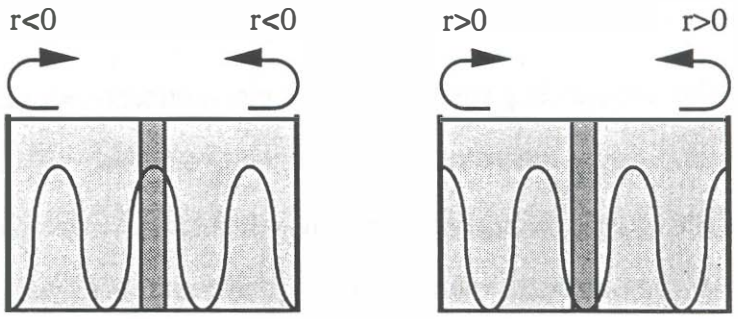


**Fig. 4.6**: Standing-wave patters for two symmetric $3\lambda/2$ cavities at resonance with different reflection phases at the mirrors.

It is a straightforward task to show that the resonance wavelength for cases (a) and (b) are identical. This is exactly true as long as there are no reflections at the gain medium. If we include the reflections on the active layer, these spurious reflections will interfere with the reflections from the cavity mirrors and slightly change the resonance wavelength. It is important to note that the contribution to the shift of the resonance wavelength changes in sign when the mirror reflectivity changes phase from zero to $\pi$. The contributions are generally different in magnitude, but are equal

for a symmetric resonator. The result of this consideration is that the measurement of free-standing cavity resonance using structure (b), which is what we can easily perform, only approximates the resonance of structure (a), which is the true free-standing cavity resonance. Fortunately, the difference between the resonances can be easily estimated by performing an exact calculation using transfer matrix calculation.

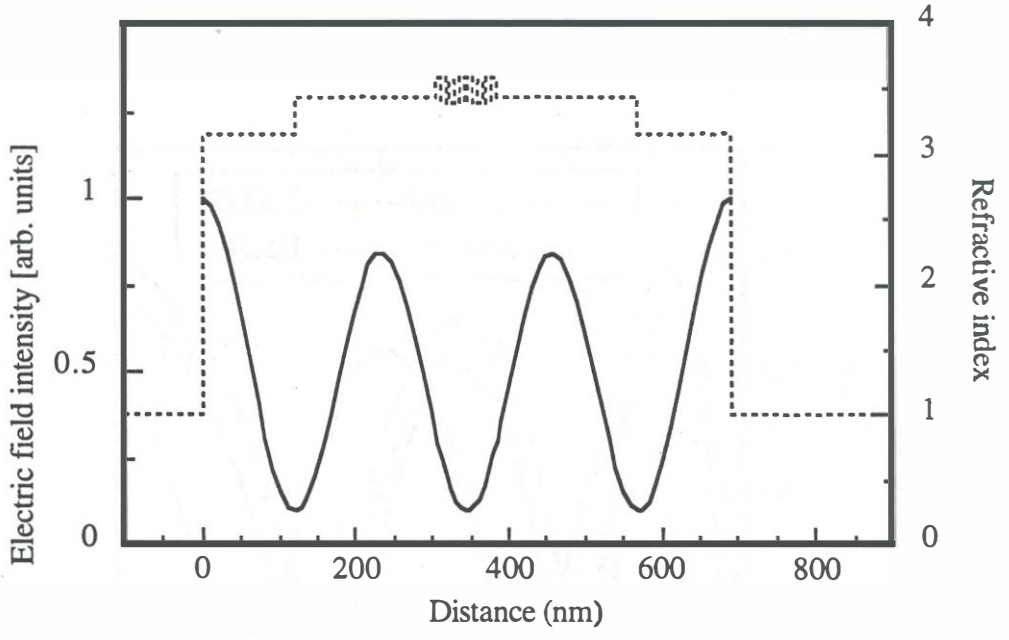


**Fig. 4.7**: Standing wave pattern in the KS2290 cavity surrounded by air (wax). The cavity is approximately $3\lambda/2$ long, and the gain region is located at the node of the standing wave pattern.

Two measurements of reflectance are performed on all active layers used in this work: One with the etch-stop layer present and one with etch-stop layer removed. The reflectivity spectra measurement performed without the etch-stop layer yields the free-standing-cavity resonance of the complementary cavity. The cavity has a thickness of approximately $3\lambda/2$. The standing-wave pattern inside the KS2290 active layer is

illustrated in Fig. 4.7. The reflectance measurements on all of the epilayers used in this work are shown in Figure 4.8. It is evident that all of the free-cavity resonance wavelengths are short. The KS2290 sample has a free-cavity resonance at 1456 nm, while the rest of the samples have their resonances at 1357 nm, 1380 nm, and 1385 nm (KS2778, KS2777 and KS2781). This information is sufficient to get an estimate on the corrections necessary to bring the fused-cavity resonance to the neighborhood of 1550 nm.

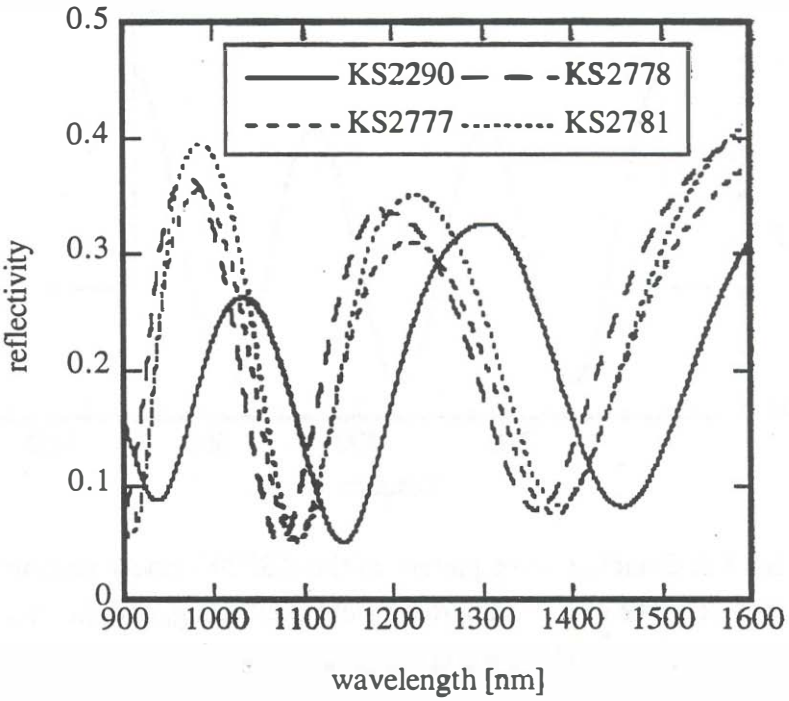


**Fig. 4.8**: Reflectance spectra measured on the free-standing cavities of all active layers: KS2290, KS2777, KS2778 and KS2781.

The first parameter that needs to be determined is magnitude of the difference between the resonance wavelength of the original and the complementary cavities. An exact calculation using the approximate cavity thickness and refractive indexes shows that

the free-standing cavity resonance of the original cavity is approximately 30 nm longer than the complementary cavity. In our case, the measured free-cavity resonances are much shorter than the desired resonance (1550 nm) and this correction is easily included. Furthermore, the error introduced by not knowing the exact values of the corrections is significantly smaller than the variation in the optical thickness of the epilayer around the wafer.

If the free-cavity resonance of the complementary cavity is denoted by $\lambda_{free}$, then the effective optical length of the original cavity can be found from $D_{free} = 3(\lambda_{free} + \Delta\lambda_{corr})/2$, where $\Delta\lambda_{corr} \approx 30\text{nm}$. Assuming that the AlAs/GaAs mirror will be tuned exactly to 1550 nm, we can shift the double-fused cavity resonance to 1550 nm if we adjust the optical length of the cavity to $D_{DF} = 3\lambda_{DF}/2$, where $\lambda_{DF} = 1550\text{nm}$. The difference in the optical length will be realized as extra GaAs layers on top of one or both GaAs mirrors. The necessary thickness of GaAs can be calculated from

$$d_{GaAs} = 3(\lambda_{DF} - \lambda_{free} - \Delta\lambda_{corr})/2n_{GaAs} \qquad (4\text{-}5)$$

For the four different epilayers (KS2290, KS2778, KS2777, and KS2781) these thicknesses are respectively, 29 nm, 73 nm, 63 nm, and 60 nm. It appears from here that resonance wavelength of the generation 1 and 2 devices can be corrected by adding an extra 30 nm of GaAs to the mirrors, while for generation 3 devices the added thickness of GaAs should be at least 60 nm. For this reason the S250 $p$-mirror (described in the next section) had been designed with an extra 30 nm of GaAs on top, while the S276 $n$-mirror had an extra 50 nm of GaAs on top. The thickness on top of the $n$-mirror was increased from the required 30 nm to accommodate the

variation of the thickness across the wafers. It is always possible to reduce the extra optical thickness by etching, while it is much more difficult to resolve a problem of a too short cavity.

These corrections worked reasonably well on the generation 2 and 3 devices. As shown in Table 4.1, in device F167 the cavity length was short in spite of the extra corrections, while F166 was matched well. The F166 device (KS2290 active layer) uses the S276 mirror with the extra 50 nm of GaAs, but still lases at 1549 nm. The reason for this is that the 50 nm GaAs layer on top of the S276 mirror has been partly etched off before fusion (approximately 30 nm). The mode adjustment worked best on the generation 3 devices, where the total added thickness equaled approximately 80 nm (30 nm on S250 and 50 nm on S276). The lasing wavelengths of F170 and F171 are within several nanometers of 1550 nm. the discrepancies are a result of the optical thickness variation across the wafer.

We now turn to the reflectivity measurement with the etch-stop layer present. Consider the cavity (b) shown in Fig. 4.9 in which we keep the wavelength unchanged, but shorten or elongate the cavity by an odd integer of quarter-wavelengths at the free-cavity resonance. This in principle describes the case of the active layer from which the etch stop (one quarter-wave) has not yet been removed. The cavity is now at anti-resonance and, as shown in Fig. 4.9, the standing-wave pattern depends on the direction of the incident beam.

If the added cavity thickness (etch-stop layer) is exactly an odd integer multiple of quarter-wavelengths thick, the resonance of the original cavity and the anti-resonance

of this modified cavity should coincide exactly. By performing this measurement, we can determine if the etch-stop layer is indeed one quarter-wavelength thick. In all of our active layers, this condition is approximately satisfied, as illustrated in Figure 4.10 where both measurements (with and without the etch-stop layer) are plotted for the KS2778 sample. Therefore, the etch-stop layer thickness is approximately equal to a quarter-wavelength at 1550 nm.

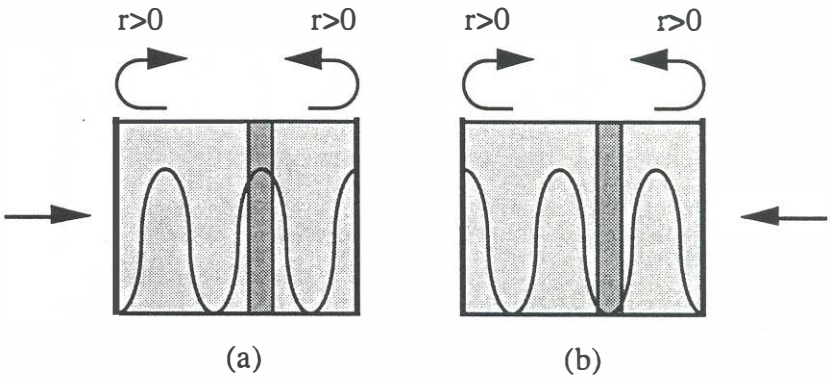


**Fig. 4.9**: Standing-wave patters for a symmetric cavity at anti-resonance with beams incident from different directions. This cavity was obtained by reducing the Fig. 4.6 case (b) cavity length by one quarter wavelength and keeping the same frequency.

Using the free-standing-cavity resonance measurement, we were able estimate the corrections to the cavity optical thickness necessary to bring the lasing wavelength to the desired wavelength, and also to check the optical thickness of the etch-stop layer. The described method for checking the cavity resonance is not the only method for mode adjustment used in this work. Another set of reflectivity measurements is performed during the fabrication: One after the first and one after the second fusion steps. The quarter-wave optical thickness of the etch-stop layer is needed to be able to

estimate the cavity resonance from these in-process reflectivity measurements of the cavity resonances. These measurements are described in Sec. 5.1.3.

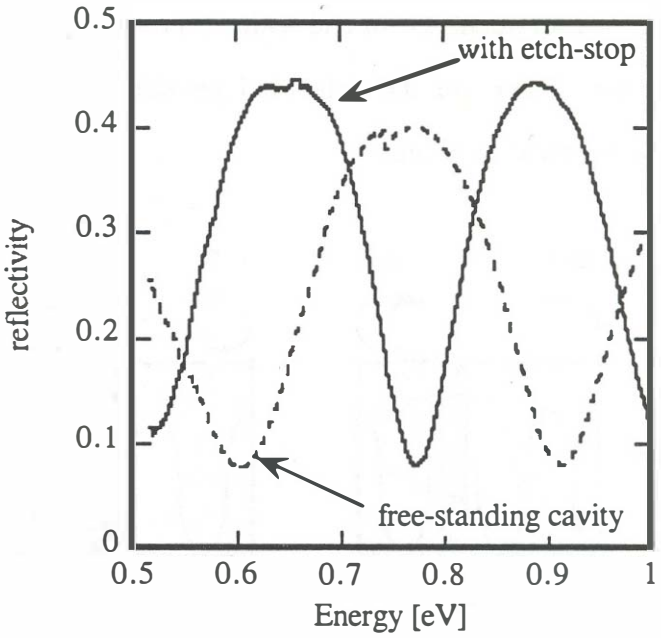


**Fig. 4.10**: Reflectance spectra measured on KS2778 with and without the etch-stop layer. The graphs was plotted vs. energy to reveal linear dependence of the reflection spectra on frequency.

4.3.3. *Standing-wave patterns*

Figures 4.11 and 4.12 show the calculated standing wave patterns in devices of generation 1 and 3, respectively. The generation 3 device uses an AlGaAs/GaAs *p*-type quarter-wave mirror and for that reason the standing wave energy falls off at a slower rate in the left mirror in comparison to the generation 1 device that uses AlAs/GaAs mirrors on both sides.

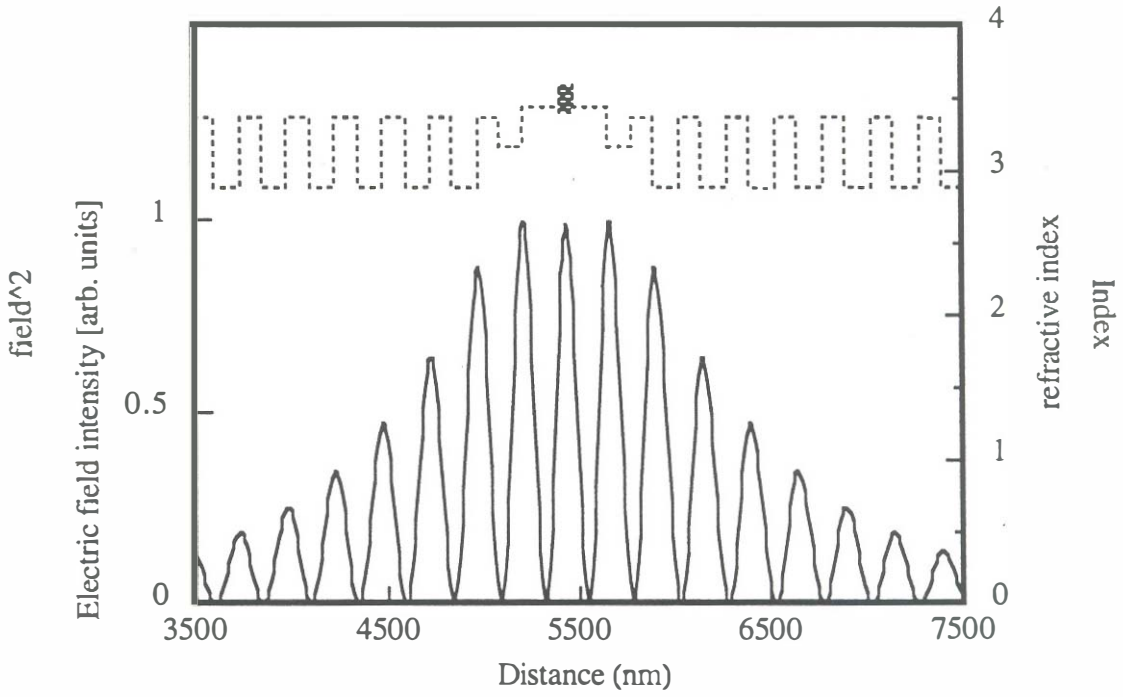


**Fig. 4.11**: Standing-wave pattern in a generation 1 device.

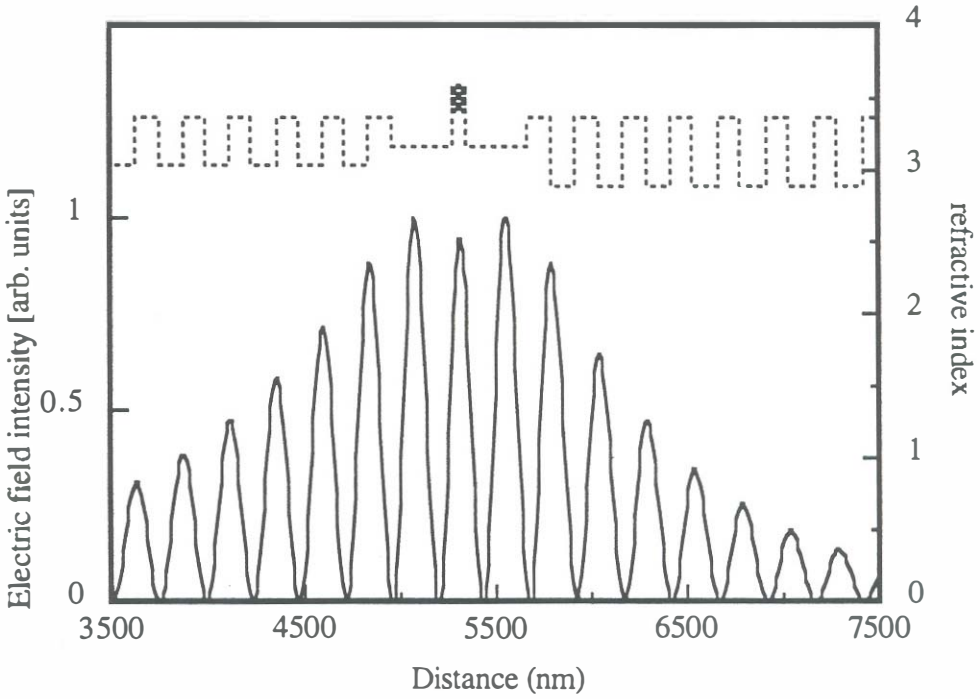


**Fig. 4.12**: Standing-wave pattern in a generation 3 device.

## 4.4. *Mirror design*

The design of any epitaxial quarter-wave mirror that is also intended for current supply involves the optimization between the reflectivity and the electrical resistance. These two parameters are connected through the free-carrier and inter-valence-band absorption which is associated with high carrier concentrations.

The resistance of the mirrors depends on the ohmic resistance of the bulk doped layers and the heterojunction resistance arising from the large number of barriers that are incorporated in a typical quarter-wave mirror (anywhere between 30 and 100). The type of carriers will also affect the conductance because the valence and conduction band offsets are typically different in most materials and the mobility of electrons is higher than that of holes. The dominant part of the voltage drop (and hence power dissipation) in vertical-cavity laser mirrors comes from the large heterojunction voltage drops. This conduction relies on a combination of tunneling and thermionic emission and is hence very temperature sensitive. The electron effective mass is lower than that of holes, and hence for the same barrier the voltage drop will be lower across $n$-type heterojunctions. A number of techniques have been devised and investigated in recent years to reduce this voltage. All of the techniques rely on engineering the bands around the heterojunctions by combining alloy grading and specially designed doping distribution that either reduce, flatten or invert the barriers that exist at the heterojunction. Inasmuch as a large number of heterojunctions appear in a real structure, even very small heterojunction voltage improvements produce large changes in the total device voltage.

Most grading schemes involve relatively high levels of doping or charge accumulation at the interfaces. The interface or bulk doping level has to be carefully selected, because the presence of carriers produces free-carrier absorption (Pankove, 1971). *N*-type AlGaAs and InGaAsP quarter-wave mirrors typically perform better than *p*-type mirrors. One of the reasons for this is that at a given doping level *n*-type GaAs (InP) exhibits less free-carrier absorption than *p*-type. For 980 nm GaAs-based VCLs, the typical values are $\alpha_N \approx 5$ cm$^{-1}$ and $\alpha_P \approx 11$ cm$^{-1}$ per $10^{18}$ cm$^{-3}$ for *n*- and *p*-type GaAs (Peters, 1995). The adjustment between the bulk doping level, interface grading/doping scheme and the peak reflectivity of the quarter-wave mirror is the subject of the optimization discussed in this chapter.

The origin of the high below-gap absorption in *p*-GaAs and *p*-InP is a combination of free-carrier and inter-valence-band absorption (Pankove, 1971). Both of these increase quite rapidly with the wavelength below the gap of the two materials and become a serious problem at optical communication wavelengths (Henry, 1983). There has been a number of reports on *p*-type GaAs and InP absorption measurements as a function of wavelength and hole concentration, but they do not cover a continuous hole concentration range. The next section describes a measurement of GaAs absorption and summarizes previously published data to provide the necessary information for mirror design.

### 4.4.1. *Absorption in p-GaAs*

Free-carrier and inter-band absorption dominate the absorption below the band-gap in extrinsic *p*-type III-V semiconductors. The absorption in heavily Be-doped and Zn-

doped InP increases rapidly with the hole concentration at 1550 nm (Yokouchi, 1992, Casey, 1984). Since heavily doped $p$-type GaAs is seldom used at optical communication wavelengths, it was not immediately evident that the effects of inter-valence-band and free-carrier absorption would directly influence the design of fused long-wavelength VCLs. Therefore, in order to use $p$-GaAs at 1.3 and 1.55 μm it was necessary to better quantify the effects of absorption. There has been a number of reports of measurements and modeling of absorption in $p$-GaAs (Henry, 1983, Braunstein, 1959, Huberman, 1991). Unfortunately, the reported studies dealt with either very high ($> 2 \cdot 10^{19}\,\mathrm{cm}^{-3}$) or moderate doping ($\leq 10^{18}\,\mathrm{cm}^{-3}$). For this reason, a measurement of the absorption coefficient was performed on several Zn-doped GaAs substrates with nominal doping levels in between the two ranges. Only two nominal doping levels were investigated ($5 \cdot 10^{18}\,\mathrm{cm}^{-3}$ and $1 \cdot 10^{19}\,\mathrm{cm}^{-3}$) because it was not possible to obtain small quantities of $p$-GaAs wafers with nominal doping below $5 \cdot 10^{18}\,\mathrm{cm}^{-3}$ and above $3 \cdot 10^{16}\,\mathrm{cm}^{-3}$.

The determination of the absorption coefficient is performed by measuring the transmission through a substrate polished on both sides. This type of absorption measurement has already been used by (Casey, 1984) for $p$-type InP. The requirement for an accurate measurement of absorption loss in a layer is that the product of the absorption coefficient $\alpha$ and the thickness of the substrate $L$ is of the order or greater than unity, namely, $\alpha L > 1$. In this case the absorption loss can be accurately de-embedded from the transmission-interference spectra. The interference between the reflections inside the substrate can be made negligible if the coherence length of the light source is shorter than the thickness of the substrate. The former requirement is easy to satisfy when measuring transmission through entire wafers

(thicknesses greater than 100 μm) using a white light sources. In this case the measured substrate transmission is given by (Pankove, 1971)

$$T_m(\lambda) = \frac{(1-R)^2 e^{-\alpha L}}{1-R^2 e^{-2\alpha L}} \qquad (4\text{-}6)$$

where $R$ is the wavelength dependent reflectivity of the air-semiconductor interface. In the case where $\alpha L >> 1$ the measured transmission through the structure is approximately given by $T_m \approx T^2 \exp(-\alpha L)$ from where it is easy to determine the absorption coefficient. The wavelength dependence of the air-semiconductor interface $T(\lambda)$ for wavelengths below the energy gap is typically negligible in comparison to the total transmission $T_m(\lambda)$ and for that reason an approximate value of $T \approx 0.7$ was used. The error introduced by not using $T(\lambda)$ calculated from the known refractive indexes of GaAs is less than 3 $cm^{-1}$ for a 150 μm thick substrate. The thickness of the substrate $L$ is measured using a micrometer, while the transmission $T_m(\lambda)$ was measured using a spectrophotometer in the range from 900 nm to 2400 nm and confirmed using a DBR laser at 1550 nm. Note that the coherence length of the 1550 nm laser is greater than the thickness of the substrate, but the effect of the interference has been made negligible due to high absorption $\alpha L >> 1$.

Three GaAs and one InP wafers were measured. Measurements were performed for two wafer thicknesses in order to eliminate any systematic errors that would depend on the slice thickness. The first measurement was performed on polished and unthinned wafers, while for the second measurement the wafers were lapped down to ≈150 μm and the polished using Br:MeOH. A number of transmission scans were performed to eliminate the substrate position and distance to the detector influencing the measurement. The sources of error in this method are the following: For large

thicknesses the absorption in the substrate is very large and the output signal is often below the detectivity of the spectrophotometer. To remove the noise, the measured data with transmission coefficients below 0.5 % was discarded. Inasmuch as the absorption coefficient dependence on $T_m(\lambda)$ and $T(\lambda)$ is logarithmic, the dominant source of error is the determination of the slice thickness. Due to uneven lapping and polishing, the error in the thickness determination was estimated to be ± 5 %. The overall accuracy of the measured absorption coefficient is estimated to be approximately ±10 %. The measurement results are shown in Figure 4.13. The doping levels given in the figure are nominal doping levels reported by the manufacturer. It is evident that the absorption loss very quickly increases below the gap and that at 1.55 μm the absorption is almost five times larger than it is around 1 μm. Furthermore, the increase of absorption for GaAs scales is approximately as $\lambda^3$ which indicates that this is *free-carrier* absorption (Pankove, 1971). The measurements on the InP wafer agree very well with previous measurements by (Casey, 1984). When this data is combined with the previously published data for *p*-GaAs we can get a complete dependence of the absorption coefficient on the hole concentration, as shown in Figure 4.14. In the doping range of interest (around $1 \cdot 10^{18}$ cm$^{-3}$) the absorption coefficient at 1550 nm follows an approximate dependence given by

$$\alpha \approx 25\text{cm}^{-1} \cdot \left( \frac{p}{10^{18}\,\text{cm}^{-3}} \right)^{1.3} . \qquad (4\text{-}7)$$

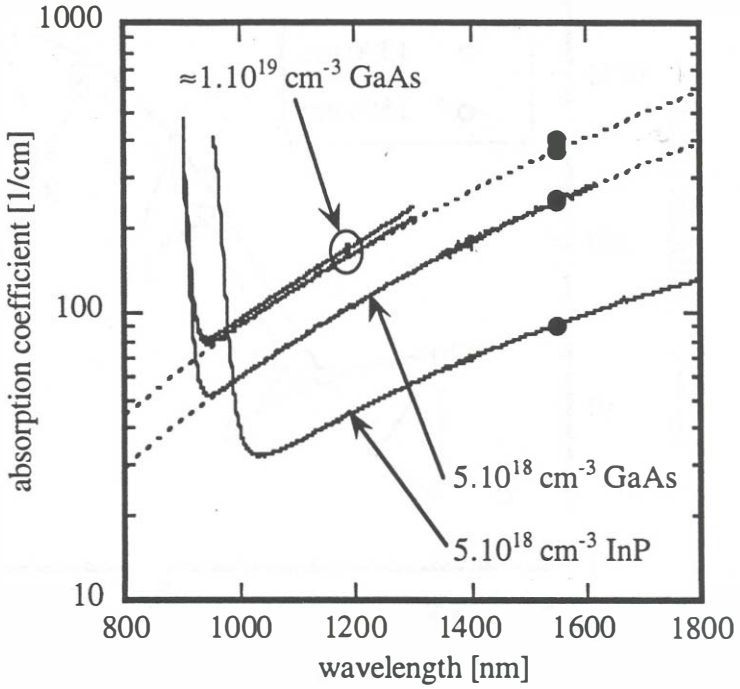


**Fig. 4.13**: Absorption coefficient in GaAs and InP for nominal LEC Zn-doped wafers determined by a transmission technique. The continuous curves have been obtained using a spectrophotometer, while the data points at 1550 nm were obtained using a semiconductor laser. The dashed lines follow a $\lambda^3$ power law.

In light of these findings the doping of mirrors with the level equal to what is commonly used in GaAs-based VCLs ($10^{18}$ $cm^{-3}$) is too high since it produces an absorption loss of approximately $25cm^{-1}$. This loss would produce a maximum reflectivity of 99.60 % if the hole distribution was uniform. To increase the reflectivity and make the design more tolerant to variations in the doping levels and free charges, we reduce the doping level in the mirror. If the light is to be taken out through a $p$-substrate, the substrate should be doped very low (less than $10^{18}$ $cm^{-3}$).

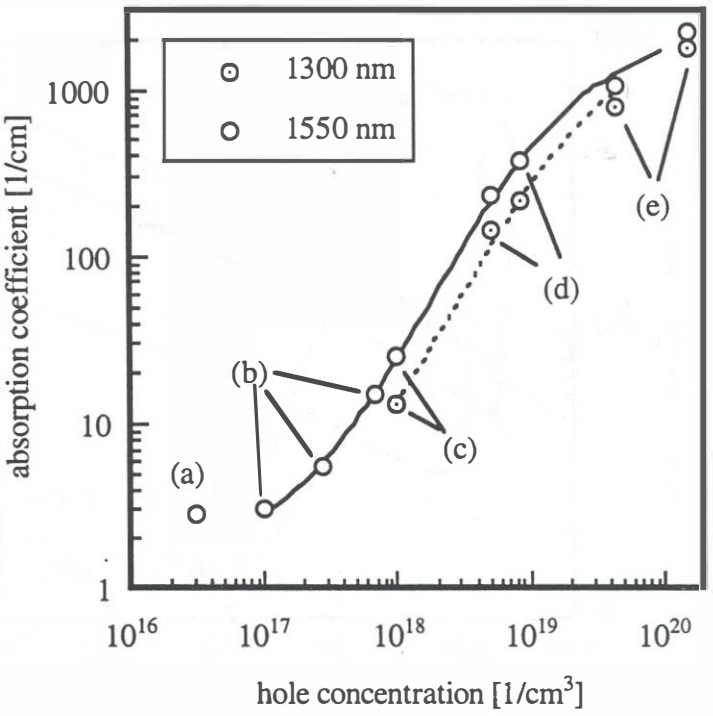


**Fig. 4.14**: Summary of $p$-GaAs absorption as a function of doping form published data and this work: a) data from (Braunstein, 1958), b) data from (Braunstein, 1959), c) (Henry, 1983), d) this work, e) (Huberman, 1991).

### 4.4.2. *Absorption in n-GaAs*

The absorption in $n$-type GaAs at optical communication wavelengths is significantly lower and has a considerably weaker wavelength dependence than that of $p$-GaAs (Pankove, 1971). At doping concentration of $5.4 \cdot 10^{18}$ cm$^{-3}$ the absorption coefficient at 1.55 μm is approximately $\alpha \approx 35$ cm$^{-1}$ (Spitzer, 1959). With the presence of this level of absorption in the substrate, a large fraction of the light can still be transmitted through the entire substrate, and at lower doping levels, such as

$1 \cdot 10^{18}$ cm$^{-3}$, very high mirror reflectivities can be achieved. For these reasons, the $n$-mirror is used as the output coupler in most VCL designs, and the light is often taken out through the $n$-type substrate. Owing to the current and heat spreading the performance of $n$-type GaAs/AlAs mirrors were not as critical in the development of fused long-wavelength lasers as the $p$-mirrors. However, an estimate of the absorption coefficient is needed to be able to predict the reflectivity of the mirrors and the substrate transmittance.

The $n$-type mirrors fabricated in the AlAs/GaAs system have an average bulk doping of $10^{18}$ cm$^{-3}$ with interfaces graded and pulse doped to approximately $5 \cdot 10^{18}$ cm$^{-3}$. Due to the slow increase of $n$-GaAs absorption with the wavelength, the absorption coefficient at 1550 nm is only 10-20 % higher than it is at 980 nm. Therefore, at the specified doping level, the absorption coefficient in GaAs is estimated to be approximately $\alpha_N \approx 6$ cm$^{-1}$. The $n$-AlAs/GaAs mirrors show relatively low resistivity, sufficient for the fabrication of electrically pumped VCLs (Peters, 1995). Low resistivity results have been reported for the InGaAsP/InP $n$-type system as well (Streubel, 1994).

The measurement of substrate absorption in $n$-type is performed using the same method as was used for $p$-GaAs in the previous section. However, since the values of the absorption coefficient are much smaller, one needs to use a thicker substrate for an accurate measurement . To determine the wavelength dependence of the absorption coefficient, the absorption coefficient measurement as performed on a substrate nominally doped in the range $1 - 3 \cdot 10^{18}$ cm$^{-3}$. Two measurements were performed: The first measurement was done on a single 500 μm thick substrate polished on both

sides, while the second measurement was performed on three such substrates stacked and wafer-fused simultaneously. The total thickness of the fused sample was 1500 μm. The measurements for two samples agreed to within $2cm^{-1}$. A slight correction was introduced into the fused substrate since the polished surfaces have roughened from the fixture pressure (Sec. 3.3.1). The resulting wavelength dependence of the absorption coefficient is shown in Fig. 4.15. The slow wavelength dependence in the 1-2 μm range is in agreement with the previous measurements reported by (Spitzer, 1959). In Chapter 7 we shall introduce another method for the estimate of substrate absorption on the actual device sample.

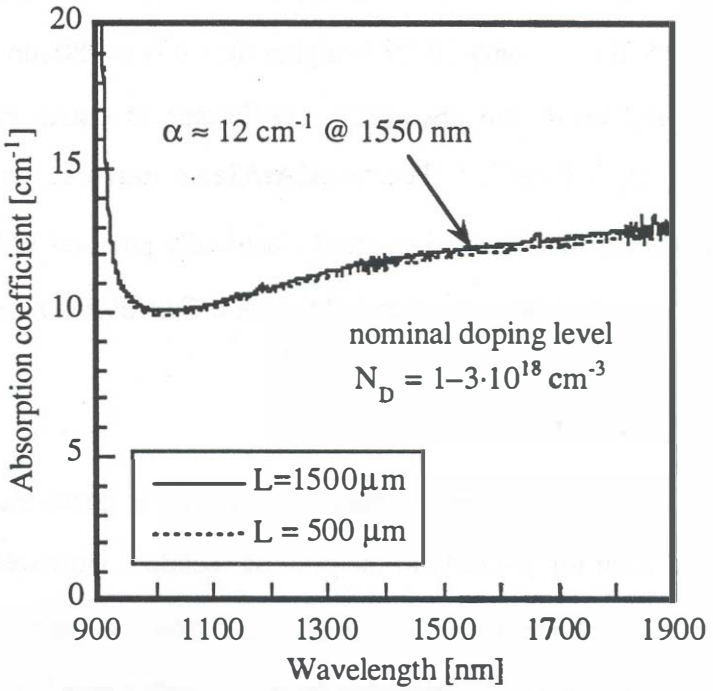


**Fig. 4.15**: Measured absorption coefficient of an $n$-GaAs substrate with nominal doping in the range $1-3\cdot10^{18}$ $cm^{-3}$.

4.4.3. *Bandgap engineering*

The realization of low resistance $p$-type quarter-wave mirrors relies on the minimizing the valence-band discontinuities at the interfaces between GaAs and Al(Ga)As. The first question that is raised in this task is: Is it possible to realize a flat band for an arbitrary combination of semiconductors and doping levels using a suitable composition grading or doping profile? The answer is: Yes, but only if both the desired grading and doping variation is slow compared to the lattice constant. This means that the solution is *exact* only within the continuous, effective-mass Poisson equation. To demonstrate this, we solve the Poisson equation with the requirement that the valence band be flat through a single heterojunction interface. The Poisson equation is given by

$$-\frac{1}{q}\frac{d}{dz}\left(\varepsilon(z)\frac{d\Phi}{dz}\right)=N(z)+p(z) \qquad (4\text{-}8)$$

Here $N(z)=N_D^+(z)-N_A^-(z)$ is the net ionized impurity distribution that may include deep levels and $p(z)$ is the hole distribution. The heterojunction is located at $z=0$. The doping levels (ionized impurity concentrations) far away from the heterojunction are assumed uniform and are denoted with $N(-\infty)=N_1$ and $N(\infty)=N_2$. The dielectric permittivity $\varepsilon(z)$ is dependent on position through the changes in the material composition. The electrostatic potential $\Phi$ is related to the valence band energy $E_v(z)$ via

$$-q\Phi(z)=E_v(z)+\Delta E_v f(z) \qquad (4\text{-}9)$$

Here $f(z)$ is the band-offset composition function: It is a dimensionless function that determines the position variation of the band offset. If the band offset is linear in composition, as is the valence band of $Al_xGa_{1-x}As$, then $f(z)$ is proportional to

$x(z)$. The conduction-band-offset composition function $Al_xGa_{1-x}As$ is more complicated, since the band changes from direct to indirect. However, once the composition grading $x(z)$ is known, $f(z)$ is uniquely defined. In the case described here, $f(-\infty) = 0$ for GaAs and $f(\infty) = 1$ when the composition equal the end alloy $Al_xGa_{1-x}As$. Positive value of $df/dz$ means the energy gap of the alloy is increasing with $z$ and the valence band edge is being lowered by $\Delta E_v f(z)$.

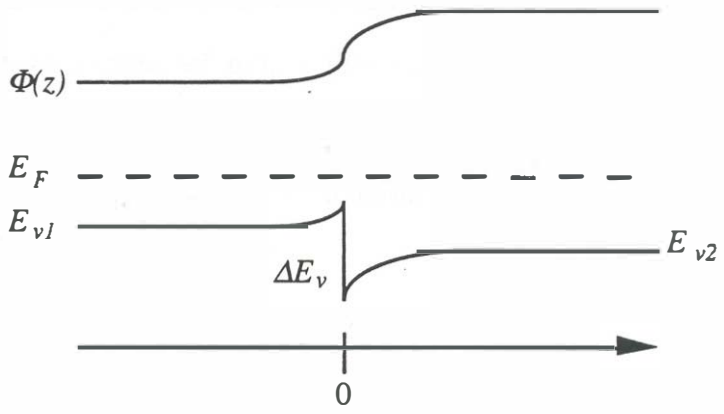


**Fig. 4.16**: Energy band-diagram for an abrupt $p$--isotype heterojunction with the associated electrostatic potential profile.

The relation $-q\Phi(z) = E_v(z) + \Delta E_v f(z)$ is derived on the basis of the following arguments: Consider an abrupt isotype heterojunction with the valence band shown in Fig. 4.16. The valence band profile contains both the electrostatic potential characteristics of the holes as well as the potential determined by quantum mechanics (the periodic potential of the crystal). The band offset $\Delta E_v$ at the abrupt heterojunction is determined by the match-up the hole wave-functions in the two semiconductors and typically does not exhibit an observable electrostatic potential difference. This is so because the electrostatic dipole that forms at the junctions is

typically very small and in most cases is negligible. When two crystals (such as 1 and 2 in Figure 4.16) are brought together, charges flow from one side to the other until all of the electrostatic balance out the diffusion forces. The band offset produces an abrupt change in the valence band, but not in the electrostatic potential. The valence band can then be written in terms of the electrostatic potential as $E_v(z) = -q\Phi(z) - \Delta E_v f(z)$, where $f(z)$ is a step function at zero. One also has to bear in mind that the reference potential can be set to zero any where in the structure and that in doing so the reference energy level for the valence band also been set.

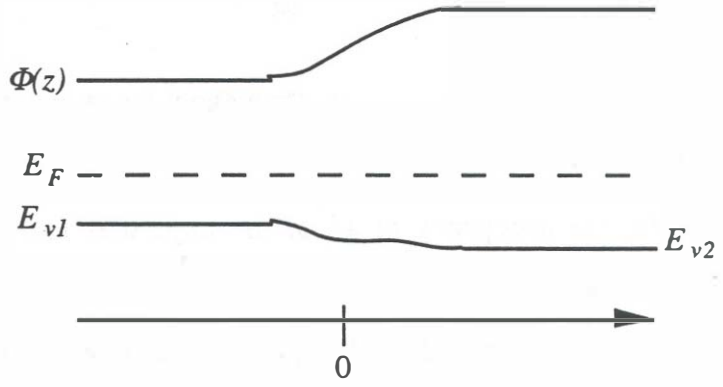


**Fig. 4.17**: Energy band-diagram for a graded $p$–isotype heterojunction with the associate electrostatic potential profile.

To continue, we need to show that the relation between the potential and the valence band edge also holds when interfaces are graded. To do this consider another heterojunction that uses the identical two semiconductors and doping levels as in Figure 4.16, but is graded. The Figure 4.17 shows such a heterojunction. Note that the total potential difference between the two semiconductors is also equal to the abrupt case. This must be true because we could in principle fabricate both junctions on the same chip and there, any closed loop that passes through the two

heterojunctions has to a have a zero potential sum. This argument was previously used in (Kroemer[a], 1985) to show that the electrostatic dipole is the same in graded or abrupt junctions. That the expression (4-9) holds everywhere within the graded junction we rely on the *transitivity* of heterojunction band offsets (Kroemer[b], 1985). This rule holds to within the accuracy of the measurements made on the heterojunction band offsets.

With this knowledge, we proceed to insert this relationship into the Poisson equation.

$$\frac{1}{q^2}\frac{d}{dz}\left(\varepsilon(z)\frac{dE_V(z)}{dz}+\Delta E_V\varepsilon(z)\frac{df(z)}{dz}\right)=N(z)+p(z) \qquad (4\text{-}10)$$

We now require that the valence band be flat throughout the structure. This means that throughout the structure $E_V(z)$ and Fermi level $E_F(z)$ are independent of position. Therefore, the occupancy of all of the impurities and deep levels is independent of position and consequently the net ionized impurity concentration $N(z)$ can be determined exactly. Using $dE_V(z)/dz = 0$, the first term in (4-10) vanishes and we are left with:

$$\frac{\Delta E_V}{q^2}\frac{d}{dz}\left(\varepsilon(z)\frac{df(z)}{dz}\right)=N(z)+p(N_V(z)) \qquad (4\text{-}11)$$

The equilibrium hole concentration depends only indirectly on position, through the changes of the effective density of states with the grading. If we assume uniform doping away from the junction, $N_1$ for $z \to -\infty$ and $N_2$ for $z \to \infty$, then the ionized impurity distribution that achieves a flat band can be written as

$$N(z)=\frac{\Delta E_V}{q^2}\frac{d}{dz}\left(\varepsilon(z)\frac{df(z)}{dz}\right)-N_1\frac{N_V(z)}{N_{V1}} \qquad (4\text{-}12)$$

This expression is *exact* and it gives the flat-band ionized impurity distribution that corresponds to a given grading function. Note that with the requested flat valence band we are obliged to provide exactly matching uniform doping levels on each side of the junction. If on side 1 the doping is $N_1$, then on side 2 we have to have a doping level of $N_2 = N_1(N_{V2}/N_{V1})$. For AlAs the doping level has to be about 10% higher than in GaAs to keep the valence-band to Fermi level spacing equal on both sides. Furthermore, since only the ionized impurity distribution is specified, the impurity profile yields a flat valence band only at one temperature.

For the AlAs/GaAs system the dielectric permittivity varies approximately linearly with composition and hence the Poisson equation of $p$-isotype heterojunction can be simplified using

$$\varepsilon(z) = \frac{\varepsilon_1 + \varepsilon_2}{2} - \frac{\varepsilon_1 - \varepsilon_2}{2}(2f(z) - 1) \tag{4-13}$$

With this simplification the equation (4-12) becomes

$$N(z) = \frac{\Delta E_V}{q^2}\left(\frac{\varepsilon_1 + \varepsilon_2}{2}\right)\left\{\frac{d^2 f}{dz^2} - \left(\frac{\varepsilon_1 - \varepsilon_2}{\varepsilon_1 + \varepsilon_2}\right)\frac{d^2(f - 1/2)^2}{dz^2}\right\} - N_1 \frac{N_V(z)}{N_{V1}} \tag{4-14}$$

The first term in the bracket is dominant in the shaping of the flatband doping distribution ($d^2 f/dz^2$). The second term only introduces a correction due to the difference in the dielectric permittivities of the two materials. The prefactor $(\varepsilon_1 - \varepsilon_2)/(\varepsilon_1 + \varepsilon_2)$ is of the order of 10%.

The most important fact visible from (4-12) or (4-14) is that there is an *infinite* number of grading and doping distribution combinations that can produce a flat band. The only limitation is the practical ability to realize the required doping or grading

distribution. For example, an abrupt heterojunction leads to a squared delta function in doping which can not be realized. To illustrate the use of the above equation, we consider the case of linear grading which leads to delta doping. Since $f(z)$ changes linearly from zero to unity over a distance equal to $\Delta z$, it is straightforward to show that

$$\frac{d^2 f}{dz^2} = \frac{\delta(z-\Delta z/2)}{\Delta z} - \frac{\delta(z+\Delta z/2)}{\Delta z} \tag{4-15}$$

and

$$\frac{d^2(f-1/2)^2}{dz^2} = -\frac{\delta(z-\Delta z/2)}{\Delta z} - \frac{\delta(z+\Delta z/2)}{\Delta z} + \frac{2P_{\Delta z}(z)}{\Delta z^2} \tag{4-16}$$

where $P_{\Delta z}(z)$ is a pulse function

$$P_{\Delta z}(z) = \begin{cases} 1 & \text{for } -\Delta z/2 < z < \Delta z/2 \\ 0 & \text{otherwise} \end{cases} \tag{4-17}$$

Using these expressions the doping profile becomes (4-18)

$$N(z) = \frac{\Delta E_V}{q^2 \Delta z}\left\{\varepsilon_1 \delta(z-\Delta z/2) - \varepsilon_2 \delta(z+\Delta z/2) - (\varepsilon_1 - \varepsilon_2)\frac{P_{\Delta z}(z)}{\Delta x}\right\} - N_1 \frac{N_V(z)}{N_{V1}}$$

The only term that has not been clarified is the term that depends on the effective density of states. Inasmuch as the density of states depends on the effective masses the variation is not very fast, and this term can in principle be approximated with a linear function, i.e. using the composition function again

$$N_V(z) = f N_{V2} + (1-f)N_{V1}. \tag{4-19}$$

The charge neutrality

$$\int_{-\infty}^{\infty} N(z)dz + \int_{-\infty}^{\infty} p(z)dz = 0 \tag{4-20}$$

is conserved since from (4-18) we find that

$$\int_{-\infty}^{\infty} N(z)dz = \frac{\Delta E_V}{q^2 \Delta z}\left\{\varepsilon_1 - \varepsilon_2 - \frac{\varepsilon_1 - \varepsilon_2}{\Delta z}\int_{-\infty}^{\infty} P_{\Delta z}(z)dz\right\} - \int_{-\infty}^{\infty} p(z)dz \qquad (4\text{-}21)$$

and from $\int_{-\infty}^{\infty} P_{\Delta z}(z)dz = \Delta z$ we have

$$\int_{-\infty}^{\infty} N(z)dz = -\int_{-\infty}^{\infty} p(z)dz \qquad (4\text{-}22)$$

The practical realization of these doping and grading schemes for achieving a flat band is never perfect. A number of researchers have investigated simple linear and double-parabolic grading schemes with very good results (Peters, 1994, Schubert, 1992, Lear, 1994). Combinations with a single-sided parabolic and a single delta-doped pulse are also possible. The two dominant problems with the practical realization of bandgap engineered junctions are: dopant diffusion and unknown composition variation in the grading. Some dopants, such as, beryllium and zinc, tend to diffuse during the 8-10 hour long growths of mirrors and completely obliterate the intended doping profile. This necessarily results in different, most often, inferior electrical properties. The situation can be greatly improved by using dopants that have lower diffusion coefficients. Recently, there has been a great progress in the use of carbon as a $p$-type dopant for GaAs (in InP it is an $n$-type dopant) and this has produced excellent quality mirrors for GaAs VCLs (Lear, 1994). The knowledge of the exact grading profile is another problem. This question is particularly important for MBE grown gradings since here the grading is realized as a digital alloy of varying composition. The growth alternates between pure AlAs and pure GaAs several monolayers at a time. It is not clear to what extent does the lattice keep its form and the grading averages out. This problem is not so prominent in MOCVD where

continuous grades are possible, but the delays in reactant supply and purging have to be accounted for.

In principle, to achieve low resistance one does not have to have perfectly flat bands. It is sufficient to eliminate the barriers, and that can easily be done by heavy doping in the region of the heterojunction. This method is called *pulse doping* and is often used for reducing the resistance of $n$-type mirrors. The drawback of this technique in $p$-mirror is that heavy doping brings on a large accumulation of holes which are then a source of absorption. Large and thin hole accumulations can be tolerated if they are located at every other mirror junction; at the nodes of the standing wave pattern. At the peaks of the waves, it is preferred to have as low carrier concentration as possible. The way to achieve this is by realizing a flat band at the junctions and keeping low carrier concentration throughout the mirror.

To characterize the doping profile in flat-band isotype heterojunctions one can use capacitance-voltage carrier concentration profiling, while the electrical characteristics can also be studied by performing temperature dependent voltage-current characteristics (Peters, 1995).

### 4.4.4. *Summary of mirrors used in double-fused VCLs*

There were three different $n$-type mirrors used in this work: S201 (Mirin), S230 (Peters) and S276 (Mars). The silicon bulk doping level on all of these mirrors was $10^{18}$ cm$^{-3}$ and the interfaces were pulsed doped approximately to $5 \cdot 10^{18}$ cm$^{-3}$. The center wavelength and the number of periods varied: Mirror S201 had 25 periods and

it was tuned to ≈1550 nm. Mirror S230 had 28 periods and was tuned to approximately to 1500 nm. Mirror S276 had 28 periods, was tuned to ≈1550 and had an extra 50 nm thick GaAs cap layer to be used for cavity optical thickness correction (described in Section 4.3.2.). The reflectivity spectra of the $n$-mirrors used in double-fused VCLs are shown in Figure 4.18.

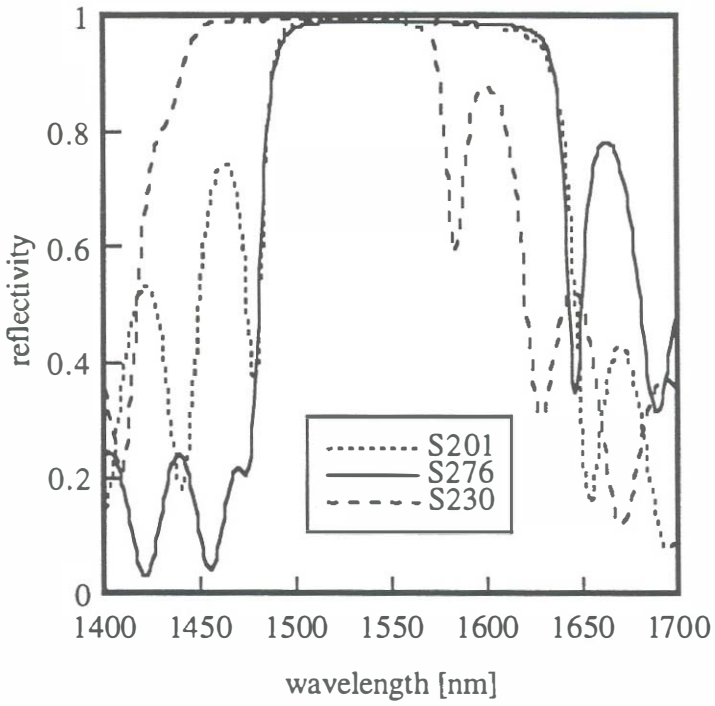


**Fig. 4.18**: The reflectivity spectra of fabricated $n$-type quarter-wave mirrors.

There were two $p$-type mirrors used in this work: S207 and S250 (Mirin). The S207 mirror was an MBE-grown Be-doped AlAs/GaAs mirror with 24 periods. The doping scheme was adjusted to increase the reflectivity structure: The first 10-periods were doped lower to reduce the absorption. The S250 mirror was an AlGaAs/GaAs mirror

with parabolic grading and overall low doping of $4 \cdot 10^{17}$ $cm^{-3}$. We shall discuss the design details of each of these separately.

The mirrors grown at UC Santa Barbara (Mirin) were tuned *in situ* using a normal incidence reflectometer (Thibeault, 1994). The method consisted of growing 6 or 8 periods of the mirror and then interrupting the growth to measure the reflectivity. During the measurement the wafer was never removed from the vacuum chamber and the temperature of the MBE sources was not changed. After the measurement was performed, a reflectivity model would indicate how much the grown 6 periods were off in wavelength and the growth rate was then accordingly adjusted.

4.4.5. *The AlAs/GaAs mirror with hybrid doping (S207)*

The increase of mirror reflectivity in a mirror with absorption is performed by reducing the doping level in the first few periods closest to the cavity where the electric field intensity is highest. In this way a section of the mirror can remain doped at a higher level and exhibit low resistance. We adjusted the optimum number of layers with low doping based on the absorption coefficient measurements and the mirror optical constants. For the value of absorption loss, we use the empirical formula (4-7) . The absorption loss in AlGaAs and AlAs was assumed to be equal to that of GaAs. Since the wavelength of laser light is much larger than the grading thicknesses and the charge distribution around it, the average absorption loss in the mirror was found by averaging the absorption loss as a function of position. For the pulse doped mirror the doping can be calculated as a weighted sum of absorption per period.

$$\bar{\alpha} = 25\frac{2d_g\left(\frac{N_g}{10^{18}}\right)^{1.3} + \left(\frac{\lambda}{4n_L} - d_g\right)\left(\frac{N_L}{10^{18}}\right)^{1.3} + \left(\frac{\lambda}{4n_H} - d_g\right)\left(\frac{N_H}{10^{18}}\right)^{1.3}}{\frac{\lambda}{4}\left(\frac{1}{n_L} + \frac{1}{n_L}\right)} \quad (4\text{-}23)$$

where the impurity concentration is given in $cm^{-3}$ and the resulting absorption loss in $cm^{-1}$.

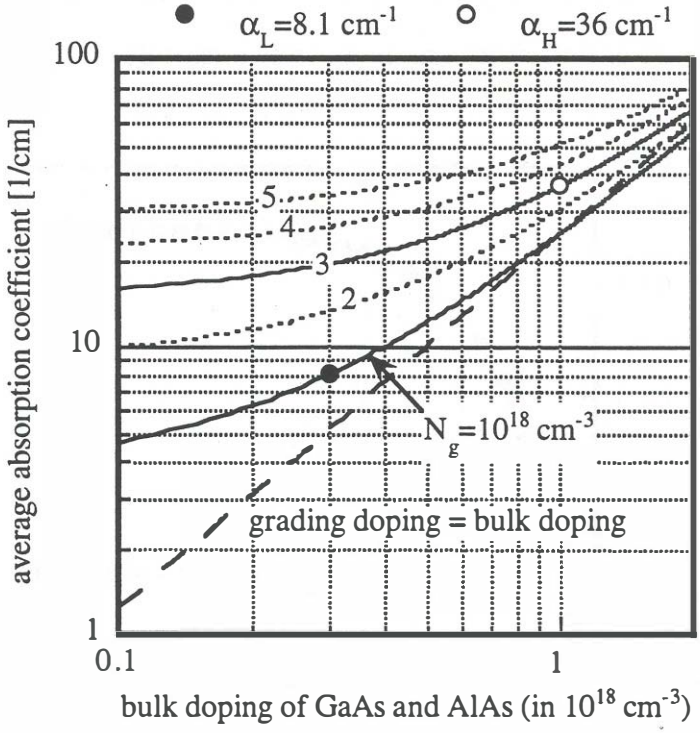


**Fig. 4.19**: Average absorption coefficient as a function of the bulk doping of AlAs and GaAs for five different pulse doping levels calculated using (4-23).

The dependence of the average loss on the bulk doping of GaAs and AlAs (kept equal) and the grading pulse doping is shown in Figure 4.19. The grading is linear and has a thickness of $d_g = 18$ nm. The two values selected for the fabrication of the mirror are shown with the bullets. The reflectivity dependence on the number of

layers with low doping is shown in Figure 4.20. The number of periods selected for the low doped section was 10, because the reflectivity already starts to saturate at that point. The reflectivity of this mirror is expected to be in the neighborhood of 99.65 %, which may have been higher if the mirror was flat-band engineered. (The peak reflectivity of a flat-band engineered mirror with uniform hole concentration of $N_A \approx 10^{18}$ cm$^{-3}$ is in the neighborhood of 99.6 %). The epilayer structure and the reflectivity spectra of this mirror are shown in Figures 4.21, 4.22, and 4.23.

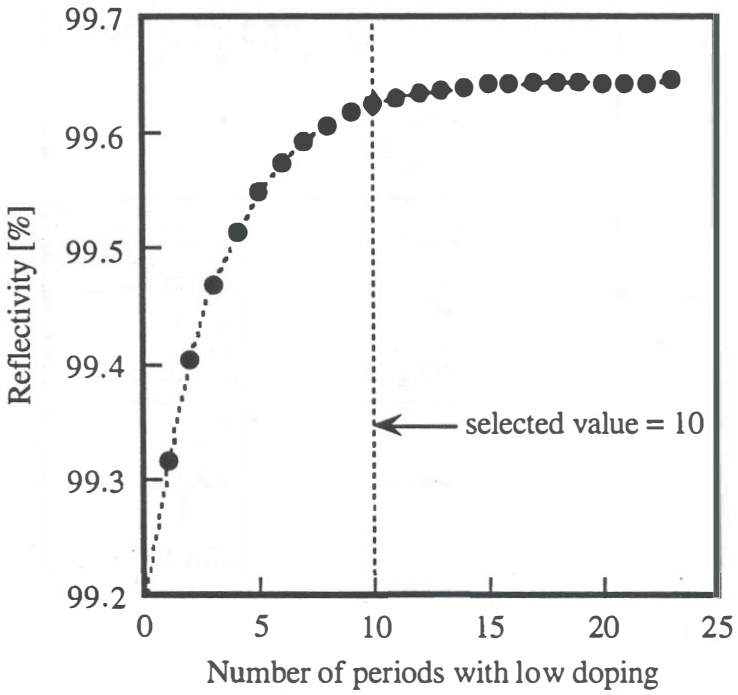


**Fig. 4.20**: The reflectivity of a hybrid doping mirror as function of number of layers with lower doping.

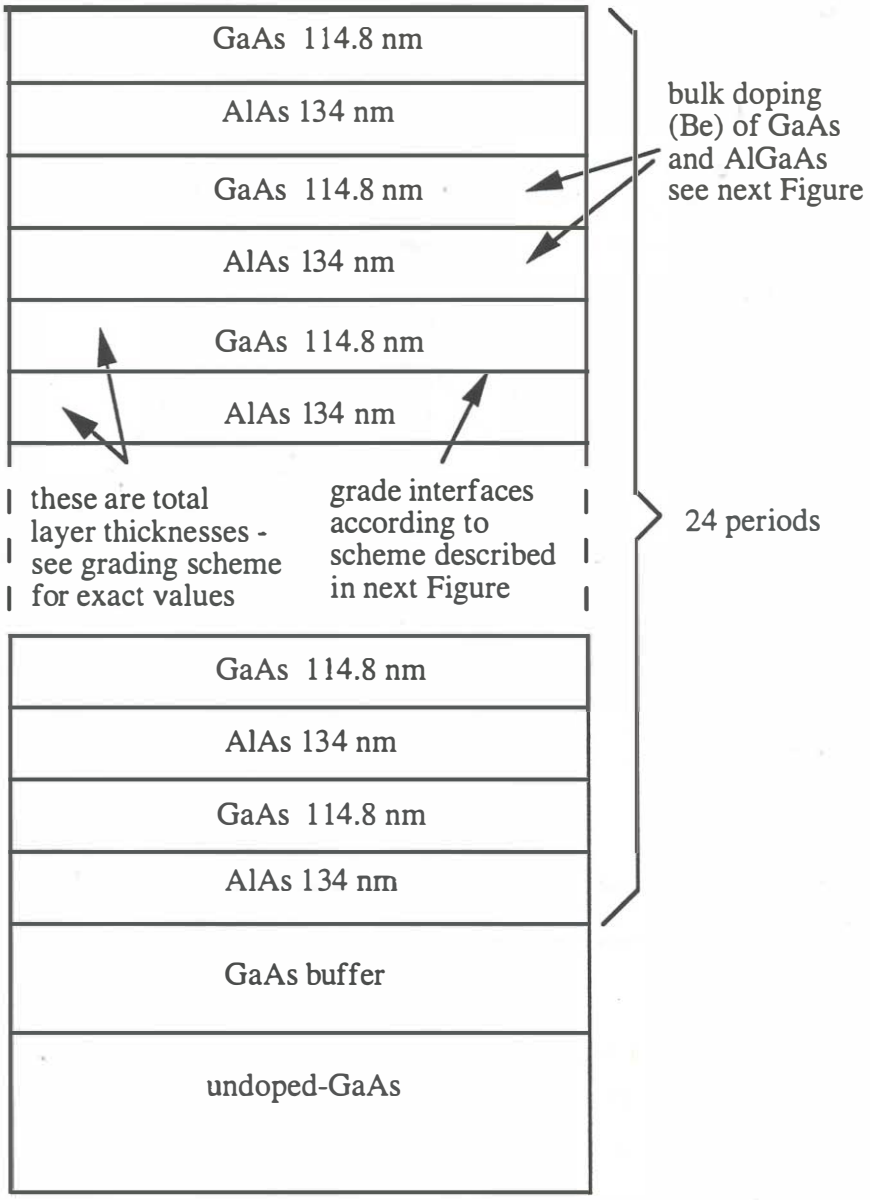


**Fig. 4.21**: Epilayer structure of the S207 mirror with hybrid doping scheme.

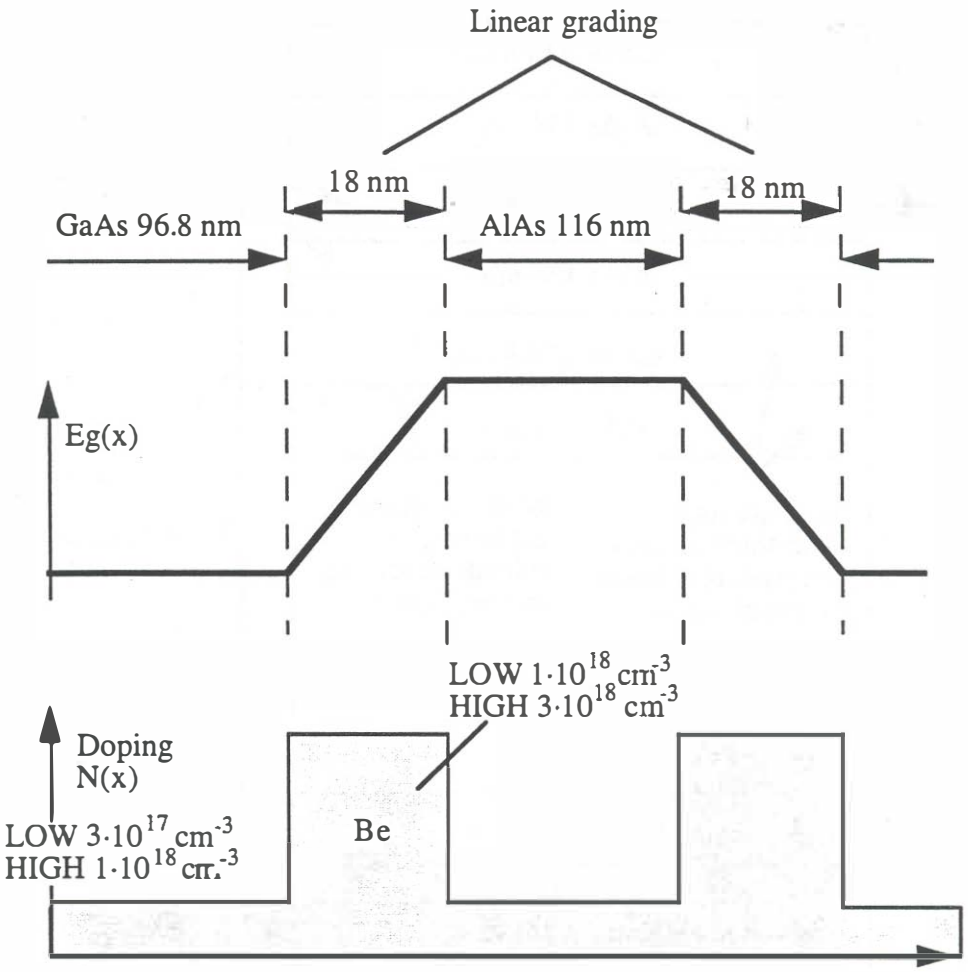


**Fig. 4.22**: Interface grading and doping scheme for the S207 hybrid doping mirror. The doping in the first 10 periods is indicated with "LOW", while in the last 14 periods the doping is indicated with "HIGH".

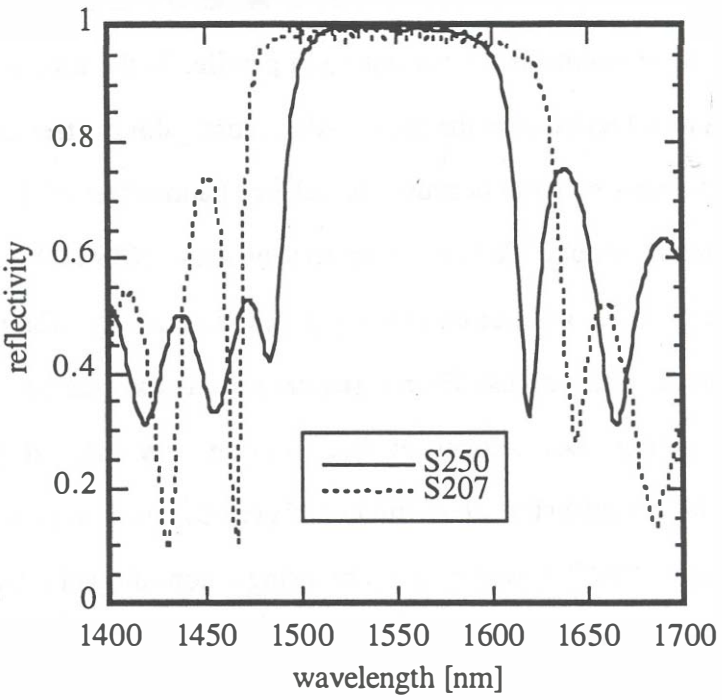


**Fig. 4.23**: Reflectivity spectra of mirrors S207 and S250. Both mirrors are tuned to approximately 1550 nm, but the bandstop widths are different because S207 is an AlAs/GaAs mirror, while S250 is an AlGaAs/GaAs mirror.

4.4.6. *The AlGaAs/GaAs mirror with parabolic grading (S250)*

The voltage drop across the S207 mirror at room-temperature pulsed thresholds of the lasers F123, F125 and F126 was greater than 10 V at threshold (see Chapters 6 and 7). The excessive power dissipation at threshold was one of the reasons why the lasers that used the S207 mirror did not operate continuously at room temperature. For this reason, the next design effort was to fabricate a $p$-type mirror with reflectivity at least as high as S207, but with lower voltage drop at the expected threshold current densities (less than $4\text{kA/cm}^2$). A number of improvements were

implemented in the next mirror (S250): 1) 67 % AlGaAs was used instead of AlAs, 2) the interfaces were engineered for a flat-band profile, 3) the mirror reflectivity was boosted with a metal reflector at the back. Aluminum gallium arsenide (67 % Al) was used as the low index material because the valence band offset of this composition to GaAs is 316 meV, about 33% lower than that of AlAs (475 meV). The interfaces were designed for a flat valence band using parabolic grading. The reason parabolic grading was used, was because Be redistribution was expected to smaller than in delta-doped gradings. Delta-doped profiles require very sharp doping variations, susceptible to higher diffusion. The number of periods necessary for a reflectivity in the neighborhood of 99.7 % was reduced by using a non-alloyed metal contact at the top of the last GaAs layer.

To determine the necessary number of layers to achieve required reflectivity, we used the estimate of absorption loss given by (4-7) and a measured value of the reflection coefficient of GaAs-to-metal interface. This reflection coefficient was measured at 1550 nm using a Fabry-Perot technique described in Appendix D. The contact used on this mirror was a Ti/Au coating with a reflection coefficient equal to $r = 0.935$. Using this data and the refractive index values $n_L = 3.045$ and $n_H = 3.377$ (Afromovitz, 1974) we generate a set of design curves for this mirror (Figure 4.24). The horizontal axis shows the average absorption in the two materials (AlAs absorption equal to GaAs), while the vertical axis shows the number of layers in the mirror in addition to the metal contact. The curves plotted are constant reflectivity curves. An approximate explicit expression for these curves can be obtained from the expressions given in Appendix B for the reduction of reflectivity of quarter-wave mirror with weak absorption loss:

$$R = \left( \frac{1 - qp^{m-1}a}{1 + qp^{m-1}a} \right)^2 \left( 1 - \frac{q\overline{\alpha}\,\lambda / n_H}{(1 - p^2)} \right) \qquad (4\text{-}24)$$

The factors $a$, $p$, and $q$ are defined in Appendix B. The number of layers is denoted with $m$. In (4-24), the peak reflectivity is assumed to be reduced by a constant factor $(1 - A)$ where $A$ is the absorptance of an infinite mirror. If one wishes to use the more accurate expressions in which the (reflection) absorptance varies with the number of layers, then expression (4-24) is no longer explicit in the number of layers and one must use an iterative solution to plot it. The expression (4-24) is valid only for the case where the first quarter-wave layer in the mirror is of high index (GaAs).

With a selected bulk doping of $N_A = 4 \cdot 10^{17}$ cm$^{-3}$ we estimate the absorption coefficient using (4-7) to be $\alpha \approx 8$ cm$^{-1}$. Since the bands are ideally flat, the hole concentration should be uniform throughout the structure. The vertical line in the graph on Figure 4.24 shows the available reflectivity values achievable with this loss coefficient. The number of periods was selected based on the curvature of the constant reflectivity curves: The optimum design is where the curves start to turn up vertically. The selected number of layers is 61 or 30.5 periods which would give a peak reflectivity greater than 99.7 %. The growth request for this mirror is shown in Figures 4.25 and 4.26, while the reflectivity spectra of the finished mirror is shown in Figure 4.23. It is evident that the S250 mirror has a narrower bandstop than the S201 mirror due to the lower reflective index ratio. In order to take advantage of a metal contact the last GaAs layer before the metal contact has to match the phase of the metal because the phase of metals on semiconductors differ depending on their optical

constants. The thickness of this layer is calculated from the measurement of the reflection phase described in Appendix D.

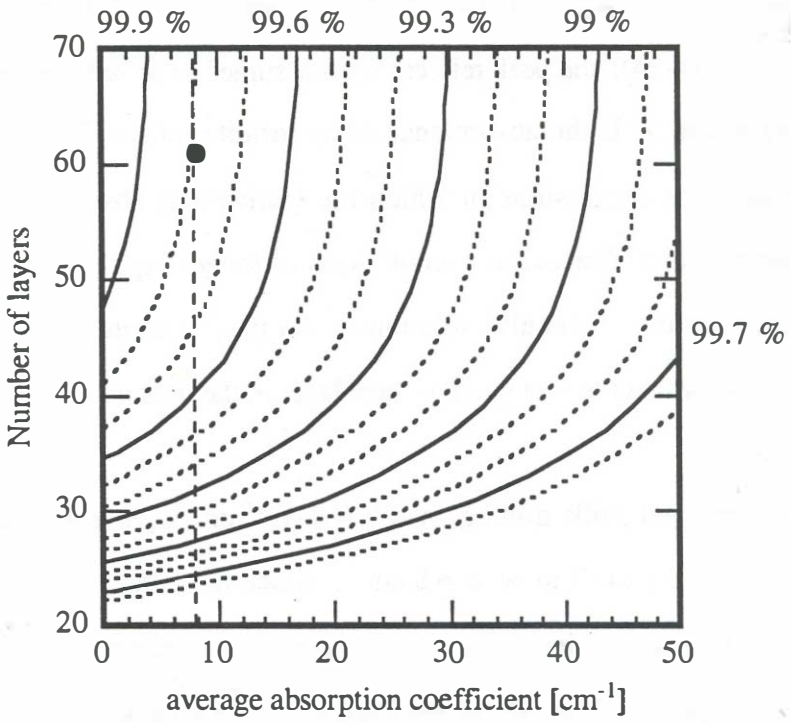


**Fig. 4.24**: Constant reflectivity curves for an AlGaAs(67%)/GaAs mirror.

The estimated reflectivity values on both S207 and S250 mirrors were based on an approximate empirical formula for the absorption coefficient. The accuracy of the formula (4-7) is now known because of insufficient data. The deviations from the predicted reflectivity will also depend on the actual value of mirror doping and the precision by which the grading and the interface doping is realized. In reality, the doping values may be as far as 50% off and this will result in quite unknown values of reflectivity. The actual cavity loss will be deduced from the measurements of the external differential quantum efficiency of the fabricated lasers.

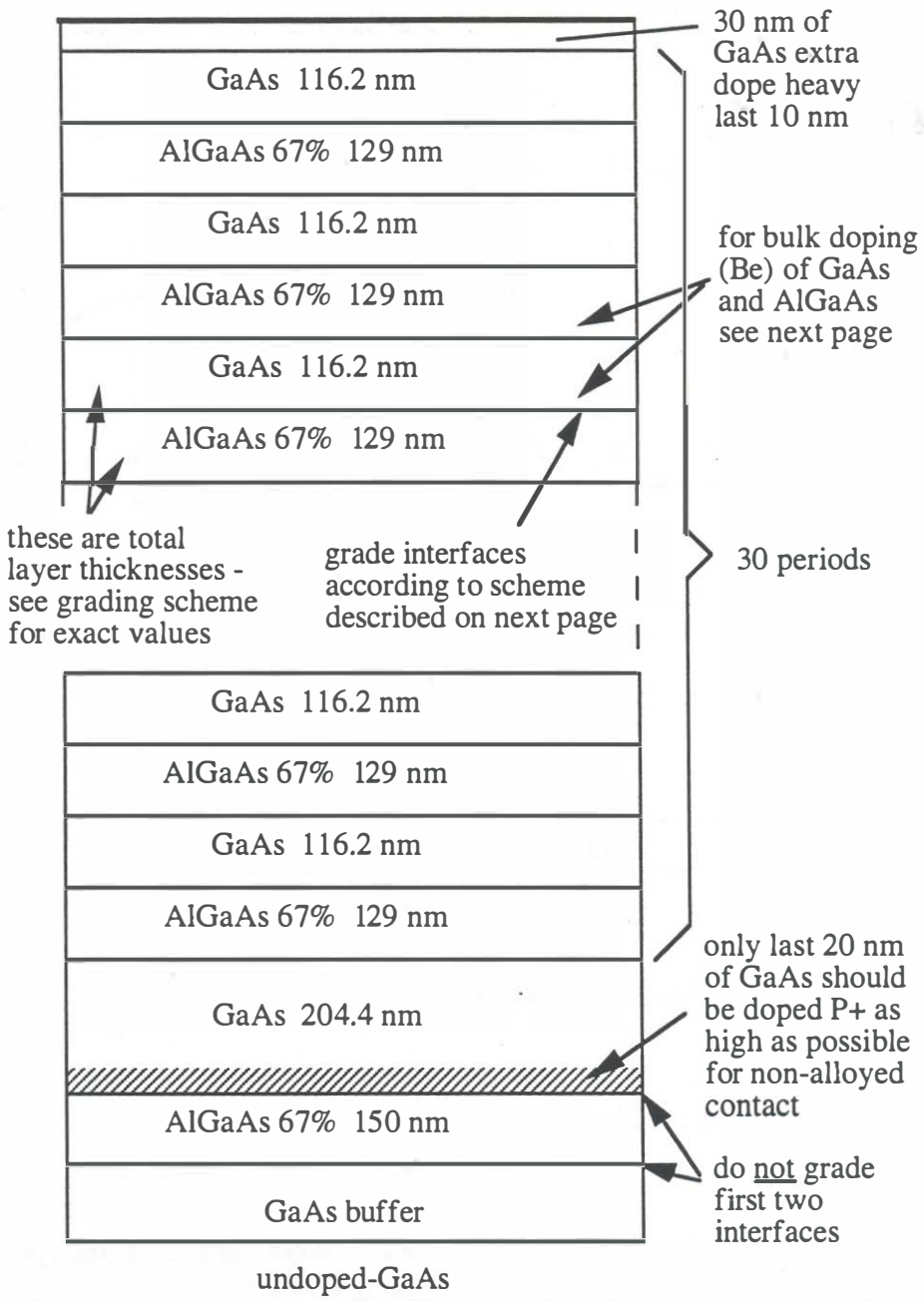


**Fig. 4.25**: Epitaxial growth request for S250 mirror.

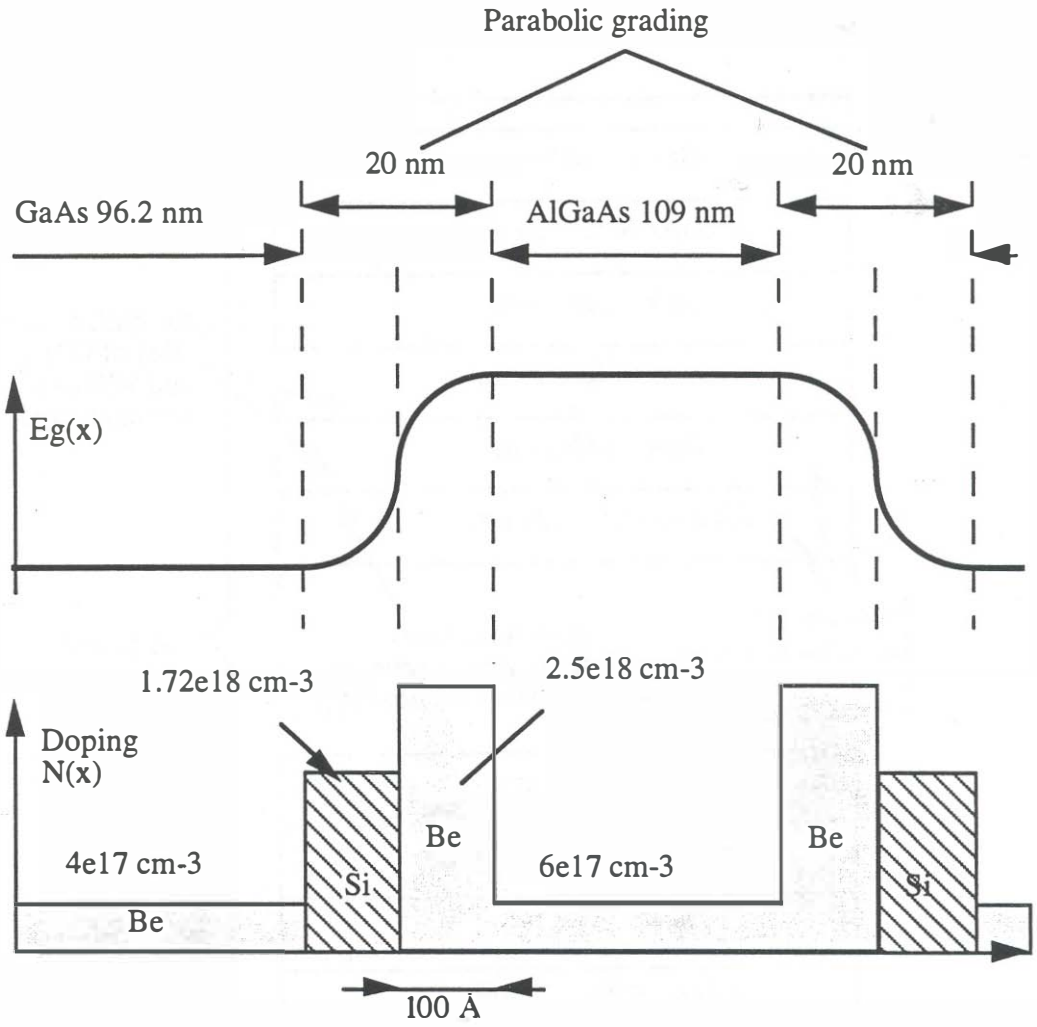


**Fig. 4.26**: Parabolic grading scheme of S250.

4.4.7. *Resistance of p-mirrors*

The resistances of mirrors S207 and S250 were measured independently by fabricating pillars as shown in Figure 4.27. The $p$-mirrors were fused to a $p^+$ InP substrate and pillars with square cross-sections were fabricated by substrate removal and chlorine reactive ion etching (Sections 5.1.4 and 5.1.5). There were two contact

pads (force and sense) which enable measurement of the mirror resistance without including the contact resistance of the pads. In addition one is able to measure the contact resistance without adding in the resistance of the mirrors. The voltage across the fused junction is included in the measurement. This type of arrangement was done because the $p$-mirrors were typically grown on semi-insulating or $n$-type substrates.

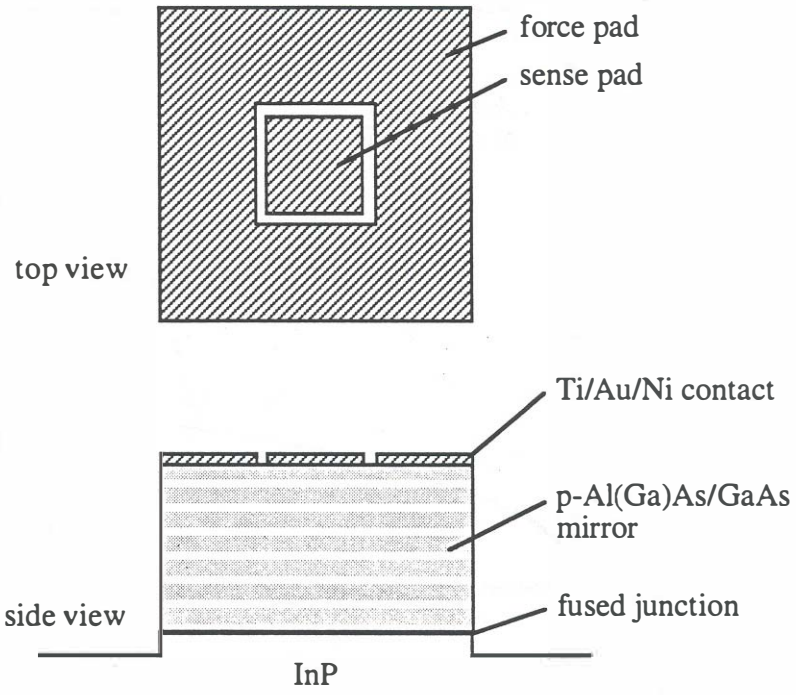


**Fig. 4.27**: Structure used for mirror resistance measurements.

The force and the sense pads had areas of 8400 $\mu m^2$ and 1225 $\mu m^2$. The mirror cross sectional area is 100 $\mu m^2$. All measurement were performed using 4 probes to eliminate any probe resistance or contact resistance. The current forcing was alternated through the sense pad to confirm that the lateral conductance was higher than the vertical. The contact resistance was approximately $2 \cdot 10^{-4}\ \Omega cm^2$ and all the

measurement were done with DC currents. The measurement results are shown in Figure 4.28. The data show that there is approximately 2.5 times improvement in the voltage drop at a given current. This improvement is not as good as has been seen by previous reports (Peters, 1995). However, the threshold power using this mirror was sufficient to allow for continuous-wave room-temperature operation of these lasers.

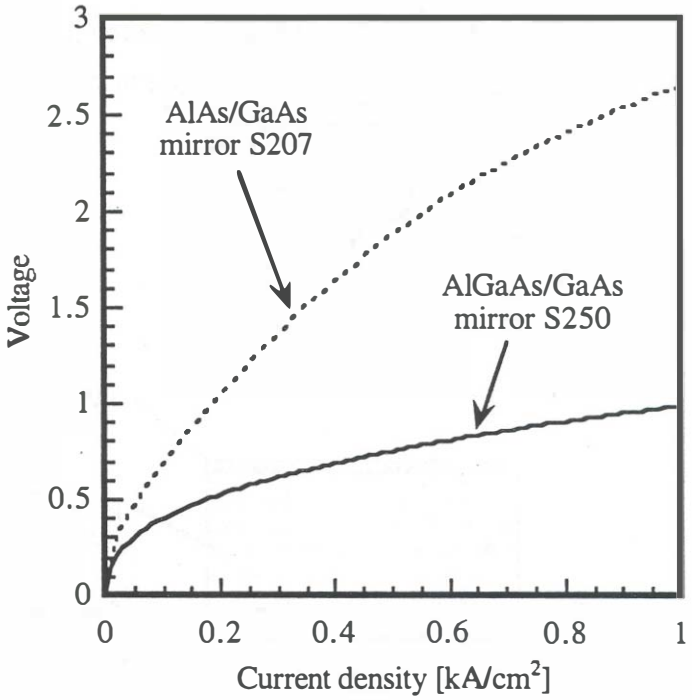


**Fig. 4.28**: Comparison between the continuous-wave $V-J$ characteristics of the two p-type mirrors used in this work. The voltage of the bandgap engineered S250 mirrors has been reduced by two and a half times in respect to the pulsed doped S207 mirror. The best fit to S250 voltage drop is given by $V(J) \cong (J/1012)^{0.4}$ V, where the current density is in $A/cm^2$.

## 4.5. *Conditions for continuous-wave operation*

With the given estimates of mirror reflectivities and the gain-current relationship we are able to determine the threshold currents and the conditions for continuous-wave operation.

To approximately account for power dissipation on the mirror resistances and the nonradiative recombination in the active layer we use a constant value for the voltage across the active layer, and fit the V-I characteristics of the mirrors. The voltage drop across epitaxial quarter wave mirrors is rarely linear. We use a fit of the form $V_{DBR}(J) \approx V_R + \beta J^{\gamma}$, where $\gamma$ is greater than zero. The total device power dissipation is then given by $P = VAJ + \beta A J^{1+\gamma}$, where $A$ is the device cross-sectional area and $V = V_R + \hbar\omega/q$.

The heat dissipation in the laser structure increases the active layer temperature $T$ to $T = T_h + \Theta P$, where $T_h$ is the ambient (heatsink) temperature and $\Theta$ is the thermal trans–resistance between the active area and the heat sink. A thermal trans-resistance $\Theta_{12}$ gives the increase in temperature at location 1 due to power dissipation at location 2. In our case we are interested in the increase in temperature of the active layer due to heat sources everywhere else in the cavity. The dominant sources of heat are the active layer and the $p$-mirror. The thermal trans-resistance at the place of the active layer due both of these two sources is approximately equal since all of the heat dissipated in the mirrors has to pass through the active layer. In other words, the value of the $p$-mirror thermal conductivity has a very weak effect on $\Theta$.

The temperature of active layer directly influences the threshold current. This dependence is empirically described using the local characteristic temperature (4-4) evaluated at room temperature: $J_{th} = J_0 \exp(T/T_0)$, where $J_0$ and $T_0$ define the behavior of the threshold current. Continuous wave threshold is achieved when the following relationship is satisfied

$$T_o \ln(J_{th}/J_0) = T_h + \Theta V A J_{th} + \Theta \beta A J_{th}^{1+\gamma}. \qquad (4\text{-}25)$$

For an arbitrary value of $\gamma$, this results in a transcendental equation in $J_{th}$. To keep the analysis simple we linearize the mirror voltage drop the current density range of interest. In this case, $\gamma = 1$ and the equation can be solved analytically to give the highest heatsink temperature $T_h^{(cw)}$ at which the device will operate continuously:

$$T_h^{(cw)} = T_0 \ln\left(\frac{J_{th}}{J_0}\right) - \frac{T_0 + \Theta V A J_{th}}{2} \qquad (4\text{-}26)$$

where $J_{th}$ is the threshold current density at $T_h^{(cw)}$ and is given by,

$$J_{th} = \frac{V}{4\beta}\left(\sqrt{1 + \frac{8\beta T_0}{\Theta V^2 A}} - 1\right) \qquad (4\text{-}27)$$

We now show the behavior of $T_h^{(cw)}$ as a function of device size for laser parameters predicted in this chapter: The S250 mirror voltage is linearized around 1 kA/cm$^2$ and expressed with $V_{DBR} \approx 0.5$ V, $\beta \approx 4.7 \cdot 10^{-4}$ $\Omega$cm$^2$, and $\gamma = 1$. We use $\hbar\omega/q = 0.8$ V and hence $V = 1.3$ V. The thermal resistance is given by $\Theta \approx 915 \cdot (12/d(\mu\text{m}))$ K/W (Sec. 6.2.), while the device area is given terms of the diameter with $A = \pi d^2/4$. From the estimated mirror reflectivities (99.7 % and 99.8 %) we expect a cavity round-trip loss of $\delta = 0.5$ %. For the active layer of structure $B$ this would require an approximate threshold gain of $g_{th} = 430\text{cm}^{-1}$. Inasmuch as we do not know what type of size dependent loss we can expect in this device, we

calculate several curves for losses that depend inversely on the diameter as $g_{th} = 430 \cdot (1 + d_0/d)\ \mathrm{cm}^{-1}$. This dependence is given only as an illustration of the influence of size dependent losses on the maximum CW operating temperature. The gain parameters are based on equations (4-1) and (4-2): $J_0 = 76.6\, N_{QW} \exp(g_{th}(cm^{-1})/846)\ \mathrm{A/cm}^2$, with $N_{QW} = 7$.

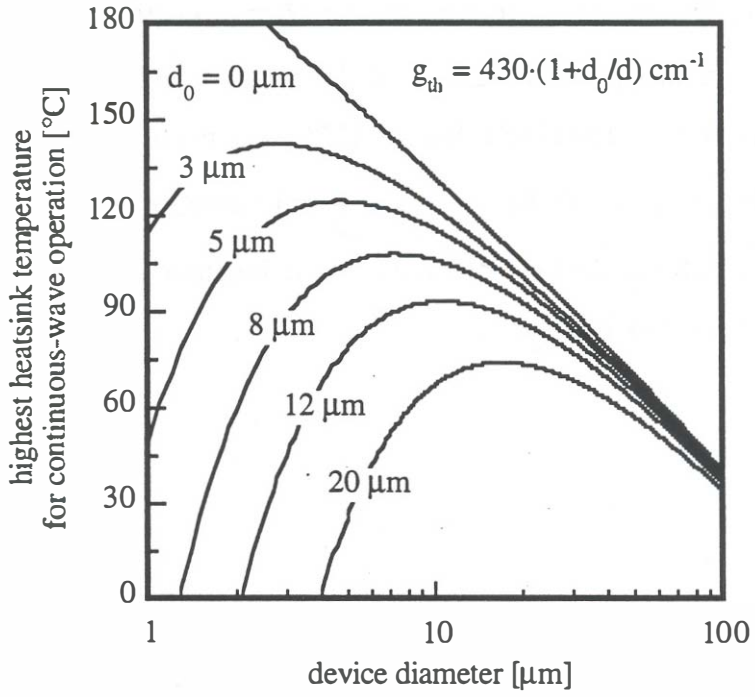


**Fig. 4.29**: Calculated highest heatsink temperature for continuous-wave operation based on the parameters given in this chapter. The size dependence of cavity loss is given only as an illustration.

The results are shown in Fig. 4.29. It is evident that in the absence of cavity dependent losses ($d_0 = 0$) the smallest devices are expected to perform continuously at highest temperatures. This is expected since for a constant threshold current density, a reducing device diameter results in a decreasing threshold power. This

power reduces faster than the increase in the thermal resistance for reducing device diameter. With the introduction of cavity dependent losses, such as, diffraction loss ($\delta \propto 1/d^3$) and sidewall scattering ($\delta \propto 1/d^2$ and $\delta \propto 1/d$), the threshold current density increases for smaller devices and limits the highest temperature for continuous-wave operation. The graphs shown in Figure 4.29 show that the lasers fabricated using the S250 p-mirror and the KS2778 active layer should operate continuously for range of diameters around 10 micrometers. The graphs in Figure 4.29 are given only as an illustration of the behavior of the highest CW operating temperature (4-26). The high values of $T_h^{(cw)}$ predicted by this model are unrealistic because the $g(J,\lambda,T)$ fit has been made only around room temperature. The temperature dependence of nonradiative recombination and absorption losses will eventually reduce the $T_0$ value and $T_h^{(cw)}$.

## 4.6. *Conclusion*

In this chapter, we have described the design and the issues important for the fabrication of continuous-wave operating fused long-wavelength vertical-cavity lasers. The information available for this design was sparse, and therefore several measurements of optical properties of used materials had to be performed. Still, the exact values of absorption coefficients, gain, and temperature dependence of optical properties are not known. These parameters will have to determined in the course of future development of these lasers. The issue of loss contribution of different layers in the cavity will be addressed again in Chapter 7, when we discuss the results on all fabricated devices.

Chapter 5

# Fabrication process

*In this business, nothing is ever exact.*

*Gerald Robinson*

The fabrication process for all working double-fused vertical-cavity lasers was in parts the same. There were three generations of laser structures, which are denoted by generation 1, 2 and 3. The active layers and mirrors used in these samples are listed in Table 4.1. The generations follow the trend of improvements in the lasers.

Generation 1 was the first working double-fused VCL that used KS2290 active layer, S207 *p*–mirror, and S201 and S230 *n*-mirrors. The mirror resistance of S207 was too high for obtaining continuous-wave operation at room temperature. The first task was to reduce the *p*–mirror resistance. The first mirror with reduced voltage drop was the S250 AlGaAs/GaAs mirror, and the lasers that used this mirror were designated as the *second* generation of double-fused vertical-cavity lasers. The active layer used in this second generation was the same as in the first generation, namely, KS2290. The laser structure of generations 1 and 2 is shown in Figure 5.1.

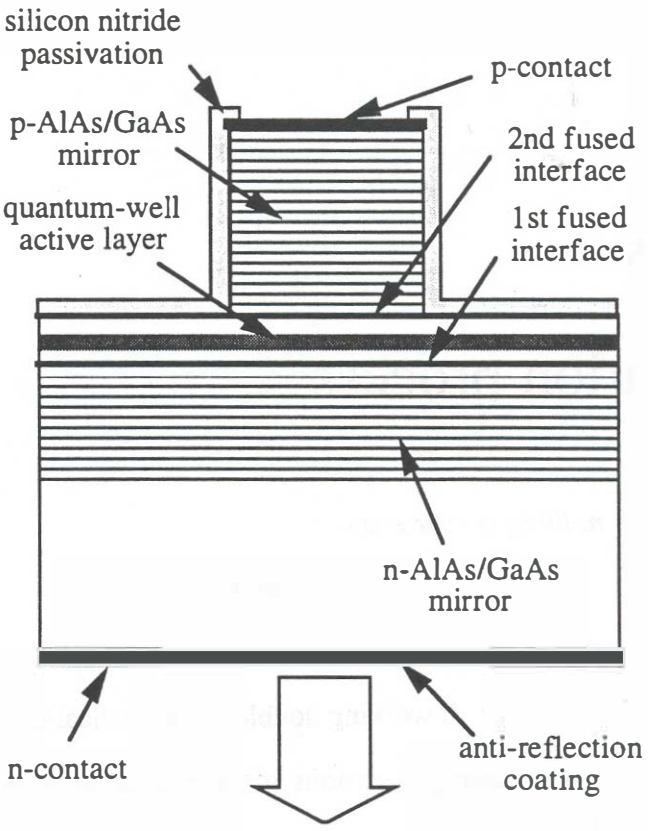


**Fig. 5.1**: Structure of generation 1 devices (F126).

The next improvement in the device performance was achieved by altering the active layer design: The separate confinement regions were removed and hence the quantum wells were embedded in InP cladding layers. Furthermore, since the active layers were grown with the *n*-type layers first, the first fusion was performed to the *p*-mirror, rather than to the *n*-mirror as it was done in generations 1 and 2. Two devices were fabricated with this new active layer (F170 and F171) and were designated as the *third* generation of double-fused vertical-cavity lasers. The structure of these devices is shown in Figure 5.2.

Apart from the epilayer changes there have been a few variations in the structures, mostly in the coating and the contact technology. All of the generation 1 and generation 2 devices except F126 had no silicon nitride coating and no anti-reflective coating on the bottom. Since the generation 2 and 3 devices had an AlGaAs mirror which oxidizes much slower than AlAs in generation 1 devices, there was no need for a silicon nitride coating. The process sequence described in this chapter follows the generation 1 and 2 device fabrication sequence. The fusion of generation 3 devices has a different order, but unless otherwise stated, the rest of the process sequence is identical to generation 1 and 2 devices.

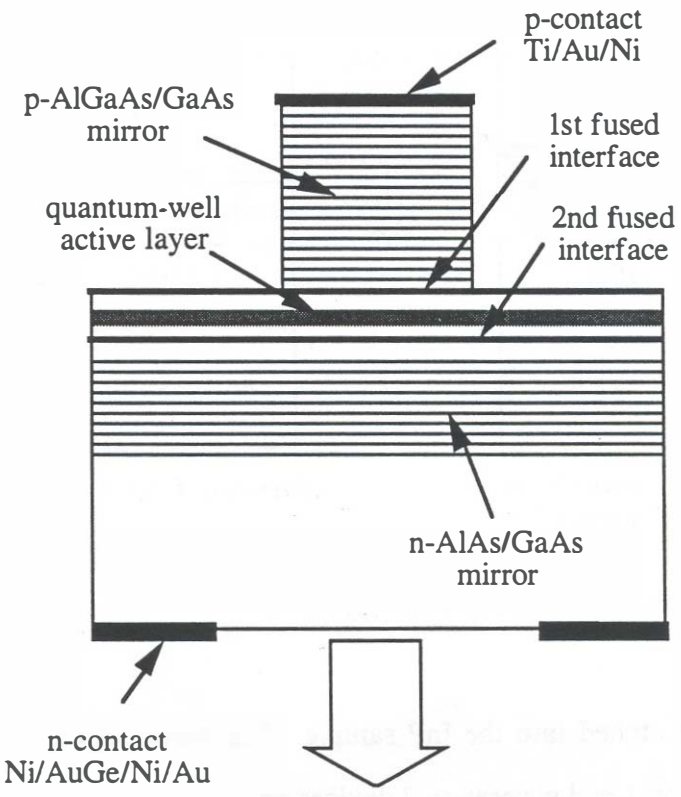


**Fig. 5.2**: The structure of generation 3 devices.

## 5.1. *Fabrication process steps*

### 5.1.1. *First fusion*

The fabrication process is illustrated with the sequence of Figures 5.3. Two MBE growths and one MOVPE growth are performed to provide the necessary epilayers. The samples to be processed are always cleaved into squares with dimensions $8\,\text{mm} \times 8\,\text{mm}$. The process sequence starts with the selection of an active layer sample and an *n*-mirror sample (Fig. 5.3a). This selection is based on the mirror center wavelength and the active layer photoluminescence peak.

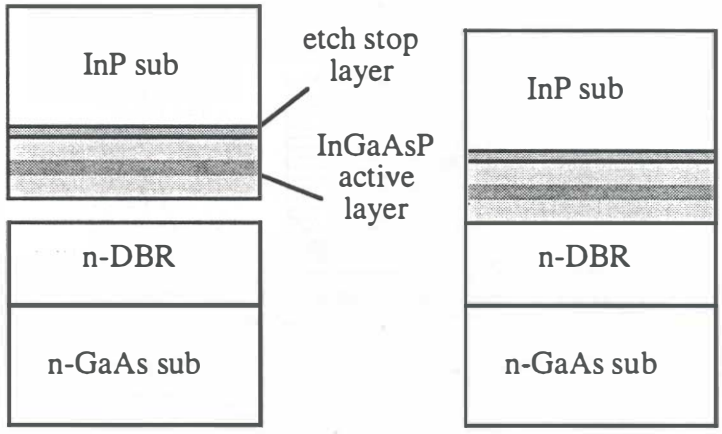


**Fig. 5.3**: Fabrication process steps (a) and (b).

Fusion channels are etched into the InP sample. The width and the depth of the channels on generation 1 and generation 2 devices was 5 μm and 122 nm. The depth was equal to the thickness of the InP cladding layers, while the channel pitch was 150 μm at all times. The channels always extended to the very end of the sample. This

was ensured by overexposing the channel mask. Before the fabrication of generation 3 devices it became evident that channels with insufficient cross-sectional area sometimes produced poor quality fusion. For this reason, all of the generation 3 devices have 10 μm wide and 300 nm deep channels (The thickness of the InP cladding on the generation 3 active layers is ≈ 300 nm). The etching of the channels is performed using 3:1 $H_3PO_4$:HCl. The etch rate of InP in $H_3PO_4$:HCl and $H_2O$:HCl mixtures at room-temperature is shown in Figure 5.4. This is a very viscous etch which is quite crystallographic at the 3:1 concentration. The etch can be made more isotropic (diffusion limited) by increasing the phosphoric acid concentration. A cross-section of a channel etched in InP substrate is shown in Figure 3.5. The chemistry of this etchant can be found in (Notten, 1991).

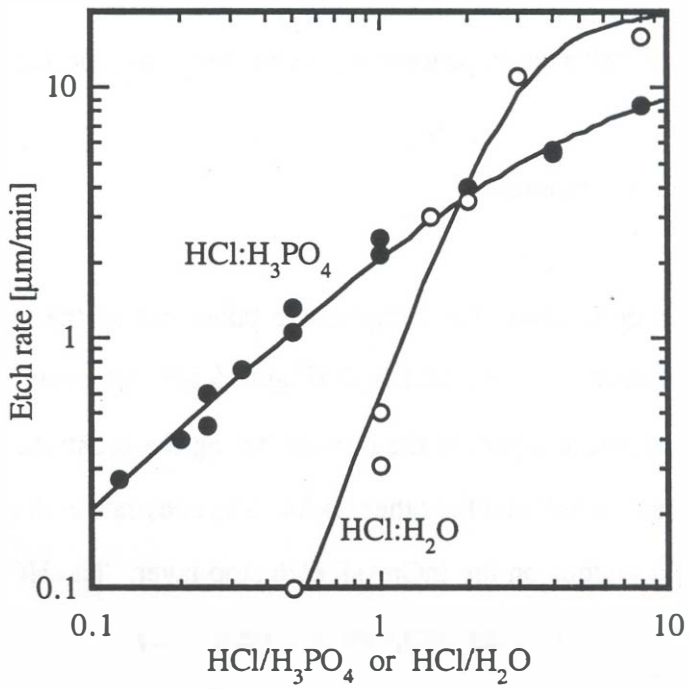


**Fig. 5.4**: The etch rate of InP in unagitated $H_3PO_4$:HCl and $H_2O$:HCl mixtures at room-temperature (12.1*N* HCl, 85%$H_3PO_4$).

After solvent cleaning and oxide removal, the *n*-type mirror is fused to the InP active layer at 630°C for 20 minutes in a hydrogen atmosphere (Figure 5.3b). During wafer fusion the two samples are aligned to fit each other exactly (cleaved edges are parallel) and uniform pressure is applied to the samples.

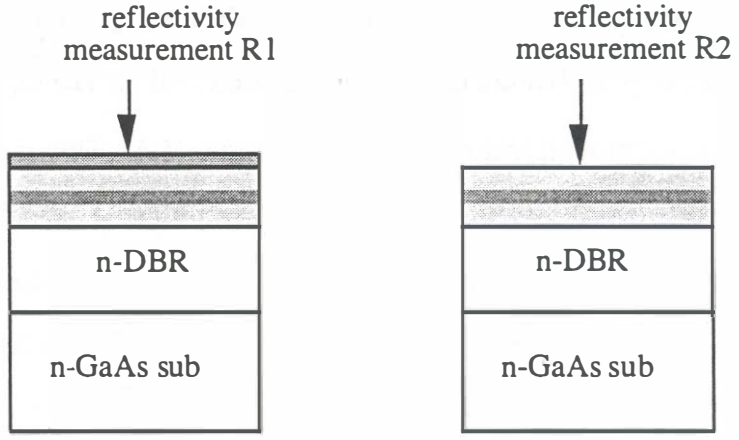


(c) InP substrate removal

(d) InGaAsP etch stop removal

**Fig. 5.5**: Fabrication process sequence. Steps (c) and (d).

5.1.2. *InP substrate removal*

After a 2 hour cool-down, the samples are taken out of the furnace and the InP substrate is removed using 3:1 HCl:$H_2O$ (Figure 5.5c). No attempt is made to protect the edges of the active layers or the mirrors during the substrate removal, since one side of the sample is InP and the other GaAs. The substrate etch typically lasts about 45 minutes and it stops on the InGaAsP etch stop layer. The HCl selectivity of InP over GaAs and Ga containing compounds is perfect at room temperature if there are no defects. One may also use concentrated acid since HCl etches InP only in the undissociated state, however, there has been some indications that too fast substrate

removal promotes cracking of fused samples (Dudley, 1994). This issue was not investigated.

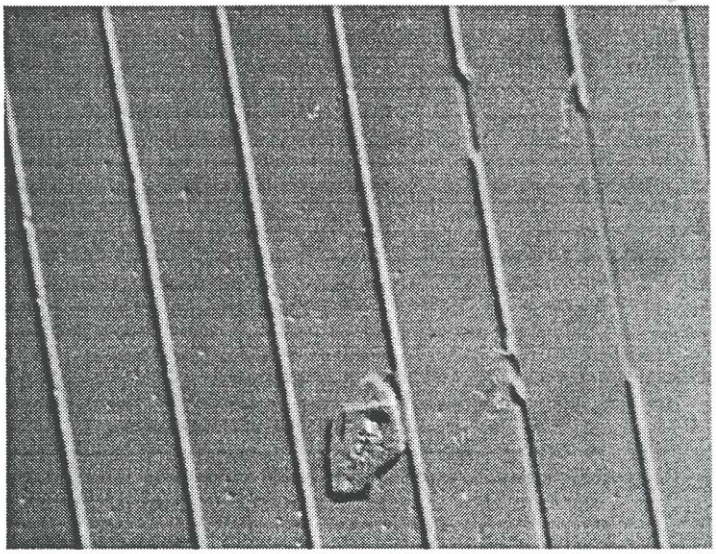

**Fig. 5.6**: Bowing of the InP epilayers into the channels after first wafer fusion and InP substrate removal. The channel pitch is exactly 150 μm.

Most of the time, especially if the channels were deep, at this point one can observe the bowing of the active layer in the places where the channels are located below the active layer. This can be seen on a microscope photograph using a Nomarski interferometer in Figure 5.6. The scale in the figure is defined by the channel pitch which is exactly 150 μm.

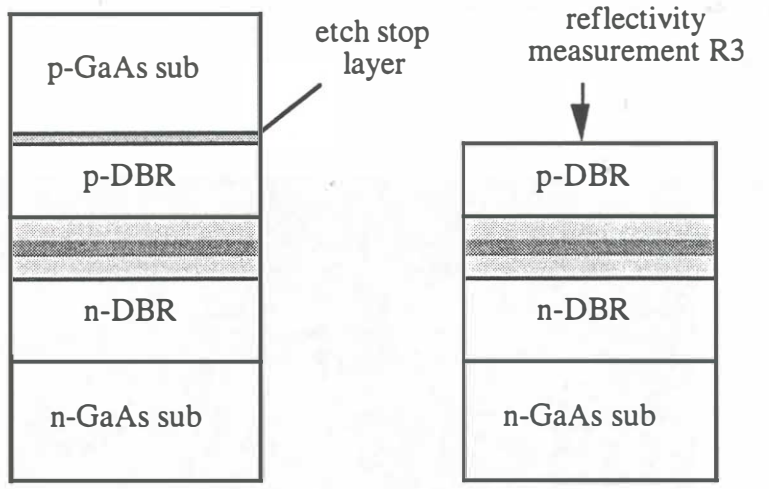


**Fig. 5.7**: Fabrication process sequence. Steps (e) and (f).

5.1.3. *Second fusion*

With the InP substrate removed, a measurement of the cavity mode wavelength is possible because the phases of the $n$-mirror and the air/InGaAsP etch stop layer interface are exactly opposite (measurement $R_1$ in Fig. 5.5c). The existence of the channels cause only a small perturbation in this reflectivity measurement since their area makes up less than 7 % of the total area. A $p$-type mirror is selected to match the measured cavity mode wavelength and in this way we maximize the $p$-mirror reflectivity based on an in-process measurement. It is for this reason that the thickness of the etch stop layer has to be exactly one quarter wavelength at the design frequency. After the removal of the etch-stop layer with $H_3PO_4$:$H_2O_2$:$H_2O$ (Fig. 5.6d) and fusion of the $p$-type mirror (Fig 5.7e), the cavity mode remains approximately at the same wavelength (Fig. 5.7f). This is confirmed a mode position

measurement $R_3$ (Fig 5.7f). The match between mode position measurements $R_1$ and $R_3$ is typically within several nanometers. Reflectivity measurement $R_2$ without the etch stop layer shows an increase in reflectivity at the mode position since both the $n$-mirror and the air/InP reflections are in phase. The three reflectivity measurements for sample F126 are shown in Figure 5.8.

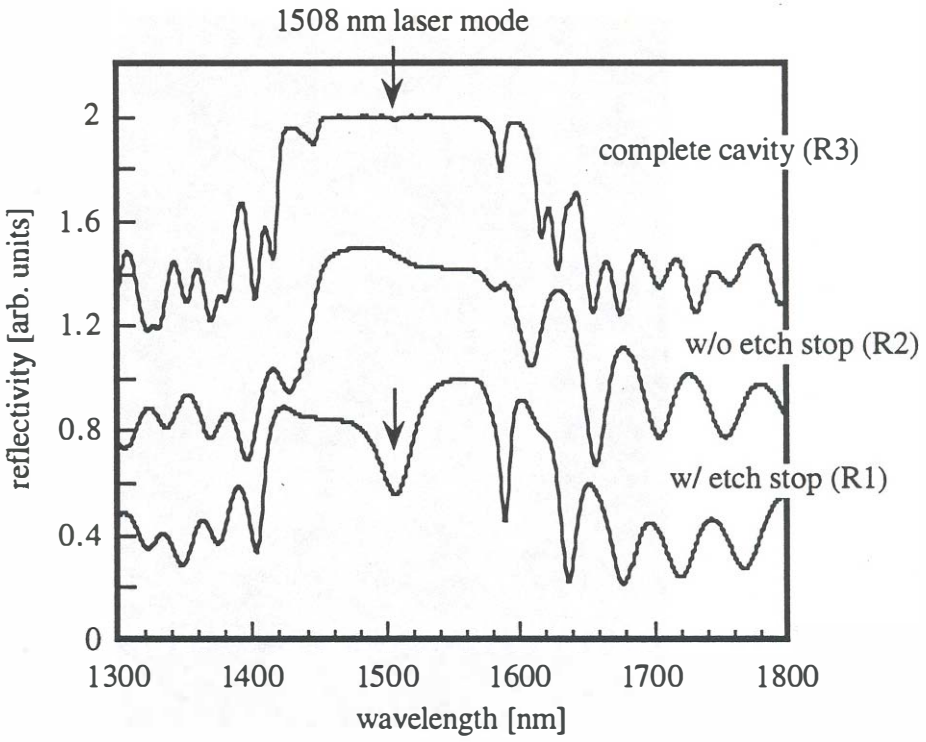


**Fig. 5.8**: In-process reflectivity measurements used to determine the cavity mode position and adjust the $p$-mirror center wavelength.

At this point is was very important to keep track which of the two sides of the fused structure is $p$ and which is $n$, because sometimes they looked very much alike. After the second fusion step, the back side of the $n$-mirror was polished using Br:MeOH if the devices used the S276 mirror (the back of S276 mirror was matte). The polishing was done by hand because it was found that mounting the samples and

polishing using a chuck increased the possibility of breaking them. After polishing, the $n$-type contact was deposited in a 1 mm stripe at the back of the sample. The contact was a standard Ni/AuGe(12%)/Ni/Au alloy evaporated using the electron-beam evaporator and alloyed at 400°C in the rapid thermal annealer. For generation 1 devices the annealing was performed at the same time as the $p$-contact (after the posts have been defined).

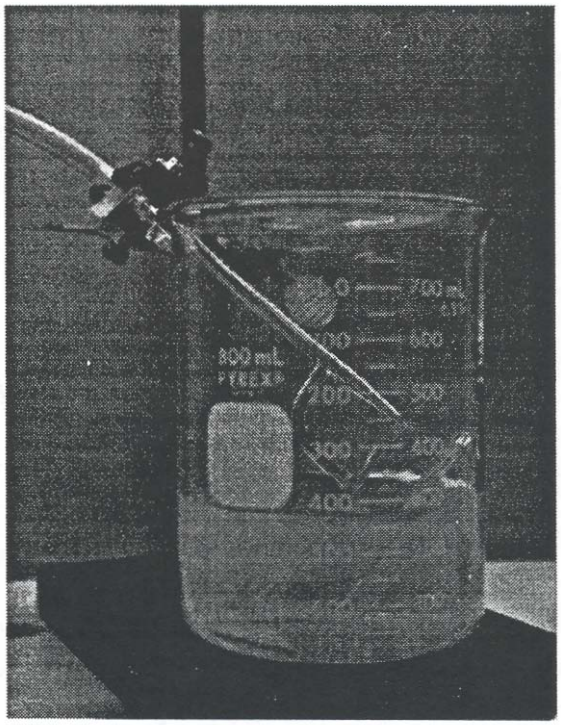


**Fig. 5.9**: A photograph of the in-house developed spray etcher.

5.1.4. *GaAs substrate removal*

After the fusion and polishing, the $p$-GaAs substrate is removed using $NH_4OH:H_2O_2$ spray etching, and the AlAs etch stop layer is removed in 25% HF. Spray etching is a common technique for selective substrate removal used in GaAs

VCL fabrication (Tanobe, 1992) and fused GaAs laser fabrication (Lo, 1993). The GaAs over AlAs selectivity in this etch is based on the difference in the solubility of Ga and Al oxides in aqueous solutions of specific pH value. When low pH values are used (less than 8) violent agitation in the form of a spray is used to help the dissolution and prevent complete oxidation of the surface. An in-house spray etcher shown in Figure 5.9 has been developed for this purpose. The etch rates of GaAs and AlAs achievable with this system are shown in Figure 5.10. The total time necessary to remove the entire substrate is around 3 hours.

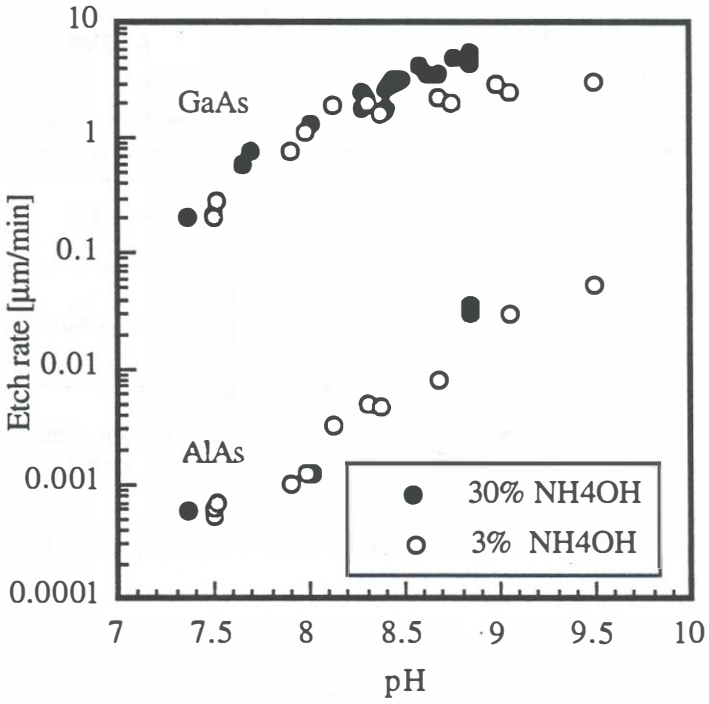


**Fig. 5.10**: Etch rates of AlAs and GaAs achievable with the spray etcher using $NH_4OH:H_2O_2$ (30%$NH_4OH$, 28% $H_2O_2$).

During the two fusion steps and the subsequent substrate removal the edges of the samples get damaged so that areas within typically 3/4 mm of the sample edge

become unusable. Note that during the first substrate etch ( HCl ), AlAs layers in the *n*-mirror and the InP in the active layer claddings are etched from the side, while during the spray etching the *n*-substrate gets etched from the corners as well as from the side. The damage from substrate removal steps ultimately reduces the usable area on the sample to approximately $40\,mm^2$. Within this area there are typically no cracks or bubbles. The only defects visible in the fused epilayers are those coming from the epilayers themselves, which are mostly oval defects in the MBE grown mirrors (see Chapter 3 for more details).

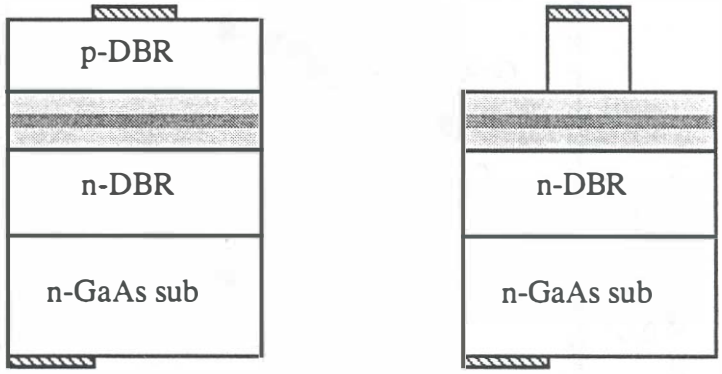


(g) *p* and *n* contact deposition

(h) Chlorine reactive ion etching

**Fig. 5.11**: Fabrication process sequence. Steps (e) and (f).

5.1.5. *Top contacts and reactive ion etching*

The generation 1 devices were defined by circular Au/AuZn/Pd/Au/Ni contacts which were fabricated by a standard lift-off process (Fig. 5.11g). The mask contained circular patterns with 10 different diameters ranging from 6 μm to 60 μm. Figure 5.12

shows the units cell of the laser mask. The dot sizes were 6, 8, 10, 12, 16, 20, 26, 36, 48, and 60 μm. The laser-dot density is 24800 $cm^{-2}$.

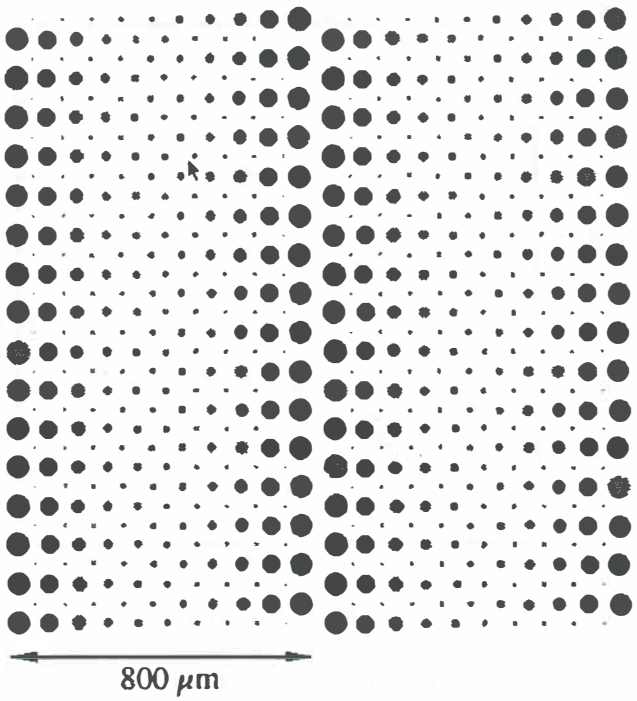


**Fig. 5.12**: Unit cell of the vertical-cavity laser mask. The pattern contains ten different sizes from 6 μm to 60 μm (inclusive) in an approximate exponential progression: 6, 8, 10, 12, 16, 20, 26, 36, 48, 60.

The top contacts ( *p*-type) were alloyed at 430°C for 20 seconds in a rapid thermal annealer (RTA) after the pillars were etched. The thicknesses were 3 nm Au, 100 nm AuZn (5%), 40 nm Pd, 100 nm Au evaporated in a thermal evaporator, followed by 150 nm of Ni evaporated in the electron-beam evaporator. For generation 2 and 3 devices the contact was not alloyed an consisted of a very thin Ti layer (approximately

5 nm), 100 nm of Au and 175 nm of Ni all evaporated in the electron-beam evaporator.

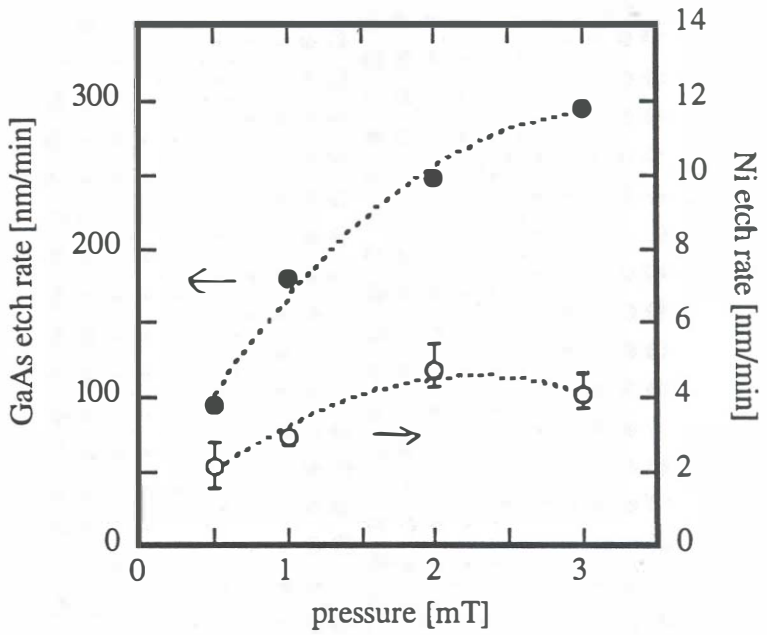


**Fig. 5.13**: The etch rates of GaAs and Ni in chlorine reactive ion etcher at different pressures.

The thickness of the nickel layer was critical since it was used as a mask in $Cl_2$ reactive ion etching. The etch rate of Ni in comparison with GaAs is shown in Figure 5.13. The posts are etched in pure $Cl_2$ plasma (1mT/350V), and a HeNe laser is used for *in situ* optical monitoring of the etching. At these conditions, Ni etches approximately 3 nm/min and hence the total thickness of the last Ni layer on top of the contact had to be adjusted to never let the Au remain exposed to the chlorine plasma. Gold does not etch chemically in chlorine, but is easily sputtered off. The thickness of the S207 mirror was approximately 5 μm, while the S250 mirror was 7 μm thick which is the reason for different Ni thicknesses on top of the contact. The

evaporation of the Ni layer was done with several cooling steps to reduce the possibly of exerting high stress on the rest of the (non-alloyed contact). It was observed that in some cases the nickel layer would peel off the contact metals if adhesion was poor. This was very common with silver which was investigated, but finally abandoned for this reason.

Figure 5.14 shows the in-situ normal-incidence reflectometer trace for the etching device F170. The total times of etching for S207 were about 35-40 minutes, while for S250 they increased to 50-60 minutes. A very low vacuum system base pressure before chlorine etching was instrumental for obtaining vertical sidewalls on the posts. The presence of oxygen increases the selectivity between AlAs and GaAs etch rates. This was particularly important in generation 1 devices which uses AlAs in the mirrors. The etching of S250 mirror was easier since AlGaAs did not oxidize as easily. The typical base pressure used was below 26 μPa ($2 \cdot 10^{-7}$ Torr).

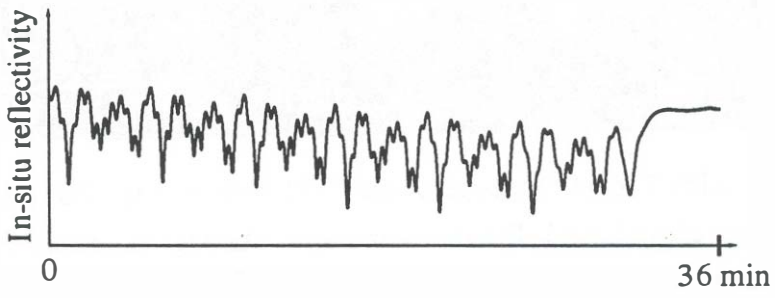


**Fig. 5.14**: In-situ normal-incidence reflectometer trace for reactive ion etching of a F170 device in chlorine.

Due to the low volatility of $InCl_3$ at the processing temperature (<60°C) InP etches more than five times slower than GaAs at these conditions. The approximate InP etch

rate at given conditions is 40 nm/min. Therefore, the InP cladding layer serves as an efficient etch stop layer and enables overetching for several minutes to eliminate any micro-loading effects around the posts. The micro-loading effects are quite pronounced around the pillars as seen in Figure 5.15 where the InP cladding of device F171 has been removed to show the width of the GaAs corner that remained after a 3 minute over-etch.

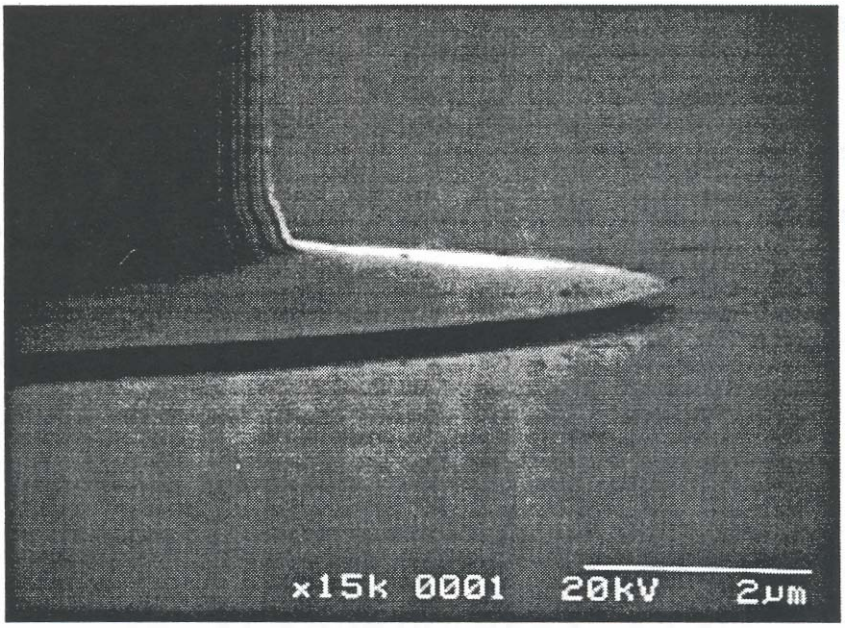


**Fig. 5.15**: The bottom edge of the F171 post with the InP p-cladding selectively removed. The free-standing GaAs edge is a result of micro-loading effects: The corners next to the pillar do not etch as well as the open areas.

Devices F123 and F125 had corrugated sidewalls resulting from selective etching of GaAs over AlAs and roughness from interruptions during the $Cl_2$ etching step. For the fabrication of devices F132 and F133, the $Cl_2$ etching was uninterrupted, the

GaAs/AlAs selectivity was reduced by lowering the base pressure before the etch from 50 μPa to 17 μPa ($1.3 \cdot 10^{-7}$ Torr), and after etching the devices were kept in $N_2$ atmosphere to slow down AlAs oxidation. For device F126, the etching was performed in the same way as for devices F132 and F133, but the sample was coated with silicon nitride immediately after the etching. For device F126, an additional patterning step was used to open the contacts at the top of the mesa and the backside was coated with an SiO anti-reflective film evaporated in the electron-beam evaporator. All of the generation 1 devices were alloyed after the chlorine etch.

A scanning electron micrograph of finished devices F126 (with silicon nitride coating) is shown in Figure 5.16. Inasmuch as all three substrates are aligned before fusion it is possible to cleave the samples smoothly along the {011} planes. An SEM of a cleave through a F126 laser post is shown in Figure 5.17. The cleaved edge has been stain etched with $H_3PO_4$:$H_2O_2$:$H_2O$ which selectively etches all the involved materials in a descending etch rate: AlAs → GaAs → InGaAsP → InP. The dark regions in Figure 5.17 are the most deeply etched AlAs layers. The last period of the $n$-mirror has a $3\lambda/4$ GaAs layer which is not crucial for the design (S230). The device was not cleaved exactly through the center and hence one can see the silicon nitride coating on the side of the pillar. The reason the silicon nitride coating edge is not vertical in the figure, is because the cleave through the pillar is not perfectly vertical.

A magnified view of the stain-etched active layer is shown in Figure 5.18 (same device as in Figure 5.17). Stain etching is also necessary to decorate the fused junctions between GaAs and InP. The presence of any micro-voids in the fused

junctions is easily detected using this stain etch since the etchant enters the void by capillary action and then increases the width of the void by etching GaAs (see Chapter 3). In Figures 5.17 and 5.18 the $n$-fused junction is visible as a very faint line. The $p$-junction is barely visible because the thickness of the GaAs above the $p$-fused junction has been reduced due to stain etching: As AlAs in the first period of the $p$-mirror etches inwards, it opens an area above the first $\lambda/4$ $p$-GaAs layer which is then thinned down very quickly.

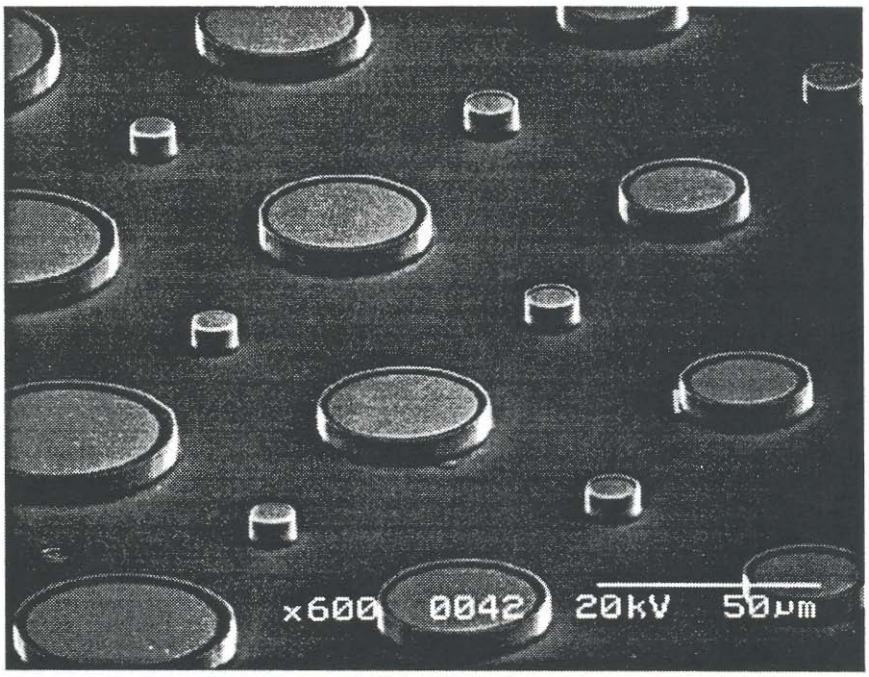


**Fig. 5.16**: Finished double-fused vertical-cavity lasers (Device F126). The ring visible on top of the mesas is the opening in the silicon nitride passivation. The clear areas are InP coated with 100 nm of silicon nitride. Large part of the processed sample is clean and without damage as shown in this scanning electron micrograph.

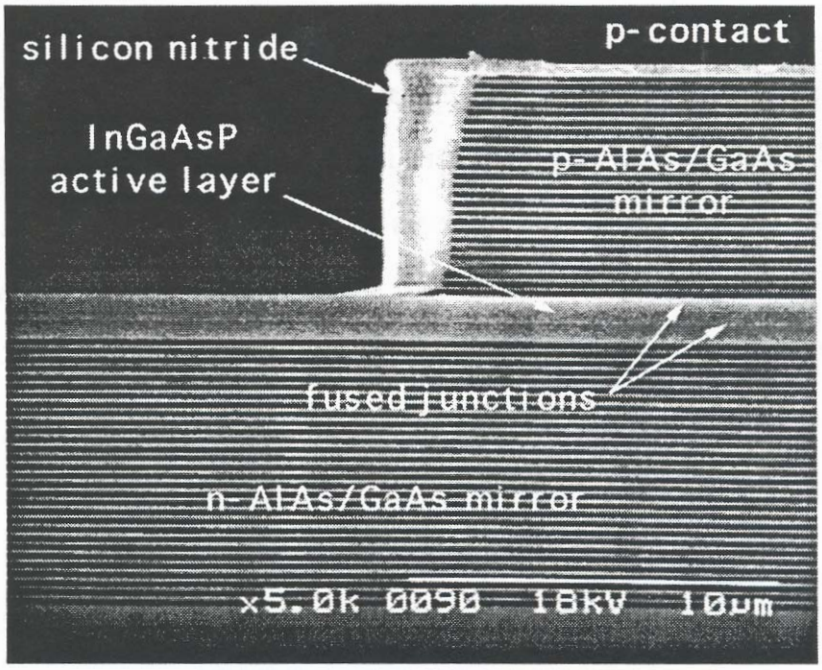


**Fig. 5.17**: Cleaved and stain-etched vertical-cavity laser (F126).

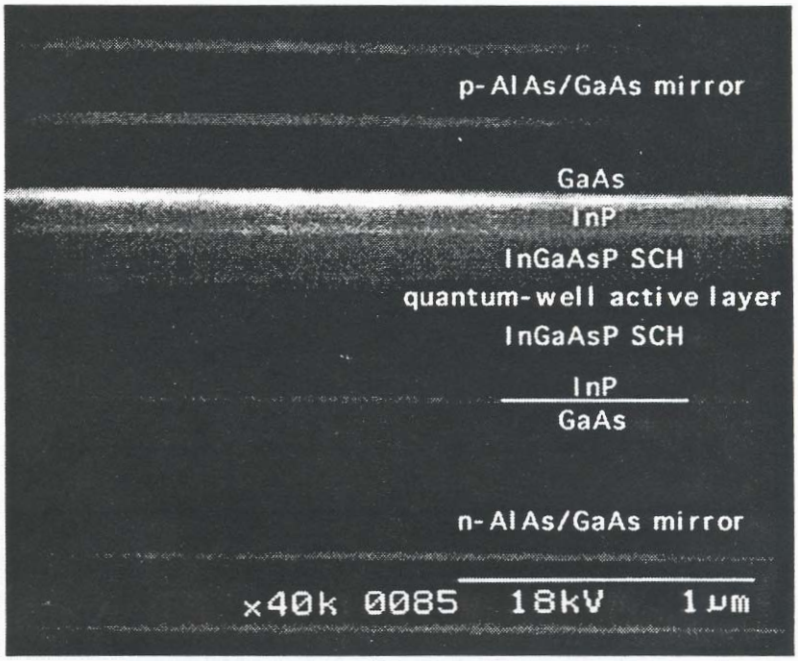


**Figure 5.18**. Stain-etched view of the active layer. Active layer in this device is KS2290.

## 5.2. *Conclusion*

In this chapter we have described the fabrication process of index-guided post double-fused vertical-cavity lasers. There is a large number of structures that can be investigated once the fused epilayers are formed and this shall be left for future developments. We have shown here a simple single mask process that produced working 1.54 μm vertical-cavity lasers.

Chapter 6

# Device characteristics

The characterization of double-fused lasers consisted of pulsed and continuous wave light-current, emission spectra and near-field pattern measurements. The summary of characterized samples is given in Table 4.1. The characteristics of the first two generations of double-fused vertical-cavity lasers are given in Section 6.1.1, while the continuous-wave operation of generation 3 devices is described in Section 6.1.3. The polarization and transverse mode studies have been performed only on the generation 1 devices (F132) and are described in Section 6.1.2. The estimate of the thermal resistance of these devices is described in Section 6.2. The analysis of a number of other laser parameters is given in Chapter 7.

The setup for measurement of calibrated light-current characteristics is shown in Fig. 6.1. The sample is placed on a copper block with a 2 mm hole in the center through which the light is taken out. Silver epoxy (Epoxy Technology, 410E) is used to improve the contact between the back contact on the sample and the gold plated copper chuck. The back of the sample was sometimes not completely flat due to hand polishing of the $n$-side (see Sec. 5.1.3 for details). The light output was measured using a calibrated Ge detector (diameter $\approx 5\,\mathrm{mm}$) and a matched power meter.

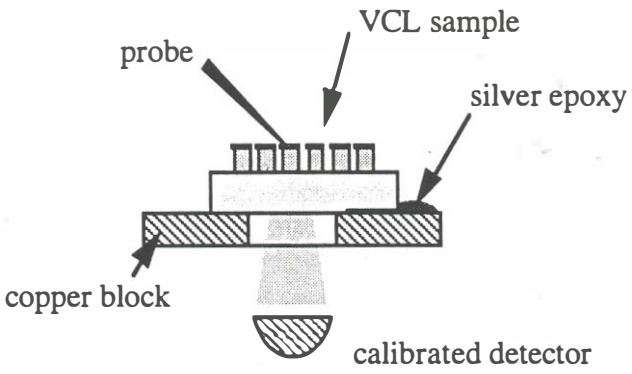


**Fig. 6.1**: Setup for the measurement of calibrated light-current characteristics.

The measurements are performed at pulsed and continuous-wave conditions using a computerized test setup. The CW voltage-current characteristics are acquired using the semiconductor parameter analyzer (HP4145) with the simultaneous acquisition of the light out using a calibrated detector (Newport 835): The current through the sample was stepped and the voltage and the light were measured. For pulsed measurements the connectors had to be changed to connect the setup to the pulse generator (HP8116). For light-current acquisition, the voltage was stepped at the pulsed generator and the current was read using an inductive current probe. The probe output was terminated with 50 ohms at the lock-in amplifier (EG&G 5209). The calibration of the current pulses and the locking amplifier readout (adjusting the sensitivity) was performed using a separate oscilloscope and a resistor. In this way the computer program directly measured calibrated Light-current-voltage characteristics for both DC and pulsed measurements. This method of calibration of pulsed measurements resulted in an uncertainty of ±5% in the current and voltage values. The spectrum of the laser was

measured by coupling the laser output directly into a multi-mode fiber that was connected to an optical spectrum analyzer.

The polarization and transverse mode characteristics were measured using a slightly modified setup shown in Fig. 6.2. The laser output was reflected on a gold mirror and collimated onto a detector or an infra-red camera. The beam was passed through a rotatable Glan-Thompson polarizer with an extinction ratio better than 30 dB. For the near-field pattern measurements we used a Hamamatsu C2741 camera.

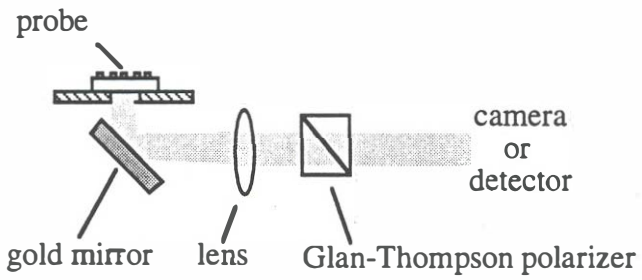


**Fig. 6.2**: Setup for measurement for measurement of polarization resolved light-current characteristics and transverse mode properties.

The temperature control of the stage is performed open-loop with a thermo-electric cooler/heater powered from a DC power supply. The temperature readout was done using a calibrated thermistor (Dale 1T1002-5) that was attached to the copper block approximately 5 mm from the sample. For "room-temperature" measurements the stage temperature was not controlled.

The thermal resistance of the lasers was measured by two methods. The first method was to monitor the shift in the lasing wavelength with temperature of the laser, while the other used the threshold current as a thermometer. The mode wavelength method was used on devices F132 since at that time no continuous-wave operation was available. With devices that operated CW at room-temperature and above room temperature (F170) it was possible to compare the CW and pulsed measurements and get a more direct measurement of the thermal resistance.

## 6.1. *Laser characteristics*

### 6.1.1. *Room-temperature pulsed measurements (GEN 1 and 2)*

The devices F125 and F123 were the first fabricated double-fused vertical-cavity lasers. All device diameters greater than and equal to 9 μm (nominally 10 μm) were found to lase under pulsed conditions (50 ns / 50 kHz / 25°C). The samples F132 and F133 were fabricated immediately after with improved processing. On this second batch of samples (F132/F133), all ten laser sizes on the mask (6 to 60 μm inclusive) operated at room-temperature under pulsed conditions (50 ns / 25 kHz / 25°C). The voltage drop at threshold across all generation 1 devices ranges from 12 V on the largest to 24V on the smallest devices. This large voltage drop is dominated by the *p*-AlAs/GaAs mirror (S207). An independent measurement of the fused junction voltage drop on a 60 μm device indicates that at threshold for this device size, less than 2 V appears across the fused junction and the ohmic contacts combined. The current-voltage characteristic of the S207 mirror is shown in Fig. 4.28. The best performance in this generation was measured on sample F126.

A large number of light-current measurements was taken to characterize the yield and determine the best performance. Since F123 and F125 were processed in parallel, only the better sample (F125) was fully characterized. The same applied to F133 and F132 where F132 performed slightly better. Devices in areas highly damaged from substrate etching (within 1 mm of the edge), were not tested. Out of 170 devices with diameters greater or equal to 9 μm measured on sample F125, 153 lased. On sample F132, 125 devices of all diameters were tested and 120 were found to lase. On sample

F126, 80 devices were tested and all lased. The overall yield is higher than 95%. The remaining 5% is attributed to oval defects in the MBE grown wafers which appear on both mirrors (Fig. 3.23), defects in the active layer, or particles trapped in the fused junctions (Fig. 3.21). Although there is the possibility of incomplete fusion within a device, there has been no indication that the fusion process reduces the yield of these lasers. A separate measurement of photoluminescence from the active layer before and after wafer fusion was performed, but no measurable change in position and the intensity of the emission spectra was observed. More investigation in this area is necessary to assess the long term impact of fusion on device reliability.

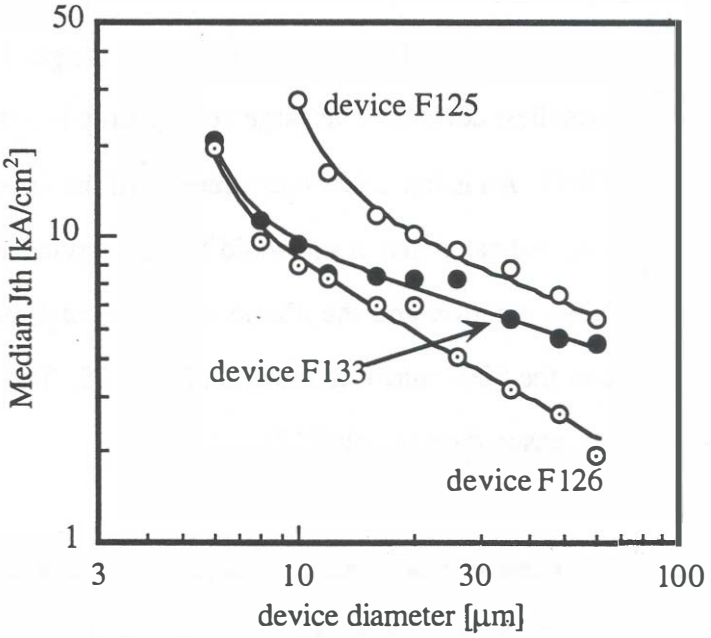


**Fig. 6.3**: Median threshold current density as a function of device diameter for 153 devices on sample F125, and 120 devices on sample F132, and 80 devices from sample F126.

The graphs in Fig. 6.3 summarize the median threshold current density as a function of device diameter for all devices that were found to lase. Due to the slight difference in the alignment of the cavity mode to the mirror reflectivity peak and the gain peak, the devices exhibit different threshold vs. temperature behavior. In all devices the lasing mode is located the short–wavelength side of the gain peak at room temperature, which causes relatively low values of the characteristic temperature $T_0$. Device F125 lased at 1522±3 nm with a characteristic temperature $T_0 \approx 40\text{K}$, device F132 lased at 1517±2 nm with $T_0 \approx 28\text{K}$, while device F126 operated at 1508±5 nm with $T_0 \approx 23\text{K}$. (Characteristic temperature is defined as $T_0 \equiv I_{th}\, dT/dI_{th}$ taken at room temperature). Maximum pulsed output of 14 mW was measured on a F132 device. The associated light-current characteristics is shown in Fig. 6.4.

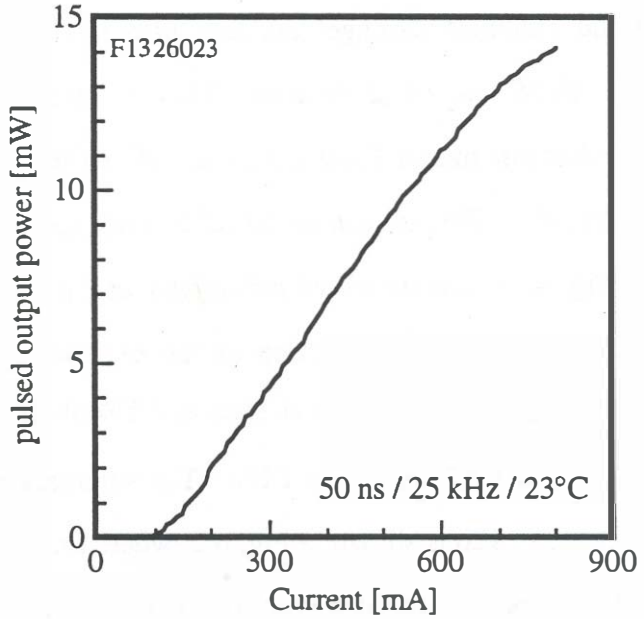


**Fig. 6.4**: Pulsed light-current characteristic of a 60 μm device delivering up to 14 mW pulse output power (F132).

The trends in the threshold current density of the three runs can be explained as follows: On device F125, light scattering from the post edges due to interrupted and selective $Cl_2$ etching produced the fast increase in the threshold current density with reduced device diameter. Consequently, the smallest operating device had a diameter of 9 μm. Once the reactive ion etching step was improved and the sidewalls protected from oxidation by keeping the lasers in $N_2$ atmosphere, the performance of the smaller devices improved, enabling the operation of the smallest devices on the mask (6 μm) and reducing the lowest threshold current by a factor of three (down to 4 mA). Since devices F125 and F132 were fabricated using similar mirrors and active layers, the threshold current density for large devices tends towards approximately the same value. In going from device F132 to F126, only a slight improvement was observed in the performance of smaller devices, while the threshold current density of the larger devices, where the sidewall damage has less effect, shows better than 30% improvement over F125 and F132 devices. This is attributed to the increased reflectivity of the bottom mirror (larger number of periods and better mode to reflectivity peak match). This is seen in the reflectivity spectra of S230 and S201 mirrors shown in Fig. 4.18. The increased reflectivity of the output coupler (bottom mirror) is also confirmed by the reduction of the external differential quantum efficiency $\eta_{ex}$ on the large devices: From as high as 2.5% observed on devices F125 and F132, it decreased to 1.3% on device F126. The summary of threshold current measurements on device F126 is shown in Fig. 6.5, where the highest and the lowest measured threshold current was denoted with the top and the bottom end of the error bar. Some improvement in the performance of the smaller devices is attributed to the sidewall passivation using silicon nitride and has resulted in a number of devices lasing at 3 mA pulsed at room temperature.

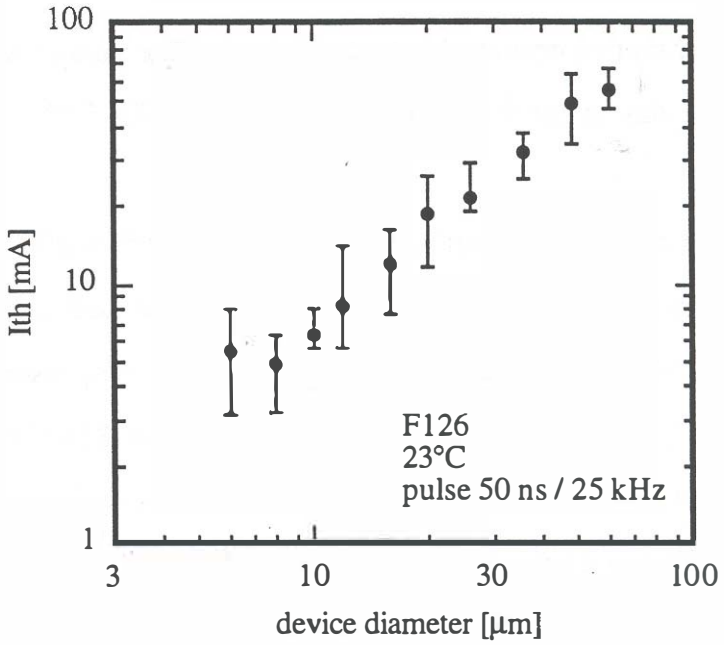


**Fig. 6.5**: Threshold current vs. device size on F126. The top and the bottom ends of the error bars show the highest and the lowest value of threshold current measured.

There has been a number of attempts to fabricate generation 2 devices. The device F139 used a non-alloyed silver contact on top, but during the chlorine reactive ion etching the silver was deeply undercut. Some lasers operated and room-temperature pulsed threshold current densities as low as 1.5 $kA/cm^2$ were observed. This was lower than any generation 1 device and indicated that generation 2 devices have lower cavity losses. The laser threshold voltage was about 2.5 times lower than in generation 1 devices. This was in agreement with the mirror resistance measurements described in Section 4.4.7. The next two attempts to fabricate this device used a non-alloyed gold mirror (F151/F152) and the laser was processed for upside down mounting with indium solder onto diamond heatsinks (See Sec. 8.1). However, due

to some contamination the fused junctions were full of voids and only very few lasers operated under room-temperature pulsed conditions. The stain-etched cleaved edge of the fused junctions on one of these devices is shown in Fig. 3.13.

The first working runs of generation 2 devices were F166 and F167. Two different *n*-mirrors were used on these two runs. The F167 device used the S201 mirror, while F166 used the S276 mirror. Based on the discussion of cavity resonance tuning given in Section 4.3, it was concluded that the combination S250, KS2290 and S276 samples would have too long a cavity length. For this reason, a part of the 50 nm of GaAs layer on top of the S276 was etched off before fusion. This was quite successful since F166 eventually operated room-temperature pulsed with a lasing wavelength of 1549 nm. No such mode adjustment was used on the F167 sample since the *n*-mirror S276 already had 50 nm GaAs layer on top to adjust the mode. This laser operated at 1532 nm. The characteristics of these lasers were not investigated to a great extent, except to compare them to the F170 device which operated continuously at room temperature. Both F166 and F167 operated with lower threshold currents and threshold current densities than any other generation 1 devices. The comparison with F170 is made in Chapter 7.

### 6.1.2. *Transverse-mode and polarization properties (GEN 1)*

The analysis of the near-field patterns and the polarization characteristics of these lasers reveals an interesting property: The light output from these lasers is very strongly polarized along the [011] direction of the active layer for both single and multiple-

transverse mode operation. Single mode operation was observed on the smallest devices (6 and 8 μm), while larger devices operated multimode already at threshold. The reasons for this strong polarization anisotropy are not as yet clear. The possible causes include the influence of biaxial stress in the active layer resulting from wafer fusion, and stress inherent to the MOVPE-grown active layer. Since the active layer is exposed between the finished devices (Fig. 5.1 without the silicon nitride coating), a polarization-resolved photoluminescence measurement can be used to investigate any polarization coming from the active layer fused to the bottom mirror. The measurement was performed on sample F125 and no anisotropy was detected. However, the anisotropy may be too weak to be observed in the photoluminescence spectrum, but may still be large enough to effect the gain and the threshold of differently polarized modes. The polarization-resolved light-current characteristic of a 6 μm device is shown in Fig. 6.6. The degree of polarization of this device is 97 % at 15 mA.

On some devices, the onset of lasing occurs at the edges with the light increasing in the center only at higher currents, as shown in the polarization-resolved light-current characteristics of a 36 μm device in Fig. 6.7. This phenomenon may be a result of the strain arising from the *p*-mirror post acting as a stressor on top of the active layer, or possibly current crowding. Even though the electric field intensity pattern resembles that of a whispering-gallery mode, the direction of the maximum output intensity clearly indicates that laser oscillation occurs in the direction perpendicular to the wafer surface.

On most devices the lasing starts in a complex field pattern which is distributed across the entire device area, as shown for a 48 μm diameter device in Fig. 6.8. Similar

irregular patterns and filamenting have been observed on large area GaAs-based gain-guided VCLs at multimode operating conditions (Tan, M., 1995). It is not clear if the irregularity of the pattern is a result of rough sidewalls or comes from the nonuniformities in the current transport over the fused junctions originating from random dislocations. The fact that the devices filament and that there are dark regions at the onset of lasing, such as is shown in Fig. 6.7 and 6.8, implies that the effective value of the threshold current density shown in Fig. 6.3 is actually higher for larger devices. However, from the shown near-field patterns it is difficult to determine the magnitude or the significance of this correction.

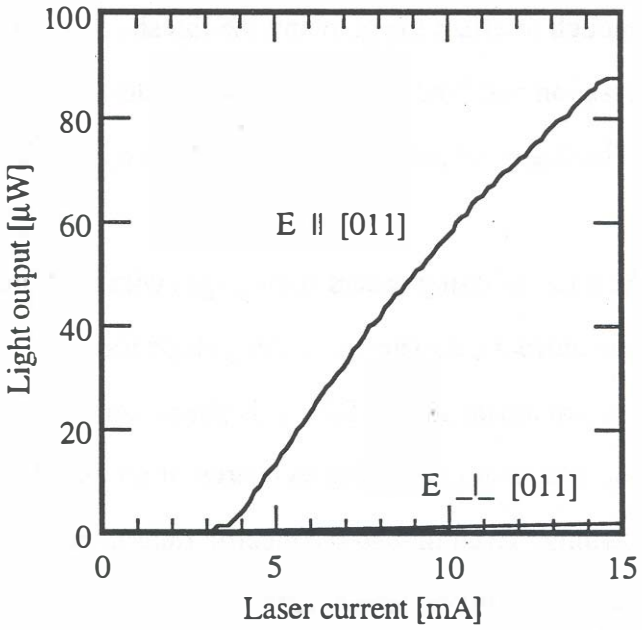


**Fig. 6.6**: Polarization-resolved light-current characteristics of a 6 μm device.

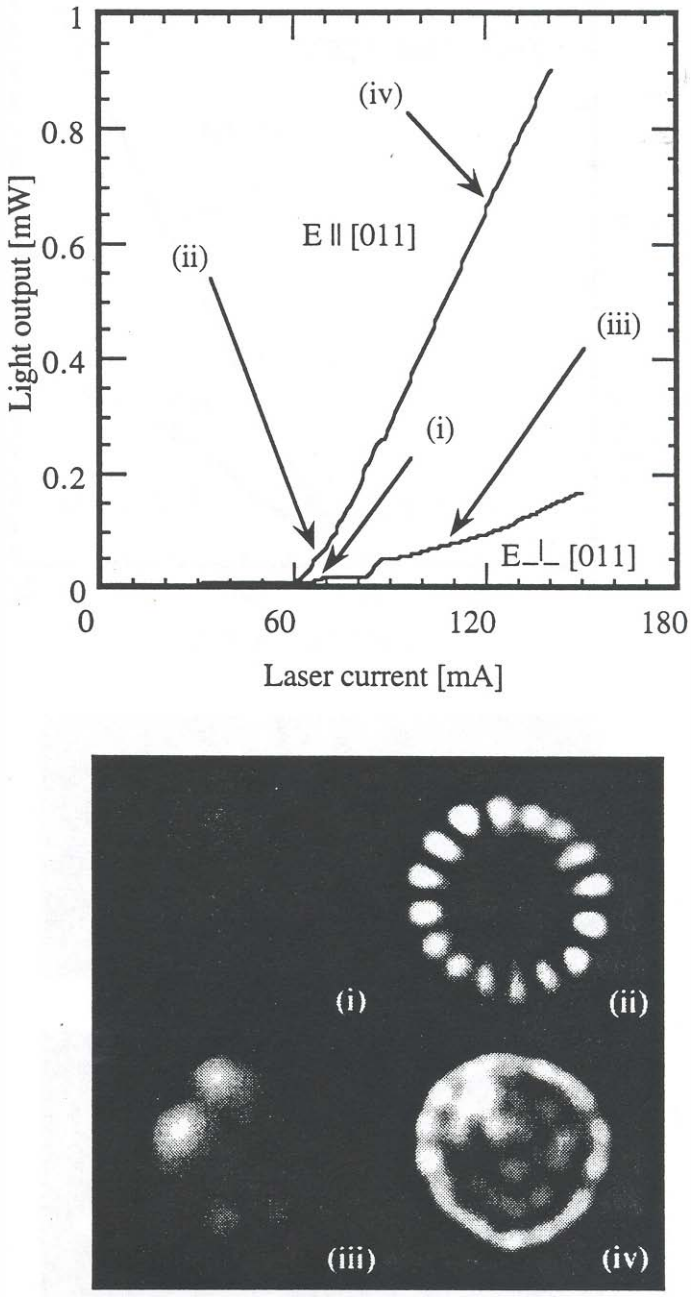


**Fig. 6.7**: Polarization-resolved light-current characteristics and associated near-field patterns of a 36 μm diameter device (F132).

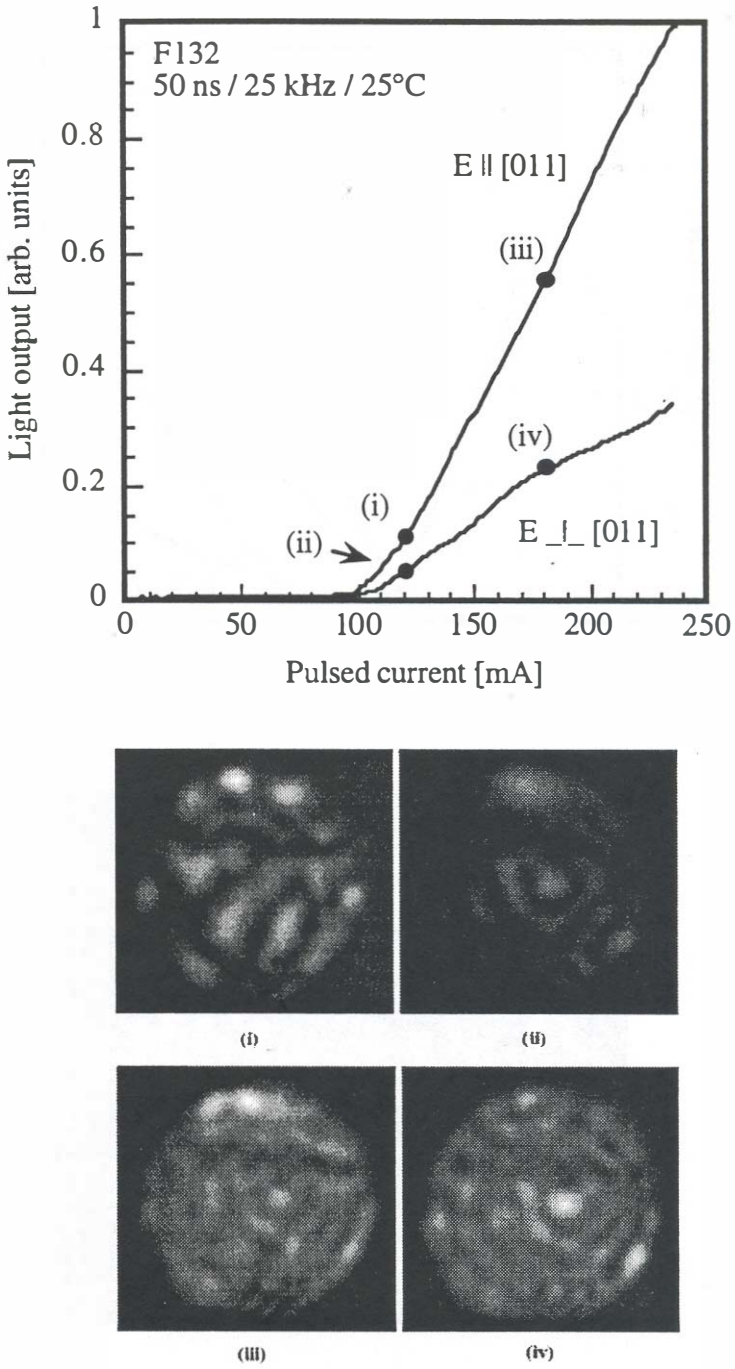


**Fig. 6.8**: Polarization-resolved light-current characteristics and associated near-field patterns of a 48 μm diameter device (F132).

The study of room-temperature pulsed performance of the first generation of double-fused vertical-cavity lasers, in particular, the size dependence of the threshold current density, has led to better understanding of device operation and to significant progress in device performance. Some of the issues that are still to be resolved are the reduction of $p$-mirror resistance and the control of the polarization characteristics. The high threshold power dissipation on the $p$-mirror and the ohmic contacts are the key reasons that prevent these lasers from operating continuous-wave at room temperature. In order to understand and possibly control the polarization characteristics of these lasers, it is necessary to fabricate lasers with various cross-sectional profiles, different types of active layers, and various epilayer orientations. Furthermore, the investigation of the effect of fusion on the active layer should be studied by fabricating lasers with varying distances between the active layer and the fused junctions.

6.1.3. *Room-temperature continuous-wave measurements (GEN 3).*

Two generation 3 samples were processed (F170 and F171) and both operated continuously at room-temperature. The device structure is shown in Fig. 5.2. Most of the characterization was performed on F170 because this sample exhibited slightly better performance. A scanning electron micrograph of finished F170 devices is shown in Fig. 6.9.

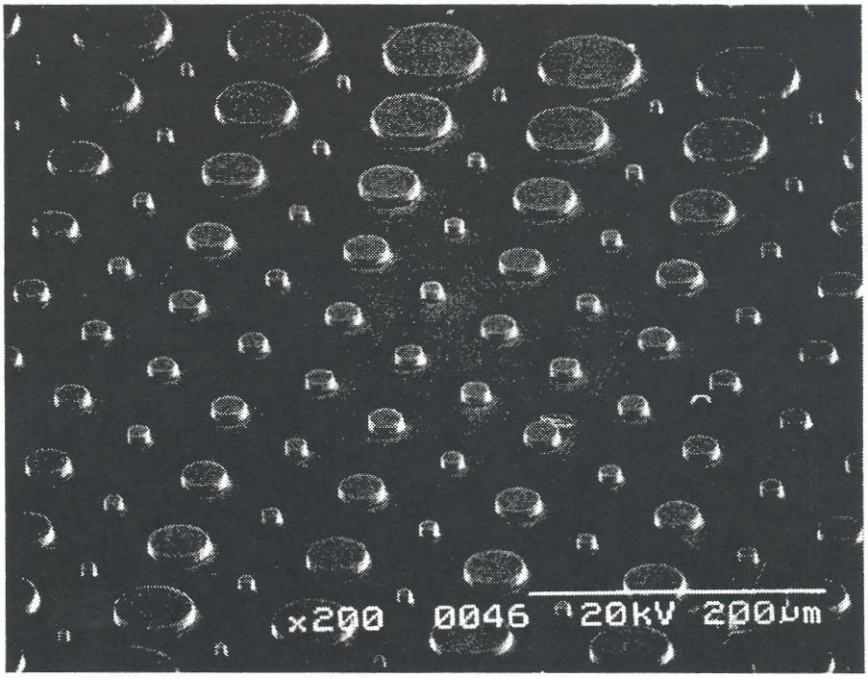


**Fig. 6.9**: Finished F170 devices. Ten different sizes from 6 µm to 60 µm are visible.

Lasers with diameters between 8 µm and 20 µm operated continuously (five sizes), while all other sizes operated pulsed at room temperature (23°C). Typical light-current characteristics for the five laser sizes are shown in Fig. 6.10. The main reason for the

oscillations in the light-current characteristics is the interference from the substrate-to-air reflection. Some small irregularities are also believed to come from multiple transverse mode operation. The oscillations are absent in the room-temperature pulsed light-current characteristics since the coherence length of the laser output is reduced by chirping during the pulse. Furthermore, the intensity of the oscillations in CW operation is reduced for on smaller devices because for the beam returning from the substrate diffracts and the coupling back into the laser is lower.

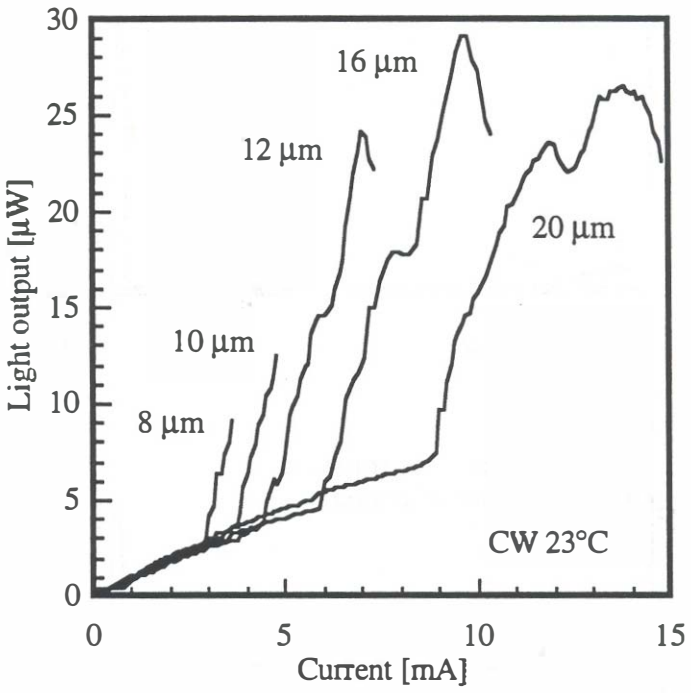


**Fig. 6.10**: Continuous-wave operation of five sizes of 1.54 μm vertical-cavity lasers.

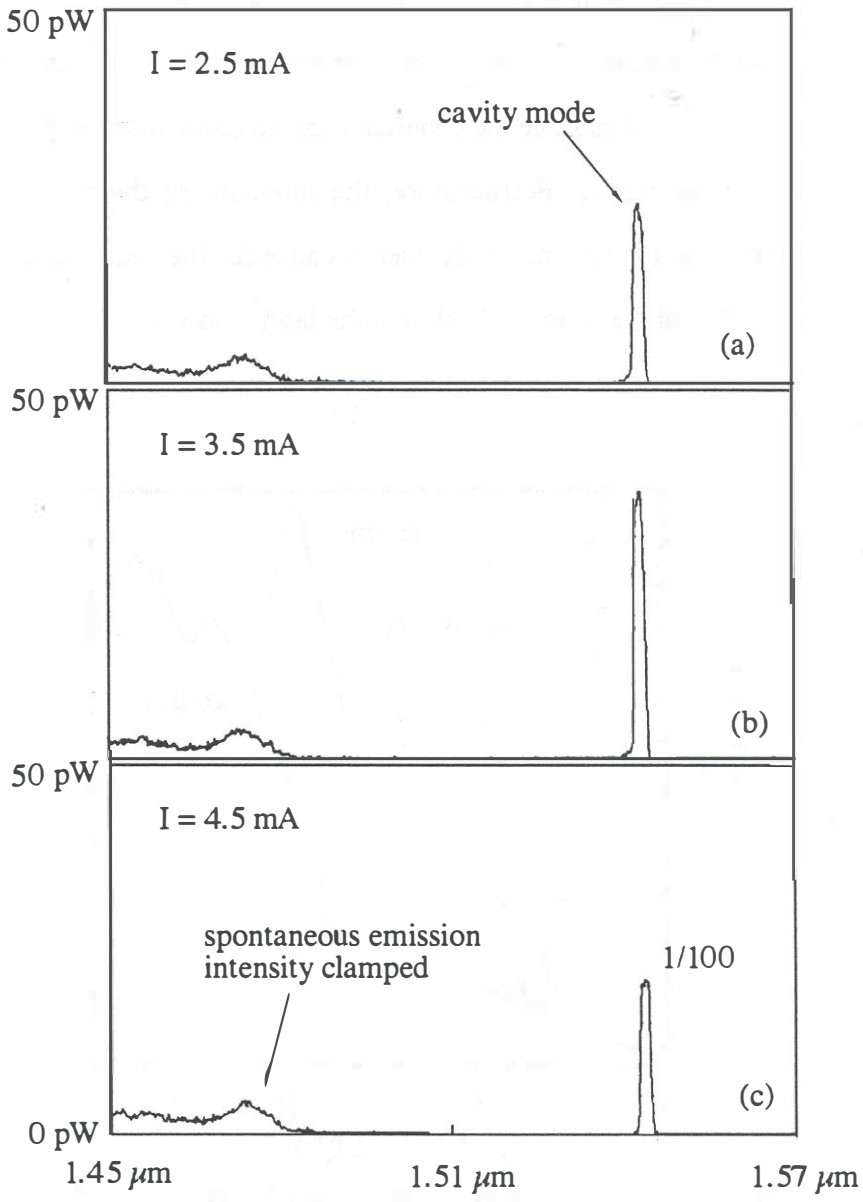


**Fig. 6.11**: Lasing threshold in the laser output spectrum.

The lasing action was confirmed by a clear threshold behavior in the light-current characteristics, and by the narrowing of the laser linewidth. Fig. 6.11 shows the onset of lasing in the output spectrum. At a current of 2.5 mA (below threshold) spontaneous emission originates from the cavity mode at 1542 nm and in two small peaks at $\lambda < 1.47\,\mu m$. These peaks correspond to the two reflection minima in the spectrum of the bottom mirror (S276), as shown in Fig. 4.18. As the bias is increased and threshold is reached the carrier concentration (and hence the spontaneous emission) is clamped while the intensity of the lasing mode dramatically increases. This is illustrated in the transition from 3.5 mA to 4.5 mA in Fig. 6.11. The dominant part of the spontaneous emission seen below threshold in Fig. 6.10 comes from wavelengths shorter than the bandstop of the bottom mirror ($\lambda < 1.47\mu m$). The narrowest linewidth measured was 0.32 nm limited by the presence of multiple transverse modes within this linewidth. An example of the multimode output spectrum is shown in Fig. 6.12. The lasing wavelength was $1542 \pm 2$ nm.

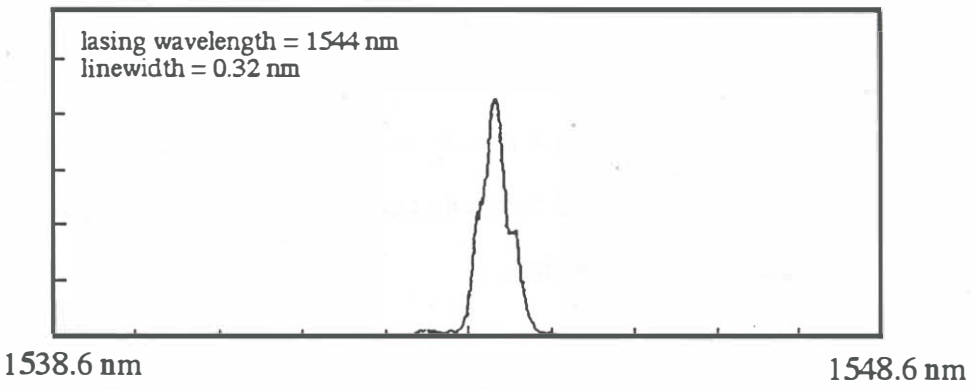


**Fig. 6.12**: Output spectrum of a 12 μm diameter device under continuous-wave room-temperature operation.

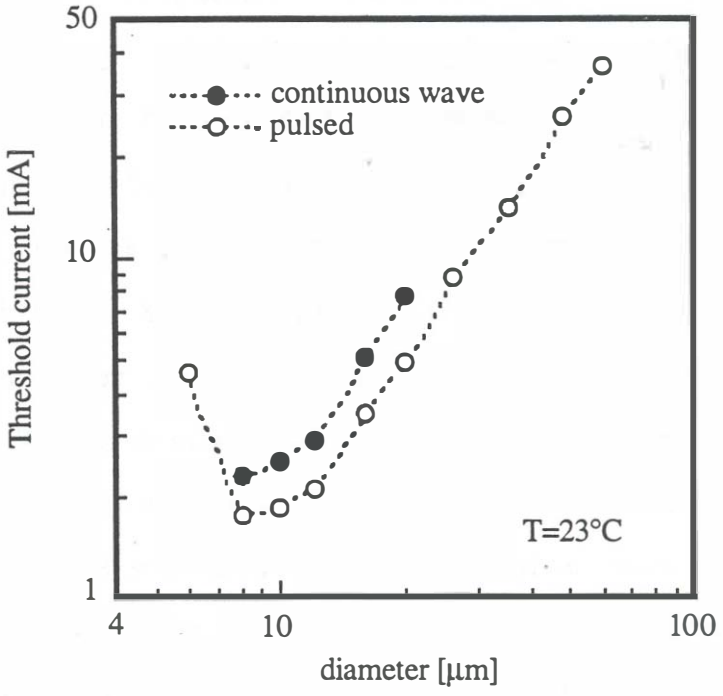


**Fig. 6.13**: A summary of room-temperature pulsed and continuous-wave threshold currents for all device sizes.

Fig. 6.13 shows a summary of room-temperature continuous-wave and pulsed threshold currents for all device sizes. The lowest continuous-wave and pulsed threshold currents are 2.3 mA and 1.8 mA, measured on an 8 μm diameter device. The lowest continuous-wave and pulsed threshold current densities are 2.5 kA/cm$^2$ (20 μm device) and 1.4 kA/cm$^2$ (60 μm device).

The 12 μm devices operate continuous-wave to temperatures above 30°C. Fig. 6.14 shows the temperature-dependent light-current characteristics of a 12 μm diameter device that operated continuously to 34°C. The continuous-wave characteristic

temperature $T_0$ at room-temperature varies between 28 and 37 K. The temperature dependence of the threshold current is discusses in Section 7.2.

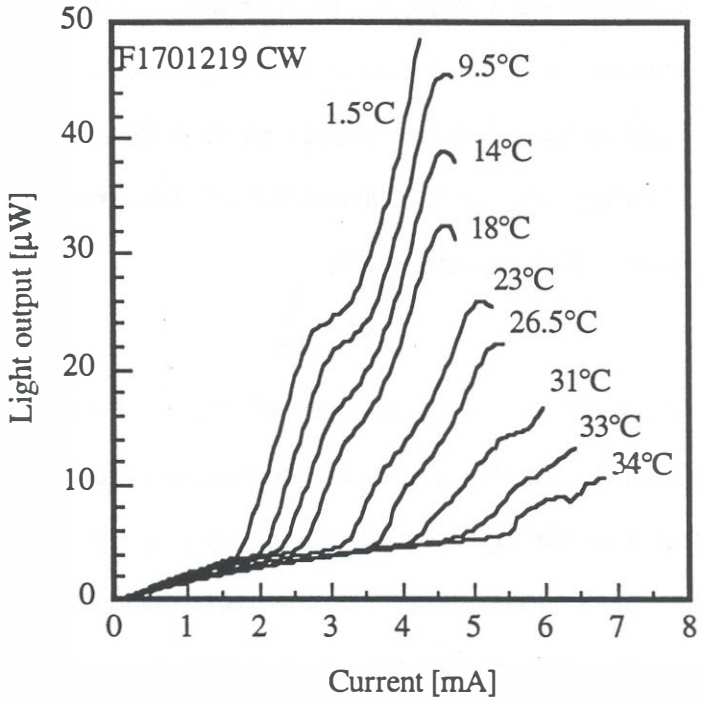


**Fig. 6.14**: Light-current characteristics of a 12 μm device as a function of temperature.

## 6.2. *Thermal resistance*

The exact calculation and the estimates of the thermal resistance of the double-fused laser are quite straightforward owing to the simple structure of this device. Since dominant heat sources are in the $p$-mirror and the active layer, its is possible to represent this structure as a disk heat source on an infinite half-space of thermal conductivity $\kappa$. The approximate thermal resistance of this structure is expressed with the analytic expression (Kutetanadze, 1966),

$$\Theta_{th} \approx \frac{1}{2\kappa d} \tag{6-1}$$

Since the structure involves a number of layers of different thermal conductivity, it is not clear how to calculate the effective thermal conductivity that could be used in (6-1). One way of estimating the equivalent conductivity is using the effective thermal resistivity method of (Osinski, 1993). In our work, the thermal resistance of the double-fused laser structure (generation 1) was calculated using a finite element program (ANSYS, 1995) by (Piprek[a], 1995). The calculated thermal resistance fits the hyperbolic relationship very well and is approximately expressed using (6-1) with an effective thermal conductivity of $\bar{\kappa} = 0.55$ W/Kcm. This conductivity represents the combined effect of the InP (0.68W/Kcm), InGaAsP ($\approx$ 0.05W/Kcm), GaAs (0.44W/Kcm) and AlAs (0.91W/Kcm) layers that all contribute to the structure thermal conductivity (Adachi, 1983, 1985). The numerically calculated thermal resistance is then approximately given by,

$$\Theta_{th} \approx 915 \cdot \left( \frac{12}{d(\mu\text{m})} \right) \ \frac{\text{K}}{\text{W}} \tag{6-2}$$

Simple thermal resistance measurements were performed on generation 1 devices (F132) by (Margalit, 1995b) using the wavelength shift method. The measured data are shown in Fig. 6.15. The large scatter in the data originates from the inconsistent thermal contact and the difficulty in determining the true mode position (due to multimode operation). The measurements of thermal resistance were fit to the following relationship,

$$\Theta_{th} \approx 1520 \cdot \left( \frac{12}{d(\mu\text{m})} \right)^{1.16} \quad \frac{\text{K}}{\text{W}} \qquad (6\text{-}3)$$

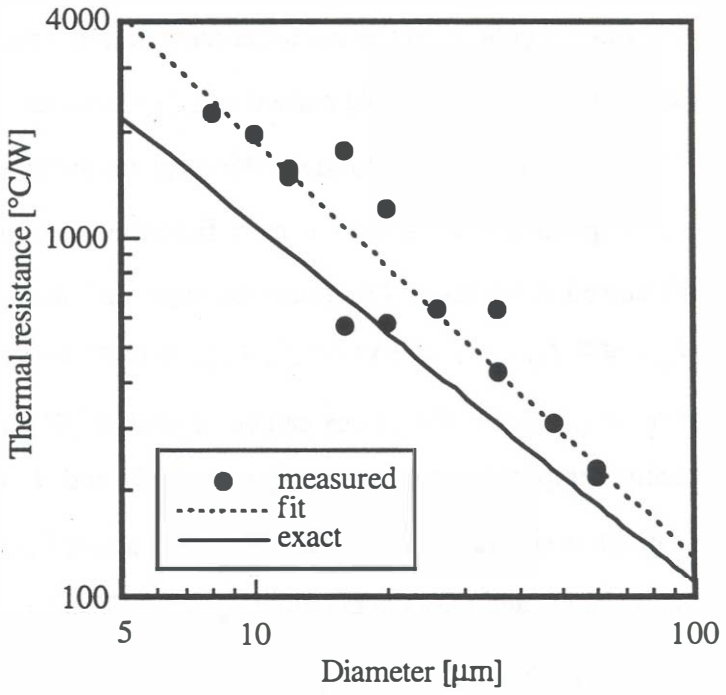


**Fig. 6.15**: Thermal resistance of double-fused vertical-cavity lasers measured by the wavelength shift technique (Margalit, 1994) and numerically calculated by (Piprek, 1995).

Strictly speaking, the wavelength shift method does not provide the thermal resistance of the active layer, but an averaged value that depends on the temperature of the entire cavity, since the mode position depends on the cavity optical length. The temperature that is most important for laser operation is the temperature of the active layer since that temperature determines the threshold current. The multimode operation of the laser makes the measurement very difficult since with the temperature changing some modes appear while others disappear. This is may be the source of the large discrepancy between the measurement and the exact calculation shown in Fig. 6.15.

Since the F170 devices operate at and above room-temperature we are able to measure the thermal resistance using the threshold current as a thermometer for the active layer temperature. The method operates as follows: We measure the threshold current and threshold power dependence of a device as a function of temperature in both continuous and pulsed operation. The pulse duration and the repetition rate are denoted with $\tau_{pulse}$ and $f_{rep}$. The duty cycle $f_{rep}\tau_{pulse}$ is made sufficiently low so that the average power dissipated at the device can be neglected. We take two threshold current vs. heatsink temperature curves $I_{pl}(T_{hs})$ (pulsed) and $I_{cw}(T_{hs})$ (CW). An example of this graph is shown in Figure 7.6. We select a threshold current value $I_{th}$ that exists on both graphs and then the equation $I_{th} = I_{cw}(T_{hs}^{(cw)}) = I_{pl}(T_{hs}^{(pl)})$ defines two heatsink temperatures $T_{hs}^{(cw)}$ and $T_{hs}^{(pl)}$. The active layer temperatures corresponding to these two heatsink temperatures are $T_a^{(cw)} = \Theta_{th}V_F^{(cw)}I_{th} + T_{hs}^{(cw)}$ and $T_a^{(pl)} = \Theta_{th}V_F^{(pl)}I_{th}(\tau_{pulse}/\tau_{th}) + T_{hs}^{(pl)}$. Here $\tau_{th}$ is the thermal time constant of the device (assuming that $\tau_{th} >> \tau_{pulse}$) and $T_a^{(pl)}$ is the approximate active layer temperature at the end of the pulse. Since the temperature of the active layer varies during the pulse (approximately linearly), it is difficult to estimate the thermal

resistance from this information, unless one can assume that the heating during the pump pulse is negligible. If we average the active layer temperature variation during the pulse, we obtain the thermal resistance from,

$$\Theta_{th} \approx \frac{T_{hs}^{(pl)} - T_{hs}^{(cw)}}{V_F^{(cw)} I_{th} - V_F^{(cw)} I_{th} (\tau_{pulse} / 2\tau_{th})} \qquad (6\text{-}4)$$

In using this equation we typically neglect the heating of the active layer during the pulse.

This method has several limitations. No matter how short the pulse, the device will always heat during the pump pulse. The magnitude of the active layer temperature rise depends on the average power dissipated in the train of pulses (duty cycle · pulse peak power) and the duration of the pulse relative to the active layer thermal time constant. To determine this temperature rise exactly, one has to numerically solve the time-dependent heat diffusion equation for a specific geometry. This has been done for a 10 μm diameter generation 1 double-fused vertical-cavity laser by (Piprek[a], 1995). With a 50 ns pulse duration and 16 mW pulse power, the temperature rise at the quantum-wells was calculated to be between 2.5°C and 4°C, depending on the lateral location (The temperature distribution in the active layer peaks in the center. ) This active layer temperature increase affects the measurement of the pulsed threshold current. If the current pulse had a value that is exactly equal to the *ideal* pulsed threshold current, then the laser would operate only during a brief moment at the beginning of the pulse. By *ideal* pulsed threshold current we mean a measurement in which the active layer and the heatsink temperatures are equal, namely, the pulse does not heat the device. To measure light emission, one has to increase the pulse current to make the laser operate

for a longer fraction of the pulse. This means that measurement of the pulsed threshold current always overestimates the ideal pulsed threshold current corresponding to the heatsink temperature. Consequently, the value of $T_{hs}^{(pl)}$ corresponding to a given current that was measured and used in (6-4) will be lower by the amount of active layer heating during the pulse. Since the threshold current is selected equal for both CW and pulsed measurement in our method, neglecting the pulse heating results in an underestimate of the thermal resistance. One can also see this from (6-4), where the thermal resistance value is higher if the heating during the pulse is included.

The second issue is the interpretation of the measurements in the presence of backside reflections. As it will be shown in Section 7.4, in continuous-wave operating VCLs the coherence length is larger than the substrate thickness and the backside substrate-to-air reflection changes the effective reflectivity of the mirror. The same device operated under pulsed conditions may not experience such reflectivity modulations due to shorter coherence length (see Figure 6.16). Since our method of thermal resistance measurement relies on the comparison between the pulsed and CW measurements of threshold current, an uncertainty in the value of thermal resistance is introduced through uncertain effective output mirror reflectivity. In addition, the interference is temperature sensitive because the optical lengths of the cavity and the substrate vary with temperature. The measurements of the continuous-wave threshold current were made by averaging the oscillations in the light-current characteristics.

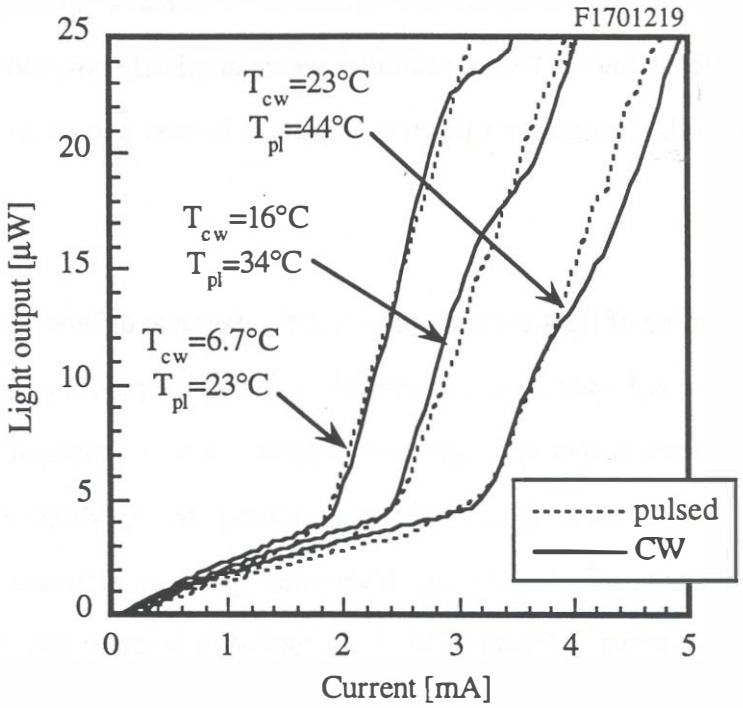


**Fig. 6.16**: Pulsed and CW light-current characteristics of a 12 μm diameter device (F170) at different temperatures. When both the threshold current and the external differential quantum efficiency match on the pulsed and the CW light-current characteristic, the active layer is approximately at the same temperature.

In the light of these issues we resort to using the thermal resistance values as an indicator of the relationship between measured pulsed and continuous-wave threshold currents, rather than as an exact indicator of the peak (or average) temperature of the active layer. In most of our measurements using the method (6-4), the measured values of thermal resistance differ drastically from the numerically determined values. The reasons for this behavior are not clear. In the following paragraphs, we shall describe the results and discuss the thermal resistance measurements performed on F170 device. It is also important to note that in our measurements the thermal

resistance is also sensitive to the device contact to the heatsink. During measurements with temperatures below ≈14°C, the samples were completely covered with condensed water. Some of the inconsistent thermal contact is believed to come from these wet surfaces.

With a large number of light-current characteristics taken at different temperatures (12 μm device shown in Figure 7.6), it is possible to match the pulsed and the continuous-wave characteristics at two different temperatures. This is shown in Figure 6.16 for three cases. It is interesting to note that matching the threshold current has also resulted in matching of the external differential quantum efficiency. The 12 μm diameter device (shown in Figure 6.16) has a room-temperature thermal resistance of $\Theta_{th} \approx 1750\ K/W$, determined using (6-4) with $V_F^{(cw)} = 3.7$ V and $I_{th} = 3.25$ mA. This is quite close to the previous value measured for a 12 μm device (6-3), but almost twice as high as the numerically calculated value (6-2). Furthermore, the thermal resistance measurement yields increasing numbers as the temperatures decreases. At the lowest temperature measurement shown, the thermal resistance is $\Theta_{th} \approx 2900\ K/W$. This large change can not be attributed to the temperature dependent thermal conductivity of the alloys. A relatively large scatter was observed in the thermal resistance values measured on different 12 μm diameter devices: Values as high as $\Theta_{th} \approx 4000\ K/W$ were measured. Another data point can be obtained from the knowledge that a 12 μm device that operates continuously at 33°C will also operate pulsed up to 55°C. Since the threshold current and voltage at 33°C are 4.9 mA and 4 V, using (6-4) we get a thermal resistance of $\Theta_{th} \approx 1120$ K/W. This is much closer the theoretically predicted value (6-2). All these measurements (done on the same device) indicate that the measured value (6-4) appears to decrease with temperature. It

is not clear whether this value represents the true thermal resistance, or is it an artifact of the measurement technique. However, the relationship between the pulsed and continuous-wave threshold current and mode shift with temperature seems to follow the large "thermal resistance" values given by (6-3) and (6-4). We illustrate this on another example that does not involve pulsed measurements. We consider the diameter dependence of the continuous-wave threshold currents.

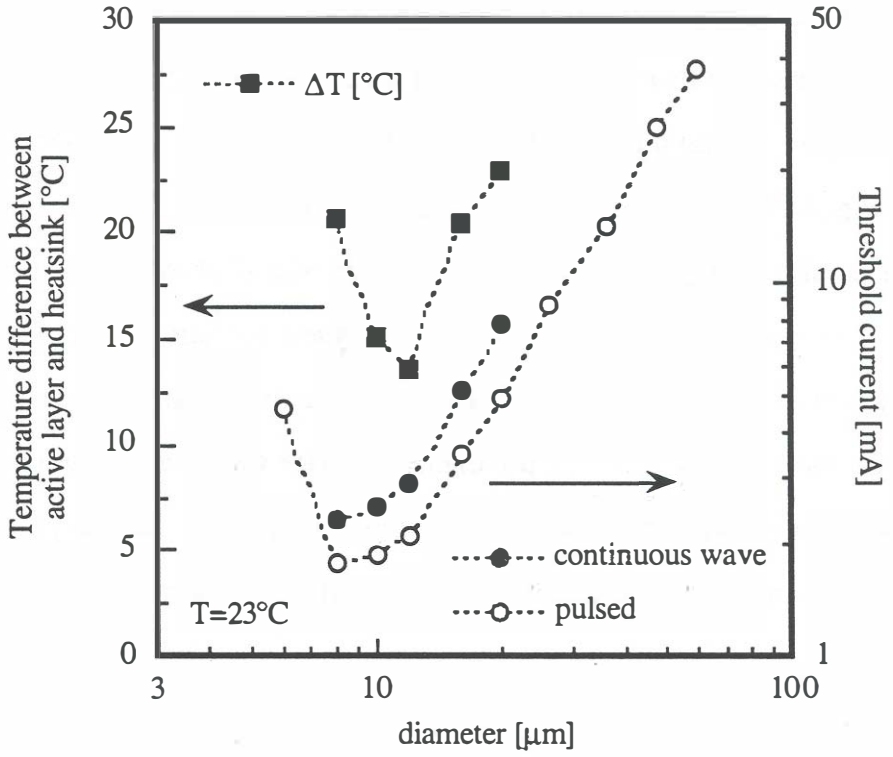


**Fig. 6.17**: Estimated temperature difference between the active layer and the heatsink at continuous-wave room-temperature operation.

We estimate the increase in active layer temperature above the heatsink for the devices shown in Figure 6.13. The exact continuous-wave threshold power was calculated using the known threshold voltage. We use equation (6-3) to estimate the active layer

temperature. The calculated temperature difference between the active layer and the heat sink is shown in Fig. 6.17. There are two interesting facts revealed from this calculation: 1) It is evident that the 12 μm diameter device operates with the lowest active layer temperature and is hence expected to have the highest continuous-wave operating temperature. This conclusion does not depend on the absolute value of the thermal resistance, but on the functional dependence of the thermal resistance on the device diameter which is approximately hyperbolic. 2) The highest active layer temperature for which there will be enough gain to reach threshold can be estimated from the largest (20μm) diameter device that lased continuously. As seen from the graph in Fig. 6.17, this maximum temperature is at least 46°C. Considering that the active layer of a 12 μm diameter device operates ≈13°C above the heatsink, it is reasonable to expect that the highest continuous-wave operation of this device size should be at least 46°C – 13°C = 33°C. This prediction is very good, since the highest continuous-wave operation of a 12 μm diameter device was measured to be 34°C. In summary, it is evident that a more comprehensive study of the thermal properties of these lasers is necessary to provide a consistent set of parameters for thermal modeling.

## 6.3. *Conclusion*

The improvement in the fabrication process and the laser design has resulted in the steady reduction in the threshold current and device threshold power dissipation, finally achieving room temperature continuous wave operation. A more detailed look at the cavity losses, efficiencies and the temperature dependence is described in the next chapter.

# Chapter 7

# Analysis

With three working generations of double-fused VCLs we are able to compare the performance and discuss some crucial questions regarding the laser design, cavity losses and efficiencies. In this section, we shall first estimate the round-trip cavity losses for the representative runs of all three generations, and then concentrate on the last (F170) sample which has operated continuously at room temperature. Even though a large number of working devices were tested, there still remains a number of issues that are not resolved and more investigation is necessary.

A great deal can be learned about the active layer performance by comparing generation 2 (F166/F167) and generation 3 (F170/F171) devices. This is possible because F166 and F170/F171 devices are identical except for the active layer. They both use S276 $n$-mirror and S250 $p$-mirror. The F167 device which has the S201 mirror operated slightly better than F166 and was used for comparison. The difference between the reflectivities of S201 and S276 mirrors in devices F167 and F170 is relatively small. Due to lower reflectivity of the S201 mirror, the round trip loss in device F167 is higher than in F170 by 0.13 %. The total round trip loss, as shown below, is 1 % or higher and therefore this difference is not very significant

In the devices of generation 1, the high mirror voltage drop and power dissipation was the reason the lasers did not operate continuously at room-temperature. The voltage drop has been significantly reduced by using the improved AlGaAs/GaAs mirror design (S250) on both generation 2 and 3 devices. The following are the reasons for better operation of generation 3 devices: 1) The active layer design was improved, 2) the $p$-mirror has lower resistance and better reflectivity using a non-alloyed metal contact, 3) the $n$-mirror has more periods, 4) the tuning between the mirrors and the cavity was improved, 5) the sidewalls of the posts were very smooth since AlGaAs does not oxidize as easily as AlAs. The improvements resulting from these facts have been expected since the design was better. The one unexpected fact is the threshold voltage on generation 3 devices: It is lower by more than one volt in comparison with generation 2 devices. This forward bias voltage also appears to be lower than the sum of the independently measured mirror voltage and the photon energy. All these factors are discussed in the next sections.

## 7.1. *Laser cavity losses*

We start the discussion by estimating the broad-area cavity losses. By *broad area* we mean large diameter VCLs in which the perimeter effects can be considered negligible. In our case, the largest device on the mask has a diameter 60 μm. We first analyze this device size, and then consider smaller devices in which the threshold gain steadily increases with the reduced size. The external quantum efficiency of a vertical-cavity laser is given by $\eta_{ex} = \eta_i T_{OC}/\delta$, where $\delta$ is the round-trip loss, $\eta_i$ is the internal quantum efficiency, and $T_{OC}$ the transmission through the output mirror and the

substrate (C-21). The round-trip loss here includes the power that is emitted from the cavity. To obtain an estimate of $\delta$, we measure $\eta_{ex}$ on the 60 μm diameter devices at room-temperature pulsed conditions. Due to scatter in the data, on some samples the lowest threshold current density and the highest external quantum efficiency were measured on devices of sizes smaller than 60 μm. In this case, the best measured data was used in the analysis. Inasmuch as we do not have an estimate for the internal quantum efficiency, we maintain $\eta_i$ equal to unity unless otherwise specified. The output coupling $T_{OC}$ is calculated from known and estimated optical properties of the output mirror and the substrate. This estimation requires a more detailed discussion and is described in the next section. The laser parameters determined in the next sections will be summarized in Table 7.2.

### 7.1.1. *An estimate of the output coupling*

The output coupling $T_{OC}$ depends on three factors: The transmission of the output mirror $T_{DBR}$, the transmission through the substrate which is reduced by the presence of the absorption $\exp(-\alpha L)$, and the transmission through the GaAs-air interface $T_S$. The resulting transmission (or reflection) depends on the relative size of the coherence length of the light beam in respect to the substrate thickness. In the pulsed measurement, due to chirping and a broad linewidth the laser coherence length is smaller than the substrate thickness, while in continuous-wave operation it is longer than the substrate. This can be easily seen by comparing the light-current characteristics in continuous-wave and pulsed operation. The continuous-wave light-current characteristics exhibit oscillations due to the interference from the GaAs-air reflection at the bottom of the substrate, as shown in Fig. 6.10, while these

oscillations are not present in the pulsed measurement, shown later in Fig. 6.4. We desire to determine the cavity round-trip loss at room temperature and hence we measure the external quantum efficiency under pulsed conditions. In this case the transmission is given by,

$$T_{OC} \cong T_{DBR} T_S \exp(-\alpha L) \qquad (7\text{-}1)$$

where the beam reflected from the back-surface has been neglected because it's intensity is negligible in comparison with the transmitted beam. From the known refractive index of GaAs at 1550 nm ($n = 3.377$), we find $T_S \approx 0.7$. We calculate $T_{DBR}$ by modeling the output mirror for each device separately using known mirror center wavelength, optical constants of GaAs and Al(Ga)As and the lasing wavelength. With calculated values for $T_{DBR}$ and $T_S$, we are only left to estimate the transmission through the substrate $\exp(-\alpha L)$.

The transmission through the $n$-GaAs substrate is reduced by free-carrier absorption. Inasmuch as the doping level varies from wafer to wafer, even in the same boule, it is advantageous to make a measurement of the absorption coefficient on the exact wafer that is used for the fabrication of devices. A simple method was developed to estimate the transmittance through the substrate on wafers with already grown quarter-wave mirrors and on completed devices. The method consists in measuring the reflectance spectra of the mirror through the substrate. Consider Fig. 7.1 and reflection measurements $R_F$ and $R_B$. The reflectivity of the semiconductor-air interface is denoted with $R_S$, while the reflectivity of the mirror seen from inside the substrate is denoted with $R_{DBR}$. The substrate has an absorption coefficient equal to $\alpha$ and thickness $L$.

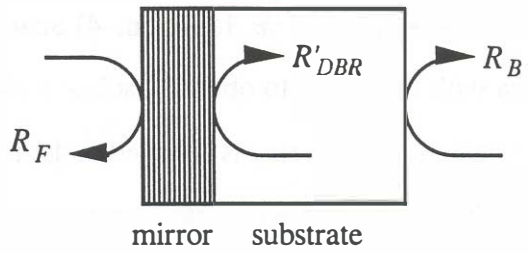


**Fig. 7.1**: Illustration of the measurement of substrate transmission

Given that the optical path through the substrate is longer than the coherence length of the measuring light, the mirror reflectivity measurement through the substrate can be expressed as

$$R_B = R_S + T_S^2 \frac{R_{DBR}\exp(-2\alpha L)}{1 - R_S R_{DBR}\exp(-2\alpha L)} \qquad (7\text{-}2)$$

Within the bandstop, the reflectivity $R_{DBR}$ is near unity and one can determine the substrate absorption from (7-2) via

$$\exp(2\alpha L)) = R_S + \frac{(1-R_S)^2}{R_B - R_S} \approx 0.3 + \frac{0.5}{R_B - 0.3} \qquad (7\text{-}3)$$

Evidently, the key factor for an accurate estimate of the absorption loss is the absolute measurement of reflectivity $R_B$. This can be done by calibrating the spectrophotometer using the forward reflectance measurement $R_F$. The procedure for measurement of the absorption loss goes as follows. 1) The spectrophotometer is calibrated using an aluminum mirror that has a relatively flat wavelength response between 1300 and 1800 nm, 2) Forward and back reflectance spectra are measured, 3) The Al mirror reflection coefficient at 1550 nm is determined using the high reflectivity region of the forward reflectance spectrum. The value of the aluminum

mirror was consistently 94 % ± 0.5 % 1550 nm. 4) Scale the forward and backward reflectance spectra with this value to obtain absolute reflectivity spectra $R_F(\lambda)$ and $R_B(\lambda)$. 5) A trial value for $\exp(-\alpha L)$ is selected and equation (7-2) is plotted using $R_F(\lambda)$ in place of $R_{DBR}(\lambda)$. The substrate transmission $\exp(-\alpha L)$ is adjusted by hand until the calculated value (7-2) matches the measured $R_B(\lambda)$. This can be done very quickly by hand and the resulting fit is shown in Fig. 7.2. Considering that the $R_F$ measurement is used only for calibration, once one knows the calibration constant (the Al mirror reflectivity), only $R_B$ measurement is sufficient to determine the absorption coefficient. Therefore, the measurement can be performed on completed lasers by simply measuring the backside reflection spectrum and fitting the spectrum with the appropriate value of $\exp(-\alpha L)$. This was done one all of the devices and the mirrors.

The measured values are summarized in Table 7.1 (the substrate transmission $\exp(-\alpha L)$ is also listed in Table 7.2). The measurements of transmission through a particular mirror and devices with the same mirrors agree to within 10% of the value quoted in Table 7.1. It is also important to note that mirrors S201 and S230 were polished on the back by the manufacturer, while S276 was polished by hand. The hand polish was sufficiently smooth not to degrade the measurement accuracy.

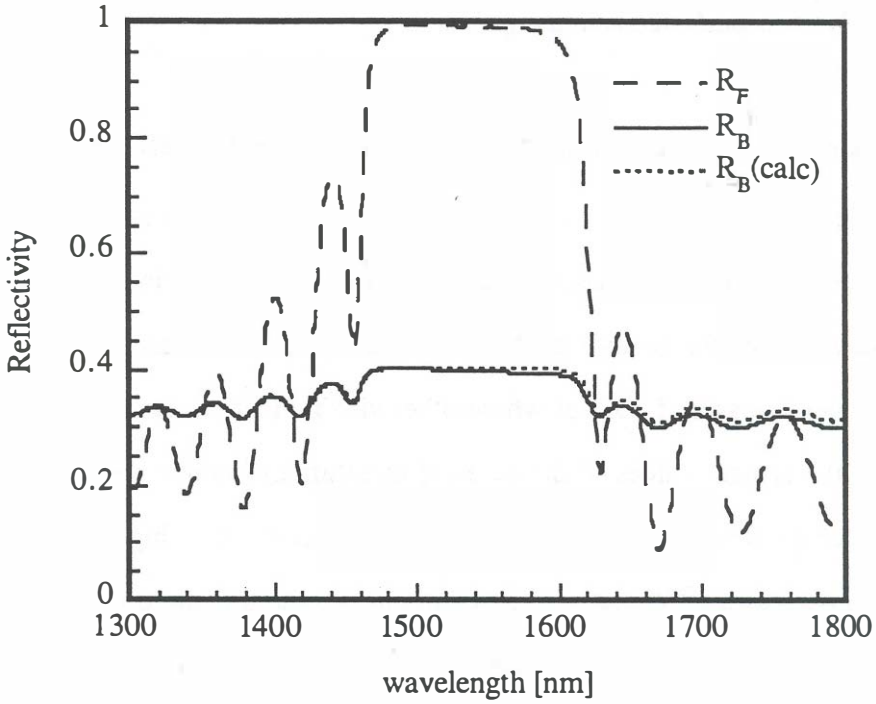


**Fig. 7.2:** Illustration of the substrate absorption measurement.

| *n*-mirror | *L* | exp(−α*L*) | α [1/cm] |
|---|---|---|---|
| S201 | 500 µm | 0.44 | 16.5 |
| S230 | 500 µm | 0.57 | 11.2 |
| S276 | 450 µm | 0.77 | 5.8 |

**Table 7.1**: Summary of substrate absorption coefficients for the three *n*-mirrors used in double-fused vertical-cavity lasers.

7.1.2. *Cavity broad-area round-trip loss*

With known output coupling $T_{OC}$ and external quantum efficiency $\eta_{ex}$ we now estimate the round-trip cavity loss for a broad-area device at room temperature. The parameters for three generations of double-fused VCLs are summarized in Table 7.2. The values listed for the threshold current density and the external quantum efficiency are the best measured, except where otherwise indicated. Due to the scatter in the values, the typical values of the external quantum efficiency are about 20 % lower, and hence the threshold gain is expected to be typically 20 % higher. We assume that internal quantum efficiency is 100%, and hence the threshold gain value quoted in Table 7.2 is in fact $g_{th}/\eta_i$. The gain enhancement factor has been calculated using (Corzine, 1993),

$$\xi = 1 + \frac{\sin(2\pi L_a/\lambda)}{2\pi L_a/\lambda} \quad L_a = N_{qw}L_{qw} + (N_{qw}-1)L_{bar} \qquad (7\text{-}4)$$

where $N_{qw} = 7$ is the number of wells, and $L_{qw}$ and $L_{bar}$ are the well and barrier thicknesses. The nominal quantum well width for the generation 1 and 2 devices is 7 nm, while for generation 3 devices it is 6 nm. The quantum well thickness is not precisely known. The value used for the generation 3 devices has been adjusted by (Piprek, 1995) to match the room-temperature photoluminescence spectra. The well thickness of the generation 1 and 2 devices has been scaled similarly since the luminescence peak occurs at an even shorter wavelength. However, the these values, as well as the estimated value of threshold gain are given only as a rough estimate.

| Generation | 1 | | 2 | | 3 | |
|---|---|---|---|---|---|---|
| Run | F125 | F126 | F166 | F167 | F170 | F171 |
| p-mirror | S207 | | S250 | | | |
| active | KS2290 | | | | KS2778 | |
| well thickness | 5.5 nm | | | | 4.75 nm | |
| gain enhancement | 1.71 | | | | 1.75 | |
| n-mirror | S201 | S230 | S276 | S201 | S276 | |
| $\lambda$ [nm] | 1522 | 1508 | 1549 | 1532 | 1542 | 1559 |
| $T_{DBR}$ [%] | 0.25 | 0.0675 | 0.0675 | 0.195 | 0.0675 | 0.0675 |
| $\exp(-\alpha L)$ | 0.44 | 0.57 | 0.77 | 0.44 | 0.77 | 0.77 |
| $T_S$ | 0.7 | 0.97 | 0.7 | 0.7 | 0.7 | 0.7 |
| $T_{OC}$ [%] | 0.0770 | 0.0373 | 0.0363 | 0.06 | 0.0364 | 0.0364 |
| $\eta_{ex}$ [%] | 2.5 % | 1.3 % | 1.6 % | 3.5 % | 3.7 % | 3.7 % |
| $\delta/\eta_i$ [%]† | 3.1 % | 2.9 % | 2.3 % | 1.7 % | 1.0 % | 1.0 % |
| $g_{th}/\eta_i$ [$cm^{-1}$]†† | 2360 | 2200 | 1750 | 1300 | 670 | 670 |
| $J_{th}$ [$kA/cm^2$] | 3 | 2 | 3* | 2.5 | 1.25 | 1.3 |
| $T_0 = dT/d(\ln J_{th})$ | 40 K | 28 K | 23 K | 37 K | 37 K | – |

**Table 7.2**: Output coupler transmission and external differential quantum efficiencies of representative runs from all three generations.
†Round trip loss is calculated using $\delta/\eta_i = T/\eta_{ex}$,
††Threshold gain is determined from $2g_{th}\xi N_{QW}L_{QW} = \delta$.
*Value may not be representative, since only a few devices were tested.

7.1.3. *The break-down of round-trip cavity losses*

Table 7.3 shows the summary of the epilayer thicknesses and the losses of F167 and F170 cavities. The thickness of the layers has been adjusted to match the lasing wavelength and all of the absorption coefficients, except the $p$-mirror absorption, have been taken from published and measured values. Since the round trip loss is approximately known from Table 7.2, the F170 cavity absorption was fine-tuned to match this value. The sources of cavity absorption are not exactly known and can only be approximated. In particular, the $p$-mirror absorption, and the existence of scattering at the fused interfaces are not known. In Chapter 5 we designed the $p$-mirror with an average free-carrier absorption of $\overline{\alpha} \approx 8\,\mathrm{cm}^{-1}$. This value will change depending on the actual doping level and the redistribution of the dopants from the bandgap engineered interfaces. For this reason, we select the average absorption in the $p$-mirror as a fitting parameter. The $p$-mirror absorption coefficient that brings the round-trip loss into the neighborhood of the value determined from the external quantum efficiency (listed in Table 7.2) is $\overline{\alpha} \approx 20\mathrm{cm}^{-1}$. This is than two times larger than the design value, and results in $p$-mirror reflectivity of 99.4 %. This absorption increase would be possible if the average mirror doping doubled due to the temperature drift in Be effusion cell. However, doubling of the doping level is a quite large deviation and it may be that the average absorption coefficient increased as a result the redistribution of the high level pulse doping profiles at the interfaces. Further analysis of the mirrors should be performed to confirm these statements by using, for example, Secondary Ion Mass Spectroscopy (SIMS) or capacitance-voltage profiling, since it is not possible to determine what the doping level is from the given data. It is not clear whether the fused interfaces provide any type of surface

scattering or absorption, since no measurements of this type have ever been reported. It may be instructive to note that the excessive absorption in these cavities (F167 and F170) can also be interpreted as surface scattering/absorption at the fused interfaces. If one wanted to keep the average mirror absorption at $\overline{\alpha} \approx 8\text{cm}^{-1}$, the round-trip cavity loss of 1 % in F170 and 1.7 % in F167, one could easily achieve this with a fused interface absorption in the range of $\alpha \Delta x \approx 0.4 - 1\,\%$. Note that, even though this value seems large, that the fused junctions are placed approximately at the nodes of the standing waves and hence their influence is minimized.

The relatively high round-trip losses of the F167 laser may be a result of a lower internal quantum efficiency, since the adjustment of the cavity losses for this device did not produce satisfactory results. For $p$-mirror absorption that is approximately equal to that of F170 device, the round-trip loss of 1.7 % was achievable only with an addition of high loss in the $p$-InP cladding and $p$-InGaAsP separate confinement regions. Very high absorption coefficients in these layers may be a result of high Zn concentration that has diffused during the MOCVD growth and later during the two fusion steps. As mentioned in the discussion on the increased $p$-mirror absorption, further analysis is necessary to confirm the actual impurity concentration in these layers. The question of decreased internal quantum efficiency, which may contribute to the apparent high round-trip loss of the F166 and F167 devices, will be discussed in a Sections 7.1.4 and 7.1.5.

| Device | | F167 | | | F170 | | |
|---|---|---|---|---|---|---|---|
| Layer | index | t [nm] | rep. | $\alpha$ [cm$^{-1}$] | t [nm] | rep. | $\alpha$ [cm$^{-1}$] |
| metal | 0.116 | — | | — | — | | — |
| GaAs | 3.35 | 115.7 | | 21 | 115.7 | | 20 |
| AlGaAs | 3.045 | 127.3 | 30 x | 21 | 127.3 | 30 x | 20 |
| GaAs | 3.35 | 115.7 | | 21 | 115.7 | | 20 |
| GaAs | 3.35 | 20 | | 21 | 20 | | 20 |
| GaAs | 3.35 | 10 | | 1000 | 10 | | 1000 |
| InP (p-clad.) | 3.17 | 111 | | 80 | 184 | | 24 |
| InP (undoped) | 3.17 | — | | — | 100 | | 2.4 |
| InGaAsP SCH | 3.37 | 166.5 | | 100 | — | | — |
| InGaAsP well | 3.6 | 5.5 | | 80 | 4.75 | | 80 |
| InGaAsP bar. | 3.4 | 8 | 6 x | 0 | 7.3 | 6 x | 0 |
| InGaAsP well | 3.6 | 5.5 | | 80 | 4.75 | | 80 |
| InGaAsP SCH | 3.37 | 168.5 | | 0 | — | | — |
| InP (n-clad.) | 3.17 | 111 | | 8 | 262 | | 8 |
| GaAs (n) | 3.35 | — | | — | 50 | | 6 |
| GaAs | 3.35 | 116.1 | 25 x | 6 | 115.7 | 28 x | 6 |
| AlAs | 2.89 | 134.5 | | 4 | 134.0 | | 4 |
| GaAs (sub) | 3.35 | 500 μm | | 16.5 | 450 μm | | 5.8 |

**Table 7.3**: Epilayer structure of F167 and F170 devices with relevant optical parameters. Round trip cavity losses for devices F167 and F170 are $\delta = 1.7\%$ and $\delta = 1.0\%$.

Based on these observations, one can give some indication on what should be done to reduce the cavity losses and increase the external quantum efficiency. 1) The absorption in the *p*mirror should be investigated and the mirror reflectivity should be optimized. 2) The presence of any fused interface absorption should also be investigated. 3) The substrate absorption can be reduced by either thinning the substrate and/or using a lower doped substrate.

### 7.1.4. *Gain-current relationship*

The gain-current density relationship of an vertical-cavity laser active layer can be de-embedded from the measured external quantum efficiency and threshold current density in a similar manner as it is done for in-plane lasers. In an in-plane laser one uses the threshold gain variation with the varying cavity length to obtain measurements of the threshold current corresponding to different values of gain. In our VCL we rely on the threshold gain varying with the lateral size of the device. The origin of cavity loss dependence on the diameter is not important for this measurement, but is believed to be a result of sidewall scattering and diffraction. The active layer gain is related to the external quantum efficiency via,

$$2g_{th}\xi N_{QW}L_{QW}\eta_{ex} = \eta_i T_{OC}. \qquad (7\text{-}5)$$

By measuring the room-temperature pulsed external quantum efficiency and the threshold current density measured on a particular device we obtain a pair of numbers $(g_{th}/\eta_i, J_{th})$. As devices of different sizes are measured, both the threshold gain and the threshold current density vary. Ideally, this variation draws out the $g-J$ relationship for a particular active layer. However, there are several difficulties connected with this method: First, we do not precisely know the value of the internal

quantum efficiency which, as seen in equation (7-5), scales the value of gain. For our consideration we shall assume $\eta_i = 1$. Secondly, nonradiative recombination at defects in the active layer introduces scatter in the threshold current density. For this reason, a large number devices were measured and only the devices with the lowest threshold current density for a given size were considered. The fact that the selection was representative was confirmed by the fact that these devices also exhibited the highest external quantum efficiency, namely, lowest round-trip loss. This experiment was performed only on the F170 and F126 devices. The functional dependence of the round-trip loss calculated from the external quantum efficiency is shown in Fig. 7.3. The data for F170 show a round-trip loss variation between 1 and 2 %. The values calculated from F126 are quite high; almost three times higher. This would require unrealistically high gain values from the quantum wells: For $\delta = 6\%$, the gain value should be in the neighborhood of $g \approx 3600\,\mathrm{cm}^{-1}$.

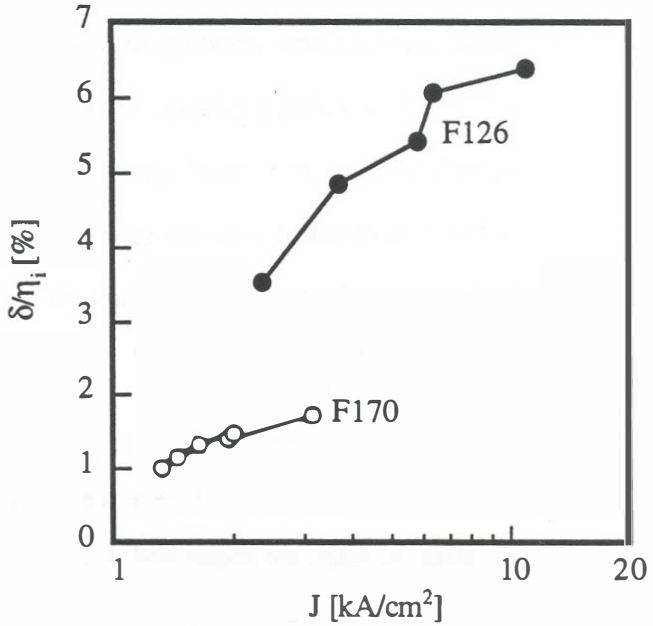


**Fig. 7.3**: Round-trip loss vs. threshold current density for samples F170 and F126.

Considering the active layers of generation 1 and 3 have the same number of quantum wells of similar thickness, it is very unlikely that these two active layers would exhibit so vastly different $g - J$ characteristics. The high value of the round-trip loss is then attributed to lower internal quantum efficiency of the active layer used in the first two generations of lasers.

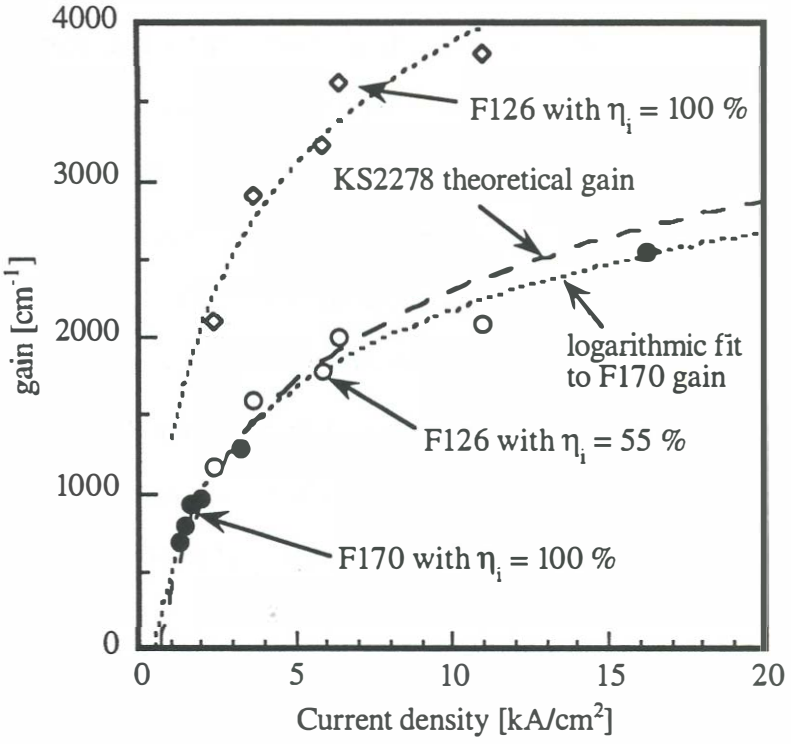


**Fig. 7.4**: De-embedded $g - J$ curves for F170 and F126 lasers.

If a certain value of the internal quantum efficiency is assumed, the graphs from Fig. 7.3 can be re-calculated to show gain vs. current density. This is shown in Fig. 7.4. We assumed a 100% internal quantum efficiency for the F170 data and fitted the resulting graph to a logarithmic gain-current dependence $g \approx g_0 \ln(J/N_{QW}J_0)$ with $g_0 = 726\text{cm}^{-1}$ and $J_0 = 72$ A/cm$^2$ ($N_{QW} = 7$). The F126 gain data can be brought in

to the neighborhood of the F170 gain data by assuming a lower internal quantum efficiency. If $\eta_i = 55\%$ is assumed for F126 active layer, then the two groups of data can be described with a single logarithmic fit, as shown in Fig. 7.4.

The physical origin of the reduction of the internal quantum efficiency lies in the current leakage in to the 1.3 μm InGaAsP separate confinement regions that were used only in generation 1 and 2 lasers. It is important to note that the internal quantum efficiency of the F126 active layer was used here only as a fitting parameter to make the $g - J$ data of the samples F126 and F170 match. The current dependence of the internal quantum efficiency has been ignored, and we have not taken into consideration that lower internal quantum efficiency leads to higher threshold current. Considering these simplifications and the uncertainty in the estimated and measured parameters that were used to determine the gain-current relationship, this fitting does not constitute a proof that the internal quantum efficiency has in fact been reduced. Further discussion of this question is undertaken in the next section.

The most significant fact presented here is that the de-embedded gain-current relationship obeys a logarithmic dependence as is expected from a quantum-well active region, and that this dependence agrees with the theoretical relationship calculated by (Piprek, 1995). The theoretical gain-current density relationship of the KS2778 active layer with 4.75 nm quantum wells and 7.33 nm barriers at 1542 nm is approximately expressed with $g_0 = 836\text{cm}^{-1}$ and $J_0 = 92\ \text{A/cm}^2$ and is shown in Fig. 7.4 for comparison.

With the known $g-J$ relationship we are in the position to determine the optimum number of quantum wells for the F170 laser. Consider that the round trip gain is given by

$$\delta = 2N_{QW}L_{QW}\xi(N_{QW})\, g_{th}(J_{th}, N_{QW}) \tag{7-6}$$

where the gain current relationship is given by $g_{th}(J_{th}, N_{QW}) = g_0 \ln(J_{th}/N_{QW}J_0)$. The gain enhancement factor depends on the number of wells via equation (7-4):

$$\xi(N_{QW}) = 1 + \frac{\sin\left[a(N_{qw}-b)\right]}{a(N_{qw}-b)} \tag{7-7}$$

where $a = 2\pi\bar{n}(L_{qw}+L_{bar})/\lambda_0$ and $b = L_{bar}/(L_{qw}+L_{bar})$. Here $\bar{n}=3.5$ is the average cavity index and $\lambda_0 = 1550\text{nm}$.

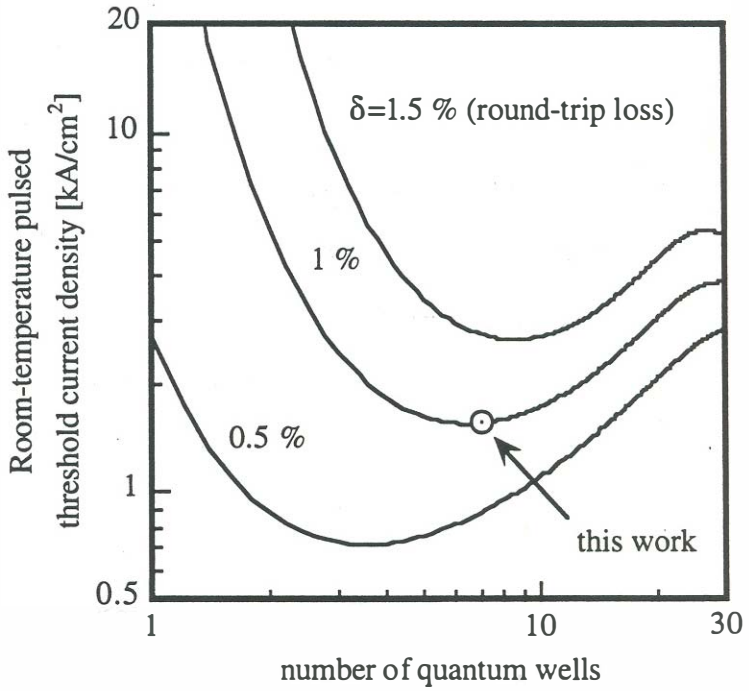


**Fig. 7.5**: Plot of room-temperature pulsed threshold current density as a function the number of wells.

We select several values of the round trip cavity loss, and plot the threshold current density as a function of the well number. These graphs are shown in Fig. 7.5. It is evident that for a 1 % round trip loss (F170) the optimum number of wells is seven, which was indeed used. This means that the round-trip cavity loss should be reduced before active layers with a smaller number of quantum wells are fabricated.

## 7.2. *Temperature dependence of laser parameters*

The characteristic temperature $T_0 = dT/d(\ln I_{th})$ of the room-temperature pulsed threshold current for all fabricated samples is summarized in Table 7.2. The difference between the between the $T_0$ values for different samples is attributed to different gain-to-mode alignment in the lasers, the absolute value of threshold gain and carrier leakage. To compare the temperature dependence in more detail, consider the threshold current dependence temperature of 12 μm F167 and F170 devices shown in Fig. 7.6. The lasing wavelengths of these two samples are close (F167 operates at 1532 nm and F170 at 1542 nm), but the F167 sample has a better gain-to-mode tuning, which can be seen from the appearance of a threshold current minimum around 5°C. It is evident that the threshold currents on the F167 are substantially higher than on F170 device. For example, at room temperature the threshold current of the F167 device is almost three times higher than on the F170 device. Using the graph in Fig. 7.4 we can easily verify that this higher threshold current agrees with the increased threshold gain. The room-temperature threshold gains and current densities of the devices from Fig. 7.6 are $g_{th} \approx \eta_i \cdot 1100\text{cm}^{-1}$ and $J_{th} \approx 1.7\ \text{kA/cm}^2$ for F170, and $g_{th} \approx \eta_i \cdot 2000\ \text{cm}^{-1}$ and $J_{th} \approx 5\ \text{kA/cm}^2$. Placing these data points on the graph in Fig. 7.4 we find that the $g_{th}/\eta_i$ value for F167 is slightly higher than the graph. This indicates that the internal quantum efficiency of the F167 device may be less than unity.

Consider now Fig. 7.7 which shows the temperature dependence of the external quantum efficiency $\eta_{ex}$ as function of temperature for F167 and F170 (12 μm device). The dependence is plotted against $1000/T$. At temperatures lower than

room temperature, $\eta_{ex}$ is approximately constant and equal to 3.5 % for F170 and as high as 3.0 % for F167. However, as the temperature rises above room-temperature the efficiency of the F167 laser rapidly decreases, while the falloff of the F170 laser is much slower.

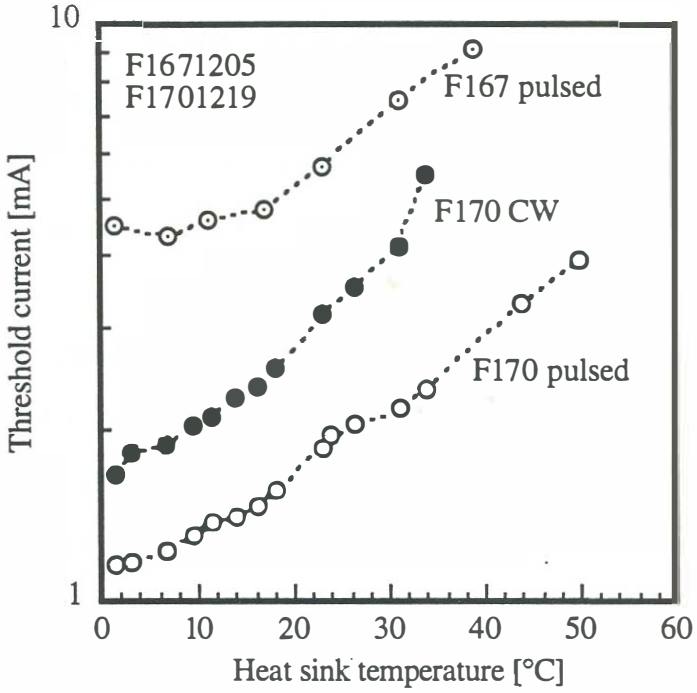


**Fig. 7.6**: Threshold current dependency on temperature.

To investigate the reasons for this temperature behavior we first consider the temperature dependence of the photon efficiency $\eta_{ph} = T_{OC}/\delta$. The cavity temperature variation effects $\eta_{ph}$ through the temperature dependent absorption and temperature dependence of the refractive indexes in the mirror. Since in GaAs/AlAs mirrors an increasing temperature increases the refractive index difference (Piprek,

1994), the output coupler transmission and hence the $\eta_{ph}$ will be reduced with increasing temperature. Using the values from (Casey, 1978, Grimmeiss, 1971),

$$\left.\frac{dn}{dT}\right|_{GaAs} \approx 4\cdot 10^{-4} \quad \left.\frac{dn}{dT}\right|_{AlAs} \approx 10^{-4} \tag{7-8}$$

we can easily calculate that over a 50°C temperature range the bottom mirror transmission decreases to 80 % of its initial value. The temperature coefficients for absorption in $p$-type GaAs and InP at $10^{18}$ cm$^{-3}$ doping levels can be estimated from the graphs in (Henry, 1983) and are given by,

$$\left.\frac{1}{\alpha}\frac{d\alpha}{dT}\right|_{GaAs} \approx 0.004 \quad \left.\frac{1}{\alpha}\frac{d\alpha}{dT}\right|_{InP} \approx 0.002 \tag{7-9}$$

Over a 50°C temperature range this absorption can raise the cavity losses at most to 120 % of its starting value. From these simple estimates we see that $\eta_{ph}$ can decrease at most down to 2/3 of its initial value over a 50°C temperature range. The effect of these two dependencies is shown also in Fig. 7.7 with a full line. Evidently, the temperature dependence of the absorption and refractive index estimated here is not sufficient to explain the decrease in the external quantum efficiency. To fit the data for F170 above room temperature the temperature coefficient of the average absorption loss in the cavity would have to be,

$$\left.\frac{1}{\alpha}\frac{d\alpha}{dT}\right|_{cavity} \approx 0.07 \tag{7-10}$$

However, this is still very far from being able to account for the sudden decrease in the external quantum efficiency of the F167 device. One possible origin of this high absorption is the intervalence band absorption in the quantum wells. The other possibilty is the higher current leakage in the generation 1 and 2 active layer. This active layer has a separate confinement region into which carriers are injected and

recombine. Since these separate confinement regions have been eliminated in the generation 3 devices, the leakage current has been reduced.

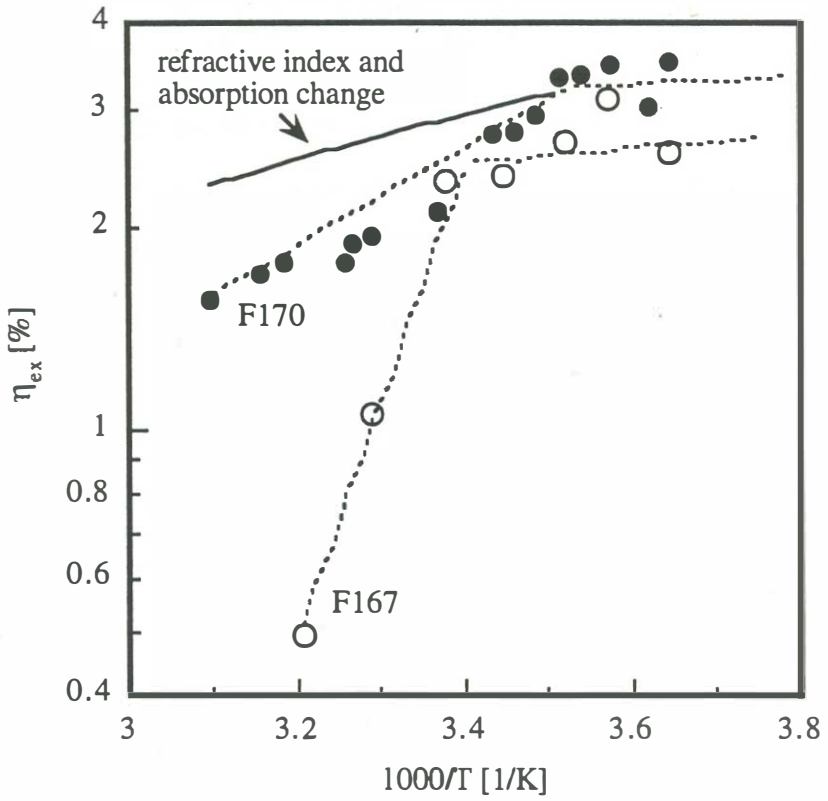


**Fig. 7.7**: Temperature dependence of the external differential quantum efficiency.

In order to confirm this statement we have searched to observe the electroluminescence from the barriers and the separate confinement regions. Two devices, one from generation 2 (F167) and one from generation 3 (F171) were biased with DC current densities up to 10 kA/cm$^2$ and the emission spectra were recorded. Note that in this experiment the F171 device lased, while F167 did not since it does not operate at CW room temperature. The emission spectra of these two samples are shown in Figures 7.8 and 7.9. In both devices the spontaneous emission extended

from 1.3 μm to 1.47 μm, but no excessive emission was observed at the barrier or separate confinement transitions (1.3 μm) in neither of the active layers. This implies that if substantial leakage current exists in the F167 devices it is predominantly non-radiative.

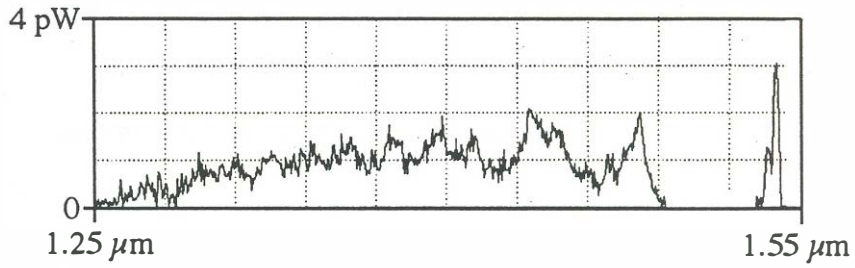


**Fig. 7.8**: Spontaneous emission from a 12 μm diameter F167 device at 10kA/cm$^2$ CW showing the cavity mode at ≈1530 nm and the emission from above the output mirror bandstop.

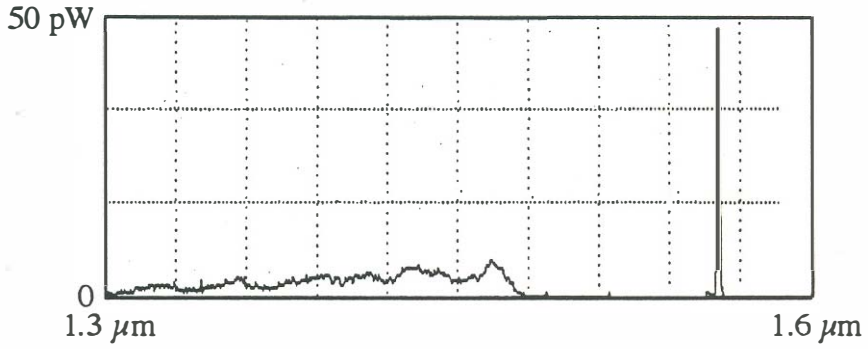


**Fig. 7.9**: Spontaneous emission from a 10 μm diameter F171 at 10kA/cm$^2$ CW showing the cavity mode at ≈1540 nm and the emission from above the output mirror bandstop.

In summary, Fig. 7.7 illustrates that using an active layer with a better carrier confinement was instrumental for obtaining continuous-wave room-temperature lasing since in the real laser the active layer is at a higher temperature than the heatsink.

The difference between the active layers of generations 2 (KS2290) and 3 (KS2778) can be attributed to partial disordering from Zn diffusion into the KS2290 quantum wells during the extended heat treatments. Furthermore, the KS2778 quantum-wells were grown directly on the binary alloy and hence resulted in higher optical quality.

## 7.3. *Device diameter dependence of laser parameters*

### 7.3.1. *Cavity losses*

In Section 7.1.4. we used the dependence of the threshold gain on the device diameter to determine the gain-current relationship. In this section we discuss the possible sources of cavity loss as function of laser diameter. To this end we measured the external quantum efficieny as a function device size, and from there calculated the threshold gain dependence on the device diameter. The results are shown in Fig. 7.10. All of the generations show a very slow increase in the cavity losses with the decreasing diameter, according to an exponent between 0.35 and 0.6. This low exponent indicates that the loss mechanism is not directly related to scattering at the post sidewalls, since it has been shown that this type of scattering leads to an inverse quadratic behavior (Thibeault, 1995).

The diffraction estimate has been made using the fit (B-112),

$$\delta_d \approx \frac{1}{1+7.23(d^2/4\chi)^{1.58}} \qquad (7\text{-}11)$$

where the $\chi = 2L_{cav}\lambda/n_{cav} + \chi_D$. Here $\chi_D$ is the diffraction range (B-113) of the AlAs/GaAs mirror at 1550 nm and equals $\chi_D = 0.87\,\mu m^2$. Using $L_{cav} = 0.705\ \mu m$ and $n_{cav} \approx 3.2$ we have $\sqrt{\chi} = 1.25\mu m$. The calculated values of loss using equation (7-11) are shown in Figure 7.10 compared to the round-trip cavity losses. Evidently the effect of diffraction does not account for all the increase in cavity loss for small diameters.

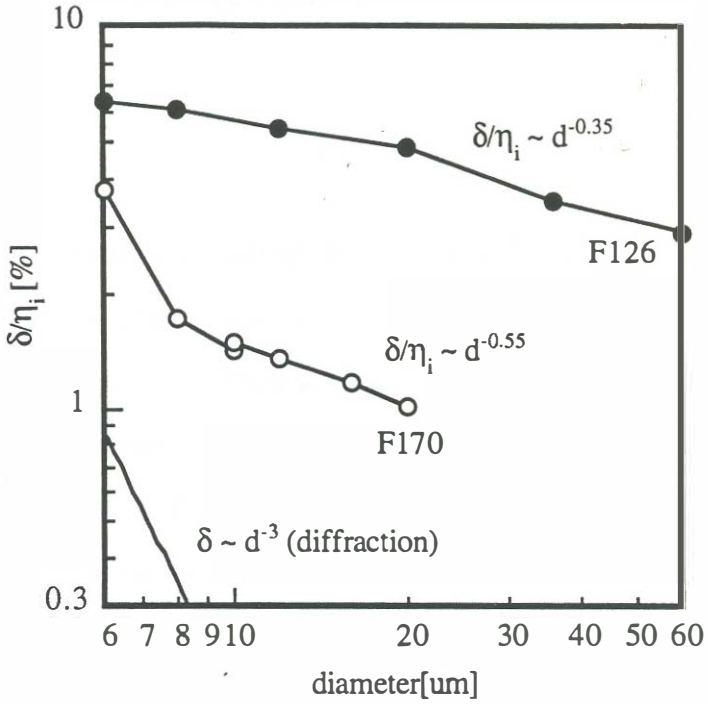


**Fig. 7.10**: Plot of round-trip loss as a function of device diameter for F126 and F170. The functional dependence is given for the sections that approximately obey a power law.

### 7.3.2. *Threshold current density*

The graphs in Fig. 7.11 compare the room-temperature pulsed performance of the F170 run to F167 and generation 1 devices. Apart from overall lower room-temperature pulsed threshold current density for all sizes, the most notable difference between the generation 3 and generation 1 devices is in the functional behavior of the pulsed threshold current density $J_{th}$ with the device size. The increase in $J_{th}$ is much more sudden for small diameters for F170 than for any generation 1 device and

consequently threshold current densities as low as 2 kA/cm$^2$ were measured for small devices (≈10 μm).

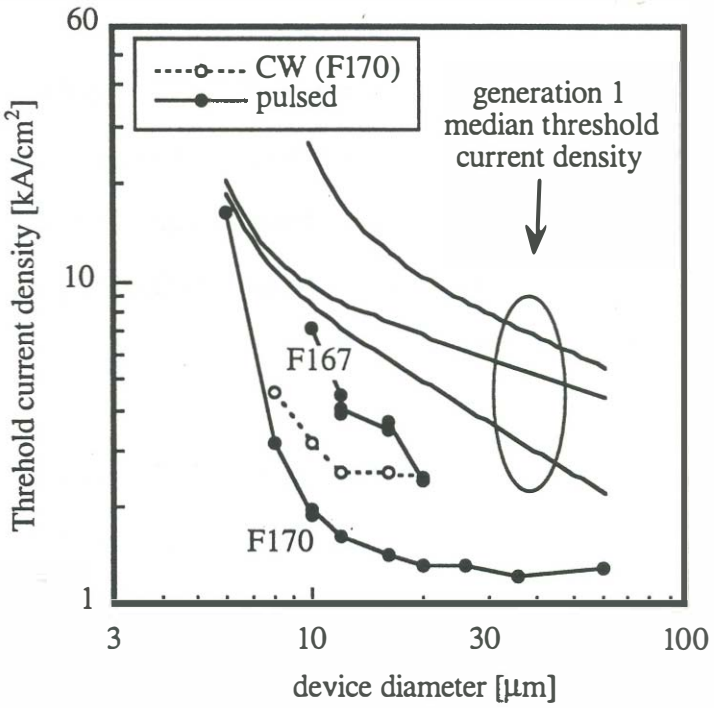


**Fig. 7.11**: Summary of threshold current density for all three generations. The values listed for F167 and F170 are best measured. Only the trends in the median threshold current density are shown for generation 1 devices.

The threshold current variation on the device size is closely related to the variation of the external quantum efficiency described in the previous section, and hence hides the same unknowns. Slow power-law dependence of the threshold current on the device diameter as was observed for the generation 1 devices, has been previously reported by (Mori, 1992). They have observed an approximate $d^{-0.8}$ dependence of the threshold current and attributed it to scattering loss.

One alternative interpretation of the threshold current increase with the reducing radius is the current spreading around the pillar. Such phenomena is driven by the perimeter to area ratio and hence should lead to a hyperbolic dependence in both the threshold current and the internal quantum efficiency. However, the threshold current density of the F170 devices does not exhibit a hyperbolic dependence in the same diameter range as the threshold gain. Therefore, from the data provided in this example, it appears that current spreading is not the dominant effect determining the increase of $\delta/\eta_i$ with reducing diameters.

Since the $p$-mirror post acts as a stressor on top of the active layer, and its influence is diameter dependent, it may me necessary to investigate the effect of stress as a possible source of optical loss and gain variation with the device size.

## 7.4. *The effect of backside reflection*

In continuous-wave operation, the linewidth of the laser output is sufficiently narrow that the coherence length is larger than the substrate thickness. For this reason the output coupler reflectivity seen from the cavity is modified by the substrate-to-air interface reflection. Depending on the relative phase between the two reflections, the equivalent output mirror reflectivity may increase or decrease in value. The two end values are denoted by $r_{eq}^{+}$ and $r_{eq}^{-}$, which correspond to constructive and destructive interference between the mirror and the back surface of the substrate,

$$r_{eq}^{\pm} = \frac{r_{DBR} \pm r_S'(r_{DBR}^2 + t_{DBR}^2)}{1 \pm r_{DBR} r_S'} \tag{7-12}$$

Here $r_{DBR}$ ($t_{DBR}$) and $r_S'$ are the quarter-wave mirror reflection (transmission) coefficient and the effective reflectivity of the substrate-to-air interface. The reflection coefficient $r_S'$ contains the effects of substrate absorption and diffraction, as illustrated in Fig. 7.12, and both of these tend to reduce the reflection coefficient.

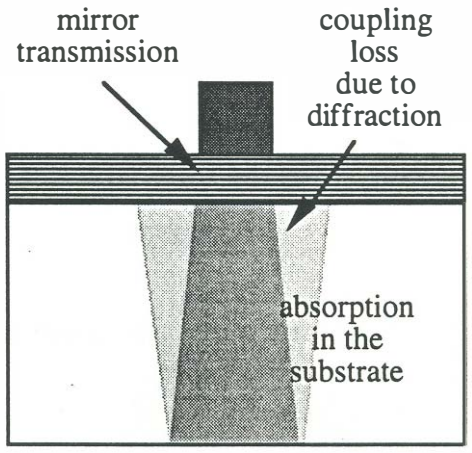


**Fig. 7.12**: Illustration of losses involved in the backside reflection interference.

The reflectivity $R_S' = r_S'^2$ can be approximately expressed using (B-112) as,

$$R_S' = R_S \frac{\exp(-2\alpha L)}{1+3.7\left(\frac{\lambda L}{nd^2}\right)^{1.58}} \tag{7-13}$$

It is seen that the effective substrate reflection is decreased by the presence of substrate absorption. Since the output beams of smaller devices diffract faster than those of large devices it is intuitive that the effective substrate reflection $R_S'$ will also reduce for smaller devices.

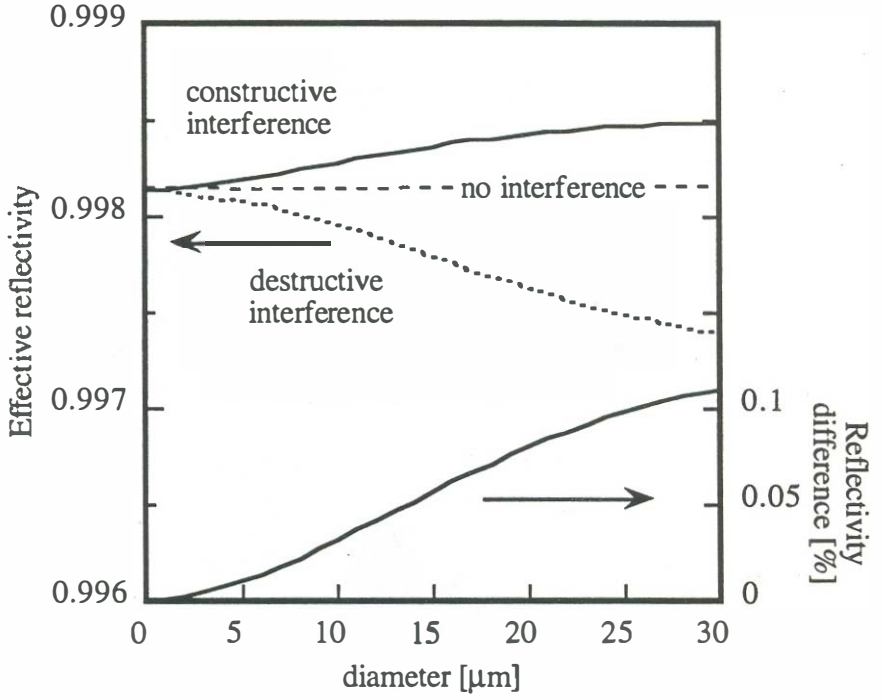


**Fig. 7.13**: Output-mirror reflectivity modulation due to backside reflection.

Using this expression we predict the depth of output-mirror reflectivity modulation of mirror S276 as a function of the device size. The reflectivity and the transmission are

99.815 % and 0.0675 %. Using expressions (7-12) and (7-13), we obtain graphs of the effective reflectivity of the output coupler for the constructive and destructive interference case (shown in Fig. 7.13). Under CW operation the device heating produces slow wavelength changes which then over the long optical length of the substrate make the effective reflectivity oscillate between the two curves shown.

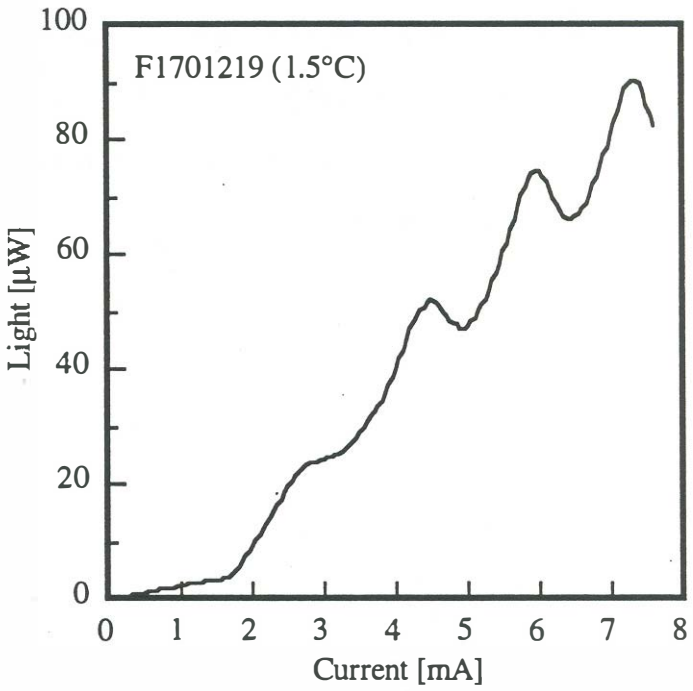


**Fig. 7.14**: Continuous-wave light-current characteristic of a 12 μm diameter measured at 1.5°C.

Since the wavelength shift is almost linear with the dissipated power (and approximately current), the oscillations are nearly periodic, as shown in Fig. 7.14. It is also visible that the difference between the reflectivity values, and hence the round trip losses increase with the diameter as a result of a reducing diffraction loss.

Considering that in these devices the round-trip loss increases with the decreasing devices size, the effect of the backside reflection monotonically reduces with the decreasing device size. This has been observed in many light-current characteristics and can also be seen from Fig. 6.10 where the oscillations in the light-current characteristics grow stronger for larger devices. The variation of the effective output coupler reflectivity and transmitivity produces changes in both the threshold current and the external quantum efficiency. For this reason, the best way to determine the continuous-wave external quantum efficiency is to take the average of the oscillations or deposited an anti-reflective coating. An anti-reflective coating will also alter the effective reflectivity, as shown in Figure 7.13.

## 7.5. *Voltage-current characteristics*

We turn now to the question of power dissipation in the devices. Consider the DC voltage vs. current density relationship measured on 10 μm and 12 μm diameter devices on runs F166, F167, F170, F171 shown in Fig. 7.15. There are two interesting fact about these measurements.

First, it is immediately evident that the voltage drop at a given current density is very different for the two generations of VCLs. The generation 2 lasers (F166/F167) have a voltage drop that is more than one volt larger than the voltage across the generation 3 devices F170/F171. This is quite unusual since all of the devices have the same $p$-mirror (S250 ) and $n$-mirror (S276). Only device F167 has a different $n$-mirror (S201), but it does not seem to have an effect on the V-J characteristics.

A second point is the comparison between the mirror and device voltages: Figure 7.15 shows the CW voltage drop measured across the S207 and S250 mirrors (fused to $p^+$ InP, as shown in Sec. 4.4.7.) with full lines. The dashed continuation of the full lines are pulsed measurements at 50°C. Both of these measurements include the contact resistance (approximately $2 \cdot 10^{-4}\ \Omega\text{cm}^2$). The voltage-current relationship for the S250 mirror without the contact is also shown (data from Figure 4.28). The S250 mirror voltage (contact included) is quite low in the low current density range ($< 1\ \text{kA/cm}^2$), but becomes comparable to the total device voltage in the higher current density range ($> 1\ \text{kA/cm}^2$). (The laser CW threshold current density is in the range $3-4\ \text{kA/cm}^2$). It quite evident from Fig. 7.15 that sum of the two parts

(the photon energy and the S250 mirror with the contact) is larger than the voltage drop across the finished device.

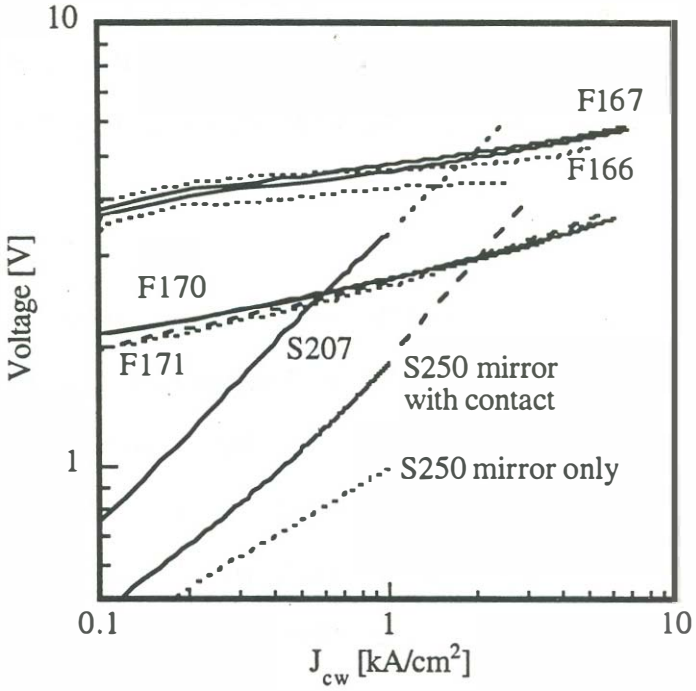


**Fig. 7.15**: Voltage-current characteristics of generation 2 and generation 3 devices (10 μm and 12 μm diameter devices combined).

The origin of the smaller voltage drop on the generation 3 devices and the discrepancy between the mirror and device voltages is not certain. It can be attributed to a number of reasons.

In the third generation of devices (F170/F171), the $p$-mirror and the $p-GaAs/p-InP$ fused junction undergo the fusion step two times: 630°C for more than 20 minutes each time. Since the surface of the $p$-mirror (S250) contains a 10 nm thick Be-doped layer with high concentration ($>2\cdot10^{19}$ cm$^{-3}$), it is possible that Be diffused during this time and doped the fused junction resulting in a lower barrier.

The question remains, whether a two times larger diffusion time, and the corresponding $\sqrt{2}$ times larger diffusion length would be able to produce such a dramatic decrease in the voltage.

Another interesting fact is the apparent correlation between the InP doping levels at the $p-\mathrm{GaAs}/p-\mathrm{InP}$ fused junction with the voltage-current characteristics. Consider that in going through the three measured structures (S250 resistance measurement, generation 2 and generation 3 devices), the doping level of the surface of InP that was fused to $p$-GaAs is decreasing: In the first experiment, S250 mirror was fused to a highly doped InP surface ($5\cdot 10^{18}$ cm$^{-3}$ nominal Zn doping). In generation 2 devices, the $p$-cladding of KS2290 was doped $2-3\cdot 10^{18}$ cm$^{-3}$ with Zn, while in generation 3, the $p$-cladding of KS2778 was Zn-doped to $10^{18}$ cm$^{-3}$. From this data it seem as if the fused junction voltage decreases with the InP doping.

The mirror voltage measurement may also be influenced by a varying contact resistance, even though the S250 current-voltage characterization described in Sec. 4.4.7. and all of the fabricated lasers used the same $p$-type contact (Ti/Au).

Within the acquired data there evidently is not enough information to claim with certainty what is the physical origin of the reduced voltage drop. However, it is quite certain that this reduced voltage drop was one of the main causes for the reduction of the threshold power and the final realization of continuous-wave operating devices.

## 7.6. *Conclusion*

The progress in understanding wafer-fused vertical-cavity lasers and the improvements in the fabrication techniques have led to the realization of the first room-temperature continuous-wave operating 1.54-μm vertical-cavity lasers. With a large number of working lasers of different sizes and structures, a vast amount of information can be deduced about the problems and the possible future improvements. Still, a number of questions remain to be answered and are left for future developments. Several important issues are: 1) The absorption properties of extrinsic (Al,Ga)As at long wavelengths must be assessed, since at the moment they seem to be the limiting factor in the achievement of lower threshold gains. 2) An investigation of the temperature dependence of the internal quantum efficiency and active layer design improvements are necessary to lower the threshold current densities. 3) Further reduction in the thermal resistance and device voltage drop is necessary for the realization of efficient double-fused long-wavelength vertical-cavity lasers.

By demonstrating the continuous-wave operation at room temperature using vertical-cavity lasers fabricated by two wafer fusion steps, we have shown that wafer fusion is a viable technique for fabricating surface-normal optoelectronic devices. However, numerous questions are still remaining regarding the physics of fusion. An investigation of nonradiative recombination in and near fused junctions, as well as optical scatter at the fused junctions is necessary for to be able to explore the full potential and properly design optoelectronic devices based on such junctions. The development of wafer-size fusion processes will then be the last frontier of bringing long-wavelength vertical-cavity lasers to commercial availability.

Chapter 8

# Future work

In the previous chapters we have described various aspects of the design and fabrication of long-wavelength vertical-cavity lasers by wafer fusion. Even though wafer bonding as a technological procedure is not new to the semiconductor fabrication field, the bonding of GaAs and InP is largely undeveloped. A large number of questions are still to be answered, and the process repeatability is yet to be verified on wafer-size samples suitable for large scale production. The future development of this field therefore holds numerous tasks, out of which the most immediate is the full understanding of the physics of bonding. The particular issues that need to be addressed and the methods that should be applied are described in the conclusion of the Chapter 3.

A separate set of issues surfaced with the use of GaAs/AlAs mirrors at long wavelengths. Inasmuch as these two materials have seldom been used in the wavelength range suitable for optical communications, the published data on absorption is sparse. Therefore, the absorption in $p$-GaAs had to estimated using a simple measurement. In the long run, more exact data are necessary to be able to develop accurate models for these lasers. If the current was to be passed through the

*p*-type mirror one must continue with the development of (Be or C-doped) band-gap engineered mirrors. Even in the lower doped mirrors used in this work, the major voltage drop originates at the heterojunction barriers rather than from the ohmic resistance of the bulk mirror layers. This indicates that there is room for mirror resistance reduction by bandgap engineering. The next step is to optimize between the mirror resistance and the absorption loss by continuing the task drawn out in Section 4.4.

Finally, the analysis of laser performance described in Chapter 7 has left many questions unanswered. This is largely due to insufficient data and the large scatter in the data measured. Only two active layers were used, and only one operated continuously at room temperature. Large part of the loss remains unaccounted for, especially in generation 1 and 2 devices. The situation is complicated even more by the unusual threshold current and external quantum efficiency dependence on the device diameter (Section 7.3) and the unusually low forward bias voltage only on generation 3 devices (Section 7.5). New devices have to be fabricated to improve the performances and reveal the underlying physics. One of the critical issues is the thermal resistance and the question of available power under continuous-wave operation. These issues, especially thermal resistance, have been with every vertical-cavity lasers designer since their invention.

In the rest of this chapter we shall discuss some improvements to present devices and show several device structures that were investigated, but due to lack of time or suitable material at the time of investigation, never resulted in working devices. However, with the advent of understanding of the material requirements for long-

wavelength vertical-cavity lasers, these structures may become practically realizable and may further improve the performance of long-wavelength vertical-cavity laser in terms of high temperature operation or fabrication process simplicity.

## 8.1. *Top down mounting*

The first step towards increasing the thermal conductance of the double-fused vertical-cavity lasers is to mount the lasers top down on to diamond heatsinks, as shown in Fig. 8.1. The silicon nitride coating on the device is necessary to insulate the gold coating from the exposed $p$-InP cladding. With the silicon nitride coating, the laser structure is similar to the one shown in Figure 5.1. The gold coating on the pillar can be done using rotating angled evaporation and then by liftoff. The overhang on the photoresist profile has to be several micrometers deep to provide efficient liftoff in this case. An example of angle-evaporated gold coating is shown in Figure 8.2, where the liftoff mask is realized using a two layer photo resist.

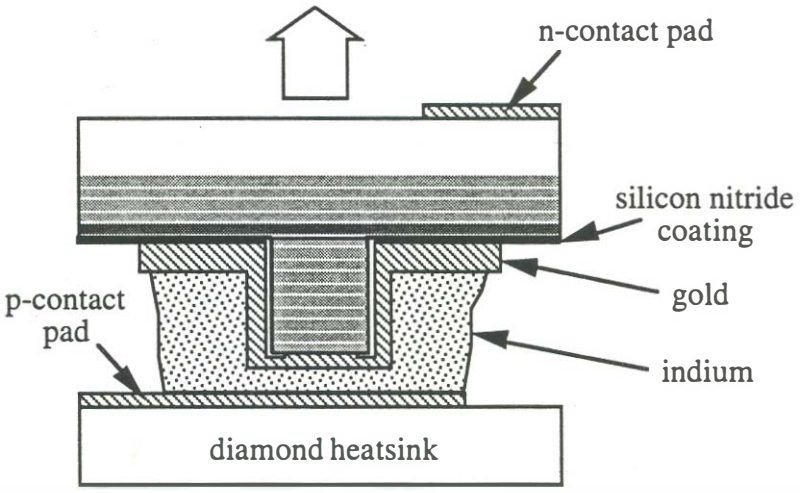


**Fig. 8.1**: Top-down mounting of double-fused vertical-cavity lasers on diamond heatsinks using indium solder.

Diamond heatsinks for this task have been fabricated. A pattern that accepts 16 vertical-cavity lasers in two rows is shown in Figure 8.3. The contact pattern is

realized using Ti/Pt/Au, while the indium bumps are 6-10 μm tall. The VCL mask used to match the heatsink is more sparse than the mask shown in Figure 5.12 to provide enough space for chip sawing.

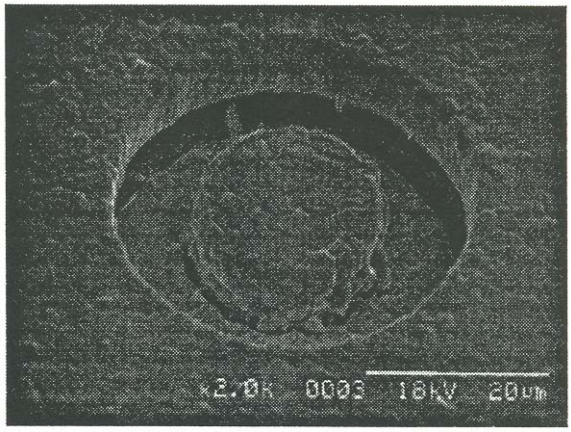


**Fig. 8.2**: Vertical-cavity laser post with rotated-angle evaporated gold.

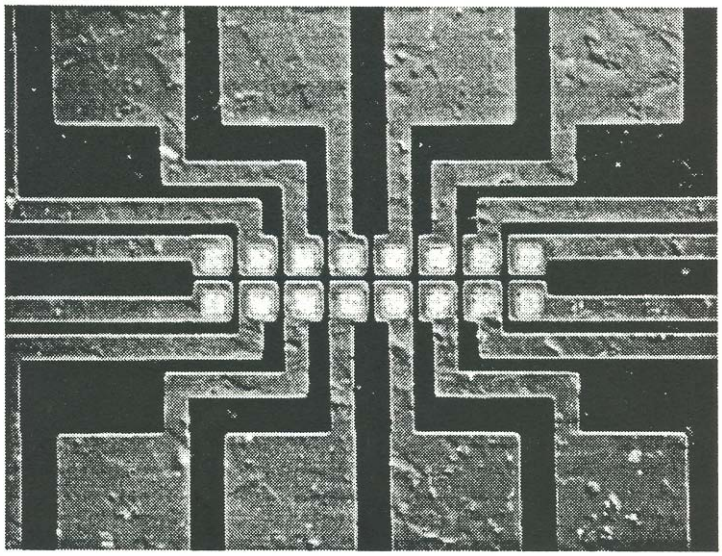

**Fig. 8.3**: Gold contact pattern and indium solder bumps on a diamond heatsink. The contact pads are 160 μm wide. The photographs was take using a Nomarski interferometer which accentuates the roughness of the diamond substrate.

This type of arrangement for efficient heat sinking has been a subject of many studies (Shimizu, 1993, Piprek, 1994a, Kajita, 1994, Peters, 1995) and appears to be a necessary technological step towards achieving low thresholds and high output powers from these lasers. The thermal resistance of the double-fused lasers is expected to reduce by a factor of two by top mounting.

## 8.2. *Current and mode confinement*

The lateral confinement of current and the optical field is necessary to minimize the perimeter effects of the VCL cavity, such as scattering and surface recombination. Three methods for achieving this are described.

### 8.2.1. *Lateral AlAs oxidation*

Recently, there has been a tremendous progress in developing ultra-low threshold and high efficiency GaAs-based vertical-cavity lasers using lateral current and mode aperturing (Lear, 1995, Hayashi, 1995, Yang, G. M., 1995, Choquette, 1994, Huffaker, 1994). Since the mirrors of double-fused vertical-cavity lasers contain AlAs they are suitable for lateral oxidation. The lateral oxidation creates a current aperture which provides gain localized away from the post edges. If the oxidized aperture is made very thin and placed at a node of the standing wave the impact on the transverse mode will be minimized and the guiding will be provided by the presence of gain (gain aperturing). One of the methods for mathematical analysis of such structures is given in Appendix C (Babić[a], 1994).

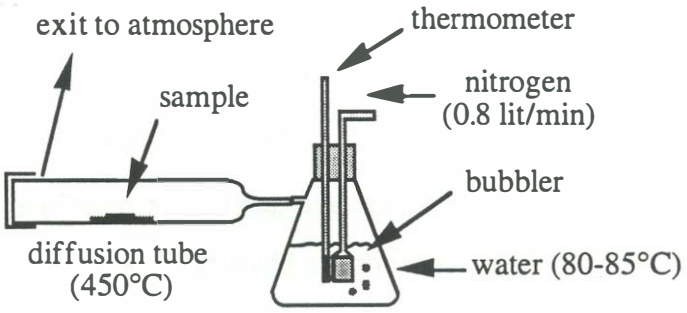


**Fig. 8.4**: Oxidation system setup.

An investigation of laterally oxidized single-fused structures has been performed, but not lasers have been fabricated. The AlAs oxidation was performed in steam at 450°C for several minutes. The oxidation system schematic and the typical process parameters are given in Figure 8.4.

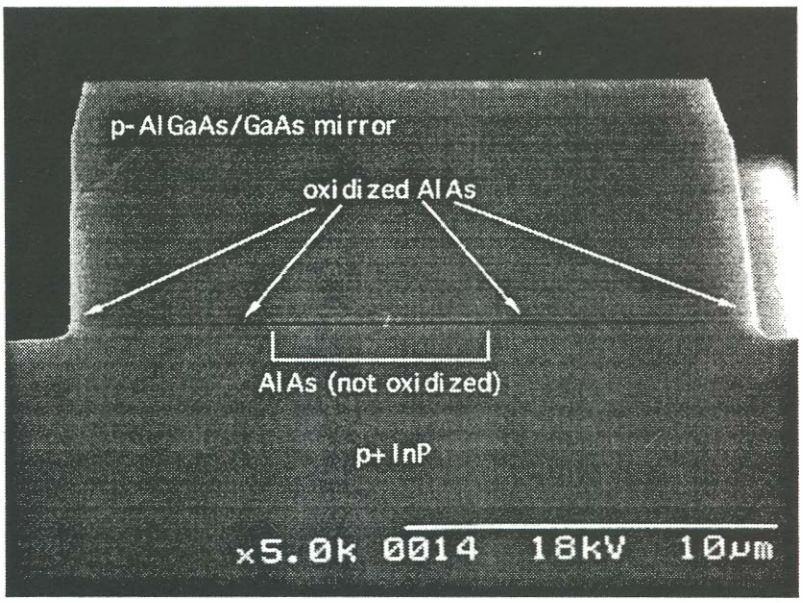


**Fig. 8.5**: Laterally oxidized AlAs layer at the bottom of a AlGaAs/GaAs mirror fused to InP.

Figure 8.5 shows a *p*-type AlGaAs/GaAs mirror fused to an InP substrate. The last mirror period has a layer of AlAs which is oxidized. Stain-etching using hydrochloric acid is used discriminate AlAs from the aluminum oxide ($AlO_x$), since HCl etches AlAs, but not $AlO_x$. The apertures realized by lateral oxidation can be made very small. A close-up view of a ≈2 µm aperture is shown in Figure 8.6. It has also been suggested that $AlO_x$ layer that forms in place of the AlAs is thinner by approximately 10%. The fact that this is true can be observed in the case when entire AlAs/GaAs mirror is oxidized and hence the total mirror thickness reduction is easily visible in a

Nomarski microscope photograph shown in Fig. 8.7. A great potential for achieving low threshold, low resistance, and hence high wallplug efficiency of a fused vertical-cavity lasers using this technique.

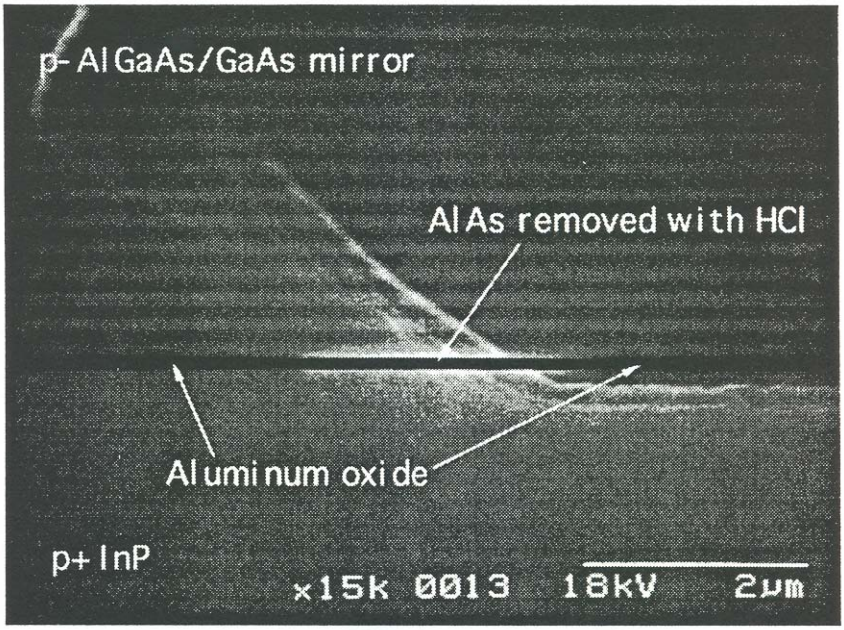


**Fig. 8.6**: A close-up view of a 2 µm aperture realized by lateral oxidation of AlAs.

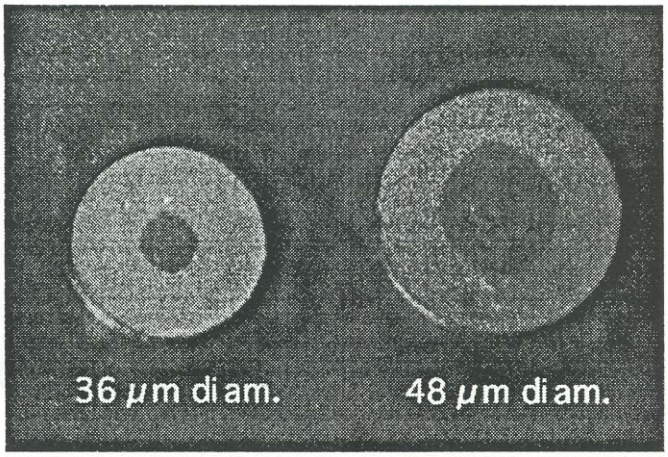


**Fig. 8.7**: Top view of laterally oxidized AlAs/GaAs mirrors.

*8.2.2. Wet chemical undercut of AlAs and InP*

Another technique for current and mode confinement is by using wet chemical undercut in place of the AlAs oxidation. Consider the double-fused vertical-cavity laser structure shown in Fig. 5.2. There are two layers that can be undercut by wet chemical etching. One may use a AlGaAs/GaAs mirror with one (last) AlAs layer and undercut this layer with a dilute hydrochloric acid. The structure required for this process is identical to the one used for oxidation, except that the AlAs is not oxidized but removed by hydrochloric acid and can be used for any GaAs-based vertical-cavity laser. The reason the HCl solution has to be sufficiently dilute is to prevent significant etching of the exposed InP cladding (For etch rates, see Figure 5.4).

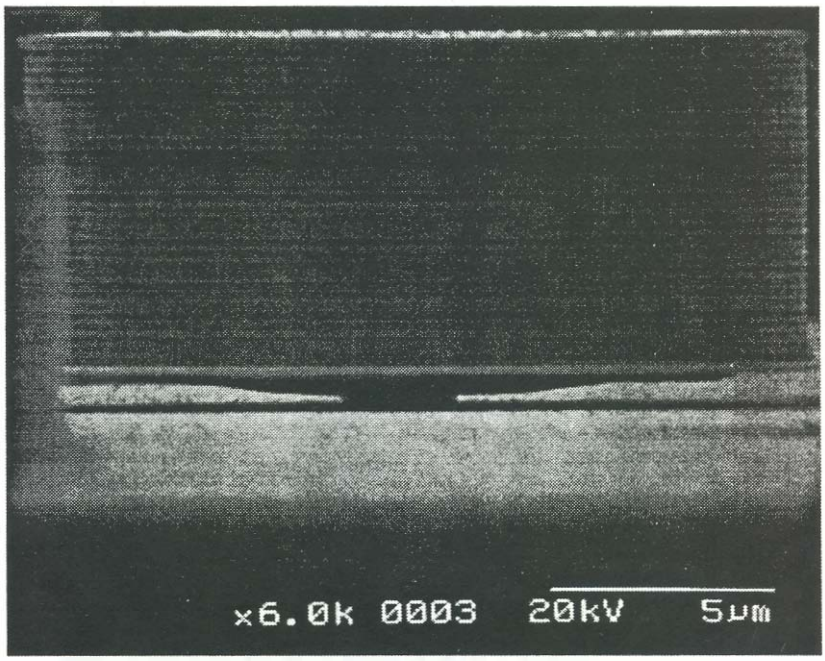


**Fig. 8.8**: An extreme case of wet chemical undercutting (Device F171). The 16 µm diameter AlGaAs/GaAs mirror (S250) is supported by a 2 µm wide InP post.

The InP cladding, exposed in double-fused lasers, can also be undercut using hydrochloric acid. To achieve this without etching the pillar, the top mirror must not contain any AlAs (InP etches much slower than AlAs at all concentrations of HCl). A wet chemical undercut experiment has been performed on the F171 sample. The F171 sample operated continuously at room temperature before the HCl etching, but after the InP layer was undercut the threshold current increased and very few devices operated at room temperature. This was attributed to the increased recombination at the exposed quantum wells exactly at the edges of the undercut pillar. Note that once the InP cladding is removed, the quantum wells of the KS2778 active layer remain exposed to air. To achieve a threshold reduction using this technique, an etch-stop layer should be introduced in the active layer just above the quantum wells. In spite of degraded performance, the undercutting has been successfully realized. An extreme case of undercutting is shown in Figure 8.8 where a 16 μm diameter pillar is supported by a 2 μm InP post.

The hydrochloric acid etching is very crystallographic, as can be seen from Figure 8.9 where a 12 μm diameter post reveals the square shape of the InP post. The sides of the square are oriented along the [100] and [010] directions. The fact that InP etches crystallographically in hydrochloric acid and GaAs isotropically in sulfuric-peroxide-water solutions is visible in Figure 8.10 where the fused junction serves as boundary between the types of etch profiles. The appearance of these profiles is a result of etching GaAs pillar after undercutting InP. The profile of InP is square, while the GaAs etching follows the circular shape of the mask.

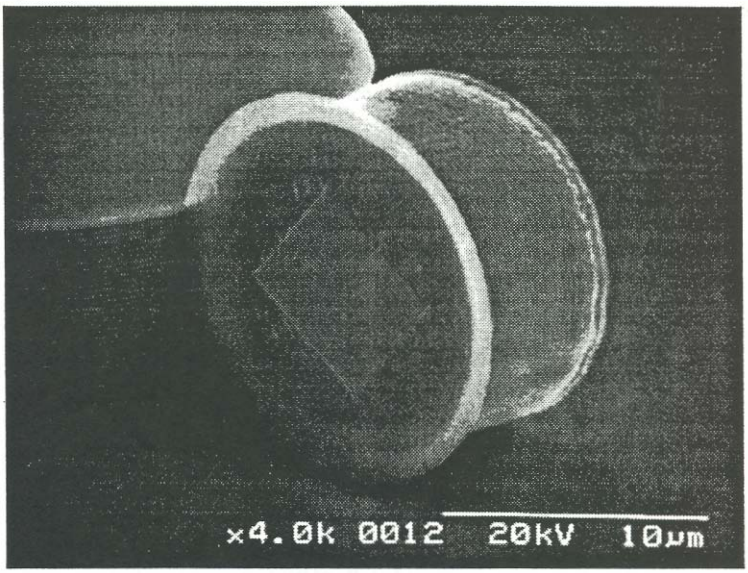


**Fig. 8.9**: A broken-off 12 µm top mirror showing the shape of the undercut InP post.

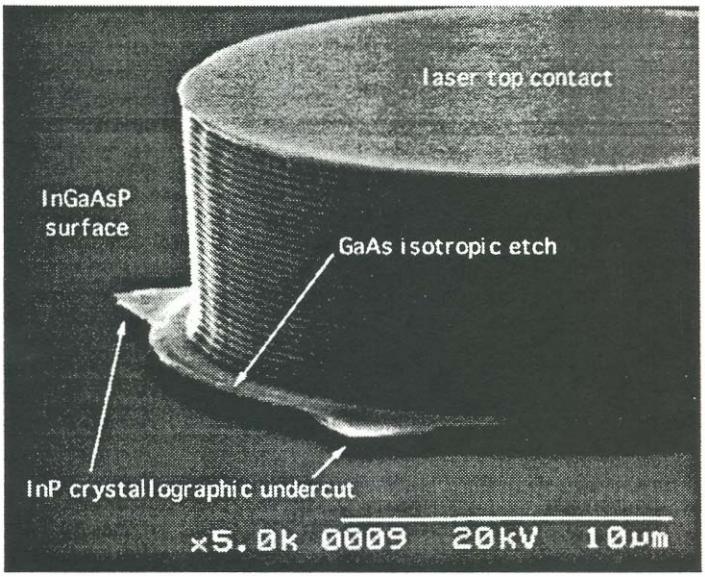


**Fig. 8.10**: Side view of an undercut post (F171). The fused junction serves as a boundary between crystallographic and isotropic etching.

Wet chemical etching is an alternative method for achieving current and mode confinement in vertical-cavity lasers. The refractive index variation and the thickness of the undercut layers are larger than in the oxidation method and hence their influence on the optical mode will be more pronounced. The appearance of recombination has to be considered when exposing to air the epitaxial layers that are adjacent to the active layer. The backfilling of the etched regions with polymers for mechanical stability is also possible.

### 8.2.3. *Proton implantation*

Creating insulating regions by proton bombardment is a very popular method for realizing current confining schemes in which there are no abrupt refractive index variations (Chang-Hasnain, 1991, Wipiejewski, 1993). The application of this method to double-fused lasers is shown in Figure 8.11. The use of proton implantation is attractive because it leads to a planar fabrication process, better thermal conductivity and top emission. The thermal conductivity is increased because the heat dissipated in the active layer can spread though the top and well as the bottom mirror. Furthermore, gain guiding in this structure ensures results in slowly diffracting beams.

A single fused proton implanted laser structure, shown in Figure 8.12, was also investigated and devices were fabricated. However, none of the devices lased. This development was performed before it was realized that $p$-GaAs absorption was limiting the $p$-mirror reflectivity. The top mirror in this device was an electron-beam

evaporated 3.5-period $Si/SiO_2$ mirror. The proton implantation energy and dose were 200 keV and $3 \cdot 10^{14}$ $cm^{-3}$. The mask for ion implantation was realized using a 3 μm thick gold layer, which was lifted off using a deep UV resist stripper.

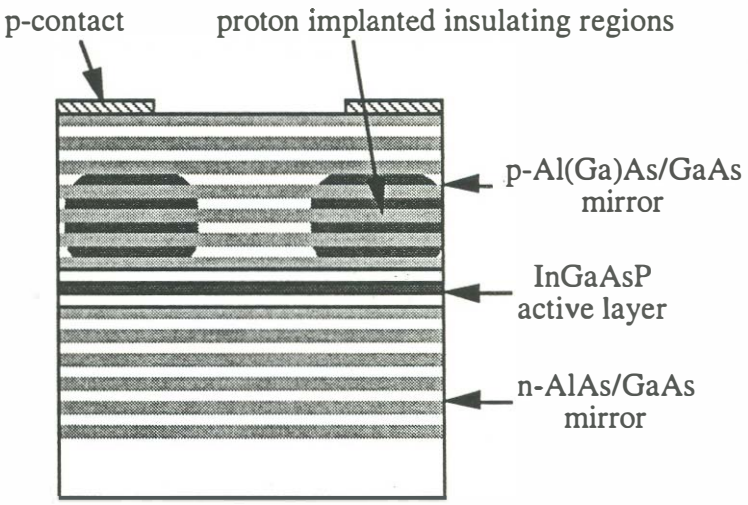


**Fig. 8.11**: Proton implanted double-fused vertical-cavity laser.

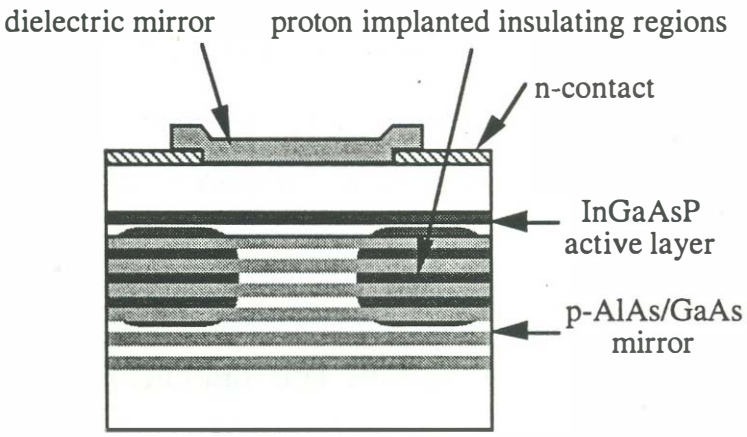


**Fig. 8.12**: Proton implanted single-fused vertical-cavity lasers.

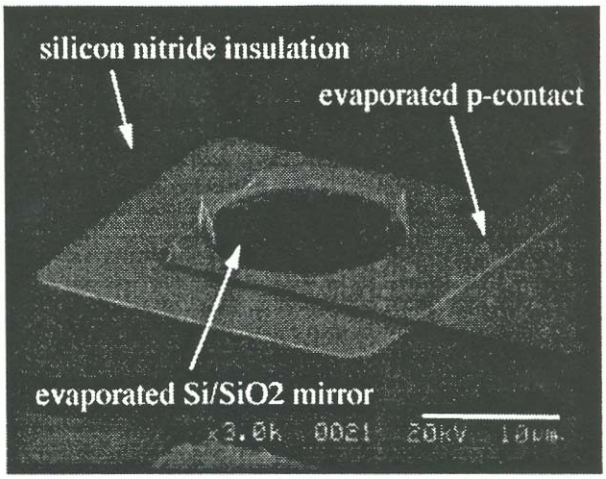


**Fig. 8.13**: Completed single-fused proton-implanted vertical-cavity structure (dummy device on silicon). The semi-transparent lip around the edges of the mirror is a result of mirror liftoff.

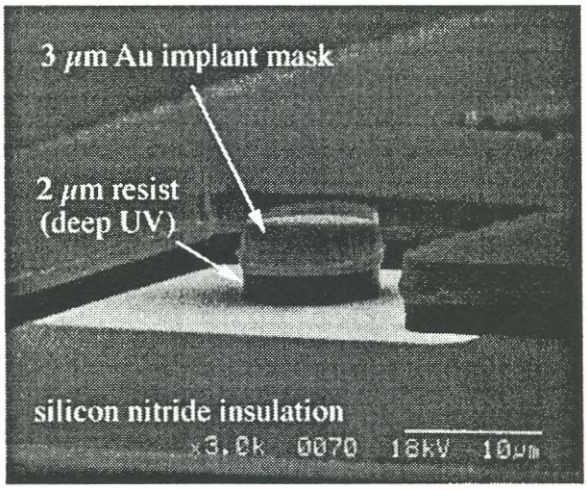


**Fig. 8.14**: Proton-implantation mask uses 3 µm thick gold on top of 2 µm thick deep UV photoresist.

## 8.3. *Single-fused all-epitaxial vertical-cavity laser*

Free-carrier and inter-valence band absorption in GaAs, InP and related alloys is a major obstacle in realizing high reflectivity $p$-type mirrors using materials with small reflective index difference, such as InGaAsP/InP and AlInGaAs/AlInAs systems. For this reason most of the research on InGaAsP/InP mirrors for long-wavelength applications has concentrated on $n$-type mirrors (Tadokoro, 1992, Streubel, 1994, Fisher, 1995), with only a few recent reports on $p$-type mirrors (Miyamoto, 1994). If one mirror is the epitaxial InGaAsP/InP mirror, the other mirror can be realized either by dielectric deposition or by wafer fusion. The structure of the wafer fused VCL with one InGaAsP/InP mirror is shown in Figure 8.15.

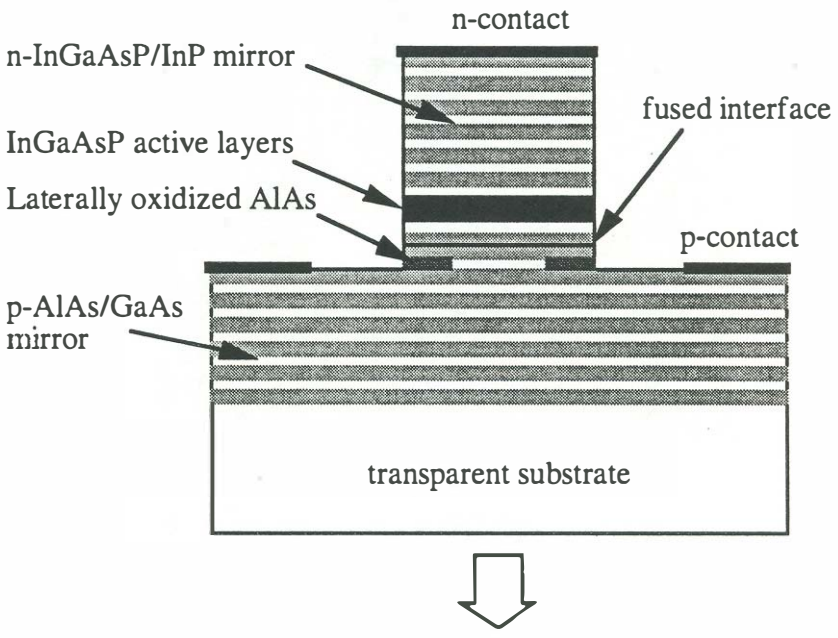


**Fig. 8.15**: Single-fused 1.55 μm vertical-cavity lasers with one AlAs/GaAs and one InGaAsP/InP mirror. Current confinement may be enhanced by lateral AlAs oxidation or wet chemical undercut.

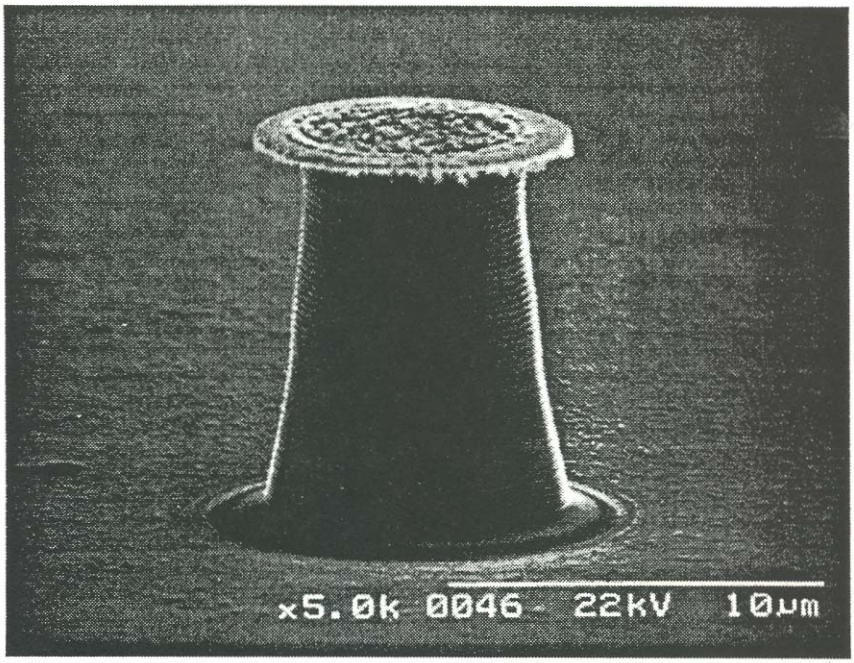


**Fig. 8.16**: Completed single-fused all-epitaxial vertical-cavity laser structure. The undercut is a result of chemical etching during methane-hydrogen-argon reactive ion etching.

Devices with this structure have been fabricated, but none lased. The AlAs/GaAs mirror was grown by MBE (Mirin), while the InGaAsP/InP was grown by MOVPE (Streubel). The fabrication of this structure is quite straightforward: After fusion and InP substrate removal, the laser mesas are defined with metal patterns and then the mirrors are etched in $CH_4/H_2/Ar$ reactive ion etching down to the first AlAs layer. Aluminum arsenide does not etch in this chemistry, hence it serves as an etch-stop layer. In fact, since $CH_4/H_2/Ar$ deposits a hydrocarbon polymer on all surfaces that do not etch, the etching comes to a complete stop on the first AlAs layer. At that point the polymer is removed with oxygen plasma and the slightly oxidized AlAs should

removed using $NH_4OH/H_2O$. Figure 8.16 shows a completed device of this type. The active layer in this device was bulk InGaAsP. The conical shape of the pillar is a result of chemical undercut during the four-hour long $CH_4/H_2/Ar$ etching. The etching conditions were $CH_4 = 4$ sccm, $H_2 = 20$ sccm, and $Ar = 10$ sccm, pressure 75 mT and 500 V self-bias. The shape of the undercut can be improved by implementing an alternating etching scheme in which the methane-hydrogen is alternated with oxygen plasma. The purpose of the oxygen plasma is twofold: It is used remove the polymer from the mask thereby keeping the mask size constant, and to oxidize the sidewalls of the pillar and inhibit further lateral etching. The resulting pillars have vertical sidewalls (Schramm, 1994). Other possible methods for obtaining vertical sidewalls include controlled mask erosion during reactive ion etching (Streubel[a], 1994).

Current and/or mode confinement can enhanced by lateral oxidation of AlAs. In this case the shape of the pillar has less influence on the cavity losses. Since the methane-hydrogen etching stopped on AlAs, after the $NH_4OH/H_2O$ clean-up the first AlAs layer in the *p*-mirror can be laterally oxidized to reduce the current aperture. The oxidation is performed at 450°C for a few minutes and hence the post should be oxidized before *n*-type contact deposition. Room temperature operation of the epilayer structure to be used in his type of device has been demonstrated using optical pumping (Babić, 1994). However, due to the low *n*-mirror resistance (Streubel[a], 1994) and the good thermal conductivity of the binary mirror on the bottom, this device holds excellent potential for continuous-wave operation at room temperature. At the time of writing this devices has not fabricated with low doped *p*-type GaAs mirrors.

## 8.4. *Conclusion*

The work presented in this dissertation describes the development of the first 1.54 μm vertical-cavity lasers operating continuously at and above room-temperature. During the course of this work, a number of theoretical models and physical phenomena that were relevant to this research and vertical-cavity lasers in general have been investigated. Naturally, many new questions regarding wafer fusion and the laser operation have been raised. Hopefully, future work will provide the answers to these questions.

# Appendix A

# Transverse-field matrix method

This appendix illustrates the calculation of plane-wave reflection and transmission coefficients from multilayer structures. Most of this mathematical formalism can be found in a number of books (Macleod, 1986, Yeh, 1988, Thielen, 1989). This material is a supplement to the theory described in this dissertation and is based on the transverse field matrices (Thielen, 1989) rather than transmission matrices (Yeh, P., 1988). To the best of our knowledge, the extension of transverse field matrices to lossy interfaces and sheet gain is original.

If a dielectric slab is parallel to the $xy$-plane and has a finite thickness in the $z$-direction, the field pattern inside can be written as a linear superposition of two waves: the forward and backward traveling waves. To introduce the matrix formalism, we first find the linear relation between the transverse fields at beginning and the end of the thin film (or section of a film) and then calculate the total reflection coefficient for a multilayer stack. This is done for two polarizations $s$ and $p$ separately, then the multilayer matrix is introduced and the formulas for the calculation of s-parameters.

## A.1. *Transverse-electric incidence (s-polarized waves)*

Consider the case where the electric field points along the $y$-direction while the magnetic field points along the $x$ and $z$ directions. The phasor of the forward and backward propagating waves at the at any place along the z-axis is denoted with $E^+(z), E^-(z)$. The amplitudes of the two waves at any place along the z-axis are given by matrix $L(z)$:

$$\begin{bmatrix} E^+(z) \\ E^-(z) \end{bmatrix} = \begin{bmatrix} \exp(ik_z z) & 0 \\ 0 & \exp(-ik_z z) \end{bmatrix} \begin{bmatrix} E^+(0) \\ E^-(0) \end{bmatrix} \tag{A-1}$$

$$L(z) = \begin{bmatrix} \exp(ik_z z) & 0 \\ 0 & \exp(-ik_z z) \end{bmatrix} \tag{A-2}$$

Note that $L$ is unitary and that $L^{-1}(z) = L(-z)$. From here on, short-hand notation $E^{\pm} = E^{\pm}(0)$ will be used. By making use of Maxwell's equations

$$\bar{\nabla} \times \bar{E} = i\omega\mu\bar{H} \quad \bar{\nabla} \times \bar{H} = -i\omega\varepsilon\bar{E} \tag{A-3}$$

we find the electric and magnetic fields at any point to be

$$\begin{aligned} \bar{E} &= \bar{E}^+ + \bar{E}^- \\ \eta_0 k_0 \bar{H} &= \bar{k}^+ \times \bar{E}^+ + \bar{k}^- \times \bar{E}^- \end{aligned} \tag{A-4}$$

$$\begin{aligned} E^{(t)} &= E^+ + E^- \\ \mu_r \eta_0 k_0 H^{(t)} &= -k_z E^+ + k_z E^- \end{aligned} \tag{A-5}$$

The transverse electric field at any place along the $z$-axis can be determined from the linear transformation given by matrix $Q_s$ where $s$ stands for $s$-polarization:

$$\begin{bmatrix} E^{(t)} \\ \eta_0 H^{(t)} \end{bmatrix} = \begin{bmatrix} 1 & 1 \\ -k_z/k_0\mu_r & k_z/k_0\mu_r \end{bmatrix} \begin{bmatrix} E^+ \\ E^- \end{bmatrix} \tag{A-6}$$

$$Q_s = \begin{bmatrix} 1 & 1 \\ -k_z/k_0\mu_r & k_z/k_0\mu_r \end{bmatrix} \quad Q_s^{-1} = \frac{1}{2}\begin{bmatrix} 1 & -\mu_r k_0/k_z \\ 1 & \mu_r k_0/k_z \end{bmatrix} \tag{A-7}$$

We relate the transverse fields at the origin ($z = 0$) to the transverse fields at some location $z$. This can be expressed in matrix form as:

$$\begin{bmatrix} E^{(t)}(0) \\ \eta_0 H^{(t)}(0) \end{bmatrix} = Q_s L^{-1}(z) Q_s^{-1} \begin{bmatrix} E^{(t)}(z) \\ \eta_0 H^{(t)}(z) \end{bmatrix} \tag{A-8}$$

The matrix that related the transverse field for a single film or a section of a film of thickness $z$ of an $s$-polarized wave (TE incidence) is denoted by $M_s$ and it is given by:

$$M_s(z) = Q_s L^{-1}(z) Q_s^{-1} = \begin{bmatrix} \cos k_z z & i\frac{k_0\mu_r}{k_z}\sin k_z z \\ i\frac{k_z}{k_0\mu_r}\sin k_z z & \cos k_z z \end{bmatrix} \tag{A-9}$$

For normal incidence we have

$$M(n,\phi) = \begin{bmatrix} \cos\phi & i\frac{1}{n}\sin\phi \\ in\sin\phi & \cos\phi \end{bmatrix} \tag{A-10}$$

## A.2. *Transverse-magnetic incidence (p-polarized waves)*

The transverse magnetic field is written in terms of the forward and backward traveling waves as (anywhere):

$$H^{(t)} = H^{+} + H^{-}$$
$$\frac{k_0 \varepsilon_r}{\eta_0} E^{(t)} = -k_z H^{+} + k_z H^{-} \qquad \text{(A-11)}$$

We can normalize all of the magnetic field to the electric field values by multiplying by the free-space impedance $\eta_0$.

$$\begin{bmatrix} E^{(t)} \\ \eta_0 H^{(t)} \end{bmatrix} = \begin{bmatrix} -k_z/k_0\varepsilon_r & k_z/k_0\varepsilon_r \\ 1 & 1 \end{bmatrix} \begin{bmatrix} \eta_0 H^{+} \\ \eta_0 H^{-} \end{bmatrix} \qquad \text{(A-12)}$$

$$Q_p' = \begin{bmatrix} -k_z/k_0\varepsilon_r & k_z/k_0\varepsilon_r \\ 1 & 1 \end{bmatrix} \quad Q_p'^{-1} = \frac{1}{2}\begin{bmatrix} -k_0\varepsilon_r/k_z & 1 \\ k_0\varepsilon_r/k_z & 1 \end{bmatrix} \qquad \text{(A-13)}$$

The matrix $Q_p'$ has a prime because it relates the transverse fields to the incident and reflected magnetic fields rather than electric fields, as in (A-6). The spatial evolution of the forward and backward propagating magnetic field amplitudes is identical as given for the electric field: (A-2). The relationship between the transverse fields in this case is:

$$M_p(z) = Q_p' L^{-1}(z) Q_p'^{-1} = \begin{bmatrix} \cos k_z z & i\frac{k_z}{k_0\varepsilon_r}\sin k_z z \\ i\frac{k_0\varepsilon_r}{k_z}\sin k_z z & \cos k_z z \end{bmatrix} \qquad \text{(A-14)}$$

In order to be able to express the electric (or magnetic) field reflection coefficient for both $s$ and $p$-polarized waves, we need to have the definition of the $Q$ matrix in terms of the electric (or magnetic) fields only. This relationship is obtained via the medium wave impedance $\eta = \eta_0\sqrt{\mu_r/\varepsilon_r}$. The magnetic and electric fields are related though:

$$\begin{bmatrix} \eta_0 H^+ \\ \eta_0 H^- \end{bmatrix} = \begin{bmatrix} -\sqrt{\varepsilon_r/\mu_r} & 0 \\ 0 & \sqrt{\varepsilon_r/\mu_r} \end{bmatrix} \begin{bmatrix} E^+ \\ E^- \end{bmatrix} \tag{A-15}$$

The $Q$ matrix for $p$ waves is then

$$Q_p = \sqrt{\frac{\varepsilon_r}{\mu_r}} \begin{bmatrix} k_z/k_0\varepsilon_r & k_z/k_0\varepsilon_r \\ -1 & 1 \end{bmatrix} \qquad Q_p^{-1} = \frac{1}{2}\sqrt{\frac{\mu_r}{\varepsilon_r}} \begin{bmatrix} k_0\varepsilon_r/k_z & -1 \\ k_0\varepsilon_r/k_z & 1 \end{bmatrix} \tag{A-16}$$

For normal incidence the equations simplify into

$$M(z) = Q L^{-1}(z) Q^{-1} = \begin{bmatrix} \cos\left(k_0 z\sqrt{\mu_r\varepsilon_r}\right) & i\sqrt{\frac{\mu_r}{\varepsilon_r}}\sin\left(k_0 z\sqrt{\mu_r\varepsilon_r}\right) \\ i\sqrt{\frac{\varepsilon_r}{\mu_r}}\sin\left(k_0 z\sqrt{\mu_r\varepsilon_r}\right) & \cos\left(k_0 z\sqrt{\mu_r\varepsilon_r}\right) \end{bmatrix} \tag{A-17}$$

## A.3. *Lossy interfaces*

The important fact to note in (A-17) is the symmetry between $\mu_r$ and $\varepsilon_r$. It is this symmetry that makes the transmission matrix approach sensitive to the origin of loss in a layer: whether it is electric or magnetic. We can this fact to model lossy interfaces, such as, scattering or absorption. The intent here is to introduce the loss phenomenologically, rather than determine the degree of scattering with the surface profile.

To derive the lossy interface matrix we consider an infinitely thin conductive sheet as a boundary between two lossless dielectric media: 1 on the left and 2 on the right. The transverse electric field across a conductive (or a current ) sheet is continuous, while the magnetic field exhibits a discontinuity equal to the linear current density. The boundary conditions across the interface is given by

$$\begin{aligned} E_1^{(t)} &= E_2^{(t)} \\ H_1^{(t)} &= H_2^{(t)} - J_t = H_2^{(t)} - \sigma_t E_2^{(t)} \end{aligned} \qquad \text{(A-19)}$$

Which leads to a transverse field matrix:

$$M = \begin{bmatrix} 1 & 0 \\ -\eta_0 \sigma_t & 1 \end{bmatrix} \qquad \text{(A-20)}$$

where $\sigma_t$ is the linear conductivity of the sheet. The fact that the origin of the loss is a result of electric field interaction manifests itself in the asymmetry of this matrix. As a check, we will bring the matrix (A-17) to the form of (A-20): We first write $\phi = k_0 z$ in (A-18) and then take the limit in which $\phi$ becomes small. Now we have

$$M = \begin{bmatrix} 1 & i\mu_r\phi \\ i\varepsilon_r\phi & 1 \end{bmatrix} \qquad \text{(A-21)}$$

Since the losses originate from current flow in a sheet of conductivity $\sigma$, we replace $\varepsilon_r \rightarrow \varepsilon_r + i\sigma/\varepsilon_0\omega$ to get:

$$M = \begin{bmatrix} 1 & i\mu_r\phi \\ i\varepsilon_r\phi - \sqrt{\frac{\mu_0}{\varepsilon_0}}\sigma z & 1 \end{bmatrix} \qquad \text{(A-22)}$$

If we let the thickness of the film go to zero, then $\phi$ goes to zero but the linear conductivity $\sigma_t = \sigma z$ remains constant in this limit. In this limit of equation (12e) evidently becomes identical to (A-20). Similar procedure could be performed on the magnetic susceptibility, in which case the upper-right element of the transverse field matrix would be real and non-zero. The case of an infinitely thin sheet of finite electrical (and/or magnetic conductivity) is the simplest way to introduce interface loss into the multilayer calculation. Surface roughness produces scattering and will be treated in the next section.

## A.4. *Scattering on interfaces*

Consider an interface that is rough or in some other way produces loss of power at an infinitely thin interface the interface. If the scattering depends on the electric field intensity the transverse field matrix should have the form (A-20).

$$M = \begin{bmatrix} 1 & 0 \\ -\delta & 1 \end{bmatrix} \tag{A-23}$$

To check the meaning of $\delta$, we suppose that the scattering interface has a finite width $\Delta x$ and the propagation across this region could be given in a form similar to (A-2), but with a complex propagation wavenumber. Using (A-7) and (A-23) we can de-embed the equivalent propagation matrix:

$$L_{int}(z) = \begin{bmatrix} 1-\delta/2 & -\delta/2 \\ \delta/2 & 1+\delta/2 \end{bmatrix} \tag{A-24}$$

Comparing (A-24) with (A-2) and assuming that the loss at the interface is small ($\delta << 1$), we see that the relationship between the absorption coefficient of this layer and $\delta$ is $\alpha\Delta x = \delta$. The reason $\delta$ appears in the off-diagonal elements is to account for loss enhancement and inhibition due to the standing wave pattern. Namely, if the forward and backward propagating waves interfere constructively at the interface then the absorption will be doubled, while if the interference is destructive there will be no absorption. In similar manner we can introduce a sheet of gain in to the interface.

To make this model more general, we phenomenologically introduce both electric and magnetic scattering into the transverse field matrix as follows:

$$M = \begin{bmatrix} 1 & -\delta_m \\ -\delta_e & 1 \end{bmatrix} \tag{A-25}$$

This interpretation is interesting if we know what the reflection and the transmission coefficients of some lossy interface are and we want to introduce these number into the model. Starting from (A-25), we derive the relations for the reflectivity and the transmission of a lossy interface.

Suppose that the incident and exit mediums have refractive indices $n_1$ and $n_2$. Using (A-7) and (A-13) we have for the electric fields,

$$\begin{bmatrix} E_1^+ \\ E_1^- \end{bmatrix} = \frac{1}{2n_1}\begin{bmatrix} n_1 & -1 \\ n_1 & 1 \end{bmatrix}\begin{bmatrix} 1 & -\delta_m \\ -\delta_e & 1 \end{bmatrix}\begin{bmatrix} 1 & 1 \\ -n_2 & n_2 \end{bmatrix}\begin{bmatrix} E_2^+ \\ E_2^- \end{bmatrix}$$

$$\begin{bmatrix} E_1^+ \\ E_1^- \end{bmatrix} = \frac{1}{2n_1}\begin{bmatrix} (n_1+n_2)+(n_1n_2\delta_m+\delta_e) & (n_1-n_2)-(n_1n_2\delta_m-\delta_e) \\ (n_1-n_2)+(n_1n_2\delta_m-\delta_e) & (n_1+n_2)-(n_1n_2\delta_m+\delta_e) \end{bmatrix}\begin{bmatrix} E_2^+ \\ E_2^- \end{bmatrix} \quad \text{(A-26)}$$

and for magnetic fields

$$\begin{bmatrix} H_1^+ \\ H_1^- \end{bmatrix} = \frac{1}{2n_2}\begin{bmatrix} -n_1 & 1 \\ n_1 & 1 \end{bmatrix}\begin{bmatrix} 1 & -\delta_m \\ -\delta_e & 1 \end{bmatrix}\begin{bmatrix} -1 & 1 \\ n_2 & n_2 \end{bmatrix}\begin{bmatrix} H_2^+ \\ H_2^- \end{bmatrix}$$

$$\begin{bmatrix} H_1^+ \\ H_1^- \end{bmatrix} = \frac{1}{2n_2}\begin{bmatrix} (n_1+n_2)+(n_1n_2\delta_m+\delta_e) & (n_2-n_1)+(n_1n_2\delta_m-\delta_e) \\ (n_2-n_1)-(n_1n_2\delta_m-\delta_e) & (n_1+n_2)-(n_1n_2\delta_m+\delta_e) \end{bmatrix}\begin{bmatrix} H_2^+ \\ H_2^- \end{bmatrix} \quad \text{(A-27)}$$

From here, the electric field reflection and transmission coefficients are given by

$$r_e = \frac{n_1-n_2+n_1n_2\delta_m-\delta_e}{n_1+n_2+n_1n_2\delta_m+\delta_e} \quad t_e = \frac{2n_1}{n_1+n_2+n_1n_2\delta_m+\delta_e} \quad \text{(A-28)}$$

and for the magnetic field we have $r_h = -r_e$, and $t_h = (n_2/n_1)t_e$. The inverse expressions for the electric and magnetic losses at the interface can be obtained from (A-28) and are quite simple:

$$\delta_e = \frac{n_1(1-r_e)-n_2t_e}{t_e} \quad \delta_m = \frac{1+r_e-t_e}{n_2t_e} \quad \text{(A-29)}$$

Note that in general the loss will depend on the standing wave pattern. If the electric field node occurs at the interface the loss will be affected only by $\delta_m$. By summing the power reflectivity and transmitivity we obtain the *scatterance* (equivalent of absorptance) of the junction.

$$A_S = 2\frac{n_1 n_2 \delta_m (\delta_e + 2n_2) + \delta_e (n_1 n_2 \delta_m + 2n_1)}{\left[(n_1 + n_2) + (n_1 n_2 \delta_m + \delta_e)\right]^2} \qquad \text{(A-30)}$$

If the scattering is only electric field related then

$$A_S = \frac{4n_1 \delta_e}{\left[n_1 + n_2 + \delta_e\right]^2} \qquad \text{(A-31)}$$

## A.5. *Multilayer structures*

Consider now the case where we have calculated the total transverse field matrix for an entire multilayer of $m$ layers. The transverse field matrix for polarization $\lambda \in (s, p)$ is given by

$$M_\lambda = \prod_{i=1}^{m} M_\lambda(i) \tag{A-32}$$

This will relate the transverse fields at the beginning and the end of the stack. Once this relationship is known we can determine the relationship between the incident and the reflected fields at both sides using the $Q$ matrices again ($s$ and $p$ suppressed):

$$\begin{bmatrix} E^+ \\ E^- \end{bmatrix}_{i=0} = Q_0^{-1} M Q_e \begin{bmatrix} E^+ \\ E^- \end{bmatrix}_{i=e} \tag{A-33}$$

Here subscripts zero and $e = m+1$ refer to the incident and the exit mediums. If we denote this matrix by $N = Q_0^{-1} M_1 M_2 M_3 \cdots M_m Q_e$ then

$$\begin{bmatrix} E^+ \\ E^- \end{bmatrix}_{i=0} = \begin{bmatrix} N_{11} & N_{12} \\ N_{21} & N_{22} \end{bmatrix} \begin{bmatrix} E^+ \\ E^- \end{bmatrix}_{i=e} \tag{A-34}$$

For the magnetic field we need to use the conversion described in equation. (A-16). So the matrix is given by

$$\begin{bmatrix} \eta_0 H^+ \\ \eta_0 H^- \end{bmatrix}_{i=0} = \begin{bmatrix} -\sqrt{\varepsilon_{r0}} & 0 \\ 0 & \sqrt{\varepsilon_{r0}} \end{bmatrix} \begin{bmatrix} N_{11} & N_{12} \\ N_{21} & N_{22} \end{bmatrix} \begin{bmatrix} -1/\sqrt{\varepsilon_{re}} & 0 \\ 0 & 1/\sqrt{\varepsilon_{re}} \end{bmatrix} \begin{bmatrix} \eta_0 H^+ \\ \eta_0 H^- \end{bmatrix}_{i=e} \tag{A-35}$$

$$\begin{bmatrix} \eta_0 H^+ \\ \eta_0 H^- \end{bmatrix}_{i=0} = \sqrt{\frac{\varepsilon_{r0}}{\varepsilon_{re}}} \begin{bmatrix} N_{11} & -N_{12} \\ -N_{21} & N_{22} \end{bmatrix} \begin{bmatrix} \eta_0 H^+ \\ \eta_0 H^- \end{bmatrix}_{i=e} \tag{A-36}$$

In order to determine the s-parameters of this system we consider the Poynting Vector $\bar{S} = \bar{E} \times \bar{H}^*$. Since for either waves (s or p) the field vectors are already defined orthogonal we can set

$$\begin{aligned} S_0^+ &= E_0^+ H_0^{+*} \quad S_e^+ = E_e^+ H_e^{+*} \\ S_0^- &= E_0^- H_0^{-*} \quad S_e^+ = E_e^+ H_e^{+*} \end{aligned} \tag{A-37}$$

Set $n = \sqrt{\varepsilon_r}$ and $\gamma = n_0^*/n_e^*$. We investigate the case with a wave incident from port 0 $E_e^- = H_e^- = 0$. Then given by

$$S_0^+ = \gamma N_{11} N_{11}^* S_e^+ \qquad S_0^+ = -\frac{N_{11} N_{11}^*}{N_{21} N_{21}^*} S_0^- \tag{A-38}$$

For waves incident from port $e$ we have $E_0^+ = H_0^+ = 0$ and:

$$S_e^+ = -\frac{N_{12} N_{12}^*}{N_{11} N_{11}^*} S_e^- \qquad S_0^- = \gamma \left| N_{22} - \frac{N_{12} N_{21}}{N_{11}} \right|^2 S_e^- \tag{A-39}$$

Now one can define s-parameters by replacing $S$ with $a = \sqrt{S}$. However, one must make sure that the incident and the exiting medium are lossless, otherwise the factor $\gamma$ will be complex. If $\gamma$ is <u>real</u> then we can define the scattering matrix

$$\begin{aligned} s_{11} &= \frac{N_{21}}{N_{11}} & s_{12} &= \sqrt{\gamma}\left( \frac{N_{22} N_{11} - N_{21} N_{12}}{N_{11}} \right) \\ s_{21} &= \frac{1}{\sqrt{\gamma} N_{11}} & s_{22} &= -\frac{N_{12}}{N_{11}} \end{aligned} \tag{A-40}$$

The sign convention between $s_{11}$ and $s_{22}$ is adjusted to agree with the electric field reflection coefficient.

Appendix B

# Optical properties of quarter-wave mirrors

The efficient and reliable fabrication of high reflectivity mirrors is instrumental for the realization of practical vertical-cavity lasers. The requirement for a high value of reflectivity ( $R > 99\%$) to a great extent dictates the choice of materials and device structure of vertical-cavity lasers. Reflectors for electromagnetic radiation can be realized using both metal or dielectric-multilayer coatings. However, in semiconductor lasers metal mirrors are not used by themselves, but only in conjunction with dielectric mirrors. The reason for this is that metal–semiconductor interface reflectivity in the near-infrared and visible wavelength range is not sufficient for use in vertical-cavity lasers ( $R < 99\%$). Furthermore, metal mirrors can not be used as efficient output couplers since they have poor or no light transmittance. For these reasons, laser mirrors are most commonly realized as multilayer interference coatings employing low loss dielectrics. The simplest and most commonly used structure is the *quarter-wave mirror* (Siegman, 1986, Herbelin, 1981). The quarter-wave mirror provides high reflectivity only over a limited frequency range, but can be fabricated with reflectivities as high as 99.999% (Rempe, 1993). In some cases, when larger mirror bandwidths are required, two quarter-wave stacks with

overlapping bandstop regions can be used (Turner, 1966) or the thicknesses of the mirror layers can be staggered in an arithmetic or geometric progression (Heavens, 1966).

Vertical-cavity laser mirrors are almost always realized as quarter-wave dielectric mirrors using either single crystal semiconductor materials or amorphous dielectrics deposited by a low temperature dielectric deposition technique. The use of hybrid mirrors in which metal is combined with a dielectric multilayer coating is also widespread. The metal coating is used to increase the reflectivity of a dielectric mirror or to replace a number of dielectric layers while keeping the same peak reflectivity. This Appendix is devoted to the description of the optical properties of quarter-wave mirrors relevant for their design and application in vertical-cavity lasers and other surface normal optoelectronic devices. The theoretical analysis of quarter-wave mirror given here is general, but the practical examples are directed towards 1.55 μm vertical-cavity lasers.

## B.1. *Introduction*

### *B.1.1. Quarter-wave mirrors - background*

The term *quarter-wave stack* or *multi-section quarter-wave transformer* encompasses a large number of structures which are used in a variety of band limited impedance transformation applications (Collin, 1955, 1966). For applications in optics these structures are realized as quarter-wave layered media with the section impedances varied by using non-magnetic materials with different refractive indices. The most

common uses here are anti-reflective (AR) coatings and high reflectivity (HR) mirrors. The quarter-wave section refractive indices of an AR coating vary monotonically with some mathematical progression, typical examples being the Binomial and Chebyshev transformers (Collin, 1955, 1966). A very high reflectivity coefficient at the design frequency can be achieved by using a structure in which the refractive index of every subsequent layer alternates in magnitude. In this way all of the reflected waves interfere constructively at the design frequency and produce a high reflection coefficient with a phase exactly zero or $\pi$. The structure that is most commonly referred to as *the* quarter-wave mirror (QWM) is a multi-section quarter-wave structure in which the section refractive indices alternate between two fixed values: high $n_H$ and low $n_L$. This is the most efficient structure for the realization of high reflectivity mirrors, since each of the interface reflections is maximized. Very high peak reflection coefficients at optical frequencies can be practically achieved in this manner. Unity reflection coefficient can not be achieved neither with finite (Haus, 1984) nor infinite number of layers due to the presence of material loss and scattering. Due to its simplicity and periodic nature the QWM structure is the most common realization of HR coatings in optics and is of primary interest in this work.

In semiconductor optoelectronics HR reflectors appear as in-plane and vertical structures. In-plane reflectors constitute Distributed Feedback (DFB) and Distributed Bragg Reflector (DBR) lasers, and are typically fabricated by e-beam lithography and holographic means. The resulting refractive index variation in these structures is typically graded and very weak, and can therefore be efficiently analyzed by perturbation methods such as Coupled-Wave Theory (CWT) (Kogelnik, 1974, Haus, 1984). The fabrication of vertical HR reflectors involves deposition of quarter-wave

layers of alternating refractive indices by epitaxial growth, evaporation, or plasma deposition. The large variety of materials used for mirror fabrication yields in a large range of available refractive index values and the interfaces are typically abrupt even though they can be graded.

The refractive profile of two quarter-wave mirrors with the relevant parameters is shown in Fig. B.1. At the center (design) wavelength, all of the layers have thickness of one quarter-wavelength and the reflectivity spectrum exhibits maximum reflectivity.

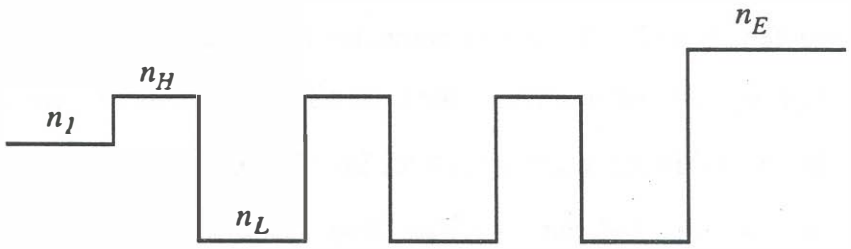


(a)

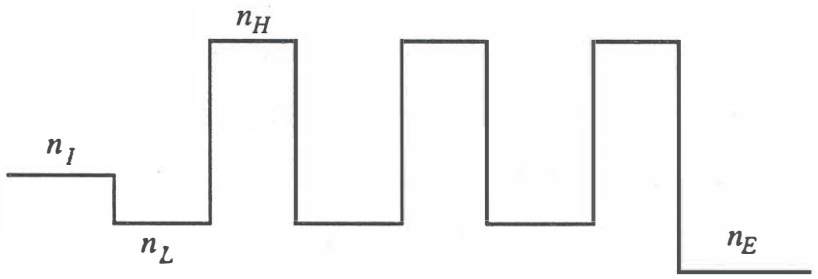


(b)

**Fig. B.1**: The refractive index profile of two quarter-wave mirrors. Mirror (a) has a reflection phase $\pi$ at the center wavelength and mirror parameters $a = n_I/n_H$, $p = n_I/n_H$, and $q = n_L/n_E$, while mirror (b) has phase zero and parameters $a = n_L/n_I$, $p = n_I/n_H$, and $q = n_E/n_H$. (Electromagnetic radiation is incident from the left).

The reflectivity spectrum will exhibit a region of high reflectivity every time the phase across each layers becomes an odd integer multiple of $\pi/2$ or in the immediate neighborhood. In an ideal situation where there is no refractive index dispersion, i.e. no frequency variation of the refractive index, the spectrum will be perfectly periodic: The high reflectivity region will appear at $\omega_c$, $3\omega_c$, $5\omega_c$, and so on. Inasmuch as all dielectric materials exhibit some degree of dispersion in the transparent region and at least one absorption region, this periodicity, if at all observable, will never be exact. If one uses dielectrics well below the fundamental absorption edge, such as, using $SiO_2$ and $Si_3N_4$ in the infrared range, then an approximate periodicity can be observed. This is shown for a $SiO_2/SiN_x$ mirror (a) in Fig. B.2.

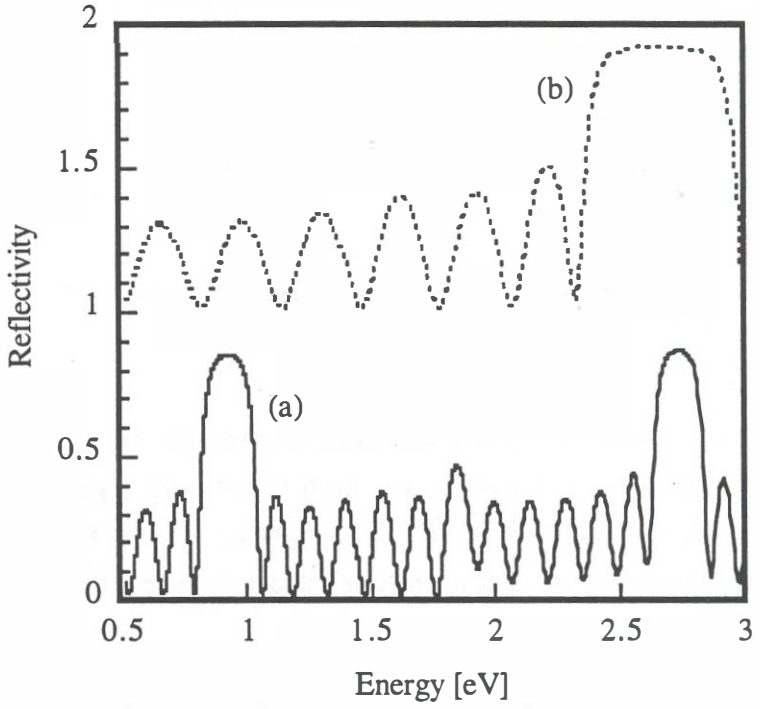


**Fig. B.2**: Measured reflectivity spectra on two $SiO_2/SiN_x$ ($x \approx 4/3$) quarter-wave mirrors deposited by reactive sputtering: Mirror (a) is a 6-period mirror tuned to 1300 nm, while (b) is an 8-period mirror tuned to 460 nm.

The mirror (b) is fabricated using the same material combination, but is tuned to a visible wavelength (blue). The width of the high reflectivity region depends on a number of parameters but is largely determined by the refractive index ratio $n_L/n_H$.The number of minima (or zeros) between any two high-reflectivity regions ( $\omega_c$ and $3\omega_c$, for example) equals the number of layers in the mirror.

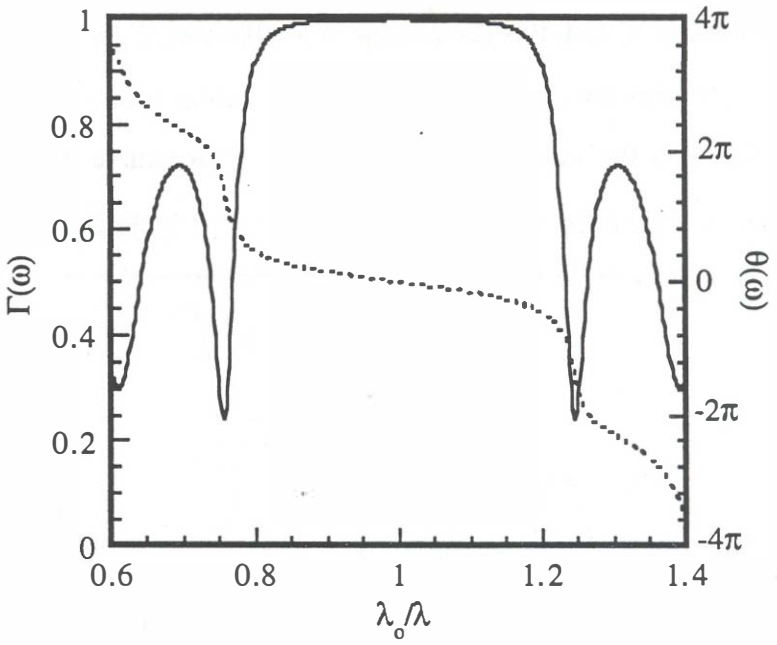


**Fig. B.3**: Calculated amplitude and phase reflectivity spectrum of a 5-period quarter-wave mirror in the high reflectivity region. The refractive indices are $n_I = 3.2$, $n_H = 3.5$, $n_L = 2.0$ and $n_E = 1.0$. For simplicity, no absorption loss or material dispersion is considered.

The quarter-wave mirror has a very complicated amplitude and phase spectrum due to its distributed (multi-reflection) nature. A numerically calculated amplitude and phase spectra of a 5-period $Si/Si_3N_4$ mirror are shown as an example in Figures B.3 and B.4. The peak reflectivity depends on the number of layers and all of the refractive

indexes involved: the incident and the exit medium, and the two materials constituting the high and low impedance sections. The phase characteristic exhibits almost linear phase within the bandstop region and then changes very rapidly outside it. The slope of the phase characteristics of a linear system is called *group delay*. It is almost constant around the center of the bandstop and increases away from it. If the group-delay is constant, an optical pulse with frequency $\omega_c$ incident on a quarter-wave mirror will be delayed by the value given by the slope of the phase characteristic. Any phase variation of higher order than linear produces pulse broadening and distortion (group delay dispersion).

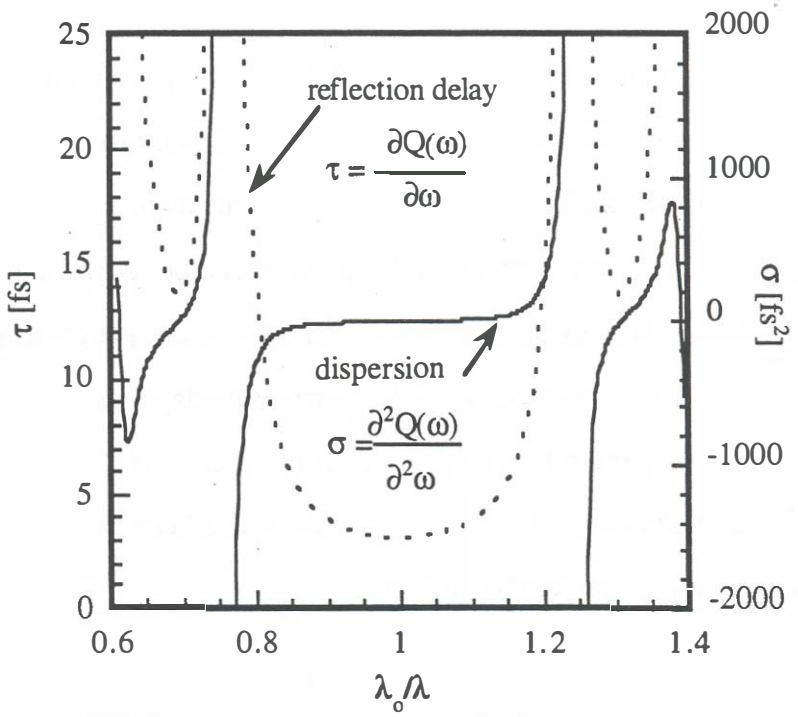


**Fig. B.4**: Calculated reflection delay and dispersion of the quarter-wave mirror shown in Fig. B.3.

In ultra-fast laser applications, high reflectivity interference coatings are sometimes used for pulse shaping (Szipöcs, 1994) since dispersion of both signs can be achieved. In semiconductor lasers the modulation bandwidths are sufficiently small that dispersion has a negligible effect on the laser high speed performance. Its only side effect is the introduction of nonlinear longitudinal mode separation, which does not have any detrimental effects on the performance of vertical-cavity lasers.

*B.1.1. Motivation and the scope of the analysis*

The quarter-wave mirror exhibits high reflectivity only at the center and in the immediate neighborhood of the center of the bandstop. This is the portion of the spectrum that is of most interest for vertical-cavity and distributed Bragg reflector (DBR) laser operation. Therefore, most of the analysis of quarter-wave mirrors for these applications is concentrated on the mirror properties at and in the vicinity of the bandstop center. The key parameters that characterize the quarter-wave mirror are the peak reflectivity, the bandstop width, the penetration depth and the mirror diffraction properties. The penetration depth and diffraction in the mirror are subjects of particular interest in this dissertation and have hence been studied more thoroughly. There are several reason for this interest:

(a) The observation that at the center of the bandstop the mirror exhibits a linear phase immediately led to the interpretation that the reflection appears as to have happened from somewhere within the actual mirror. The distance from the first mirror interface to the location of the apparent reflection was named *penetration depth.* Inasmuch as the penetration depth concept was first used in conjunction with DBR lasers where the

refractive index variations were small, another intuitive interpretation became popular: The penetration depth was defined as the depth at which the standing wave energy falls to $1/e$ of its initial value. Due to the small size of the refractive index perturbation in DBRs, these definitions were more or less equivalent and exact expressions for the penetration depth were obtained using Coupled Mode Theory (Kogelnik, 1974, Koyama, 1983). However, it was not until mirrors with large refractive index variations came to use (in vertical-cavity lasers) that it became necessary to clarify these definitions and rigorously analyze the physical quantities associated with them. (Coupled mode theory can not be applied to problems with large refractive index variations.) A detailed investigation of the "penetration depth" approximation showed that, in general, the two definitions do not lead to the same "penetration depth", and exact analytic expressions for both quantities were given (Babić, 1992).

(b) The clarification of the penetration depth concept and subsequent formalism has led to a number of original analytic expressions for physical quantities related to the penetration depth: the group-delay, scattering parameters, absorptance and reduction of peak reflectivity due to small absorption loss. All of these make the design of the quarter wave mirrors simpler and enable the study of physical quantities without the use of massive numerical calculators. The primary examples of surface-normal devices that utilize quarter-wave mirrors and benefit from this study are all vertical-cavity lasers, Fabry-Perot modulators and resonant cavity photodetectors.

*B.1.3. Lumped mirror model*

The penetration depth in quarter-wave mirrors is a very useful concept that provides both an intuitive picture and a simplified mathematical treatment of quarter-wave mirrors near the center frequency. The basic idea lies in the replacement of the very complicated phase behavior of a quarter-wave mirror with a single lumped mirror placed at a suitable distance deeper into the original mirror. The lumped mirror model describes the distributed mirror *exactly* at normal incidence and center frequency, and can be adjusted to *approximate* the mirror behavior in the vicinity of the resonance. The actual location of the lumped mirror depends on which physical quantity we wish to conserve when going from the exact mirror and the lumped equivalent. The conserved quantities can be time, energy or diffraction (free-space propagation).

Consider *time* as the conserved quantity first: It is well known from signal and system theory that a linear system with a constant amplitude and a linear phase characteristic does not introduce any distortion to the signal except for a change in amplitude equal to the transfer function amplitude and a delay equal to the slope of the (linear) phase characteristic. The QWM approximately satisfies this constant amplitude / linear phase requirement at the center frequency. The constant amplitude is modeled by a fixed reflection coefficient (fixed amplitude and fixed phase), while the delay is modeled by placing the lumped mirror at a suitable distance from the reference plane. The distance at which the lumped mirror has to be placed and the fixed phase that this mirror has to have depends on the group delay and center wavelength of the quarter-wave mirror. These parameters have to be adjusted so that the frequency response of the equivalent construction is identical to the original QWM when seen from the some

reference plane. This constitutes a lumped-mirror equivalent a quarter-wave mirror that is *time*- or *phase*-conserving. We can similarly introduce energy and diffraction conserving models: In the energy conserving model the lumped mirror is placed at the location within which all of the quarter-wave mirror electromagnetic energy would be contained if the energy did not attenuate with the number of layers. In the diffraction conserving model, a reflected light beam has diffracted by the same amount as it would if it propagated freely over a distance equal twice the diffraction equivalent distance. All three of these equivalent constructions will be valid for frequencies (and angles) close to the center of the bandstop (normal incidence).

The most important fact is that the equivalent distances based on the phase, energy and diffraction conserving models are generally *not* equal to each other. For this reason care must be taken when the term penetration depth is used, since it must be clear what is the conserved quantity. These three models are discussed in detail in sections B.4., B.6. and B.9.

### *B.1.4. Appendix outline*

We proceed now with a step by step analysis of the quarter-wave mirrors at the center wavelength relevant to small vertical-cavity optoelectronic device design. The reflectivity and the bandwidth are discussed in Sections B.2 and B.3. We continue then by discussing the reflection delay which is crucial to the understanding of phase penetration depth (Section B.4). After introducing the mirror energy capacity and the energy conserving model of a quarter-wave mirror in Section B.6 we compare the two models in Section B.7. Both models are very efficiently used to determine the

effect of weak absorption loss on the absorptance and the peak reflectivity reduction described in Section B.8. In Section B.9 we describe the diffraction conserving model of quarter-wave mirrors.

## B.2. *Peak reflectivity of lossless quarter-wave mirrors*

The calculation of the amplitude and phase characteristics of the quarter-wave mirrors and other multilayer structures can be performed exactly using transmission matrices (Yeh, 1988) or transverse field matrix calculation (Thielen, 1989, Appendix A). The peak reflectivity of a lossless quarter-wave mirror at the center wavelength can be determined analytically using quarter-wave transformation formulas (Haus, 1984). However, an elegant substitution using *tanh*() function originally introduced by Ran H. Yan (Yan, 1991) provides a simple way to determine the reflectivity of combinations of quarter-wave and half-wave multi-layer structures at the resonant frequency. We shall illustrate use this substitution to calculate the peak reflectivity of the quarter-wave mirror of a QWM. For more general applications with non-abrupt index profiles and half-wave layers, the reader is referred to (Corzine, 1991) where the *tanh* substitution has been discussed in detail.

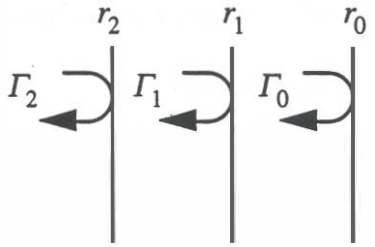


**Fig. B.5**: Partial reflectivities of a quarter-wave stack. The reflection coefficients of individual interfaces between two layers are denoted by $r_i$ (seen from the left), and the cumulative reflection coefficients of $i$-layer structure are denoted by $\Gamma_i$.

Consider the reflection of a single quarter-wave layer structure $\Gamma_1$ in Fig. B.5. In terms of $r_1$ and $\Gamma_0$, $\Gamma_1$ is given by

$$\Gamma_1 = \frac{r_1 + \Gamma_0}{1 + r_1 \Gamma_0} \tag{B-1}$$

Using the substitution

$$s_i = \left|\tanh^{-1} r_i\right| \tag{B-2}$$

and the hyperbolic tangent addition formula

$$\tanh(a+b) = \frac{\tanh a + \tanh b}{1 + \tanh a \cdot \tanh b} \tag{B-3}$$

we arrive at:

$$|\Gamma_1| = \tanh(s_1 + s_0) \tag{B-4}$$

The relation for the peak reflectivity of the entire stack can be derived by repeated application of (B-1), (B-2) and (B-3):

$$|\Gamma_2| = \tanh(s_2 + s_1 + s_0) \tag{B-5}$$

.

.

$$|\Gamma_m| = \tanh\left(\sum_0^m s_i\right) \tag{B-6}$$

The summation goes over all interfaces in the structure: for $m$ layers there are $m+1$ interfaces. Each interface is characterized by a factor $s_i$ which can be expressed in terms of material indices at the interfaces: Using (B-2) we write,

$$|r_i| = \frac{1-e^{-2s_i}}{1+e^{-2s_i}} = \frac{1-\frac{n_{Li}}{n_{Hi}}}{1+\frac{n_{Li}}{n_{Hi}}} \tag{B-7}$$

and find that $s_i$ is given by,

$$s_i = -\frac{1}{2}\ln\left(\frac{n_{Li}}{n_{Hi}}\right) \tag{B-8}$$

The reflectivity of the entire structure is then given by

$$\Gamma_m = \frac{1-b_m}{1+b_m} \tag{B-9}$$

with $b_m$ being the product of the refractive index ratio for all interfaces in the stack:

$$b_m = \prod_{i=0}^{m}\left(\frac{n_{Li}}{n_{Hi}}\right) \tag{B-10}$$

(Note that $0 < b_m < 1$). For an arbitrary quarter-wave structure or half-wave structure the coefficients $b_i$ are all different. Inasmuch as the quarter-wave mirror is a structure with some incoming index $n_I$, exit medium $n_E$, and a *periodic* sequence of layers with alternating indexes $n_L$ and $n_H$ one can write a simpler relationship for the reflectivity. Four parameters are sufficient to achieve this: $a$, $p$, $q$ and the number of quarter-wave layers $m$. The parameters $a$, $p$, and $q$ are refractive index ratios at the three types of interfaces that characterize the mirror, and are shown in Figure B.1. All of the ratios are taken as low/high, i.e. $a$, $p$, and $q$ are real numbers smaller than 1.

$$q = \frac{n_{II}}{n_{HI}} \qquad p = \frac{n_L}{n_H} \qquad a = \frac{n_{LE}}{n_{HE}} \qquad \text{(B-11)}$$

Factor $q$ is the ratio of the refractive indices at the interface between the *incident* medium (subscript *I*) and the *first* QWM section, factor $a$ is the ratio of the refractive indices at the *last* QWM section and the *exit* medium (subscript *E*), and factor $p$ is the ratio of the refractive indices of the two materials that constitute the QWM structure. This very elegant notation has been introduced by Scott Corzine (Corzine, 1993) and will be used extensively in this dissertation. The reflectivity of a quarter-wave stack expressed using (B-6) and (B-8) or by

$$R = \left( \frac{1 - qap^{m-1}}{1 + qap^{m-1}} \right)^2 \qquad \text{(B-12)}$$

This expression is valid only for lossless materials, but can also be used for quarter-wave mirrors with metal cladding, as described in Section B.8.6. When weak absorption loss is present in one or both of the materials the reflectivity can be approximated using expressions given in section B.8.

## B.3. *Bandstop width*

The *bandstop width* is the approximate wavelength range over which the quarter-wave mirror exhibits high reflectivity. There is no definition of the bandstop width that is practical and exact at same time. A practical definition, such as the full width at half maximum (FWHM) depends on too many parameters (all of the refractive indexes involved and the number of layers) and is too complicated to determine and use analytically. A definition that is most commonly used is the bandstop of an infinite mirror. This quantity can be determined analytically and depends only on the refractive index ratio $n_L/n_H$, but only approximately describes bandstops of finite mirrors.

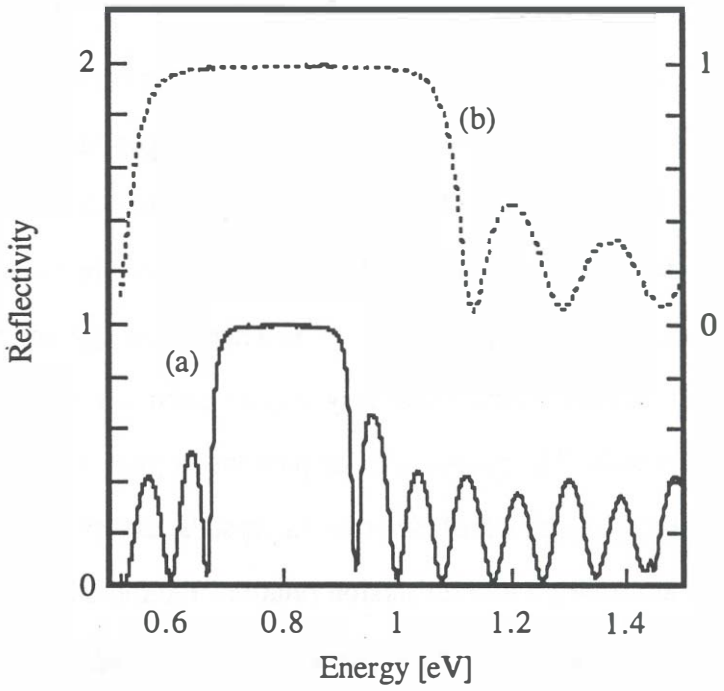


**Fig. B.6**: Measured reflectivity spectra on two 1550 nm quarter-wave mirrors: (a) 8-period electron-beam deposited $SiO_2/TiO_2$ mirror, (b) reactively sputtered 3-period $Si/SiO_2$ mirror.

A large refractive index ratio results in a large bandstop width. This is illustrated in Fig. B.6 where a $Si/SiO_2$ mirror ($n_L/n_H \approx 1.46/3.5$) is compared to $SiO_2/TiO_2$ mirror ($n_L/n_H \approx 1.46/2.1$). We shall use the mirror bandstop width as a figure-of-merit when discussing the necessary precision of the mirror fabrication process and the ability to tune the laser wavelength to a specified value. The reason for this is that the behavior of the phase characteristics of the mirror within the bandstop depends on the bandstop width. We shall first discuss the character of an infinite quarter-wave mirror and derive an exact expression for the bandstop width, and then discuss its relevance for practical finite mirrors.

B.3.1. *Quarter-wave mirror as a photonic bandgap structure*

The infinite quarter-wave stack represents the simplest form of a photonic band-gap structure (Yablonovitch, 1990). A photonic band-gap structure structure is one within which the propagation of electromagnetic radiation is suppressed in a range of frequencies (forbidden gap) and allowed to propagate for frequencies above and below this range (energy bands). The occurrence of energy bands and bandgaps is observed in crystalline solids where they play an important role in the conduction of electrons (or holes). The propagation of photons in photonic-bandgap structures is analogous to the propagation of electrons in crystals, except for the difference in the free electron and free photon dispersion relation. Photonic band-gap crystal can be made to efficiently suppress electromagnetic wave propagation in one (the quarter-wave mirror), two (Philal, 1991, Gerard, 1994, Villeneuve, 1992) and three (Yablonovitch, 1991) dimensions. It is important to note that the photonic-bandgap crystals are not the only structures capable of suppressing electromagnetic wave

propagation: A waveguide operated below the cutoff frequency will behave in the same way. The interest in photonic bandgap crystals in recent years arose from a number of experiments and potential applications that were and could be performed by creating spaces which were devoid of all radiation (in a certain frequency range). Experiments with spontaneous emission inhibition and enhancement were the most popular (Martorell, 1990, Yablonovitch, 1991, Ram, 1995a).

In an infinite quarter-wave stack, the propagation of electromagnetic waves for frequencies within the bandstop is suppressed in one direction. At the wavelength at which the phase across each of the layers is an odd integer multiple of $\pi/2$ all of the individual interface reflections add up in phase and no wave can propagate. This happens at the center of the forbidden gap of an optical crystal created by an infinite quarter-wave mirror. At the edges of the forbidden gap are the first extended states in which light can propagate (reflectivity is zero). This edge is sometimes called, the mobility edge, from the electron propagation analogy. The is an infinite number of modes that light can propagate through in this crystal. The existence of these modes can also be observed in the reflectivity spectrum of a real, finite mirror shown in Figure B.6. Every minimum in this curve represents an extended state in which the photons propagate through the mirror. As the number of independent states always equals the number of layers, by increasing the number of periods, the modes become more dense. When the mirror becomes infinite, the band becomes continuous. The dispersion relation of an infinite quarter-wave mirror can be determined using the Kronig-Penney model of propagation through a periodic potential as described in many textbooks (Liboff, 1980). We apply this model to a quarter-wave stack and use it to determine the bandstop width.

Consider a periodic structure in which each period consists of two layers across which the phases equal $\phi_1$ and $\phi_2$. The length of the period is equal to $d = \lambda_0/2\bar{n}$, where $\lambda_0 = 2\pi c/\omega_0$ is the mirror center wavelength (frequency), and $\bar{n}$ is the average refractive index in the mirror defined by $2/\bar{n} = 1/n_1 + 1/n_2$. The dispersion relation for this structure is given (Liboff, 1980) by

$$\cos\phi_1 \cos\phi_2 - \frac{1+r^2}{1-r^2}\sin\phi_1 \sin\phi_2 = \cos Kd \qquad \text{(B-13)}$$

where

$$r = \frac{n_1 - n_2}{n_1 + n_2} \qquad \text{(B-14)}$$

is the amplitude reflectivity of a single interface that constitutes the mirror and $K$ is the Bloch wave number. Since at $\omega = \omega_0$ the layers are one quarter-wavelength thick $\phi_1 = \phi_2$, one can write the dispersion relation for an infinite quarter-wave stack as,

$$\cos 2\phi = r^2 + (1-r^2)\cos\theta. \qquad \text{(B-15)}$$

Here $\phi = (\pi/2)(\omega/\omega_0)$ is the phase change across a single quarter-wave film and $\theta = Kd$ is the normalized Bloch wave-number. This dispersion relation is illustrated in Fig. B.7 for three values of $r$: Around $K = 0$ the propagation is largely unaffected by the periodic index perturbation and the dispersion curve is linear with a slope determined by the average index of the mirror $\omega \cong (c/\bar{n})K$. As the Bloch vector approaches the Bragg wave number $Kd \approx \pi$ the dispersion relation becomes sub-linear and a gap is formed at $Kd = \pi$. To determine the width of the forbidden gap

$\Delta\omega$ we set $\phi_1 = \phi_2 = \pi/2 + \delta$, where $\delta = \pi\Delta\omega/4\omega_0$ is the fractional gap width. Introducing this into (B-15) we obtain $2\sin^2\delta = (1+r^2) \pm (1-r^2)$. When $\cos kd = 1$ each of the layers is one half wavelength thick, $\sin\delta = \pm 1$. The band edge occurs when $\cos kd = -1$ (the period is exactly one half-wavelength thick) and is given exactly by $\sin\delta = \pm r$, or

$$\sin\left(\frac{\pi}{4}\frac{\Delta\omega}{\omega_0}\right) = \frac{n_H - n_L}{n_H + n_L} \qquad \text{(B-16)}$$

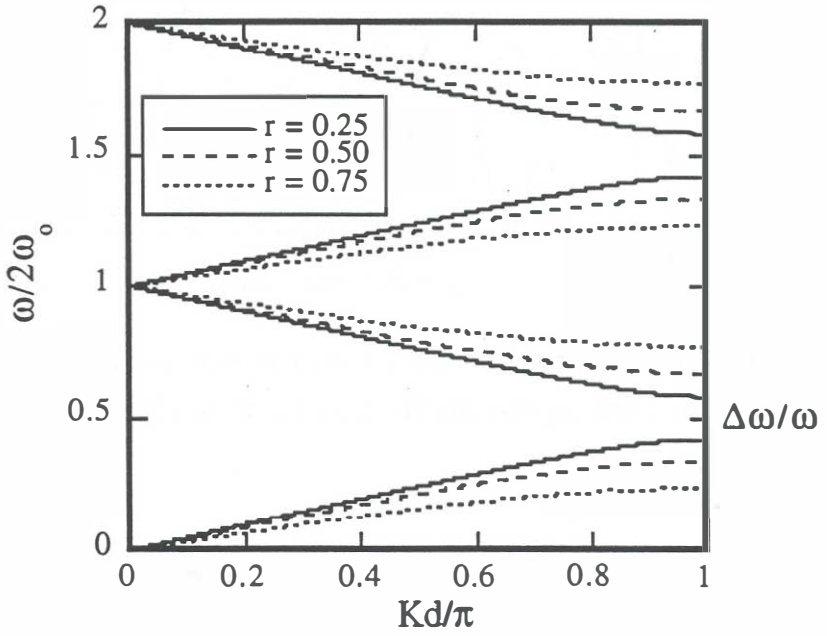


**Fig. B.7**: Infinite quarter-wave stack dispersion curve calculated for three different refractive index ratios. The bandstop width is denoted with $\Delta\omega$.

The standing wave pattern at the mobility edge of an infinite quarter-wave mirror is shown in Fig. B.8. It resembles the probability density function for an electron in a

period crystal, due to the analogy of propagation. The wave with more energy in the low index material ( $n = 1$ ) has higher frequency.

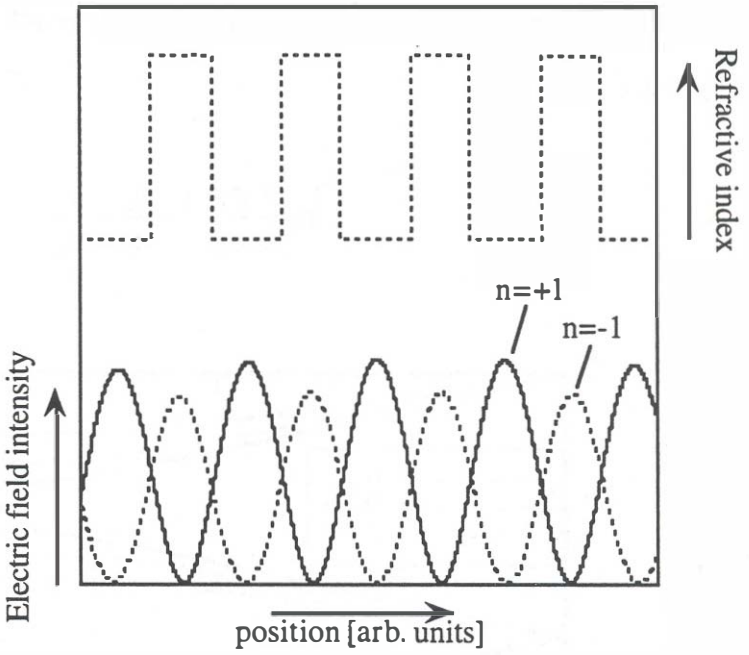


**Fig. B.8**: Standing wave pattern in an infinite quarter-wave mirror at the band edges approximately depicted using a 30 period AlAs/GaAs mirror.

The number of minima between any two high-reflectivity regions equals to the number of quarter-wave layers in the mirror. This fact can understood if one considers that a stack of $m$ quarter-wave layers operated at twice the mirror center frequency ( $2\omega_0$) in fact represents a stack of $m$ coupled half-wave resonators. It is well know that the resonance peak of a resonator splits into two when coupled to a second resonator. Similarly, the frequency response of $m$ coupled resonators will have $m$ resonances. (In our case we have $m$ identical resonators.) The mode

splitting is illustrated in Fig. B.9 where the transmittance spectra of one, two and three layer quarter-wave stacks are shown. In order to exaggerate the effect the coupling between the resonators was made weak by setting $n_H = 10n_L$. The dots above the graphs indicate the locations of the resonance peaks for stacks with the number of layers varying from one to eight.

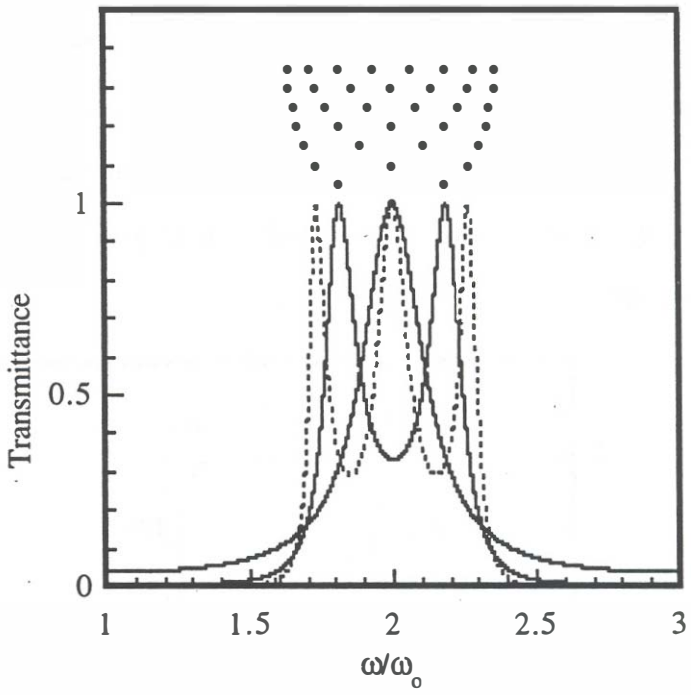


**Fig. B.9**: Transmission spectra of one, two and three layer quarter-wave stacks illustrating the resonance splitting as a function of number of coupled resonators (half-wave layers).

The location of the minima has been determined exactly when all of the reflections have equal strength, i.e. $q = a = p$. For this case the minima in the quarter-wave mirror reflectivity spectra occur at

$$\sin^2 \delta_n = r^2 + (1 - r^2)\sin^2\left(\frac{n\pi}{m+1}\right) \qquad \text{(B-17)}$$

where $n$ is the serial number of the minimum starting with $n = \pm 1$ for the minimum adjacent to the bandstop and ending with $n = \pm m$ with minimum adjacent to the next higher (or lower) bandstop. The frequency deviation of the $n$th minimum $\omega_n$ is given by

$$\delta_n = \frac{\pi}{2}\frac{\omega_n - \omega_0}{\omega_0} \tag{B-18}$$

If the first and/or the last reflections are weaker ($q, a < p$), the exact frequency deviation will be larger than the one calculated by (B-17), and similarly if $q, a > p$, the exact deviation will be smaller. These deviations from exact predication are result of the departure from the perfectly periodic index profile for which the Kronig-Penney model applies.

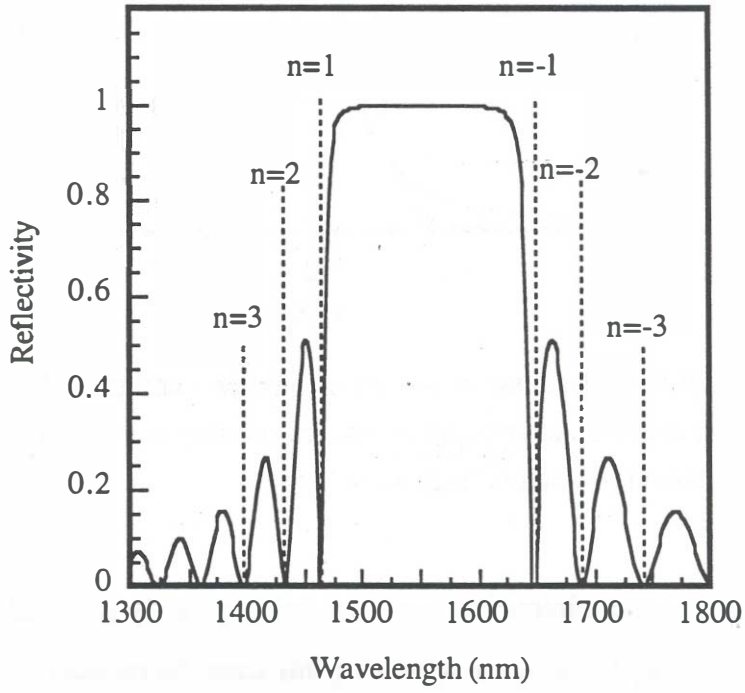


**Fig. B.10**: Reflectivity spectrum of a 30-period AlAs/GaAs mirror with $n_I = n_L = 2.893$, and $n_E = n_H = 3.377$.

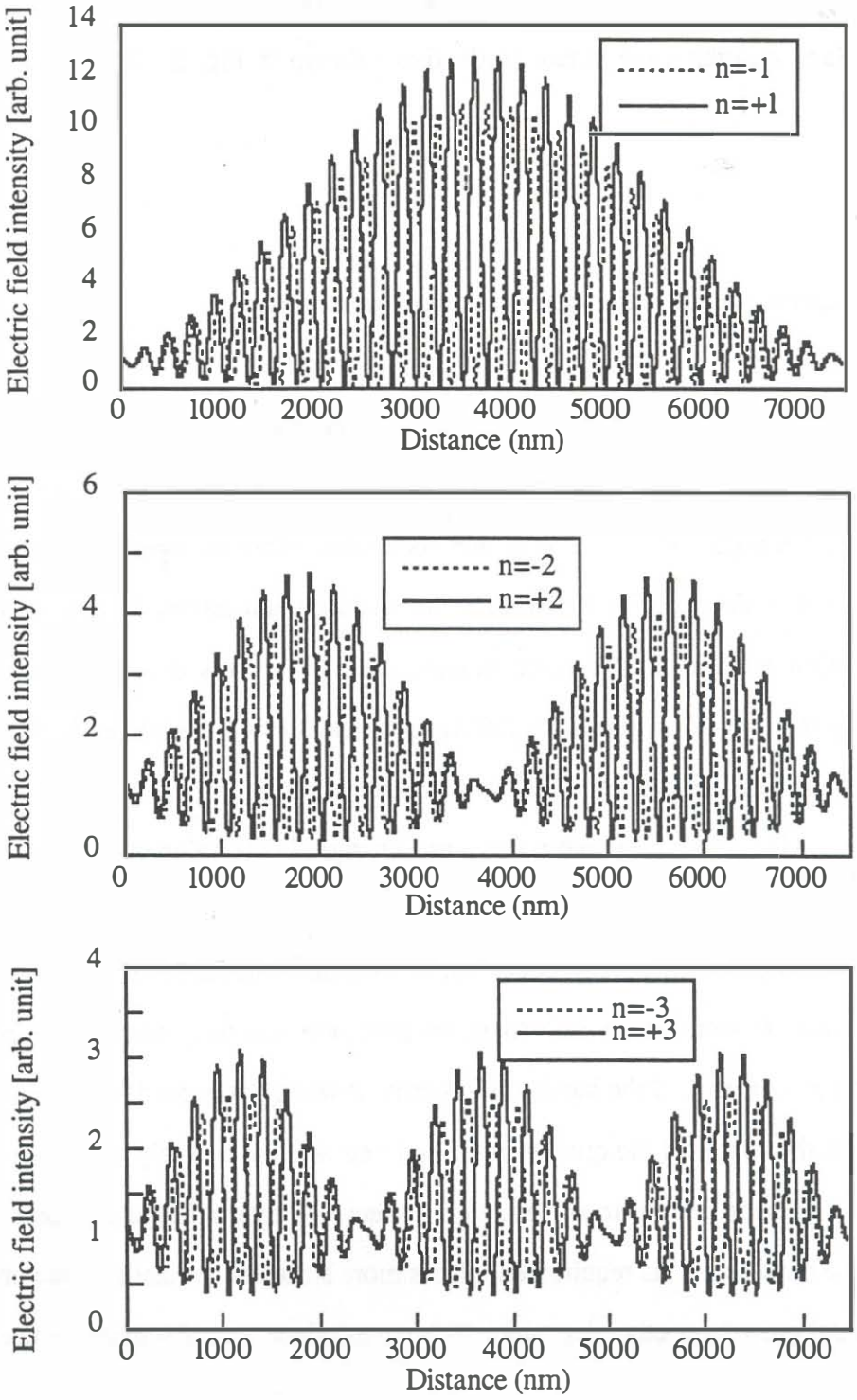


**Fig. B.11**: Standing wave patterns in the first three resonances of the mirror shown in Fig. B.10.

An example of the standing wave patterns in the first three resonances of a 30-period AlAs/GaAs quarter-wave mirror (reflectivity shown in Fig. B.10) is shown in Fig. B.11.

B.3.2. *Bandstop width and practical quarter-wave mirrors*

There are two reasons why the knowledge of the bandstop width is relevant for cavity design: (a) the bandstop with is the approximate wavelength range within which the reflectivity is high, and (b) the reflection coefficient phase changes by approximately $2\pi$ over this range. For this reason no matter what cavity length is used on conjunction with a quarter-wave mirror, there is always one mode within the bandstop (B-14). What makes the difference in cavities with misaligned mode is the fact that the peak reflectivity of the mirror always varies slightly over the bandstop, and this is what sometimes makes very large changes in the value of threshold gain.

The mode adjustment is very important in VCSELs and the phase variation of the quarter-wave mirror directly influences the precision necessary for the fabrication of quarter-wave mirrors. If the bandstop is narrow it will be very hard to place the mode exactly at the center of the quarter-wave and one will have to rely on increasing the number of mirror periods to achieve high reflectivity over a larger frequency range within the bandstop. This requirement places more stringent demands on the precision of epitaxial growth (or other deposition techniques) since the reflectivity reduces if the mirror chirped or mistuned. The fractional bandstop width is a figure of merit that indicates how difficult is it to practically use a quarter-wave mirror when one is to

make a laser cavity. Mirrors with wide bandstops are very forgiving to errors in the thicknesses and refractive index values and are hence easy to fabricate and use. Very narrow bandstops such as in InGaAsP/InP system at 1.3 μm operation are not practical due to the very large number of layers necessary to achieve sufficient reflectivity at the center and large susceptibility to errors.

## B.4. *Reflection delay*

At the center of the bandstop of a losses mirror with no material dispersion, the dispersion is zero and the reflection delay is at a minimum. Both quantities increase in magnitude for frequencies away from the center. The reflectivity amplitude and phase spectra of an $a-Si/Si_3N_4$ quarter-wave mirror are shown as an example in Fig. B.3. Fig. B.4 shows the reflection delay and dispersion dependence on frequency in the neighborhood of the band-stop frequency. We shall describe here the derivation of the reflection delay at the center frequency for the QWMs with no material loss or dispersion.

### B.4.1. *Reflection delay recursion relation*

The frequency and time response of dielectric mirrors is described by its complex amplitude reflectivity spectrum:

$$\tilde{\Gamma}(\omega) = \Gamma(\omega)e^{i\Theta(\omega)} \tag{B-19}$$

where $\Gamma(\omega)$ and $\Theta(\omega)$ are real functions. (The tilda ~ denotes a phasor). The QWM exhibits a *real* impulse response, and hence $\Gamma(\omega)$ is an even function, while the phase $\Theta(\omega)$ is an odd function of the frequency. For a lossless mirror with no material dispersion this is also true around the center frequency $\omega_0$ where as a consequence the phase characteristic has an inflexion, as seen from Fig. B.3. For continuous signals at frequency $\omega_0$ the QWM can be characterized by two parameters: the reflectivity $\Gamma(\omega_0)$ and the phase, which for a QWM stack is either zero or $\pi$ at the center frequency. When the carrier is modulated both the reflected signal amplitude

and the phase are determined by the portion of the mirror reflectivity spectrum that overlaps with the modulated signal spectrum. As seen from FiguresB.2 and B.3, for very narrow modulation bandwidths close to the center of the mirror band-stop the relevant portion of the spectrum can be assumed to have uniform amplitude and a linear phase:

$$\tilde{\Gamma} = \Gamma(\omega_0)\exp\left(-j(\omega-\omega_0)\tau\right) \tag{B-20}$$

where $\tau$ is the *reflection delay* at frequency $\omega_0$ given by

$$\tau = -\left.\frac{\partial\Theta(\omega)}{\partial\omega}\right|_{\omega=\omega_0} \tag{B-21}$$

The quantity $\tau$ is the time by which an input pulse will be delayed upon reflection (Silvestri, 1984a), also called group-delay time. The fixed phase term $\Theta(\omega_0)$ present in equation (B-19) has been included into the amplitude $\Gamma(\omega_0)$ of equation (B-20) for simplicity of upcoming mathematical derivations. The sign of $\Gamma(\omega_0)$ can then take both positive and negative values depending on the orientation of the stack. (The phase of the QWM stack at the Bragg frequency can be determined from the phase of the first reflection, since all of the reflections are in phase at the center frequency. Refractive index sequence HL at the first interface gives $\Gamma(\omega_0)>0$, while the opposite sequence LH gives $\Gamma(\omega_0)<0$.)

In order to calculate reflection delay $\tau$ we will derive a recursion relation between the reflection delay $\tau_m$ of an $m$–section stack and the group delay $\tau_{m-1}$ of an $(m-1)$-section stack. Let $Z_{m-1}$ be the input impedance of the $(m-1)$-section structure shown in Fig. B.14. We now proceed building the stack by adding a quarter-wave layer to the top. The refractive index of the added layer must be of the proper relative

magnitude so that the indices of the overall structure alternate. (It is irrelevant which of the two material indices is being used, as long as the phase is properly adjusted). Once the refractive index of the $m$-th layer is specified, by knowing $Z_{m-1}$ one can easily determine $\Gamma_{m-1}$: the reflectivity of the $(m-1)$-layer stack as seen from within the added quarter-wave layer, and $Z_m$ the input impedance of the $m$-layer stack. With the next quarter-wave layer added we will can determine the reflectivity $\Gamma_m$ and $Z_{m+1}$, and so on. The reflectivities $\Gamma_m$ and $\Gamma_{m-1}$ are then related by:

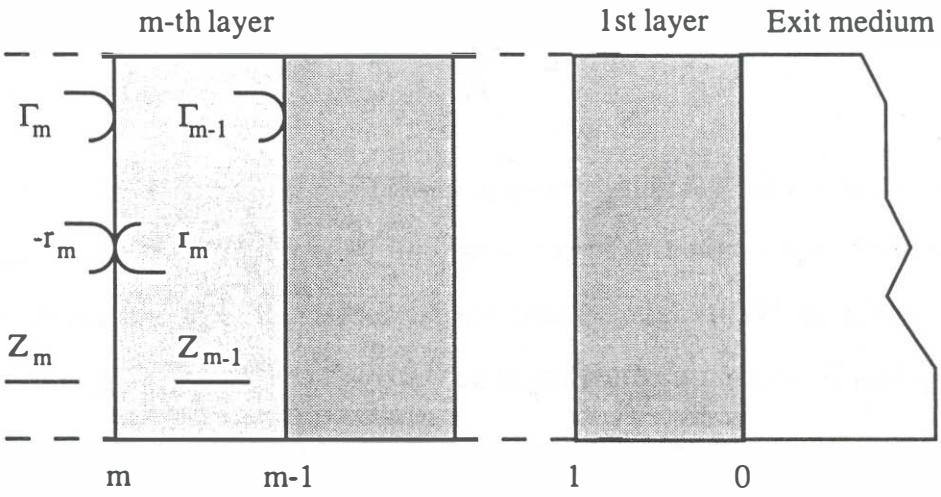


**Fig. B.14**: The structure and notation used in the derivation of the group-delay recursion relation. Figure shows on ()-section quarter-wave stack with one quarter-wave layer added on top.

$$\tilde{\Gamma}_m = \frac{r_m - \tilde{\Gamma}_{m-1} e^{-j2\omega\Delta\tau}}{1 - r_m \tilde{\Gamma}_{m-1} e^{-j2\omega\Delta\tau}} \qquad \text{(B-22)}$$

where $r_m$ is the amplitude reflectivity of the interface between the quarter-wave layers $m+1$ and $m$, and $\Delta\tau$ is one quarter period time, $4f\Delta\tau = 1$ ($f$ is the band-stop center frequency). Using equation (B-20) we express $\Gamma_m$ and $\Gamma_{m-1}$.

$$\tilde{\Gamma}_m = \Gamma_m \; e^{-j(\omega-\omega_0)\tau} \tag{B-23}$$

We now simplify (B-22) using the tanh substitution (B-2):

$$s_m = \tanh^{-1}(r_m) \qquad \tilde{S}_m = \tanh^{-1}\left(-\tilde{\Gamma}_m e^{-j2\omega\Delta\tau}\right) \tag{B-24}$$

Using the tanh(z) addition rule (B-3) we obtain:

$$\tilde{\Gamma}_m = -\tanh\left(s_m + \tilde{S}_{m-1}\right) \tag{B-25}$$

By differentiating (B-23) and (B-25) with respect to ω and evaluating at $\omega_0$ we obtain:

$$\left.\frac{\partial\tilde{\Gamma}_m}{\partial\omega}\right|_{\omega=\omega_0} = -j\tau_m\Gamma_m \tag{B-26}$$

$$\left.\frac{\partial\tilde{\Gamma}_m}{\partial\omega}\right|_{\omega=\omega_0} = j(\tau_{m-1}+2\Delta\tau)\left(\frac{1-\Gamma_m^2}{1-\Gamma_{m-1}^2}\right)\Gamma_{m-1} \tag{B-27}$$

Here we have used the fact that $\Gamma_m(\omega)$ is maximum at $\omega_0$ and that $\omega_0\Delta\tau = \pi/2$. Equating (B-26) and (B-27) we obtain a recursion relation for the reflection delay $\tau_m$ in terms of the delay $\tau_{m-1}$ and the associated reflection coefficients $\Gamma_m$ and $\Gamma_{m-1}$:

$$\gamma_m\tau_m = \gamma_{m-1}(\tau_{m-1}+2\Delta\tau) \tag{B-28}$$

where factors $\gamma_i$ are given by:

$$\gamma_i = (-)^i\frac{\Gamma_i}{1-\Gamma_i^2} \tag{B-29}$$

For quarter-wave mirrors, the factors $\gamma_i$ are always of the same sign since the phase of the reflection coefficients $\Gamma_i$ alternates between zero and $\pi$. This recursion relation can be easily applied to mirrors in which each layer has thickness of $n$ quarter-wavelengths where $n$ is odd. In this case, we would replace $\Delta\tau$ with $n\Delta\tau$. When $m = 0$ the quarter-wave structure reduces to a single interface between the incident and exit medium: There is no reflection delay and we can set $\tau_0 = 0$. By repeated application of (B-28) we can find the reflection delay of a QWM of an arbitrary number of layers. The recursion relation (B-28) leads to the sum:

$$\tau_m = \frac{1}{2f} \cdot \frac{\sum_{i=0}^{m-1} \gamma_i}{\gamma_m} \qquad \text{(B-30)}$$

Since we have not in any way specified the individual quarter-wave section impedances (indexes), equation (B-30) is *exact* for *any* multi-section quarter-wave transformer at the design frequency. In the case of matching transformers the value of $\Gamma_m$ is ideally zero while the $\Gamma_i (i < m)$ are in general non-zero. Equation (B-30) then implies that the reflection delay time is infinite which means that the signal never returns, which is indeed the goal of perfect matching. It is possible to generalize this derivation, starting with equation (B-22), to arbitrary structures that involve both quarter-wave and half-wave layers and this has been done in (Tan, 1992). However, in this paper we will concentrate only on the QWM structure and refer the reader to reference (Corzine, 1991) for a more detailed treatment of the *tanh substitution* and its application in calculating reflectivities of more complex quarter and half wave structures.

*B.4.2. Reflection delay for a quarter-wave stack*

For the case of a QWM structure the expression (13) can be reduced to an explicit relation due to the simplicity of the relations for the partial reflectivities $\Gamma_i$ and the factors $\gamma_i$. The phase of the reflectivity of every subsequent quarter-wave section alternates between 0 or $\pi$, and therefore no generality will be lost by setting:

$$\gamma_i = \frac{|\Gamma_i|}{1-\Gamma_i^2} \tag{B-31}$$

By substituting (B-9) into (B-31) ($m$ replaced with $i$) we get,

$$\gamma_i = \frac{1-b_i^2}{4b_i} \tag{B-32}$$

The expression (B-30) now becomes a sum of two series:

$$\tau_m = \frac{1}{2f} \cdot \frac{\sum_{i=0}^{m-1} \left( \frac{1}{b_i} - b_i \right)}{\left( \frac{1}{b_m} - b_m \right)} \tag{B-33}$$

The coefficients $b_i$ are all different, but can be expressed in a simple way using (B-10) and (B-11). For $i < m$ we have

$$b_i = \left( \frac{n_L}{n_H} \right)^i \left( \frac{n_{LE}}{n_{HE}} \right) = p^i a \tag{B-34}$$

and at $i = m$ we have

$$b_m = \left( \frac{n_{LI}}{n_{HI}} \right) \left( \frac{n_L}{n_H} \right)^{m-1} \left( \frac{n_{LE}}{n_{HE}} \right) = q p^{m-1} a \tag{B-35}$$

Introducing these variables into (B-33) we are left with a sum of two finite geometric series which after some manipulation yield the expression:

$$\tau_m = \frac{1}{2f} \cdot \frac{q}{1-p} \cdot \frac{(1-a^2 p^{m-1})(1-p^m)}{(1-q^2 a^2 p^{2m-2})} \qquad \text{(B-36)}$$

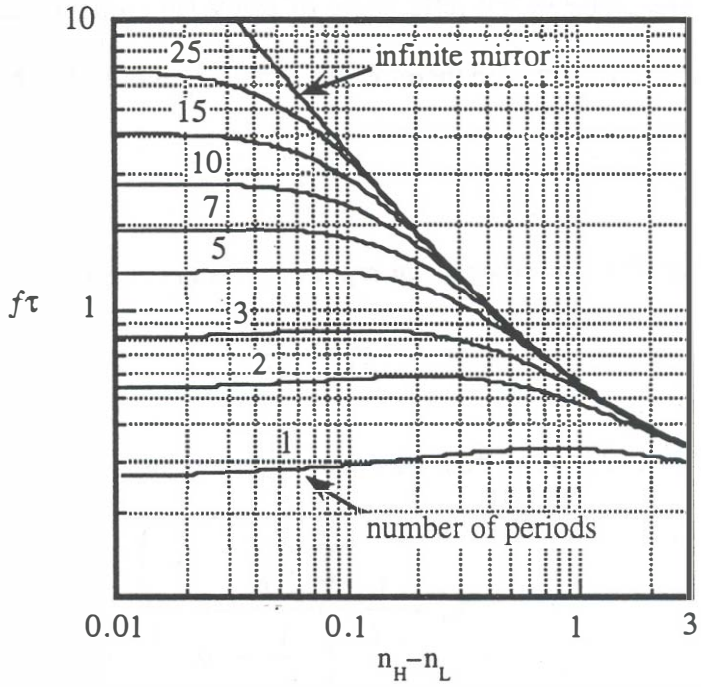


**Fig. B.13**: A family of curves illustrating the functional dependence of the reflection delay – center frequency product $f\tau$ on material properties. The values used in this plot are $n_I = 3.2$ (InP), $n_E = 1.0$ (air), and $n_L = 1.46$ ($SiO_2$). The refractive index $n_H$ was varied continuously from 1.46 to 4.45 for illustration. Multiple curves correspond to different number of periods.

Equation (B-36) is the exact relation for the reflection delay of a lossless quarter-wave mirror with an arbitrary number of sections and material indices at the mirror band-stop center frequency. An important fact to note is that the reflection delay from the front and the back of a QWM is in general not equal, since it depends on the incident

and exit medium indices. The functional dependence of equation (B-36) is illustrated in Fig. B.13 for several number of layers and a continuous variation of the refractive index $n_H$. The general trend in Fig. B.13 shows that mirrors with large index differences produce short delay times. The small reduction in the delay for very small index difference occurs because the reflection at the exit medium interface starts dominating (the exit medium in Fig. B.13 is air). A fact not apparent in this figure is that any decrease in the refractive index difference for a fixed number of periods will also decrease the maximum reflectivity of the mirror.

For a large number of periods the curves approach that of an infinite QWM. The reflection delay of an infinite mirror (unit reflectivity) is the maximum delay a QWM can realize at the center frequency and it is obtained by taking the $m \to \infty$ limit in (B-36). (The second term in the product tends to unity.) For a mirror in which the incident medium refractive index $n_I$ is lower than that of the first layer $n_H$ we have,

$$\tau_\infty = \frac{1}{2f} \cdot \frac{n_I}{n_H - n_L} \qquad \text{(B-37)}$$

If the first layer has index $n_L$ lower than the incident medium $n_I$ we have

$$\tau_\infty = \frac{1}{2f} \cdot \frac{n_L n_H}{n_I (n_H - n_L)} \qquad \text{(B-38)}$$

For the special case when the incident medium has the same refractive index as one of the mirror materials, namely, $n_I = n_L$ in (B-37) and $n_I = n_H$ in (B-38), the group delay becomes equal for both mirror orientations: $2f\tau_\infty = n_L/(n_H - n_L)$. This equation has previously been derived (Seeley, 1964) in an analysis of the resolving power of Fabry-Perot interferometers with distributed mirrors.

B.4.3. *Partial group-delay times*

Using the expressions (B-33)-(B-36) one can determine the expected time a light pulse spends in the material of low or high index. These two times will be called *partial* group-delay times: $\tau_L$ and $\tau_H$, and the total reflection group-delay is given by the sum: $\tau = \tau_L + \tau_H$. This separation does not mean that the electromagnetic wave spends more time in one layer type, but is states what is the contribution of each type of layer to the total group delay time. To derive the expressions for the partial group delays we explicitly denote the dependence of the group delay on the refractive indexes of the layers using a dimensionless group delay:

$$\Phi(n_L,n_H) = 2f\tau \tag{B-39}$$

From the recursive relation (B-28) and the expressions (B-32), (B-33) and (B-11) we see that if we change the sign of one of the refractive indexes, for example $n_L$, that the individual time contributions in (B-28) change sign if the delay has occurred in the layer of refractive index $n_L$. Therefore, four combinations of group delays are possible:

$$\begin{aligned} \Phi(n_L,n_H) &= \Phi_L + \Phi_H & \Phi(-n_L,n_H) &= -\Phi_L + \Phi_H \\ \Phi(-n_L,-n_H) &= -\Phi_L - \Phi_H & \Phi(n_L,-n_H) &= \Phi_L - \Phi_H \end{aligned} \tag{B-40}$$

Using any two linearly independent expressions from this set we determine the partial group-delay times:

$$\Phi_L = \frac{\Phi(n_L,n_H) + \Phi(n_L,-n_H)}{2} \qquad \Phi_H = \frac{\Phi(n_L,n_H) - \Phi(n_L,-n_H)}{2} \tag{B-41}$$

Partial delay times can be used when one needs to estimate a physical quantity that depends on times spent in the two layers of the DBR. We shall use this concept in section B.8. to derive an approximation for the reduction of peak reflectivity from

loss, in section B.9. To estimate the properties of quarter-wave mirrors for wave with small off-normal incidence.

B.4.4. *Phase penetration depth*

The reflection delay in a distributed reflector is most commonly associated with an *apparent* depth of penetration into the mirror. The interpretation of the delay *time* with *distance* is potentially misleading since one needs to know the *velocity* of propagation in the medium. Nevertheless, for the practical use of the penetration depth concept one never needs the real propagation constant in the medium. The idea behind the penetration depth approximation is that the group delay time (strictly defined by the mirror) is interpreted as a reflection from a lumped, fixed phase mirror at some distance in to the mirror. The distance to the lumped mirror depends on the value of the refractive index we use for the medium that precedes the lumped mirror. If the quarter-wave mirror is adjacent to a cavity then it only makes sense to use the cavity refractive index for this extension. In this way there are no extra reflections at the mirror/cavity boundary that need to be considered - the cavity is simply extended by a distance equal to $L_\tau$.

The penetration depth depends on what is the refractive index of the material used in front of the mirror. This fact is of crucial importance for proper use of the concept: The quarter-wave mirror determines the group delay time, but the refractive index of the cavity in front of the mirror determines the group velocity of the wave to be reflected. Only with both of these quantities defined can we speak of penetration depth into the quarter-wave mirror. To make things clearer, it does not make sense to

ask for the value of the penetration depth of a particular mirror without specifying the group velocity in the medium in front of it.

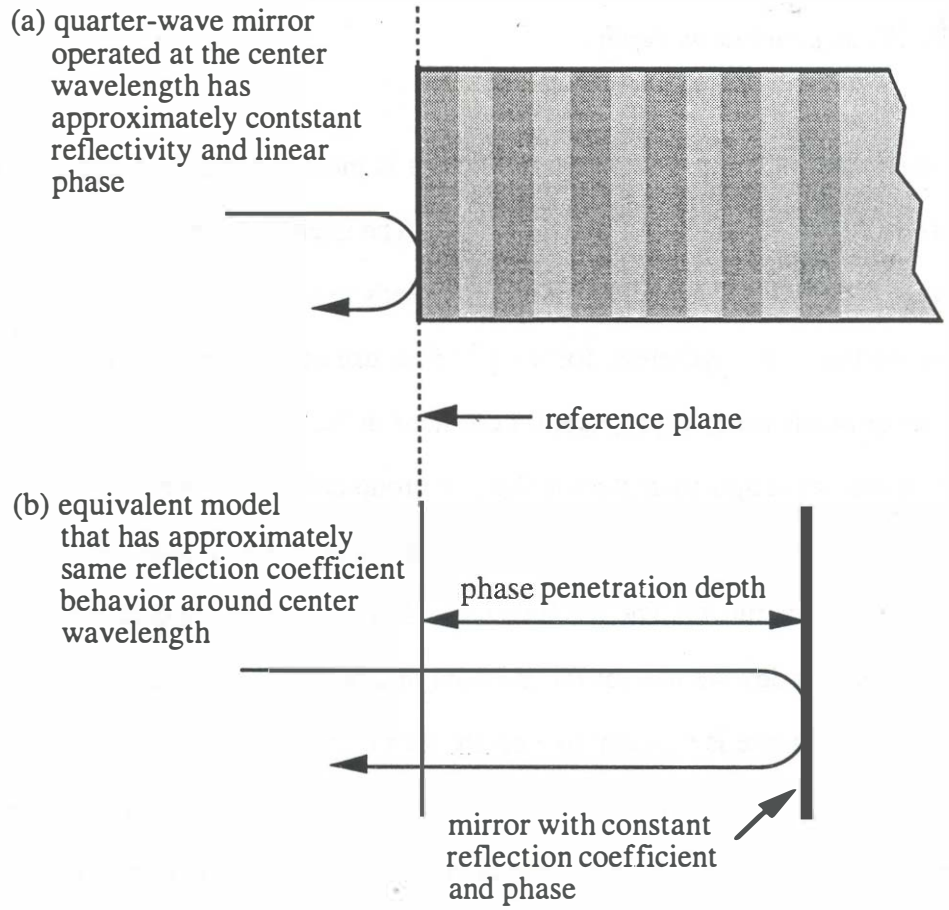


**Fig. B.14**: Interpretation of phase penetration depth.

The interpretation of the penetration depth concept is illustrated in Figure B.14: A wave is incident from a medium with refractive index $n_1$ onto a distributed mirror with linear phase. Its reflection is delayed by $\tau$ and scaled by the value of the reflectivity $\Gamma$. The equivalent model for the distributed mirror is realized by extending the incident medium beyond the reference plane and by placing a lumped

mirror with a fixed phase $\theta_0$ at depth $L_\tau$. To the observer placed to the left of the reference plane, the mirrors will appear equivalent if the reflectivity and the phase characteristics of the two cases are equal. This is satisfied if:

$$L_\tau = \frac{c\tau}{2n_I} \qquad \theta_0 = \omega_0 \tau \tag{B-42}$$

where $L_\tau$ is the *phase penetration depth.* The use of the equivalent lumped mirror model is completely transparent to any calculations involving the mirror phase as long as the QWM can be assumed to have a uniform amplitude and a linear phase in the spectral range of interest. Introducing (B-36) into (B-42) we obtain:

$$L_\tau = \left(\frac{\lambda_0}{4n_I}\right)\frac{q}{1-p}\cdot\frac{(1-a^2p^{m-1})(1-p^m)}{(1-q^2a^2p^{2m-2})} \tag{B-43}$$

$$\omega_0\tau_m = \pi\cdot\frac{q}{1-p}\cdot\frac{(1-a^2p^{m-1})(1-p^m)}{(1-q^2a^2p^{2m-2})} \tag{B-44}$$

## B.5. *Transmission delay*

A lossless quarter-wave mirror is a reciprocal linear network and therefore the frequency behavior of the transmission coefficient is determined from the reflection coefficients seen the incident and exit ports (Haus, 1984). This means that from the knowledge of the reflectivity and the reflection group-delays from the two ports we can determine all the scattering parameters for a quarter-wave mirror, which is a useful tool when we want to apply circuit analysis models to multi-cavity resonators that employ quarter-wave mirrors in the neighborhood of the center frequency.

### B.5.1. *Scattering parameters of a lossless quarter-wave mirror*

We determine the scattering parameters from knowing the complex amplitude reflectivities from both sides $s_{11}$ and $s_{22}$:

$$s_{11} = r\exp\left[-j(\omega-\omega_0)\tau_{11} - j\phi_{11}\right] \tag{B-45}$$

$$s_{22} = r\exp\left[-j(\omega-\omega_0)\tau_{22} - j\phi_{22}\right] \tag{B-46}$$

Here $\omega_0$ is the center frequency and $\phi_{ii}$ are the fixed phases of the mirror at the center frequency seen from port $i$. This phase depends on the orientation of the stack and can be either zero or $\pi$ ($\phi_{11}$ and $\phi_{22}$ are generally different). We assume that the mirror is lossless and hence $s_{21}$ and $s_{12}$ are equal due to reciprocity. The $s$-parameters are related through (Haus, 1984),

$$|s_{11}|^2 + |s_{21}|^2 = 1 \qquad |s_{12}|^2 + |s_{22}|^2 = 1 \qquad s_{11}^* s_{12} + s_{21}^* s_{22} = 0 \qquad \text{(B-47, 48,49)}$$

From here we quickly find that find that

$$s_{21} = s_{12} = \sqrt{1-r^2}\exp\left[-j(\omega-\omega_0)\tau_{21} - j\phi_{21}\right] \tag{B-50}$$

where if $\phi_{11} = \phi_{22} = 0$ or $\pi$ then $\phi_{21} = \pi/2$, and if $\phi_{11} = 0$ and $\phi_{22} = \pi$ then $\phi_{21} = 0$. The transmission-group delay $\tau_{21}$ is the average of the two reflection-group delays:

$$\tau_{21} = \frac{\tau_{11} + \tau_{22}}{2} \tag{B-51}$$

Using (B-36) in (B-51) we arrive at an analytic expression for the transmission-group delay of a lossless quarter-wave mirror at the center wavelength:

$$\tau_{21} = \frac{1}{4f}\cdot\frac{a+q}{1-p}\cdot\frac{(1-p^m)}{(1+qap^{m-1})} \tag{B-52}$$

With equation (B-12) for the reflectivity, the equation (B-36) for the two reflection-group delays, and the equation (B-52) for the transmission-group delay, we have a *completely* analytical definition of mirror scattering parameters of a lossless quarter-wave mirror operated near the center frequency.

B.5.2. *Transmission-delay time and causality.*

A careful inspection of the formulas given in Section B.5.1 shows that the transmission group delay (B-52) can be many times smaller than the time a light pulse needs to traverse the physical distance equal to the thickness of the mirror. This implies that light travels faster than $c$ in the mirror and that (relativistic) causality is hence violated. Even though this may appear impossible, the fact that the pulse delay

through a quarter-wave mirror can be shorter than the physical thickness of the mirror is *true* and it has also been experimentally confirmed (Steinberg, 1993). The phenomenon in question is associated with tunneling of light through the quarter-wave mirror forbidden gap. Consider a pulse incident on a quarter-wave mirror at the center frequency. The pulse linewidth is assumed to be much narrower than the mirror bandstop in order to observe an approximately constant transmission-group delay, and the pulse rise distance (time) is assumed to be longer than the mirror. The rising edge of this pulse passes through the mirror unattenuated because during this beginning time the multiple reflections and the standing wave in the mirror have not had a chance to set up and attenuate the signal. The time necessary for the standing wave to set up is determined by the mirror transmission-group delay. By the time the head and the tail of the pulse appear the field in the mirror has been established and the rest of the pulse is attenuated. Therefore, at the output side of the mirror only the rising edge of the pulse has emerged with some appreciable amplitude while the rest was attenuated. The exact delay of the rising edge depends on the properties of the mirror and can most certainly appear before the head of the pulse that would travel through vacuum. Hence, causality is not violated.

An experiment of the photon tunneling time through the forbidden gap of a 5.5-period $TiO_2/SiO_2$ quarter-wave mirror has confirmed that the transmission-group delay time is the most realistic estimate of the delay in transmission through quarter-wave mirrors (Steinberg, 1993) . Here we briefly illustrate experiment results and use equation (B-52) to obtain the transmission-group delay. A $TiO_2/SiO_2$ mirror with indexes given by $n_H = 2.22$ ($TiO_2$) and $n_L = 1.41$ ($SiO_2$) is tuned to 692 nm. The time it takes light to propagate a distance equal to the thickness of a symmetrical

quarter-wave mirror with $N+1/2$ periods in vacuum is given by $\tau_{vac}=(N/n_L+N/n_H+1/n_H)/4f$, while the time it takes light to propagate through the stack based on the mirror optical length is $\tau_{qwm}=(2N+1)/4f$. The transmission–group delay is given by (B-52) with $m=2N+1$. These times can be very different for long mirrors, since the group delay saturates for large number of layers. Fig. B.15 shows the comparison between these times as a function of the number of periods. The value of 1.47 fs measured for 5.5-periods is also included showing that the transmission-group delay gives the best estimate.

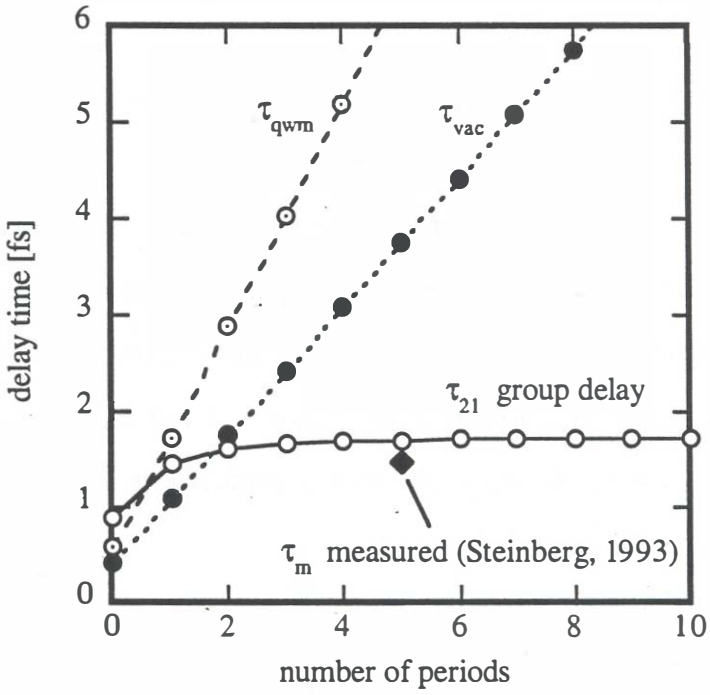


**Fig. B.15** Comparison between different propagation times through a $SiO_2/TiO_2$ quarter-wave mirror at 692 nm.

## B.6. *Quarter-wave mirror energy capacity*

When a plane wave is incident on a quarter-wave mirror at the center frequency a standing wave of decreasing intensity sets up within the mirror, as shown in Fig. B.16. In this section we shall derive exact analytic expressions for amount of energy stored in a lossless quarter-wave mirror at the center wavelength and relate it to the energy density in front of the mirror, namely, the incident power. We shall use these expressions in later sections to determine the absorptance of quarter-wave mirror in the limits of small material absorption.

### B.6.1. *Dimensionless energy capacity of a quarter-wave mirror*

In Fig. B.16 we show the energy density distribution in a QWM at the center frequency. The total electromagnetic energy in each quarter-wave layer is constant (electric and magnetic), but we only show the electric field intensity. We first introduce a dimensionless mirror *energy capacity* $\Lambda$ as the ratio of the total amount of energy within the mirror $W_T$ to the energy contained in the quarter-wavelength of space in front of the mirror $W^*$.

$$\Lambda = \frac{W_T}{W^*} \tag{B-53}$$

The meaning of $\Lambda$ is illustrated graphically in Fig. B.16: The total area under the monotonically decreasing waves of electric field intensity is now contained in a uniform (wavy) distribution vanishing abruptly at depth of $\Lambda$ quarter-wavelengths. The standing wave pattern in the model does not oscillate in with the same periodicity as the original field intensity because it is determined using the refractive index of the

incident material. In order to determine $\Lambda$ we first find the expression for the total energy $W_T$. The Poynting vector magnitude in each section $S_i$ vector is given by

$$S_i = |\bar{E}_i \times \bar{H}_i| = \frac{n_i}{Z_0} |E_i|^2 (1 - R_{i-1}) \tag{B-54}$$

where $Z_0$ is the characteristic impedance of vacuum, $n_i$ the refractive index of section $i$ and $R_{i-1}$ the power reflectivity of the $i-1$-section quarter-wave mirror seen from the section $i$. The energy contained in section $i$ is obtained by integrating the energy density over one quarter-wave period:

$$W_i = \frac{n_i}{4 f Z_0} |E_i|^2 (1 + R_{i-1}) \tag{B-55}$$

In a QWM with no loss the Poynting vector is constant throughout the structure: $S_i = S$. This condition gives us the means of connection between (B-54) and (B-55) yielding:

$$W_i = \frac{S}{4f} \cdot \frac{1 + R_{i-1}}{1 - R_{i-1}} \tag{B-56}$$

The total energy in the mirror is now a sum of all $W_i$. We just need to sum (B-56) for all sections in the mirror. Using the *tanh substitution* again with (B-3) and (B-9) we have:

$$W_i = \frac{S}{f} \left( \frac{1 + b_{i-1}^2}{8 b_{i-1}} \right) \tag{B-57}$$

The energy capacity $\Lambda$ is then given by the sum,

$$\Lambda = \frac{\sum_{i=0}^{m-1}\left(\frac{1}{b_i} + b_i\right)}{\left(\frac{1}{b_m} + b_m\right)} \qquad \text{(B-58)}$$

Introduction $a$, $q$ and $p$ after some manipulation we arrive at,

$$\Lambda = \frac{q}{1-p} \cdot \frac{(1+a^2p^{m-1})(1-p^m)}{(1+q^2a^2p^{2m-2})} \qquad \text{(B-59)}$$

The general behavior of $\Lambda$ as a function of mirror refractive indices is very similar to the one shown for $f\tau$ in Fig. B.13.

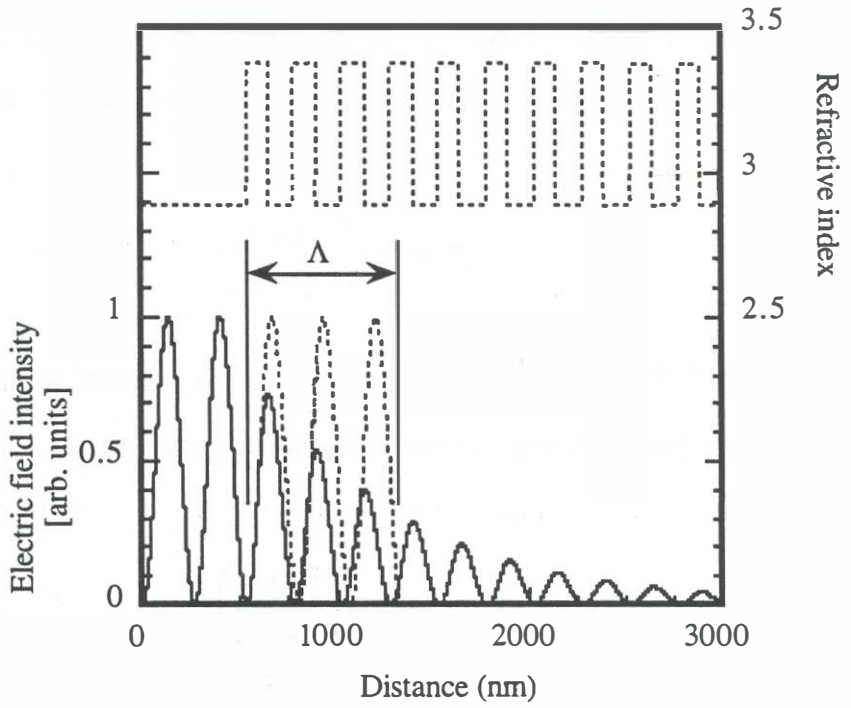


**Fig. B.16**: Energy distribution inside a quarter-wave stack at the band-stop frequency $f$. The horizontal axis is normalized to the optical path so that all layers have equal width and the energy-per-layer distribution falls monotonically.

B.6.2. *Fraction of energy in two mirror materials*

Using the idea of partial group-delay times described in Section B.4.3, we can similarily determine fraction of energy present in each of the materials (H and L). Consider the relation (B-58): the total energy in the mirror is a sum of partial energies in each quarter-wave layer. The total energy $\Lambda^+$ as a sum of two terms: the energy present in the two materials $\Lambda^+ = \Lambda_L + \Lambda_H$, where $\Lambda_L$ and $\Lambda_H$ factor give the fraction of the total energy that is present in the materials with indexes $n_L$ and $n_H$. At the center wavelength a standing wave establishes itself in the mirror and the energy is not distributed equally between the two materials, but clearly depends on the optical parameters of the mirror. In order to determine $\Lambda_L$ and $\Lambda_H$ analytically we first express the explicit dependence of $\Lambda$ given by (B-59) on the two refractive indexes by $\Lambda(n_L,n_H)$. From the expression (B-57) we see that if we change the sign of one of the refractive indexes, for example $n_L$, that the individual energy contributions in (B-57) change sign in the layers of refractive index $n_L$. By changing $n_H$ or both indexes we can obtain four combinations of $\Lambda$ :

$$\begin{aligned} \Lambda(n_L,n_H) &= \Lambda_L + \Lambda_H \qquad \Lambda(-n_L,n_H) = -\Lambda_L + \Lambda_H \\ \Lambda(-n_L,-n_H) &= -\Lambda_L - \Lambda_H \qquad \Lambda(n_L,-n_H) = \Lambda_L - \Lambda_H \end{aligned} \tag{B-60}$$

Using two of these four expressions, one can obtain $\Lambda_L$ or $\Lambda_H$.

$$\Lambda_L = \frac{\Lambda(n_L,n_H)+\Lambda(n_L,-n_H)}{2} \qquad \Lambda_H = \frac{\Lambda(n_L,n_H)-\Lambda(n_L,-n_H)}{2} \tag{B-61}$$

The partial energies in a DBR serve as a basis to an excellent approximation for the prediction of the absorptance of a quarter-wave mirror due to small absorption loss

(Section B.8.1). The fraction of energy in the two materials constituting the mirror are shown in Fig. B.17.

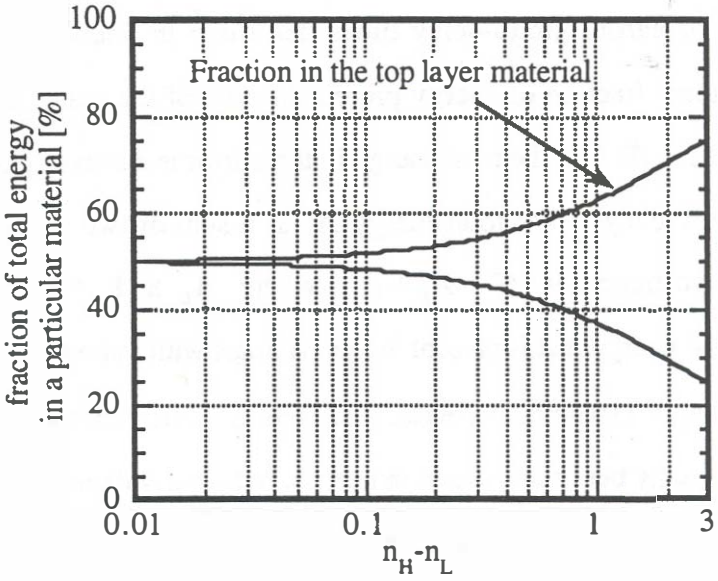


**Fig. B.17**: Calculated distribution of total energy in the mirror between the two mirror materials: The top material always contains more energy.

B.6.3. *Energy penetration depth*

Expression (B-59) is exact for an arbitrary QWM at the center frequency. We now define the *energy penetration depth* with the dimensions of distance as:

$$L_e = \left(\frac{\lambda_0}{4n}\right)\Lambda \qquad \text{(B-62)}$$

Its physical interpretation can be inferred from Fig. B.16. Similarly to the definition of the phase penetration depth, $L_e$ depends on the wavelength and the refractive index of the medium in front of the mirror, since the same medium is assumed to extend past the physical boundary of the mirror to the equivalent lumped mirror.

## B.7. *Phase and energy penetration depths – A comparison*

By taking the ratio of equations (B-62) and (B-36) one can see that for a finite $m$, $L_e$ is always greater than $L_\tau$.

$$\frac{L_e}{L_\tau} = \frac{\Lambda}{\Phi} = 1 + 2a^2 p^{m-1} \frac{(1 - q^2 p^{2m-2})}{(1 - a^2 p^{m-1})(1 + a^2 q^2 p^{2m-2})} \qquad \text{(B-63)}$$

The two penetration depths become practically equal if $2a^2 p^{m-1} << 1$ and the difference between them decreases with the degree by which this condition is met. This means that either the number of layers is large, in which case $p^m << 1$, or the last interface in the mirror dominates the reflectivity: $a << 1$. Note the similarity between the expressions (B-36) and (B-59): The difference arises from the fact that loss of energy through transmission reflects differently on the group delay and the energy stored in the mirror. To illustrate this difference, consider a single quarter-wave layer sandwiched between identical media ($a = q = p$ and $m = 1$). The ratio between $L_e / L_\tau$ is given by (B-63),

$$\frac{L_e}{L_\tau} = 1 + \frac{2p^2}{(1 + p^4)} \qquad \text{(B-64)}$$

The highest ratio between these two numbers equals 2 and it occurs when $p \to 1$, namely, when the refractive indexes become negligibly different. For $p \cong 1$ the energy distribution in the layer is uniform and therefore $L_e \to L$. Since the reflection delay is an average of reflections from all interfaces, it is natural to expect that $L_e \to L/2$ in this limit.

B.7.1. *Unified expression*

Using the expressions derived in Section B.7 and B.8 we can derive some unified expressions for the phase and energy penetration depths and the associated partial reflection times and fractions of energy in different materials. Note that $L_e$ and $L_\tau$ can be written in a unified way: Letting the exit medium index change $n_E \to in_E$ gives $L_\tau \to L_e$, since,

$$L_\tau = \left(\frac{\lambda_0}{4n_I}\right)\Phi(a) \quad L_e = \left(\frac{\lambda_0}{4n_I}\right)\Phi(ia)$$
$$\Phi(x) = \frac{q}{1-p}\cdot\frac{(1-x^2p^{m-1})(1-p^m)}{(1-x^2q^2p^{m-1})} \tag{B-65}$$

This means that the difference between the phase and energy penetration depths originates only from the presence of the exit medium. To develop a unified formula for all the partial times ( $\Phi_L$, $\Phi_H$ ) and energy capacities ( $\Lambda_L$, $\Lambda_H$ ) that is suitable for programming, we introduce several integer variables: Variable $s$ determines whether $\Phi_L$ or $\Phi_H$ ( $\Lambda_L$ or $\Lambda_H$ ) are calculated: $s=1$ for $\Phi_L$ and $s=-1$ for $\Phi_H$. Variable $\varepsilon$ determines the index of the first layer in the mirror: $\varepsilon=1$ if $n_1=n_L$, and $\varepsilon=-1$ if $n_1=n_H$ . In order to avoid using imaginary arguments required to distinguish between $\Phi$ and $\Lambda$, we set $d=1$ for group delay and $d=-1$ for energy capacity. The unified formula is then (B-66):

$$\Phi_{s\varepsilon d}^{(m)}(q,p,a) = q\frac{(1+p)(1-da^2p^{m-1})(1-p^m)+s\varepsilon(1-p)(1-da^2(-p)^{m-1})(1-(-p)^m)}{2(1-dq^2a^2p^{2m-2})(1-p^2)}$$

$$\Phi_{s\varepsilon d}^{\infty}(q,p,a) = q\frac{(1+p)+s\varepsilon(1-p)}{2(1-p^2)} \tag{B-67}$$

$$\Phi_L^\infty - \Phi_H^\infty = \frac{\varepsilon q}{1+p} \quad \Phi_L^\infty + \Phi_H^\infty = \frac{q}{1-p} \qquad \text{(B-68, 69)}$$

B.7.2. *The small refractive index difference limit*

A special case of interest is the behavior of $\tau_m$ when the index difference between all of materials involved is very small $n_I$, $n_E$, $n_L$, $n_H \approx n$, and $\Delta n = n_H - n_L << n$. In this case the reflection delay (and the penetration depth) can be found by differentiating the phase of the expression for the DBR reflectivity obtained by CWT (Koyama, 1983):

$$\tau = \frac{n}{c}\frac{\tanh(\kappa L)}{\kappa} \qquad \text{(B-70)}$$

where $L$ is the thickness of the mirror (length of the grating) and $\kappa$ is the coupling coefficient. For a square index perturbation $\kappa = 2\Delta n/\lambda_0$, where $\lambda_0$ is the design wavelength ( $\lambda_0 = 2\pi c/\omega_0$ ). To verify the analytic expression given in (B-36) we show that equation (B-70) can be derived from (B-36) by applying the noted assumptions about the values of the refractive indices. To this end we let $n_H = n + \Delta n/2$ and $n_L = n - \Delta n/2$, and set $qa \cong a^2 \cong p$. The equation (B-36) then reduces to:

$$\tau_m = \left(\frac{1}{2f}\right)\frac{q}{1-p}\cdot\frac{1-p^m}{1+p^m} \qquad \text{(B-71)}$$

The factor $p^m$ can be approximated by $p^m \cong (1-\Delta n/n)^m$, while the thickness of the mirror is related to $m$ by $L = m\lambda_0/4n$. We let $\Delta n$ become very small while keeping $\kappa L$ constant:

$$p^m = \lim_{m\to\infty}\left(1-\frac{2\kappa L}{m}\right)^m = e^{-2\kappa L} \qquad \text{(B-72)}$$

Using (B-71) and (B-72) we easily arrive at (B-70), which shows that in this limit the equation (B-36) and the results of the Coupled-Wave Theory agree. The importance of equation (B-36) then lies in its application to abrupt multi-layered structures with large index differences such as amorphous dielectric media, where the coupled mode theory can not be applied.

Using the same method we can show that the phase penetration and energy penetration depths become:

$$L_\tau = \frac{\tanh \kappa L}{2\kappa} \quad \text{and} \quad L_e = \frac{\tanh(2\kappa L)}{2\kappa}. \qquad \text{(B-73)}$$

As shown here even in the small refractive index limit, applicable to DFB and DBR structures the two penetration depths are not equal. However, the difference between them has little practical significance since the energy penetration depth is rarely used.

## B.8. *Absorptance and other sources of peak reflectivity reduction*

The reflectivity of a quarter-wave mirror is reduced by the presence of absorption and scattering losses. The analysis of mirrors with absorbing materials is done in a straightforward fashion using transverse field matrices (Appendix 1), whereas the treatment of scattering losses can be quite involved (Stover, 1990). In this section we present a first order approximation to the values of the peak reflectivity, transmission and the absorptance of quarter-wave mirrors with weak material absorption operating at the center wavelength. We will give analytic expressions for all of these parameters that are exact in the limit of small loss.

### B.8.1. *Total absorptance*

An electromagnetic wave is incident on a quarter-wave mirror. The fraction of the incident power that is neither reflected nor transmitted, but is lost in the mirror, is specified by the mirror *absorptance* (Macleod, 1986): $A = P_{diss}/P_{inc}$. Here $P_{diss}$ and $P_{inc}$ are the total power dissipated in the mirror and power incident on the mirror. In order to differentiate between the *reflection* and *transmission* absorptances, introduced in later text, this absorptance will sometimes be referred to as the *total* absorptance. The power balance in the mirror is given by $R+T+A=1$, where $R$ and $T$ are the reflectivities of the lossy mirror. A good estimate of the total absorptance is obtained by integrating the power loss in the mirror determined from the knowledge of the absorption coefficient and the electromagnetic field energy at each location. This model is applicable if the loss has a negligible effect on the standing wave pattern in the mirror. Fortunately, this is largely the case in practical high reflectivity mirrors.

As long as the extinction coefficients of the mirror layers are much smaller than the refractive indexes the individual interface reflection coefficients will remain unperturbed leaving the standing wave pattern largely intact. The total dissipated power in the mirror is given by the weighted integral of the energy distribution in the mirror:

$$\frac{dW}{dt} = -c\int_0^L \frac{\alpha(x)w(x)}{n(x)}dx \qquad W_T = \int_0^L w(x)dx \qquad \text{(B-74)}$$

The integrals are to be taken over the entire length of the mirror ($0 \rightarrow L$). Here $\alpha(x)$ and $n(x)$ are the position dependent power loss coefficient (1/length) and the refractive index within the mirror. The energy density per unit length is denoted by $w(x)$ and the total energy present in the mirror by $W_T$. Taking into account the periodic nature of $\alpha(x)$ and $n(x)$ in the quarter-wave mirror we quickly arrive at,

$$P_{diss} = -\frac{dW_T}{dt} = 4\pi f\left\{\frac{k_L}{n_L}W_L + \frac{k_H}{n_H}W_H\right\} \qquad \text{(B-75)}$$

where $W_L$ and $W_H$ are the amounts of energy present in the two materials. The material extinction coefficients are denoted by $k_L$ and $k_H$. (The extinction coefficients are related to the absorption coefficients via $\alpha = 4\pi k/\lambda$). To determine $W_L$ and $W_H$ as functions of the incident power $P_{inc}$ and the physical parameters of the quarter-wave mirror we first relate the energy in the quarter-wavelength in front of the mirror $W^*$ to the incident power $P_{inc}$, and then relate $W_L$ and $W_H$ to $W^*$ using the fractional quarter-wave mirror energy capacities $\Lambda_L$ and $\Lambda_H$. The energy stored in one quarter-wavelength of incident medium in front of the mirror can be found from (B-56) by setting $i = m+1$.

$$W^* = \frac{S}{4f} \cdot \frac{1+R_0}{1-R_0} \qquad \text{(B-76)}$$

Where $R_0$ is the reflectivity of the complete lossless mirror given by (B-12). The Poynting vector can be related to the incident power via $S = P_{inc}(1-R_0)$, which introduced into (B-76) and together with the definitions given in Section B.6.2 yields an analytic expression for the absorptance:

$$A = \pi(1+R_0)\left\{\frac{k_L}{n_L}\Lambda_L + \frac{k_H}{n_H}\Lambda_H\right\} \qquad \text{(B-77)}$$

In the limit of small loss $n_j >> k_j$ this expression gives the correct value of the QWM absorptance for any combination of refractive indices and number layers. For very long mirrors ($m \to \infty$), the energy capacity saturates at $\Lambda = q/(1-p)$ and with known orientation of the quarter-wave sequence we can obtain the maximum absorptance of quarter-wave mirrors. For the two infinite mirror orientations, we have:

$$A_{n_1=n_H} = 2\pi\frac{n_I(k_L+k_H)}{n_H^2-n_L^2} \qquad A_{n_1=n_L} = 2\pi\frac{n_L^2k_H+n_H^2k_L}{n_I(n_H^2-n_L^2)} \qquad \text{(B-78)}$$

These two expressions are known approximate relations for the absorptance of the quarter-wave stack in the presence of small loss given in (Macleod, 1986). The equation (B-77) is a general result applicable to quarter-wave mirrors of any number of layers (odd or even) and optical parameters of both the mirror materials and the surrounding media. The absorptance of a quarter-wave stack with weak absorption was also estimated by (Hemingway, 1973) using a different method. Their approach yielded two absorptance expressions that differed depending on whether the total

number of layers is odd or even, and assumed that the incident and the exit medium refractive indices equal to one of the mirror material indices. Both of the absorptance expressions given in (Hemingway, 1973) can be obtained from equation (B-77).

B.8.2. *Reflection and transmission absorptances*

Besides the information on how much energy is lost in the mirror, one often needs to know how much does this energy loss influence the reflection or the transmission coefficients. The absorptance $A$ only provides the information on what is the *total* power lost to the mirror. It does not provide the information on how does this loss effect the reflectivity or the transmission seen from two ports. The reason it does not make this distinction is because of the way we chose to estimate it, namely, through the energy stored in the standing wave. In order to estimate the reduction of reflectivity due to absorption loss we take a slightly different approach: We consider the time the electromagnetic wave spends in the mirror rather than the energy stored. With known loss rate and time spent in the mirror we have yet another estimate of dissipated power. However, the advantage of the latter approach is that it is port specific. The reflection-group delay provides the information on what time does a signal, that eventually reflects, spend in the mirror. Consider a mirror which in the absence of loss has reflectivity $R_0$. A fraction of the power that enters this mirror is lost to absorption. Since we know the loss rate $\alpha(x)v_g(x)$ in every layer of the mirror and the amount of time the electromagnetic wave appears to spend in the mirror (reflection-group delay) we can estimate the amount of dissipated power.

$$P_{diss} = P_{inc} \int_0^{\tau} \alpha(x) v_g(x) dt \tag{B-79}$$

To first order, the reflectivity of the mirror is given by $R \cong R_0(1 - A_R)$, where $A_R$ is called *reflection absorptance* and it is defined as the fraction of the incident power which is lost to absorption, but would otherwise be reflected. The reflection absorptance $A_R$ is generally different from the total absorptance $A$. We similarly define transmission absorptance $A_T$, using $T = T_0(1 - A_T)$. These three quantities satisfy the following energy balance relation:

$$R_0 A_R + T_0 A_T = A \tag{B-80}$$

In a quarter-wave mirror the rate of power dissipation depends on how much time the electromagnetic wave *appears* to spend in each of the two mirror materials. As pointed out, to estimate the reduction of reflectivity this is precisely what we are interested in: The *apparent* influence of the mirror delay times on the reflection. Inasmuch as the two materials have different absorption coefficients we use the partial reflection-group delay times $\tau_L$ and $\tau_H$ to obtain an analytic expression for the reflection absorptance,

$$A_R = 2\pi \left( \frac{k_L}{n_L} \Phi_L + \frac{k_H}{n_H} \Phi_H \right) \tag{B-81}$$

where $\tau = \Phi / 2f$ was used. This equation and the idea for the reflection absorptance was originally suggested by Scott Corzine and given in (Corzine, 1993). Here we have discussed the physical rationale behind the reflection absorptance and the role of the material-specific delay time of propagation in the mirror. To appreciate the significance of equation (B-81), one needs to remember that previous analytic expressions for the reflectivity of low-loss quarter-wave mirrors were based on an

arbitrary split of the total absorptance between the reflectance and transmittance based on the value of $R$ and $T$ (Macleod, 1986), (Giacomo, 1961), (Babić, 1992): $R = R_0(1-A)$ and $T = T_0(1-A)$. These expressions provide very good approximation for the peak reflectivity when the number of layers is very large ($m \to \infty$), since then $A_R \to A$, but discrepancies surface when the number of layers is small. It is for low number of layers that expression (B-81) provides a better fit. The expressions (B-77) and (B-81) become identical when the number of layers tends to infinity ( $R_0 = 1$). This is expected since the is no transmission and the dissipated power equals the difference between incident and reflected powers. For this limiting case equations (B-78) can be used to estimate the reflection absorptance.

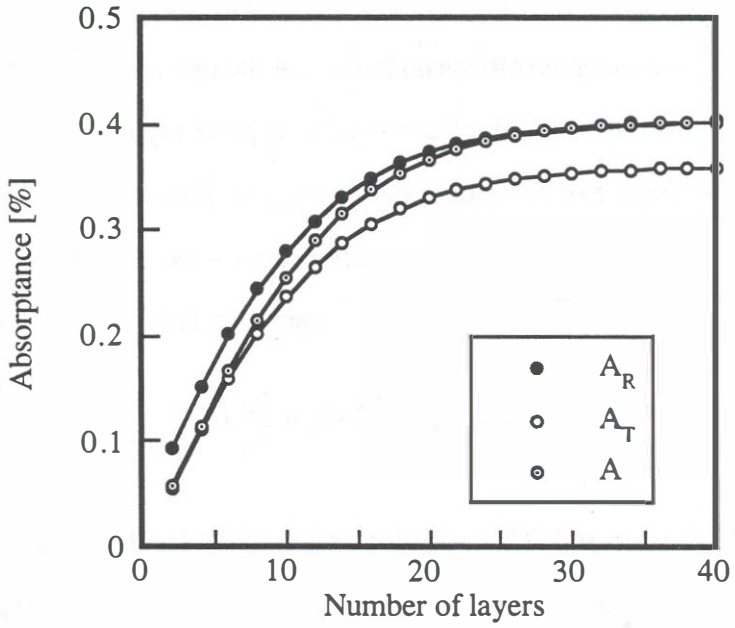


**Fig. B.18**: Graph of exact and analytically calculated $A$, $A_R$ and $A_T$ for an AlAs/GaAs quarter-wave mirror as function of number of layers. The full lines are exact solutions, while the dots represent the approximate values given by equations (B-77), (B-80) and (B-81).

Figure B.18 shows the comparison between exactly calculated and analytically determined absorptances $A$, $A_R$ and $A_T$ for an AlAs/GaAs mirror. The mirror transmission is most susceptible to errors in using $A$ instead of $A_R$ and $A_T$.

B.8.3. *Optimal-pair mirror*

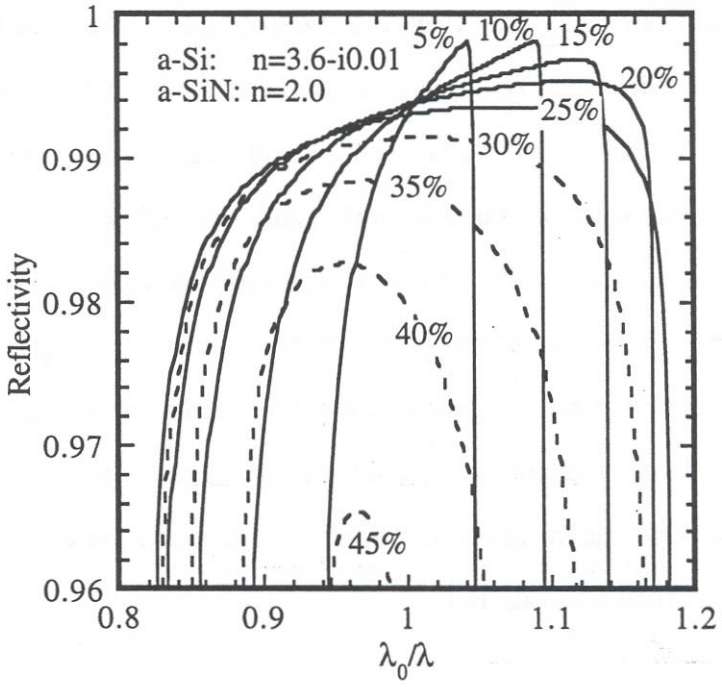


**Fig. B.19**: The reflectivity spectra of a periodic multilayer with constant resonance frequency. Each period has two layers and the thickness of the high index material is expressed as a fraction of the wavelength, i.e. when the fraction is 25% then the multilayer is a quarter-wave stack. The high index material is lossy amorphous silicon ($n_H = 3.6 - i0.01$) and the loss index is losses silicon nitride ($n_L = 2.0$).

The maximum reflectivity of mirrors in which one of the materials has a higher absorption loss than the other, generally occurs at a frequency that is slightly detuned from the mirror center. The reason for this is the following: As the wavelength changes from the center towards one of the band edges, the energy within the mirror (already unevenly split between the materials) tends to shift towards one of the two materials. For higher frequency the energy distribution shifts to the low index material (and vice versa) as can be seen from the standing wave pattern at the edge of the forbidden gap in Fig. B.8. This opens possibility for designing quasi-quarter-wave mirrors where the thickness of the layers have been slightly altered to achieve highest possible reflectivity with a given loss coefficient. The peak reflectivity value and the detuning at which it occurs varies occurs at a different detuning is a complicated function of the optical constants of the materials and the number of layers. A multilayer stack that is has its quarter-wave layers adjusted to maximize the peak reflectivity is referred to as the *optimal pair* stack. An example of the variation of the peak reflectivity with the thickness of the layers while the mirror center frequency was kept constant, is shown in Fig. B.19.

### B.8.4. *Scattering in mirrors*

Besides the bulk material absorption, light energy in the quarter-wave mirror can be lost by scattering. By scattering we mean that the light energy is redirected from the useful (laser) mode of propagation into other directions. The scattering of electromagnetic waves occurs in optically inhomogeneous bulk materials and on rough interfaces between two media with different homogenous optical properties.

For use in dielectric coatings were are primarily interested in weak scattering in the long wavelength regime where the size of the scatterers is small compared to the wavelength, such as, Rayleigh scattering. Bulk scattering can be treated similarly as bulk absorption, by introducing an imaginary part of the refractive index (Jackson, 1986). Scattering at the interfaces between two media is of particular interest in quarter-wave mirrors for near-infrared and visible light applications because the typical roughness of the deposited or grown dielectric layers may produce significant reduction in the peak reflectivity of these mirrors. In amorphous films deposited by e-beam, reactive sputtering, and plasma enhanced chemical deposition techniques the defects in the mirrors occur from contaminants and dust, as well as three-dimensional nucleation of deposited materials. In epitaxial films the interface scattering will be affected by oval defects, dislocations and compositional non-uniformities. One of the important factors determining whether an epitaxial multilayer structure is adequate for surface-normal optoelectronic device, is the relative size of the device and the defect. Large defects, such as, pinholes in deposited films or oval defects in epitaxially grown materials have sizes comparable to optoelectronic devices and their presence directly influences the yield. Uniformly distributed micro-roughness on height and lateral extend of several nanometers degrade the performance of all optoelectronic devices. It is the latter type of surface roughness that sets the true limit of reflectivity and the application of a particular multilayer scheme.

There are a number of ways to characterize the optical properties of rough surfaces. A measurement of the angular distribution of the scattered light from a sample yields information about the surface roughness and the lateral surface variation (Stover, 1990, Gourley, 1991). The surface roughness can be directly measured using

Atomic Force Microscopy (AFM), and then the interface reflectivity can be calculated from this information (Bennett, 1961). The reduction in reflectivity of quarter-wave mirrors can approximately determined using analytic expressions of (Arnon, 1977) or using the transverse matrix approach described in Appendix A.

B.8.5. *Layer thickness and refractive index variation*

The fabrication of high reflectivity quarter-wave mirrors often requires the deposition of a large number of quarter-wave layers. The requirement for the realization of a perfect quarter-wave mirrors is that all of the layers have the exact thickness. However, this is rarely the case because the deposition / growth rate varies with a large number of process parameters, some of which are very difficult to control. The factors that influence the deposition / growth rate are the temperature variation, base pressure and source depletion. Random variations of mirror parameters typically has a detrimental effect on the peak reflectivity of the mirror and also changes the phase properties, as has been investigated theoretically by several authors (Weber, 1990, Law, 1993). Systematic variation of the thickness of the layers due to process variation with change the mirror center wavelength and reduce the peak reflectivity. The temperature variation of the refractive index may have a similar result (Dudley, 1992), but may also increase the reflectivity of the mirror (Piprek, 1994).

B.8.6. *Metal clad quarter-wave mirrors*

It is a common practice to use non-alloyed metal reflector on top of an epitaxial quarter-wave mirror to provide and ohmic contact and to boost the reflectivity of the

mirror and thereby reduce the number of periods of the quarter-wave stack necessary to achieve some given reflectivity value. In order to increase the overall reflectivity of the mirror, the last layer in front of the metal has to adjust the phase of the metal reflection to match the phase of the quarter-wave mirror at the design wavelength. The thickness of this *phase-matching* layer depends on the phase of the metal reflection, while the increase of the overall mirror reflectivity depends on the reflectivity of the semiconductor-metal interface. In order to simplify the calculation of the reflectivity of metal-clad quarter-wave mirrors and the number of periods necessary for a certain reflectivity the metal-clad quarter-mirror is replaced with an equivalent dielectric structure as shown in Figure B.20.

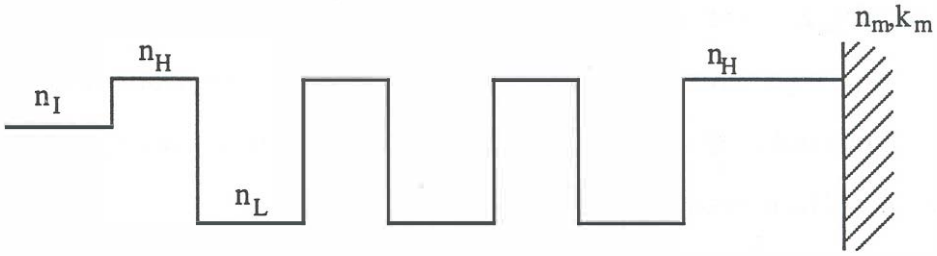


(a) metal-clad quarter-wave mirror

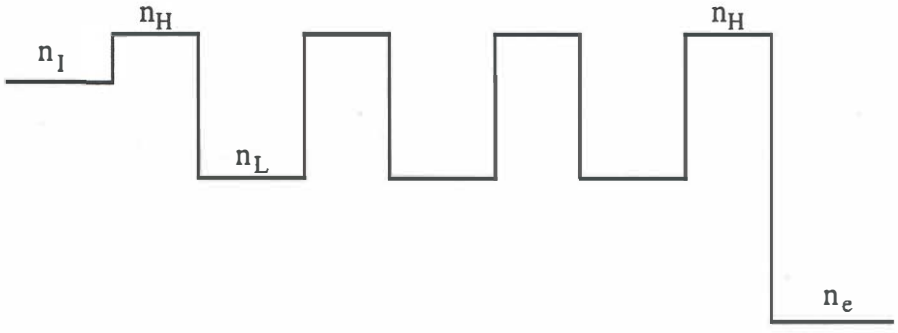


(b) equivalent dielectric mirror
(quarter-wave mirror of same reflectivity)

**Fig. B.20**: Refractive index profile of metal-clad and all-dielectric quarter-wave mirrors.

The phase matching layer and the metal reflector are replaced with a single dielectric interface which gives the same phase and reflection strength at the quarter-wave position. Hence, at the mirror center wavelength the reflection coefficient of the quarter-wave mirrors is equal to the one that would be obtained if the phase matching layer and the metal were considered. This equivalence, however, works only at the center wavelength. It does not work for any other wavelength, i.e. it can not be used to determine the penetration depth of the DBR exactly, but only approximately. In this case one either ignores the extra phase in the phase matching layer when calculating $L_\tau$ or ignores the extra energy stored in the phase matching layer when calculating $L_E$. The relative size of the equivalent index of the exit medium depends whether the phase matching layer is of index $n_H$ or $n_L$. If the phase matching layer is of the high index (typically it is - GaAs), then the effective index $n_e$ should be lower than $n_H$. The rigorous definition of $n_e$ is

$$n_e = n_H \frac{1-|r|}{1+|r|} \tag{B-82}$$

where $r$ is the reflection coefficient of the semiconductor to metal interface. If we wish to determine $n_e$ using the bulk optical constants of the metal $n_m - ik_m$ and the phase matching layer $n_s$, we equate the reflectivity of the actual metal-semiconductor interface $R$ with the reflectivity of the semiconductor - effective exit medium interface $R_e$: Set $R = R_e$.

$$R = \frac{(n_s - n_m)^2 + k_m^2}{(n_s + n_m)^2 + k_m^2} \quad R_e = \left(\frac{n_s - n_e}{n_s + n_e}\right)^2 \tag{B-83}$$

and solve for $n_e$ exactly:

$$\frac{n_e}{n_s} = \frac{(n_s^2 + n_m^2 + k_m^2)}{2n_m n_s}\left(1 - \sqrt{1 - \frac{4n_m^2 n_s^2}{(n_s^2 + n_m^2 + k_m^2)^2}}\right) = \frac{z - \sqrt{z^2 - 4}}{2} \quad \text{(B-84)}$$

where $z$ is a new variable given by $z = (n_s^2 + n_m^2 + k_m^2)/n_m n_s$. The exact reflectivity of the metal interface is given by $R = (z-2)/(z+2)$. Most good metal reflectors the effective index of the exit medium is approximately equal to:

$$n_e \cong \frac{n_m}{1 + (n_m^2 + k_m^2)/n_H^2} \quad \text{(B-85)}$$

With these two expressions we can use (B-12) to find the peak reflectivity of a lossless mirror. If loss is present we can use $R = R_0(1 - A_R)$ as an approximation. Note that the use of effective exit medium index (B-82) in $A_R$ we are neglecting the additional delay in the metal phase matching layer. For mirrors with a large number of layers this omission does not produce significant errors in the reflectivity.

## B.9. *Diffraction properties of quarter-wave mirrors*

In this section we develop a diffraction conserving lumped mirror model for a quarter-wave mirror. The model is developed for an infinite lossless quarter-wave mirror and is only approximately applicable to mirrors with a finite number of layers and absorption loss. The model is based on representing propagation and reflection on a quarter-wave mirror as a case of free-space propagation over a specified distance determined by the optical properties of the mirror. This distance is named: diffraction equivalent distance, because the spatial evolution an electromagnetic wave during the reflection from an infinite lossless quarter-wave mirror can be well approximated with simple free-space propagation. The use of an unit reflectivity quarter-wave mirror greatly simplifies the analysis because in this case the reflection conserves energy in the same sense as free-space propagation.

### B.9.1. *Reflection operator for paraxial waves*

Consider a single frequency paraxial light beam propagating in free space. The beam propagates in the $+z$ direction with wave-number $k = n_l \omega / c$. We observe the transverse field profile on surface $S_z$ positioned at an arbitrary location $z$, as shown in Fig. B.22. The surface $S_z$ is perpendicular to the propagation direction and $\bar{\rho}$ is the coordinate on the surface, $\bar{\rho} \in S_z$. If the mode pattern is known at $z = 0$, the diffraction of the beam is governed by the Fresnel Transformation (Haus, 1984, Kojima, 1975, Aoyagi, 1973) $f \rightarrow \tilde{\boldsymbol{T}}(z) f$ given in real-space coordinates by:

$$\tilde{\boldsymbol{T}}(z) f(\bar{\rho}) = \frac{k}{i 2\pi z} \int d^2\rho' \, f(\bar{\rho}') \exp\left( ikz + ik|\bar{\rho} - \bar{\rho}'|^2 / 2z \right) \qquad \text{(B-86)}$$

where the integration is performed over the entire $S_0$ plane. This transformation is applicable only for small diffraction angles, in which case the observation distance $z$ can be made arbitrarily small. If we express the initial transverse field $f(\bar{\rho})$ in terms of its angular spectrum (Goodman, 1968) $F(\bar{k}_\rho)$,

$$F(\bar{k}_\rho) = \int d^2\rho\, f(\bar{\rho}) e^{-i\bar{k}_\rho \cdot \bar{\rho}} \tag{B-87}$$

then the $k$-space representation of the free-space paraxial propagation operator is given by

$$\tilde{\boldsymbol{T}}(z) = \exp\left( ikz - i\frac{k_\rho^2 z}{2k} \right). \tag{B-88}$$

Here $\bar{k}_\rho$ is the transverse wave vector.

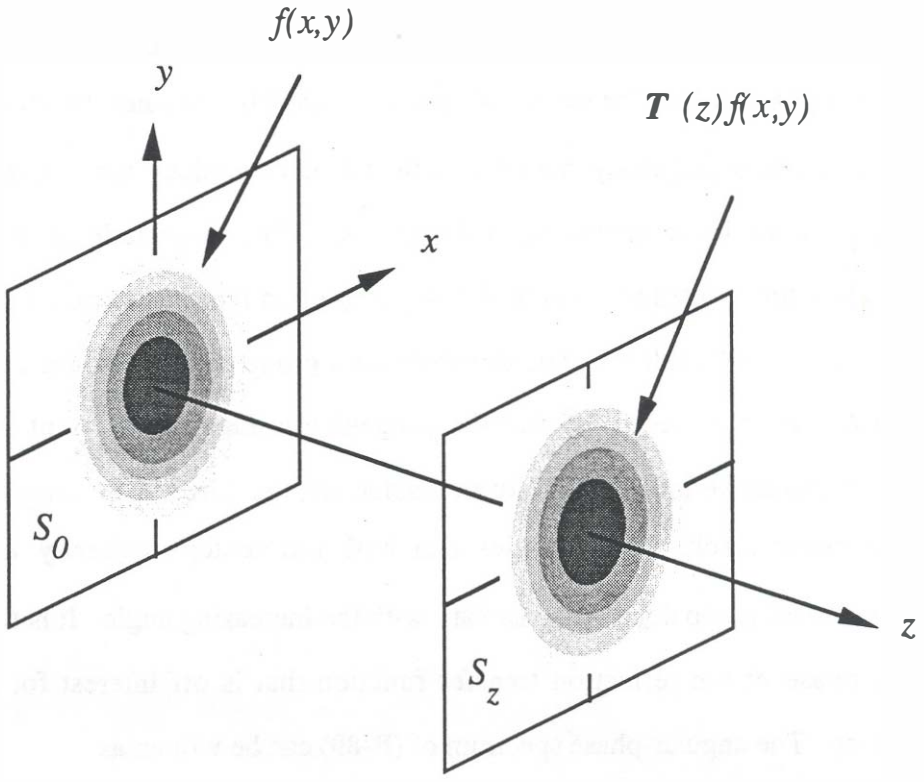


**Fig. B.22**: Free-space propagation of a beam with transverse electric field profile $f(x,y)$.

Consider now the case in which we place an infinitely long lossless quarter-wave mirror parallel to surface $S_0$ at $z = 0$. We consider the case where the observation frequency $\omega$ is near the center of the bandstop and the electromagnetic wave is incident with an angle sufficiently small so that the magnitude of the reflection coefficient is still unity, but the phase varies with the angle and the detuning. The angular-reflection spectrum is then written as,

$$\tilde{R}_{DBR} = r_{mc} \exp i\phi_m \cdot \exp i\phi_{m1}(k_{\bar{\rho}}) \tag{B-89}$$

where $r_{mc}$ is the real and positive amplitude reflection coefficient at the mirror center ($r_{mc} = 1$ for an infinite mirror), and $\phi_{mc}$ is the mirror fixed phase (either zero or $\pi$). At the center wavelength the normal incidence reflectivity is given by (B-20): $\phi_{m1} = \pi(\omega/\omega_c - 1)\Phi$. The factor $\Phi$, given by (B-40), does not directly depend on the mirror center frequency, but only on the refractive indices, namely, the reflection strength of the layer interfaces in the mirror. The magnitude of the reflection coefficient for frequencies within the bandstop of an infinite quarter-wave mirror is unity for normal incidence. The dimensionless group delay of an infinite mirror is given by $\Phi^{\infty} = q/(1-p)$. Since the propagation angle is different in layers of different refractive index at off-normal incidence, the mirror is no longer tuned as a quarter-wave stack. This implies that both the center frequency $\omega_c$ and the dimensionless group delay $\Phi$ will vary with the increasing angle. It is the variation in the phase of the reflection transfer function that is off interest for diffraction modeling. The angular-phase spectrum of (B-89) can be written as

$$\phi_m(k_\rho) = \pi\left(\frac{\omega}{\omega_c}\frac{\omega_c}{\omega_c'(k_\rho)} - 1\right)\Phi(k_\rho) \tag{B-90}$$

Here $\omega_c$ and $\omega_c'$ are the center frequencies of the mirror at normal incidence and at some small angle, respectively. In order to simplify the $k_\rho$ dependence (B-90) we consider the two terms: $\omega_c/\omega_c'(k_\rho)$ and $\Phi(k_\rho)$, separately. The first term indicates how much does the mirror center wavelength change with the angle, while the second term shows how much does the dimensionless group delay change with the angle. We expand the ratio $\omega_c/\omega_c'$ in powers of $k_\rho^2$. The expression that relates the shift of the mirror center frequency and the transverse wave number is obtained from the requirement that the phase shift across a single period of the mirror stack in the $z$-direction equals $\pi$ at the new mirror center frequency $\omega_c'$:

$$\frac{2\omega_c}{\omega_c'} = \frac{2k_c}{k_c'} = \sqrt{1 - \frac{k_\rho^2}{n_L^2 k_c'^2}} + \sqrt{1 - \frac{k_\rho^2}{n_H^2 k_c'^2}} \tag{B-91}$$

We solve for $k_c'^2$ explicitly,

$$\left(\frac{k_c'}{k_c}\right)^2 = 1 + \frac{1}{2}\left(\frac{1}{n_L^2} + \frac{1}{n_H^2}\right)\left(\frac{k_\rho}{k_c}\right)^2 + \frac{1}{16}\left(\frac{1}{n_L^2} - \frac{1}{n_H^2}\right)^2\left(\frac{k_\rho}{k_c}\right)^4 \tag{B-92}$$

and expand the result to first order in $k_\rho^2/k_c^2$ to obtain

$$\frac{\omega_c}{\omega_c'} \equiv 1 - \frac{A}{2}\left(\frac{k_\rho}{k_c}\right)^2 \tag{B-93}$$

where the mirror refractive indexes have been merged into $2A = 1/n_L^2 + 1/n_H^2$. The factor $\Phi(k_\rho)$ dependence on $k_\rho$ is twofold: (a) The change in the angle of

propagation though each layer alters the reflection strength at each interface. The factors $p$ and $q$ vary as

$$p \cong \frac{n_L}{n_H}\left\{1-\frac{\gamma}{2}\left(\frac{1}{n_L^2}-\frac{1}{n_H^2}\right)\frac{k_\rho^2}{k_0^2}\right\} \quad q \cong \frac{n_{LI}}{n_{HI}}\left\{1-\frac{\gamma}{2}\left(\frac{1}{n_{LI}^2}-\frac{1}{n_{HI}^2}\right)\frac{k_\rho^2}{k_0^2}\right\} \tag{B-94}$$

The direction of the correction also depends on the polarization of the incident beam: $\gamma = +1$ for $s$ (TE) and $\gamma = -1$ $p$ (TM) polarized waves. (b) The optical thickness of the layers at the new resonance frequency are not equal to a quarter wavelength: The low index quarter-wave appears thinner, while the high index layer appears thicker. The exact expressions for the change in the quarter-wave time are given below,

$$\frac{\Delta\tau_L}{\Delta\tau} = 1-\frac{1}{4}\left(\frac{1}{n_L^2}-\frac{1}{n_H^2}\right)\left(\frac{k_\rho}{k_c}\right)^2 \quad \frac{\Delta\tau_H}{\Delta\tau} = 1+\frac{1}{4}\left(\frac{1}{n_L^2}-\frac{1}{n_H^2}\right)\left(\frac{k_\rho}{k_c}\right)^2 \tag{B-95}$$

Note that the sum of these two times is equal to a half wave time at the new frequency (B-91). The estimate of $\Phi(k_\rho)$ dependence on $k_\rho$ due to unequal times in the two mirror materials is based on correcting the partial group delay times $\Phi_L$ and $\Phi_H$ before adding them to obtain the total group delay time . We shorten $\Phi_L$ and prolong $\Phi_H$ by scaling with (B-95) to obtain the total group delay time:

$$\Phi(k_\rho) = \left(\Phi_L(k_\rho)+\Phi_H(k_\rho)\right) - B\left(\frac{k_\rho^2}{k_c^2}\right)\left(\Phi_L(k_\rho)-\Phi_H(k_\rho)\right) \tag{B-96}$$

where $2B = 1/n_L^2 - 1/n_H^2$. The partial group-delays $\Phi_L(k_\rho)$ and $\Phi_H(k_\rho)$ still depend on $k_\rho$ because we did not yet introduce the correction due to individual reflections (B-94). To do this we derive the angular variation using (B-94),

$$\Phi_L^{\infty} - \Phi_H^{\infty} = \frac{\varepsilon q}{1+p}\left\{1 - \frac{\gamma}{2}\left[B + \varepsilon A - \varepsilon\frac{1}{n_I^2} + \frac{1}{n_H}\left(\frac{1}{n_L} - \frac{1}{n_H}\right)\right]\left(\frac{k_\rho}{k_c}\right)^2\right\}$$

$$\Phi_L^{\infty} + \Phi_H^{\infty} = \frac{q}{1-p}\left\{1 - \frac{\gamma}{2}\left[B + \varepsilon A - \varepsilon\frac{1}{n_I^2} + \frac{1}{n_H}\left(\frac{1}{n_L} + \frac{1}{n_H}\right)\right]\left(\frac{k_\rho}{k_c}\right)^2\right\} \qquad \text{(B-97)}$$

Bringing it all together and keeping only terms up to the second power in $k_\rho/k_c$ we get

$$\Phi(k_\rho) = \frac{q}{1-p}\left\{1 - \frac{V}{2}\left(\frac{k_\rho}{k_c}\right)^2\right\}$$

$$V = \frac{\gamma}{2}\left\{\varepsilon\left(\frac{1}{n_L^2} + \frac{1}{n_H^2} - \frac{2}{n_I^2}\right) + \left(\frac{1}{n_L} + \frac{1}{n_H}\right)^2\right\} + \varepsilon\left(\frac{1}{n_L} - \frac{1}{n_H}\right)^2 \qquad \text{(B-98)}$$

Finally, the phase of an infinite quarter-wave mirror changes as

$$\phi_m(\omega, k_\rho) = (\omega - \omega_c)\tau_\infty - \frac{1}{2}\left(\omega\tau_\infty A + V(\omega - \omega_c)\tau_\infty\right)\left(k_\rho/k_c\right)^2 \qquad \text{(B-99)}$$

at this point we discard the term containing $V$, because $\omega >> \omega - \omega_c$ while $A$ and $V$ are of the same order. By doing this we also eliminated the polarization dependence of the phase. We argue that for paraxial waves the polarization dependence can be ignored, namely, none of the terms preceded by $\gamma$ or smaller should enter the final expression. With these approximations the phase change becomes

$$\phi_m(\omega, k_\rho) = (\omega - \omega_c)\tau_\infty - \frac{\omega\tau_\infty A}{2}\left(\frac{k_\rho}{k_c}\right)^2 \qquad \text{(B-100)}$$

Introducing (B-100) into (B-89) the mirror reflection function can be written as

$$\tilde{R}_{DBR}(\omega, k_\rho) = r_{mc}\exp i\left(\phi_m - ikz + (\omega - \omega_c)\tau_\infty\right)\cdot\exp\left(ikz - i\frac{k_\rho^2 z}{2k}\right) \qquad \text{(B-101)}$$

with

$$z = \frac{n_I c \tau_\infty}{2}\left(\frac{1}{n_L^2}+\frac{1}{n_H^2}\right)\left(\frac{\omega^2}{\omega_c^2}\right) \qquad \text{(B-102)}$$

We identify two terms in the transfer function, the reflection $\tilde{R}^*(\omega)$ which represents a lumped mirror and the free-space propagation term $\tilde{T}(\omega,k_\rho)$ which represents space in front of a lumped mirror. The free-space propagator $\tilde{T}(\omega,k_\rho)$ is only approximate since the frequency appears in the numerator rather than the denominator, however, $\omega \cong \omega_c$ and this difference can be ignored. The distance at which the lumped mirror is located is given by $L_D = z/2$. From (B-102) using $(\omega^2/\omega_c^2) \cong 1$ we quickly find

$$L_D = \beta L_\tau^\infty \qquad \beta = \frac{n_I^2}{2}\left(\frac{1}{n_L^2}+\frac{1}{n_H^2}\right) \qquad \text{(B-103)}$$

$$\tilde{R}_{DBR}(\omega,k_\rho) = r_{mc}\exp i\left(\phi_m + (\omega-\omega_c)\tau_\infty\right)\cdot\exp\left(-i\beta L_\tau^\infty k_\rho^2/k\right) \qquad \text{(B-104)}$$

A very important fact is revealed here: The reflection of electromagnetic waves from an infinite quarter-wave mirror (at near-normal incidence and small detuning from the center wavelength) can be treated as a case of free-space propagation over a fixed distance determined by the frequency and the optical parameters of the quarter-wave mirror. An intuitive understanding of this effect is obtained if one represents the action of the operator (B-104) by a lumped mirror of unit reflectivity and a fixed phase placed at a suitable distance away from the beginning of the original quarter-wave mirror. The distance at which the equivalent lumped mirror should be placed is named diffraction equivalent distance and it is given by $L_D = \beta c\tau_\infty/2n_I$ .

A few noteworthy characteristics of (B-104) are: Only at the center frequency or at normal incidence can one split the (B-104) operator into a lumped mirror with fixed

reflectivity and phase and free-space propagation. As soon as one lets the frequency vary at the same time as the angle this separation is no longer possible unless the factor $\beta$ equals unity. Therefore, the *penetration depth* model of the quarter-wave mirror leads to two different penetration depths $L_\tau$ and $L_D$ depending on whether one considers time or diffraction as the conserved quantity in the pumped mirror model. All of this analysis has been carried out for paraxial beams with a linewidth that is small compared to the mirror bandstop. The hard mirror model has been shown (Ram, 1995b) to be very applicable in the case of spontaneous emission from atomic systems within cavities that used distributed mirrors and emit into all directions. The use of lumped (hard) mirror approximation to determine effective models for cavities with distributed mirrors and analytic expressions for the spontaneous emission rate and factor has been described in a paper by Rajeev Ram (Ram, 1995). In this work we study only paraxial wave reflection on quarter-wave mirror that is applicable to vertical-cavity lasers.

The paraxial reflection operator of a quarter-wave mirror was derived for an infinite lossless mirror (unit reflectivity). Real quarter-wave mirrors have finite numbers of layers and their reflectivity is reduced by absorption loss. The inclusion of all of these other effects into the above formalism would severely complicate the mathematical approach and introduce additional mirror parameters. In subsequent calculation and comparisons between exact and approximate formalism, we show that very good agreement can be obtained with a first order approximation in which the reflection operator (B-104) is simply scaled by the value of the actual peak reflectivity of the quarter-wave mirror. This means that the angular and polarization dependence of $|r_{n1}|$ which is strong for $r_{nic} < 1$, is neglected. The lowest non vanishing order of

$k_\rho$ in the expansion of $|r_m|$ is two. We also use the actual value of the reflection-group delay in (B-89). These corrections for finite mirrors have proven to be very good approximations in the high reflectivity region, which is interesting for VCSELs applications. Numerical calculation of modal reflectivity of finite lossles quarter-wave mirrors performed in this work (Babić, 1993) and by (Ram, 1995) show that the noted approximation provides sufficient accuracy for practical use.

B.9.2. *Free-space modal reflection and its scaling*

The quality factor of open resonators, described in more detail in Appendix C, is directly influenced by the diffraction of electromagnetic waves. These resonators typically exhibit some form of lateral beam shaping that involves either aperturing or spatial beam filtering by finite mirrors. A beam that left an aperture has to eventually enter back though this aperture and reinforce itself in order to continue the oscillation. In this process, some power is lost because if the beam has any chance to propagate unguided it will never come back to itself exactly, there will always be some shape change present and the beam will not couple back into itself with unity coupling coefficient. The topic of this section is discuss the properties of the coupling coefficient of paraxial beams coupling back into themselves after free-space propagation. Inasmuch as we have shown in the previous section that mirror reflection can be modeled as free-space propagation the same characteristics will apply to the coupling coefficient after a reflection from a quarter-wave mirror. This in turn will offer means for treating the diffraction properties of all quarter-wave mirror on equal footing, using a single analytically determined parameter called diffraction range. The diffraction loss arising from non-ideal coupling will be a monotonic

function of the diffraction range and will serve as a means for comparison between mirrors of different wavelengths and optical properties.

Consider a paraxial beam of transverse mode shape $f(\bar{\rho})$ at $z=0$ propagating in $+z$ direction. This beam first propagates over distance $z/2$, then it reflects from a lumped mirror with a fixed phase and reflectivity ($r_h = r_0 \exp(i\phi_0)$, $r_0$ and $\phi_0$ real constants and $0 \le r_0 \le 1$). It travels back over the distance $z/2$, and finally couples back into the original mode shape We evaluate the coupling of the reflected mode into the original mode at $z=0$ by taking reflection coefficient back into itself is given by the overlap integral (Snyder, 1983),

$$\kappa = \frac{\int d^2\rho \; f_R(\bar{\rho}) f^*(\bar{\rho})}{\int d^2\rho \; f(\bar{\rho}) f^*(\bar{\rho})} . \qquad \text{(B-105)}$$

Here the subscript $R$ refers to the reflected field pattern. Using Parseval's theorem and (B-88) the overlap in the frequency domain is given by,

$$\kappa = A r_h \exp(ikz) \int d^2k_\rho |F(\bar{k}_\rho)|^2 \exp(-ik_\rho^2 z/2k) \qquad \text{(B-106)}$$

where

$$A^{-1} = \int d^2k_\rho |F(\bar{k}_\rho)|^2 .$$

For a plane wave at normal incidence all $F(\bar{k}_\rho)$ are zero except for $\bar{k}_\rho = 0$ where the reflection coefficient becomes $\kappa = r_h \exp(ikz)$. It is evident that if we exclude the intrinsic properties of the hard mirror (setting $r_h = 1$), the coupling coefficient depends on two factors: the geometric phase $\exp(ikz)$ and the integral which we write as

$$\kappa_0(\chi) = A\int d^2k_\rho \, |F(\bar{k}_\rho)|^2 \exp(-ik_\rho^2\chi/4\pi) \tag{B-107}$$

The importance of this representation is that for a particular mode pattern $\kappa_0(\chi)$ depends *only* on the normalized variable

$$\chi = \lambda z/n \quad , \tag{B-108}$$

where $n$ is the refractive index of the material through which the mode is propagating and $\lambda$ is the free space wavelength ($k = 2\pi n_i/\lambda$). The dimension of $\chi$ is distance squared. The coupling loss is defined as $\delta(\chi) = 1 - \kappa^*\kappa$. It does not depend on the geometric phase and can therefore always be written as a function of $\chi$.

To take this one step further, consider a set of mode patterns which are scaled versions of each other. If for some characteristic radius $a_0$ the field and its angular spectrum are given by $f_0(\bar{\rho})$ and $F_0(\bar{k}_\rho)$, then for all other modes in this set the field pattern and its angular spectrum are given by $f(\bar{\rho}) = f_0(\bar{\rho}/\gamma)$ and $F(\bar{k}_\rho) = \gamma F_0(\gamma \bar{k}_\rho)$. Since the characteristic radius of any other mode in the set is $a = \gamma a_0$, the coupling coefficient can always be expressed as a function of the Fresnel Number $N = a^2 n/\lambda z$:

$$\kappa_0(N) = A\int d^2k_\rho \, |F_0(\bar{k}_\rho)|^2 \exp\left(-ik_\rho^2 a_0^2/4\pi N\right) \tag{B-109}$$

The power coupling loss is then expressed as $\delta_N(N)$. This property is known as a part of a more general set of *equivalence relations* for spherical mirror resonators (Gordon, 1964). Note that we have used the original definition (Siegman, 1986) of the Fresnel Number arbitrary to a multiplicative constant, whereas in general it depends on the mode and structure geometry (Kogelnik, 1966), (Fox, 1961), (Iga,

1984). Modes of cylindrical dielectric waveguides can not be scaled, unless they are far from cutoff and practically all of the energy is confined in the core (Snyder, 1983). In this case they scale approximately with the waveguide diameter and consequently $\kappa_0$ can be written as a function of the Fresnel Number. (For rectangular waveguides two Fresnel Numbers are needed (Fox, 1961, Vainstein, 1963). Cylindrical metal waveguides and Laguerre-Gaussian beams have scalable mode patterns. For a Gaussian beam, the coupling coefficient can be obtained analytically by solving of the Fresnel-Kirchoff integral in two dimensions. Assuming that the minimum mode waist occurs at $z = 0$ we obtain,

$$\kappa_0(N) = \frac{1}{1 - i/4\pi N} \qquad \delta_N(N) = \frac{1}{1 + (4\pi N)^2} \tag{B-110}$$

where $N = s^2/\chi$ and $s$ is the initial beam waist defined (Iga, 1984) by $E^*E \sim \exp(-r^2/s^2)$.

Fig. B.22 shows the functional behavior of $\delta_N(N)$ for the Gaussian beam and other modes considered in this work. The two lowest order modes of a dielectric waveguide far from cuttoff are denoted with $q$-$\mathrm{TEM}_{00}$ and $q$-$\mathrm{TEM}_{10}$ which approximately corespond to the case of index-guide post VCLs. The mode discrimination of the free-space reflection for q-$\mathrm{TEM}_{00}$ and q-$\mathrm{TEM}_{10}$ modes is approximately a factor of three and their coupling loss is an order of magnitude higher than for a Gaussian beam. The large size of this ratio for a Gaussian is partly a consequence of the Fresnel Number definition used (Iga, 1984). The fundamental mode of the cylindrical metal waveguide is $\mathrm{TE}_{11}$ and as seen in Fig. B.22 it diffracts

very quickly. The reason for this is the presence of the abrupt field variation at the edge of the waveguide. The same situation occurs for the $TM_{01}$ mode. The field pattern of the $TE_{01}$ mode does not have any abrupt changes and hence it diffracts slower. The $TE_{01}$ mode of the metal waveguide is equivalent to the $TE_{01}$ mode of the dielectric waveguide (Snyder, 1983) and can be obtained by the superposition of two q-$TEM_{10}$ modes rotated by $\pi/2$. The metal waveguide mode is, however, more sharply confined to the core. This is the reason why the free-space coupling loss of the $TE_{01}$ mode in Fig. B.22 is only slightly higher than that of the q-$TEM_{10}$ mode. All of the curves show an approximate power law dependence $\delta \sim N^{-\alpha}$ over the region plotted. For the Gaussian beam $\alpha \approx 2$ as seen from (B-110). For q-$TEM_{00}$, q-$TEM_{10}$, and $TE_{01}$ we find $\alpha \approx 3/2$, for $TE_{11}$ and $TM_{01}$ $\alpha \approx 1/2$.

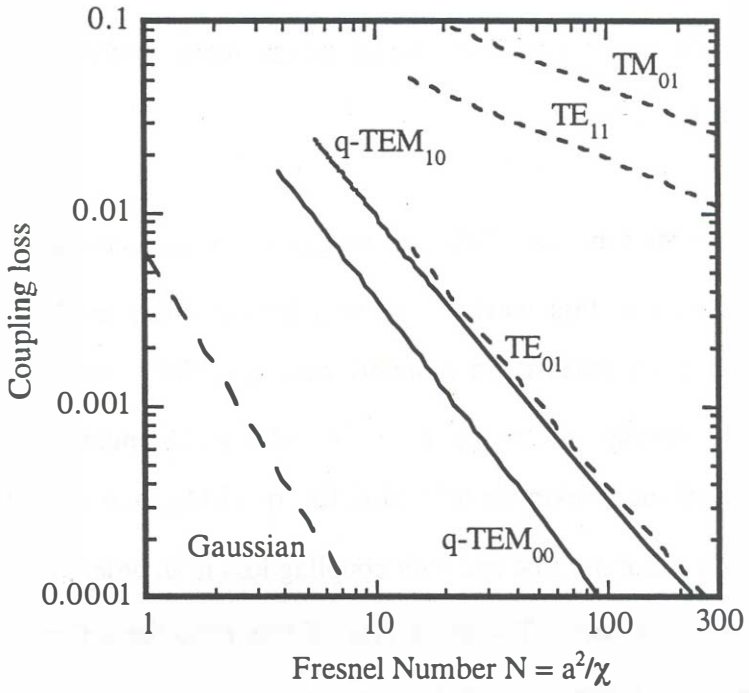


**Fig. B.22**: Coupling loss after free space propagation

For a Gaussian beam, the coupling loss can be expressed analytically by introducing $N_D$ into (B-110):

$$\delta = \frac{1}{1+\left(4\pi\frac{s^2}{\chi_D}\right)^2} \qquad \text{(B-111)}$$

The coupling loss of the dielectric waveguide modes, which are most interesting for this work, is approximately given by

$$\delta_{\mathrm{TEM}_{00}} = \frac{1}{1+7.23N^{1.58}} \quad \delta_{\mathrm{TEM}_{10}} = \frac{1}{1+2.94N^{1.54}} \qquad \text{(B-112)}$$

B.9.3. *Modal reflection on an infinite mirror – diffraction range*

The reflection coupling coefficient for any multilayer structure depends on the rate of diffraction of a particular mode pattern in a homogeneous medium between the reflections and the strength of individual reflections at the multilayer interfaces (considering the polarization as well). In the Fresnel diffraction limit we neglect the polarization dependence of the interface reflections and for an infinitely long lossless DBR we can separate the diffraction and the reflection phenomena by representing $\kappa_{DBR}$ as $\kappa(\chi_D)$. Here $\kappa(\chi)$ is the coupling loss for free space propagation reflected at a unit reflectivity hard mirror located at $z/2 = n\chi/2\lambda$ which, most importantly, depends *only* on the mode shape. The argument $\chi_D$ is called the *diffraction range* of the DBR, and it depends *only* on the optical properties of the mirror and the center wavelength. Therefore, a hard mirror with unit reflectivity positioned at $L_D = n\chi_D/2\lambda$ away from the $S_0$ plane exhibits the same coupling coefficient as the infinite DBR at $z = 0$. The coupling loss is then given by $\delta(\chi_D)$. Since $\delta(\chi)$ is

monotonic in $\chi$, the diffraction range $\chi_D$ is a useful quantity in comparing different DBR mirrors independently of the mode shape and the wavelength. If the mode shape is scalable, $\chi_D$ can be replaced by the Fresnel Number and the coupling loss written as $\delta_N(N_D)$. in (B-89). By normalizing the round trip $2L_D$ as in (B-108), we obtain the diffraction range of the DBR:

$$\chi_D = \frac{2\lambda L_D}{n_i} = \frac{\lambda\lambda_c}{4}\left(\frac{1}{n_L^2}+\frac{1}{n_H^2}\right)\frac{q}{1-p}. \qquad \text{(B-113)}$$

Here $\lambda$ is the free space wavelength of the beam, while $\lambda_c$ is the center (free-space) wavelength of the DBR. By combining (B-88) and (B-89) we can determine the coupling coefficient at an arbitrary location in front of the mirror $z_a$ by using $\tilde{\boldsymbol{R}} = \tilde{\boldsymbol{T}}(z_a)\tilde{\boldsymbol{R}}_{DBR}\tilde{\boldsymbol{T}}(z_a)$. The usefulness of $\chi_D$ lies in the fact that it is a single parameter that characterizes the mirror diffraction to first order. It can therefore be used for quick analytic estimates and comparisons between different DBR structures. Since the expression of $\chi_D$ is analytic it also provides insight in the sensitivity of the coupling loss to various mirror parameters. If we denote the maximum reflectivity of an $m$-layer mirror by $R_m$, then the maximum possible coupling magnitude is approximately given by $R_m^{(\text{modal})} \cong R_m |\kappa(\chi_D)|^2$. This is a very good approximation in the high reflectivity region of DBRs, which is interesting for VCSELs applications.

Before we conclude this section, it will be useful to illustrate how to use the knowledge of $\chi_D$ to evaluate the coupling loss and compare different mirrors. First, in designing mirrors to be used with no lateral guiding (as index-guided post devices Figure 5.1) the goal should be to minimize the distance of unguided propagation and minimize the diffraction range $\chi_D$, since this implies minimum coupling loss.

Second, to determine the actual coupling loss of a particular mirror structure one must know the shape of the mode that will be incident on this structure. With the known mode pattern and using a suitable numerical or analytic calculation we can determine the free-space propagation coupling loss $\delta$ as a function of $\chi$ (Equation (B-105)). We then evaluate this function at $\chi_D$ and to obtain the coupling loss for the DBR.

Consider a beam launched from a dielectric waveguide that propagates for some distance equal to $L/2$ before it reflects on a mirror with reflectivity $R$ and diffraction range $\chi_D$. The beam propagates back another distance $L/2$ and then couples back into the waveguide. The coupling loss for the fundamental mode is approximately given by (B-114) with $N = a^2/\chi$ and $\chi = \lambda L/n + \chi_D$. For a Gaussian mode the coupling loss is expresses analytically and hence one can directly introduce $\chi$ or $\chi_D$ into (B-111). The coupling of a Gaussian beam after reflection on a AlA/GaAs mirror was calculated by (Frateschi, 1995) using scalar beam propagation, and shows excellent agreement with the analytic expression (B-111).

## B.10. *Conclusion and future work*

Due to their periodicity and the possibility of exact treatment, the properties of quarter-wave mirrors possess numerous peculiarities. The topic of this chapter was to address some of these characteristics which are pertinent for the design and use of small surface-normal optoelectronic devices, and also to provide a different perspective on the physics involved. Future work in this field would include 1) the determination of approximate analytic expressions for the increase in mirror dispersion around the center wavelength, 2) the behavior of the reflectivity as a function of the angle, and 3) the reduction of reflectivity due to rough interfaces. The introduction of polarization dependence in the diffraction characteristics is also a topic of interest.

# Appendix C

# Resonators with distributed mirrors

The operation of semiconductor lasers is determined by the efficiency of the electron/hole supply, the interaction between light and charge carriers, and subsequent extraction of light from the cavity. To maximize that interaction, the starting point of any laser design is the realization of a good overlap between the gain and the electric field. In a vertical-cavity laser the critical optical design issues involve producing a high quality resonator in which the electromagnetic field oscillates in the direction perpendicular to the wafer surface. The primary concern of electrical design is the efficient delivery of electrons and holes to the gain region and their subsequent confinement at that location to recombine radiatively. An efficient thermal design implies effective dissipation of heat generated from the electrical resistance and the non-radiative recombination in the laser.

The mathematical modeling of the VCL operation is a very complex problem because it involves the interaction of a wide range of physical phenomena. Optical, electrical and thermal properties of materials and structures have to be considered in a self-consistent solution to provide a complete model of the laser's operation. There have been numerous studies reported in literature that describe such modeling

(Fox example, Scott, 1993, Shimizu, 1991, Piprek, 1996). No such complete solution is attempted in this work, but rather a survey of important factors determining the laser's performance is given.

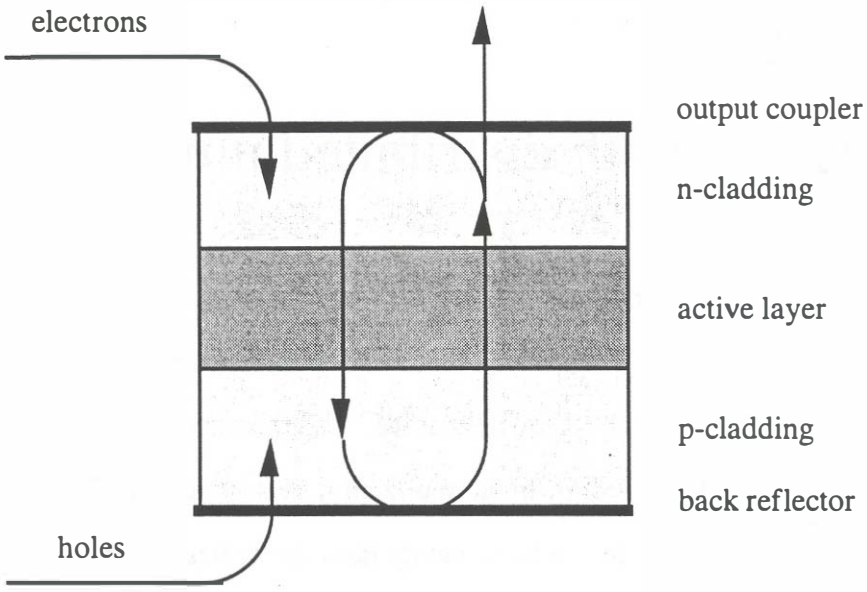


**Fig. C.1**: Schematic illustration of a vertical-cavity laser.

The VCL mirrors are flat multilayer coatings with high reflection coefficients fabricated from semiconductor or insulating amorphous materials. The laser cavity, shown schematically in Figure C.1, is in most cases fabricated by planar epitaxial growth and consists of the *active layer*, which produces optical gain when holes and electrons recombine in it, and *cladding layers* which are used to confine the carriers in the active layer and through which the carriers are supplied. The fundamental transverse-mode electric-field pattern, shown in Figure C.2, is at maximum in the center of the cavity and therefore efficient interaction of light and charge interaction requires lateral carrier and current confinement. The active layers are realized as

either bulk semiconductor or multiple quantum-well structures with the lowest transition being near the desired oscillation wavelength of the laser. The electron and hole confinement is achieved by using barriers provided by heterojunctions at the interface between the cladding and the active layer or by multi-quantum well barriers.

In order to maximize the overlap between the charge and the electromagnetic field, one must first consider the effects that determine the shape of the oscillating modes in a VCL and then the type of charge supply and confinement that can be realized in conjunction with the particular optical confinement scheme.

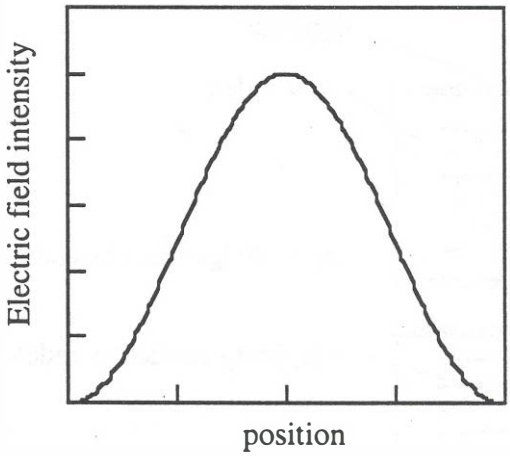


**Fig. C.2**: Lateral electric field intensity variation for the fundamental mode in the cavity shown in Fig. C.1.

The determination of oscillating modes in a real vertical-cavity laser is quite complex since it involves the solution of three-dimensional open resonator problems which also may include non-linear effects such as non-uniform current injection,

spatial hole burning, and/or gain guiding. It is however, possible to separate VCL structures by the dominant type of transverse-mode defining scheme. These categories are shown in Figure C.3 and are (a) index guiding, (b) gain guiding or (c) aperturing. The horizontal lines in the figure illustrate the approximate shape of the phase fronts. Only in an index guided resonator shown in case (a) are the phase fronts approximately flat. In the case (b) and (c) the light beam is not laterally guided and freely diffracts, leading to curved phase fronts. In real vertical-cavity lasers, the mechanism of gain-guiding is by far more complex than what can be inferred from using an imaginary refractive index: It also involves index guiding, arising from the change of the refractive index due to temperature and carrier concentration. These are in turn strong functions of the electrical current and light intensity.

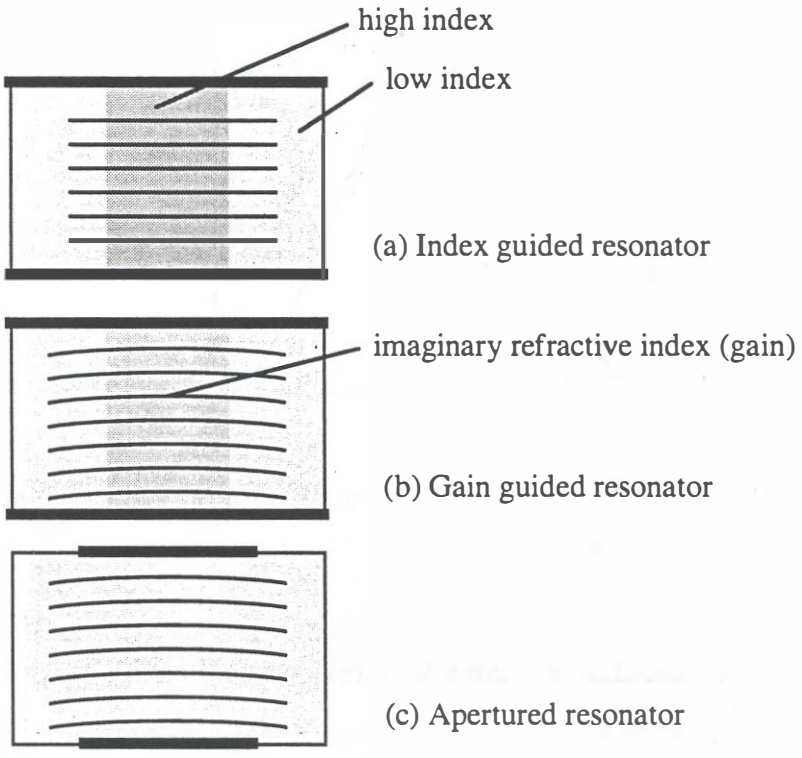


**Fig. C.3**: Three mode defining schemes in vertical-cavity lasers.

In a gain-guided laser the lateral placement and size of the gain region has a strong effect on the mode shape. In index guided and apertured resonators, the mode defining mechanism is typically stronger than the perturbation introduced by the lateral extent of the gain region. This effect can then be used to independently define the transverse modes and the gain they experience from a suitably positioned active layer (Moriki, 1987). In all of the mentioned cases the current may be injected through the mirrors, in which case the mirrors have to be conductive, or if the mirrors are insulating, the current has to be supplied from the side. Whether the laser mirrors are conductive or insulating is probably the most significant fact influencing the vertical-cavity laser structure, as shown in Figure C.4. This is primarily due to the fact that in cavities with insulating mirrors the lateral current flow requires ring contacts and potentially leads to higher resistance to conduct the current to the active layer. Furthermore, the cavity length has to be large enough to allow for lateral current paths. With conductive mirrors there is no limit to the length of the cavity other than the lasing wavelength. Short cavity length is necessary to minimize absorption and diffraction losses. The overlap between the electric field intensity and the gain region depends on the spatial profile of both the field intensity and the gain distribution. The fundamental transverse mode has a peak in the center of the cavity, while the shape of the gain profile is a strong function of the current injection scheme and the position dependent recombination. The gain profile may exhibit a minimum at the edges caused by surface recombination, or a minimum in the center, caused by spatial hole burning or non-uniform current injection (Scott, 1993, Wada, 1992, Shimizu, 1990). The problems arising from non-uniform injection are not only limited to poor gain overlap and

providing more gain to higher order modes, but with higher resistance and heating arising from current crowding.

There are number of lateral current confinement schemes that have been investigated up to date. They include, a) wet chemical undercutting of the active layer (Wada, 1991, Dudley, 1994) or a layer above the active layer introduced for this purpose (Scott, 1993, Chapter 8), b) lateral oxidation of AlAs as a confining layer (Choquette, 1995), c) regrowth of insulating Fe:InP semiconductors (Baba, 1993), and d) insulating hydrogen or helium implantation. The use of a current confining scheme is closely related to the type of mirrors used in the cavity.

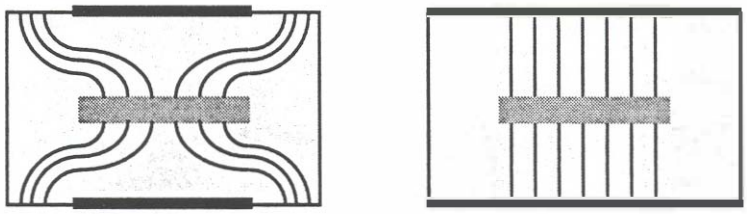

(a) current injected around the mirrors

(b) current injected through the mirrors

**Fig. C.4**: Vertical-cavity laser structures with conductive and insulating mirrors

The heating of the device due to resistances and/or non-radiative recombination during continuous wave operation sets up a temperature profile in the device. This influences the operation of the laser in several ways: As the temperature increases, both the peak gain value and the peak wavelength decrease. This occurs because of the changes in the tails of the Fermi-Dirac probability distributions and the lattice

expansion with temperature. Furthermore, Auger recombination which is a dominant source of non-radiative recombination in long-wavelength lasers increases with temperature. In unguided portions of the vertical-cavity laser the temperature distribution, which typically exhibits a strong peak in the center of the device, produces a lateral index variation and effectively forms a waveguide. This effect, known as, thermal lensing, helps guiding and reduces diffraction losses, but is difficult to control since it depends on the device pumping and power dissipation.

The analysis of vertical-cavity lasers will here be separated into *axial* and *radial* design. The axial design deals with the issues that related to plane wave propagation in the cavity: design of mirrors, active layers, cavity absorption, standing wave pattern, and the charge confinement scheme. The radial design deals with the transverse mode definition, current confinement scheme, and other three dimensional issues, such as thermal and electrical resistance. Only optical properties are considered in this Appendix.

## C.1. *Axial design*

In this section we shall first examine the threshold condition for gain and wavelength, and the external differential quantum efficiency for a simplified Fabry-Perot cavity with two different mirrors. We then extend the discussion to real VCL cavities which involve multilayer structures and non-zero thickness gain regions.

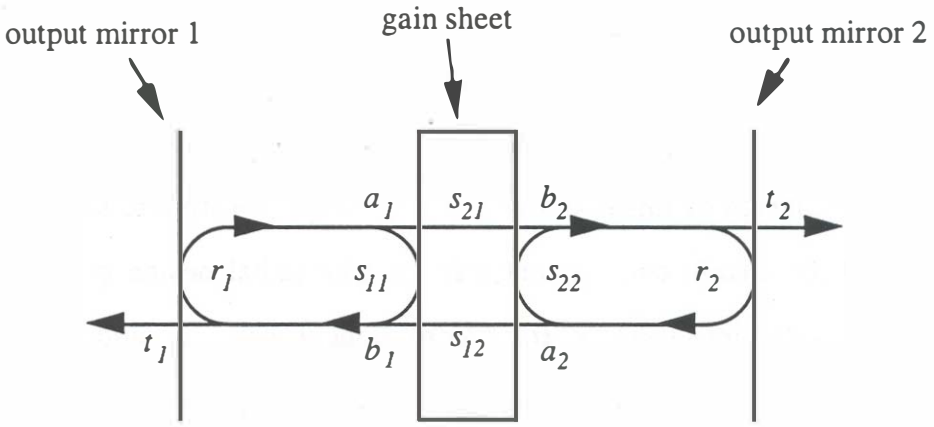


**Fig. C.5**: One-dimensional Fabry-Perot resonator with a gain sheet.

### *C.1.1. Threshold of a classical planar resonator*

Consider a Fabry-Perot resonator shown in Figure C.5. The gain region is vanishingly thin and the two mirrors are different. The sheet gain is represented as a layer with negative conductance $\delta$. The transverse electric fields are continuous across this sheet, while the magnetic fields have a discontinuity proportional to the gain value, as

$$\begin{bmatrix} E_1^t \\ \eta_0 H_1^t \end{bmatrix} = \begin{bmatrix} 1 & 0 \\ \delta & 1 \end{bmatrix} \begin{bmatrix} E_2^t \\ \eta_0 H_2^t \end{bmatrix} \qquad \text{(C-1)}$$

The gain medium is described with $s$-parameters as follows,

$$\begin{bmatrix} b_1 \\ b_2 \end{bmatrix} = \frac{1}{1-\gamma} \begin{bmatrix} \gamma & 1 \\ 1 & \gamma \end{bmatrix} \begin{bmatrix} a_1 \\ a_2 \end{bmatrix} \qquad \text{(C-2)}$$

where $\gamma = \delta/2n$ and $n$ is the cavity refractive index. The phase that the light acquires in traversing the free-space distances between the gain and the mirrors are included into the complex mirror reflectivities. Using the mirror complex reflectivities $a_1 = r_1 b_1$ and $a_2 = r_2 b_2$, we obtain resonator equations:

$$b_1 = \frac{\gamma r_1 b_1}{1-\gamma} + \frac{r_2 b_2}{1-\gamma} \quad b_2 = \frac{r_1 b_1}{1-\gamma} + \frac{\gamma r_2 b_2}{1-\gamma} \qquad \text{(C-3)}$$

subtracting these two equations we get $b_1(1+r_1) = b_2(1+r_2)$. At threshold, all of the fields can be determined from any single field amplitude, but for the sake of symmetry we use a new *symmetric* field amplitude $\Phi = b_1(1+r_1) = b_2(1+r_2)$. To determine the threshold condition for this resonator we find the denominator of the resonator transmission and set it to zero. The threshold condition is,

$$\gamma = \frac{1-r_1 r_2}{(1+r_1)(1+r_2)} \,. \qquad \text{(C-4)}$$

We require that the gain value is always real. Since the reflectivities are generally complex, we have to adjust the cavity length or any one complex reflectivity to make the gain real. To emphasize this we write the threshold gain as

$$1+\gamma = \frac{1}{1+r_1} + \frac{1}{1+r_2} \qquad \text{(C-5)}$$

and require that the imaginary part of the right side of the equation must be zero.

$$\mathrm{Im}\left(\frac{1}{1+r_1}\right)+\mathrm{Im}\left(\frac{1}{1+r_2}\right)=0 \qquad \text{(C-6)}$$

In the case of arbitrary complex reflectivities this leads to a complicated, but explicitly solvable equation.

The power that is dissipated in the gain sheet comes from the excess current above threshold:

$$P_d=\eta_i\eta_{ph}\frac{\hbar\omega}{q}(I-I_{th}), \qquad \text{(C-7)}$$

where $\eta_i$ is the injection efficiency and $\eta_{ph}$ the *photon efficiency* . The photon efficiency of port 1 is given as the ratio $\eta_{ph}^{(1)}=\Delta P_1/\Delta P_d$. The relationship between the power dissipated in the active layer $P_d$ and the powers outputted from each mirror, $P_1$ and $P_2$ can be written as

$$P_d=(1-R_1)|b_1|^2+(1-R_2)|b_2|^2 \quad P_1=T_1|b_1|^2 \quad P_2=T_2|b_2|^2 \qquad \text{(C-8)}$$

where $R_i=|r_i|^2$ and $T_i=|t_i|^2$. Note that in general, the output mirrors are lossy so $R_i+T_i<1$. Expressing the field amplitudes in terms of $\Phi$ we have

$$\frac{P_d}{|\Phi|^2}=\frac{1-R_1}{|1+r_1|^2}+\frac{1-R_2}{|1+r_2|^2} \quad \frac{P_1}{|\Phi|^2}=\frac{T_1}{|1+r_1|^2} \quad \frac{P_2}{|\Phi|^2}=\frac{T_2}{|1+r_2|^2} \qquad \text{(C-9)}$$

The final expression for $\eta_{ph}^{(1)}$ is

$$\eta_{ph}^{(1)}=\frac{T_1}{|1+r_1|^2}\cdot\frac{1}{\frac{1-R_1}{|1+r_1|^2}+\frac{1-R_2}{|1+r_2|^2}} \qquad \text{(C-10)}$$

where the efficiency from the other port is obtained by cycling the port index. The photon efficiency depends on the phases of $r_1$ and $r_2$ because the interaction with

the gain medium depends on the standing wave pattern. If in addition $r_1$ and $r_2$ are different, the power gain will be different for the forward or backward propagating wave. To simplify this expression, let us assume that the active layer is positioned optimally – exactly at the peak of the standing wave. If the cavity is more than one half-wavelength long, there will be more than one location to place the active layer. In each of these cases, both $r_1$ and $r_2$ will be real and positive and the photon efficiency will always be given by

$$\eta_{ph}^{(1)} = \frac{1}{2}\frac{T_1}{1-r_1 r_2}\cdot\frac{1+r_2}{1+r_1}. \qquad \text{(C-11)}$$

In vertical-cavity lasers, the reflectivities of the two mirrors are very close to unity and hence $1+r_1 \cong 1+r_2 \cong 2$. The photon efficiency becomes,

$$\eta_{ph}^{(1)} = \frac{1}{2}\frac{T_1}{1-r_1 r_2} \qquad \text{(C-12)}$$

This also means that the power gain seen by the forward and the backward traveling waves is very close to being equal.

We shall now use this fact to our advantage to derive (approximate) expressions for gain and gain enhancement factor that are commonly used in the analysis of vertical-cavity lasers. We start the analysis with a slightly different gain region $s$-parameter matrix (C-2). We keep the gain region at the standing wave peak, and hence both reflectivities are real, positive and very close to unity. The field $b_2$ consists of two parts: The transmitted $a_1$ and the reflected $a_2$ field, $b_2 = a_1/(1-\gamma) + a_2\gamma/(1-\gamma)$. Since $a_1$ and $a_2$ approximately equal, we shall simplify the matrix by replacing $a_1$ field with $a_2$ and obtain $b_2 = a_1(1+\gamma)/(1-\gamma)$.

This replacement simplifies the mathematics and still keeps the track of the gain enhancement. The s-parameter matrix is now,

$$\begin{bmatrix} b_1 \\ b_2 \end{bmatrix} = \frac{1+\gamma}{1-\gamma}\begin{bmatrix} 0 & 1 \\ 1 & 0 \end{bmatrix}\begin{bmatrix} a_1 \\ a_2 \end{bmatrix} \tag{C-13}$$

and the threshold gain is given by

$$\gamma = \frac{1-\sqrt{r_1 r_2}}{1+\sqrt{r_1 r_2}} \tag{C-14}$$

The photon efficieny from port 1 is given by

$$\eta_{ex}^{(1)} = \frac{T_1}{1-r_1 r_2} \cdot \frac{r_2}{(r_1+r_2)} \tag{C-15}$$

Now let us compare expressions (C-11) and (C-15) with the expression that is commonly used for in-plane lasers. In in-plane lasers the gain medium extends through the cavity and the gain reflections are effectively included into the mirror reflectivities. Furthermore, the reflectivities are real and can be very different. To model this, we neglect the reflections at the gain sheet described by the matrix (C-2) and (C-13) and obtain $s$-parameter matrix,

$$\begin{bmatrix} b_1 \\ b_2 \end{bmatrix} = \frac{1}{1-\gamma}\begin{bmatrix} 0 & 1 \\ 1 & 0 \end{bmatrix}\begin{bmatrix} a_1 \\ a_2 \end{bmatrix} \tag{C-16}$$

The threshold of this resonator is

$$\gamma = 1-\sqrt{r_1 r_2} \tag{C-17}$$

while the photon efficiency now takes the form,

$$\eta_{ph}^{(1)} = \frac{T_1}{1-R_1}\frac{1}{1+\frac{\sqrt{R_1}}{\sqrt{R_2}}\left(\frac{1-R_2}{1-R_1}\right)} \tag{C-18}$$

which is *exactly* expression (C-15). Compare now expressions (C-11) and (C-15). The difference occurs from the exclusion of the reflections at the gain sheet. Since in in-plane lasers the two mirror reflectivities can be very different (using coatings), the ratio $r_2/(r_1+r_2)$ in the expression for $\eta_{ph}^{(1)}$ (C-15) can be substantially different from 1/2. In vertical-cavity lasers, $r_1 \equiv r_2 \equiv 1$ and hence (C-11) and (C-15) lead to practically identical values of photon efficiencies. Therefore, for vertical-cavity lasers the expression (C-12) provides the most accurate estimate of $\eta_{ph}$. The error in using this expression is smaller than the error made by neglecting multiple reflections at the active layer and claddings. To solve for the photon efficiency exactly we need to use the transverse field matrix method (Appendix A). Let us look at some other simple situations involving vertical-cavity lasers. If the resonator is symmetric $r_1 = r_2 = r$ and we have $\eta_{ex} = T/(1-R)/2$ for a single mirror in both cases. If in addition the output mirrors are not lossy we have $\eta_{ex}^{(1)} = 1/2$. If $r_2 = 1$, the output efficiency of the other port is $\eta_{ex}^{(1)} = T_1/(1-R_1)$.

Consider now the case in which the cavity medium has a small absorption coefficient $\alpha$. The absorption coefficient is sufficiently small so it does not perturb the fields in the cavity. The reflectivity of the mirrors is reduced by approximately, $r_1 \rightarrow r_1 \exp(-\alpha L_1)$, where $L_1$ is the distance between the mirror 1 and the gain region. Introducing this into (C-12) we have

$$\eta_{ph}^{(1)} = \frac{1}{2}\frac{T_1}{1-\exp\{\ln(r_1 r_2) - \alpha L\}} \qquad \text{(C-19)}$$

where $L = L_1 + L_2$ is the total cavity length. Considering that the losses are small and that the reflectivities are close to unity we may use the expansion $\exp(x) \approx 1 + x$ for small $x$, and obtain

$$\eta_{ph}^{(1)} = \frac{T_1}{2\alpha L - \ln(R_1 R_2)} \qquad \text{(C-20)}$$

which is a well known expression for the photon efficiency and can be summarized in words as

$$\eta_{ph} \cong \frac{\text{Port transmission}}{\text{Round trip loss}} \qquad \text{(C-21)}$$

Consider now the threshold phase condition (C-5) or (C-6): If the gain sheet is located at the standing wave peak, both $r_1$ and $r_2$ have to be real and positive to provide constructive interference at the gain location. Lets look at what happens when the gain medium is shifted towards one of the mirrors. The position change can be simulated by a phase change in the reflectivities: While the phase of one mirror increases, the other decreases. The exact relationship between the two phases has to be determined from equation (C-6), because the threshold condition has to be satisfied at all times. This problem is tractable, but quite cumbersome to do analytically. To illustrate the effect of gain enhancement we can simplify the mathematics by making the resonator symmetric. In this case the two mirror reflectivities will be replaced with $r_1 = r\exp(i\phi)$ and $r_2 = r\exp(-i\phi)$, where the shift of the gain sheet from the center is expressed in terms of the phase of the propagating light. With these assumptions the threshold phase condition (C-6) is always satisfied and the threshold gain equals

$$\gamma = \frac{1-r}{1+r} \cdot \frac{1}{1 - \frac{4r}{(1+r)^2}\sin^2(\phi/2)} \qquad \text{(C-22)}$$

Evidently, as the gain sheet moves it changes the interaction strength between the gain and the electromagnetic field. The functional dependence of equation (C-22) is illustrated in Figure C.6.

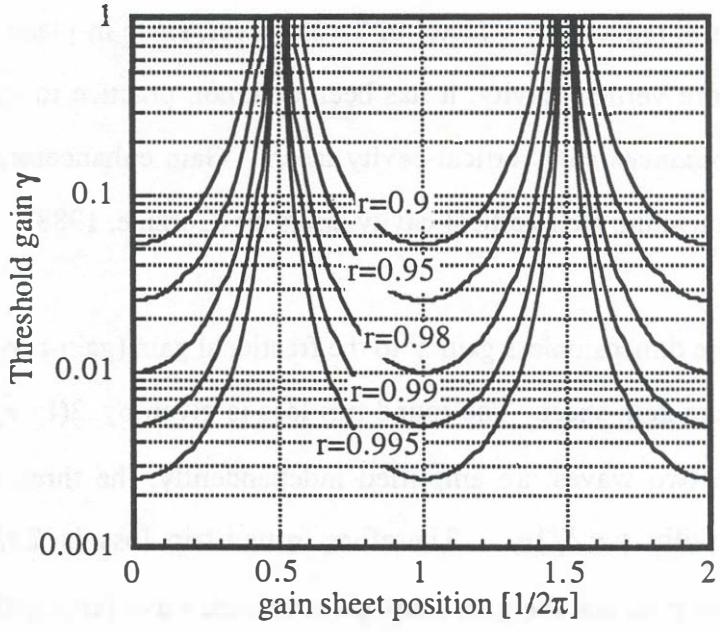


**Fig. C.6**: Threshold gain dependence on the position of the gain sheet in the cavity.

Now we can compare the expressions for threshold gain derived for both VCLs and in-plane lasers. The three expressions are (C-4), (C-14), and (C-17). For vertical-cavity lasers, where the mirror reflectivities are real, positive and close to unity expressions (C-4), (C-14) give approximately equal gain $\gamma \cong (1 - r_1 r_2)/4$, while (C-17) leads to twice larger gain $\gamma \cong (1 - r_1 r_2)/2$. This discrepancy is a result of neglecting the effect of the standing wave in the cavity. In in-plane lasers the gain medium is very long compared to the wavelength of light in the laser and hence encompassed a large number of standing waves. Since the standing wave oscillates

between zero and maximum with an approximate functional dependence of $\sin^2 x$, the interaction with the gain medium is averaged to 1/2. In vertical-cavity laser, the gain medium can be placed exactly at the peak of the standing wave and hence the interaction is maximized. One may say then that, due to averaging, the usable gain in in-plane lasers is reduced by a factor of 2. However, since in-plane lasers were investigated before vertical-cavity, it has been common practice to speak of this effect as *gain enhancement* vertical-cavity lasers. Gain enhancement has been investigated for quantum well vertical-cavity lasers by (Corzine, 1988).

We shall relate the dimensionless gain $\gamma$ to the fractional gain (gain-per-pass) given to the wave by the gain sheet. The round-trip loss is given by $2(1-r_1r_2)$ and we know that when two waves are amplified independently, the threshold gain is $\gamma \cong (1-r_1r_2)/2$ with $\gamma = \delta/2n$. Therefore, round-trip loss is $2\delta/n$ and the fractional gain per pass that the gain sheet gives to each wave propagating through is equal to $\delta/n$. If the gain sheet was a quantum well of thickness $L$, then the gain is $g = \delta/nL$, where $nL$ is the optical thickness of the gain medium.

C.1.2. *Planar vertical-cavity resonator analysis*

The relations derived in Section C.1.1 are exact, but they were developed for an idealized classical resonator with an infinitely thin sheet gain. Real VCL resonators have gain sheets of finite thickness which may be comparable or even larger than the wavelength. Furthermore, the resonators are constructed with a large number of layers with different refractive indexes and loss coefficients. This introduces numerous reflections in the cavity which can be treated exactly, but is very

cumbersome to do by hand. Computer programs, based on transmission (Yeh, 1988) or transverse field (Appendix A) matrices, are used for this purpose. Satisfying the threshold condition requires finding both the value of gain for which the transmission diverges and the wavelength for which the round trip phase is an integer multiple of $2\pi$. An infinite transmission coefficient implies that with a finite input, the resonator delivers infinite output. This is equivalent to the classical definition of threshold which says that with an infinitesimal input, in the form of spontaneous emission, the output increases without bounds until it becomes limited by the charge supply. The refractive index profiles and associated standing wave patterns of three different structures used for long-wavelength vertical-cavity lasers are shown in Figures C.7--C.9. (All of the structures are shown with a quantum well active layer). It is seen that in all of the structures the active layer is positioned exactly at the peak of the electric field intensity.

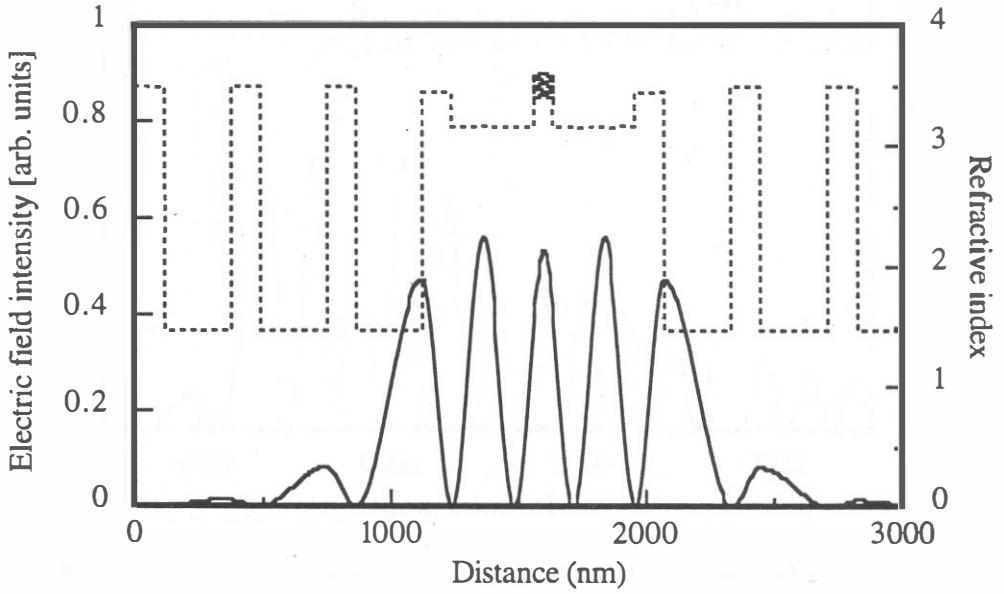


**Fig. C.7** Standing-wave pattern in an etched-well vertical-cavity laser with two $Si/SiO_2$ mirrors.

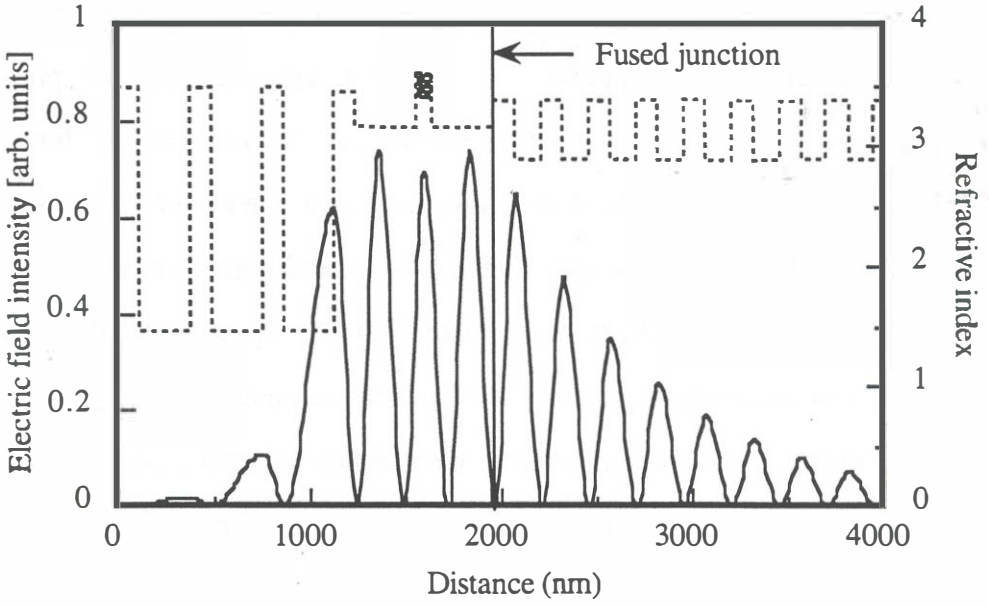


**Fig. C.8**: Standing-wave pattern of a single-fused vertical-cavity laser with one AlAs/GaAs and one $Si/SiO_2$ mirror.

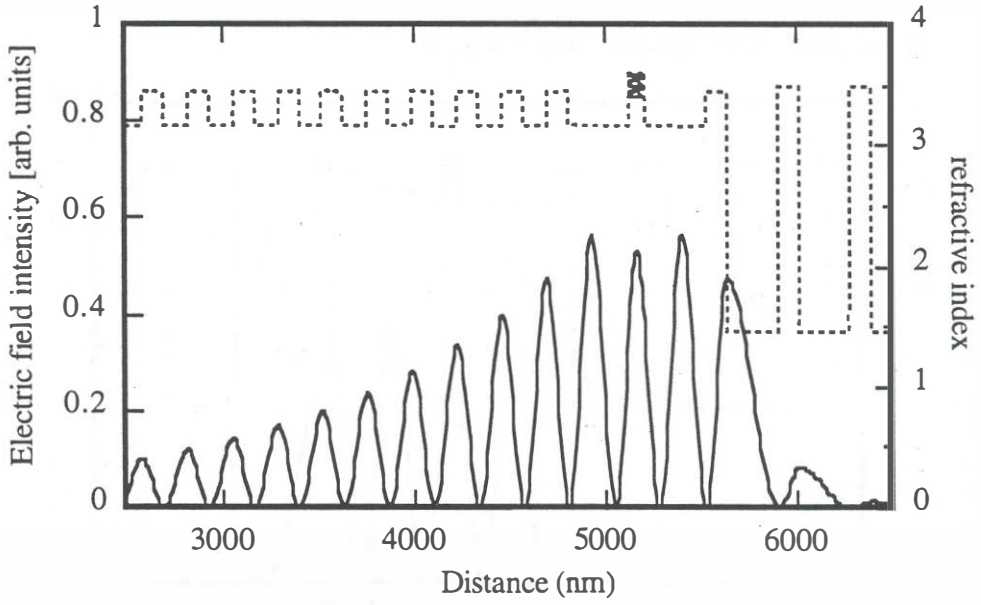


**Fig. C.9**: Standing wave pattern in a vertical-cavity laser with one $Si/SiO_2$ and one InGaAsP/InP mirror.

The etched-well structure, shown in Figure C.7, uses $Si/SiO_2$ or similar amorphous mirrors on both sides of the resonator. The field intensity falls of very rapidly in these mirrors due to the large refractive index ratio. Since amorphous silicon is lossy it is advantageous to start the mirror with silicon oxide because it has a lower absorption coefficient than silicon.

It can be shown using the analytic expressions for peak reflectivity of lossy mirrors derived in Appendix B, that for a given amount of loss in one of the layers the order in which the layers are deposited may make a substantial difference in the reflectivity. The fact that the gain region has to placed at the peak of the electric field pattern to maximize the interaction with the electromagnetic radiation in the cavity, one desires to minimize the effect of any lossy layers on the cavity quality factor. For this reason, one places the lossy layers at the nodes of the standing wave. The best examples are placing rough interfaces or interfaces with high absorption at the nodes of the standing wave patterns. This is a common technique in engineering of doped epitaxial mirrors where for the reduction of electrical resistance the heterojunction interfaces have to be doped heavily to reduce the voltage drop across the mirror. In fused vertical-cavity lasers, the fused-heterojunction may contain voids or other sources of scattering; it may also be the site of increased absorption. Therefore, it is advantageous to place the fused junction at the node of the standing wave pattern. This has been the practice in all of the fused vertical-cavity lasers reported in this work. Figure C.8 shows the refractive index and the standing wave pattern of a single-fused vertical-cavity laser that uses one AlAs/GaAs mirror and one Si/SiO2 mirror. Except for the quantum-well active layer and a thinner first GaAs layer, the index profile corresponds to the single-

fused VCL fabricated by (Dudley, 1994). Here one can also note that the fused junction has been placed at the node of the standing wave. The last index profile corresponds to a structure that uses one InGaAsP/InP and one $Si/SiO_2$ mirror. The energy fall-off in the InP mirrors is quite slow due to the small refractive index difference. The index profiles of the fabricated double-fused VCLs were discussed in Chapter 4.

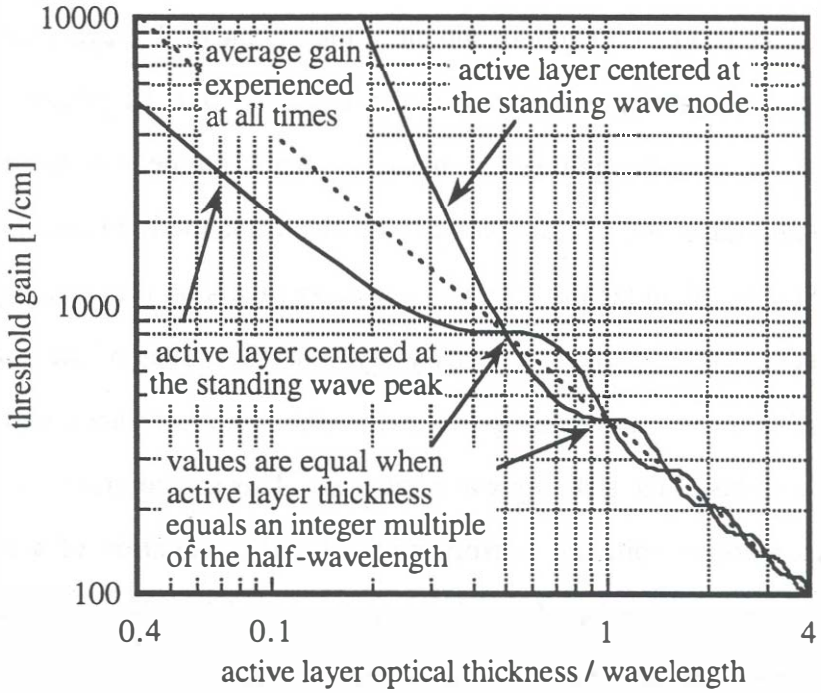


**Fig. C.10**: Threshold gain vs. active layer thickness.

As shown in the previous section, when the active layer thickness becomes small in comparison with the wavelength, the location of the active layer in respect to the standing wave pattern becomes critical. As the thickness of the active layer is increased the layer encompasses more of the standing wave pattern and eventually

experiences an averaged gain value. The functional dependence of the threshold gain for a simple Fabry-Perot cavity with the active layer placed at the node and at the peak of the standing wave pattern is shown in Figure C.10. The cavity is symmetric and the mean power reflectivity of the mirrors is 98%. Extrapolated to zero thickness gain region, the average gain becomes approximately twice the value a thin gain region would experience at the same place.

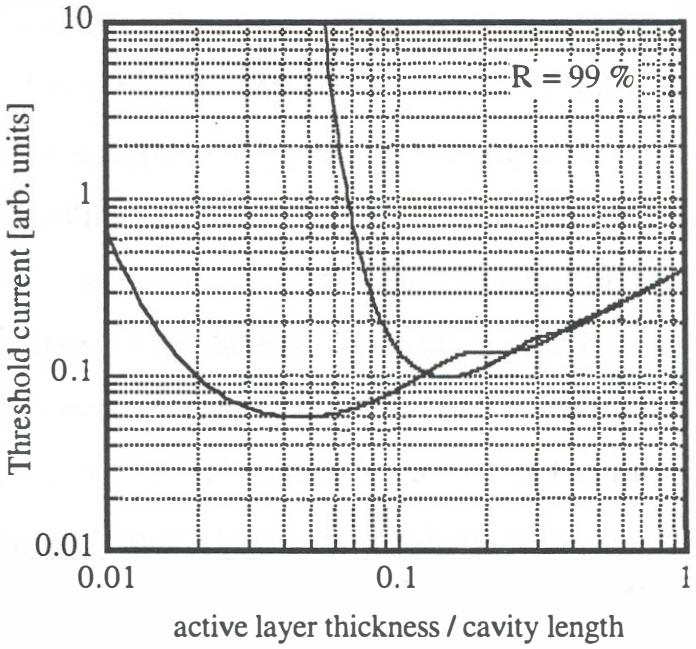


**Fig. C.11**: Functional dependence of threshold current as a function of the active layer thickness for a given reflectivity.

From Figure C.10 it may seem that with the increasing active layer thickness one can also reduce the threshold current to arbitrary low values. However, the threshold current does not follow the functional behavior of the threshold gain because the volume of the gain region increases when the active layer thickness increases. Furthermore, due to non-radiative recombination and gain saturation the

gain–current relationship is sub-linear. One can illustrate the typical behavior of the threshold current as a function of the active layer size by assumes a sub-linear material gain dependence as $g(J) = g_0 \ln(J/J_0)$, where $g_0$ and $J_0$ are fitting parameters. A qualitative dependence of the threshold current on the active layer thickness is shown in Figure C.11. There always exists an optimum active layer thickness which gives lowest threshold current. The increase of threshold current for smaller than optimal values is very sharp, while for larger values of active layer thicknesses the threshold current increases more-or-less linearly. It is evident from here, that if the cavity loss is not precisely known, it is always better to make the active layer thick. The drawbacks of this method is the possible nonuniformity of the carrier profile in the active layer. The electron and hole diffusion lengths may be very short in materials with high non-radiative recombination, such as, long-wavelength InGaAsP material. Furthermore, as the laser is biased to higher powers the stimulated emission lifetime drops further reducing the carrier diffusion length. When the carrier diffusion length becomes compared to the thickness of the active layer the distribution of carriers in the active layer (bulk or multi-quantum well) becomes non-uniform in the axial direction. This again results in lower gain at given current. The non-uniformity on injected carrier distributions have been investigated in connection with high-power PIN diodes (Ghandi, 1977).

### C.1.3. *Threshold gain and mode positions*

The calculations of threshold gain presented in Section C.1.2. have been performed exactly using the transverse field matrix method described in Appendix A. The

threshold gain and the lasing wavelength was solved using a suitable searching technique.

An important feature of the index profiles shown in Figures C.7–C.9 is the fact that all the layers in involved are adjusted so the reflections at their mutual interfaces increase the cavity finesse. This means that each of the layers, with the exception of the active layer and the neighboring cladding, is an odd integer multiple of quarter-wavelength thick. The thickness of the active layer (and the cladding) is determined by the number of quantum wells and the round trip cavity loss. The sum of the active layer and the cladding optical thicknesses has to equal to an integer multiple of quarter-wavelength at the lasing wavelength. Based on this observation we divide the laser resonator into separate sections, each of which will be approximately treated depending on their primary function. The resonator is divided into two mirrors and the cavity: The distributed mirror will be replaced with a lumped mirror according to the approximations described in Appendix B, while the remainder of the cavity is simplified by ignoring any spurious reflections at the cladding/active region or any other interfaces. The problem with these reflections is that they are not always in phase with the mirror reflections and they slightly alter the cavity resonance and the gain and is correctly accounted for in the exact calculations presented in the previous section. Since the cavity is fabricated using a single epitaxial technique where the refractive index variations are not very large, the reflections at these interfaces are weak in comparison with the reflectivity of the mirror. More importantly, the error made by ignoring is them less than the uncertainty one has in all other cavity parameters. We process now to determine the threshold gain and resonance of this simplified cavity.

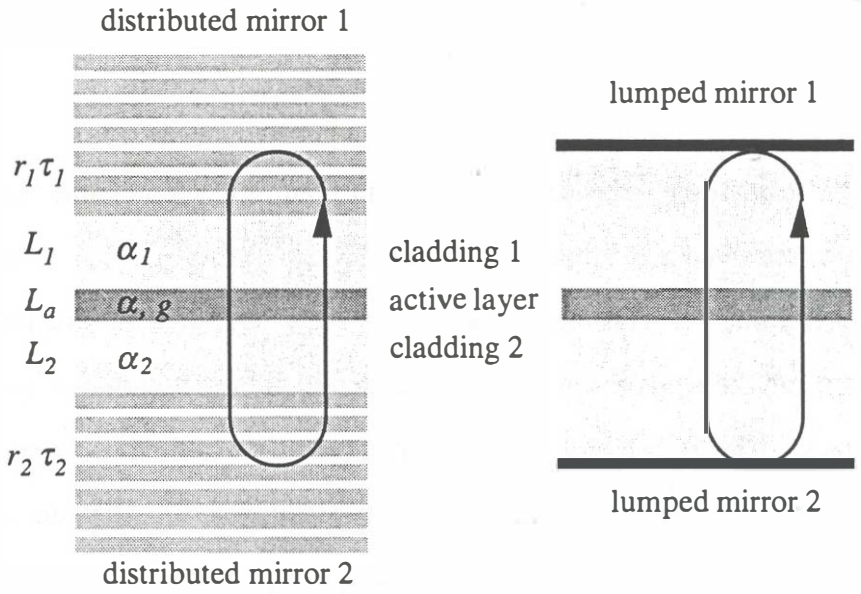


**Fig. C.12**: (a) Vertical-cavity laser refractive index structure, and (b) and equivalent cavity with lumped mirrors.

Consider a planar laser cavity with two different distributed mirrors shown in Figure C.12(a). The top mirror may also include a metal coating to boost the reflectivity. The cavity has a gain medium of thickness $L_a$ with refractive index $n_a$, gain coefficient $g$ and loss coefficient $\alpha_a$. The thicknesses, refractive indexes and absorption coefficients of the claddings are denoted with $L_i$, $n_i$ and $\alpha_i$ $(i=1,2)$. The expected lasing mode wavelength and the center wavelengths of both mirrors are close and hence the distributed mirrors can be replaced with their lumped equivalents as described in Appendix B and shown schematically in Figure C.12(b). Each mirror has a constant reflectivity and a linear phase.

$$\tilde{r}_i(\omega) = r_i \exp\left[-j(\omega-\omega_i)\tau_i + \phi_i\right] \qquad \text{(C-23)}$$

Here $\tilde{r}_i$ are the complex amplitude reflectivities, and $r_i$ are peak reflectivities the mirror at the center frequency (taken as real and positive), $\omega_i$ are the mirror center frequencies ( $\omega_1 \approx \omega_2$ for the linear phase model to apply), and $\tau_i$ are $\tau_2$ the mirror group-delays at the center frequency. The phase of the mirrors at the respective center frequencies can be either 0 or $\pi$ and for both mirrors and are denoted by: $\phi_i$. The threshold condition is achieved when the round-trip amplitude and phase of plane wave signal in this resonator remains unchanged. Two independent parameters are necessary to achieve this. Both the amplitude and the phase conditions must be satisfied. The amplitude condition is,

$$\xi g_{th} L_a = \alpha_a L_a + \alpha_1 L_1 + \alpha_2 L_2 - \ln\sqrt{r_1 r_2} \qquad \text{(C-24)}$$

The factor $\xi$ is the *gain enhancement factor* that accounts for the overlap between the active layer and the standing wave pattern. If the active layer is narrow compared to the wavelength and placed at the peak of the standing wave, $\xi \approx 2$, while if the active layer thin, but is placed at the node we have $\xi \approx 0$. For active layers centered exactly at the peak of the standing wave and thicknesses comparable to the wavelength the interaction is calculated from the overlap and is given by (Corzine, 1993).

$$\xi = 1 + \frac{\sin(2\pi L_a/\lambda)}{2\pi L_a/\lambda} \qquad \text{(C-25)}$$

where $\lambda$ is the wavelength in the cavity material. The round-trip phase has to be equal to an integer multiple of $2\pi$:

$$2\omega_m(n_1 L_1 + n_2 L_2 + n_a L_a)/c + (\omega_m - \omega_1)\tau_1 + \phi_1 + (\omega_m - \omega_2)\tau_2 + \phi_2 = 2\pi m \qquad \text{(C-26)}$$

where $m$ is the integer mode number, $\omega_m$ the $m$th mode frequency. The penetration depth of the two mirrors are $L_{\tau 1} = c\tau_1/2n_1$ and $L_{\tau 2} = c\tau_2/2n_2$ and cavity mode frequencies are given by,

$$\omega_m = \frac{c}{2} \cdot \frac{2\pi m + \omega_1\tau_1 + \omega_2\tau_2 - \phi_1 - \phi_2}{n_a L_a + n_1(L_1 + L_{\tau 1}) + n_2(L_2 + L_{\tau 2})} \qquad \text{(C-27)}$$

The denominator is the effective optical length of the cavity $D_{eff} = n_a L_a + n_1(L_1 + L_{\tau 1}) + n_2(L_2 + L_{\tau 2})$. If we may assume some unique value of refractive index in the cavity $n_{eff}$ then we can define *effective cavity length* as $L_{eff} = D_{eff}/n_{eff}$. The effective cavity length is a very popular quantity used to characterize the length of cavities with distributed mirrors, but it is misleading for the same reasons as the penetration depth is as described in Chapter 2: The physical quantity that enters expression (C-27) is the time of propagation rather than distance, and hence one needs to specify the velocity of propagation to be able to associate time with distance. The effective cavity length is arbitrary because the value of $n_{eff}$ is arbitrary. Even with the linear phase mirror approximation in real multilayer cavities, the usefulness and the physical meaning of the effective cavity length is at best only approximate. Only if we may set $n_1 \approx n_2 \approx n_a = n_{eff}$ does the effective cavity length equal to the sum of the cavity and the penetration depths of the mirrors: $L_{eff} = L_a + L_1 + L_{\tau 1} + L_2 + L_{\tau 2}$. The other important fact to note in equation (C-27) is that the fixed phase of the equivalent lumped mirrors ($\omega_1\tau_1$ and $\omega_2\tau_2$) as well as the fixed phases of the original quarter-wave mirror ($\phi_1$ and $\phi_2$) enter in the expression for the mode frequency. Omitting the lumped mirror phase is probably the most common error encountered in using the penetration depth concept in Fabry-Perot cavities. In other words, a simple replacement of the

physical cavity length $L_a + L_1 + L_2$ by the effective cavity length $L_{eff}$ will never give correct mode frequencies unless a fixed phase equal to $\omega_i \tau_{i1}$ is not given to the mirrors of the new (effective) resonator (see Appendix B for discussion).

The mode separation is given by $\Delta\omega_{VCL} = c\pi/\tilde{n}_{eff} L_{eff}$, where $\tilde{n} = n + \omega\, dn/d\omega$ is the group index. Using the typical values for VCL cavity length of 3 μm, from this expression one would expect that the mode separation would be approximately ≈100 nm. However, this expression was derived assuming a linear phase relationship for the distributed mirrors and this approximation holds only for frequencies close to the center wavelength. In reality, the mode locations are determined by phase characteristic of the distributed mirrors which become non-linear phase characteristics away from the center wavelength. For this reason expression (C-27) only has limited applicability: It works very well for determining the lasing wavelength, because that wavelength, hopefully, occurs very close to the center wavelength of both mirrors. Its applicability in finding the wavelengths of the other modes is very limited. Only if the other modes fall well within the narrowest bandstop of the two mirrors will equation (C-27) give accurate prediction for the mode wavelength. This restriction can be expressed in other words as: Equation (C-27) can be used to determine modes other than the lasing mode, *if the product of the mode number $m$ and the fractional bandstop width of the narrowest quarter-wave mirror $\Delta\omega/\omega_0$ is greater than unity*. To find the true cavity modes one has to use exact calculation (Appendix A). In a single-longitudinal mode cavity, the longitudinal mode closest to the lasing mode will be at the edge of the bandstop of the mirror with the narrowest bandstop. This can very nicely be seen in

the reflection spectra of a single-longitudinal mode resonator with one AlAs/GaAs and one InGaAsP/InP mirror shown in Figure C.13.

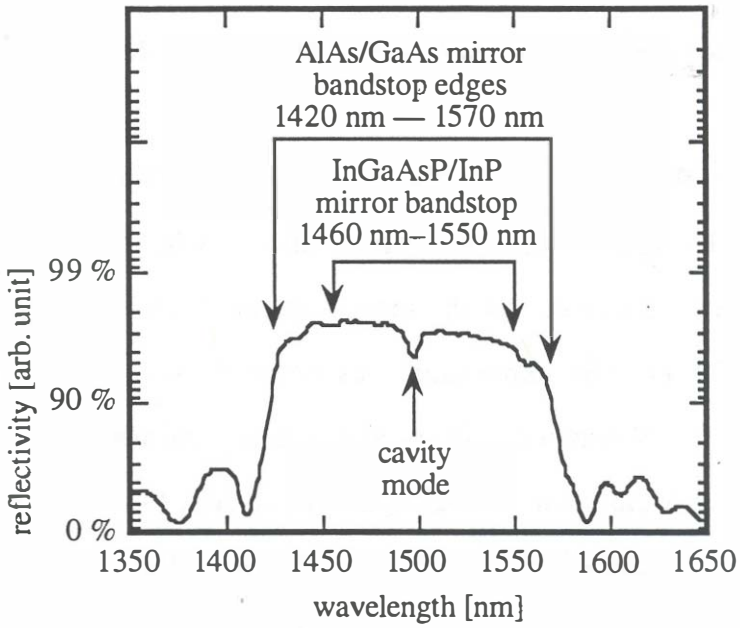


**Fig. C.13**: Reflectivity spectra of a cavity that has one AlAs/GaAs and one InGaAsP/InP mirror.

Existence of multiple longitudinal modes is not an inherent disadvantage. The problems arise when more than one longitudinal or transverse modes experience threshold or near threshold gain. The key cavity parameters that determine whether this will happen are 1) position and the spectral width of the active layer gain relative to the mode wavelengths, 2) the mode dependent losses (frequency and/or spatially dependent), and 3) gain enhancement fact of particular mode (if thin active layer is used). The spectral width of the gain of semiconductor active region is typically less than 100 nm and can be estimated from the photoluminescence spectra. For cavities with short effective lengths, at most one or two of the vertical-cavity longitudinal modes may fall within this range and experience the gain.

Vertical-cavity lasers are typically built to have very short cavities, with only one (lasing) longitudinal mode within the mirror bandstop. The modal losses of all other modes are typically too high that they never lase. The situation is quite different with transverse modes of vertical-cavity lasers, which are very often observed to lase simultaneously.

## C.2. *Radial design*

### C.2.1. *Open and lossy resonators*

There are two sources of decay of the energy stored in the oscillating electromagnetic field in an unpumped resonator. The radiation can be either absorbed within the resonator or given off to the outside world, and therefore, the resonator quality is determined by both the amount of absorption and the degree of output coupling. A lossy resonator is a resonator with intra-cavity absorption, while an open resonator is a resonator that is coupled to the outside world. Lossless resonators are idealized structures which do not occur in nature, and closed resonators are not practical since no energy can be extracted from them. Nevertheless, the mathematical analysis of these idealized cases is often much simpler than that of real resonators, and they are often used as approximate models for lossy and open resonators. The electromagnetic energy that emanates from an open resonator can be collected and used. However, there is always some loss associated with this collection: scattering and diffraction losses. In an ideal open resonator, all of the energy emanating from the resonator is collected and used.

It is important to define the terms: scattering and diffraction. The removal of energy from an incident beam and subsequent redistribution of the a portion of that energy is called *scattering* (Hecht, 1974). If the direction of redistributed energy is collinear with the incident wave we speak of reflection and transmission, and refraction if the exit medium is of different refractive index. Under the term light scattering, we typically understand the phenomenon in which the redistributed

energy is dispersed in many directions, such as non-specular reflection from rough surfaces and reflection form a large collection of particles with sizes of the order of the wavelength. The interference and the subsequent propagation of scattered light is called *diffraction.* It has originally been studied as "deviation from rectilinear light propagation", but generally means the interference of many waves produced by obstructing an incident wave with either transparent or opaque obstacles (Hecht, 1974). In vertical-cavity resonators, scattering will occur at intra-cavity obstacles. The resultant fundamental mode will be determined by the diffraction of the light scattered, reflected and refracted at the sharp edges of mirrors, waveguides and other intra-cavity structures. It is hard to give a separate definition of scattering losses and diffraction losses, since scattering and diffraction occur simultaneously in any propagation problem that involves boundaries. The discrimination between the phenomena that will be used in this dissertation is based on the fact that diffraction loss is associated with light propagation, while scattering loss is associated with light interaction with boundaries (matching boundary conditions at interfaces). Therefore, if the rate of energy loss from cavity to the outside world can be controlled by changing the physical size or shape of the cavity, such as, length, width, and any other free-space propagating distance, it is called diffraction loss. On the other hand, if the rate of energy loss can be altered by changing the shapes of dielectric interfaces, the loss is by scattering.

Open resonators with spherical and plane mirrors (Kogelnik, 1966, Siegman, 1986) have been extensively studied since the introduction of the Fabry-Perot laser resonator (Schawlow, 1958). The fundamental issue in the study of open resonators is the determination of the normal modes and their associated propagation constants.

This is a difficult problem to solve exactly even for simple geometries because it involves the solution of boundary problems in an infinite three-dimensional space. Therefore, the analysis of open resonators has been numerically intensive (Fox, 1961, Barone, 1963, Li, 1965, Checcacci, 1966, Lotsch, 1968, 1969). Analytical expressions can be given only for some simple structures that approximately describe real resonators: If the mirrors are spherical the resonator can be treated approximately as an ideal resonator and leads to Gauss-Hermitian mode patterns (spherical resonator). Analytical expressions for the propagation constants and the mode patterns have also been derived for the parallel plane mirror resonator with finite mirrors (Vainshtein, 1963).

### C.2.2. *The "Fox and Li" problem*

In order to appreciate the complexity of the open resonator problem, consider the simplest plane parallel mirror resonator shown in Figure C.14. The mirrors have unit reflectivity. The beam of light traveling from the bottom towards the top mirror diffracts and when it arrives at the top mirror part of the energy reflects back towards the bottom mirror, while a fraction continues past the mirror. In steady state solution of this resonator the resonator "mode" is an excited radiation mode. If the mirror diameter is very large and the mirror separation very small compared to the wavelength, the diffraction of the light beam will be relatively small — only a small fraction of energy will be lost with each pass of the wave. This mode has a complex propagation constant because the resonator mode involves irreversible power loss resulting from the excitation of states in the outside world. The resonance in this cavity occurs at a higher frequency than in the plane wave case

which would be expected from the separation of the mirrors, because of the lateral mode confinement. Furthermore, this resonator is not an ideal open resonator, because the power emanating from it is difficult to collect. Note however, that if a laser was built using this type of resonators, coherent radiation and threshold behavior would be observed in the output and the diffracted beams. This circular plane mirror resonator has been the subject of numerous studies, both numerically (Fox, 1961, Barone, 1963, Li 1965) and analytically (Vainshtein, 1963).

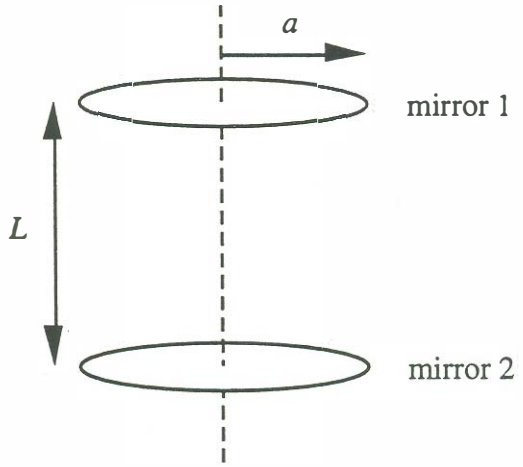


**Fig. C.14**: Circular parallel plane mirror open resonator.

The simplest solution of the modes of this resonator is obtained by an iterative solution of the Fresnel-Kirchoff integral (Fox, 1961). An example of the electric field profile at one of the mirrors calculated in the same manner as in (Fox, 1961), is shown in Figure C.15. The solution of this resonator problem is used as a check in this work for scalar (two-dimensional) Beam Propagation Method and scalar plane wave expansion (similar to the one described in (Babić, 1993) always yielding the same results for diffraction loss. Note that the electric field amplitude does not go

to zero at the edge of the mirror. This indicates that a fraction of the energy has been lost upon reflection. The discontinuity in the reflected electric field profile produces higher order ripples in the pattern visible both in the amplitude and the phase characteristic. The ripples appear in the exact solution (Fox, 1961), but not in the approximate analytic solutions of (Vainshtein, 1963, 1969) because there the calculation is bandlimited. A survey of techniques used to analyze these resonators is given in (Kogelnik, 1966, Lotsch, 1968, 1969).

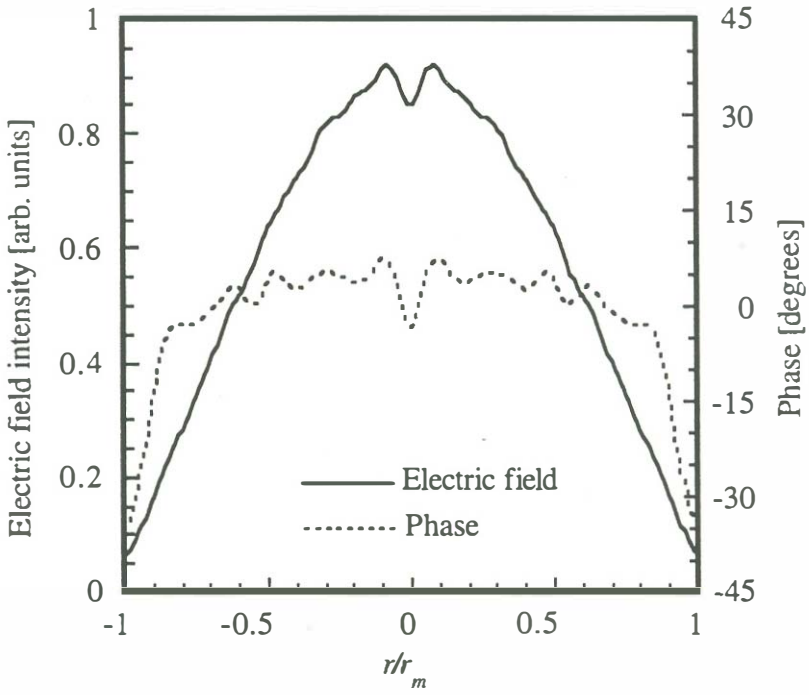


**Fig. C.15**: Electric field amplitude and phase at a resonator mirror for resonator shown in Figure C.14 with mirror to mirror separation of 3 μm and mirror diameter of 10 μm. The wavelength was 489 nm (1550 nm / 3.2). The calculation was done by numerical integration of the Fresnel-Kirchoff integral as given in (Fox, 1961). The number of iteration was 700.

C.2.3. *Applicability of Fresnel diffraction limit*

Historically, laser cavities were large compared to the wavelength and the mirror diameter small compared to the mirror separation. It was therefore possible to employ scalar diffraction theory and the Fresnel approximation to solve for the cavity modes. Semiconductor optoelectronic devices, on the other hand, have dimensions of the order of a wavelength and often require rigorous treatment of the electromagnetic wave propagation that considers the vector nature of the electromagnetic field as well.

Real vertical-cavity lasers are lossy open resonators. The optical losses arise in varying degrees from both scattering and diffraction, depending on the cavity structure. Inasmuch as all dimensions in VCL cavities are of the size of a wavelength, any imperfections, sharp edges and unguided wave propagation will result in either light scattering or increased diffraction loss in the resonator. The structure of a VCL cavity is a compromise between the optical, electrical and thermal requirements and is often less than ideal from the standpoint of diffraction. The normal modes of such three-dimensional problems are difficult to determine exactly, and a general formalism is hard to give in a simple form since there are many different structures presently used for the fabrication of VCSELs. The transverse field profile of the oscillating electromagnetic wave in the cavity is shaped by spatial and angular frequency filtering. In high-quality vertical resonators, the transverse mode behavior is well described by Fresnel (near-field) diffraction. In order to support this statement, we note that: (a) The lateral and longitudinal size of vertical-cavity lasers is of the order of the wavelength.

Therefore, if free-space beam propagation existed within the resonator, *geometric optics* would not be sufficient to accurately describe the wave propagation within the resonator, (b) The other limit, *Fraunhofer diffraction*, occurs for distances larger than $d^2/4\lambda$ (Hecht, 1974), where $d$ is the lateral size of the resonator, and $\lambda$ the wavelength in the resonator. For a typical vertical cavity laser where the lateral sizes are of the order of a few micrometers and wavelength of the order of one micrometer, Fraunhofer diffraction can be considered only if the unguided fraction of the resonator length is larger than several micrometers — this is rarely the case in practical vertical-cavity lasers. Consequently, the most commonly used method for analysis of such structures is the scalar (Yevick, 1990, Feit, 1978, Chung, 1991a, Shimizu, 1991) or vector beam propagation method (Chung, 1991b, Huang, 1992).

The motivation for analysis of diffraction and open resonator comes from the need to understand the optical properties of vertical-cavity lasers. All the effects that involve diffraction and scattering, and are difficult to evaluate, represent sources of cavity loss which must be minimized. There are then two reasons why one needs to study the effects of diffraction in vertical-cavity laser resonators: (a) Estimation of the diffraction loss to design better laser cavities, and (b) study diffraction for the purpose of transverse mode discrimination. Higher order modes diffract faster and hence the fundamental mode can be selected by simply making a cavity whose quality is limited by diffraction loss.

In the course of the development of long-wavelength VCLs, diffraction properties of VCL resonators have taken an important role. In comparison with the GaAs-based VCLs, the wavelength was up to 50 % longer, and because of technological

difficulties the structures were different, typically longer with larger unguided sections than in GaAs-based VCLs. For these two reasons, diffraction of the cavity modes within the cavity was expected to play a more pronounced effect on the overall cavity loss. Up to the writing of this work, no experimental quantification of the diffraction effects in long-wavelength VCLs had been given in the literature. Part of the reason for this is the paucity of such lasers, and hence of data available for such studies. However, with the advancement of this technology, this information will surface and more correlation between modeling and experimental evidence of diffraction will be established. For this reason, in this work, diffraction is studied only theoretically; the most important contribution being the estimate of the single reflection coupling loss of a mode emerging from a dielectric waveguide reflection from a quarter-wave mirror and returning back into the waveguide. These results are described in the next section.

## C.3. *Index guided resonators*

The structure of the double-fused vertical-cavity lasers fabricated in the course of this work is that of a post index-guided laser shown in Figure 1.2. The determination of propagation modes in this cavity is quite difficult since it involves numerous waveguide junctions. This implies that for the analysis one has to work with large sets of orthogonal modes (guided and radiation) to a get a realistic field distribution in the cavity. Most researchers have employed simplified optical solution in order to be able to include other effects, such, as spatial hole burning (Shimizu, 1991), and heating (Scott, 1993, Piprek[b], 1994). The most interesting sources of optical loss in this type of resonator are sidewall scattering and diffraction loss. The roughness at the waveguide sidewalls produces scattering losses and the free-space propagation though the unguided fraction of the bottom mirror produces coupling losses. We discuss these losses separately.

### C.3.1. *Scattering losses*

Even a perfectly smooth vertical waveguide, such as is shown in Figure 2.5, experiences power loss through electromagnetic radiation from abrupt refractive index variations. A sidewall profile of an AlAs/GaAs etched in Chlorine reactive ion etching is shown in Figures C.16. There are two sources of sidewall corrugation: Etching undercut and AlAs oxidation. The undercut comes from the difference between the etch rates of the two materials that constitute the mirrors. The darker regions in Figure C.16 are oxidized AlAs.

The degree to which the sidewalls effect the propagation of the electromagnetic wave through the waveguide is determined by the energy density that is present at the edges of the waveguide. Consequently, smaller devices will suffer from scattering losses more than large devices. The exact mathematical treatment of this loss mechanism is quite difficult and hence in this section we only estimate the loss for a vertical post-mirror. More importantly, we show, based on simplified modeling, that the functional behavior of the scattering is $1/a^{\gamma}$ where $a$ is the post radius and $\gamma$ is approximately 2 but may be higher. The magnitude of loss depends on the corrugation depth.

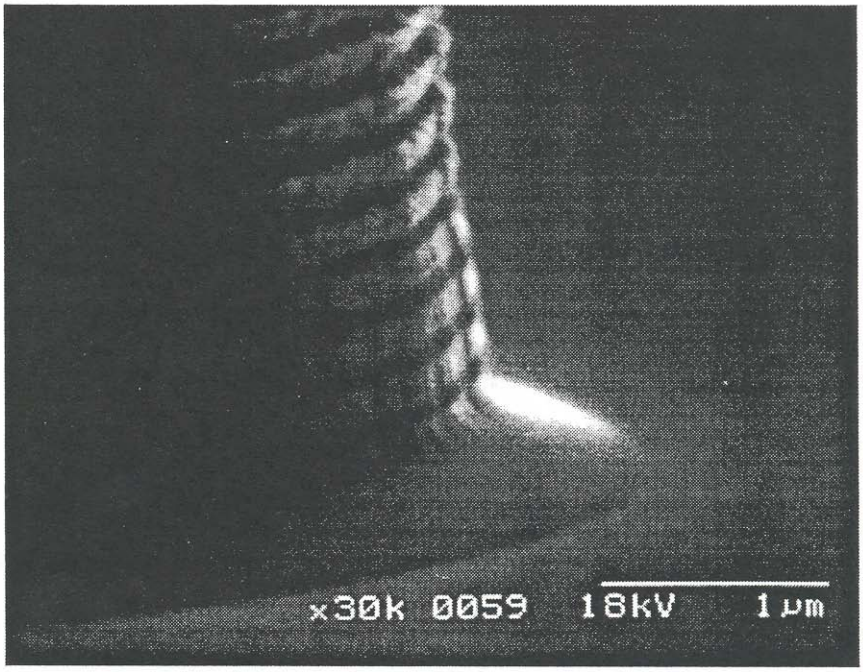


**Fig. C.16**: A sidewall of an AlAs/GaAs mirror etched in $Cl_2$reactive ion etching.

Consider a cylindrical post with a quarter-wave mirror shown in Figure C.17. Due to etching undercut or oxidation, one of the layers is narrower. Even though the actual shape of the corrugation is irregular as shown in Figure C.16, the shape will be modeled as rectangular. There are two approaches one can take to estimate the energy loss of a wave propagating along this waveguide:

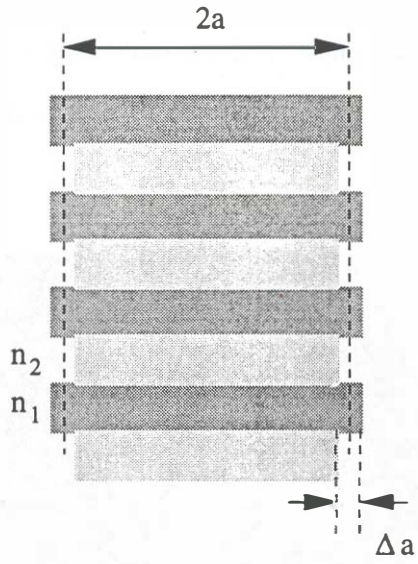


**Fig. C.17**: Cylindrical post with corrugated sidewalls.

The first approach models the propagation as occurring in an effective waveguide with an absorbing ring. This idea is based on the fact that the waveguide sections between two adjacent interfaces are thin compared to the wavelength (one quarter wavelength) and that therefore the energy is carried from one interface to the other by both guided and leaky modes. One may then assume that the light actually propagates through an effective waveguide of some average radius $a$ and that the portions of the field pattern in the rough regions are lost to radiation. The simplest way of modeling this is to phenomenologically introduce lossy regions of some

width $\Delta a$ around the edges of the waveguide. This was done using the fundamental and first higher order mode of a cylindrical dielectric waveguide. The modes were determined by solving the scalar Helmholtz equation in cylindrical coordinates, the solutions being Bessel functions inside and Modified Bessel functions outside the waveguide. The refractive index was taken to be the average between GaAs (3.377) and AlAs (2.893), and the width of the absorbing region was made equal to the corrugation depth. Even though the model is very crude it shows that the losses at each interface, and hence the entire mirror, vary as,

$$\delta_s \propto \frac{\Delta a}{a^{2.8}} \qquad \text{(C-28)}$$

The second approach to estimate the scattering losses assumes quite the opposite: Even though leaky and high order modes propagate through the quarter-wave sections they eventually radiate out after many reflections (in a high reflectivity quarter-wave mirror there is a large number of reflections). The only mode that carries the energy is the fundamental mode of the waveguides. Since the waveguides (1) and (2) have different radii and different refractive indexes the modes will not look exactly the same. There will be imperfect coupling between these modes at each junction. We can easily calculate what this coupling will be as a function of the waveguide radius and the corrugation depth. Again, this was done using the scalar waveguide solutions. The coupling loss was calculated for a single interface of a 1.55 μm AlAs/GaAs mirror/waveguide as a function of the radius and the results show that the functional dependence of the single interface coupling approximately obeys,

$$\delta \propto \frac{(\Delta a - \Delta a_0)^2}{a^2} \qquad \text{(C-29)}$$

where $\Delta a_0$ is the corrugation depth which produces lowest coupling loss. The reason this value is not zero, as one would intuitively expect, is because the mode of the lower index waveguide is spread out slightly more so the coupling coefficient happens to be better when that waveguide is made a bit narrower (in this case $\Delta a_0 = 14.5\,\text{nm}$). In order to estimate the reflectivity of the quarter-wave mirror we model each of the junctions as a interface between two dielectrics ($n_1$ and $n_2$) that has loss equal to (C-28). Multilayer calculation using transverse field matrices was used to estimate the reduction on reflectivity. At each junction a matrix is added to include loss, as described in the Appendix A. This calculation shows that the cavity loss depends inversely on the radius squared.

The numerical calculations performed here indicate that the scattering loss calculated from the overlap model is more sensitive to the assumed corrugation depth, than the absorption model. Based on this fact and calculated absolute values of interface loss for the two methods, we conclude that for strong sidewall perturbation the overlap model dominates the scattering loss, and that, consequently, for weak sidewall perturbation the scattering is better described using the absorption model. However, these conclusions are somewhat hypothetical, since the models are over–simplifications of the real phenomena. The experimental study of sidewall scattering performed by (Thibeault, 1995) indicates that for AlGaAs/GaAs posts etched in $Cl_2$ plasma, the scattering loss dependence on the diameter is

approximately $1/a^2$. This observation seems to indicate that, possibly, the overlap model seems to model the scattering better.

Note that the perturbation depth $\Delta a$ can be used as a fitting parameter to real data that scales the loss using both methods. One must, however, keep in mind that the rectangular corrugation profile is a clear oversimplification of the real scattering profile and that the estimate of interface loss given by (C-28) and (C-29) should not be used to estimate the absolute value of mirror reflectivity.

### C.3.2. *Diffraction loss*

The second source of optical loss based on the structure geometry is the imperfect coupling of the wave reflected from the bottom mirror in a post index-guided structure. The interesting part of this problem is the reflection in a multilayer structure – the quarter-wave mirror. Even when we ignore the fact that the top waveguide has a quarter-wave mirror in it, and treat it as a cylindrical waveguide, the exact solution of the waveguide junction problem requires a numerical solution that includes all the guided, evanescent and radiation modes of the structure (Jackson, 1986, Snyder, 1983). A solution of this type of problem has been performed for the reflection of a slab waveguide on a cleaved edge by (Ikegami, 1972). The main difficulty in solving this problem exactly is the determination of the field profile in the junction. In this work, we simplify the analysis by assuming that this field is completely determined by the sum of two waves: the forward and backward propagating fundamental mode of the waveguide. Furthermore, we assume that the transverse modes of this cavity are completely determined by the

waveguide, while the laterally infinite quarter-wave mirror only introduces a power loss to the propagation constants. An important simplification of the problem is achieved by ignoring the reflections at the junction between the two sections. We approximate the solution by applying boundary conditions between the two sections that are similar to Kirchoff boundary conditions (Jackson, 1986) and are given as: 1) Across the surface where the mode is assumed significant (calculation surface) the field distribution of the incident wave and its derivative are exactly the same as they would be in the absence of the interface, and 2) On the part of the boundary surface that lies outside of the calculation surface the field distribution and its derivative are identically zero. This implies that there is no mode conversion nor any radiation loss due to impedance mismatch at the junction, but only due to the reflection at the mirror. The amount of light that couples back into the waveguide after the reflection is determined from the overlap integral between the incident and reflected mode profiles (Jackson, 1986). We therefore concentrate our study on the behavior of the coupling coefficient $\kappa$ as defined in Appendix B, which we also refer to as the modal reflection coefficient. A similar study of coupling loss has been performed for quarter-wave mirror facet coating for long-wavelength in-plane lasers (Ohtsu, 1983).

The purpose of this analysis is to be able to compare different mirrors (GaAs and InP based) adjacent to an identical waveguide (top section). For this reason, the core of the waveguide is assumed homogeneous with the refractive index equal to that of InP. Assuming that the cladding index is unity (air) the confinement of this mode is so high that it makes a little difference if the index of the core is 3.17 (InP) or GaAs (3.5). In fact the average index of AlAs/GaAs mirrors falls in the vicinity of the InP

in this wavelength range. In practice there are many options for the cladding material, such as, air, polyimide, metal, or regrowth, and by proper selection of this material one can achieve low beam diffraction. We are interested in studying the worst possible cases: the air and the metal cladding. In both cases, the fundamental waveguide mode will be far from cutoff since the practical sizes of etched posts are greater than 4 μm. This furthermore implies that the electromagnetic field components normal to the mirror surface are small compared to the transverse and that the field pattern in the waveguide does not significantly change shape in the transition from the top to the bottom section of the cavity. In a dielectric waveguide with air cladding the electric field at the edges of the core is small compared to its maximum value, hence the mode pattern can be determined by solving the scalar wave equation. We consider the two lowest order modes of the dielectric waveguide: $q-\mathrm{TEM}_{00}$ and $q\text{-}\mathrm{TEM}_{10}$ (quasi-TEM). We determine the fields patterns analytically and assign pure linear polarization to the them. This approximation agrees well with the experimentally observed polarization states of VCSEL transverse modes (Chang-Hasnain, 1991). In the analysis of the dielectric waveguide, we concentrate on two core diameters: 5 μm and 10 μm. These two core sizes will be quite representative since for diameters larger than 10 μm the diffraction loss will become very small, whereas the smaller diameter is at the brink of violating the paraxial requirement ($D \sim 10\lambda$ for $\lambda = 1.55\,\mu\mathrm{m}$ in InP). The boundary conditions at the edge of the metal waveguide are quite different than in the dielectric, since for some modes the electric field magnitude can change abruptly at the edge of the guide. Here we consider the three lowest order modes: $\mathrm{TE}_{01}$, $\mathrm{TE}_{11}$ and $\mathrm{TM}_{01}$ for which the field patterns are given exactly (Harrington, 1961).

The numerical calculation of the modal reflectivity is performed using plane-wave vector expansion which is described in detail in (Babi[cb], 1993). The analysis was performed for three practical semiconductor and one amorphous mirror with their optical parameters given in Table C.1. Mirrors M1 and M2 are AlAs/GaAs mirrors at two wavelengths 0.98 μm and 1.3 μm. The refractive indices given for AlAs and GaAs correspond to $\lambda = 0.98\mu m$ (Afromovitz, 1974). When the wavelength is changed to 1.3 μm, the indices of both materials will change, but the index difference will remain almost the same. We intentionally used the same refractive index values for both mirrors to single out the effect of the wavelength change on the coupling loss. Long wavelength mirrors are typically fabricated using InGaAsP/InP or AlInGaAs/AlInAs materials, and the refractive indices of these two quaternaries lattice matched to InP are very similar at 1.55 μm (Mondry, 1992). Hence we only analyze the InGaAsP/InP system (Mirror M4). Mirror M3 is a $SiO_2/Si_3N_4$ quarter-wave mirror, which is a low loss alternative to the $SiO_2$/Si material combination.

| ID | Material | $\lambda$ [nm] | Phase | $n_i$ | $n_L$ | $n_H$ | $n_e$ | $\chi_D[\mu m^2]$ |
|---|---|---|---|---|---|---|---|---|
| M1 | AlAs/GaAs | 980 | 0 | 3.52 | 2.95 | 3.52 | 3.52 | 0.243 |
| M2 | AlAs/GaAs | 1300 | 0 | 3.52 | 2.95 | 3.52 | 3.52 | 0.428 |
| M3 | $SiO_2/Si_3N_4$ | 1300 | 0 | 3.17 | 1.45 | 1.95 | 1 | 0.557 |
| M4 | InGaAsP/InP | 1550 | $\pi$ | 3.17 | 3.17 | 3.47 | 3.17 | 1.147 |

**Table C.1**: Numerical data for modeled quarter-wave mirrors.

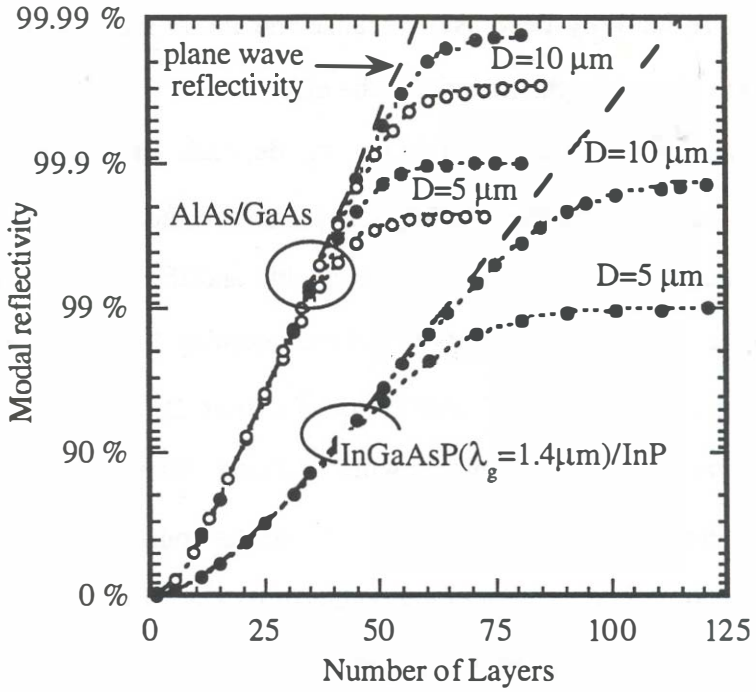


**Fig. C.18**: Modal reflectivity of three practical quarter-wave mirrors as a function of number of layers.

With the mathematical apparatus described in Appendix B we investigate two topics: 1) We calculate the modal reflection coefficient for select beam patterns on practical DBRs and 2) We compare different mirrors, and estimate the reflection coefficient using the parameter $\chi_D$ in an analytic approach to the diffraction characterization of DBRs (confirm analytic predictions from Appendix B). We first calculate the modal reflection for the q-$TEM_{00}$ mode for the semiconductor mirrors M1, M2 and M4 listed in Table C.1. The results of the numerical calculation for two mode diameters are shown in Figure C.18. Mirror M1 (AlAs/GaAs 0.98 μm) has the smallest diffraction range and hence the modal reflection is very high even for diameters as small as 5 μm. When we change the

wavelength from 0.98 μm to 1.3 μm and model the M2 mirror (AlAs/GaAs 1.3 μm), the modal reflectivity decreases because the mode size has decreased in respect to the wavelength in the material. The effect of the wavelength change can also be seen from the Equation (B-113): $\chi_D$ depends on the square of the wavelength. We can estimate the coupling loss for any of the mirrors in Table C.1: We take the calculated values of $\chi_D$ from this table and the radius of a particular mode to calculate $N = a^2/\chi_D$. Then we read the coupling loss from the graph in Figure B.22. The maximum modal reflectivity of a finite DBR is approximated by $R_m^{(\text{modal})} \equiv R_m(1-\delta(N))$ and it is shown in with the dashed lines in Figure C.18. The accuracy of this prediction is approximately 10% of the coupling loss value and is limited by the calculation error. The remarkable fit between the numerical and our semi-analytic approach using the equivalent hard mirror concept illustrates the importance of the parameter $\chi_D$ in characterizing paraxial beam reflection on DBRs. If we now change to mirror M4 that is tuned to a longer wavelength and has a smaller refractive index difference, the diffraction range increases drastically. The coupling loss for mirror M4 is an order of magnitude larger than in mirror M1. This limits the range of mode sizes that can be used in long wavelength mirrors fabricated using the quaternary alloys AlInGaAs or InGaAsP: They can not be used without lateral guiding for mode diameters below ~10 μm. This limitation should be considered in addition to the difficulty in the practical realization of high reflectivity long wavelength mirrors and the relatively narrow bandwidth. The coupling loss of AlAs/GaAs mirrors is so small that it is difficult to observe the difference between the operation of guided and unguided mirror structures. If very narrow mode diameters are used, the laser threshold current was typically

dominated by other mechanisms that depend on the laser size, such as, surface recombination and scattering at the waveguide junction.

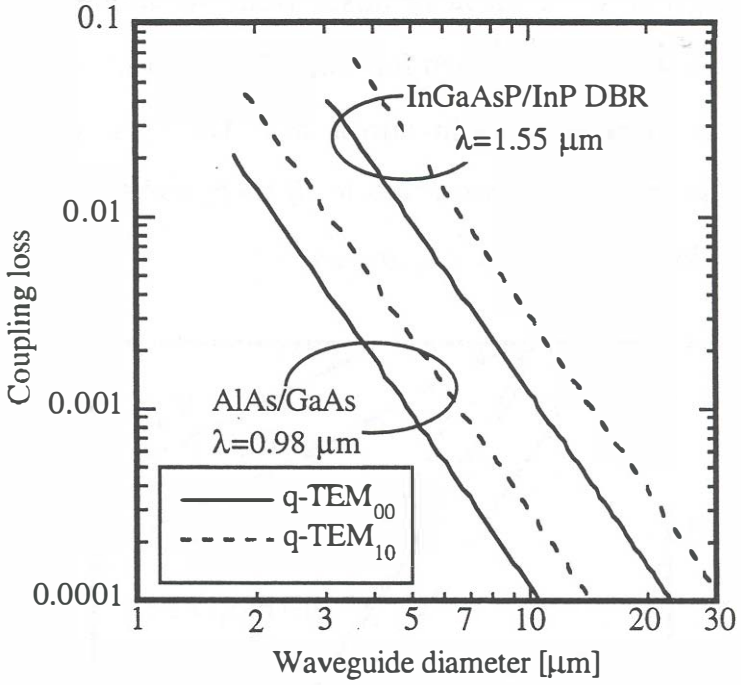


**Fig. C.19**: Coupling loss vs. waveguide diameters

In Figures C.19 and C.20 we show the coupling loss calculated for the mirrors in Table C.1 as a function of the waveguide diameter. We also calculated the coupling loss by using $\chi_D$ and the free-space coupling loss shown in Figure B.22. In Figure C.19 the two calculations overlap to within accuracy of the numerical calculation over the range shown for both q-$TEM_{00}$ and q-$TEM_{10}$ modes. The mode discrimination is approximately a factor of three for all radii and the uncertainty in the data is better than 10% of the coupling loss value. In Figure C.20 we show the coupling loss for mirrors M2 and M3 for all modes described in section II. It is evident that the $SiO_2/Si_3N_4$ mirror shows higher diffraction loss than the

AlAs/GaAs mirror. The reason for this is faster diffraction of the beam in the mirror with a low average refractive index. The deviation from the pure power law visible in the range of small diameter arises from violation of the paraxial approximation. Note that this transition for mirror M2 happens at approximately two times smaller diameter than in mirror M3. The limit of the paraxial approximation from this figure corresponds to $d/\lambda \sim 5$, and the equivalent hard mirror concept breaks down for smaller diameters.

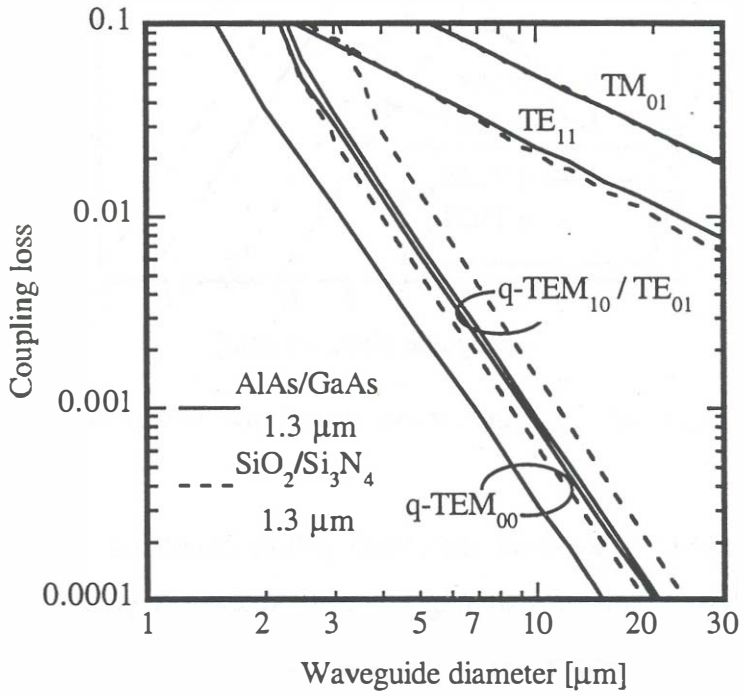


**Fig. C.20**: Coupling loss vs. waveguide diameter.

Long-wavelength mirrors lattice matched to InP (InGaAsP/InP) exhibit large diffraction range. This in turn produces serious limitation on the smallest size of a mirror with no lateral guiding one can employ in long-wavelength VCLs. Evidently, the structures that need to be used with mirrors have to be laterally

guided or another material system should be used. Using the AlAs/GaAs mirror is clearly a good choice because of the larger refractive index difference.

Based on these calculations we have also seen that coupling loss can also substantial on a dielectric mirror, if the refractive index difference is small and the average index is low. Typically, in amorphous mirrors ($Si/SiO_2$) large refractive index differences produce a very short penetration depth and hence negligible diffraction. The knowledge of the diffraction range enables analytic comparison between these mirrors and it has correctly predicted their relative performance in respect to diffraction loss.

## C.4. *Apertured resonators*

The other type of transverse mode determination in VCLs, that is becoming very interesting in recent years is by lateral oxidation and or wet chemical undercutting, with structures to be shown later in Chapter 8. In this case the mode is apertured by large refractive index change. The weakly-apertured resonator, discusses in Section C.5, is of special interest here, since it effectively models a vertical-cavity laser with a thin oxidized layer for current confinement placed at the node of a standing wave pattern.

Let us first define what we mean by aperturing: A resonant mode in a resonator is fundamentally determined by a combination of spatial and spatial frequency filtering. The two processes are conjugate to each other in the same sense as gating in time is conjugate to frequency filtering.

An aperture is a electromagnetic wave scatterer that produces spatial filtering. Its aperture function is given by its position dependent transmission and/or reflection coefficient. For the sake of simplicity, in this work, an aperture is infinitely thin and conforms to the approximations associated with Kirchoff diffraction theory. The position dependent reflection and transmission coefficient varies slowly enough to be able to neglect the fringing evanescent fields. For simplicity, the aperture function has no angular dependence. In addition, in this work an aperture includes an opening or an obstacle in a semi-transparent screen as well.

The spatial frequency or angular spectrum filtering is the conjugate of spatial filtering. It is used to selectively attenuate or transmit plane waves depending on the angle of incidence. The best example is the quarter-wave mirror, which reflects the near-normal incident waves, while transmits waves incident at angles larger than the critical angle. The quarter-wave mirror is an angular spectrum low-pass reflection filter.

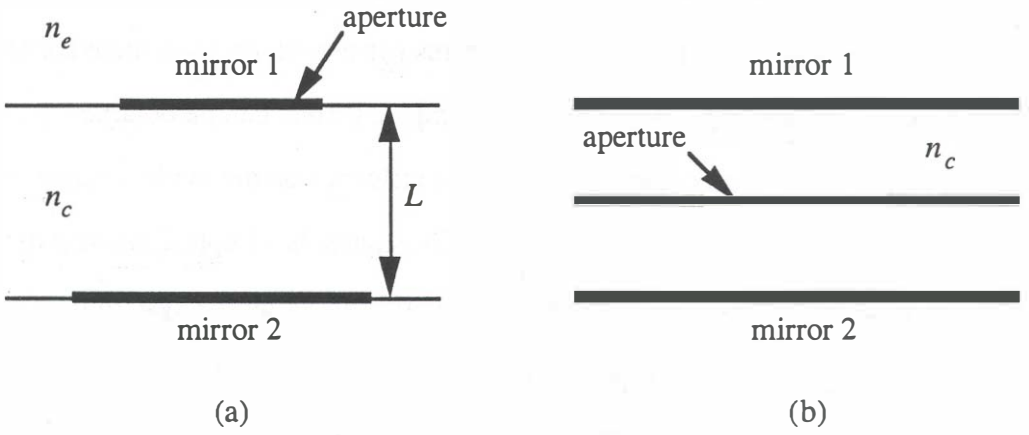


**Fig. C.21**: Two types of apertured resonators.

The following sections present a simplified treatment of resonators with infinitely thin apertures. The spatial filtering realized by an aperture and angular filtering realized by a multilayer structure is represented and manipulated by linear operators, which act on the mode. There is a number of resonator types in which apertures are used to define and select the transverse modes, and couple in or out of the resonators. In this work we are primarily interested in open resonators with plane mirrors and at least one aperture. Figure C.21 illustrates two types of apertured resonators (simplified) which are interesting for vertical-cavity laser resonators. We discuss these cases in more detail.

C.4.1. *Asymmetric aperture resonator*

In the case (a) of Figure C.21, two laterally finite mirrors are separated by free-space. The electromagnetic field in this cavity can be viewed as a wave packet oscillating between the two mirrors. This implies that the propagation is determined by an infinite set of screens (Fox, 1961) through which the wave propagates as being iteratively shaped. The apertures are now complementary to mirror shapes. The period of the sequence contains two apertures per period, because there are two different mirrors in the original resonator. A simpler system can be obtained if one of the mirrors is much larger than the other so its influence on the mode shaping can be ignored. This equivalent model in principle illustrates the simplest mathematical method of solution, i.e. the power method of iterative applying the system operator to the state until it converges. This is called *asymmetric aperture resonator*. The operator equation that defines the modes of this resonator is given by

$$\lambda \Phi = \tilde{L}\tilde{S}_1 \tilde{L}\tilde{S}_2 \Phi \tag{C-30}$$

where $\tilde{L}$ is the free-space propagator over distance $L$, $\tilde{S}_i$ are the aperture functions and $\lambda$ is the eigenvalue. At resonance the eigenvalue is real, and at threshold it is unity. The important fact to note is that $\tilde{S}_i$ and $\hat{L}$ do not commute, i.e. $[\tilde{L},\tilde{S}_i] \neq 0$. The $k$-space representation of $\hat{L}$ is given by (B-88):

$$\tilde{L} = \exp(-ik_\rho^2 L/2k) \tag{C-31}$$

while the aperture function is a top-hat function and in position representation is given by,

$$\tilde{S}(\rho) = \begin{Bmatrix} 1 & for & \rho < 1 \\ 0 & for & \rho > 1 \end{Bmatrix} \tag{C-32}$$

which in $k$-space is denoted by $aS(ak_\rho) = J_1(ak_\rho)/k_\rho$ (Goodman, 1968). The simpler cases of this resonator are when the two mirrors are identical (symmetric apertured resonator) and when one mirror is much wider (single-apertured resonator). These operator equation for the symmetric resonator is given by

$$\lambda\Phi = (\tilde{L}_{sym}\,\tilde{S})^2\ \Phi \tag{C-33}$$

while for the single-sided resonator we have

$$\lambda\Phi = \tilde{L}_{ss}^2\,\tilde{S}\ \Phi. \tag{C-34}$$

To get from (C-30) to (C-34) we have used the property that *similar* matrices have identical eigenvalue spectra (Ortega, 1987). (The meaning of $\Phi$ changes depending on the resonator shape.) We consider these two cases are interesting because the solutions of the single-sided resonator are a subset of the solutions of the symmetric resonator. Since the (C-33) represents a symmetric problem we can slit it into in $\pm\sqrt{\lambda}\,\Phi = \tilde{L}\tilde{S}\,\Phi$ and have the following $k$-space representation

$$\pm\sqrt{\lambda}\,\Phi = \exp\left(-i\frac{\kappa^2 L_{sym}}{2a^2k}\right)\cdot\left(S(\kappa)\otimes\Phi\right) \tag{C-34}$$

where $\kappa = k_\rho a$. Similarly, the single-sided resonator operator equation can be written as

$$\lambda\Phi = \exp\left(-i\frac{\kappa^2 L_{ss}}{a^2k}\right)\cdot\left(S(\kappa)\otimes\Phi\right) \tag{C-35}$$

Evidently, the solutions of the single-sided aperture resonator with cavity length $L_{ss}$ are a subset of the solutions of a symmetric resonator with cavity length $L_{sym} = 2L_{ss}$. The most important fact evident in these equations is that the eigenvalues and the eigenvectors are determined by a single variable $L/2a^2k$, where $L$ corresponding cavity length. This dimensionless parameter that completely characterizes any resonator of this form is called Fresnel number, and is given by

$$F = \frac{L\lambda}{a^2 n} \tag{C-36}$$

There are many definitions of Fresnel number depending on the resonator structure. The use of Fresnel number characterizes resonator problems in the Fresnel diffraction limit. In the case of rectangular apertures (mirrors) and Fresnel diffraction limit, the separation of variables yield a simplification of the mathematics. We have $S_1(x,y) = S_{1x}(x)S_{1y}(y)$ and $\Phi(x,y) = \Phi_x(x)\Phi_y(y)$. It is easy to show now that this equation splits into two independent relations:

$$\Phi'_x \Phi'_y = \tilde{L}_x \tilde{S}_{1x} \Phi_x \cdot \tilde{L}_y \tilde{S}_{1y} \Phi_y \tag{C-37}$$

$$\lambda_x \Phi_x = \hat{L}_x \hat{r}_{1x} \hat{L}_x \hat{r}_{2x} \Phi_x \quad \lambda_y \Phi_y = \hat{L}_y \hat{r}_{1y} \hat{L}_y \hat{r}_{2y} \Phi_y \tag{C-38}$$

The eigenvalue of the problem is $\lambda = \lambda_x \lambda_y$. The propagation in symmetric rectangular aperture resonators ($\hat{r}_1 = \hat{r}_2$) can be completely described with two Fresnel numbers, one for each propagation direction. This has been used by (Fox, 1961) in rectangular shaped open resonators and by (Shimizu, 1991) to obtain an estimate of diffraction loss in vertical-cavity lasers.

### C.4.2. *Aperture–coupled resonator*

In the case (b) of Figure C.21, two laterally infinite mirrors separated by free-space and a semi-transparent aperture. This resonator is in fact two resonators coupled through a semi-transparent aperture. We call this resonator *aperture-coupled resonator*.

A large number of vertical-cavity laser cavities are structurally similar to the aperture--coupled resonator with the laterally infinite mirrors. The mirrors are quarter-wave stacks with widths much larger than the characteristic width of the aperture. Since the quarter-wave mirrors are effective angular spectrum filters, the complexity of the resonator has increased since we have now a combination of both spatial and angular frequency filtering in the resonator. A similar problem appears in the single-aperture resonator shown in Figure C.21 if the bottom mirror is replaced with a quarter-wave mirror. In a real vertical-cavity laser the laterally finite mirror (in Figure C.21) can be a quarter-wave mirror, and in this case the aperture is no longer infinitely thin and becomes a waveguide with an embedded multilayer such as was described in Section C.1.4.

The problem of a wave bouncing back and forth between spatial and angular filtering is a problem encountered in signal and system theory with a signal that is passing though an infinite sequence of time gates and sharp low pass filters. The exact solution of this problem is involves spherical-prolate functions (Slepian, 1961). The solution of the apertured resonator problems, as shown in Figure C.21, is much more complicated, but has one significant simplification: For high Q resonators with planar mirrors, low diffraction loss can be achieved only with beams of very low divergence. The angular bandstop of quarter-wave mirrors in use in surface-normal optoelectronic devices is much larger than the diffraction angle of the resonator beams. Therefore, only the very narrow portion of the quarter-wave mirror angular spectrum needs to be considered in the analysis of these resonators. In this chapter, we shall use the analytic behavior of practical quarter-wave mirrors under the single reflection of a real VCL waveguide mode, and also the behavior of

a DBR in a resonator. We shall show that the difference between quarter-wave mirror angular spectrum and a constant reflectivity (but variable phase) angular spectrum is negligible for all practical purposes. This realization has enables a substantially simpler treatment of quarter-wave mirrors and resonator that employ them. However, even with this simplification, the case shown in Figure C.21(b) is quite complicated because it involves two resonators coupled with an aperture. We will set up an operator equation defining the modes of this resonator that includes all of the reflections, but will not solve it for the general case. In Section C.5 we shall numerically solve the special case of a weakly apertured resonator.

The operators defining the mirror reflections are $\hat{R}_1$ and $\hat{R}_2$ and the aperture transmission and reflection functions are given by $\hat{r}$ and $\hat{t}$. The free-space propagation in front of the mirrors is included into the mirror reflection operators, since the free-space operator commutes with the mirror reflection operator. The mirror reflection operator and free-space propagation are eigen states of plane wave functions:

$$\hat{R}_i|k\rangle = R_i(k)|k\rangle \qquad \text{(C-39)}$$

while the aperture operators are eigenstates of the position eigenstates.

$$\hat{r}|x\rangle = \hat{r}(x)|x\rangle \quad \hat{t}|x\rangle = \hat{t}(x)|x\rangle \qquad \text{(C-40)}$$

To derive the operator equation that specifies the resonator modes we first write the system equations as similarly as in section 3.2.1, except that in our derivation, now

we have to watch that some of the operators do not commute, $[\hat{t},\hat{R}_i]\neq 0$ and $[\hat{r},\hat{R}_i]\neq 0$.

$$f_1=\hat{t}\hat{R}_2 f_2+\hat{r}\hat{R}_1 f_1 \quad f_2=\hat{r}\hat{R}_2 f_2+\hat{t}\hat{R}_1 f_1 \tag{C-41}$$

Subtracting these equations we get the symmetric field function,

$$\Phi=[1+(\hat{t}-\hat{r})\hat{R}_1]f_1=[1+(\hat{t}-\hat{r})\hat{R}_2]f_2 \tag{C-42}$$

and also $\Phi=\hat{t}(\hat{R}_2 f_2+\hat{R}_1 f_1)$. Now we add equations (C-41) and after some manipulation get the final operator equation that defines the resonator:

$$\left\{(1-\hat{r}\hat{R}_1)\left(1+(\hat{t}-\hat{r})\hat{R}_1\right)^{-1}+(1-\hat{r}\hat{R}_2)\left(1+(\hat{t}-\hat{r})\hat{R}_2\right)^{-1}\right\}\Phi=\lambda\Phi \tag{C-43}$$

Inasmuch as none of the denominators ever become zero for finite mirrors, this system can be solved. For scattering at a single dielectric interface, we have $\hat{r}+1=\hat{t}$ and the operator equation reduces to

$$\left\{\frac{1}{1+\hat{R}_1}+\frac{1}{1+\hat{R}_2}\right\}\Phi-\hat{r}\left\{\frac{\hat{R}_1}{1+\hat{R}_1}+\frac{\hat{R}_2}{1+\hat{R}_2}\right\}\Phi=\lambda\Phi \tag{C-44}$$

or at threshold when $\lambda=1$ we have

$$\hat{r}\Psi=\left\{\frac{1-\hat{R}_2\hat{R}_1}{\hat{R}_1(1+\hat{R}_2)+\hat{R}_2(1+\hat{R}_1)}\right\}\Psi \tag{C-45}$$

with the substitution

$$\Psi=\left\{\frac{\hat{R}_1}{1+\hat{R}_1}+\frac{\hat{R}_2}{1+\hat{R}_2}\right\}\Phi \tag{C-46}$$

The solution of this problem now has to performed numerically. Note that to obtain threshold there have to exist values of $\hat{r}$ that have gain otherwise (C-45) will never be satisfied.

A special case of the aperture–coupled resonator is where the aperture becomes so weak that the multiple reflections can be neglected, namely, the coupling is so strong that it behaves as a single resonator rather than as two coupled resonators. This provides a simple means for modeling of gain guiding, even though in reality gain-guiding involves thermal lensing and anti-guiding due to refractive index depression with carrier presence. A resonator of this type can also be realized by aperturing the current with an oxidized or chemically undercut layer that is thin compared to the wavelength and placed at a node of the standing wave. In this way, the influence of the oxidized aperture on the wave is minimized. The gain sheet should then placed at a standing wave peak nearby to maximize the interaction with the electromagnetic wave. The region with gain (laterally confined is what then performs the aperturing).

To further motivate this analysis we show that in the weakly-apertured resonator, the aperture does not have to *weak* if the mirror reflectivities are high, as in vertical-cavity lasers. In Section C.1.1. we have seen that the intensity of a beam passing through an active layer has contributions from the amplified (transmitted) and the reflected beam. In vertical-cavity lasers, due to high mirror reflectivities, these contributions are practically equal in size. Consider now the approximation performed in going from the exact *s*–parameter matrix (C-2) to the approximate (C-13). The matrix (C-13) includes the gain enhancement, but approximates the reflected beam with the transmitted since they are approximately of the same size in vertical-cavity lasers. In this way, the reflections are approximately accounted without neglecting their magnitude. In the next section, we numerically analyze this case.

## C.5. *Weakly–apertured resonator*

Most gain-guided VCSEL cavities are high finesse, open resonators with flat mirrors, and therefore the output beams of these lasers diffract very slowly. These lasers can therefore be analyzed accurately using the paraxial approximation, and that their geometry can be described using a Fresnel number. In order to realize this simplified picture, we reduce the large number of parameters used to describe the DBRs (center wavelength, number of layers and refractive indices of all materials involved) by approximating the DBR reflectivity spectrum with that of an equivalent hard mirror (constant reflectivity and fixed phase) as shown in Appendix B. By combining the phase- and diffraction-conserving models of the DBR, the cavity is replaced with an equivalent hard mirror resonator. The separation between the hard mirrors in this cavity is called the *diffraction effective cavity length* and is used in the definition of the Fresnel number. This hard mirror gain-guided resonator is shown to be completely specified by two parameters: the mean mirror reflectivity and the Fresnel number. For vertical cavity lasers the mean reflectivities are very high (greater than 98%) and under this additional condition the resonator can be completely specified with a single parameter: the ratio of the Fresnel number to the passive cavity finesse. All of the resonator variables - the threshold gain, the frequency spectrum, and the transverse mode patterns are functions of this ratio. We verified these scaling laws by a self-consistent solution for the two lowest order modes of a two-dimensional (the direction of propagation and one transverse dimension) vertical cavity with distributed mirrors. By performing a two-dimensional rather than a three-dimensional calculation we have significantly reduced the computation requirement, without reducing the generality

of the analytic approach. In this section we present an analysis of diffraction and cavity loss mechanism as starting point for a normalized theory for vertical cavity laser operation. In practical vertical cavity lasers the transverse mode definition is also influenced by thermal lensing and spatial hole burning. These effects depend on the material properties and the cavity structure details, they may have to be treated individually as deviations from the presented theory.

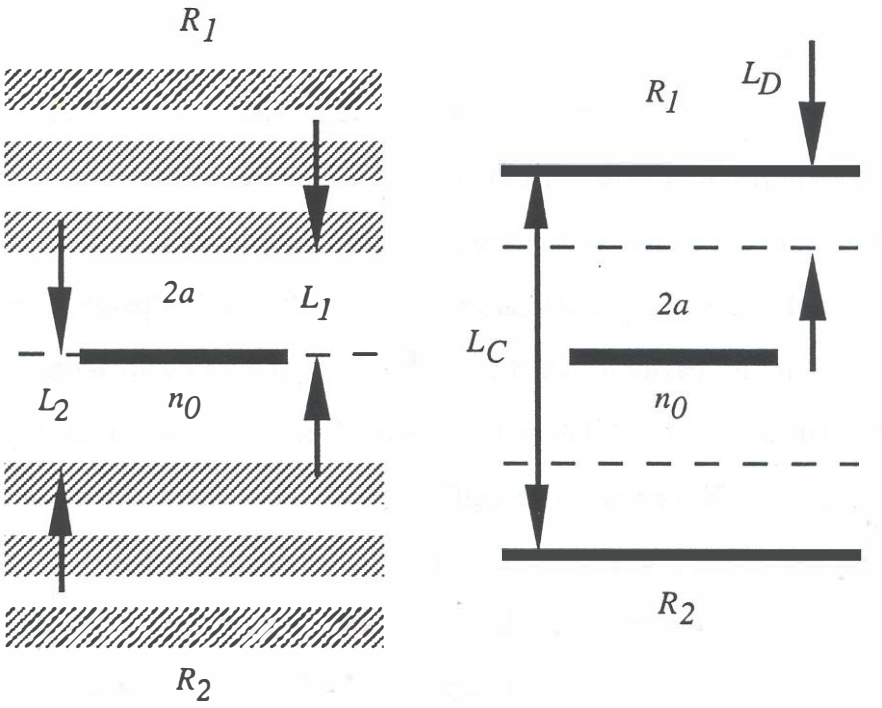


**Fig. C.22**: a) Two-dimensional vertical cavity structure with distributed mirrors 1 and 2. The gain region is an infinitely thin strip of width $2a$ and the mirror-to-mirror separation is equal to $L_1 + L_2$. b) Equivalent hard mirror cavity with diffraction equivalent cavity length equal to $L_C = L_{D1} + L_1 + L_{D2} + L_2$.

C.5.1. *Analysis*

The simplified VCSEL cavity structure used in this model is shown in Figure C.22(a). The gain region is infinitely thin, while the shape of the gain is defined by a real localized function $S(x/a)$ of characteristic width 1. In this analysis, we use a uniform aperture function defined by $S(\chi)=1$ if $|\chi|<1$ and zero otherwise. Two counter-propagating waves in the cavity are amplified independently, each of them experiencing field amplification equal to $1+g$. The total gain is $2g$, and the fractional power gain is $\xi g_a L_a$. (Gain that would have to be achieved with a gain region of thickness $L_a$, gain per length $g_a$, and gain enhancement factor $\xi$ located at the same position). The transverse mode field $\psi(x)$ is selectively amplified in the gain region according to $\psi(x) \rightarrow \tilde{\mathbf{G}}\psi(x)$, where $\tilde{\mathbf{G}} = 1+gS(x/a)$. The evanescent fields produced by sharp edges of the gain profile are confined to the immediate neighborhood of the gain region. The spatial region over which the reflected and the amplified beams interact is limited to half a wavelength in the material (Goodman, 1968). After passing the gain region, the beam enters the DBR. The shape of the reflected mode $\psi_r(x)$ is determined by decomposing the incident mode pattern $\psi_i(x)$ into plane waves, reflecting each plane wave component from the DBR and then reconstructing the real space field by linear combination of the reflected waves. The reflection coefficient of each plane wave component is calculated using the transmission matrix approach and is given for each mirror ($m=1,2$) by $\Gamma_m(k,\lambda)$, where $k$ is the transverse wave-number and $\lambda$ is the free-space wavelength. This reflectivity spectrum is different for $s$ and $p$ polarizations, and it includes the spacer layer of thickness $L_m$ in front of mirror $m$. The field reflected from mirror $m$ is given by $\psi_r = \tilde{\Gamma}_m \psi_i$ where $\tilde{\Gamma}_m$ is a linear

operator given by $\tilde{\Gamma}_m \psi_i(x) = F^{-1}\{\Gamma_m(k,\lambda) \cdot F\{\psi_i(x)\}\}$ ($F$ indicates Fourier Transform). The transverse modes of the entire structure are then described by the integral equation $\gamma \psi_r = \tilde{\Gamma}_2 \tilde{G} \tilde{\Gamma}_1 \tilde{G} \psi_r$, where $\gamma$ is the round-trip propagation eigenvalue. By neglecting spontaneous emission the threshold condition becomes $\gamma = 1$. The solutions of this equation for symmetric 0.98 μm AlAs/GaAs cavities with two different cavity lengths and three values of the peak mirror reflectivity are shown in Figure C.23.

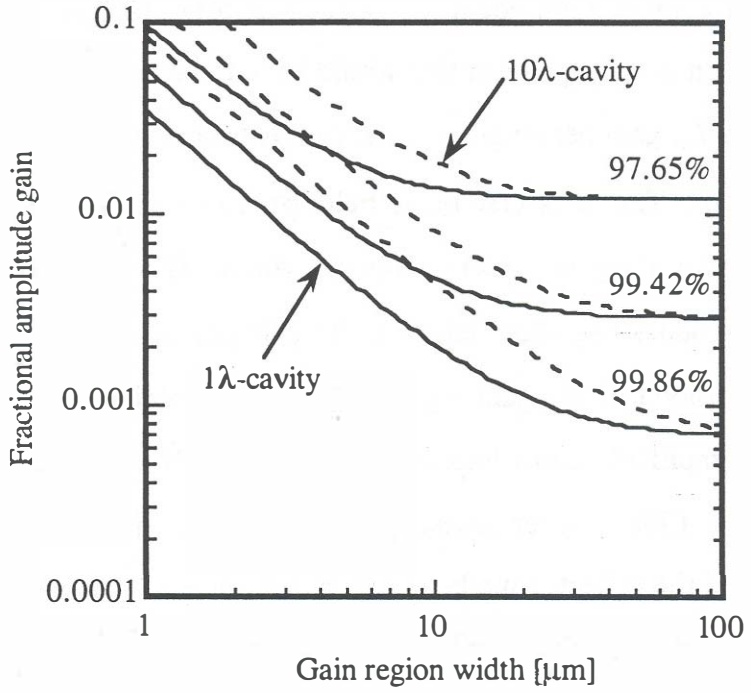


**Fig. C.23**: Threshold amplitude gain of symmetric $1\lambda$ and $10\lambda$ cavities with three different AlAs/GaAs mirrors plotted as function of the gain region width. The refractive indices are: cavity $n_0 = 2.95$, $n_H = 3.52$, $n_L = 2.95$ and substrate $n_e = 3.52$. The number of periods (peak reflectivity) for the three mirrors are 14 (97.65%), 18 (99.42%), and 22 (99.86%).

We now restrict the study to paraxial beams and follow the formalism described in Appendix B to replace each of the distributed mirrors by a hard mirror, as shown in Figure C.22(b). The $k$-space representation of the mirror reflectivity operation is then simplified to: (C-47)

$$\Gamma_m(k,\lambda) = \Gamma_m \exp(-ik^2(L_{Dm} + L_m)/k_0 n_0 + i2n_0(k_0 - k_{cm})L_{Pm} + i2n_0 k_0 L_m + i\theta_m)$$

The peak reflectivity amplitude is real and positive ($0 < \Gamma_m < 1$) while the fixed phase is absorbed in the $\theta_{ni}$ term. The free-space wave-numbers of the oscillation and the mirror centers are denoted by $k_0$ and $k_{cm}$. The distances $L_{Pm}$ and $L_{Dm}$ are the phase penetration depth and diffraction equivalent distance of the quarter-wave mirrors, which can both be determined analytically (Appendix B). We denote the *diffraction effective cavity length* by $L_C = L_{D1} + L_{D2} + L_1 + L_2$ and the *phase-effective cavity length* by $L_E = L_{P1} + L_{P2} + L_1 + L_2$. The plane wave resonance wave-number $k_n$ is given by $2n_0 k_n L_E = 2n_0(k_{c1}L_{P1} + k_{c2}L_{P2}) + n\pi - (\theta_1 + \theta_2)$, where $n$ is the longitudinal mode number. The fractional resonance offset is denoted by $\delta = (k_0 - k_n)/k_n$. The resonance of any laterally confined mode will be slightly detuned ($\delta > 0$) from the plane wave resonance. In general, the equivalent hard mirror resonator (Figure C.22(b)) will be asymmetric ($R_1 \neq R_2$ and $L_{D1} + L_1 \neq L_{D2} + L_2$). A significant simplification of the integral equation is obtained by restricting our study to the case where the active region is placed in the center of the diffraction effective cavity ($L_{D1} + L_1 = L_{D2} + L_2$). This is not a strong restriction since to first order, the position of the gain region has no effect on the threshold gain, provided that is placed at the peak of the standing wave. The integral equation is now separated into two symmetric parts similarly as in Section C.4.1,

one for each half of the cavity and the reflectivity angular spectrum of each half is given by

$$\Gamma(k,\lambda) = (-)^n \sqrt{R}\ \exp(-ik^2a^2/4\pi N + i\phi/2) \tag{C-48}$$

The Fresnel number is defined by $N = (1+\delta)a^2 n_0/L_C\lambda$, $R = \Gamma_1\Gamma_2$ is the mean mirror power reflectivity and the resonance offset $\phi = 2\delta n_0 k_n L_E$. Setting $\chi = x/a$ and $\gamma = 1$ we obtain a transformed integral equation $\Psi(\chi) = \left[\tilde{\Gamma}(\chi{:}R,N,\phi)\tilde{\mathbf{G}}(\chi{:}g)\right]^2 \Psi(\chi)$ in which the operators depend only on $g$, $\phi$, $N$ and $R$. For every pair of $N$ and $R$, this equation yields a pair of $g$ and $\phi$, and a family of mode patterns described by the eigenfunction $\Psi(\chi)$. To proceed with the introduction of scaling we note that for paraxial beams the angular spectrum is narrow $\Delta k^2 << 2k_0 n_0/L_C$ and that the plane wave cold cavity finesse $F = \pi\sqrt{R}/(1-R)$ of vertical cavity surface emitting lasers is large. We define $g_0$ as the gain of a infinitely wide gain region resonator (for a given reflectivity value $R(1+g_0)^2 = 1$), and note that under the established conditions the resonance offset $\delta$ and $g_0$ are both very small compared to unity. By expanding the exponential function in (C-48), the integral equation can be written in terms of the product $Ng_0$, the normalized gain $g/g_0$, and the normalized resonance offset $\phi/g_0$. Rearranging the terms and merging into exponential functions the integral equation is given approximately by,

$$\Psi_k(\kappa) = (g/g_0)\exp(-i\phi/2g_0)\ \exp(i\kappa^2/4\pi N g_0)\ S_k(\kappa a) \otimes \Psi_k(\kappa) \tag{C-49}$$

($S_k(ka)$ and $\Psi_k(ka)$ are Fourier Transforms of $S(x/a)$ and $\Psi(x/a)$, and $\otimes$ indicates convolution). Since for small $g_0$ the finesse is given by $F \cong \pi/2g_0$ the ratio $N/F$ becomes the single parameter necessary to completely describe any

resonator. The effect of this scaling is illustrated in Figure C.24, where the gain curves of the six AlAs/GaAs cavities shown in Figure C.23 have been reduced to a single curve by simply plotting the normalized gain versus the ratio $N/F$. The smallest gain region width considered was equal to one wavelength.

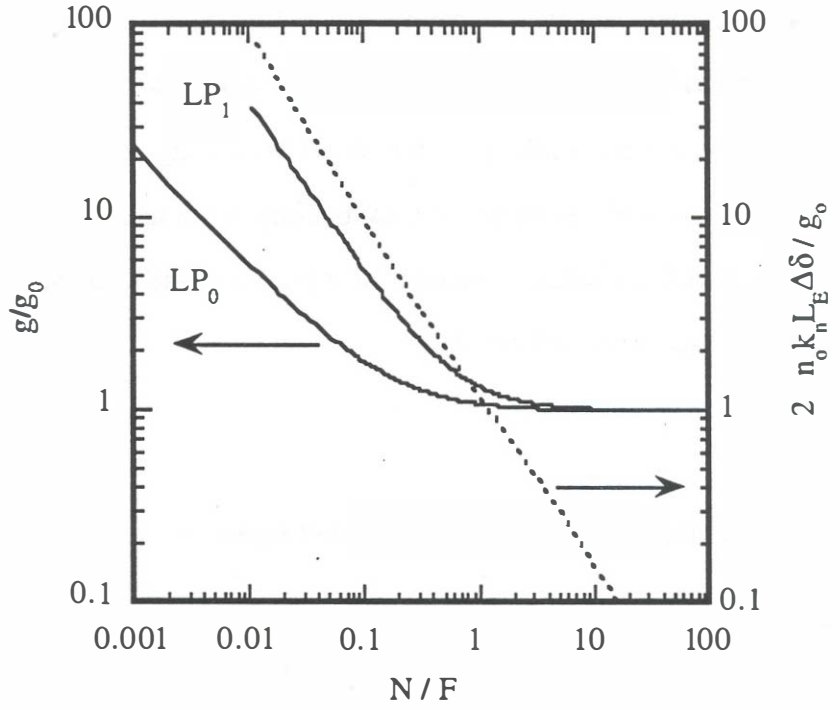


**Fig. C.24**: Normalized threshold amplitude gain $g/g_0$ and the normalized mode spacing between the two modes $4\pi\Delta\delta n_0 L_E/\lambda\, g_0$ for two-dimensional gain-guided cavities plotted as a function of $N/F$. The lowest order even and odd modes are denoted with $LP_0$ and $LP_1$.

In order to verify the scaling for a different wavelength, we have determined the modes and propagation constants of $1\lambda$ and $10\lambda$ cavities with two InGaAsP/InP DBRs tuned to 1.55 μm. The results are also shown in Figure C.24, since the

scaling of the threshold gain and the mode spacing was confirmed in all studied cases to within the numerical accuracy of our calculation. The widths of the field $\Delta x/a$, the mode angular spectrum $\Delta k/a$, and the uncertainty product $\Delta x\Delta k$ were more susceptible to the violation of the paraxial requirement (small $N$), but have exhibited very little error even for the smallest gain region widths. For $s$ and $p$ polarized modes in the $10\lambda$ AlAs/GaAs cavity $\Delta x\Delta k$ differed by less than 10% at $2a = 0.5\mu\text{m}$, while $\Delta x\Delta k$ for the equivalent hard mirror cavity was 20% larger than the $s$ polarized mode for the same gain width. The scaling laws have been numerically verified for two-dimensional cavities, but due to the scaling property of the Fourier transform and the radial symmetry of equation (C-49) this analysis is fully applicable to three-dimensional cavities.

### C.5.2. *Derivation of scaling for weak-aperture coupled resonator*

To derive the scaling for a symmetric weakly-apertured resonator, consider the structure shown in Figure C.22(b). The gain operator $\hat{g}$ is defined via position dependent aperture function:

$$\hat{g}|x\rangle = g\,S(x)|x\rangle \tag{C-50}$$

where $\hat{g}$ is a constant and $S(x)$ is the shape function. The equations defining the system are derived similarly as in (C-41).

$$f_1 = (1+\hat{g})\hat{r}_2 f_2 + \hat{g}\,\hat{r}_1 f_1 \quad f_2 = (1+\hat{g})\hat{r}_1 f_1 + \hat{g}\,\hat{r}_2 f_2 \tag{C-51}$$

Threshold is obtained when the eigenvalue $\gamma = 1$ in equation

$$\gamma f_1 = \frac{1}{1-\hat{g}\hat{r}_1}(1+\hat{g})\hat{r}_2 \frac{1}{1-\hat{g}\hat{r}_2}(1+\hat{g})\hat{r}_1 f_1 \qquad \text{(C-52)}$$

In order to get a representation with a single operator equation we subtract the two equations (C-51) and get $(1+\hat{r}_1)f_1 = (1+\hat{r}_2)f_2$. This equality represents the total transverse field in the center of the cavity. We now define the symmetric field $\Phi = \hat{r}_1 f_1 + \hat{r}_2 f_2$, and quickly obtain the resonator equation that resembles (C-45).

$$\frac{1-\hat{r}_1\hat{r}_2}{\hat{r}_1(1+\hat{r}_2)+\hat{r}_2(1+\hat{r}_1)}\Phi = \hat{g}\Phi \qquad \text{(C-53)}$$

Equation (C-53) is the starting point for the introduction of scaling laws. First note that close to resonance $\hat{r} \cong 1-\hat{\varepsilon}$ where $\|\hat{\varepsilon}\Phi\| << \|\Phi\|$, and that for the same reason $\|\hat{g}\Phi\| << \|\Phi\|$. Now we can express the mirror reflectivities in terms of reflection amplitude $\Gamma_i$ and propagation $\exp(-i\chi^2/N_i)$:

$$r_i = \Gamma_i \exp(-i\chi^2/N_i) \qquad \text{(C-54)}$$

With this we have selected the representation of the operators to be in $k$-space. the integral equation is now:

$$\frac{1-\Gamma_1\Gamma_2\exp(-i\kappa^2/N)}{\Gamma_1\exp(-i\kappa^2/N_1)+\Gamma_2\exp(-i\kappa^2/N_2)+2\Gamma_1\Gamma_2\exp(-i\kappa^2/N)}\Phi = gS\otimes\Phi \qquad \text{(C-55)}$$

where $\chi = ka$ and $1/N = 1/N_1 + 1/N_2$. The numerator of the left-hand side operator has a phase that varies much faster with $\kappa$ than the denominator. This is instrumental to the introduction of scaling.

$$\frac{1-\Gamma_1\Gamma_2}{\Gamma_1+\Gamma_2+2\Gamma_1\Gamma_2}\cdot\frac{1+i\dfrac{\Gamma_1\Gamma_2}{1-\Gamma_1\Gamma_2}\dfrac{\kappa^2}{N}}{1-i\kappa^2\left\{\dfrac{\Gamma_1/N_1+\Gamma_2/N_2+2\Gamma_1\Gamma_2/N}{\Gamma_1+\Gamma_2+2\Gamma_1\Gamma_2}\right\}} \qquad \text{(C-56)}$$

We place the gain region exactly at the center of the effective cavity, but leave the mirror reflectivities different. Since $\Gamma$'s are close to unity (at resonance) the operator can be approximated by

$$\frac{1-\Gamma_1\Gamma_2}{4}\frac{1+i\dfrac{1}{1-\Gamma_1\Gamma_2}\dfrac{\kappa^2}{N}}{1-i\dfrac{3\kappa^2}{4N}} \cong \frac{1-\Gamma_1\Gamma_2}{4}\exp\left(i\frac{1}{1-\Gamma_1\Gamma_2}\frac{\kappa^2}{N}\right) \tag{C-57}$$

Finally, using $R=\Gamma_1\Gamma_2$ the integral equation becomes

$$\exp\left(i\frac{\chi^2}{N}\cdot\frac{1}{1-R}\right)\Phi(\chi)=\frac{4g}{1-R}S(\chi)\otimes\Phi(\chi) \tag{C-58}$$

It is possible to approximately relate this scaling to the cavity finesse

$$F=\frac{\pi\sqrt{R}}{1-R}\cong\frac{\pi}{1-R} \tag{C-59}$$

since $R\cong 1$, then $2R>>1-R$ and

$$\frac{1}{N'}\cong\frac{F}{\pi N} \qquad g'=\frac{4}{\pi}Fg \tag{C-60}$$

then (C-58) becomes

$$\exp\left(i\frac{\chi^2 F}{\pi N}\right)\Phi(\chi)=\left(\frac{4}{\pi}Fg\right)S(\chi)\otimes\Phi(\chi) \tag{C-61}$$

C.5.3. *Practical significance of scaling*

The use of the paraxial approximation is instrumental to a simplified analysis of weakly-apertured vertical-cavity resonators with distributed mirrors. We have shown that in the absence of other mode determining mechanisms these resonators can be completely described by a single number: the ratio between the Fresnel number and the cold cavity finesse. The origin of the scaling arises from the simplification of the wave propagation in the cavity to two mechanisms: beam

diffraction and loss of energy to the mirrors. The ratio $N/F$ describes the competition between these two mechanisms in determining the transverse modes and their propagation constants. There is a unique mode shape of every order associated with each value of $N/F$. As shown in Figure C.25, in the region where $N > F$ the gain is dominated by the mirror loss, the effect of diffraction is negligible and hence the confinement factor is near unity. For $N < F$ the diffraction within the cavity broadens the mode, which in turn reduces the confinement factor and causes the increase in threshold gain.

The practical significance of the $N/F$ scaling can be appreciated in the following examples. For minimum threshold gain the laser should be designed so that $N > F$. This ensures that the confinement factor is close to unity and that most of the gain is used for supporting the mirror and cavity losses. However, this regime provides a very weak transverse mode discrimination. Since the mode discrimination improves and the threshold gain of the fundamental mode increases for $N < F$, the optimum design for low threshold single transverse mode gain-guided VCLs will evidently lie in the range where $N \approx F$. In the neighborhood of this breakpoint, the confinement factors of higher modes change much faster than for the fundamental mode thereby producing fast increase in the mode discrimination while only weakly affecting the threshold gain of the fundamental mode.

The next step in this analysis is the extension to three-dimensional cavities and the vector-plane wave expansion. , and experimental verification of the scaling. Hopefully, with the advance of laterally oxidized vertical-cavity lasers this may be possible.

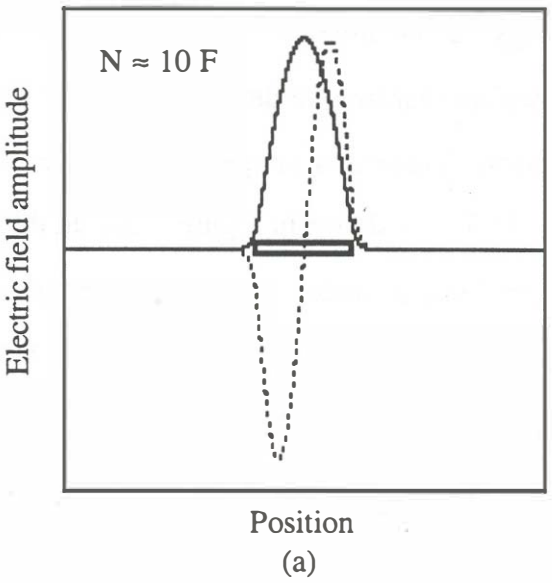


(a)

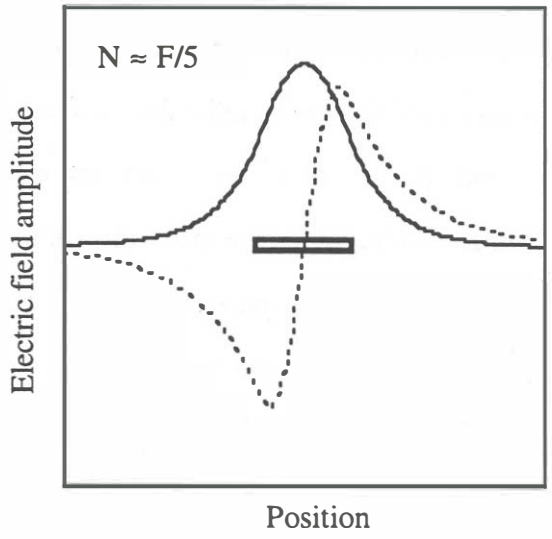


(b)

**Fig. C.25:** Transverse mode profiles for a) $N \approx 10F$ and b) $N \approx F/5$.

Appendix D

# Characterization of metal mirrors on GaAs

It is a common practice to use nonalloyed metal reflector on top of quarter-wave mirror to boost the reflectivity of the mirror and thereby reduce the number of periods of the quarter-wave stack necessary to achieve some given reflectivity value. In order to increase the overall reflectivity of the mirror, the last layer in front of the metal has to adjust the phase of the metal reflection to match the phase of the quarter-wave mirror at the design wavelength. The thickness of this *phase-matching* layer depends on the phase of the metal reflection, while the increase of the overall mirror reflectivity depends on the reflectivity of the semiconductor-metal interface. In this appendix we describe a Fabry-Perot technique for the determination of the reflection coefficient (amplitude and phase) of the interface between GaAs and several metal contact structures: Ti/Au, Au and Ag deposited by e-beam evaporation and Pd/Au deposited by thermal evaporation.

The structure that was used to characterize the metal-semiconductor interface is shown in Figure D.1. The incident medium has the reflective index $n_o$, while the cavity has

index $n_s$. The exit medium can be either a dielectric with a real refractive index $n_e$, or a metal with complex refractive index $n_m - ik_m$.

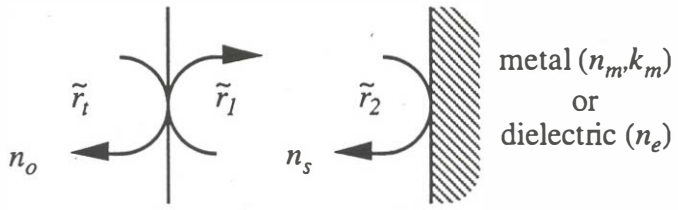


**Fig. D.1**: A Fabry-Perot cavity formed by the phase matching layer of index $n_s$ and the metal (or dielectric) coating. The reflection coefficients seen from the cavity are denoted by $\tilde{r}_1$ and $\tilde{r}_2$, while the total reflection is $\tilde{r}_t$. The reflection 2 can be either metal or dielectric.

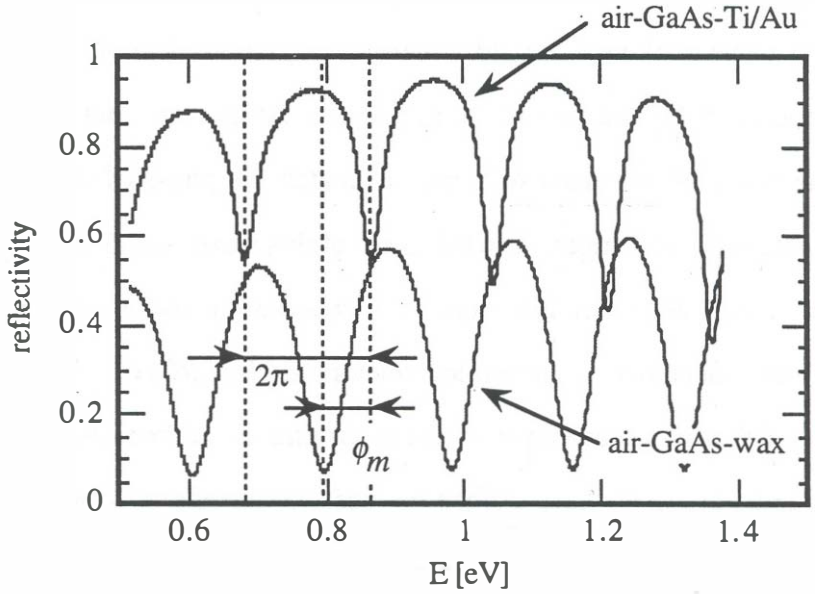


**Fig. D.2**: The measured reflectivity spectra on sample P247–M1. The phase measurement is illustrated.

The reflection spectra of this structure when terminated with metal and a dielectric are periodic: An example is shown in Figure D.2. The depth of the Fabry-Perot fringes

depends on the strength of the reflections of the two interfaces, while the offset between the extrema of the semiconductor/metal trace and the semiconductor/wax trace depends on the phase of the semiconductor-metal reflection (GaAs–wax reflection phase is zero – see later text).

## D.1. *Measurement of the fringe ratio and reflection phase*

To determine the reflection strength quantitatively we measure the fringe ratio of the Fabry-Perot reflectivity spectra. Consider a Fabry-Perot interferometer shown in Figure D.1. We set $r_2 = |\tilde{r}_2|$ and $r_1 = \tilde{r}_1$, since $n_o$ and $n_s$ are real. The phase of the semiconductor/metal reflection $\phi_m$ is absorbed in the round-trip phase term $\theta = 2\beta L + \phi_m$, where the wave number in the cavity and the length of the cavity are denoted by $\beta$ and $L$. The power reflectivity $R(\theta) = |r_t(\theta)|^2$ of the resonator is then given by

$$R(\theta) = \frac{r_1^2 + r_2^2 - 2r_1 r_2 \cos\theta}{1 + r_1^2 r_2^2 - 2r_1 r_2 \cos\theta} \qquad \text{(D-1)}$$

The extrema of this reflectivity function occur when $\theta = 0$ and $\theta = \pi$.

$$R(0) = \left(\frac{r_1 - r_2}{1 - r_1 r_2}\right)^2 \quad R(\pi) = \left(\frac{r_1 + r_2}{1 + r_1 r_2}\right)^2 \qquad \text{(D-2)}$$

The *fringe ratio* is defined by $\rho = R_{min}/R_{max}$, where $R_{min}$ is the reflectivity at the resonance (bottom of the valley in the reflectivity curve), and $R_{max}$ is the reflectivity at the anti-resonance if anti-resonance would occur at the same wavelength. This, of course, never happens so we calculate $R_{max}$ as the average of the two neighboring

anti-resonances. The relation between the fringe ratio and the reflection coefficients $r_1$ and $r_2$ is given by:

$$\frac{1-\sqrt{\rho}}{1+\sqrt{\rho}} = \left| \frac{r_2(1-r_1^2)}{r_1(1-r_2^2)} \right|^{\pm 1} \qquad \text{(D-3)}$$

The exponent is adjusted so that the fringe ratio is always less than unity. With the known (assumed) value of $r_1$ and the measured value of $\rho$, this relation can be solved analytically to yield the value of $r_2$. It is important to note that the presence of loss in the semiconductor decreases the obtained value of $r_2$. What is in fact measured is

$$r_2' = r_2 \exp\left(-\int_0^L \alpha(x)dx\right) \qquad \text{(D-4)}$$

where $\alpha(x)$ is the position dependent absorption loss in the cavity. This equation holds for the case where the absorption is weak enough not to perturb the fields in the cavity; $n_s$ is approximately real. Therefore, one must account for the presence of loss in the layers preceding the metal to correctly determine the metal reflection strength.

The measurement of the metal reflection phase is obtained by comparing the shift between the reflection spectra of a known reflection (semiconductor to dielectric) and the cavity with the metal mirror. Figure D.2 illustrates how the data is extracted from the graph. The minima of the reflectivity spectra are offset by exactly the amount of the metal reflection phase. As an example, consider the case where an ideal metal with the reflection phase equal to $\pi$ is compared to the dielectric reflection which has zero phase. In this case the minima of one curve would coincide with the maxima of

the other. Since real metals are not nearly perfect at optical frequencies this phase is offset from 180° down to the 130-170° range.

## D.2. *Fabrication and characterization*

The samples were fabricated in the following way: A structure shown in Figure D.3 was grown using MBE and sample of 10 x 8 mm was cleaved. The desired metal was evaporated on one half of the sample (Figure D.4) in order to make reflection measurements on two places which were close enough so the epilayer thickness can be assumed equal.

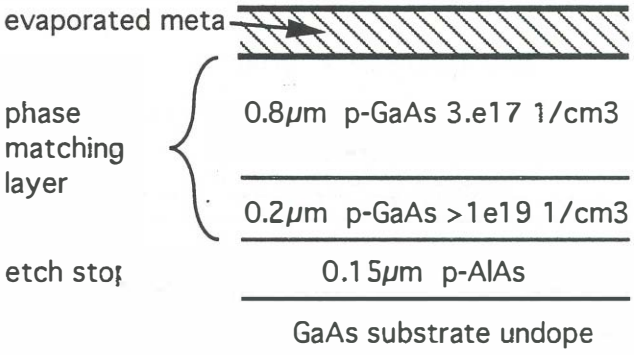


**Fig. D.3**: MBE grown structure S234 for characterization of GaAs-metal interface. The S235 epi structure is identical to S234 except that it was capped with 10 nm of highly *p*-doped GaAs.

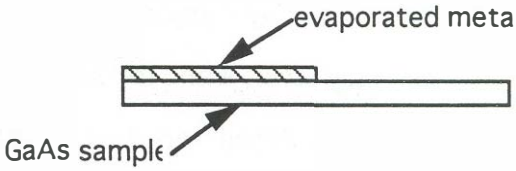


**Fig. D.4**: A half of the sample was covered to evaporate the metal.

After the evaporation, the sample was mounted on a glass slide for GaAs substrate removal using $NH_4OH:H_2O_2$ spray etching with pH 8.3. The etch stop layer (AlAs) was removed using $NH_4OH:H_2O$ and $HF:H_2O$ mixtures. The first of three reflectivity measurements is performed at this time (measurement 1). The GaAs layers were subsequently etched in 1:1:50 $H_3PO_4:H_2O_2:H_2O$ for 4 minutes to remove ≈ 280 nm ( 1st etch) and then for 2 minutes to remove ≈ 130 nm (2nd etch) of GaAs. The reflectivity was measured after each of these two etches (measurements 2 and 3). This was done to observe the fringe strength and phase measurements dependence on the thickness of the epilayer. In fact, this additional etching and measurements were instrumental to obtaining accurate measurements of the reflectivity.

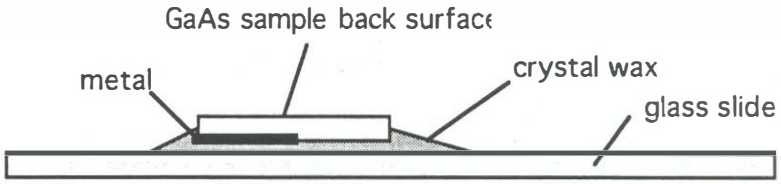


**Fig. D.5**: Substrate removal using $NH_4OH:H_2O_2$ spray etching.

Inasmuch as there is a 200 nm thick highly doped layer in the structure (Figure D.3) the reflection coefficient of the GaAs–metal interface $r_2$ was reduced due to absorption loss, which resulted in an erroneous reading of the reflectivity. An accurate measurement was accomplished by comparing the three measurements: The 1st measurement is includes the lossy layer, while the 2nd and the 3rd measurement do not, since the rest of the GaAs is doped very low ($3 \cdot 10^{17}\,cm^{-3}$). All of the reflectivity measurements were performed at two places on the sample: One over the metal and one over the wax. The GaAs to wax reflection is assumed to have phase

zero. This is true for wax that has very low loss in the wavelength range of interest. Using a transmission measurement through a 1 mm thick slab, the IR absorption in crystal wax was measured to be below $30\ cm^{-1}$ in the entire wavelength range of measurement. Table D.1 contains the summary of samples that were analyzed along with the results of the measurements.

## D.3. *Results and discussion*

Using these measurements we have obtained an estimate of the metal-semiconductor interface reflection strengths for Pd/Au, Ti/Au, Au and Ag. Using three reflectivity measurements (and two etching steps) we were able to eliminate the influence of loss and get a consistent measurement of the reflection coefficient. Figure D.6 shows an example of the three reflectivity curves for sample P249M1. As seen from Figure D.3, the high absorption region extends only over the first 200 nm of the measured epilayer. To account for the absorption in the lossy layer we compare the three reflection measurements: The reflection coefficient of the metal with the absorbing layer is $r_2' = r_2 \exp(-\alpha L)$ where $L = 200\,\text{nm}$ and $r_2$ is the reflection coefficient of GaAs–metal interface. Once the lossy layer is etched off we perform the second measurement which yields $r_2$ since we are assuming that the loss in the remaining layers is negligible. If this in fact were true, then the third measurement (after the second etch) should yield equal value of $r_2$. This is in fact what can be very easily seen from the data in Table D.1: The $r_2$ measurements 2 and 3 are approximately equal and are consistently higher than the first measurement for all samples.

From these measurements we can estimate the absorption coefficient of GaAs at 1.55 μm using $\alpha = \ln(r_2/r_2')/L$. The estimates of this coefficient are also listed in Table D.1 showing that measured $\alpha$ values fit in the range of published values for *p*-GaAs absorption at 1.55 μm ($800 - 1400\ \mathrm{cm}^{-1}$). Note that for most samples the phase measurement is independent of the presence of the absorption layer, which is to be expected since the absorption is still to low to produce any significant changes in the phase. The two Ag/GaAs measurements P249–M1/M2/M5 and P249–M3/M4/M6 were done on slightly different epi structures: The structure of S234 is shown in Figure D.3. The structure of P249(S235) is the same except that the 10 nm next to the metal is very highly doped, which could explain some of the difference in the fringe ratio.

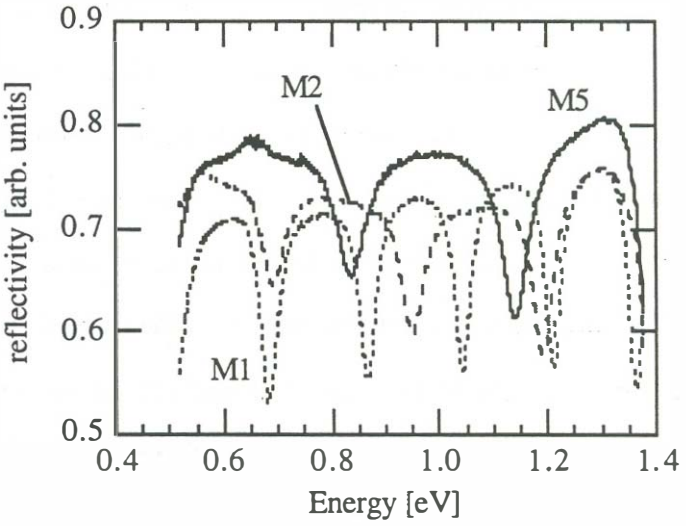


**Fig. D.6**: The three reflectivity measurements on the silver coated sample P249M1.

The comparison between the measurements and the published data is shown in Figure D.7. The discrepancy may originate from a number causes: surface preparation and

roughness, presence of oxide on the semiconductor prior to evaporation and finally the quality of the evaporated metal. Nevertheless, the agreement with the published values is not so critical here. The importance of this method lies in that it can be used to characterize the reflection strength of a metal scheme *as it will be made* in the finished device – including the effects of surface roughness, cleaning, and metal deposition.

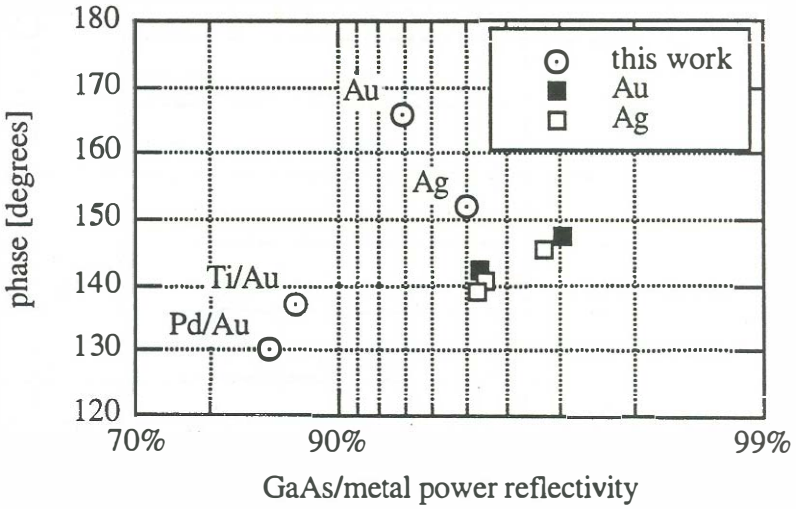


**Fig. D.7**: Reflectivity and phase of GaAs/metal interface at 1.55 μm compared to values calculated from published optical constants of Ag and Au.

| sample # | epi thick [μm] | epi/metal | thick. [nm] | $\rho/\phi_m$ 1.55 μm | $\rho/\phi_m$ 1.3 μm | $\approx \alpha$ $cm^{-1}$ | $r_2$ 1.55μm |
|---|---|---|---|---|---|---|---|
| P245–M1 | ≈ 1.0 | S234–Ti/Au | 2/160 | 0.59/— | 0.58/— | | 0.9177 |
| P245–M2 | 1st etch | ··· | ··· | 0.70/— | 0.64/— | 1380 | 0.9434 |
| P245–M3 | 2nd etch | ··· | ··· | 0.70/— | 0.64/— | | 0.9432 |
| P247–M1 | ≈ 1 | S234–Ti/Au | 2/170 | 0.59/134° | 0.55/125° | | 0.9177 |
| P247–M2 | 1st etch | ··· | ··· | 0.67/137° | 0.59/118° | 940 | 0.9367 |
| P247–M3 | 2nd etch | ··· | ··· | 0.66/137° | 0.59/127° | | 0.9333 |
| P249–M1 | 0.94 | S234–Ag | 120 | 0.76/150° | 0.76/152° | | 0.9561 |
| P249–M2 | 0.66 | ··· | ··· | 0.86/153° | 0.83/— | 960 | 0.9756 |
| P249–M5 | 0.54 | ··· | ··· | 0.85/152° | 0.83/150° | | 0.9739 |
| P249–M3 | ≈ 1 | S235–Ag | 120 | 0.74/140° | 0.73/128° | | 0.9520 |
| P249–M4 | 1st etch | ··· | ··· | 0.85/128° | 0.82/115° | 1060 | 0.9737 |
| P249–M6 | 2nd etch | ··· | ··· | 0.84/— | 0.81/120° | | 0.9711 |
| P256–M1 | ≈ 1 | S234–Au | 100 | 0.70/166° | 0.69/163° | | 0.9434 |
| P256–M2 | 1st etch | ··· | ··· | 0.80/166° | 0.76/165° | 1100 | 0.9641 |
| P256–M5 | 2nd etch | ··· | ··· | .80/172° | 0.76/163° | | 0.9645 |
| P256–M4 | 1st etch | S234–Pd/Au | 3/100 | 0.62/137° | 0.54/120° | — | 0.9251 |
| P256–M6 | 2nd etch | ··· | ··· | 0.61/130° | 0.54/— | | 0.9234 |

**Table D.1**: List of samples. The fringe ratio has been rounded to two and the phase to three significant digits.

# Appendix E

# Long-wavelength vertical-cavity lasers at UCSB (A personal log)

The invention of the vertical-cavity laser was a result of an effort to fabricate single-mode monolithic semiconductor lasers that was conducted in the mid-seventies at the Tokyo Institute of Technology under the guidance of Professors Yasuharu Suematsu and Kenichi Iga. In the course of development of such lasers, a number of structures, such as etched facet lasers and Distributed Feedback lasers were explored. It was one night in March of 1977, according to Professor Iga (Iga[b], 1995), he had the idea of making a laser in which light oscillates in the direction perpendicular to the wafer surface. This type of device could be fabricated monolithically and with a short cavity could operate in a longitudinal single mode. He noted this idea in his notebook, which he would take home with him just for cases like these, and the concept of *surface-emitting laser*, as Professor Suematsu later named it, was born. The technological and application promises of surface-emitting lasers were many. Since it could be fabricated monolithically and its lateral structure defined by photolithographic means, it held many of the manufacturing advantages of light-emitting diodes and other monolithic semiconductor devices, in addition to some inherent performance advantages over in-plane lasers.

The long-wavelength VCL research at UCSB started in 1988 as a joint effort of Professors John Bowers and Evelyn Hu. James Dudley, one of Professor Bowers' first graduate students, started this effort at Santa Barbara by developing optical coatings and the fabrication process for etched well VCLs operating at 1.3 μm. At that time there were no growth facilities at UCSB that could be used for growing phosphides. The MOVPE system was purchased and installed two years later. The active layer materials were provided by several groups outside of UCSB: Dr. Barry Miller from AT&T Bell Laboratories in Holmdel, NJ and Prof. Gary Robinson from Colorado State University. In 1988 Dr. Deborah Crawford joined Prof. Bowers' research group as a post-doctoral researcher, while I joined in 1989 as a graduate student on a joint project with Professors Bowers and Hu. While James and Deborah were developing the fabrication process for an etched-well VCL, I was developing high reflectivity mirrors. My first project involved customizing a donated commercial sputtering machine for deposition of $Si/SiN_x$ mirrors. I spent several months developing a multi-tasking software that would automate this machine and enable flexible programming that was needed for making mirrors and various optical coatings (Babić[a], 1991). Using this machine we started depositing 8 to 10 period mirrors $Si/SiN_x$ for the first 1.3 μm VCLs.

Our efforts came to fruition with the visiting researcher from OKI Electric (Japan), Hiroshi Wada, who arrived in 1990 and eventually built the first 1.3 μm VCL at UCSB. This was an etched well vertical-cavity laser with $Si/SiN_x$ mirrors on both sides of the cavity, that operated at a record low room-temperature pulsed current of 50 mA (Wada, 1991). The structure of this laser is shown in Figure E.1.

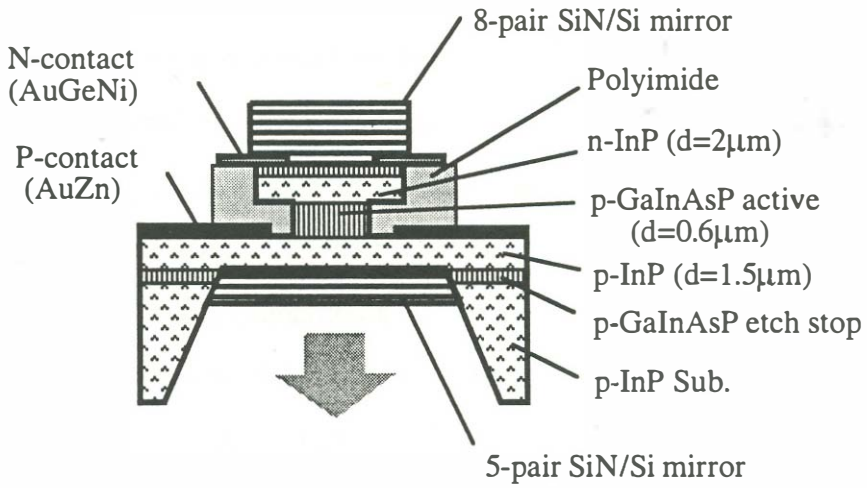


**Fig. E.1**: The structure of the first long-wavelength vertical-cavity laser fabricated at University of California, Santa Barbara (Wada, 1991).

Many interesting issues relevant for the future direction of UCSB long-wavelength VCL research surfaced in the characteristics of these lasers. Hiroshi Wada noticed that the threshold current density increased with the increasing diameter of the devices (Figure E.2). This was attributed to nonuniform current injection resulting from ring contacts and lateral current flow through poorly conductive *p*-type region (Wada, 1992). Furthermore, with high current densities, and hence high gain, at the edges of the active layer, one would expect the higher order transverse modes to reach threshold before the fundamental mode. However, even on the largest device (20 μm) the near-field pattern and the spectrum revealed a single mode, and this mode had only one lobe with the maximum in the center (Figure E.3). This fact turned our attention to diffraction which results in mode selective cavity loss. Since the cavities of these resonators had to be rather long to provide for lateral current flow, they could

not be scaled to very small sizes without increasing the diffraction loss. Scaling devices to small volumes was advantageous for reducing active layer operating temperature. This issue was very important since the thermal properties of etched-well VCLs were very poor owing to the low thermal conductivity of the amorphous mirrors. Looking at the very low external quantum efficiency of these lasers which was less than 0.5 % we concluded that the cavity losses were still too high than we expected. It was subsequently found that amorphous silicon used in our mirrors was quite lossy, as high as $\alpha_{Si} \approx 1000\text{cm}^{-1}$ at 1.3 μm (Babić, 1992), which limited the reflectivity of our $Si/SiN_x$ mirrors to 99.0 % at 1.3 μm.

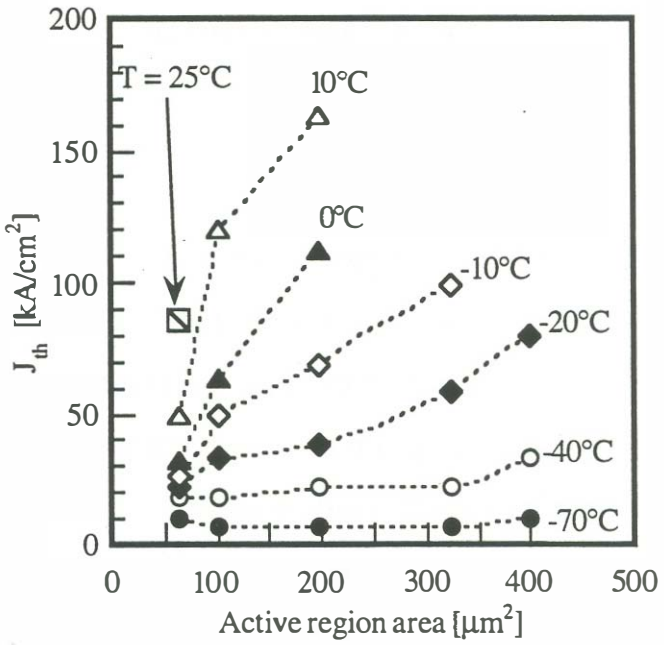


**Fig. E.2**: Threshold current density dependence on device area (diameter) indicating that nonuniform current injection is present (Wada, 1992).

At this point our efforts branched off to several directions; a new type of device had to developed. The year 1992 saw the departure of Hiroshi Wada and Deborah Crawford, and the arrival of a new visiting researcher, Mitsuaki Shimizu from Tokyo Institute of Technology. Dr. Shimizu concentrated on numerical modeling of etched-well VCLs with regrown active layers to find the conditions for continuous wave room temperature operation (Shimizu, 1993). I started working on reducing loss in amorphous silicon by hydrogenation, i.e. silicon sputtering in $Ar/H_2$ plasma. Hydrogenation did not produce good results because the refractive index of silicon was reduced in the hydrogenated layers and the reduction in absorption coefficient was not as high as was expected. Using a large refractive index ratio, such as, $Si/SiO_2$ seem to be the only way to fabricate better mirrors using the existing technology. For this purpose, I converted our sputtering machine to an RF source. Now we were able to perform RF and DC sputtering simultaneously of silicon, silicon nitride and silicon oxide. Furthermore, Thomas Reynolds from UCSB and I installed a 1.3 μm laser reflectometer on the machine. To accomplish this we designed a hollow anode with a window through which the laser beam could be normally incident on to the wafer. Using this system were we able to perform in-situ optical deposition rate calibration and tuning of mirrors (Babić, 1991). Most researchers in other institutions that were investigating long-wavelength VCLs were using electron-beam evaporated amorphous mirrors (Imajo, 1990, Oshikiri, 1991, Tadokoro, 1992, Baba, 1993), while we were using RF reactive sputtering. This was done because of the greater control over the deposition rates that was achievable with our computerized sputtering machine. Furthermore, we did not have an in-situ monitoring system for the electron-beam evaporator.

During the first years of graduate school, I devoted a lot of time studying theoretical aspects of quarter-wave mirrors. In Fall of 1990, while playing with numerically calculated penetration depths of quarter-wave mirrors, I noticed that for some special cases the penetration depth depended inversely on the difference between the refractive indexes of the two mirror materials. This relationship led me to believe that maybe there was an analytic expression for this parameter. I pursued this for a few months until I finally derived an analytic expression for the group delay and the penetration depth of arbitrary quarter-wave mirrors at the center wavelength (Babić, 1991). With the help of Youngchul Chung and Scott Corzine I expanded the concept to diffraction quarter-wave mirrors (Babić, 1991) and with the help of Rajeev Ram to resonators with distributed mirrors (Babić, 1993). The latter idea was later fully developed by Rajeev Ram (Ram, 1995).

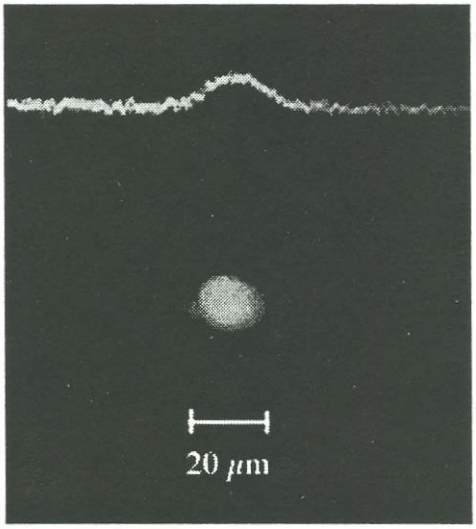


**Fig. E.3**: Near-field pattern of a 20-μm diameter device showing single-lobed field intensity profile (Wada, 1992).

My interest in laser fabrication centered on building a 1.55 μm vertical-cavity laser with InGaAsP/InP mirrors with either implantation or regrowth used for current and mode confinement (structure of the type shown in Figure 1.2(b)). I experimented with methane-hydrogen-argon etching of these mirrors for mode confinement (Section 8.4).

James Dudley, on the other hand, was searching for completely new ways of making mirrors. One of the things he tried were air-bridge mirrors (Ho, 1990), but this did not seem to be easily manufacturable. Finally, he ran across recent interesting results on wafer fusion (Liau, 1990, Lo, 1991), a method for bonding InP to GaAs or silicon by forming what was believed to be a covalent bond. Provided that this bond was optically transparent and thermally and electrically conductive, James thought, one could make a VCL using InGaAsP active layers and AlAs/GaAs mirror tuned to long wavelengths. This was a revolutionary idea because it completely avoided all the problems that we had with epitaxial or amorphous mirrors. Using an AlAs/GaAs mirror on at least on one side would improve the thermal and electrical properties of the laser. James made the first fusion experiments at UCSB in the discarded LPE furnace using weights with Masayuki Ishikawa, a visiting researcher from Furukawa. They first made fused in-plane lasers and then demonstrated the high temperature operation of a single fused VCL structure with one AlAs/GaAs mirror and one $Si/SiO_2$ mirror using optical pumping (Dudley, 1992[b], 1993). The active layers for these devices were grown by Dr. Barry Miller from AT&T Bell Labs in Holmdel, while the AlAs/GaAs mirror was grown by Richard Mirin at UCSB. With this result, Richard Mirin became the official supplier of GaAs mirrors for fused long-wavelength vertical-cavity lasers.

After the demonstration of the fused optically pumped VCLs, Rajeev Ram, a first year graduate student in John Bowers' group went to work as a summer intern in Hewlett-Packard, Palo Alto. The group at Hewlett-Packard Laboratories in Palo Alto, Dr. Kent Carey and Dr. Long Yang, had similar interests. They also felt that wafer fusion may be a good way to fabricate long-wavelength vertical-cavity lasers. This started a collaboration between UCSB and HP Labs in developing wafer-fused VCLs that is active to present day. Rajeev Ram spent the summer with Dr. Long Yang at Hewlett-Packard experimenting with fusion of InP to GaAs and other materials and made the first studies of the electrical and optical quality of the junctions (Ram, 1993, 1995[b]). They also developed a cleaning procedure, which with some modifications, has been being used to date at UCSB.

Meanwhile, many of the potential sources of InGaAsP/InP mirrors that I needed for my project were losing interest. The mirrors were too thick (15 μm) to be grown by GSMBE, and too difficult to control the wavelength. I was very fortunate that I met Dr. Klaus Streubel from KTH, Stockholm in Spring of 1993, while he was visiting UCSB for a QUEST workshop. We quickly realized that our common interest is the fabrication of 1.55 μm VCLs using InGaAsP/InP mirrors at least on one side of the resonator. Unlike many others, Klaus was able to grow these mirrors using MOVPE with astonishing control of the center wavelength and composition. We decided to collaborate on building 1.55 μm VCLs, and Klaus started sending material to UCSB for me to fabricate lasers. The design I decided to pursue used an $n$-InGaAsP/InP post and $p$-type GaAs/AlAs mirror on the bottom bonded by wafer fusion, as shown in Sec. 8.4.

The end of summer of 1993 brought the first electrically-pumped wafer-fused VCL (Dudley, 1994). This device used an $n$-type AlAs/GaAs quarter-wave stack as the bottom mirror and a $Si/SiO_2$ mirror on top (Figure E.4). The current and mode confinement was realized by wet chemical undercut of the active layer. Later the same year I demonstrated the first photopumped operation of a single-fused all-epitaxial 1.52 μm VCL (Babić[a], 1994).

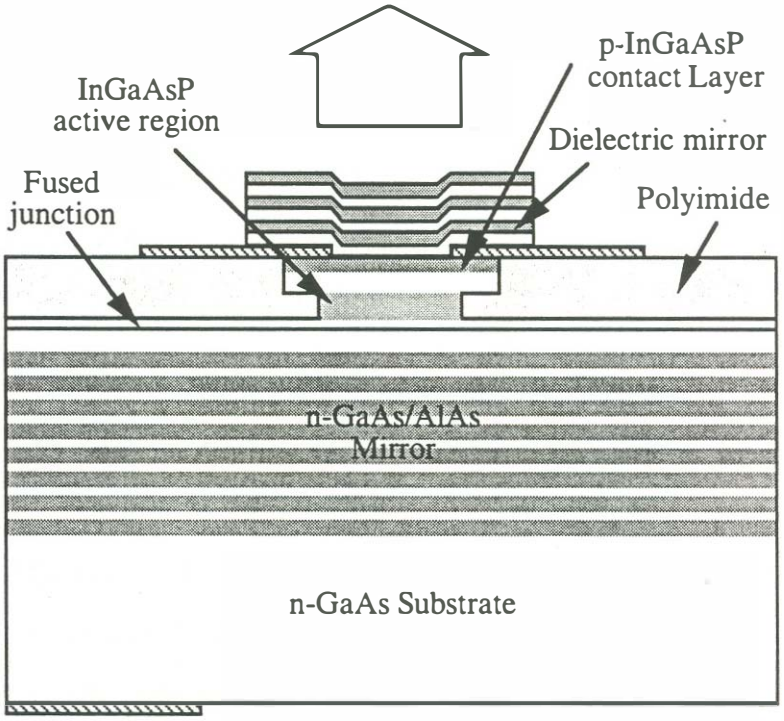


**Fig. E.4**: The structure of the first fused vertical-cavity laser fabricated by James Dudley at UC Santa Barbara (Dudley, 1994).

The following year passed in unsuccessful attempts to fabricate continuous wave operating lasers using wafer fusion. In Fall 1994, after having fabricated several more runs of fused VCLs, James graduated and left UCSB for Hewlett-Packard

Optoelectronic Division in San Jose. Before departing he made one try in fabricating a *double-fused vertical-cavity laser*. The double-fused vertical-cavity laser promised to outperform all other long-wavelength VCL structures due to its optical, electrical, and thermal properties. The idea for this device came across in one of our weekly VCL meetings in 1993. The record of this invention is noted in James' research notebook and the first attempt to fabricate this device is described in his dissertation (Dudley, 1994). Dr. Long Yang at Hewlett-Packard tried to fabricate this device as well. However, none of these attempts produced working lasers, and the reason why became clear only later that year.

The origin of the problem was in the insufficient reflectivity of the *p*-AlAs/GaAs mirror. Free carrier and inter-valence-band absorption, which in extrinsic *p*-GaAs increase very rapidly for wavelengths below the energy gap, reduced the reflectivity of the mirrors. I ran into the same problem wanting to use *p*-AlAs/GaAs mirrors in conjunction with an *n*-InGaAsP/InP mirror for the all-epitaxial VCL (Sec. 8.4). Before this fact became evident, all of us kept designing *p*-mirrors with the same doping level as for 980 nm VCLs. This doping level (≈1e18) was too high and all of the mirrors had too low reflectivity due to absorption. The first indication that the *p*-AlAs/GaAs mirrors may be the problem was in spring of 1994 when Klaus Streubel visited UCSB to perform optical pumping on his 1.55 μm VCLs. Klaus brought with him a selection of completed lasers with bulk and quantum well active layers with one InGaAsP/InP and one $Si/SiO_2$ mirror (Streubel[a,b], 1994). The quantum-well lasers (with the $Si/SiO_2$ mirrors) operated photopumped at room-temperature using the 1064 nm line of Nd:YAG laser. I performed an interesting experiment then: I took an unpatterned quantum-well sample that we knew lased at room

temperature, removed the $Si/SiO_2$ mirror and fused to it a $p$-AlAs/GaAs mirror. To our surprise, no lasing was observed even though the cavity mode was almost at the same wavelength (reflection spectra shown in Figure C.13). Evidently, the reflectivity of the $p$-mirror AlAs/GaAs was lower than the reflectivity of the 3.5-period $Si/SiO_2$ mirror that was originally used on the same sample. I subsequently researched the topic of below-gap absorption in extrinsic semiconductors, and made absorption coefficient measurements (Section 4.4.1.) to confirm that there in fact was between three and five times more free carrier absorption in $p$-GaAs at 1.55 μm than at 0.98 μm. This required a special design of the $p$-AlAs/GaAs mirror for use in future fused VCL designs.

Wanting to get electrically pumped results with my all-epitaxial VCLs, Richard and I decided to try a hybrid doping scheme in which the 10-periods of the $p$-AlAs/GaAs mirror were doped very low ($3 \cdot 10^{17}\,cm^{-3}$), while the rest of the mirror (13-periods) were doped higher ($10^{18}\,cm^{-3}$). We made no attempt of engineering the heterojunction interfaces and hence the electrical resistance of this mirror was very high. Nevertheless, it was with this mirror and the newly grown strain-compensated quantum-well active layers obtained from Sweden (KS2290) that I built the first double-fused vertical-cavity laser (Babić[a], 1995). The performance of this laser set new records for room-temperature pulsed operation of 1.55 μm VCLs. The fact that there did not seem to be any indication that wafer fusion is limiting the development of these lasers, but the quality of the mirrors and the active layer, made us believe that continuous-wave operation could be obtained with the double-fused structure. Following the first success of the double-fused laser, we proceeded developing lower resistance $p$-mirrors to reduce the threshold power dissipation. A discussion with

Professor John Bowers resulted in the idea to redesign the active layer without the separate confinement regions. In May of 1995 I went to the Indium Phosphide and Related Materials Conference that was held in Sapporo, Japan. I met Klaus Streubel there, and as he handed me a box with three newly grown wafers of active layers, he said: "This is CW room temperature". He was right.

With a newly designed AlGaAs/GaAs mirror and the improved active layer, on June 18, 1995 I measured the first room-temperature continuous-wave operating 1.54 μm (double-fused) vertical-cavity lasers. This was reported only a week later at the 10th International Conference on Integrated Optics and Optical Fibre Communications in Hong Kong (IOOC'95). It was quite hot and humid in Hong Kong, but these new lasers operated continuously at temperatures as high as 33°C, and hence became the first *Hong Kong street-temperature continuous-wave operating 1.54-μm vertical-cavity lasers.*

Further improvements of laser characteristics are now under way. The project is being taken over by a new student of Professor Bowers, Near Margalit, whose first fabricated double-fused lasers (ever), operated continuously at room temperature. Prof. Joachim Piprek from University of Delaware is currently developing comprehensive models for these lasers, while long-wavelength transmission experiments and modulation characteristics are being measured by Peter Blixt, a visiting researcher from KTH in Stockholm.

# References


Adachi, S., "GaAs, AlAs and $Al_xGa_{1-x}As$: Material properties for use in research and device applications", *J. Appl. Phys.*, Vol. 58, No. 3, pp. R1-R29 (1985).

Adachi, S., "Lattice thermal resistivity of III-V compound alloys", *J. Appl. Phys.*, Vol. 54, No. 4, pp. 1844-1848 (1983).

Adachi, S., "Refractive indices of III-V compounds: Key properties of InGaAsP relevant to device design", *J. Appl. Phys.*, Vol. 53, No. 8, pp. 5863-5869 (1982).

Afromowitz, M. A., "Refractive Index of $Ga_{1-x}Al_xAs$", *Solid State Comm.*, Vol. 15, pp. 59-63 (1974).

Anan, T., H. Shimomura, S. Sugou, "Improved reflectivity of AlPSb/GaPSb Bragg reflector for 1.55μm wavelength", *Electronics Letters*, Vol. 30, No. 25, 2138 (1994).

ANSYS®, Ansys, Inc., 201 Johnston Rd., Houston, PA 15342, revision 5.1 (1995).

Aoyagi, N., and S. Yamaguchi, "Functional Analytic Formulation of Fresnel Diffraction", *Jpn. J. Appl. Phys.*, Vol. 12, No. 3, pp. 366-370 (1973).

Arnon, O., "Loss mechanisms in dielectric optical interference devices", *Appl. Opt.* Vol. 16, No. 8, pp. 2147-2151 (1977).

Baba, T., Y. Yogo, K. Suzuki, F. Koyama, K. Iga, "Near room-temperature continuous wave lasing characteristics of GaInAsP/InP surface-emitting laser", *Electron. Lett.*, Vol. 29, No. 10, pp. 913-914 (1993).

Babić, D. I., J. J. Dudley, M. Shirazi, E. L. Hu, J. E. Bowers, "Sputter deposition of precision $Si/SiN_x$ Bragg reflectors using multitasking interactive processing control", *J. Vac. Sci. Technol. A*, Vol. 9, No. 3, pp. 1113-1117 (1991).

Babić, D. I., T. E. Reynolds, E. L. Hu, J. E. Bowers, "Reactive sputtering of Si/$SiN_x$ quarter-wave dielectric mirrors using in-situ laser reflectometry", SPIE Techn. Symp. on Microelectron. Processing Integration, San Jose (1991).

Babić[b], D. I., and S.W. Corzine, "Analytic Expressions for the Reflection Delay, Penetration Depth, and Absorptance of Quarter Wave Mirrors", *IEEE J. Quantum Electron.,* Vol. 27, No. pp. 514 (1992).

Babić[a], D. I., T. E. Reynolds, E. L. Hu, J. E. Bowers, "In situ characterization of thin film optical coatings using a normal incidence laser reflectometer", *J. Vac. Sci. Technol.* A, Vol. 10, No. 2, pp. 514-524 (1992).

Babić[a], D. I., D. Bimberg, J. J. Dudley, J. E. Bowers, E. L. Hu, — Discussion on MOCVD growth of Si, GaP and AlP for possible use in vertical-cavity lasers — meeting at U.C. Santa Barbara (1993).

Babić[b], D. I., Y. Chung, N. Dagli, J. E. Bowers, "Modal reflectivity of quarter-wave mirrors in vertical-cavity lasers", IEEE J. Quantum Electron., Vol. 29, No. 6, pp. 1950-1962 (1993).

Babić[c], D. I., Epilayers grown by MBE (Mark J. Mondry, UCSB), amorphous mirror deposited by reactive sputtering (1993).

Babić[a], D. I., R. J. Ram, J. E. Bowers, M. Tan, L. Yang, "Scaling laws for gain-guided vertical-cavity lasers with distributed Bragg reflectors", *Appl. Phys. Lett.*, Vol. 64, No. 14, pp. 1762-1764 (1994).

Babić[b], D. I., "Improved fusion using channels", UCSB research cleanroom notebooks #16 and #17, processes P219, P222, and P229, Aug 10 – Sep 6 (1994).

Babić[c], D. I., J. J. Dudley, K. Streubel, R. P. Mirin, E. L. Hu, J. E. Bowers, "Optically-pumped all-epitaxial wafer-fused 1.52 μm vertical-cavity lasers", *Electron. Lett.*, Vol. 30, No. 9, pp. 704-706 (1994).

Babić[a], D. I., J. J. Dudley, K. Streubel, R. P. Mirin, J. E. Bowers, E. L. Hu, "Double-fused 1.52 μm vertical-cavity lasers", *Appl. Phys. Lett.*, Vol. 66, No. 9, pp. 1030-1032 (1995).

Babić[b], D. I., K. Streubel, R. P. Mirin, N. M. Margalit, J. E. Bowers, E. L. Hu, Dan E. Mars, L. Yang, K. Carey, "Room-temperature continuous-wave

operation of 1.54 μm vertical-cavity lasers", 10th Int. Conf. Integ. Opt. Opt. Fibre Comm. (IOOC'95), Hong Kong, paper PD1.5 (1995).

Barbé, H., R. L. Van Meirhaeghe, F. Cardon, "The growth of thin oxide layers on GaAs in methanol", *Semicond. Sci. Technol.*, Vol. 3, pp. 853-858 (1988).

Barone, S. R., "Resonances of the Fabry-Perot Laser", *J. Appl. Phys.* Vol. 34, No. 4, pp. 831-843 (1963).

Bengtsson, S., "Semiconductor wafer bonding: A review of interfacial properties and applications", *J. Electon. Mat.*, Vol. 21, No. 8, pp. 841-862 (1992).

Bennett, H. E., and J. O. Porteus, "Relation between surface roughness and specular reflectance at normal incidence", *J. Opt. Soc. Am.*, Vol. 51, No. 2, pp. 123-129 (1961).

Bennett, H. E., J. M. Bennett, E. J. Ashley, and R. J. Motyka, "Verification of the anomalous-skin-effect theory for silver in the infrared", *Phys. Rev.*, Vol. 165, No. 3, pp. 755-764 (1968).

Beyler, C. A., S. G. Hummel, N. Frateshi, P. D. Dapkus, "Small dimension Bragg reflectors formed by air-isolated GaAs layers", Electron. Lett., Vol. 27, No. 7, pp. 588-590 (1991).

Blum, O., I. J. Fritz, L. R. Dawson, A. J. Howard, T. J. Headley, J. A. Olsen, J. F. Klem, T. J. Drummond, "Molecular beam epitaxy grown AlAsSb/GaAsSb distributed Bragg reflector on InP substrate operating near 1.55 μm", *J. Vac. Sci. Technol. B*, Vol. 12, No. 2, pp. 1122-1124 (1994).

Bower, R. W., M. S. Ismail, B. E. Roberds, "Low temperature $Si_3N_4$ direct bonding", *Appl. Phys. Lett.*, Vol. 62, No. 26, pp. 34853487 (1993).

Braunstein, R., and E. O. Kane, "The Valence Band Structure of III-V Compounds", *J. Phys. Chem. Solids*, Vol. 23, pp. 1423-1431 (1962).

Braunstein, R., "Intervalence band transitions in Gallium Arsenide", *J. Phys. Chem. Solids*, Vol. 8, pp. 280-282 (1959).

Braunstein, R., "Optical Absorption in *p*-Type Gallium Arsenide", *Phys. Rev.*, Vol. 111, No. 2, pp. 480-481 (1958).

Bruce, C. F., and P.E. Ciddor, "Phase Dispersion in Multilayer Films", *J. Opt. Soc. Am.*, vol. 50, pp. 295-299, 1960.

Casey, H. C., and P. L. Carter, "Variation of intervalence band absorption with hole concentration in $p$-type InP", *Appl. Phys. Lett.*, Vol. 44, No. 1, pp. 82-83 (1984).

Casey, H. C., and Panish, Heterostructure lasers, PartA, Academic Press, New York, p. 31 (1978).

Chailertvanitkul, K. Iga, K. Moriki, "GaInAsP/InP surface-emitting laser ($\lambda = 1.4\mu m$) with heteromultilayer Bragg reflector", *Electron. Lett.*, Vol. 21, pp. 303-304 (1985).

Chandra, P., L. A. Coldren, K. E. Strege, "Refractive index data from $Ga_xIn_{1-x}As_yP_{1-y}$ films", *Electron. Lett.*,

Chang-Hasnain, C. J., J.P. Harbison, G. Hasnain, An.C. Von Lehmen, L.T. Florez, N.G. Stoffel, "Dynamic, Polarization, and Transverse Mode Characteristics of Vertical Cavity Surface Emitting Lasers", *J. Quantum Electron.*, Vol. 27, No. 6, pp. 1402-1409 (1991).

Checcacci, P.F., A. Consortini, A. Scheggi, "Modes, Phase Shifts, and Losses of Flat-Roof Open Resonators", *Proc. IEEE*, Vol. 54, No. 10, pp. 1329-1334 (1966).

Choa, F. S., K. Tai, W. T. Tsang, S. N. G. Chu, "High reflectivity 1.55μm InP/InGaAsP Bragg mirror grown by chemical beam epitaxy", *Appl. Phys. Lett.*, Vol. 59, No. 22, pp. 2820-2822 (1991).

Choquette, K. D., G. Hasnain, Y.H. Wang, J.D. Wynn, R.S. Freund, A.Y. Cho, R.E. Leibenguth, "GaAs Vertical-Cavity Surface Emitting Lasers Fabricated by Reactive Ion Etching", *IEEE Photon. Technol. Lett.*, Vol. 3, No. 10, pp. 859-862 (1991).

Choquette, K. D., R. P. Schneider, Jr., K. L. Lear, K. M. Geib, "Low therhold voltage vertical-cavity lasers fabricated by selective oxidation", *Electron. Lett.*, Vol. 30, No. 24, pp. 2043-2044 (1994).

Chua, C. L., C. H. Lin, Z. H. Zhu, Y. H. Lo, M. Hong, J. P. Mannearts, R. Bhat, "Long wavelength vertical-cavity laser using strain-compenstaed multiple quantum wells on GaAs substrates", 1994 IEEE LEOS Ann. Mtg., paper SL7.1 (1994).

Chua, C. L., Z. H. Zhu, Y. H. Zhu, Y. H. Lo, R. Bhat, M. Hong, "Low-threshold 1.57-μm VC-SEL's using strain-compensated quantum wells and oxide/metal backmirror", *IEEE Phot. Technol. Lett.*, Vol 7, No. 5, pp. 444-445 (1995).

Chung[a], Y., and N. Dagli, "Analysis of Z-invariant and Z-variant semiconductor Rib Waveguides with Non-uniform Mesh Configuration", *IEEE J. Qunatum Electron.*, Vol. 27, No. 10, pp. 2296-2305 (1991).

Chung[b], Y., N. Dagli, and L. Thylén, "Explicit Finite Difference Vectorial Beam Propagation Method", *Electron. Lett.*, Vol. 27, No. 23, pp. 2119-2121 (1991).

Collin, R. E., *Foundations of Microwave Engineering*, McGraw-Hill (1966).

Collin, R. E., "Theory and Design of Wide-Band Multisection Quarter-Wave Transformers", *Proceedings of the IRE*, pp. 179-185 (1955).

Corzine, S. W., "Design of vertical-cavity surface-emitting lasers with strained and unstrained quantum well active regions", Ph. D. Dissertation, University of California, Santa Barbara, ECE Tech. Rep. #93-09 (1993).

Corzine, S. W., R. S. Geels, J.W. Scott, L.A. Coldren, "Surface-emitting laser with periodic gain", IEEE Lasers and Electro-Optics Soc. Ann. Mtg., paper OEl .2, Santa Clara, CA (1988).

Corzine, S. W., R. S. Geels, R. H. Yan, J.W. Scott, L.A. Coldren, "Efficient, narrow-linewidth distributed-Bragg-refrector surface-emitting laser with periodic gain", IEEE Phot. Technol. Lett., Vol. 1, p. 52 (1989).

Corzine, S. W., R.H. Yan, and L.A. Coldren, "A Tanh substitution Technique for the Analysis of Abrupt and Graded Interface Multi-Layer Dielectric Stacks", *IEEE J. Quantum Electronics*, Vol. 27, No. 9., 2096 (1991)

Cristel, L., K. Petersen, P. Barth, F. Pourahmadi, J. Mallon, Jr., and J. Bryzek, "Single-crystal silicon pressure sensors with 500x overpressure protection", *Sensors Actuators*, Vol. A21-A23, pp. 84-88 (1990).

De Silvestri, S., P. Laporta, and O. Svelto, "Analysis of quarter-wave dielectric-mirror dispersion in femto-second dye-laser cavities", *Opt. Lett.*, vol. 9, pp. 335-337 (1984).

De Silvestri, S., P. Laporta, and O. Svelto, "The Role of Cavity Dispersion in CW Mode-Locked Lasers", *IEEE J. Quantum Electronics*, vol. QE-20, pp. 533-539 (1984).

Deppe[a], D. G. , N. Chand, J. P. van der Ziel, G. J. Zdyzik, "$Al_xGa_{1-x}As$ – GaAs vertical-cavity lasers surface-emitting lasers grown on on Si substrate", *Appl. Phys. Lett.*, Vol. 56, No. 8, pp. 740-742 (1990).

Deppe[b], D. G., S. Singh, R. D. Dupuis, N. D. Gerrard, G. J. Zydzik, J. P. van der Ziel, C. A. Green, C. J. Pinzone, "Room-temperature photopumped operation of an InGaAsP/InP vertical-cavity surface-emitting laser", *Appl. Phys. Lett.*, Vol. 56, No. 22, pp. 2172-2174 (1990).

Dobbelaere, D. Huang, M. S. Ünlü, and H. Morkoç", AlGaAs/GaAs multiple quantum well reflection modulators grown on Si substrates", Appl. Phys. Lett., Vol. 53, No. 12, pp. 94-96 (1988).

Dudley[a], J. J., D. L. Crawford, J. E. Bowers, "Temperature dependence of the properties of DBR mirrors used in surface normal optoelectronic devices", *IEEE Phot. Technol. Lett.*, Vol. 4, No. 4, pp. 311-314 (1992).

Dudley[b], J. J., M. Ishikawa, B.I. Miller, D.I. Babić, R. Mirin, W.B. Jiang, M. Shimizu, "InGaAsP (1.3-μm) vertical-cavity lasers using GaAs/AlAs mirrors", presented at Ann. Mtg. Opt. Soc. America, Albuquerque, New Mexico, paper FKK7 (1992).

Dudley, J. J., M. Ishikawa, D. I. Babić, B. I. Miller, R. Mirin, W. B. Jiang, J. E. Bowers, and E. L. Hu, "144°C operation of InGaAsP vertical-cavity lasers on GaAs substrates", *Appl. Phys. Lett.*, Vol. 61, pp. 3095 (1993).

Dudley, J. J., D. I. Babić, R. P. Mirin, L. Yang, B. I. Miller, R. J. Ram, T. E. Reynolds, E. L. Hu, J. E. Bowers, "Low threshold, wafer fused long-wavelength vertical-cavity lasers", Appl. Phys. Lett., Vol. 64, No. 12, pp. 1463-1465 (1994).

Dudley, J. J., "Wafer-fused long-wavelength vertical-cavity lasers", Ph.D. dissertation, University of California, Santa Barbara, unpublished (1994).

Entran Sensors and Electronics, Fairfield, NJ, USA: Model number: ELF-13/5-250.

Epoxy Technology Inc., Part A of epotek® 410E silver epoxy.

Feit, M. D., and J.A. Fleck, "Light Propagation in graded-index optical fibers", *Appl. Opt.*, Vol. 17, No. 24, pp. 3990-3998 (1978).

Fisher, M. A., A. J. Dann, D. A. O. Davies, D. J. Elton, M. J. Harlow, C. B. Hatch, S. D. Perrin, J. Reed, I. Reid, M. J. Adams, "High temperature

photopumping of 1.55 μm vertical-cavity surface emitting lasers", *Electron. Lett.*, Vol. 29, No. 17, pp. 1548-1549 (1993).

Fisher, M. A., Y.-Z. Huang, A. J. Dann, D. J. Elton, M. J. Harlow, S. D. Perrin, J. Reed, I. Reid, M. J. Adams, "Pulsed electrical operation of 1.5-μm vertical-cavity surface-emitting lasers", *IEEE Phot. Technol. Lett.*, Vol. 7, No. 6, pp. 608-610 (1995).

Fox, A. G., and T. Li, "Resonant Modes of a Maser Interferometer", *Bell Sys. Tech . J.*, Vol. 40, pp. 453-488 (1961).

Frateschi, N. C., P. D. Dapkus, S. S. Ou, J. J. Yang, and M. Jansen, "Analysis of Nonplanar Wave Propagation Through Multilayer Bragg Reflectors for Folded Cavity and Vertical Cavity Surface Emitting Laser Structures", *IEEE J. Quantum Electron.,* Vol. 31, No. 4, pp. 627-635 (1995).

Gabriel, M. C., H. A. Haus, E. P. Ippen, "Thermal index changes by optical absorption in group II-V semiconductor waveguides", IEEE J. Lightwave Technol., Vol. 4, No. 10, pp. 1482-1492 (1986).

Gates, D. M., C. C. Shaw, D. Beaumont, "Infrared reflection of Evaporated Metals Films", *J. Opt. Soc. Am.* Vol. 48, No. 2, 88-89 (1958).

Geels, R. S., S.W. Corzine, L.A. Coldren, "InGaAs Vertical-Cavity Surface Emitting Lasers", *IEEE J. Quantum Electron.*, Vol. 27, No. 6, pp. 1359-1367 (1991).

Geels, R., and L. A. Coldren, "Submilliamp threshold vertical-cavity laser diodes", Appl. Phys. Lett., Vol. 57, No. 16, pp. 1605-1607 (1990).

Gerard, J. M., A. Izrael, J. Y. Marzin, R. Padjen, et al, "Photonic bandgap of 2-dimensional dielectric crystals", *Solid State Electron.*, Vol. 37, No. 4, pp. 1341-1344 (1994).

Ghandi, S. K., *Semiconductor power devices: Physics of operation and fabrication*, John Wiley, New York (1977).

Giacomo, P., "Les couches reflechissantes multidielectriques appliquees a l'interferometre de Fabry-Perot. Etude theorique et experimentale des couches reelles", *Rev. Opt.*, vol. 35 pp. 317-54 (1956).

Goodman, J. W., *Introduction to Fourier Optics*, McGraw-Hill (1968).

Gordon, J. P., and H. Kogelnik, "Equivalence Relations among Spherical Mirror Optical Resonators", *Bell Sys. Tech. J.*, Vol. 43, pp. 2873-2886 (1964).

Gösele, U., T. Abe, J. Haisma, M. A. Schmidt, eds., Proc. of the First Int. Symposium on Semicond. Wafer Bonding, Electrochem. Soc., Pennington, New Jersey (1992).

Gourley, P. L., L. R. Dawson, T. M. Brennan, B. E. Hammons, J. C. Stover, C. F. Schaus, S. Sun, "Optical scatter in epitaxial semiconductor multilayers", Appl. Phys. Lett., Vol. 58, No. 13, pp. 1360-1362 (1991)

Grimmeiss, H. G., and B. Monemar, "Temperature dependence of the refractive index of AlAs and AlP", *Phys. Stat. Sol. A*, Vol. 5, pp. 109-114 (1971).

Guy, P., K. Woodbridge, M. Hopkinson, "High reflectivity and low resistance 1.55μm $Al_{0.65}In_{0.35}As/Ga_{0.63}In_{0.37}As$ strained quarter-wave Bragg reflector stack", *Electron. Lett.* Vol. 29, No. 22, pp. 1947-1948 (1993).

Haisma, J., B. A. C. M. Spierings, U. K. P. Biermann, A. A. van Gorkum, "Diversity and feasibility of direct bonding: a survey of a dedicated optical technology", *Appl. Opt.*, Vol. 33, No. 7, pp. 1154-1169 (1994).

Harendt, C., B. Höfflinger, H.-G. Graf, E. Penteker, "Silicon direct bonding for sensor applications: Characterization of the bond quality", Sensors and Actuators A, Vol. 25-27, pp. 87-92 (1991).

Harrington, R. F., *Time Harmonic Electromagnetic Fields*, McGraw-Hill (1961).

Hasnain, G., K. Tai, L. Yang, Y.H. Wang, R.J. Fischer, J.D. Wynn, B. Weir, N.K. Dutta, A.Y. Cho, "Performance of Gain-Guided Surface Emitting Lasers with Semiconductor Distributed Bragg Reflectors", *IEEE J. Quantum Electron.*, Vol. 27, No. 6, pp. 1377-1385 (1991).

Haus, H., *Waves and Fields in Optoelectronics*, Prentice-Hall (1984).

Hawkins, A., T. E. Reynolds, D. England, D. I. Babić, M. J. Mondry, J. E. Bowers, "Silicon hetero-interface photodetector", submitted to *Appl. Phys. Lett.* (1995).

Hayashi, Y., T. Mukaihara, N. Hatori, N. Ohnoki, A. Matsutani, F. Koyama, K. Iga, "Record low-threshold index-guided InGaAs/GaAsAs vertical-cavity surface-emitting laser with native oxide confinement structure", *Electron. Lett.*, Vol. 31, No. 7, pp. 560-562 (1995).

Heavens, O. S., and H. M. Liddell, "Staggered Broad-Band Reflecting Multilayers", *Applied Optics*, Vol. 5, No. 3, 373-376 (1966).

Hecht, E., and A. Zajac, *Optics*, Addison-Wesley (1974).

Hecht, E., *Optics*, Addison-Wesley Publishing Company, Reading, Massachusetts (1987).

Hemingway, D. J., and P.H. Lissberger, "Properties of weakly absorbing multilayer systems in terms of the concept of potential transmittance", *Optica Acta,* vol. 20, pp. 85-96, 1973.

Henry, C. H., R. A. Logan, F. R. Merrit, J. P. Luongo, "The Effect of Intervalence Band Absorption on the Thermal Behavior of InGaAsP Lasers", *IEEE J. Quantum Electron.*, Vol. QE-19, No. 6, pp. 947-952 (1983).

Herbelin, J. M., and J. A. McKay, "Development of laser mirrors or very high reflectivity using cavity-attenuated phase-shift method, *Applied Optics*, Vol. 20, 3341-3344 (1981).

Ho, S.-T., S. L. McCall, R. E. Slusher, L. N. Pfeiffer, K. W. West, A.F. J. Levi, G. E. Blonder, J. L. Jewell, "High index contrast mirrors for optical microcavities", *Appl. Phys. Lett.*, Vol. 57, No. 14, pp. 1387-1389 (1990).

Hsin, W., G. Du, J. K. Gamelin, K. J. Malloy, S. Wang, J. R. Whinnery, Y. J. Yang, T. G. Dziura, S. C. Wang, "Low threshold distributed Bragg reflector surface emitting laser diode with semiconductor air-bridge-supported top mirror", *Electron. Lett.*, Vol. 26, No. 5, pp. 307-308 (1990)

Huang, W. P., C.L. Xu, S.K. Chaudhuri, "A Finite-Difference Vector Beam Propagation Method for Three Dimensional Waveguide Structures", *IEEE Photon. Technol. Lett.,* Vol. 4, No. 2, pp. 148-151, (1992).

Huberman, M. L., A. Ksendzov, A. Larsson, R. Terhune, J. Maserjian, "Optical absorption by free holes in heavily doped GaAs", *Phys. Rev. B.*, Vol.. No. 3, pp. 1128-1133 (1991).

Huffaker, D. L., D. G. Deppe, T. J. Rogers, "Transverse mode behavior in native-oxide-deined low threshold vertical-cavity lasers", *Appl. Phys. Lett.*, Vol. 65, No. 13, pp. 1611-1613 (1994).

Ibaraki, A., S. Ishikawa, S. Ohkouchi, K. Iga, "Pulsed oscillation of GaAlAs/GaAs surface-emitting injection laser", *Electron. Lett.* Vol. 20, pp. 420-422 (1984).

Iga, K, F. Koyama, S. Kinoshita, "Surface Emitting Semiconductor Lasers", *IEEE J. Quantum Electron.,* Vol. 24, No. 9, pp. 1845-1855, (1988).

Iga, K., H. Soda, T. Terakado, S. Shimizu, "Lasing characteristics of improved GaInAsP/InP surface emitting injection lasers", *Electron. Lett.* Vol. 19, pp. 457-458 (1983).

Iga, K., private communication at the 1995 Indium Phosphide and Related Materials conference in Sapporo, Hokkaido, Japan, May 10, (1995).

Iga, K., Y. Kokubun, M. Oikawa, *Fundamentals of Microoptics*, Academic Press, (1984).

Ikegami, T., "Reflectivity of Mode at Facet and Oscillation Mode in Double-Heterostructure Injection Lasers", *IEEE J. Quantum Electron.*, Vol. QE-8, No. 6, pp. 470-476 (1972).

Imajo, Y., A. Kasukawa, S. Kashiwa, H. Okamoto, "GaInAsP/InP Semiconductor Multilayer Reflector Grown by Metalorganic Chemical Vapor Deposition and its Application to Surface Emitting Laser Diodes", *Jpn. J. Appl. Phys.* Vol. 29, No. 7, pp. L1130-L1132 (1990).

Ismail, M. S., R. W. Bower, J. L. Veteran, O. J. Marsh, "Silicon nitride direct bonding", *Electron. Lett.*, Vol. 26, No. 14, pp. 1045-1046 (1990).

Jackson, J.,*Classical Electromagnetics,* John Wiley & Sons (1986).

Jewell, J. L., A. Scherer, M. Walther, J.P. Harbison, L.T. Florez, "Low-Voltage-Threshold Microlasers", presented at Proc. CLEO '92, Anaheim, California, 1992.

Jewell[a], J. L., J. P. Harbison, and A. Scherer, "Microlasers", *Scientific American*, Vol. 265, No. 5, November 1991, pp. 86-94 (1991)

Jewell[b], J. L., J.P. Harbison, A. Scherer, Y.H. Lee, L.T. Florez, "Vertical-Cavity Surface-Emitting Lasers: Design, Growth, Fabrication, Characterization", *IEEE J. Quantum Electron.*, Vol. 27, No. 6, pp. 1332-1346 (1991).

Jewell[a], J. L., K. F. Huang, K. Tai, Y. H. Lee, R. J. Fisher, S. L. McCall, A. Y. Cho, "Vertical-cavity single quantum well laser", *Appl. Phys. Lett.*, Vol. 55, No. 5, pp. 424-426 (1989).

Jewell[b], J. L., S. L. McCall, Y. H. Lee, A. Scherer, A. C. Gossard, J. H. English, "Lasing characteristics of GaAs microresonators", *Appl. Phys. Lett.*, Vol. 54, No. 15, pp. 1400-1402 (1989).

Jewell[c], J. L., A. Scherer, S. L. McCall, Y. H. Lee, S. Walker, J. P. Harbison, L. T. Florez, "Low-threshold electrically pumped vertical-cavity surface-emitting microlasers", *Electron. Lett.*, Vol. 25, No. 17, pp. 1123-1124 (1989).

Jing, X. L., J.C. Ho, P.K.L. Yu, "Hemispherical resonator study for surface-emitting InGaAsP/InP lasers", *Appl. Phys. Lett.*, Vol. 56, No. 5, pp. 432-433 (1990).

Johnston, G. T., "Wavelength dependence of dn/dT in infrared-transmitting semiconductor materials", *Appl. Opt.*, Vol. 16, No. 7, pp. 1796-1797 (1977).

Kajita, M., T. Numai, K. Kurihara, T. Yoshikawa, H. Saito, Y. Sugimoto, M. Sugimoto, H. Kosaka, I. Ogura, K. Kasahara, "Thermal Analysis of Laser-Emission Surface-Normal Optical Devices with a Vertical Cavity", *Jpn. J. Appl. Phys.*, Vol. 33, Pt. 1, No. 1B, pp. 859-863 (1994).

Kales, D., "Review and forecast of laser markets: 1993", *Laser Focus World*, pp. 70-88, January (1993).

Kinoshita, S., T. Kobayashi, T. Sakaguchi, and K. Iga, "Room temperature pulse operation of GaAs surface-emitting laser by using TiO2/SiO2 dielectric multilayer reflector", *Trans. IECE Japan*, Vol. J69-C, pp. 412-420 (1986).

Kish, F. A., F. M. Steranka, D. C. DeFevere, D. A. Vanderwater, K. G. Park, C. P. Kuo, T. D. Osentowski, M. J. Peanasky, J. G. Yu, R. M. Fletcher, D. A. Steigwald, M. G. Craford, and V. M. Robbins, "Very high-efficiency semiconductor wafer-bonded transparent-substrate $(Al_xGa_{1-x})_{0.5}In_{0.5}P$/GaP light-emitting diodes, *Appl. Phys. Lett.* Vol. 64, No. 21, pp. 2839-2841 (1994).

Kissinger, G, and W. Kissinger, "Hydrophilicity of silicon wafers for direct bonding", *Phys. Stat. Sol. A*, Vol. 123, No. 1, pp. 185-192 (1991).

Knauer, A., D. Hirsch, R. Staske, U. Zeimer, "Oxide-free etching of (100) InP surfaces", *Cryst. Res. Technol.* Vol. 24, No. 4, pp. 443-451 (1989).

Kogelnik, H., and C.V. Shank, "Coupled-Wave Theory of Distributed Feedback Lasers", *J. Appl. Phys.*, vol. 43, pp. 2327-2335 (1972).

Kogelnik, H., and T. Li, "Laser Beams and Resonators", *Proc. IEEE.*, Vol. 54, No. 10, pp. 1312-1329 (1966).

Kojima, K., and S. Yamaguchi, "Functional Analysis of Diffraction Integral Transform. I.", *Jpn. J. Appl. Phys.*, Vol. 14, No. 11, pp. 1799-1805 (1975).

Kowalsky, W, and J. Mähnss, "Monolithically integrated InGaAlAs dielectric reflectors for vertical-cavity optoelectronic devices", *Appl. Phys. Lett.*, Vol. 59, No. 9, pp. 1011-1012 (1991).

Koyama, F., Kinoshita S., K. Iga, "Room temperature CW operation of GaAs vertical-cavity surface-emitting laser", *Trans. IEICE*, Vol. E71, No. 11, pp. 1089-1090 (1988) and also, "Room-temperature continuous-wave lasing characteristics of a GaAs vertical-cavity surface-emitting laser", *Appl. Phys. Lett.*, Vol. 55, No. 3, pp. 221-222 (1989).

Koyama, F., Y. Suematsu, S. Arai, and T. Tawee, "1.5-1.6 um GaInAsP/InP Dynamic-Single-Mode (DSM) Lasers with Distributed Bragg Reflector", IEEE J. of Quantum Electronics, vol. QE-19, pp. 1042-1051, (1983).

Kroemer[a], H., "Determination of heterojunction band offsets by capacitance-voltage profiling through nonabrupt isotype heterojunctions", *Appl. Phys. Lett.*, Vol. 46, No. 5, pp. 504-505 (1985).

Kroemer[b], H., "Theory of heterojunctions: A critical review", *Molecular Beam Epitaxy and Heterostructures*, Ed. L. L. Chang, and K. Ploog, NATO ASI Series, No. 87, pp. 331-379 (1985).

Kubota, S. , F. Koyama, K. Iga, "Low Threshold GaInAsP/InP transmission-type surface emitting laser", *Jpn. J. Appl. Phys.*, Vol. 31, No. pp. L175-L176, (1992).

Kubota, S., F. Koyama, K. Iga, "Low Threshold Current Density Operation of 1.3μm GaInAsP/InP Transmission Type Surface Emitting Laser", presented at CLEO '92, Anaheim, California, paper JThD5, 1992.

Kutateladze, S. S., and V. M. Borishanski, *A Concise Encyclopedia of Heat Transfer*, Pergamon Press, Oxford (1966).

Lambert, B., Y. Toudic, Y. Rouillard, M. Baudet, B. Guenais, B. Deveaud, I. Valiente, J. C. Simon, "High reflectivity 1.55 μm (Al)GaSb/AlSb Bragg mirror grown by molecular beam epitaxy", *Appl. Phys. Lett.*, Vol. 64, No. 6, pp. 690-691 (1994).

Laporta, P., and V. Magni, "Dispersive effects in the reflection of femtosecond optical pulses from broadband dielectric mirrors", *Appl. Opt.*, vol. 24, pp. 2014-2020, 1985.

Lasky, J. B., Appl. Phys. Lett., Vol. 48, p. 78 (1986).

Lasky, J. B., S. R. Stiffler, F. R. White, J. R. Abernathey, "Silicon-on-insulator (SOI) by bonding and etch-back", 1985 Proc. Int. Elec. Dev. Mtg. (IEDM), pp. 684-687, paper 28.4 (1985).

Law, K-K., and D. I. Babić, "The effect of layer thickness variation on propagation delay and penetration depth of a quarter-wave distributed Bragg reflector", *IEEE Phot. Technol. Lett.*, Vol. 5, No. 11, pp. 1294-1297 (1993)

Lear, K., R. P. Schneider, Jr., K. D. Choquette, S. P. Kilcoyne, J. J. Figiel, J. C. Zolper, "Vertical-cavity surface-emitting lasers with 21% efficiency by metalorganic vapor phase epitaxy", *IEEE Photonics Technol. Lett.*, Vol. 6, No. 9, pp. 1053-1055 (1994).

Lear, K., K. D. Choquette, R. P. Schneider, Jr., S. P. Kilcoyne, K. M. Geib, "Selectively oxidised vertical-cavity surface emitting lasers with 50 % power conversion efficiency", *Electron. Lett.*, Vol. 31, No. 3, pp. 208-209 (1995).

Lee, Y. H., J.L. Jewell, B. Tell, K.F. Brown-Goebeler, A. Scherer, J.P. Harbison, L.T. Florez, "Effects of etch depth and ion implantation on surface emitting microlasers", *Electron. Lett.*, Vol. 26, No. 4, pp. 225-227 (1990).

Li, T., "Diffraction Loss and Selection of Modes in Maser Resonators with Circular Mirrors", *Bell Sys. Tech. J.*, Vol. 44, pp. 917-932 (1965).

Liau[a], Z. L. and D. E. Mull, "Wafer fusion: A novel technique for optoelectronic device fabrication and monolithic integration", *Appl. Phys. Lett.*, Vol. 56, No. 8, pp. 737-739 (1990).

Liau, Z. L., J. N. Walpole, D. Z. Tsang, *IEEE J. Quantum Electron.*, Vol. QE-20, p. 855 (1984).

Liau[b], Z. L., J.N. Walpole, L.J. Missaggia, D.E. Mull, "GaInAsP/InP buried-heterostructure surface-emitting diode laser with monolithic integrated bifocal microlens", *Appl. Phys. Lett.*, Vol. 56, No. 13, pp. 1219-1221 (1990b).

Liboff, R. L., *Introductory Quantum Mechanics*, Holden-Day, Inc. San Francisco (1980).

Lin, C. H., C. L. Chua, Z. H. Zhu, F. E. Ejeckam, T. C. Wu, Y. H. Lo, R. Bhat, "Photopumped long-wavelength vertical-cavity surface-emitting lasers using strain-compensated multiple quantum-wells", *Appl. Phys. Lett.*, Vol. 64, No. 25, pp. 3395-3397 (1994).

Lo, Y. H., R. Bhat, D. M. Hwang, M. A. Koza, T. P. Lee, "Bonding by atomic rearrangement of InP/InGaAsP 1.5 μm wavelength lasers on GaAs substrates", *Appl. Phys. Lett.*, Vol. 58, No. 18, pp. 1961-1963 (1991).

Lo, Y.-H., R. Bhat, D.M. Hwang, C. Chua, C.-H. Lin, "Semiconductor lasers on Si substrtaes using the technology of bonding by atomic rearrangement", *Appl. Phys. Lett.*, Vol. 62, No. 10, pp. 1038-1040 (1993).

Lotsch, H. K. V., "The Fabry-Perot Resonator", *Optik* 28, pp. 65-75, pp. 328-345, pp. 555-574 (1968) and *Optik* 29, pp. 130-145 (1969).

Lott, J., R. P. Schneider, K. J. Malloy, "All-InAlGaP visible (672 nm) vertical-cavity surface-emitting laser", 1993 Conf. Lasers and Electro-Optics, Tech. Dig. paper CWJ56, p. 328, Baltimore, MD (1993).

Lu, Z. H., B. Bryskiewicz, J. McCaffrey, Z. Wasilewski, M. J. Graham, "Ultraviolet-ozone oxidation of GaAs(100) and InP(100)", *J. Vac. Sci. Technol.* B, Vol. 11, No. 6, pp. 2033-2037 (1993).

MacDougal, M. H., P. D. Dapkus, V. Pudikov, H. Zhao, G. M. Yang, "Use of AlAs oxide/GaAs distributed Bragg reflectors to fabricate ultralow-threshold-current VCSELs", 1995 Conf. Lasers and Electro-Optics Tech. Dig. p. 56, paper CTuB4, Baltimore, Maryland, May 21-26 (1995).

MacDougal, M.H., P. D. Dapkus, V. Pudikov, H. Zhao, G. M. Yang, "Ultralow threshold current vertical-cavity surface-emitting lasers with AlAs oxide-GaAs distributed Bragg reflectors", *IEEE Phot. Technol. Lett.*, Vol. 7, No. 3, pp. 229-231 (1995).

Macleod, H. A., *Thin-film optical filters*, Adam Hilger Ltd, Bristol (1986).

Madelung, O. (Ed.), *Semiconductors - Group IV Elements and III-V Compounds*, Data in Science and Technology, Springer-Verlag Berlin Heidelberg (1991).

Manning, J., R. Ohlansky, C. B. Su, "The carrier-induced index change in AlGaAs and 1.3 μm InGaAsP diode lasers", IEEE J. Quantum Electron., Vol. 19, No. 10, pp. 1525-1530 (1983).

Margalit, N. M., "Measurement of GaAs etch rate in 30% $NH_4OH$", laboratory notebook, unpublished (1995).

Margalit, N. M., "Measurements of thermal resistance of double-fused vertical-cavity lasers", unpublished note, January (1995).

Mars, D. E., S276, MBE growth number M2630 (1995).

Martorell, J., N. M. Lawandy, "Observation of inhibted spontaneous emission in a periodic dielectric structure", *Phys. Rev. Lett.*, Vol. 65, No. 15, pp. 1877-1879 (1990).

Mathine, D. L., H. Fathollahnehad, R. Droopad, S. Daryanani, G. N. Maracas, "InGaAs quantum well vertical-cavity surface-emitting lasers integration onto silicon substrates", IEEE LEOS Ann. Mtg. Boston, MA, Oct. 31-Nov. 4, paper SL7.2 (1994).

Mirin, R. P., S201, MBE growth number 940629D (1994).

Mirin, R. P., S207, MBE growth number 940712C (1994).

Mirin, R. P., S250, MBE growth number 941220A (1994).

Mitani, K., V. Lehmann, R. Stengl, D. Feijoo, U. M. Gösele, H. Z. Masood, "Cause and prevention of temperature-dependent bubbles in silicon wafer bonding", *Jpn. J. Appl. Phys.*, Vol. 30, No. 4, pp. 615-622 (1991).

Miyamoto, T., K. Mori, H. Maekawa, Y. Inaba, et al. "Carrier transport in p-type GaInAsP/InP distributed Bragg reflectors", *Jpn. J. Appl. Phys.*, Vol. 33, Pt. 1, No. 8, pp. 4614-4616 (1994).

Mondry, M. J., D.I. Babić, J.E. Bowers, L.A. Coldren, "Refractive Indexes of (Al, Ga, In)As Epilayers on InP for Optoelectronic Applications", *IEEE Photon. Technol. Lett.*, Vol. 4, No. 6, pp. 627-630 (1992).

Mori, K., K. Tokutome, K. Nishi, S. Sugou, "High-quality InGaAs/InP multiquantum-well structures on Si fabricated by direct bonding", *Electron. Lett.*, Vol. 30, No. 12, pp. 1008-1009 (1994).

Mori, K., T. Asaka, H. Iwano, M. Ogura, S. Fujii, T. Okada, S. Mukai, "Effect of cavity size on lasting characteristics of a distributed Bragg reflector-surface emitting laser with buried heterostructure", *Appl. Phys. Lett.*, Vol. 60, No. 1, pp. 21-22 (1992).

Moriki, K., H. Nakahara, T. Hattori, K. Iga, "Single Transverse Mode Condition of Surface Emitting Injection Lasers", *Trans. IEICE.* ,Vol. J70-C, No. 4, pp.

501-509, (1987) (in Japanese), also: *Electronics and Communications in Japan*, Part 2. Vol. 71, No. 1, pp. 81-90, (1988) (in English).

Moss, T.S., *Optical properties of semionductors*, Butterworth (1959).

Motegi, Y., H. Soda, K. Iga, "Surface-emitting GaInAsP/InP injection laser with short cavity length", *Electron. Lett.* Vol. 8, pp. 461-463 (1982).

Mouton, A., C. S. Sundararaman, H. Lafontaine, S. Poulin, J. F. Currie, "Etching of InP by $H_3PO_4$, $H_2O_2$ solutions", *Jpn. J. APpl. Phys.*, Vol. 29, No. 10, pp. 1910-1913 (1990).

Mukai, S., M. Watanabe, H. Yajima, "Analysis of modes in a vertical-cavity surface-emitting laser with multilayer Bragg reflectors", IEICE Trans. Electron., Vol. E77-C, No. 9, pp. 1479-1488 (1994).

Mukihara, T., Y. Hayashi, N. Hatori, N. Ohnoki, A. Matsutani, F. Koyama, K. Iga, "0.33-mA-threshold InGaAs/GaAs VCSEL grown by MOCVD", 1995 Conf. on Lasers and Electro-Optics, paper CTuB5, Baltimore, MD, May 21-26 (1995).

Notten, P. H.L., J. E. A. M. van den Meerakken, and J. J. Kelly, *Etching of III-V semiconductors*, Elsevier Advanced Technology, Oxford, UK (1991).

O'Gorman, J., A. F. Levi, T. Tanbun-Ek, D. L. Coblentz, R. A. Logan, "Temperature dependence of long-wavelength semiconductor lasers", Appl. Phys. Lett., Vol. 60, No. 9, pp. 1058-1060 (1992)

Ohashi, H., J. Ohura, T. Tsukakoshi, M. Shimbo, "Improved dielectrically isolated device integration by silicon-wafer direct bonding (SDB) technique", 1986 Proc. Int. Elec. Dev. Mtg. (IEDM), pp. 210-213, paper 9.1 (1985).

Ohashi, H., J. Ohura, T. Tsukakoshi. M. Simbo, "Improved dielectrically isolated device integration by silicon-wafer direct bonding (SDB) techniques", 1986 International Electron Device Mtg. Digest, paper 9.1, pp. 210-213 (1986).

Ohtsu, M., H. Kotani, H. Tagawa, "The alternating quarter-wavelength layers coating on 1.55 μm GaInAsP/InP laser facets", *Jpn. J. Appl. Phys.*, Vol. 22, No. 5, pp. 815-820 (1983).

Ohura, J. , T. Tsukakoshi, K. Fukuda, M. Shimbo, H. Ohashi, "A dielectrically isolated photodiode array by silicon-wafer direct bonding", *IEEE Elec. Dev. Lett.*, Vol. EDL-8, No. 10, pp. 454-456 (1987).

Okuda, H., H. Soda, K. Moriki, Y. Motegi, K. Iga, "GaInAsP/InP surface emitting injection laser with buried heterostructures", *Jpn. J. Appl. Phys.* Vol. 20, pp. L563-L566 (1981).

Okuno[a], Y., K. Uomi, M. Aoki, T. Taniwatari, M. Suzuki, M. Kondow, "Anti-phase direct bonding and its application to the fabrication of InP-based 1.55 μm wavelength lasers on GaAs substrates", *Appl. Phys. Lett.*, Vol. 66, No. 4, pp. 451-453 (1995).

Okuno[b], Y., M. Aoki, T. Tsuchiya, K. Uomi, "Fabrication of (001) InP-based 1.55-μm wavelength lasers on a (110) GaAs substrate by direct bonding (A prospect for free-oreintation integration)", *Appl. Phys. Lett.*, Vol. 67, No. 6, pp. 810-812 (1995).

Orenstein, M., A. C. Von Lehmen, C. Chang-Hasnain, N. G. Stoffel, J. P. Harbison, L. T. Florez, "Matrix addressable vertical-cavity surface-emitting laser array", Electron.Lett., Vol. 27, No. 5, pp. 437-438 (1991).

Ortega, J. M., *Matrix theory*, Plenum Press, New York (1987).

Oshikiri, M., F. Koyama, and K. Iga, "Flat surface circular buried heterostructure surface-emitting laser with highly reflective $Si/SiO_2$ mirrors", *Electron. Lett.*, Vol. 27, No. 22, pp. 2038-2039 (1991).

Osinski, M., and W. Nakwaski, "Effective thermal conductivity analysis of 1.55 μm InGaAsP/InP vertical-cavity top-surface-emitting mircolasers", Electron. Lett., Vol. 29, No. 11, pp. 1015-1016 (1993).

Otsubo, K., H. Shoji, T. Fujii, M. Matsuda, H. Ishikawa, "High-reflectivity $In_{0.29}Ga_{0.71}As/In_{0.28}Al_{0.72}As$ ternary mirrors for 1.3 μm vertical-cavity surface-emitting lasers grown on GaAs", *Jpn. J. Appl. Phys.*, Vol. 34, Pt. 2, No. 2B, pp. L227-L229 (1995).

Pankove, J. I., *Optical processes in semiconductors*, Dover Publications, Inc., New York (1971).

Pauling, L., *General Chemistry*, Dover Publications, Inc. New York (1970).

Peters, M. G., D. B. Young. F. H. Peters, B. J. Thibeault, J. W. Scott, S. W. Corzine, R. W. Herrick, L. A. Coldren, "High wall-plug efficiency temperature-insensitive vertical-cavity surface-emitting lasers with low-barrier p-type mirrors", *Proc. SPIE*, Vol. 2147, pp. 1-11 (1994).

Peters, M. G., *Molecular beam epitaxial growth of vertical-cavity lasers for optical communications*, Ph. D. dissertation, University of California, Santa Barbara, ECE Report #95-05 (1995).

Peters, M. G., S230, MBE growth number unknown (1994).

Philal, M., A. A. Maradudin, "Photonic band structure of 2-dimensional systems - the triangular lattice", Phys. Rev. B, Vol. 44, No. 16, pp. 8565-8571 (1991).

Piprek[a], J., "Heat flow analysis of long-wavelength VCSELs with varius DBR materials", Proc. 1994 IEEE/LEOS Ann. Mtg., pp. 286-287, Boston, MA (1994).

Piprek[b], J., H. Wenzel, and G. Stefka, "Modeling thermal effects on the light vs. current characteristics of gain-guided vertical-cavity surface-emitting lasers", *IEEE Phot. Technol. Lett.*, Vol. 6, No. 2, pp. 139-142 (1994).

Piprek[a], J., Numerical modeling of thermal properties of generation 1 devices, unpublished (1995).

Piprek, J., D. I. Babić, J. E. Bowers, "Modeling and characterization of double-fused vertical-cavity lasers", to be submitted to Appl. Phys. Lett. (1995).

Ram, R. J., L. Yang, K. Nauka, Y. M. Huong, M. Ludowise, D. E. Mars, J. J. Dudley, S. Y. Wang, "Analysis of wafer fusion for 1.3 μm vertical-cavity surface-emitting lasers", *Appl. Phys. Lett.*, Vol. 62, No. 20, pp. 2474-2476 (1993).

Ram[a], R. J., D. I. Babić, R. A. York, J. E. Bowers, "Spontaneous emission in cavities with distribued mirrors", *IEEE J. Quantum Electron.*, Vol. 31, No. 2, pp. 399-410 (1995b).

Ram[b], R. J., J. J. Dudley, J. E. Bowers, L. Yang, K. Carey, S. J. Rosner, K. Nauka, "GaAs to InP wafer fusion", to be published *J. Appl. Phys.* (1995).

Rempe, G., R. J. Thompson, H. J. Kimble, R. Lelezari, "Measurement of ultralow losses in an optical interferometer", *Opt. Letters*, Vol. 17, No. 5, 363-365 (1992).

Sakaguchi, T., F. Koyama, K. Iga, "GaAlAs/AlAs DBR surface emitting laser grown by MOCVD", *Electron. Lett.*, Vol. 24, p. 928 (1988).

Schawlow, A. L., C.H. Townes, "Infrared and Optical Masers", *Phys. Rev.* Vol. 112, No. 6, pp. 1940-1949 (1958).

Scherer, A., J. L. Jewell, Y. H. Lee, J. P. Harbison, L. T. Florez, "Fabrication of microlasers and microresonator optical switches", Appl. Phys. Lett., Vol. 55, No. 26, pp. 2724-2726 (1989).

Schramm, J., D. I. Babić, E. L. Hu, J. E. Bowers, J. L. Merz, "Anisotropy control in the reactive ion etching of InP using oxygen in methane/hydrogen/argon", 6th In. Conf. on InP and Related Materials, Santa Barbara, paper WE4, March 28-31 (1994).

Schubert, E. F., L. W. Tu, G. J. Zdyzik, R. F. Kopf, A. Benvenuti, M. R. Pinto, "Elimination of heterojunction band discontinuities by modulation doping", Appl. Phys. Lett., Vol. 60, No. 4, pp. 466-468 (1992).

Scott, J. W., R. S. Geels, S. W. Corzine, L. A. Coldren, "Modelling Temperature effects and spatial hole burning to optimize vertical-cavity surface-emitting laser performance", *IEEE J. Quantum Electron.*, Vol. 29, pp. 1295-1308 (1993).

Seeley, J. S., "Resolving power of multilayer films", J. Optical Society of America, Vol. 54, No. 3, pp. 342-346 (1964).

Shimada, M., T. Asaka, Y. Yamasaki, H. Iwano, M. Ogura, S. Mukai, "Low-threshold surface-emitting laser diodes with distributed Bragg reflectors and current blocking layers", *Appl. Phys. Lett.*, Vol. 57, No. 13, pp. 1289-1291 (1990).

Shimbo, M. K. Furukawa, K. Fukuda, K. Tanzawa, J. Appl. Phys., Vol. 60, p. 2987 (1986).

Shimbo, M., K. Fukuda, Y. Ohwada, "Method of manufacturing semiconductor substrate", Europian patent application 0,161,740 (1985).

Shimizu, M., D.I. Babić, J. J. Dudley, W. B. Jiang, J. E. Bowers, "Thermal resistance of 1.3-μm InGaAsP vertical-cavity lasers", Micro. Opt. Technol. Lett., Vol. 6, No. 8, pp. 455-457 (1993).

Shimizu, M., F. Koyama, K. Iga, "BPM Simulation of transverse mode characteristics in surface emitting lasers", *Trans. IEICE*, Vol. E74, No. 10, pp. 3334-3340 (1991).

Shimomura, H., T. Anan, K. Mori, S. Sugou, "High -reflectance AlPSb/GaPSb distributed Bragg reflector mirrors on InP grown by gas-source molecular beam epitaxy", *Electron. Letters*, Vol. 30, No. 4, 314-315 (1994).

Siegman, A, *Lasers*, University Science Books, Mill Valley, CA (1986).

Slatter, J. A. G., H. E. Brockman, J. Haisma, "Method of manufacturing a semiconductor device including a static induction transistor", U. S. Patent 5,089,431 (1992).

Slepian, D., and H. O. Pollack, "Prolate Spheroidal Wave Functions, Fourier Analysis and Uncertainty", *Bell Sys. Tech. J.*, Vol. 40, pp. 43-84 (1961).

Snyder, A. W., and J.D. Love, *Optical Waveguide Theory*, Chapman and Hall (1983).

Soda, H., K. Iga, C. Kitahara, and Y. Suematsu, "GaInAsP/InP Surface Emitting Injection Lasers", *Jpn. J. Appl. Phys.*, Vol. 18, No. 12, pp. 2329-2330 (1979).

Soda, H., Y. Motegi, K. Iga, "GaInAsP/InP surface emitting injection lasers with short cavity length", *IEEE J. Quantum Electron.*, Vol. 19, pp. 1035-1041 (1983).

Spitzer, W. G., and J. M. Whelan, *Phys. Rev.*, Vol. 114, p. 59 (1959).

Steinberg, A. M., P. G. Kwiat, R. Y. Chiao, "Measurement of the Single-Photon Tunneling Time", Phys. Rev. Lett., Vol. 71, No. 5, pp. 708-711 (1993).

Stern, F., "Band-tail model for optical absorption and for the mobility edge in amorphous silicon", Phys. Rev. B, Vol. 3, No. 8, pp. 2636-2645 (1971).

Stover, J. C., *Optical Scattering*, McGraw-Hill, New York (1990).

Streubel[a], K., J. Wallin, L. Zhu, G. Landgren, I. Queisser, "High-reflective 1.5 μm GaInAsP/InP Bragg reflectors grown by metal organic vapor phase epitaxy", Mat. Sci. Eng., Vol. B28, pp. 285-288 (1994).

Streubel[b], K., J. André, J. Wallin, G. Landgren, "Fabrication of 1.5 μm optically pumped $Ga_{1-x}In_xAs_yP_{1-y}$/InP vertical-cavity surface-emitting lasers", Mat. Sci. Eng., Vol. B28, pp. 289-292 (1994).

Sugo, M., H. Mori, Y. Sakai, Y. Itoh, "Stable cw operation at room temperature of a 1.5 μm wavelength multiple quantum well laser on a Si substrate", *Appl. Phys. Lett.*, Vol. 60, No. 4, pp. 472-473 (1992).

Swaminathan, V., A.T. Macrander, *Material Aspects of GaAs and InP Based Structures*, Prentice-Hall, Englewood Cliffs, New Jersey (1991).

Szipöcs, R., K. Ferenz, C. Spielmann, and F. Krausz, "Chirped multilayer coatings for broadband dispersion control in femtosecond lasers", *Opt. Lett.* Vol. 19, No. 3, pp. 201-203 (1994).

Tadokoro, T., H. Okamoto, Y. Kohama, T. Kawakami, and T. Kurokawa, "Room Temperature pulsed operation of 1.5mm GaInAsP/InP vertical cavity surface emitting lasers", *IEEE Photon. Technol. Lett.*, Vol. 4, No. 5, pp. 409-411 (1992).

Tai, K., F. S. Choa, W. T. Tsang, S. N.G. Chu, J. D. Wynn, A. M. Sergent, "Room temperature photopumped 1.5 μm quantum-well surface-emitting lasers with InGaAsP/InP distributed Bragg reflectors", *Electron. Lett.*, Vol. 27, No. 17, pp. 1540-1542 (1991).

Tai, K., L. Yang, Y.H. Wang, J.D. Wynn, and A.Y. Cho, "Drastic reduction of series resistance in doped semiconductor distributed Bragg reflectors for surface emitting lasers", *Appl. Phys. Lett.*, vol. 56, pp. 2496-2498, 1990.

Tai, K., R. J. Fisher, A. Y. Cho, K. F. Huang, "High reflectivity $AlAs_{0.52}Sb_{0.48}$/GaInAs(P) distributed Bragg mirror on InP substrate for 1.3–1.55 μm wavelengths", *Electronics Letters*, Vol. 25, No. 17, pp. 1159-1160 (1989).

Tai, K., S. L. McCall, S. N. G. Chu, W. T. Tsang, "Chemical beam epitaxially grown InP/InGaAsP interference mirror for use near 1.55 μm wavelength", Appl. Phys. Lett., Vol. 51, No. 11, pp. 826-827 (1987).

Tai, K., Y. Lai, K. F. Huang, T. C. Huang, T. D. Lee, C. C. Wu, "Transverse mode emission characteristics of gain-guided surface-emitting lasers", Appl. Phys. Lett., Vol. 63, No. 19, pp. 2624-2626 (1993).

Takagi, T., "Refractive index of $Ga_{1-x}In_xAs$ prepared by vapor-phase epitaxy", Jpn. J. Appl. Phys., Vol. 17, No. 10, pp. 1813-1817 (1978).

Tan, I-H., J. J. Dudley, D. I. Babić, D. A. Cohen, B. D. Young, E. L. Hu, J. E. Bowers, B. I. Miller, U. Koren, M. G. Young, "High quantum efficiency and narrow absorption bandwidth of the wafer-fused resonant cavity $In_{0.53}Ga_{0.47}As$ photodetectors", IEEE Phot. Technol. Lett., Vol. 6, No. 7, pp. 811-813 (1994).

Tan, M. R. T., K. H. Hahn, Y. M. Young, S. Y. Wang, "SELs for distance optical links using multimode fibers", Tech. Dig. Conf. Lasers and Electro-Optics, Baltimore, Maryland May 21-26, paper CTuB1 (1995).

Tanobe, H., F. Koyama, K. Iga, "Etching and Optical Characteristics in GaAs/GaAlAs Surface Emitting Laser Fabrication Using a Novel Spray Etch", *Jpn. J. Appl. Phys.*, Vol. 31, pp. 1597-1601 (1992).

Tanobe, H., M. Oshikiri, M. Araki, F. Koyama, K. Iga, "A preliminary study on MgO/Si multilayer reflectors for improving thermal conductance in surface-emitting lasers", 1992 IEEE Lasers Electro-Optics Soc. Ann. Mtg., Boston, MA, paper. DLTA12.2 (1992).

Thibeault, B. J., Fiber coupled white light reflectometer for measurement of normal incidence reflectivity. Used on the MBE system while wafers are still under vacuum (1994).

Thibeault, B. J, T. A. Strand, T. Wipiejewski, M. G. Peters, D. B. Young, L. A. Coldren, J. W. Scott, "Evaluating the effects of optical and carrier losses in etched post vertical-cavity lasers", submitted to *J. Appl. Phys.* (1995).

Thielen, A., *Design of Optical Interference Coatings*, McGraw-Hill, (1989).

Tong, Q.-Y., H.-Z. Zhang, M. Qing, "Void elimination by lateral gap diffusion in silicon direct bonding (SDB) technology", *Electron. Lett.*, Vol. 27, No. 3, pp. 288-289 (1991).

Turner, A. F., and P.W. Baumeister, "Multilayer Mirrors with High Reflectance Over an Extended Spectral Region", *Appl. Opt.*, vol. 5, no. 1, pp. 69-76 (1966).

Tuttle, G., J. Kavanaugh, S. McCalmost, "(Al, Ga)Sb long-wavelength distributed bragg reflectors", IEEE Phot. Technol. Lett., Vol. 5, No. 12, pp. 1376-1378 (1993).

Uchida, T., T. Miyamoto, N. Yokoushi, Y. Inaba, F. Koyama, K. Iga, "CBE grown 1.5 μm GaAsInAs-InP surface emitting lasers", *IEEE J. Quantum Electron.*, Vol. 29, No. 6, pp. 1975-1980 (1993).

Uchiyama, S., S. Kashiwa, "1.3 μm GaInAsP/InP SBH Surface Emitting Laser with $Si/Al_2O_3$ Stacked Mirror", 10th Int. Conf. Integrated Optics and Optical Fibre Communications, Hong Kong, June 26-30, paper TuB1-3 (1995).

Uomi, K., S. J. B. Yoo, A. Scherer, R. Bhat, N. C. Andreadakis, C. E. Zah, M. A. Koza, T. P. Lee, "Low threshold, room temperature pulsed operation of 1.5 μm vertical-cavity surface-emitting lasers with an optimized multi-quantum well active layer", *IEEE Phot. Technol. Lett.*, Vol. 6, No. 3, pp. 317-319 (1994).

Vaînshteîn, L. A., *Open Resonators and Open Waveguides*, The Golem Press, Boulder Colorado (1969).

Vaînshteîn, L. A., "Open Resonators for Lasers", *Sov. Phys. JETP.*, Vol. 17, No. 3, pp. 709-719 (1963).

Vakhshoori, D., J. D. Wynn, G. J. Zydzik, "Top-surface-emitting lasers with 1.9 V threshold voltage and the effect of spatial-hole burning on their transverse mode operation and efficiences", APpl. Phys. Lett., Vol. 62, No. 13, pp. 1448-1450 (1993).

Villeneouve, P. R., M. Piche, "Photonic band gaps in 2-dimensional square and hexagonal lattices", Phys. Rev. B, Vol. 46, No. 8, pp. 4969-4972 (1992).

Von Lehman, A. C., C. Chang-Hasnain, J. Wullert, L. Carrion, N. G. Stoffel, L. T. Florez, J. P. Harbison, Electron. Lett., Vol. 27, p. 583 (1991).

Wada, H., and T. Kamijoh, "Effects of heat treatment on bonding properties in InP-to-Si direct wafer bonding", *Jpn. J. Appl. Phys.*, Vol. 33, Pt. 1, No. 9A, pp. 4878-4879 (1994).

Wada, H., D.I. Babić, D.L. Crawford, T.E. Reynolds, J.J. Dudley, J.E. Bowers, E.L. Hu, J.L. Merz, B.I. Miller, U. Koren, M.G. Young, "Low-Threshold, High-Temperature Pulsed Operation of InGaAsP/InP Vertical Cavity Surface Emitting Lasers", *IEEE Photon. Technol.*, Lett. Vol. 3, No. 11, pp. 977-979 (1991).

Wada, H., D.I. Babić, M. Ishikawa, J.E. Bowers, "Effects of nonuniform current injection in GaInAsP/InP vertical cavity lasers", *Appl. Phys. Lett.*, Vol. 60, No. 24, pp. 2974-2976 (1992).

Weber, J.-P., and S. Wang, "Effect of layer thcikness variations in a distributed-Bragg-reflector mirror on the phase of the reflected light", Opt. Lett., Vol. 15, No. 10, pp. 526-528 (1990).

Wiliams, R. E., *Gallium arsenide processing techniques*, Artech House, Dedham, MA (1984).

Wilson, G. C., D. M. Kuchta, J. D. Walker, J. S. Smith, "Spatial hole burning and self-focusing in vertical-cavity surface-emitting lasers", Appl. Phys. Lett., Vol. 64, No. 5, pp. 542-544 (1994).

Wipiejewski, T., K. Panzlaff, E. Zeeb, B. Weigl, K. G. Ebeling, "Efficient alignment tolerant coupling of vertical-cavity laser to single mode fiber", Proc. 19th European Conference on Optical Communication, Montreaux, Switzerland, 333 (1993).

Wipiejewski, T., K, Panzlaff, E. Zeeb, K. J. Ebeling, "Tnable extremely low threshold vertical-cavity laser diodes", IEEE Phot. Technol. Lett., Vol. 5, No. 8, pp. 889-892 (1993).

Yablonovitch, E., D. M. Hwang, T. J. Gmitter, L. T. Florez, and J. P. Harbison, "Van der Waals bonding of GaAs epitaxial liftoff films on arbitrary substrates", *Appl. Phys. Lett.*, Vol. 56, No. 24, pp. 2419-2421 (1990).

Yablonovitch, E., T. J. Gmitter, K. M. Leung, "Photonic Band Structure: The Face-Centered-Cubic Case Employing Nonspherical Atoms", *Phys. Rev. Lett.* Vol. 67, No. 17, pp. 2295-2297 (1991)

Yablonovitch, E., T. Sands, D. M. Hwang, I. Schnitzer, and T. J. Gmitter, S. K. Shasty, D. S. Hill, J. C. C. Fan, "Van der Waals bonding of GaAs on Pd leads to a permanent, solid-phase topotaxial, metallurgical bond", Appl. Phys. Lett., Vol. 59, No. 24, pp. 3159-3161 (1991).

Yamaguchi, H., S. Fujino, T. Hattori, Y. Hamakawa, "Superjunction by wafer direct bonding", Jpn. J. Appl. Phys., Vol. 34, Pt. 2, No. 2B, pp. L199-L202 (1995).

Yamamoto, Y., S. Machida, G. Bjork, "Micro-cavity semicondcutor lasers with conrolled spontaneous emission", *Opt. Quantum Electron.*, Vol. 24, pp. S215-S243 (1992).

Yan, R. H, "High-Performance Transverse Electro-Optic Modulators Using Fabry-Perot Modulators", Ph.D. Dissertation, University of California, Santa Barbara, 1990.

Yan, R. H., R.J. Simes, and L.A. Coldren, "Analysis and Design of Surface-Normal Fabry-Perot Electrooptic Modulators", *IEEE J. Quantum Electron.* Vol. QE-25, pp. 2272-2280 (1989).

Yang, L. Y., private communication (1994).

Yang, L., M. C. Wu, K. Tai, T. Tanbun-Ek, R. A. Logan, "InGaAsP(1.3 μm)/InP vertical-cavity surface-emitting laser grown by metalorganic vapor phase epitaxy", *Appl. Phys. Lett.*, Vol. 56, No. 10, pp. 889-891 (1990).

Yang, Y. J., T.G. Dziura, and S.C. Wang, "Submilliampere continuous-wave room-temperature lasing operation of a GaAs mushroom structure surface-emitting laser", *Appl. Phys. Lett.*, Vol. 56, No. 19, pp. 1839-1840 (1990).

Yang, Y. J., T.G. Dziura, T. Bardin, S.C. Wang, and R. Fernandez, "Continuous wave single transverse mode vertical-cavity surface-emitting lasers fabricated by helium implantation and zinc diffusion", presented at CLEO '92, Anaheim, California (1992).

Yang, G. M., M. H. Dougal, P. D. Dapkus, "Ultralow threshold current vertical-cavity surface-emitting lasers obtained with selective oxidation", Electron. Lett., Vol. 31, No. 11, pp. 886-888 (1995).

Yano, M., H. Imai, M. Takusagawa, "Analysis of electrical, threshold, and temperature characteristics of InGaAsP/InP double-heterojunction lasers", IEEE J. Quantum Electron., Vol. 17, No. 9, pp. 1954-1963 (1981).

Yeh, C-F., S. Hwangleu, "The novel preparation of p-n junction mesa diodes by silicon-wafer direct bonding (SDB)", *Jpn. J. Appl. Phys.*, Vol. 31, Pt. 1, No. 5A, pp. 1535-1540 (1992).

Yeh, P., *Optical waves in layered media,* John Wiley & Sons, New York (1988).

Yevick, D., and B. Hermansson, "Efficient Beam Propagation Techniques", *IEEE J. Quantum Electron.,* Vol. 26, No. 1, pp. 109-112, (1990).

Yokouchi, N., T. Uchida, T. Miyamoto, Y. Inaba, F. Koyama, K. Iga, "An Optical Absorption Property of Highly Beryllium-Doped GaInAsP Grown by Chemical Beam Epitaxy", *Jpn. J. Appl. Phys.*, Vol. 31, Pt. 1, No. 5A, pp. 1255-1257 (1992).

Zhao, Y.-G., R. A. Morgan, "Temperature dependence of transverse mode evolution in vertical-cavity surface-emitting lasers", Opt. Eng., Vol. 33, No. 2, pp. 3917-3919 (1994).